

# Nucleation Behavior of Oxygen-Acetylene Torch-Produced Diamond Films

*F.E. Roberts*

*Marshall Space Flight Center, Marshall Space Flight Center, Alabama*

## The NASA STI Program Office...in Profile

Since its founding, NASA has been dedicated to the advancement of aeronautics and space science. The NASA Scientific and Technical Information (STI) Program Office plays a key part in helping NASA maintain this important role.

The NASA STI Program Office is operated by Langley Research Center, the lead center for NASA's scientific and technical information. The NASA STI Program Office provides access to the NASA STI Database, the largest collection of aeronautical and space science STI in the world. The Program Office is also NASA's institutional mechanism for disseminating the results of its research and development activities. These results are published by NASA in the NASA STI Report Series, which includes the following report types:

- **TECHNICAL PUBLICATION.** Reports of completed research or a major significant phase of research that present the results of NASA programs and include extensive data or theoretical analysis. Includes compilations of significant scientific and technical data and information deemed to be of continuing reference value. NASA's counterpart of peer-reviewed formal professional papers but has less stringent limitations on manuscript length and extent of graphic presentations.
- **TECHNICAL MEMORANDUM.** Scientific and technical findings that are preliminary or of specialized interest, e.g., quick release reports, working papers, and bibliographies that contain minimal annotation. Does not contain extensive analysis.
- **CONTRACTOR REPORT.** Scientific and technical findings by NASA-sponsored contractors and grantees.

- **CONFERENCE PUBLICATION.** Collected papers from scientific and technical conferences, symposia, seminars, or other meetings sponsored or cosponsored by NASA.
- **SPECIAL PUBLICATION.** Scientific, technical, or historical information from NASA programs, projects, and mission, often concerned with subjects having substantial public interest.
- **TECHNICAL TRANSLATION.** English-language translations of foreign scientific and technical material pertinent to NASA's mission.

Specialized services that complement the STI Program Office's diverse offerings include creating custom thesauri, building customized databases, organizing and publishing research results...even providing videos.

For more information about the NASA STI Program Office, see the following:

- Access the NASA STI Program Home Page at <http://www.sti.nasa.gov>
- E-mail your question via the Internet to [help@sti.nasa.gov](mailto:help@sti.nasa.gov)
- Fax your question to the NASA Access Help Desk at (301) 621-0134
- Telephone the NASA Access Help Desk at (301) 621-0390
- Write to:  
NASA Access Help Desk  
NASA Center for AeroSpace Information  
7121 Standard Drive  
Hanover, MD 21076-1320  
(301)621-0390



# Nucleation Behavior of Oxygen-Acetylene Torch-Produced Diamond Films

*F.E. Roberts*

*Marshall Space Flight Center, Marshall Space Flight Center, Alabama*

National Aeronautics and  
Space Administration

Marshall Space Flight Center • MSFC, Alabama 35812

Available from:

NASA Center for AeroSpace Information  
7121 Standard Drive  
Hanover, MD 21076-1320  
(301) 621-0390

National Technical Information Service  
5285 Port Royal Road  
Springfield, VA 22161  
(703) 487-4650



## TABLE OF CONTENTS

1. INTRODUCTION .....	1
1.1 Background and Relevance of Diamond Film Research.....	1
1.2 Methods of Diamond Film Production .....	2
1.3 General Introduction to Vapor-Phase Nucleation .....	10
1.4 Background on Clusters and Embryos .....	25
2. DESCRIPTION OF THE NUCLEATION EXPERIMENTS .....	35
2.1 Introduction .....	35
2.2 Torch Experiments .....	35
2.3 Torch Operation .....	40
2.4 Sample Preparation .....	41
2.5 GAMoly Experiment .....	41
2.6 Gas Flow and Substrate Experiment .....	42
2.7 Torch Tip Modification Experiments .....	43
2.8 High-Velocity Oxygen Fuel Gun Experiments .....	44
2.9 Two-Dimensional Kinetics Simulations .....	47
3. ANALYSIS METHODS .....	48
3.1 Optical Microscopy: A Study of Morphology .....	48
3.2 Chemical Vapor Deposition Homoepitaxial Morphological Background.....	52
3.3 Natural Diamond and Other Diamond Morphological Notes .....	54
3.4 Prior Morphology Studies Using the Oxygen-Acetylene Torch .....	54
3.5 Morphology Method of Study (Optical Microscopy) .....	58
3.6 Raman Spectroscopy Background .....	58
3.7 Prior Raman Spectroscopy on Diamond Films .....	64
3.8 Raman Spectroscopy Method .....	66
3.9 Atomic Force Microscopy Background .....	67
3.10 Previous Results of Atomic Force Microscopy Work on Diamond .....	68
3.11 Atomic Force Microscopy Method .....	69
3.12 Designed Experiments .....	79
4. EXPERIMENTAL RESULTS .....	80
4.1 GAMoly Experimental Results .....	80
4.2 Flow Rate and Substrate Experimental Results .....	127
4.3 Tip Modification Experiment Results .....	150

## TABLE OF CONTENTS (Continued)

4.4	Substrate Tip Experiment Results .....	158
4.5	High-Velocity, Oxygen Fuel Gun—Discussion of Results .....	165
5.	DISCUSSION .....	168
5.1	Previous Work on the Low-Pressure Nucleation of Diamond .....	168
5.2	Outline of the Proposed Mechanism for Nucleation of Diamond .....	175
5.3	Discussion of Experimental Conditions Similar to GAMoly .....	177
5.4	Discussion of Relevant Simulation Prior Work .....	179
5.5	Relevance of GAMoly and Simulation to Proposed Mechanism .....	181
5.6	Discussion of Experimental Conditions Similar to the Flow and Substrate Experiment .....	183
5.7	Relevance of Flow Rate and Substrate to Proposed Mechanism .....	190
5.8	Work Related to Torch Tip Modification .....	191
5.9	Relevance of Torch Tip Modifications to Proposed Mechanism .....	192
5.10	Diamond Jet High-Velocity Oxygen Fuel Experiment .....	194
5.11	Relevance of Proposed Mechanism to Prior Literature .....	195
6.	CONCLUSIONS .....	201
	APPENDIX—ALGORITHM FLOW DIAGRAMS AND BLOCK DIAGRAMS .....	207
	REFERENCES .....	283

## LIST OF FIGURES

1.	Expanded Ostwald rule of stages .....	18
2.	Dimerization of $C_2$ .....	30
3.	Depiction of an $sp^3$ bond structure .....	30
4.	$\pi$ -bond structure from Friedel.....	32
5.	$O_2$ - $C_2H_2$ torch diamond deposition gas flow path setup .....	36
6.	Torch positioning and mounting apparatus .....	36
7.	Substrate cooling block showing interchangeable mounting plates .....	36
8.	Constituent calculation subprogram equations .....	39
9.	Carbon monoxide addition versus CO line position as relevant to Bachmann diagrams .....	46
10.	Toluene addition relative to CO line position on a Bachmann diagram .....	47
11.	Cubic diamond showing staggering of interlayer bonds .....	48
12.	Hexagonal diamond showing eclipsed bonds .....	48
13.	Competition between $\{100\}$ and $\{111\}$ facets, growth habit progressing left to right .....	51
14.	Primary active Raman mode of cubic diamond .....	59
15.	Primary diamond Raman signal at $1,332\text{ cm}^{-1}$ .....	60
16.	First-order Raman spectrum of graphite .....	61
17.	First Brillouin zone of a two-dimensional lattice .....	61
18.	The $1,355\text{ cm}^{-1}$ peak appearance with graphite crystal size .....	62
19.	Raman spectra of $C_{60}$ .....	62

## LIST OF FIGURES (Continued)

20.	Demonstration of hardness calculation.....	74
21.	Sample of Young's modulus calculation .....	75
22.	Typical one-segment curve .....	76
23.	Typical two-segment curve .....	77
24.	Box plots of hardness .....	78
25.	GAMoly No. 1 five-sided growth structures, $\times 40$ .....	81
26.	GAMoly No. 1 growth steps, $\times 100$ .....	81
27.	GAMoly No. 1 boundary and mound-region boundary, $\times 20$ .....	81
28.	GAMoly No. 1 nest of $\langle 111 \rangle$ facets, $\times 20$ .....	81
29.	GAMoly No. 2 lower-level focus showing a series of square-terminated pillars, $\times 40$ .....	82
30.	Visible Raman results on GAMoly No. 1 .....	82
31.	FTRaman results on GAMoly No. 1 .....	83
32.	AFM two-dimensional scan for GAMoly No. 1 .....	83
33.	AFM three-dimensional scan for GAMoly No. 1 .....	84
34.	AFM scan analysis for GAMoly No. 1 .....	84
35.	Force versus distance trace breakdown for GAMoly No. 1 .....	85
36.	GAMoly No. 2 identical pillars forming a forest, $\times 100$ .....	86
37.	GAMoly No. 2 $\langle 111 \rangle$ faceting at midlevel heights, $\times 100$ .....	86
38.	GAMoly No. 2 $\langle 100 \rangle$ summit facing, $\times 100$ .....	86
39.	GAMoly No. 2 edge faceting, $\times 40$ .....	86
40.	Visible Raman results for GAMoly No. 2 .....	87
41.	FTRaman results for GAMoly No. 2 .....	87

## LIST OF FIGURES (Continued)

42.	AFM two-dimensional for GAMoly No. 2 .....	88
43.	AFM three-dimensional scan for GAMoly No. 2 .....	88
44.	AFM scan analysis for GAMoly No. 2 .....	89
45.	AFM force-versus-distance breakdown for GAMoly No. 2 .....	90
46.	GAMoly No. 3 surface <111> facets, $\times 40$ .....	91
47.	GAMoly No. 3 surface <100> facets, $\times 150$ .....	91
48.	Raman results for GAMoly No. 3 .....	91
49.	AFM two-dimensional scan for GAMoly No. 3 .....	92
50.	AFM three-dimensional scan for GAMoly No. 3 .....	92
51.	AFM scan analysis for GAMoly No. 3 .....	93
52.	GAMoly No. 4 a-C and cauliflower morphology, $\times 100$ .....	94
53.	GAMoly No. 4 small triangular structure, $\times 100$ .....	94
54.	Visible Raman spectra of GAMoly No. 4 .....	94
55.	FT-Raman spectra of GAMoly No. 4 .....	95
56.	GAMoly No. 5 pillars with {111} and {100} facets, $\times 40$ .....	96
57.	GAMoly No. 5 isolated pillars, $\times 40$ .....	96
58.	GAMoly No. 5 covered {111} surfaces, $\times 100$ .....	96
59.	Visible Raman data for GAMoly No. 5 .....	97
60.	AFM two-dimensional scan for GAMoly No. 5 .....	97
61.	AFM three-dimensional scan for GAMoly No. 5 .....	98
62.	AFM scan analysis for GAMoly No. 5 .....	98
63.	AFM force-versus-distance breakdown for GAMoly No. 5 .....	99

## LIST OF FIGURES (Continued)

64.	GAMoly No. 6 {100} facets with secondary growth, $\times 100$ .....	100
65.	GAMoly No. 6 secondary growth on midlevel facets, $\times 100$ .....	100
66.	GAMoly No. 6 surface facets with growths, $\times 100$ .....	101
67.	GAMoly No. 6 sample backside, $\times 20$ .....	101
68.	Visible Raman results on GAMoly No. 6 .....	101
69.	AFM two-dimensional scan for GAMoly No. 6 .....	102
70.	AFM three-dimensional scan for GAMoly No. 6 .....	102
71.	AFM scan analysis for GAMoly No. 6 .....	103
72.	AFM force-versus-distance breakdown for GAMoly No. 6 .....	104
73.	GAMoly No. 7 blanket of crystals of mostly {100} facets, $\times 40$ .....	105
74.	GAMoly No. 7 clean faceting, $\times 40$ .....	105
75.	GAMoly No. 7 growth steps or heavily twinned facets, $\times 100$ .....	105
76.	GAMoly No. 7 whiskers on bottom of sample, $\times 100$ .....	105
77.	GAMoly No. 7 bottom of sample, $\times 100$ .....	106
78.	Visible Raman for GAMoly No. 7 .....	106
79.	AFM two-dimensional scan for GAMoly No. 7 .....	107
80.	AFM three-dimensional scan for GAMoly No. 7 .....	107
81.	AFM scan analysis for GAMoly No. 7 .....	108
82.	AFM two-dimensional scan for GAMoly No. 7 .....	108
83.	AFM three-dimensional scan for GAMoly No. 7 .....	109
84.	AFM scan analysis for GAMoly No. 7 .....	109
85.	AFM two-dimensional scan for GAMoly No. 7 .....	110

## LIST OF FIGURES (Continued)

86.	AFM three-dimensional scan for GAMoly No. 7 .....	110
87.	AFM scan analysis for GAMoly No. 7 .....	111
88.	AFM force-versus-distance breakdown for GAMoly No. 7 .....	112
89.	Lack of faceting in GAMoly No. 8, $\times 100$ .....	113
90.	GAMoly No. 8 lack of facets on scratch, $\times 100$ .....	113
91.	Visible Raman data for GAMoly No. 8 .....	113
92.	GAMoly No. 9 clean {100} pillars, $\times 100$ .....	114
93.	GAMoly No. 9 smooth facets with one or no secondary growth sites, $\times 100$ .....	114
94.	GAMoly No. 9 base of pillar, $\times 100$ .....	115
95.	GAMoly No. 9 isolated pillars, $\times 100$ .....	115
96.	GAMoly No. 9 heavy secondary growth, $\times 100$ .....	115
97.	GAMoly No. 9 foreign material interspersed with crystallites, $\times 100$ .....	116
98.	GAMoly No. 9 coverage by small square facets, $\times 100$ .....	116
99.	GAMoly No. 9 coverage by small square facets, $\times 100$ .....	116
100.	Visible Raman data for GAMoly No. 9 .....	117
101.	AFM two-dimensional scan for GAMoly No. 9 .....	117
102.	AFM three-dimensional scan for GAMoly No. 9 .....	118
103.	AFM scan analysis for GAMoly No. 9 .....	118
104.	AFM force-versus-distance breakdown for GAMoly No. 9 .....	119
105.	Response of qualitative optical rating .....	121
106.	Response of Raman linewidth for GAMoly .....	121
107.	Response of relative peak height between diamond and the background .....	122

## LIST OF FIGURES (Continued)

108.	Surface finish response .....	122
109.	Young's modulus results .....	123
110.	Graph of <100> hardness results .....	123
111.	Graph of <111> hardness results .....	123
112.	Combustion temperature response of GAMoly simulation .....	124
113.	Enthalpy response of GAMoly simulation .....	124
114.	Entropy response of GAMoly simulation .....	124
115.	Carbon monoxide fraction from GAMoly simulation .....	125
116.	Carbon fraction from GAMoly simulation .....	125
117.	Triatomic carbon fraction from GAMoly simulation .....	125
118.	Hydroxide fraction from GAMoly simulation.....	125
119.	Singly terminated, diatomic carbon fraction from GAMoly simulation .....	126
120.	Acetylene fraction from GAMoly simulation .....	126
121.	Atomic hydrogen fraction from GAMoly simulation.....	126
122.	Hydrogen fraction from GAMoly simulation.....	127
123.	Flow No. 1 general deposit, $\times 40$ .....	127
124.	Flow No. 1 octagonal faceted growth, $\times 40$ .....	127
125.	Flow No. 1 rectangular faceted growth, $\times 40$ .....	128
126.	FTRaman data for flow No. 1 .....	128
127.	Flow No. 2 carbon-like surface material, $\times 40$ .....	129
128.	Flow No. 2 poorly faceted material, $\times 100$ .....	129
129.	Flow No. 2 background, underneath pillar, $\times 100$ .....	129



## LIST OF FIGURES (Continued)

130.	FTRaman data for flow No. 2 .....	130
131.	Small, isolated deposits on flow No. 3 with primarily top surface faceting, $\times 40$ .....	131
132.	Larger deposits on flow No. 3 showing no faceting, $\times 40$ .....	131
133.	Background of flow No. 3 showing no faceted material, $\times 40$ .....	131
134.	FTRaman results on flow No. 3 .....	132
135.	Discolorations noted on flow No. 4, $\times 100$ .....	132
136.	Isolated pillars of heavily faceted crystalline material flow No. 5, $\times 20$ .....	133
137.	Isolated pillars of heavily faceted crystalline material flow No. 5, $\times 40$ .....	133
138.	Flow No. 5 facets showing hexagonal aspects, $\times 100$ .....	133
139.	Pitting on upper surface of flow No. 5 facets, $\times 100$ .....	133
140.	FTRaman data for flow No. 5 .....	134
141.	Flow No. 6 isolated pillars of faceted material, $\times 20$ .....	135
142.	Regular flower structure of $\langle 111 \rangle$ and $\langle 100 \rangle$ facets, $\times 10$ .....	135
143.	Picture of $\langle 111 \rangle$ facets with secondary growths, $\times 100$ .....	135
144.	FTRaman data for flow No. 6 .....	136
145.	Flow No. 7 adhered region showing no faceting, $\times 100$ .....	137
146.	Flow No. 7 debond region showing strong small $\{111\}$ faceting, $\times 100$ .....	137
147.	Flow No. 7 debond region showing strong small $\{111\}$ faceting, $\times 100$ .....	137
148.	Small $\langle 111 \rangle$ crystals showing uniform coverage of GAMoly No. 7, $\times 40$ .....	137
149.	Small $\langle 111 \rangle$ crystals showing uniform coverage of GAMoly No. 7, $\times 100$ .....	138
150.	Small $\langle 111 \rangle$ crystals showing uniform coverage of GAMoly No. 7, $\times 150$ .....	138
151.	Flow No. 7 $\langle 111 \rangle$ compact of facets, $\times 100$ .....	138

## LIST OF FIGURES (Continued)

152.	Flow No. 7 <111> facets on raised portion, $\times 100$ .....	138
153.	Flow No. 7 <111> facets in dense compact film, $\times 100$ .....	139
154.	Raman results on flow No. 7 .....	139
155.	Flow No. 8 pillars depth profile top, $\times 40$ .....	140
156.	Flow No. 8 pillars depth profile middle, $\times 40$ .....	140
157.	Flow No. 8 pillars depth profile base, $\times 40$ .....	140
158.	Flow No. 8 outlier pillars top focus, $\times 100$ .....	140
159.	Flow No. 8 outlier pillars base, $\times 100$ .....	141
160.	Raman data for flow No. 8 .....	141
161.	Flow No. 9 samples center crystals top, $\times 40$ .....	142
162.	Flow No. 9 samples center crystals midlevel, $\times 40$ .....	142
163.	Flow No. 9 samples center crystals base, $\times 40$ .....	142
164.	Flow No. 9 edge pillars showing tendency to broaden, $\times 20$ .....	142
165.	Flow No. 9 edge pillars showing tendency to broaden midlevel, $\times 40$ .....	143
166.	Flow No. 9 edge pillars showing tendency to broaden base, $\times 40$ .....	143
167.	Twin-like structures on tabletop <100> facets, $\times 40$ .....	143
168.	FTRaman results on flow No. 9.....	144
169.	Weak signal FTRaman data flow No. 3 .....	144
170.	Weak signal FTRaman data flow No. 6 .....	145
171.	Weak signal FTRaman data flow No. 9 .....	145
172.	Weak signal FTRaman data flow No. 7 .....	146
173.	Qualitative optical results from flow and substrate experiment .....	147

## LIST OF FIGURES (Continued)

174.	Qualitative hexagonal diamond results from flow and substrate experiment .....	147
175.	Raman diamond linewidth results from flow on substrate experiment .....	148
176.	Raman diamond linewidth results from flow and substrate experiment .....	148
177.	Raman diamond linewidth versus graphite linewidth results from flow and substrate experiment .....	149
178.	Raman diamond linewidth versus a-C linewidth results from flow and substrate experiment .....	149
179.	Gas tip No. 1 island morphology in tip No. 1 samples, $\times 5$ .....	150
180.	Gas tip No. 1 clean $\langle 100 \rangle$ terminated facets, $\times 10$ .....	150
181.	Gas tip No. 1 $\{111\}$ terminated facets with growth structures, $\times 40$ .....	150
182.	Gas tip No. 1 depth profile $\{100\}$ top surface, $\times 100$ .....	151
183.	Depth profile for gas tip No. 1 samples, $\{111\}$ midlevel facets, $\times 40$ .....	151
184.	Depth profile for gas tip No. 1 samples, $\{111\}$ midlevel facets, $\times 40$ .....	151
185.	Depth profile for gas tip No. 1 samples, unfaceted base materials, $\times 40$ .....	151
186.	FT-Raman data for tip No. 1 samples .....	152
187.	Gas tip No. 2 samples showing a lack of faceting, $\times 40$ .....	152
188.	Gas tip No. 2 unusual structures, $\times 100$ .....	152
189.	Gas tip No. 2 unusual structures, $\times 100$ .....	153
190.	FT-Raman data for tip sample No. 2 .....	153
191.	Faceted pillars for gas tip No. 3, $\times 100$ .....	154
192.	Faceted pillars for gas tip No. 3, $\times 150$ .....	154
193.	Faceted pillars for gas tip No. 3, $\times 40$ .....	154
194.	Pillars and nonfaceted material for gas tip No. 3, $\times 10$ .....	154

## LIST OF FIGURES (Continued)

195.	Pillars and nonfaceted material for gas tip No. 3, $\times 100$ .....	155
196.	Pillars and nonfaceted material for gas tip No. 3, $\times 150$ .....	155
197.	Raman data for tip No. 3 samples.....	155
198.	Hexagonal structures on tip No. 4 samples, $\times 100$ .....	156
199.	Transparent structures on tip No. 4 samples, $\times 40$ .....	156
200.	Transparent structures on tip No. 4 samples, $\times 40$ .....	156
201.	Raman data for tip No. 4 samples.....	157
202.	Raman linewidth for gas tip experiment .....	157
203.	Substrate tip No. 1 Raman results .....	158
204.	Substrate tip No. 1 nonfaceted material, $\times 10$ .....	159
205.	Substrate tip No. 1 nonfaceted material, $\times 10$ .....	159
206.	Substrate tip No. 1 nonfaceted material, $\times 20$ .....	159
207.	Substrate tip No. 1 nonfaceted material, $\times 40$ .....	159
208.	Substrate tip No. 2 nonfaceted material, $\times 40$ .....	160
209.	Substrate tip No. 2 transparent structure, $\times 40$ .....	160
210.	Substrate tip No. 2 transparent structure, $\times 100$ .....	160
211.	Substrate tip sample No. 2 ball-like growths, $\times 40$ .....	160
212.	FTRaman results for subtip No. 2 .....	161
213.	Substrate tip No. 3 island-like morphology, $\times 40$ .....	161
214.	Substrate tip No. 3 $\langle 100 \rangle$ terminated facets, $\times 20$ .....	161
215.	FTRaman results for substrate tip No. 3 .....	162
216.	Isolated pillars of $\{111\}$ faceting on substrate tip No. 4, $\times 40$ .....	162

## LIST OF FIGURES (Continued)

217.	Substrate tip No. 4 depth profile No. 1, $\times 40$ .....	162
218.	Substrate tip No. 4 depth profile No. 2, $\times 40$ .....	163
219.	FTRaman results for substrate tip No. 4 .....	163
220.	Tip suboptical response .....	164
221.	Tip sub-Raman linewidth response .....	164
222.	Tip sub-Raman linewidth comparison between diamond and graphite .....	165
223.	Tip sub-Raman linewidth comparison between diamond and a-C .....	165
224.	Designed experiment for addition of toluene .....	166
225.	Surface roughness by facet .....	183
226.	Plot of $C_7H_8$ experiment on Bachmann diagram .....	194
227.	Alto system setup .....	208
228.	Motion controller setup .....	217
229.	Setup remote control for copy .....	219
230.	Pyrometer auto setup .....	224
231.	Basic statistics .....	228
232.	Pyrometer st transfer VI .....	233
233.	Read continuous pyrometer .....	238
234.	Constituent calculations .....	241
235.	Flow control VI .....	243
236.	Output voltages from flow control .....	247
237.	Input voltages for flow control .....	249
238.	Temperature-only control .....	251

## LIST OF FIGURES (Continued)

239.	Logarithmic switch .....	254
240.	Sine wave switch .....	256
241.	Bounded CO line .....	258
242.	Screen flow comparison VI .....	260
243.	Kill switch .....	262
244.	Global array 1D pass .....	263
245.	Safety switch.....	264
246.	New torch control system .....	267
247.	Flow controller VI .....	280
248.	Motion controller setup .....	281
249.	Setup remote control for copy .....	282
250.	Front panel .....	282

## LIST OF TABLES

1.	Classification of binding in clusters .....	26
2.	Designed experiment for GAMoly trials .....	42
3.	Designed experiment for flow trials .....	43
4.	Gas tip modification designed experiment .....	43
5.	Designed substrate tip experiment .....	44
6.	Designed experiments for C <sub>7</sub> H <sub>8</sub> addition .....	47
7.	Carbon Raman peaks .....	63
8.	Variation of diamond hardness with type, direction, and plane .....	71
9.	Published literature on Young's modulus of diamond .....	72
10.	TDK results for C <sub>7</sub> H <sub>8</sub> addition .....	167

## LIST OF ACRONYMS AND SYMBOLS

a-C	amorphous carbon
AES	Auger electron spectroscopy
AFM	atomic force microscopy
Al	aluminum
Al <sub>2</sub> O <sub>3</sub>	alumina
Ar	argon
ArF	argon fluoride
B	boron
B <sub>2</sub> H <sub>6</sub>	diborane
BeC	beryllium carbide
BeO	beryllium oxide
BN	boron nitride
BO <sub>2</sub>	boron dioxide
C	carbon
C-13	carbon-13
C <sub>2</sub>	diatomic carbon
C <sub>2</sub> H	singly terminated diatomic carbon
C <sub>2</sub> H <sub>2</sub>	acetylene
C <sub>2</sub> H <sub>4</sub>	ethylene
C <sub>3</sub>	triatomic carbon
C <sub>3</sub> H <sub>6</sub>	propane
C <sub>4</sub>	carbon 4 quatriatomic carbon
C <sub>7</sub> H <sub>8</sub>	toluene
Ce	cesium
CH	carbon hydrogen
CH <sub>3</sub>	methyl
CH <sub>3</sub> OH	methanol
CH <sub>4</sub>	methane



## LIST OF ACRONYMS AND SYMBOLS (Continued)

CH <sub>4</sub> -H <sub>2</sub>	methane-hydrogen
CHO	carbon-hydrogen-oxygen
CO	carbon monoxide
CO <sub>2</sub>	carbon dioxide
CO/H	carbon monoxide and hydrogen
Co	cobalt
Cu	copper
CVD	chemical vapor deposition
CVI	chemical vapor infiltration
dc	direct current
DLC	diamond-like carbon
ECR	electron-cyclotron resonance
F	fluorine
Fe	iron
FTIR	Fourier transform infrared
FTIRaman	Fourier transform Raman
FWHM	full width at half maximum
G	Gibbs free energy
Ga	gallium
GaAs	gallium arsenide
GAMoly	gas additions on molybdenum substrates
Ge	germanium
GPa	gigapascals
H	atomic hydrogen
H <sub>2</sub>	hydrogen
HA	lower enthalpy
HB	higher enthalpy
H/C	hydrogen to carbon
HOPG	highly oriented pyrolytic graphite
HPHT	high pressure, high temperature
HREM	high-resolution electron microscopy

## LIST OF ACRONYMS AND SYMBOLS (Continued)

HVOF	high-velocity oxygen fuel
HWHM	half width at half maximum
I/O	input/output
IR	infrared
LaB <sub>6</sub>	lanthanum boron-6
MgO	magnesium oxide
Mo	molybdenum
MoC	molybdenum carbide
MPCVD	microwave plasma chemical vapor deposition
MSFC	Marshall Space Flight Center
N <sub>2</sub>	nitrogen
NaCl	sodium chloride
Ne	neon
Ni	nickel
NICM	Normarski differential interference-contrast microscopy
NiH	nickel hydride
NIST	National Institute of Standards and Testing
NMR	nuclear magnetic resonance
NRL	Naval Research Laboratory
O	atomic oxygen
O <sub>2</sub>	oxygen
O/C	oxygen-to-carbon
OH	hydroxyl
PACVD	plasma-assisted chemical vapor deposition
PBC	periodic bond chain
PID	proportional internal derivative
PIM	pulse interval modulation
PMMA	polymethyl methacrylate
PSI	phase shifting interferometry
Pt	platinum

## LIST OF ACRONYMS AND SYMBOLS (Continued)

<i>R</i>	acetylene-to-oxygen ratio
Ra	arithmetic
Re	rhenium
rf	radio frequency
RHEED	reflected high-energy electron diffraction
rms	root mean square
SA	lower entropy
SB	higher entropy
SEM	scanning electron microscope
Si	silicon
SiC	silicon carbide
SiCl <sub>4</sub>	silicon tetrachloride
SIMS	secondary ion mass spectroscopy
Si <sub>3</sub> N <sub>4</sub>	silicon nitride
SiO <sub>2</sub>	silicon dioxide
Sk	critical cluster
sLpm	standard liter per minute
Sn	tin
Ta	tantalum
TaB <sub>2</sub>	tantalum diboride
TDK	two-dimensional kinetics
TEM	transmission electron microscopy
Ti	titanium
TiC	titanium carbide
TiN	titanium nitride
UHV	ultrahigh vacuum
UV	ultraviolet
W	tungsten
WC	tungsten carbide
XPS	x-ray photoelectron spectroscopy

## LIST OF ACRONYMS AND SYMBOLS (Continued)

XRD	x-ray diffraction
Z	ambient phase
Z'	kinetic coefficient
ZnO:Al	zinc oxide-aluminum compound
ZnS	zinc sulfide
ZnSe	zinc selenide

## NOMENCLATURE

$A_n^\circ$	surface area on a critical nuclei
$a$	specific free surface energy of the crystal-ambient interface
$D$	diffusion constant
$d$	jumping distance of the sticking atom
$dG$	Gibbs free energy
$d_i$	initial number of molecules
$dn/dt$	absorption rate
$E$	energy
$G$	total Gibbs function of the vapor phase
$g_j$	geometric factors independent of size for a given crystal
$H$	function of the vapor phase
$h$	plank constant
$I$	frequency of nucleation in unit volume per unit time
$I_o$	initial nuclearion rate
$i$	number of molecules
$J$	steady-state nucleation rate
$j_c$	gross condensation flux
$j_e$	gross evaporation flux for a spherical liquid drop
$k$	Boltzmann constant; gas constant per molecule
$kt$	rate constant (time)
$m$	nuclei within time interval $0 \leq t \leq 1$
$N$	average number of nuclei to be expected over the time interval
$N_\infty$	maximum number of particles nucleated after a very long time
$N_\infty$	concentration of the saturated vapor that is in equilibrium with the bulk liquid at the same temperature
$N_i$	density of the particles in the nutrient phase; partial concentration of $i$ clusters in the initial vapor; total number of $i$ sized clusters
$N_n^\circ$	critical number and nucleated particles
$N_T$	surface density of nuclei
$n$	critical nuclei density

## NOMENCLATURE (Continued)

$n_c$	capture site density per unit area
$n_s^\circ$	critical nucleus
$O_i$	spherical isolated stationary $i$ clusters
$P$	total pressure of the vapor
$P$	vapor pressures above the drop
$P_i$	vapor pressure of an $i$ cluster
$P_\infty$	bulk liquid pressure
$p$	adsorption probability
$p^{2/3}$	pressure
$p dV$	pressure $\times$ derivative or volume
$pV$	pressure $\times$ volume
$Q$	heat
$R$	acetylene to oxygen ratio
$r$	radius of droplet
$S$	entropy
$S dT$	(entropy) derivative or temperature
$sv$	surface tension
$T$	temperature
$T dS$	(temperature) derivative or entropy
$TS$	temperature $\times$ entropy
$t$	time
$t_N$	nucleation time
$U$	internal energy
$V$	volume
$V_c$	total volume of the crystal
$V dP$	volume $\times$ derivative or pressure

## NOMENCLATURE (Continued)

$\nu$	adsorption frequency
$\nu$	vapor pressure
$\nu n_s^\circ$	adsorption frequency; critical nucleus
$\nu_o$	atomic vibration frequency
$\int_{\pi}^{\pi+\Delta\pi} \nu dp$	Zel'dovich factor expressing steady state critical nucleation density/equilibrium density integral from $\pi$ to $\Delta\pi$ of (vapor pressure) (derivative of pressure)
$\beta_c$	frequency of an atom sticking to a critical nucleus
$\Delta G_a$	activation energy for the attachment of a new single particle to the nucleus
$\Delta G_d$	interface activation energy
$\Delta\mu$	difference in chemical potentials of the initial and final phases
$\Delta\pi$	infinitesimal amount
$\partial G$	partial derivative of Gibbs free energy
$\partial N_i$	partial derivative of number of molecules
$\partial N_i \mu^\infty$	chemical potential of single molecules in the vapor in equilibrium with the bulk liquid
$\partial P$	partial derivative of pressure
$\partial U$	partial derivative of internal energy
$\partial\mu$	particle derivative or chemical potential
$\lambda$	latent heat
$\lambda'$	new latent heat
$\mu_d$	chemical potential of single molecules in the vapor in equilibrium with the drop
$\mu_i$	chemical potential of the single molecules at the concentration $N_i$ in the gas phase
$\sum \mu_i dN_j$	summation of the “ith” chemical potential $\times$ derivative or the “jth” number or molecules
$\Omega$	volume of one particle of the crystal
$\Omega_i$	chemical potential of $i$ clusters at their equilibrium concentrations $N_i$ in the vapor phase
$\S_j$	surface Gibbs function of formation per unit area for a given face





## TECHNICAL PUBLICATION

# NUCLEATION BEHAVIOR OF OXYGEN-ACETYLENE TORCH-PRODUCED DIAMOND FILMS

## 1. INTRODUCTION

### 1.1 Background and Relevance of Diamond Film Research

Synthetic or manmade diamond synthesis was first accomplished in the high-pressure, high-temperature (HPHT) region of diamond stability using nickel (Ni) as a catalyst solvent.<sup>1</sup> Since that time, a few tons of diamonds have been made for a variety of manufacturing applications.<sup>2</sup> Worldwide sales of synthetic diamond have been 330 million carats (73 tons) with a market price of between \$500 million and \$1 billion.<sup>3</sup> Eversole,<sup>4</sup> followed by Deryagin and Feedosev,<sup>5</sup> first produced diamond synthesis at low pressure in the region where diamond is thermodynamically metastable. The growth rates reported in these experiments were very, very low and interest was not overwhelming until Spitsyn et al.<sup>6</sup> noted that atomic hydrogen (H) etches graphite preferentially over diamond. This launched the synthesis of low-pressure, chemical vapor deposition (CVD) diamond.

Development of diamond films has progressed such that the central issues for commercialization are not whether diamond can be grown in sufficient amounts or with sufficiently attractive properties, but rather how the processing routes can be made appropriately cost effective.<sup>7</sup> Specifically, for the high growth rate torch process, assuming full utility of the deposit, Kosky and McAtee<sup>8</sup> have calculated that the best case efficiency is about  $2.3 \times 10^{-3}$ . Their calculations use a reported growth rate of 1  $\mu\text{m}/\text{min}$  over a 3-mm spot using  $\approx 1$  standard liter per minute (sLpm) of acetylene ( $\text{C}_2\text{H}_2$ ). This means that for bottled  $\text{C}_2\text{H}_2$  with a cost of 1¢/g, the carbon (C) cost alone is more than \$400 per gram or \$80 per carat. They note that this is approximately one order of magnitude higher than commercial prices for similar diamond.

An interesting aspect of diamond synthesis was the phase diagram using concentrations of C, hydrogen ( $\text{H}_2$ ), and oxygen ( $\text{O}_2$ ) put forth in a publication by Bachmann, Leers, and Lydtin.<sup>9</sup> Their phase diagram was irrespective of the type of precursor gas and deposition process used. Yet, they were able to accommodate data from most of the prior literature on diamond deposition and define a region where diamond growth was possible.

The work presented here is a study of the nucleation method of oxygen-acetylene ( $\text{O}_2\text{-C}_2\text{H}_2$ ) produced diamond. A new suggestion on a mechanism of torch diamond nucleation is presented.

## 1.2 Methods of Diamond Film Production

### 1.2.1 Chemical Vapor Deposition Methods

**1.2.1.1 Plasma-Assisted Chemical Vapor Deposition.** Some of the highest quality early production of diamond at low pressures was performed by use of microwave plasma for decomposition of methane ( $\text{CH}_4$ ).<sup>10,11</sup> Very early into research on actual production of diamond by CVD, it was found possible to produce diamond of some quality with a large number of source gases.<sup>12</sup> It was found that diamond growth was enhanced by the addition of water vapor into a source gas of  $\text{CH}_4$  and  $\text{H}_2$ .<sup>13</sup> Plasma-assisted chemical vapor deposition (PACVD) has a number of possible process configurations. The most prevalent mechanism appears to be the use of a microwave to excite the plasma. Other configurations, such as spiral hollow cathode PACVD<sup>14</sup> or magnetoactive microwave discharges, have been investigated. Electron-cyclotron resonance (ECR) will be discussed later. Variations in discharge frequency<sup>15</sup> and alternate electromagnetic field patterns<sup>16</sup> have also been reviewed. The spiral hollow cathode method provides additional hot electron bombardment of the surface as well as providing a plasma environment from the direct current (dc) discharge.<sup>14</sup> When the plasma frequency range is varied in the lower or radio frequencies (rf's), diamond-like C is obtained, whereas in the microwave region, high-quality diamond is grown.<sup>15</sup> Notably, at microwave frequencies,  $\text{H}_2$  enters its highest excitation state and a new C-containing species appears in the emission spectra.<sup>15</sup>

In microwave plasma chemical vapor deposition (MPCVD), a microwave plasma is typically created directly above or encompassing the deposition substrate. Reactant gases are then passed through the plasma and onto the substrate. The plasma power density and the substrate temperature are often linked. Independent control of the temperature and microwave power has shown that both parameters have an effect on the final composition of the diamond deposit.<sup>17</sup> The MPCVD method has proven an excellent tool for investigation of diamond film precursors and various effects of process gases. Unlike hot filament CVD, MPCVD not only uses hydrocarbon-based process gases but excellent results have also been noted using carbon monoxide (CO) with and without the addition of  $\text{H}_2$ .

Considering the  $\text{C}_2\text{H}_2$  and  $\text{H}_2$  system for MPCVD,<sup>18–23</sup> the residence time of process gas has been studied by variation of the gas flow rate through the chamber.<sup>18</sup> It was shown that a number of effects, including texture and surface morphology, were affected by variations in the gas flow rate. Among other things, H has been suggested as an etchant, as a method for stabilizing and passivating the growing diamond surface, and as a control on substrate temperature. The influence of H gradients has been shown, to a first approximation, to control substrate temperature.<sup>19</sup> This same series of experiments indicated a dependence of mean crystallite diameter and a power law dependence of the linear growth rate, normal to the surface, on H concentration.<sup>19</sup> The H results are well supported by the effect of noble gas addition on diamond deposition from methane-hydrogen ( $\text{CH}_4\text{-H}_2$ ) microwave plasmas.<sup>20</sup>

As noble gases are mixed into the  $\text{CH}_4\text{-H}_2$  system, the atomic weight of the noble gas increases, and so correspondingly does the substrate temperature. Addition of noble gases can also increase the deposition rate through energy and charge transfer by creating additional C-containing activated species.<sup>20</sup> The effect of  $\text{O}_2$  addition into the  $\text{CH}_4\text{-H}_2$  system has been shown to reach a maximum with an improvement in crystallite size and idiomorphism. Additionally, a decrease in film thickness is consistently noted with the addition of  $\text{O}_2$ .<sup>20–22</sup> In an experiment using a high enough flow rate to avoid the interconversion of  $\text{CH}_4$  and  $\text{C}_2\text{H}_2$ , carbon-13 ( $\text{C-13}$ ) was used to trace the use of  $\text{CH}_4$  versus  $\text{C}_2\text{H}_2$  in a growing diamond film.<sup>23</sup>

Looking at the carbon monoxide and hydrogen (CO/H) system,<sup>24–26</sup> an experiment, analogous to that given in reference 23, was undertaken to distinguish the roles of CO and CH<sub>4</sub> in diamond growth.<sup>24</sup> Again, CH<sub>4</sub> was found to contribute much more strongly to diamond growth than CO. In the CO/H system, the addition of argon (Ar) was found to suppress C<sub>2</sub>H<sub>2</sub> formation in the plasma, resulting in higher crystallinity films.<sup>25,26</sup> Growth was also found to be significantly improved as the content of H increased.<sup>25,26</sup> The increase in H was assumed to suppress nondiamond C formation and allow transition of CO species to methyl (CH<sub>3</sub>) growth species.<sup>26</sup> It does appear, however, that in the CO system, there is a possibility of forming diamond without going through CH<sub>3</sub>.<sup>24</sup>

In a comprehensive investigation of most of the systems responsible for diamond growth in microwave plasmas, including halogen carrier systems, Mitomo et al.<sup>18</sup> delineated three equilibrium chemical systems using an in situ Fourier transform infrared (FTIR) spectrophotometer. These results, in conjunction with the results of Joeris et al.,<sup>19</sup> where H<sub>2</sub> is not used in the feed gas, help clarify the role of CH<sub>4</sub>-derived radicals in the growth of microwave plasma-grown films. An early piece of work by Williams, Kong, and Glass<sup>20</sup> looked at defects present in MPCVD diamond films. There has been a fair amount of study on the defects in various films. This will be discussed later in regard to diamond film morphology.

While a number of microwave plasma experiments used the CO/H system for the creation of diamond, this chemistry does not seem to be effective in the hot filament approach to diamond growth.<sup>24</sup> In microwave plasma systems, the chemistry does not proceed toward thermodynamic equilibrium, primarily due to the high-energy electrons activating the gas-phase species. A hot filament reactor is a thermally driven system in which the reactions proceed toward thermal equilibrium.<sup>24</sup> Carbon monoxide is one of the most stable constituents under thermodynamic equilibrium conditions in the presence of H<sub>2</sub>. A CO/H system driven toward thermodynamic equilibrium may not be able to generate sufficient hydrocarbons for diamond growth.

**1.2.1.2 Hot Filament Chemical Vapor Deposition.** Hot filament CVD has quickly become one of the most useful and inexpensive methods for diamond synthesis, paralleling the use of microwave plasma deposition of diamond. There can be a large amount of process variation in this method. Hot filament CVD uses a heated filament, typically tungsten (W) or rhenium (Re), placed in the flow path of gaseous reactants slightly above a thermally controlled substrate. The substrate is kept cool (800–1,000 °C) on, typically, a water-cooled pedestal. No diamond or graphite are deposited unless the W wire is heated.<sup>21</sup> Growth rate of the diamond depends critically on the filament temperature, the substrate temperature, or the distance between the substrate and the filament.<sup>22</sup> Because the filament and the substrate are maintained in close proximity, large temperature variations across the deposition substrate are often possible. Interestingly, radiative heat transfer from the filament dominates the control of substrate temperature in hot filament reactors.<sup>23</sup> A calculation of thermal radiation flux correlates well with growth rate profiles from filament-grown films.<sup>23</sup> Substrate voltages have been applied in electron assisted CVD to accelerate thermal electrons through the reactive surface region.<sup>24</sup>

Hot filament CVD has often been used for absorption studies and for studies involving the direct monitoring of surface species because of the relatively slow growth rates and easy control of process gases.<sup>25–28</sup> By sampling the species present at the surface<sup>26,27</sup> and correlating that with relative surface temperatures, a stronger understanding of the mechanism of diamond growth has arisen. In the case of hot filament growth, embryonic surface constituents have been studied in an excellent Auger electron spectroscopy (AES) study on the role of the hot filament on sticking probabilities of activated precursor gases.<sup>28</sup>

Hot filament CVD is versatile enough to be used in conjunction with C-13 as a substitute growth species.<sup>22,29-32</sup> Experiments with C-13 were groundbreaking because they provided one of the stronger arguments that identified CH<sub>3</sub> radicals as a dominant growth species during hot filament diamond growth. The use of hot filament growth with C-13 has allowed nuclear magnetic resonance (NMR) studies of CVD diamond films. The simplicity of hot filament CVD makes it an appealing candidate for process control and modeling studies.<sup>28,33,34</sup> Hot filament CVD has also been used to deposit diamond directly on transmission electron microscopy (TEM) imaging grids<sup>35,36</sup> and conventionally in films for sectioning.<sup>37</sup> The direct deposition onto TEM imaging grids has resulted in a novel theory of diamond nucleation, which will be discussed in a later section. Hot filament reactors have been used for commercial application of diamond films, specifically for diamond thin films with semiconductor properties.<sup>38</sup> Hot filament reactors are currently used for creation of diamond tubes and diamond fibers by the U.S. Naval Research Laboratory (NRL).<sup>39</sup>

**1.2.1.3 Plasma-Jet Chemical Vapor Deposition.** Plasma-jet CVD arose directly from experiments seeking to increase the surface bombardment by electrons and to decrease the temperature dependence of diamond deposition on filament size and shape.<sup>40</sup> Similar to the torch method, it is both a high rate process and one that shows a dependence on the tip-to-substrate distance.<sup>41,42</sup> Typically, the arc-jet process uses only H<sub>2</sub> and CH<sub>4</sub> as the process gases although an Ar-H<sub>2</sub> plasma has been used as well<sup>43</sup> with CH<sub>4</sub> addition and with CH<sub>4</sub> and C<sub>2</sub>H<sub>2</sub> addition.<sup>44</sup> The high growth rate and uniform gas-phase environment have proven reasonably amenable to process and kinetic simulation.<sup>45</sup> As in other methods, the addition of O<sub>2</sub> has been found to produce higher quality films. Takeuchi and Yoshida<sup>46</sup> suggest that O<sub>2</sub> may react selectively with C<sub>2</sub>H<sub>2</sub> in a boundary layer adjacent to the surface. This would slow the formation of nondiamond C and might account for the high film quality noted in plasma-jet work.

The plasma-jet technique is the only current process using mixtures of metals and diamond during film deposition.<sup>47</sup> Early work with plasma jets was troubled by contamination from the cathode and anode material. More recently, a process of incorporating metal and metal carbide material in with the diamond to create a functional gradient material has been demonstrated.<sup>48</sup> They use a mixture of CH<sub>4</sub> and metal powder for feedstock in the plasma jet. This work highlights some of the promise that the plasma-jet process shows for application. The strongest argument for the applicability of plasma-jet CVD comes from the success in the commercial market with the process by Norton Diamond Film Co.<sup>49</sup> They have provided a large number of technical papers<sup>49</sup> on a variety of applications for films produced from their patented plasma-jet process.

**1.2.1.4 Electron-Cyclotron Resonance Chemical Vapor Deposition.** Electron-cyclotron resonance plasma-assisted CVD has an inherently low growth temperature without the need for substrate cooling. This makes it particularly attractive for many applications of diamond films where the substrate materials are temperature-sensitive; i.e., optical materials such as zinc selenide (ZnSe) and zinc sulfide (ZnS).<sup>50</sup> Because of lower substrate temperatures, ECR plasmas have been used for deposition onto a wide range of substrate materials such as copper (Cu), aluminum (Al), and silicon (Si).<sup>51</sup> Electron-cyclotron resonance systems also possess the advantage of being able to produce conformal coatings on three-dimensional objects with only moderate use of H<sub>2</sub> during deposition.<sup>52</sup> Two gas-phase precursor systems are typically used in ECR systems: CO:H and CH<sub>4</sub>:O<sub>2</sub>:H<sub>2</sub>.<sup>50-55</sup> One unusual aspect of the ECR system diamond is that, in some cases,<sup>51</sup> a better diamond film was produced without use of either CH<sub>4</sub> or C<sub>2</sub>H<sub>2</sub> as a precursor gas. Another advantage of the ECR system is the possibility of using magnetic confinement to provide uniform

depositions over large areas.<sup>55,56</sup> This brings up the potential applicability of continuous feed systems for scrolling depositions.<sup>55</sup> Currently, these systems are used for diamond-like C; however, should diamond be possible in such a system, a much wider variety of applications will become available.

**1.2.1.5 Flow-Tube Reactor Chemical Vapor Deposition.** An interesting CVD variant, flow tube CVD, has been used for the investigation of various growth species. The flow tube typically uses  $H_2$  and Ar excited in plasma, then sent down a flow tube toward the substrate. Mass transfer in such a system is governed by flow rather than diffusion. Directly in front of the substrate, a pipette is used to add various process gases. The entire assembly is constrained within a tube furnace. Since the hydrocarbons do not pass through the plasma discharge, the species in the diamond growth region are closely related to the hydrocarbon added, and the species are determined by reaction rates rather than by equilibria.<sup>57-59</sup>

**1.2.1.6 Laser and Laser-Assisted Chemical Vapor Deposition.** Recognition that plasma generation, required in many types of diamond growth, could be efficiently accomplished with a laser has spurred the development of a number of laser-based, diamond-film formation methods. Early experiments that were successful with diamond ranged from the suspected production of diamond from a direct laser excited plasma<sup>60,61</sup> to hot filament assisted with laser plasma formation,<sup>62</sup> and use of C ion implantation into a subsequently laser-annealed Cu metal catalyst.<sup>63</sup> Direct production of diamond from an argon fluoride (ArF) excimer laser-induced plasma<sup>60</sup> required an almost parallel orientation of the beam to the surface ( $1^\circ$  to more than  $5^\circ$ ) and a focused beam. These results were dependent on reflected high-energy electron diffraction (RHEED) data that, upon further analysis, indicated the deposits were graphitic.<sup>61</sup> The initial hot filament work showed increased density of diamond crystallites compared to traditional hot filament crystallite densities. The higher growth and nucleation rates were directly accredited to laser CVD. Considering the ion implantation, it was found that pulsed laser melting and rapid solidification were required for the formation of diamond.<sup>63</sup>

The more current production of laser-assisted diamond follows a number of distinct but direct routes for the production of diamond films. Molian and Waschek<sup>64</sup> show a laser CVD system where the laser decomposes a mixture of  $CH_4$  and  $H_2$ . An unfocused carbon dioxide ( $CO_2$ ) laser was directed either parallel or normal to a gallium arsenide (GaAs) substrate. In the experiments with a parallel beam, no diamond growth occurred. On the other hand, diamond growth was noted for normal incident beams. This was accredited to activation and heating of the substrate in the normal case. Rebello and Subramanian<sup>65</sup> used an ArF excimer laser to substantially perform the same function with the result that high-quality diamond was formed in both normal and parallel configurations. Recently, Latsch and Hiraoka<sup>66</sup> demonstrated diamond film formation from laser ablation of polymethyl methacrylate (PMMA) in the presence of  $O_2$  and  $H_2$ .

## 1.2.2 Oxygen-Acetylene Torch Production of Diamond Films

Hirose<sup>67</sup> was involved in an experiment wherein  $O_2$  addition to microwave plasma increased the deposition rate an order of magnitude.<sup>68</sup> I speculate that at some point after examining the beneficial effects of  $O_2$  (noting the advantage of small amounts of Ar, utilizing a process pressure one order of magnitude away from atmospheric, and recognizing the parallels between a thermal combustion system and a thermal CVD system), Hirose decided the vacuum chamber was unnecessary and a conventional  $O_2$ - $C_2H_2$  torch was capable of producing diamond. Nevertheless, whatever the mechanism of insight, the



first mention of an  $O_2$ - $C_2H_2$  torch is generally credited to Hirose and Kondo.<sup>69</sup> The torch was first picked up in the United States by Hanssen, Carrington, Butler, and Snail of the NRL.<sup>68</sup> The use of flame species for crystal deposition had been used previously in the case of “vapor-axial deposition” where a  $CH_4$ - $O_2$  flame was fed with silicon tetrachloride ( $SiCl_4$ ) to form silica optical fiber material.<sup>70</sup> The work by Hanssen et al.<sup>68</sup> was extended soon thereafter to combustion using  $O_2$ -ethylene ( $C_2H_4$ ) flames. The change in process was successful but not advantageous.<sup>71</sup>

Flame structure, radical concentrations, and C formation in premixed flames had been studied previously.<sup>72,73</sup> In fact, it is highly probable that low-pressure (1 atm) deposition of diamond would have been noted in 1967 by Homann<sup>72</sup> had RAMAN spectroscopy been available. They investigated the luminous yellow C streak that forms at or after the flame tip. The critical ratio of fuel to oxidizer in the initial mixture of unburnt gas at which C formation can just be detected in any part of the flame is dependent on the  $H_2$  content, aromatic character, and flame parameters such as structure and temperature. They found that hydrocarbons in the burnt gas promote C formation and that hydroxyl (OH) inhibits C formation. Looking at formation of C in the flame, they state that the conception of a C nucleus in a flame is somewhat vague.

“It is not possible to think of it in the same way as in the process of condensation of a vapor since there is no critical size of a carbon particle which can be correlated with a supersaturated carbon-particle vapor.”<sup>72</sup>

I take this to mean that in the absence of etchants the critical size nucleus is one C atom in the flame environment.

They also show a normal distribution of particle size in the burnt gas of an  $O_2$ - $C_2H_2$  flame, depending on flame temperature and distance from the burner. Again, this relates, in our case, to the importance of the region within the flame in which diamond is possible. It also indicates that as the temperature goes up, the downstream environment becomes less and less hospitable for stable maintenance of diamond. In 1977, a large absorption of the OH bands observed in the flame spectra showed a high concentration of OH radicals in the combustion zone.<sup>73</sup> The amounts of atomic oxygen (O), H, and OH radicals in the flame were noticed as being much larger than expected by chemical equilibrium.<sup>73</sup>

The first in-depth study of the mechanisms of flame diamond came from the labs of Y. Hirose in a study done by Matsui.<sup>74</sup> The flame structure was analyzed using laser-induced fluorescence and mass spectrometry. Diamond formation had been reported only within the region of the flame called the flame feather. The main gaseous species in the flame and feather region were CO and  $H_2$ . The concentration of  $C_2H_2$  and other  $C_2$ -containing radicals was almost equilibrated near the tip but decreased linearly toward the tip of the flame feather. This might have been expected from the reduction in cone area experienced by the feather.

Carbon-hydrogen (CH) bond and  $C_2$  radicals were suggested as growth species or precursors because their acetylene-to-oxygen ratio ( $R$ ) dependencies were in good agreement with the growth rate. Hydroxyl radicals were observed in the intermediate and outer zones, and the maximum values were found to be independent of distance from the tip<sup>74</sup> (within the flame and feather).

From the nitrogen ( $N_2$ ) fraction, they calculated that the volume of dilution or (ambient) air was about three times the volume of the reactant gases. The overall reaction for  $R=1$  is  $C_2H_2+O_2 \rightarrow 2CO+H_2$ .<sup>74</sup> They noted that the growth rate was almost proportional to the mixture flow rate at low flow, but the growth rate became saturated at high flow rates, showing that the growth is mass-transport limited. They surmised that the concentration of  $CH_3$  was not sufficient for the growth rate when they considered the sticking coefficient.

An excellent account of the thermodynamics of the flame feather is presented by Kosky and McAtee.<sup>75</sup> They neglect the diffusion of ambient gases and then calculate the free energy change of gaseous C to solid C with respect to temperature. They note that the small free energy difference between diamond and graphite appears insignificant in respect to the activity change.<sup>75</sup>

Cappelli and Paul<sup>76</sup> present a detailed study on the secondary flame front. This is the flame front of the feather region of the flame from which appears to come the species responsible for growth. Typically, diamond growth occurs in a narrow annular region defined by the intersection of the flame feather with the cooled substrate.<sup>76,77</sup> They also explain laser fluorescence results by an increase in molecular C in the growth region.<sup>76</sup> Fiber-optic waveguide studies on emission spectra of the flame growth region have indicated a strong signal from O and H as well as  $C_2$  and CH radicals.<sup>78,79</sup> The authors<sup>78</sup> proposed that the thermodynamically, unequilibrated primary combustion zone having excess radical formation is the most favorable region for diamond growth. An alternate approach to emission intensity measurement localized the  $C_2$  and CH radicals at the feather boundary, while OH radicals were found primarily in the intermediate zone.<sup>79</sup>

The turbulence of the flame in  $O_2$ - $C_2H_2$  diamond film growth has been shown to have a considerable effect on film quality.<sup>80-82</sup> Snail and Craigle<sup>80</sup> first noted the beneficial effect of eddies within the flame which improved the effective diffusion coefficient of active species. They also noted the decrease in growth rate of the diamond in such a flame. This suggests the influx of etchant species into the growth regime. This is in direct contrast to later work by Alers et al.<sup>81</sup> where the growth rate of turbulent flames was reported to be twice as high as laminar flames. They noted, however, that due to conventional burner design, flow calculations show that it is impossible to create both a turbulent and a laminar flame on the same burner given the flow rates reported. When burners with the same exit opening size, the same flow rate, and the same position in the flame are compared, the higher efficiency of mixing has been shown to provide a higher growth rate for the diamond films.<sup>81</sup> The original work from reference 80 was revisited and expanded; however, the inconsistency between the two references remains.<sup>82</sup> The second study proposed that the amount of room or entrained air may be held accountable for the difference.<sup>82</sup> In later work, it was also noted that the rounding and blurring of the conical laminar flame front is actually the time-averaged envelope of a fluctuating, wrinkled flame front.<sup>82</sup>

Morphology provides a number of strong clues relating to the nucleation and growth of torch-produced diamond films. In most experiments, the morphology is invested because it provides a simple and convenient measure of processing variations. By way of introduction, we start by summarizing a few studies where the primary emphasis was on an examination of the morphology and processing effects on morphology.<sup>83-88</sup> An early look involves the morphology, which is an indicator of possible changes in nucleation.<sup>83</sup> Ravi et al.<sup>83</sup> in starting their work note that the annular ring given by other researchers

appears to be absent in their results. On abraded molybdenum (Mo) surfaces, for times of 90 min, they obtained cubo-octohedrons with well-formed (100) facets. In switching to molybdenum carbide (MoC) substrates, they noted similar growth with no apparent change in nucleation density. Their most dramatic results occurred on a substrate of diamond-like carbon (DLC) deposited by the torch for 30 sec prior to diamond deposition. In this case, they developed contiguous, relatively fine-grained films. They note that the observed increase in growth rate for the films may instead be a decrease in incubation time for the initial nucleation of diamond.<sup>83</sup> Four processes suggested to explain the enhancement of diamond nucleation by diamond-like C layers are:

1. A regasification of C from the DLC providing more C in the near-surface gas phase
2. Solid-state renucleation from DLC to diamond
3. An increase in the density of surface defect sites for nucleation
4. The functioning of the DLC layer as a source of H during deposition.<sup>83</sup>

Importantly, in the absence of high nucleation density, the morphology appears to be related to surface energies, growth anisotropies, and the chemistry of the gas in the diamond synthesis ambient environment. When substrate temperatures are higher, the cube morphology tends to dominate, while octahedral faces tend to form at lower temperatures.<sup>2</sup> There is a large portion of  $\langle 110 \rangle$  orientation in this region, indicating decomposition from  $\{100\}$  crystals to  $\{111\}$  oriented crystals.<sup>84</sup> This information is complemented by studies where the radial temperature distribution is correlated with the dominant growth habit.<sup>85</sup> The growth toward the center of the flame appears dominated by  $\{111\}$  facets going radially outward. Following this,  $\{100\}$  planes start to appear with  $\{111\}$  planes growing or twinning from the  $\{100\}$  planes toward the outside where  $\{111\}$  planes dominate.<sup>85</sup>

The radial dependence of morphology is based on a variation of active flame species with position in the flame.<sup>86</sup> As the flow ratio of  $O_2$  to  $C_2H_2$  decreases in a flame, the C supersaturation should increase, while the fraction of H may decrease. The  $H_2$  termination of the growth surface will be reduced at higher temperatures as thermal desorption of  $H_2$  takes place so that the interaction between increasing supersaturation of C and the increased  $H_2$  content, in the higher temperature regions of the flame, can help account for the growth-oriented morphology variances.

Ravi et al.<sup>87</sup> provide a noteworthy presentation of morphological instability in the low-pressure synthesis of diamond films. This work presents data based on the classification of diamond growth as being a combination of diffusion limited and ballistic aggregation, with the process becoming increasingly ballistic as the growth rate increases. They bring up work from Janssen in which vapor growth is essentially an unstable process while vapor etching is essentially a stable process. By varying only the growth times, they observe an onset of morphological instabilities relating to nutrient starvation and competitive shadowing.<sup>87</sup> Additional review of torch film morphologies will be presented with the morphology results presented in following sections. Growth of transparent diamonds and diamond films has been produced on nondiamond substrates by a couple of labs,<sup>80,88</sup> with the more recent results<sup>80</sup> providing cohesive free-standing films of sufficient quality to allow newsprint to be read through the film.

Although the vast majority of torch-produced diamond has been produced with various grades of  $C_2H_2$  and  $O_2$ , there have been successful variations on the production of diamond films using a torch.



Variation in process gas has been tried with the introduction of  $\text{H}_2$ <sup>89</sup> and  $\text{CH}_4$ <sup>90</sup> into a  $\text{H}_2$ - $\text{O}_2$  flame torch, and methanol ( $\text{CH}_3\text{OH}$ )<sup>91</sup> or aerosol<sup>91</sup> into an  $\text{O}_2$ - $\text{C}_2\text{H}_2$  torch. The effect of  $\text{H}_2$  was examined by  $\text{H}_2$  addition and  $\text{H}_2$  substitution.<sup>90</sup>

A torch was started with a fixed  $\text{O}_2/\text{C}_2\text{H}_2$  ratio that was known to produce good quality diamond.  $\text{H}_2$  was then added to the flame. The quality of the diamond increased across the deposition region; however, once the  $\text{H}_2/\text{C}_2\text{H}_2$  ratio rose above 0.25, the growth density significantly decreased.<sup>89</sup> The increase in quality was most profound in the center of the deposit and least significant at the edges of the deposit. At the temperature of the inner flame core, 11 percent of the molecular  $\text{H}_2$  is expected to disassociate. The addition of  $\text{H}_2$  is expected to enhance the amount of H available in the feather region where diamond formation is expected. In the case where  $\text{H}_2$  was substituted for  $\text{C}_2\text{H}_2$ , the substitution was quickly able to completely suppress the formation of diamond. Before the substitution limit was reached, however, an increase in quality was again noted.<sup>89</sup>

Diamond has been successfully grown by inserting  $\text{CH}_4$  into a  $\text{H}_2$ - $\text{O}_2$  torch flame.<sup>90</sup> The  $\text{H}_2$ - $\text{O}_2$  flat flame is somewhat of a bridge between CVD-type processes and torch processes. The flat flame burner operates just like a torch; however, it operates in a vacuum chamber at pressures of 30–40 torr.<sup>90</sup> Both vertical and horizontal injection produced diamond. Outside the diamond growth region there was no C deposition. This suggests that, like the torch, the flame environment outside the protected jet flow region is too oxidizing for C or diamond survival.<sup>90</sup> The highest quality diamond noted was at the outer edges of the deposit, where the injected gases are subject to the most mixing with the  $\text{H}_2$ - $\text{O}_2$  flame.<sup>90</sup> Doping of flame-grown diamond films has been tried by incorporation of a liquid phase dopant before the flame front.<sup>91</sup> The effect of  $\text{CH}_3\text{OH}$  was studied as a precursor to this work and high-quality “white” diamond was obtained. The boron (B)-doped samples, in general, showed a smaller size than the undoped films.<sup>91</sup>

Variations on the torch process itself include use of a flat flame,<sup>92</sup> a sheathed flame,<sup>93</sup> a multiple flame,<sup>93</sup> and a multinozzle diffusion flame.<sup>76,94</sup> The variants of the torch process often apply themselves toward the practical application of torch deposition processes for an industrial large-area deposition scheme. A flat-flame burner has been used to demonstrate the deposition of uniform, high growth rate films. The flat flame used has a flat-flame front stabilized above the substrate surface. This flat-flame front contains the flame feather region; however, it has been homogenized by the flat-flame stabilization. The principal advantage is a homogeneity of temperature and species concentration.<sup>92</sup> This provides uniform deposit without radial dependence on temperature and species concentration.<sup>92</sup>

The sheathed-flame torch design was also applied to address the uniformity of diamond film combustion processes.<sup>93</sup> In the sheathed-flame design, an Ar sheath separates the  $\text{O}_2$ - $\text{C}_2\text{H}_2$  flame from the atmosphere. In this system, the length of the feather region was noted as doubling, as was the deposition region when the Ar shielding was applied.<sup>93</sup> Multiple flame deposition of diamond is a logical step toward industrial application and growth of larger area films. The results of a nine-nozzle system showed surprising internal consistency; however, a radial dependence of thickness and quality was noted. Films of 20-mm thickness were produced with the highest quality diamond produced in the center of the deposit and the quality suffering the most drastic dropoff at the edge of the deposit.<sup>94</sup> The use of a multinozzle diffusion flame has been suggested and current work is involved with developing such a system, the purpose being to lower the deposition temperatures and use the C species generated in the flame more efficiently.<sup>76,95</sup>

### 1.2.3 High Pressure and Other Novel Methods of Diamond Synthesis

The defining work on high-pressure synthesis of diamond is generally credited to researchers at General Electric.<sup>96</sup> In HPTH synthesis, it has been supposed that all C incorporated into the diamond passed through a monatomic state.<sup>97</sup> Other theories have involved the direct catalytic transformation without the need for dissolution of C in the melt.<sup>97</sup> The H<sub>2</sub> content in the starting melt also has a large effect on the pressure of diamond synthesis. There are still a number of unsolved questions on the high-pressure<sup>98–100</sup> and shock-induced formation of diamond.<sup>101,102</sup> Shock wave-synthesized diamonds, like CVD diamond, are typically very thin sheets of transparent diamond.<sup>103</sup> A new phase of C has been proposed (H-6, H-8) based on results from the iron (Fe)-Ni-C system at HPHT, which relates to structures in the electrically conducting surface of CVD diamond.

The transformation mechanism suggested for shock formation provides a reasonable contrast of mechanisms to compare the renucleation mechanism proposed by Singh<sup>36</sup> for CVD diamond. There are a number of other methods that have recently arisen for production of diamond or diamond-thin films that provide insight into the mechanism of diamond nucleation and growth. Nonhydrostatic pressures of 20 gigapascals (GPa) have been shown to transform fullerenes into the cubic form of diamond.<sup>104</sup> Sputtering, with assistance from a W filament (triode),<sup>105</sup> has been shown to produce diamond samples from graphite starting materials. This method, however, mainly shows the inconsequence of starting material for hot-filament-type reactions. True sputtering results for diamond have previously been shown by Kitabatake and Wasa<sup>106</sup> from graphite precursors in H<sub>2</sub> on Ni. A diamond/diamond composite has been produced using the chemical vapor infiltration (CVI) process densifying nonmined diamond into a relatively stress-free coating.<sup>107</sup> Growth of diamond-on-diamond seed crystals has been found to occur using two independent supersonic jets of H and CH<sub>3</sub> radicals. A novelty of this method is that radical production is decoupled from radical reaction until they are a few mean free paths from the surface. The gas phase radical concentrations have been found to be independent of each other and of temperature until the jets impinge in the near surface region.<sup>108</sup>

## 1.3 General Introduction to Vapor-Phase Nucleation

Vapor-phase nucleation, in its simplest form, considers nucleation of a material from a supersaturated vapor of the same material. Initially, putting aside the effects of other constituents present in the vapor or plasma and the consideration of precritical nuclei, we will start a discussion of nucleation with a review of Ostwald's rule.<sup>109</sup>

The Ostwald rule can be understood by looking at two structures of a material: (1) Structure "B," a higher temperature equilibrium phase with a higher enthalpy (HB) and a higher entropy (SB), and (2) structure "A," a lower temperature equilibrium phase with a lower enthalpy (HA) and a lower entropy (SA). As the temperature rises, the contribution of SB rises and, therefore, Gibbs free energy ( $G$ )<sub>i</sub> decreases, favoring the formation of the high temperature phase. Similarly, as the temperature decreases, the enthalpy term dominates and HB is less than HA and the A phase is the equilibrium phase.<sup>109</sup> Ostwald specifies that during formation: "...not the form with the smallest amount of free energy is achieved during the spontaneous ensuing departure of a state but rather the form, which can be achieved with the least possible loss of free energy, or the form with the next largest amount of free energy."<sup>109</sup>

The Ostwald stage rule has been subsequently derived from the Volmer nucleation theory.<sup>110</sup> One view of this approach is that the high entropy phases, in particular amorphous phases, will, therefore, be favored as the first, if short lived, stage from a vapor.<sup>111</sup> Production of nuclei from a vapor is described as either (1) homogeneous, where the supersaturation and the undercooling are responsible for the embryonic germination resulting in a critical nucleus, or (2) heterogeneous, where a catalyst such as a suspended vapor-phase particle, surface particle, or bulk surface provides an energetic advantage to the formation of a critical nucleus.<sup>112</sup>

Ions can be particularly apt at catalyzing the formation of heterogeneous nuclei such as in a Wilson cloud chamber.<sup>112</sup> To appropriately consider a nucleation mechanism, we start with the thermodynamics of the phase transition that we define as nucleation.

### 1.3.1 Thermodynamics

Thermodynamics and statistical mechanics concerned with systems in equilibrium are not strictly applicable to flow and irreversible chemical reactions.<sup>113</sup> The results below are used as a guide to understanding the forces involved and do not necessarily represent an accurate formulation of the mechanisms involved. These are powerful tools for analysis, and their use is an aid in our understanding of the nucleation process.

The driving force for nucleation, whether equilibrium or kinetic, is a reduction in local free energy. A pleasant aspect of the description of free energy is that it is applicable for all phases of material (i.e., discussing nucleation from an undercooled melt of a solid, nucleation of a liquid from a vapor, or nucleation of a solid from a vapor). The description of free energy for our purposes, heavily relying on reference 113, is as follows:

$$dQ = dU + pdV \text{ (first law of thermodynamics (conservation of energy))} \quad (1)$$

$$TdS \geq dQ \text{ (second law of thermodynamics) .} \quad (2)$$

Combining eqs. (1) and (2) gives the chemical potential and the relation for internal energy  $U$ :

$$\mu_i \int (\partial U / \partial N_i)_{S,V,N_j(j \neq i)} , \quad (3)$$

and

$$dU = TdS - pdV + \sum \mu_i dN_j . \quad (4)$$

The Gibbs free energy and the enthalpy are defined as

$$G = H - TS \quad (5)$$

and

$$H = U + pV . \quad (6)$$

When combining eqs. (3) through (6), we arrive at an equation for the Gibbs free energy:

$$dG = -SdT + VdP + \sum \mu_i dN_i . \quad (7)$$

Because a system containing clusters at the critical size is unstable (the clusters can either decrease or increase in size), we need to look at the number of nuclei of critical size for equilibrium conditions and then look at the rate of incorporation of new atoms into the nuclei. First, we look at the number of equilibrium nuclei present. Borrowing from reference 111, we can consider nucleation of a spherical drop of liquid. The surface tension on a drop of liquid creates a higher internal pressure than pressure outside of the drop, much like a balloon. The chemical potential and the vapor pressure of a drop will be greater than those of the same liquid having a plane surface. Since, in general,

$$(\partial \mu / \partial P)_T = v . \quad (8)$$

Transferring an infinitesimal amount from a liquid having a plane surface to a drop will involve increasing the pressure inside the drop an infinitesimal amount  $\Delta \pi$ . Integrating over this pressure change will provide the change in chemical potential. From mechanical considerations, the change in pressure is equal to  $2$  (surface tension)/radius droplet:

$$\mu_d - \mu_\infty = \int_{\pi}^{\pi + \Delta \pi} v dp = 2sv / r , \quad (9)$$

where  $\mu_d$  is the chemical potential of single molecules in the vapor in equilibrium with the drop, and  $\mu_\infty$  is the chemical potential of single molecules in the vapor in equilibrium with the bulk liquid. The difference in chemical potentials of the liquids must be equal to the difference in chemical potentials of the vapors with which they are in equilibrium. This in turn will be equal to  $kT \ln(P/P_\infty)$ , where  $k$  is the gas constant per molecule and  $P$  and  $P_\infty$  are the vapor pressures above the drop and bulk liquid, respectively:

$$\mu_d - \mu_\infty = kT \ln(P / P_\infty) = 2sv / r . \quad (10)$$

Equation (10) is sometimes referred to as the Thomson equation.<sup>111</sup> For the creation of critical nuclei from the liquid, it is assumed that a subcritical embryo will gain more atoms than it loses by chance, causing it to reach the critical size. The time dependence of the mean number of nuclei formed at a constant supersaturation can either be obtained experimentally or estimated using probability theory, as noted by Toshev.<sup>114</sup> For a nonsupersaturated vapor at equilibrium, clusters will be in chemical equilibrium with single molecules. Where  $\Omega_i$  is the chemical potential of  $i$  clusters at their equilibrium concentration  $N_i$  in the vapor phase, then:

$$\Omega_i = i\mu_1 \quad , \quad (11)$$

$$\Omega_i = (\partial G / \partial N_i)_{T,P} \quad , \quad (12)$$

and

$$\mu_1 = (\partial G / \partial N_1)_{T,P} \quad , \quad (13)$$

from eq. (7), where  $G$  is the total Gibbs function of the vapor phase,  $N_i$  is the total number of  $i$  (sized) clusters, and  $\mu_1$  is the chemical potential of the single molecules at their concentration  $N_1$  in the gas phase.

When  $d_i$  molecules are transferred from the bulk liquid to a drop, both under the same total pressure, the overall change in Gibbs function will be from the Thomson eq. (10),

$$(\mu_d - \mu_\infty)d_i = 2(\text{surface tension})vd_i / r_i \quad , \quad (14)$$

and, therefore, to build a complete drop, the change in Gibbs function will be

$$\Delta G_i = \int_0^{d_i} (\mu_d - \mu_\infty)d_i = \int_0^{d_i} 2(\text{surface tension})vd_i / r_i \quad . \quad (15)$$

We can solve for the chemical potential of the  $i$  clusters by performing the following reversible cycle of isothermal operations:

1. Extract a small number of  $i$  clusters at their partial concentration,  $N_i$  in the vapor phase, the total pressure on the vapor phase being held constant both in this and all subsequent stages. During this extraction, there will be no change in the total Gibbs function. Then convert the  $i$  clusters to single molecules at their concentration in the vapor phase  $N_1$ . From eq. (11) it will be seen that there is again no change in total Gibbs function. If  $\Delta G(1)$  is the change in total change in Gibbs function in stage (1), then  $\Delta G(1)=0$ .
2. Change the concentration of the resulting single molecules from  $N_i$  to  $N_\infty$ , the concentration of the saturated vapor that is in equilibrium with the bulk liquid at the same temperature. The change in total Gibbs function per single  $i$  cluster is given by

$$\Delta G(2) = ikT \ln(N_\infty / N_1) \quad . \quad (16)$$

3. Convert to a liquid at pressure  $P_\infty$  and  $\Delta G(3)=0$ .
4. Convert bulk liquid to spherical isolated stationary  $i$  clusters, using

$$O_i = 4\pi r_i^2, \text{ where } r_i = (3v / 4\pi)^{1/3} i^{1/3} \quad (17)$$

and

$$dO_i / d_i = 2v / r_i \quad (18)$$

Substituting eq. (18) into eq. (15), we obtain  $\Delta G(4) = SO_i$ .

5. Dissolve the  $i$  clusters in a gas phase consisting of  $i$  clusters at concentration  $N$ . (This is an entirely imaginary state.) Let  $\Delta G(5) = x_i$ .
6. Change the concentration from  $N$  to  $N_i$ , which is the partial concentration of  $i$  clusters in the initial vapor, and reintroduce to the initial vapor producing  $\Delta G(6) = kT \ln(N_i/N)$  (from reference 111, pp. 8 and 9).

The previous six steps constitute a reversible cycle for which the overall change in Gibbs function must be zero, producing over the cycle,

$$ikT \ln(N_\infty / N_1) + (\text{surface tension}) O_i + x_i + ikT \ln(N_i / N) = 0 \quad (19)$$

This can be rewritten as

$$N_i = \exp\left\{(-1 / kT) [(\text{surface tension}) O_i - ikT \ln(N_1 / N_\infty) + x_i]\right\} \quad (20)$$

This describes the equilibrium number of clusters of size  $i$  in a vapor in equilibrium.

Nucleation rate may be approached from a number of directions depending on the system and the modeling approach.<sup>115</sup> A linear law model gives a constant nucleation rate. A constant nucleation rate can be expected when a large number of nucleation sites or embryos are present. The nucleation equation for the linear model is:

Number of particles nucleated = (rate constant) (time) or

$$N_T = kt \quad (21)$$

This law is expected in many systems during the initial stages of nucleation.<sup>115</sup> Considering an undercooled melt and a linear model,<sup>116</sup> the nucleation rate is equal to

$$I = N_n^\circ (dn / dt) \quad (22)$$

The absorption rate  $(dn/dt)$  is the product of an adsorption frequency,  $\nu$ , and the density of sites where the atoms can be adsorbed by the critical nucleus  $n_s^\circ$  where

$$(dn / dt) = vn_S^\circ \quad . \quad (23)$$

The adsorption frequency,  $v$ , is

$$v = v_o \exp(-\Delta G_d / k_B T) p \quad . \quad (24)$$

The atomic vibration frequency is  $v_o$  and  $\exp(-\Delta G_d / k_B T)$  is the fraction of atoms with sufficient energy to overcome the interface activation energy  $\Delta G_d$ . The adsorption probability is “ $p$ .”

$$n_S^\circ = A_n^\circ n_c \quad . \quad (25)$$

The previous equation is the site density with  $A_n^\circ$  as the surface area on a critical nuclei and  $n_c$  as the capture site density per unit area. Combining equations and using  $I_o = N_I v_o p A_n^\circ n_c$ , we can write the nucleation rate as

$$I = I_o \exp(-\Delta G_n^\circ + \Delta G_d / k_B T) \quad . \quad (26)$$

The exponential law model arises when formation of a stable particle also corresponds to a decrease in the number of nucleation sites or embryos<sup>115</sup> such that

$$dN_T / dt = (N_\infty - N_T) / t_N \quad , \quad (27)$$

where  $N_\infty$  is the maximum number of particles nucleated after a very long time and  $t_N$  is the nucleation time. Integrating this gives<sup>115</sup>

$$N_T = N_\infty (1 - e^{-t/t_N}) \quad , \quad (28)$$

with

$$t = t / t_N \quad . \quad (29)$$

Frade<sup>115</sup> provides equations that use a linear rate but additionally account for an induction time. For derivation of the equations, the original reference is listed in reference 115.

$$N_T = ktV(t / t_1) \quad , \quad (30)$$

and

$$V(x) = 1 - \pi^2 / 6x - 2 \sum_{n=1}^{\infty} (-1)^n / [n^2 x \exp(n^2 x)] \quad . \quad (31)$$

Multistep nucleation models are usually based on nucleation that occurs by a series of elementary steps written

$$dN_i / dt = k_{i-1}N_{i-1} - k_iN_i \quad . \quad (32)$$

With  $i = 1, 2, \dots$  and  $dN_o/dt = k_oN_o$ , an approximate solution for small times where  $kt_i \ll 1$  is

$$NP = ktP \quad . \quad (33)$$

Based on interfacial controlled growth, Frade<sup>115</sup> provides solutions for the four models noted above. Discussing nucleation of a liquid from a vapor in equilibrium, we can correlate the previous thermodynamic approach with a kinetic approach that starts using the Thomson equation derived in eq. (10).

### 1.3.2 Kinetics

We will first look at steady-state kinetics. The rate of condensation and the rate of evaporation must be equal at equilibrium, although nucleation is obviously not an equilibrium process. This is necessary so that if  $j_c$  is the gross condensation flux and  $j_e$  is the gross evaporation flux for a spherical liquid drop, we can use eq. (17) and write

$$j_c N_{i-1} O_i = j_e N_i O_i \quad , \quad (34)$$

and

$$N_{i-1} / N_i = j_e / j_c \quad . \quad (35)$$

These results only consider those clusters for which  $N_{i-1}/N_i \geq 1$ , then

$$N_{i-1} / N_i \approx 1 - (d \ln N_i / di) \quad , \quad (36)$$

$$j_e / j_c \approx 1 + \ln(j_e / j_c) \quad , \quad (37)$$

and

$$d \ln N_i / di = -\ln(j_e / j_c) \quad . \quad (38)$$

Assuming that condensation and evaporation occur by a direct process, with  $P_i$  being the vapor pressure of an  $i$  cluster and  $P$  being the total pressure of the vapor, then

$$j_e / j_c = P_i / P \quad . \quad (39)$$



Now using the Thomson eq. (10)

$$d \ln N_i / di = 1 / kT \left[ 2s_v / r_i + kT \ln(P / P_\infty) \right] . \quad (40)$$

Using eq. (15) and integrating gives

$$N_i = \exp \left\{ (-1 / kT) \left[ sO_i + ikT \ln(P / P_\infty) + \text{constant} \right] \right\} . \quad (41)$$

If the constant in this equation is taken as  $x_i - kT \ln N$  and written as  $\partial - kT \ln N$  to separate the methods of derivation, eq. (41) may now be written as

$$N_i = \exp \left\{ (-1 / kT) \left[ sO_i - ikT \ln(P / P_\infty) + \partial - kT \ln N \right] \right\} , \quad (42)$$

which is virtually identical to eq. (20),

$$N_i = \exp \left\{ (-1 / kT) \left[ (\text{surface tension}) sO_i - ikT \ln(N_i / N_\infty) + x_i \right] \right\} . \quad (43)$$

If for convenience  $\Delta G = [sO_i - ikT \ln(N_i / N_\infty) + x_i]$ , then

$$N_i = N \exp(-\Delta G_i / kT) . \quad (44)$$

In the previous methods of calculation, it has been assumed that the temperatures of the forming nuclei will remain constant during the processes of evaporation and condensation. However, as the free energy of a molecule decreases upon absorption by a cluster, the cluster free-energy average must increase, and, typically, this may be expressed in the thermal profile. The effect is, of course, smaller as the size of the cluster, whose average energy will increase, gets larger.

The kinetics used above considers the average number of nuclei and relates this to the macroscopic properties of the system. To minimize errors, this average is taken over as many experiments as possible; however, the statistical distribution of the number of nuclei does not yield any information concerning the kinetics of the process.

### 1.3.3 Transient Kinetics of Nucleation

Transient kinetics is of considerable interest in considering torch-produced diamond. The flow properties of the particles and the constant structure of the flame indicate that as species traverse the flame locus, their environment shows drastic change. Even in the absence of chemical reaction, equilibrium conditions are not likely to be attained.

The initial development of transient kinetics is credited to Zeldovich and Frenkel. Work by Gutzow and Toshev,<sup>117,118</sup> in a couple of papers, expands the theory to encompass nucleation in the formation of anisotropic (crystalline) phases from the vapor. The incorporation of particles into the nucleation of a crystalline phase involves an energetic barrier above that of isotropic or amorphous phases. Using the fact that the work of cluster formation  $\Delta G$  is a maximum for a critical-sized cluster, they simplify the equations of Zeldovich and Frenkel. They state that the molecular flux toward the critical nucleus<sup>117</sup> is the decisive parameter in the equations for nonsteady-state nucleation.

The molecular flux can be expressed as the surface area of the critical cluster  $S_k$  multiplied by the collision frequency of the molecules in the ambient phase  $Z$  again multiplied by a kinetic coefficient  $Z'$ . This process is used to arrive at an equation for the time lag of nucleation. In evaluation of  $Z'$ , they consider growth of a subcritical nucleus by a “normal” mechanism, a spiral growth mechanism, and a two-dimensional growth mechanism. Because of the relative cluster size and the appropriate dislocation density theory, spiral growth is ruled out as extremely unlikely. Their theoretical treatment states that in the case of small clusters, the normal mechanism and the two-dimensional growth mechanism will compete during subcritical nucleus growth.<sup>117</sup> Their work expands Ostwald’s rule of stages (fig. 1) as discussed earlier, such that only when the following conditions are met will the thermodynamically stable phase be ensured. A brief glance shows that this relates the chemical potential difference applicable from the thermodynamics, the surface energy of the appropriate phases and their kinetic coefficients, and the ratio of surface energies. The mathematics of their work is not as clear as their conclusions. Referral is made to reference 117.

$$\left( \frac{\Delta\mu_c}{\Delta\mu_1} \right)^2 > \left( \frac{\sigma_c}{\sigma_1} \cdot \frac{Z'_1}{Z'_c} \right) > \left( \frac{\sigma_c}{\sigma_1} \right)^3 > 1$$

Figure 1. Expanded Ostwald rule of stages.

In 1987, Inoue et al.<sup>119</sup> provided the first conclusive proof of nucleation time lag. They dealt with oxide precipitates in Si. However, their summarization and contribution to classical theory was general—considering steady-state nucleation to be represented by the following equations:

$$n(r) = n_1 \exp[-\Delta G(r) / kT] , \quad (45)$$

$$\Delta G(r) = (4/3)\pi r^3 \Delta G_v + 4\pi r^2 (\text{surface tension}) , \quad (46)$$

and

$$\Delta G_v = \Delta H_v (TE - T) / TE , \quad (47)$$

where the critical radius, given by

$$r_c = 2s / \Delta G_v \quad (48)$$

is a minimum in the individual size-distribution curve. Nucleation is defined by the adjoining of an additional atom to a critical nucleus. The steady-state nucleation rate is given by

$$J_c = n_c Z \beta_c \quad , \quad (49)$$

with  $J$  being the steady-state nucleation rate,  $n$  the critical nuclei density,  $Z$  the Zeldovich factor expressing steady-state critical nucleation density/equilibrium density, and  $\beta_c$  the frequency of an atom sticking to a critical nucleus. Then,

$$\beta_c = 4\pi r^2 c^{n_1} (D / d) \quad (50)$$

with  $D$  as the diffusion constant and  $d$  the jumping distance of the sticking atom. For transient nucleation when a system is suddenly supercooled, the time lag associated with the transient nucleation portion is due to the time lag for the system to develop an equilibrium embryo size distribution. Inoue et al.<sup>119</sup> carry the theory through to the calculations required for experimental determination of the nucleation lag time based on observations of increases in precipitation density. Their calculated results, however, differ from the observed time lag by two orders of magnitude. They concluded, using their data and results from Probstein<sup>119</sup> where a similar discrepancy was noted, that a theoretical assumption is in error. Convincingly, they list the following four theoretical assumptions:

1. The impinging number of atoms to unit area of the embryo surface is independent of embryo size  $i$ .
2. All of the impinging atoms stick to the embryo regardless of the embryo size (accommodation coefficient = 1).
3. The thermodynamic barrier for atom impinging and sticking may be neglected.
4. The heating of the embryo by an atom sticking may be neglected.

Previous papers have suggested that assumptions 1, 3, and 4 should give only a slightly different induction time from the correct one. Inoue decided that indeed assumption 2 may be responsible for their discrepancy and an accommodation coefficient of  $\approx 10^{-2}$  may be practical.

Although the statistical distribution of the number of nuclei has not yet been shown to provide information on the nucleation kinetics, the statistical distribution of time to formation for the first nucleus does provide information on the kinetic characteristics.<sup>112</sup> Toshev et al.<sup>112</sup> describe utilization of the probability distribution of the time to form the first nuclei, which will distinguish steady state and transient nucleation. They consider nucleation as a sequence of random, discrete, independent events along a time axis. The Poisson formula is used to find  $m$  nuclei within time interval  $0 \geq t$ , with  $N$  as the average number of nuclei to be expected over the time interval:

$$P_m = \left[ N^m \exp(-N) \right] / m! \quad . \quad (51)$$

Using  $I = dN/dt$  as the momentary rate of nucleation, the differential distribution of times between the initial point and the  $m$ th event can be given by

$$dP \geq m = I \left( N^{m-1} / m! \right) \exp(-N) dt . \quad (52)$$

This is integrated to yield a probability function that at least  $m$  nuclei are formed by time  $t$ :

$$P \geq m = I - \exp(-N) \sum_{k=0}^{m-1} N^k / k! . \quad (53)$$

Plots of these two equations can determine the presence of a time lag in the nucleation kinetics or the strict adherence to a linear time dependence of nucleation.

Shi et al.<sup>120</sup> consider transient nucleation in situations where there is a sudden change in supersaturation. They mention the applicability of their work to free jet expansion in expansion nozzles. This hints at the applicability of transient nucleation to the nozzle-directed expansion of gases in our growth torch. Importantly, they also consider the effect of foreign particles within the nucleation environment that scavenge particles otherwise used for the growth of embryo toward nuclei. Using single perturbation theory, they arrive at a transient-cluster nucleation distribution, a transient nucleation rate, and the time-dependent number density of critical clusters nucleated. They also look at these parameters in the presence of cluster scavenging. According to their results for the establishment of the transient cluster size distribution, the time required for subcritical clusters to attain a steady state is not overly dependent on the critical cluster size. Instead, it is dependent on the number of polymers present in the subcritical cluster (i.e., the subcritical clusters attain a steady state first in the smaller clusters, then in the larger clusters, and finally in the critical clusters). As the critical cluster size increases, more time is spent in establishing a steady-state cluster distribution outside the region of the critical cluster size.

For diamond nucleation, the consideration is interesting because, by assuming that both diamond and C and graphite nuclei are capable of being produced, the time given to the gas stream in which particles (growth elements) are carried may determine the state to which nucleation is carried. For example, the change in supersaturation at the nozzle exit through the initial reaction region gives a time for nucleation only in the inner flame cone (stoichiometric region). The change in supersaturation, however, also occurs when the gases enter the flame feather by passing through the plasma region (cone). Finally, the supersaturation changes again when the particles leave the feather and enter the diffusion flame. If C embryo grow at a given rate, an embryo may start, for example, as amorphous carbon (a-C) sp<sup>1</sup> bonded. With addition of additional C atoms, it may be considered as sp<sup>3</sup> bonded a-C. Further addition of C atoms and the presence of H may stabilize the structure as diamond. An even longer nucleation time or the scavenging of H<sub>2</sub> may allow graphite to form.

Looking at cluster scavenging, their equations indicate that, when cluster scavenging is present, the time to reach a steady-state distribution of cluster sizes is not affected. However, the steady-state number density of subcritical clusters is smaller than without cluster scavenging (i.e., the rate of development is not affected; however, the number of final nuclei is affected). Interestingly, the presence of scavenging shortens the time lag needed for the nucleation rate to approach the steady state.

Shi and Seinfeld<sup>121</sup> address transient nucleation from the viewpoint of cluster concentration at the instrumentally detectable size. Starting by noting that the steepest variation in cluster concentration occurs at the critical region, they recognize that since the critical cluster only has an equal probability of growth or decay, the detected clusters must be related to the size of the nucleated cluster, which has a 100-percent chance of growing to detectable size given sufficient time. Much like their previous work on subcritical clusters, the detectable cluster size distribution time lag can be considered supercritical nucleation density and therefore relates to the total height of the Gibbs free energy barrier.

Relevant to nucleation behavior in diamond systems and the focus of this work is the occurrence of nucleation in the gas phase or nucleation on the substrate surface. Understanding where nucleation occurs is the first handle on nucleation control mechanisms. Nucleation on surfaces can be described as homogeneous (on a pure two-dimensional plane) or heterogeneous (as in kink or ledge sites). Gas-phase nucleation can be either heterogeneous (on foreign or catalyst particles) or homogeneous. Looking first at surface nucleation, Volmer<sup>122</sup> is first credited with development of stabilization of nonthermodynamically stable phases by surfaces. Turnbull<sup>122</sup> applied this to nucleation sites retained by thermal history. He then noted that, depending on the rate of undercooling, these retained sites could dominate nucleation of the final undercooled phase.

#### 1.3.4 Heterogeneous Nucleation

General surface-nucleation work considers nucleation from the vapor onto a substrate, nucleation from the melt, or solid phase nucleation. Calvert and Uhlman<sup>123</sup> consider the separation of the surface nucleation mechanism into a small crystal and a large crystal. The small crystal model is relevant when the time for a nucleated layer to propagate across the surface is much less than the time between nucleation events. In the large crystal model, the crystal assumes that a nucleation event occurs between the coverage by propagating layers. In the large crystal model, which they hold to be generally applicable, they define  $t_3$  and  $t_g$ , respectively, as the time between the initiation of two successive layers and the time between initiation and completion of a layer. The result of their work looks at the results obtained by Gutzow and Toshev.<sup>118</sup>

Hirth<sup>124</sup> considers atomistic and capillarity theories of heterogeneous nucleation from the vapor phase onto a substrate. He presents work with a general picture of nucleation and supercritical growth starting with nucleation and surface diffusional growth of clusters that deplete a surrounding area of adatoms, thus suppressing nucleation in said surrounding area. Impingement of these depleted areas leads to a decrease in maximum supersaturation and eventually a diminution in continued nucleation. Also, contact of nuclei leads to sintering agglomeration or Ostwald ripening agglomeration driven by capillarity. They argue convincingly for Ostwald ripening on a nucleated surface using the size dependence of the local adatom concentration in equilibrium with a cluster via the Gibbs-Thomson equation. Their central premise is refuted, however, by Lewis and Halpern<sup>125</sup> in considering the effect of monomer density on the growth of clusters growing through the critical size. They refute the use of the equilibrium equations. Lewis and Halpern recall that nucleation is an irreversible process and the nucleation flux represents a departure from equilibrium. From their references, the arrival rate of monomer to a surface cluster is much greater from surface migration than from direct vapor impingement. With desorption as the principal loss process, they specify the monomer migration rate using the diffusion coefficient, and conclude that the relevant capture rate in surface nucleation theory is the diffusion limited capture rate of monomer by critical nuclei.

Surface nucleation theory is often primarily concerned with nucleation on homogeneous surfaces. Trofimov<sup>126</sup> considers the contribution of homogeneous (nucleation on a pure surface) and heterogeneous (nucleation on defects, ledges, vacancies, or adatoms). Two models are presented. One where nuclei are not required and defects play the role of cluster sites. The other considers adatoms that form nuclei that are localized on either homogeneous or defect sites and growth occurs onto these nuclei. The principal difference between the two models is that coalescence occurs in model one only after nucleation sites have become exhausted, whereas in model two, coalescence can have a significant effect while nucleation is in progress. The principal difference, due to the consideration of an inhomogeneous surface, is the occurrence of a plateau on the kinetic curve resulting from nucleation at defects.

In discussing a variety of full- and partial-condensation conditions, he notes that, for full condensation, high fluxes or low defect densities will cause heterogeneous nucleation to occur only in the very first stages of nucleation. For incomplete condensation, the nucleation on defects takes on proportionally greater importance. Ookawa<sup>127</sup> looks mostly at a crystal in equilibrium with its melt for the growth of crystal surfaces. Although not directly related to nucleation, a note of the work is worthwhile here. He points out that a small entropy change may favor the creation of a diffuse or rough interface and a large entropy change may favor a more two-dimensional interface (planar or sharp interface). Work was done by Osaka and Kasukabe<sup>128</sup> with tin (Sn) on silica. The results indicate that the Sn deposits as a liquid on small radius of curvature steps and that crystallization occurs from this liquid graphoeptaxially.

### 1.3.5 Homogeneous Nucleation

Homogeneous nucleation theories are most often considered for the situation of crystallization in a liquid melt. Forces and methods are applicable, as at least a first approximation to crystallization in the gas phase.

An excellent and reasonably recent treatment of homogeneous nucleation kinetics is given by Rasmussen et al.<sup>129</sup> They propose that the thermodynamic potential that controls the system stability is a continuous function of the cluster size and that this energetics produces a Frenkel cluster distribution. Further, they propose that an  $i$ th cluster consists of only  $i-1$  condensed monomers and one still gas-like monomer. This differs from classical theory that condenses all monomer. The result is that a classical cluster, because of the density difference between the condensed phase and the monomer phase, can grow in a volume smaller than that occupied by the first atom. The classical approach for this reason requires a statistical mechanics correction factor as applied by Lothe and Pound<sup>129</sup> (some materials have been referred to as Lothe-Pound fluids). Rasmussen et al.<sup>129</sup> incorporate the curvature dependence of the surface tension as given by Gibbs to permit the continuity of the thermodynamic potential. They consider the thermodynamic potential controlling system stability to be the sum of the following:

1. The product of the number of monomer gas atoms in the system and the partial molecular Gibbs potential per monomer in the vapor phase
2. The product of the number of condensed monomers in the cluster and the partial molecular Gibbs potential per monomer in the condensed phase
3. The product of the surface energy per monomer in the cluster and the surface energy of said cluster.

Use of the Frenkle distribution provides a continuous decrease in population as a function of the size  $i$ . This eliminates the need for a steady-state distribution different from the equilibrium distribution. Considering the steady-state kinetics, the incorporation of the Frenkle distribution decreases the nucleation rate in comparison to the classical theory. Demo and Kozisek,<sup>130</sup> in their work on homogeneous nucleation, also use the approach of a Frenkle distribution for the development of kinetics. The work of Rasmussen was expanded by Jayaraman et al.<sup>131</sup> to the situation where a heterogeneous cap nucleus is used.

Fluctuations in density have been noted to produce diffusionless nucleation up to a subcritical size embryo.<sup>132</sup> This mechanism starts the crystallization using, as a relaxation mechanism, a diffusionless atomic rearrangement leading to a subcritical nucleus. The mechanism is noted here because of the high possibility of density or pressure gradients within the torch environment. Exact application of this, however, requires sufficient atomic density to allow the diffusionless transformation, which is difficult to assume in a plasma or gaseous environment.

Drastic changes in pressure are considered by Lee and Wang<sup>133</sup> where they look at the collapse of cavitation bubbles created by a sound wave. This situation is much closer to the situation present in an operating torch system; however, this is simply conjecture by this author. Specifically, they look at the pressure dependence of the surface energy term starting with Turnbull's observation that the surface energy of a substance is proportional to its latent heat of fusion. If a substance contracts during freezing in the presence of a pressure change, the resulting work is stored as an increase in latent heat. The new latent heat at the new melting point, as dictated by the Claperon equation, is given by

$$\lambda' = \lambda(1 + E) \quad , \quad (54)$$

where

$$E = \Delta p \Delta / \lambda \quad , \quad (55)$$

such that

$$s' / p^{2/3} = (1 + E) s' / p^{2/3} \quad . \quad (56)$$

If  $p$  and  $v$  are positive, there will be an increase in undercooling. This will give an increase in the nucleation rate, principally due to the increase in the melting point. If  $v$  is negative, the nucleation rate is decreased as in Si, water, gallium (Ga), and others. Cavitation can trigger nucleation for an undercooled liquid if the liquid is close to the verge of normal nucleation. For the case of diamond, it would seem that this is only a minor enhancement of nucleation as cavitation is unlikely, although acoustic vibrations and turbulent flow are not.

### 1.3.6 Nucleation of Metastable Phases

Two or more free-energy minima may exist for a given environment. In any situation, the lowest free-energy state is considered the stable phase and any other phase is considered a metastable phase. According to the Ostwald rule of stages mentioned previously, the metastable phase will be traversed



before the stable phase is obtained. The relative stability of a metastable phase is determined not by the magnitude of free energy difference but instead by the activation energy barrier between the phases. The activation energy can be compared to the free-energy maxima noted by Wilcox.<sup>134</sup> A demonstration that the free energy can exhibit a maximum and a minimum with respect to the quantity of a new phase that has formed has been given by Wilcox<sup>134</sup> in a NaCl-H<sub>2</sub>O system. A maximum is a metastable equilibrium that can be represented by the barrier to nucleation, and the minimum is a stable equilibrium corresponding to the solubility conditions. Spitsyn<sup>135</sup> has presented work on the growth of a number of crystals directly in their range of metastability.

Considering homogeneous nucleation of a metastable phase, Spitsyn<sup>135</sup> starts by using the frequency of nucleation  $I$  in unit volume per unit time as given by

$$I = 2N_1(kT/h)^{1/2} \exp(-\Delta G_a/kT) \exp(-16\pi\Omega^2 a^3/3kT\Delta\mu^2) , \quad (57)$$

where  $\Omega$  is the volume of one particle of the crystal,  $N_1$  is the density of particles in the nutrient phase,  $k$  and  $h$  are the Boltzmann and Plank constants, respectively,  $a$  is the specific free surface energy of the crystal-ambient interface,  $\Delta G_a$  is the activation energy for the attachment of a new single particle to the nucleus, and  $\Delta\mu$  is the difference in chemical potentials of the initial and final phases.

When the preexponential factors are ignored, a relation stating the condition of the predominant nucleation of the metastable phase is derived:

$$\left( G_{\text{metastable}} + 16\pi\Omega_m^2 a_m^3 / 3\Delta\mu_m^2 \right) < \left( G_{\text{stable}} + 16\pi\Omega_s^2 a_s^3 / 3\Delta\mu_s^2 \right) . \quad (58)$$

The significance of eq. (58) lies in the controlling factors for the observed predominance of the metastable phase. The three controlling factors are again:

1. The specific free interfacial surface energy of the crystal-ambient interface is  $a$ .
2.  $\Delta G$  is the activation energy (for the attachment of a new single particle to the nucleus).
3.  $\Delta\mu$  is the difference in chemical potentials of the initial and final phases (liquid/vapor  $\geq$  solid).  
Spitsyn notes that metastable phases usually seem to have a lower surface energy.

### 1.3.7 Direct Nucleation of a Solid

The thermodynamic and kinetic approaches reviewed are similar for both the direct nucleation from a vapor of a liquid and a solid, with the important distinction of the application of the crystal shape into the derivation process for the nucleation of crystals. The Gibbs-Wulff theorem affects only (as in our case) the shape of very small crystals.<sup>111</sup> For solids, there is an analogous equation to the Thomson equation, eq. (10):

$$\mu_c - \mu_\infty = kT \ln(P/P_\infty) = 2v/\lambda = 2\gamma_j v/h_j . \quad (59)$$



By using  $g_j$  as geometric factors independent of size for a given crystal,  $V_c$  is the total volume of the crystal and  $\S_j$  is the surface Gibbs function of formation per unit area for a given face,

$$\lambda = \left[ 3V_c / (g_j \S_j^3) \right]^{1/3} . \quad (60)$$

It shows how the importance of chemical potential and vapor pressure increases as the size decreases. The surface Gibbs functions are assumed to be constants independent of the area of the crystal faces. However, the area change represented by the addition of molecules to a small crystal is larger than that for a large crystal so that there is more energy available to change less crystal for small clusters.

## 1.4 Background on Clusters and Embryos

### 1.4.1 Cluster Definition and Introduction

When considering a mechanism for nucleation, it is appropriate to investigate the embryonic state (precritical) of the nucleating cluster. Nucleation at both gas and surface locations requires growth of an embryo or cluster past a critical size in order to form a statistically stable nucleus. In our case, the nucleus then progresses to bulk diamond. Embryos must nucleate. The nucleation of a cluster, for the sake of clarity, will be referred to as germination. Germination involves the formation of a cluster from individual molecules. A cluster grows or decays and a molecule, by comparison, joins, attaches, or bonds. The properties of a solid are thought to gradually evolve as atoms are brought together. When a new atom is brought onto a cluster, all of the atoms in the cluster completely rearrange and the cluster reconstructs.<sup>136</sup> The gradual appearance of bulk properties and bulk material structure are manifestations of the cluster-to-nucleus-to-solid-growth process. For example, when examining the thermal properties of clusters, note that clusters may coexist as liquids and as solids over a range of temperatures;<sup>137</sup> i.e., the melting temperature and the freezing temperature are not the same.

Within a range of coexistence temperatures, the number of clusters that are solid versus those that are liquid depends on the exact cluster size and the difference in free energy between the two competing forms. Additionally, the number of clusters depends on the intermediate stages that are possible and present between the solid and liquid phases. This is due to Ostwald's rule of stages. Considering the formation of clusters and, from them, nuclei, Ostwald<sup>138</sup> mentioned the form that can be achieved with the least possible loss of free energy, or the form with the next largest amount of free energy that is involved in the spontaneous transformation from state to state. Ostwald further notes that states A and D have no reason to change, but that once state A has changed to state B, due to the presence of another state being adjacent, state B is driven to change to C and state C is driven to change to D. Because of the small number of atoms in a cluster and the large surface-to-volume ratio, some transformations may be possible in clusters that are not feasible in bulk material.

Berry<sup>139</sup> notes that the Born-Oppenheimer approximation is accurate enough to permit the use of an effective potential surface for describing the motion of the component molecules of a cluster. Using the potential surface as a descriptor, clusters, like conventional molecules, have some well-defined geometry corresponding to the absolute minimum energy of their potential surfaces. There is a well around the minimum of this surface within which a classical cluster would vibrate. At higher energies, local stable

minima are found in which alternate geometries are preferred. Berry presents an example using sodium chloride (NaCl). The tetramer of NaCl has two stable geometries—a planar ring and a cube. The cube has energy 0.27 eV below that of the planar ring. The barrier between the two forms is quoted as being no more than 0.56 eV above this so that conversion between the two can occur at least at the rate of thermal hopping. The implication is that under most conditions both forms would be present. Clusters then may be thought of as having complex potential surfaces that they may explore. The hydrologic term, catchment regions, has been used to describe the wells within the potential surface.

### 1.4.2 Cluster Bonding

Clusters may be classified as either weakly bonding (Van der Waals' molecular and H<sub>2</sub>-type bonds) or as strongly bonding (ionic, valence, and many metallic systems). Table 1 is a classification table that came from Jortner et al.<sup>140</sup>

Table 1. Classification of binding in clusters.

Type	"Canonical" Cases	Cause of Binding	Average Binding Energies	Occurrence
Van der Waals clusters	Rare gases R <sub>n</sub> , (N <sub>2</sub> ) <sub>n</sub> , (CO <sub>2</sub> ) <sub>n</sub> , (SF <sub>8</sub> ) <sub>n</sub>	Dispersive plus weak electrostatic	Weak binding D≤0.3 eV	Aggregates of rare gases and closed-shell molecules
Molecular clusters	Organics (M) <sub>n</sub> , (I <sub>2</sub> ) <sub>n</sub>	Dispersive electrostatic (weak valence)	Moderate binding D≤0.3–1 eV	Aggregates of organic molecules and some closed-shell molecules
Hydrogen bond clusters	(HF) <sub>n</sub> , (H <sub>2</sub> O) <sub>n</sub>	H-bonding electrostatic charge transfer	Moderate binding D≤0.3–0.5 eV	Closed-shell molecules containing H and electronegative elements
Ionics clusters	(NaCl) <sub>n</sub> , (CaF) <sub>n</sub>	Ionic bonds charge-charge interactions shell effects ih+EA	Strong binding D≤2–4 eV	Metals from left side of periodic table plus right side electro-negative element
Valence clusters	C <sub>n</sub> , S <sub>8</sub> , AS <sub>4</sub>	"Conventional" chemical bonds	Strong binding D≤1–4 eV	Isoteric molecules and radicals
Metallic clusters	Na <sub>n</sub> , Al <sub>n</sub> , Cu <sub>n</sub> , W <sub>n</sub>	"Metallic" bond low KE of electrons	Moderate to strong binding D≤2–4 eV	Wide occurrence to the left of B, Si, Ge, Sb, Po in rows 2–6 of the periodic table

Friedel<sup>141</sup> emphasizes the importance of electron-electron interactions and electronegativity in the choice between compact and dimerized clusters. The possibility of frustrations between the forces involved in cluster bonding and those involved in large aggregate bonding is also emphasized. These frustrations can determine the final macroscopic structural form, say amorphous versus crystalline. In looking

at bonding, Friedel<sup>141</sup> starts with the bonding patterns in dimerization and proceeds toward the bonding prevalent in larger nuclei or aggregates.

In the transition from dimers to trimers, the principal tradeoff involves the localization of the electron shells. Delocalization favors close packing of the atomic configurations, whereas localization favors the formation of bound dimers. This can be generalized to the case where large values of  $U_e$ , and thus large values of electronegativity, are expected to have stable dimerized trimers, and correspondingly low values of electronegativity are expected to produce close packed trimers. In a limit of strong delocalization, the exact structure of the close packing will be determined by the directionality of bonding.

### 1.4.3 Thermodynamic Structure of Clusters

The surface-to-volume ratio plays a large part in the behavior of clusters. For example, consider a simple spherical geometry with 100 atoms, 72 of these should be surface atoms. A 20-atom cluster, likewise, would have 18 to 19 surface atoms.<sup>142</sup> The number of surface atoms compared to the total number of atoms for a cluster size can be seen to increase with decreasing size for larger size clusters. This is shown below:<sup>140</sup>

$n_s/n = 4/n^{1/3}$  for  $n = 106$ ,  $n_s/n = 0.04$ ; for  $n = 104$ ,  $n_s/n = 0.2$ ; for  $n = 103$ ,  $n_s/n = 0.4$  with the ratio obviously approaching one as the molecular regime is approached.

Quantum size effects are also of importance in cluster behavior. The dependence of electric susceptibility on cluster geometrical dimension stems from the fact that the excitation (interaction) wavelength is comparable in length with the cluster dimensions. Additionally, the sample size is so small that the energy gap for excitations is comparable with the thermal energy  $KbT$ , the magnetic interactions  $H$ , or to the spectral resolution. Thermodynamic size effects are related to the dependence of some intensive thermodynamic properties such as surface tension, vapor pressure, and phase transitions on surface-to-volume ratios.

The melting of small clusters may be synonymous with fast isomerization between distinct nuclear configurations. Jortner et al.<sup>140</sup> show a hierarchical development of structural transformations for NaCl with  $n = 4$ ,  $n = 16$ , and  $n = 108$ . The structural phase diagram of the smaller clusters of 4 and 16 are shown to be characterized by branches corresponding to stable isomers separated by isomer coexistence regions. Olivei<sup>143,144</sup> presents the following assumptions for nonisothermal nucleation on a substrate from the vapor:

1. Direct impingement rate of molecules from vapor to substrate is considered negligible compared to surface diffusion of atoms on the substrate. This may be acceptable for torch diamond considering the rationale that the gas flow over the surface behaves to a first approximation like the classic flow against a plate. For example, there is a stagnation region where the rate of gas flow is zero and mass transfer must occur by diffusion.
2. Because of high substrate temperatures, the clusters are assumed to possess a liquid-like structure. Looking at nonisothermal nucleation and growth of embryos in a condition of supersaturation, formation of phase A onto substrate B may occur by condensation, layer by layer, at an

undersaturation of phase A—or phase A may form on substrate B by three-dimensional island condensation at a supersaturation of phase A. When the binding energy A–A becomes lower than the binding energy A–B, then layer-by-layer growth takes place.<sup>143,144</sup> The two cases may also be distinguished in terms of the A–B interfacial energy and the surface energy of phase A. When critical supersaturation is reached in conjunction with high nucleation rates, Jortner et al.<sup>140</sup> note that the rate usually turns out to be proportional to the equilibrium concentration of clusters of critical size multiplied by the rate at which the clusters are capable of acquiring additional atoms. He uses two methods to calculate the equilibrium concentration of liquid islands on a substrate for a given degree of supersaturation:

- a. The first method uses the change in standard Gibbs free energy when the vapor is concentrated into a liquid. The law of mass action is then used to calculate the concentration of islands.
- b. The second method minimizes the Helmholtz free energy of a vapor containing clusters of various size classes with respect to concentration of the various size classes with constraints of constant temperature, constant volume, and constant mass of material. Assumptions of constant temperature, constant volume, and constant mass of material to a first approximation relate to torch deposition as those properties are held constant through a gas flux region over the surface.

Olivei<sup>143,144</sup> provides convincing work on the lack of thermal influence by the thermal conduction of the substrate on nucleation of embryos from the vapor phase onto a substrate. He notes a caveat to his proof that nuclei that he considers are not much larger than the critical size. The thermal influence of substrate thermal conduction occurs in the removal or the retention of latent heat acquired by an embryo during the acquisition of an additional monomer. The thermal conduction of the substrate would seem to provide an important mechanism for stimulating growth by the removal of this heat. A critical cluster characteristically contains on the order of a few molecules, giving a critical radius of a few angstrom. The thermal propagation of the latent heat released by an impinging atom is typically restricted to 10–25 Å, thus, the thermal process in the substrate occurs in distances  $\approx 20$  times shorter than the mean free path of the electrons and phonons in the surface (the mean free path in metals and insulators is about 100–500 Å). For nuclei larger than about three critical diameters, the thermal dissipation of the substrate should be taken into account. The mean free path of carriers in the embryo increases and is better able to couple with the mean free path of carriers in the substrate.

Chow<sup>145</sup> considers the rapid condensation of a sputtered vapor. Material removed from a sputtering source is mainly in the form of atoms and a small fraction of atom clusters. The energy of sputtered atoms approaches the thermal energy of the ambient gas. Chow demonstrates that the major material transport mechanism is via convective transport. He also notes that nucleation aided by the presence of ions may be important for homogeneous nucleation in regions of high convection, where convection aides the process of adiabatic expansion and supercooling, resulting in a supersaturated vapor. Klots<sup>146</sup> brings the kinetics of evaporation in as an upper limit to the range of temperatures accessible by clusters of a given size. A temperature for small clusters signifies an energy location, in particular the high-energy edge of the cluster ensemble. This is also the edge of the cluster or the size of cluster where evaporation is predominantly occurring. In comparison, he equates the temperature scales present in the phenomena of energy

release and electron scattering. The conclusion asserts that with comparably sized clusters, the relationship is presumed to be more evident. Clusters can isomerize by thermal excitation or by tunneling or by a combination.<sup>147</sup>

#### 1.4.4 Production of Clusters From Free Jet Expansion

During free jet expansion, the thermal energy of the molecule is progressively converted to kinetic energy. Along the jet axis, the pressure and temperature are decreasing while the gas velocity reaches a constant value. At constant nozzle diameter, condensation can occur homogeneously due to a decrease in inlet pressure or a decrease in inlet temperature.<sup>148</sup> The mean cluster size is controlled by varying the outlet pressure. During the growth phase, after a molecule has been added to the cluster, the heat gained by the cluster from condensation must be released before another molecule can be added. The release of heat acquired from condensing molecules may be dumped by nonsticking collisions with the surrounding gas, by evaporation, or by radiation. The temperature of the clusters produced depends only on the condensation and evaporation properties of the condensing gas rather than on the mean cluster size. Conical and cylindrical nozzles have been found to yield different distributions of cluster sizes.<sup>139</sup>

#### 1.4.5 Electronic Structure of Clusters

It is of interest to see how discrete electronic levels within a structure form in the transition from the molecular to the solid-state regime. For the case of C, the electronic band gap difference between forms is large as the electronic structure arranges to form either graphite, glassy C, C<sub>6</sub>O, or diamond. The electronic states of clusters are directly related to the bonding and atomic structure. These electronic states, however, provide an important and unique probe of atomic structure. Reverting to the relationship between bonding and electronic cluster structure, Friedel<sup>141</sup> provides figure 2 on the dimerization of diatomic carbon (C<sub>2</sub>). This figure shows the variation of bond energy with bond distance for the  $\sigma$  and  $\pi$  one-electron state of the C<sub>2</sub> dimer. For macroscopic aggregates with sp<sup>3</sup> covalent bonding, the hybrid bonds are roughly additive so that the total cluster energy may be estimated from addition of the number of bonds and their energy. This may be shown for sp and sp<sup>2</sup> bonds as well. The sp<sup>3</sup> bonds that build a quasi-complete set to develop delocalized electronic states show developing band structures for sites in the cluster where the energetic upper limit of four neighbors has not been reached. The structure is considered nonalternate and the band structure does not yet provide a specific crossing point between the *s* and *p* bands (fig. 3). As atoms are added to the cluster, the bands fill in energy (from a greater concentration of delocalized electrons). This filling process is roughly additive so that the character of the bonds present in the cluster (depending somewhat on position) go through a gradual change in character, eventually behaving as bulk sp<sup>3</sup> bonds (fig. 3). This is important in the stabilization of the eventual nuclei structure.

The smaller bandwidth of the  $\pi$  bands is expected to stabilize the  $\pi$  bonding with respect to the  $\sigma$  bonding, especially in C with its high value of internal bonding energy. This may explain the stability (in bulk) of graphite over diamond. For small aggregates, the delocalization required for the states to be smeared enough to make the assumption of strong delocalization may not hold (i.e., stability of small diamond over small graphite).

Clusters can ionize both positively and negatively. A complete review of small C-cluster ionization by Weltner and Van Zee will be covered later. Ionization of a molecule within a cluster involves a lowering

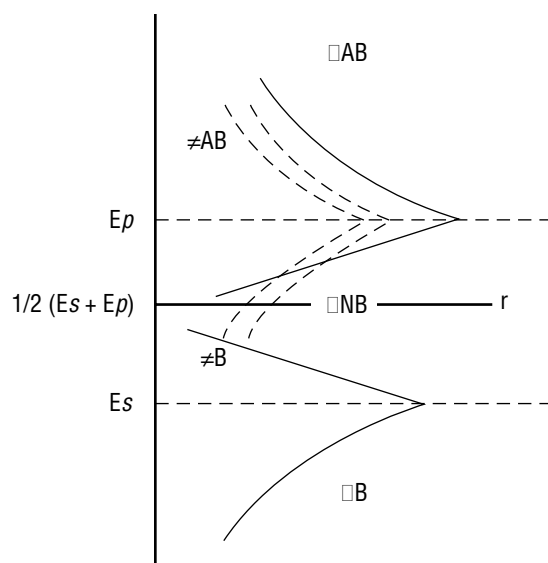


Figure 2. Dimerization of  $C_2$ .<sup>141</sup>

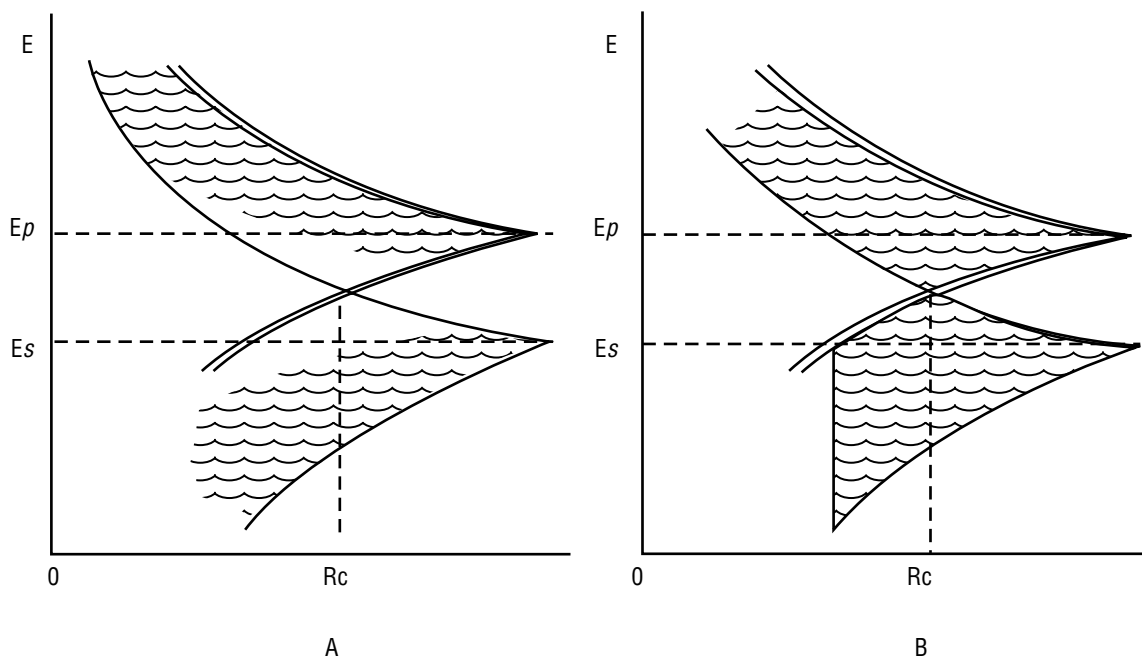


Figure 3. Depiction of an  $sp^3$  bond structure.<sup>141</sup>

of the overall ionization potential of the entire cluster with respect to monomer ionization. Electron localization in clusters may involve quasi-free states on the one hand and bulk and surface states on the other. Jortner provides an extensive review of these methods. Here, however, we will consider only the solvation of an excess electron to stabilize a negative ion or cluster. Nonreactive electron localization in water clusters has been documented as originating from electron binding during cluster nucleation or from electron attachment to preexisting clusters in water. The localization of a free electron constituted a novel, excess-electron surface state on the cluster. With an increase in size, the ability to internalize the localization of the electron became favored over the creation of novel surface states. Here, a convergence to the bulk behavior is noted.

#### 1.4.6 Vibrational Contributions to Melting and Phase Transformations

Melting and thermal expansion of phase transformations are caused by the anharmonic effect of atomic vibrations.<sup>149</sup> An interesting simulation experiment has been done by Cheng and Landman.<sup>150</sup> They performed simulations on the energetics of collisions of crystalline phase nanoclusters impinging on fluid films that are adsorbed on solid surfaces. Their simulations used NaCl vibrationally cold crystals that were impinging on a bare {001} NaCl surface, a bare {001} NaCl surface with an adsorbed film of liquid neon (Ne), and a bare {001} NaCl surface with an adsorbed film of liquid Ar. The results look at the nature of energy conservation, melting, cooling, and shock generation. In fact, they note an ability to control the nature (shape and crystalline/glassy structure) of the nanoscale growth units by means of appropriate selection of a target liquid film. Interruption of the incident cluster motion at the target surface results in heating, structural deformations, possible fragmentations, and the development of shock conditions. For collisions with the lower density Ne film, the cluster tends to preserve the overall shape and crystalline order of the structure—although rapid heating is noted. The difference appears to be the attenuation length of the impact energy. For the higher density Ar fluid, the collision leads to ultrafast heating of the cluster followed by a fast cooling stage involving melting and disordering of the cluster. During these collisions with the Ar film, the clusters tend to melt and undergo disordering, while maintaining compositional integrity. As the cooling process continues, the disordered cluster approaches the underlying crystalline substrate where it is eventually deposited. Throughout the evolution of the process, the cluster remains in a disordered state characterized by a significant excess of potential energy above the ground state. The initial jump to high temperature, coupled with the quench cooling, prevents reordering and structural annealing of the cluster.

To additionally investigate the results on Ar films, they performed a simulation where the cluster was incident with a higher relative velocity. In the simulation where the energy of incidence was higher, they noted a consistently higher internal potential energy. They note that this allows access of the cluster to various local minima of the multidimensional configuration and potential surface comprising, in their case, the glassy states of the cluster. Zajfman et al.<sup>151</sup> show a variation in the ratio of different isomers present in a C ion beam between a cesium (Ce) sputtering apparatus and laser vaporization.

#### 1.4.7 Carbon Clusters

Carbon clusters can be examined from  $C_2$  and its ions through the recently discovered stable  $C_6O$  and  $C_7O$  phases. At some point in the growth of pure diamond from the gas phase, constituents must form diamond nuclei—an excellent review is presented in reference 152. Except where noted, the subsequent information on C clusters has been taken from this reference.



Clusters of pure C and the various ionic embryos are of considerable interest. At some point in the growth of diamond, C atoms preferentially choose to arrange themselves in the diamond-cubic lattice structure. Control of this germination and nucleation process will ultimately determine the utility of diamond as an engineered material. Proposed stable geometries of pure C are shown in figure 4.

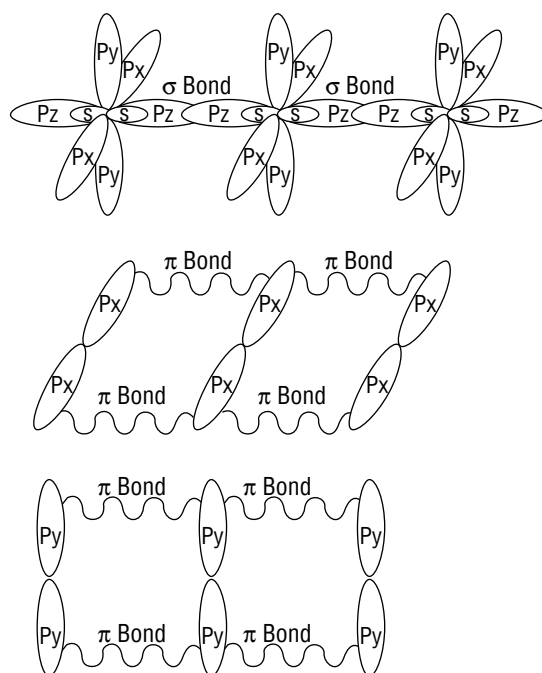


Figure 4.  $\pi$ -bond structure from Friedel.<sup>141</sup>

### 1.4.7.1 Carbon

**1.4.7.1.1 Atomic Bonding.** A natural question that arises for diamond formation is whether the close-packed trimer state should be identified as an intermediary in the formation of C nuclei. Friedel notes that the linear chain configuration of C is a close-packed trimer. When  $P$  bonding is present, the linear configuration is preferred to that of an equilateral triangle because of the ability to stabilize the linear chain, with the  $P_x$  and  $P_y$  orbitals, with the formation of  $\pi$  bonds (fig. 4). If the linear chain becomes long enough, the expectation is that it will dimerize slightly, forming nodes along the chain. Because the  $\sigma$  bonding is stronger than the  $\pi$  bonding, the chain will only dimerize when the number of atoms is large enough to treat the multitude of localized  $\pi$  bonds as quasi-continuous. Considering completely delocalized electrons in covalent aggregates, Friedel suggests for large aggregates that three-dimensional bonds should be based on the diamond tetrahedron and  $\sigma$   $sp^3$  bonding because it is the strongest bonding. As the number of atoms goes down, he brings up an expectation of two-dimensional aggregates based on  $sp^3$   $\sigma$  bonds and  $\pi$  bonds characteristic of graphite. For aggregates with  $N < 10$ , the linear chains discussed are expected with  $\sigma$ ,  $sp$ , bonds and 2  $\pi$  bonds in evidence.



1.4.7.1.2 **Electronic Structure.** The electronic structure of group IVa covalent clusters reveals an important difference between C and Si or germanium (Ge) clusters.<sup>152</sup>  $C_n$  clusters are dominated  $\pi$  interactions; this results in linear forms for odd-numbered clusters through 9 and distorted ring structures for even-number clusters through 10. Reverting to the relationship between bonding and electronic cluster structure, the dimerization of  $C_2$  is provided by Friedel in figure 2. This shows the variation of bond energy with bond distance for the  $\sigma$  and  $\pi$  one electron state of the  $C_2$  dimer.

**1.4.7.2 Diatomic Carbon.** Seventeen electronic states of  $C_2$  have been identified. When graphite is heated,  $C_2^-$ ,  $C_3^-$ , and  $C_4^-$  were the most abundant species.  $C_2^-$  was first noticed in the flash discharge of  $CH_4$ .  $C_2^-$  was prepared in an Ar matrix at 4 K by photolysis of  $C_2H_2$ . Implantation of 250 KeV  $C^+$  ions into Ar matrices has also been found to create  $C_2^-$  ions. The appearance potential of  $C_2$  in C vapor was measured to be 12.0 +0.06 eV by Raghavachari and Binkley.<sup>153</sup> Passing from  $C_2^+$  to  $C_2$  to  $C_2^-$  involves successive additions of electrons to the  $\pi_u$  bonding orbital. An electric discharge through CO at  $\approx 0.1$  atm and in the ultraviolet (UV) fragmentation produces a progression through the specific emission spectrum called the high-pressure bands of  $C_2$ .

**1.4.7.3 Triatomic Carbon.** The spectrum of triatomic carbon ( $C_3$ ) beginning at 4,050 Å was seen in 1882 in the emission from comets. These bands are observed in an  $O_2$ - $C_2H_2$  flame on top of a strong underlying continuum. From an analysis of the rotational structure of the 4,050-Å band, Douglas found that the molecule was linear in both states, with the C-C bond distance increasing from 1.281 Å in the lower state to 1.305 Å in the upper state.

The  $\pi_g$  molecular orbital is not occupied in  $C_3$  in the ground electronic state; however, excitation occurs in the  $1\pi_u$  level. There is a corresponding abrupt rise in the bending frequency, which is attributed to the occupation of this antibonding  $\pi_g$  orbital having a strong stabilizing influence on the linear structure. As electrons continually add to this orbital, the  $\nu_2$  frequencies steadily increase in the molecules CCN, NCN, boron dioxide ( $BO_2$ ), and  $CO_2$ . Narayan et al.<sup>154</sup> demonstrate that the low bending frequency of  $C_3$  has a significant effect on the thermodynamics of the vaporization and the high temperature behavior of C.

**1.4.7.4  $C_4$ - $C_{10}$ .** No  $C_4$ - $C_{10}$  molecules have been detected in the gas phase except through mass spectrometry. The consideration of these molecules in relation to diamond formation is intriguing. In structures larger than  $n=9$ , it appears that the ring structure is favored for C cluster geometries. For diamond formation then to take place, either a recrystallization-type phenomena must occur after the embryo has been formed in order to achieve the diamond structure, or the diamond structure must be achieved through stabilization using bonded  $O_2$ ,  $N_2$ , or  $H_2$ . Following this second chain of logic, if the structure is to be a bulk diamond structure, the stabilization can only take place on the surface of the growing embryo, as the additional bonded atoms must be removed prior to growth.

For an unstabilized C cluster of diamond, the crystal basis consists of four singly bonded C atoms. The  $C_4$  molecule would appear to be the critical unit in unstabilized C for the structuring of a diamond lattice.

Calculations by Whiteside<sup>154</sup> concluded that a bicyclic form of  $C_4$  was more stable by 6 Kcal/mol than the linear form. Calculations by Nemukhin et al.<sup>154</sup> show the linear triplet form to be more stable. The exact value of the energy difference between the two forms is still undetermined; however, the two forms

appear to be almost isoenergetic. To switch between forms of  $C_4$  requires passing through a planar square form with very high energy between the rhombic (bicyclic) and the linear forms. If one form is chosen, the transfer to the other configuration would be slow, if it occurred at all, due to the high energy requirements of the planar square intermediate. Evidence has been found that neutral  $C_4$  prefers the rhombic form.<sup>152</sup>

The rhombic form has been established as the theoretical equilibrium form of  $C_4$  by Ott.<sup>155</sup> Bonding in linear  $C_4$  has been established by Weltner et al.<sup>154</sup> to be cumulene-like and not  $C_2H_2$ -like so that they are in their lowest triplet states. Several authors have pointed out that if equilibrium prevails, the linear species will dominate in the vapor from graphite due to the SB contribution.

**1.4.7.5  $C_5$ .**  $C_5$  appears to be a more rigid linear molecule than  $C_3$ . The spectrum of  $C_5$ , however, is expected to be very similar to  $C_3$  where a  $\sigma$  to  $\pi$  transition occurs near 3 eV. The dominant fragmentation path is found to involve the loss of  $C_3$ . This is common among the neutral polycarbons because of the stability of  $C_3$ .

**1.4.7.6  $C_7$  and  $C_9$ .** These molecules are linear with  $\sigma$  ground states and appear to have a dominant fragmentation path involving loss of  $C_3$ .

**1.4.7.7  $C_6$ ,  $C_8$ , and  $C_{10}$ .** There is some evidence of two forms of  $C_{10}$  which, Weltner notes, suggests two slightly bent isomers. The  $C_6$  molecule showed signs of cumulene-type bonding with the unpaired electrons in the  $p\pi$  orbitals on the C chains as in  $C_4$ . In  $C_{10}$ , there is an abrupt change in the even/odd alternation, and the pattern looks like that of  $C_7$  or  $C_9$ . Weltner has proposed that this is the beginning of the transition to monocyclic rings.

**1.4.7.8 Magic Numbers and Larger Molecules.** Mandich<sup>156</sup> notes that the indications are that clusters in the size range of 15–20 Å do not form association complexes; therefore, they only weakly interact with  $C_2H_2$  as compared to clusters in the 10–14 Å atom range.

In an examination of an ion signal detected by mass spectrometry versus C cluster size, a number of molecular sizes are detected in disproportionate numbers. Magic numbers for  $C_n^+$  satisfy the relationship  $n=4m-1$ , with  $m=2, 3, \dots, n$ , with groupings of four. Weltner notes that this is not the  $4n+2$  distribution predicting the most stable species for planar aromatic cyclic molecules. Magic numbers are usually interpreted as designating clusters of unusual stability. The recently discovered high stability forms of  $C_{60}$  and  $C_{70}$  fall into this group.

Simulations by Jing<sup>157</sup> indicate that the morphology of large clusters such as  $C_{60}$  are only weakly dependent on the initial configuration. They note that clusters change more easily in their simulation during a process of monomer addition rather than a simulation where the number of atoms is held constant.

The work presented in this technical publication seeks to build on this background of nucleation and cluster theory in the specific field of torch-produced diamond film. A series of five experiments plus related computer simulations were derived to investigate the nature of embryo germination and cluster nucleation for diamond films from a torch system. The next section will describe the structure of these experiments.

## 2. DESCRIPTION OF THE NUCLEATION EXPERIMENTS

### 2.1 Introduction

Five experiments have been performed looking at the nucleation of diamond film in a torch production environment. Three experiments were conducted using an  $O_2$ - $C_2H_2$  torch and the other two experiments were conducted using a high-velocity oxygen fuel (HVOF) gun. In this section, the experiments and equipment used to carry them out will be covered. The  $O_2$ - $C_2H_2$  experimental apparatus is described first, followed by an explanation of general operating procedures, and then a discussion of experiments undertaken. This procedure is then repeated for the experiments performed using the Metco HVOF gun.

### 2.2 Torch Experiments

#### 2.2.1 Hardware

The author assembled all the hardware and completely wrote all the software. Tracing first the flow path of the gases, technical grade  $C_2H_2$  (98-percent purity), technical grade  $O_2$  (99 percent), standard grade (2)  $CH_4$ , and standard grade (2.3)  $CO$  were used. All bottles were used at standard bottle pressures. Flow regulators were used to step down the gas pressures so that input into the mass flow controllers was typically 15–20 psi, dependent upon the gas. Flow controllers from Porter Instrument Company were connected to standard pressure bottle gas. The flow controllers were chosen specifically for their response time and their internal proportional internal derivative (PID) set point control. The flow controllers were recalibrated and a least-squares fit was determined to be appropriate as an approximation of the calibration curves. Coefficients of the least-squares fit were incorporated into the flow-control software subprogram used for monitoring and control. The mass flow controllers were operated through a computer interface with a Porter Instruments pulse interval modulation (PIM) manual interface controller. The PIM controller offered the convenience of computer operation with a backup capability of manual operation. The computer operation will be discussed at length in the software section. The gas flow to the torch is shown in figure 5. The three C containing fuel gases “T” into a common line. Both the fuel line and the  $O_2$  line are sent through backflow check valves for safety.

The torch itself was a modified version of a standard, unwelded  $O_2$ - $C_2H_2$  torch, where the gas metering adjustment valves were replaced with direct-flow connections. The torch was mounted on a simple internally threaded block mounted on a rotating screw so that the height of the torch above a sample could be accurately controlled by rotating the screw as shown in figure 6.

During operation, the torch was directed at a water-cooled substrate holder. Water flow was measured with a Brooks Instruments high-volume flowmeter. Because of the complexity and number of variables involved, no attempt was made to correlate the water flow with heat transfer rates. The water was controlled with a simple spigot and this was found to be sufficient. In fact, variations of 5–10 gal/min were found to equate well with temperature variations of 10–20 °C in the operating range of 600–1,000 °C. The water flow, after passing through the flowmeter, passed into a large Cu block (shown in fig. 7). The block consisted of a flow channel into and out of the block and a series of substrate holders or substrates that fit

into the block using a keyway and four tie-down screws. The keyway and tie-down screws were used to maintain strong mechanical contact for thermal transfer during deposition.

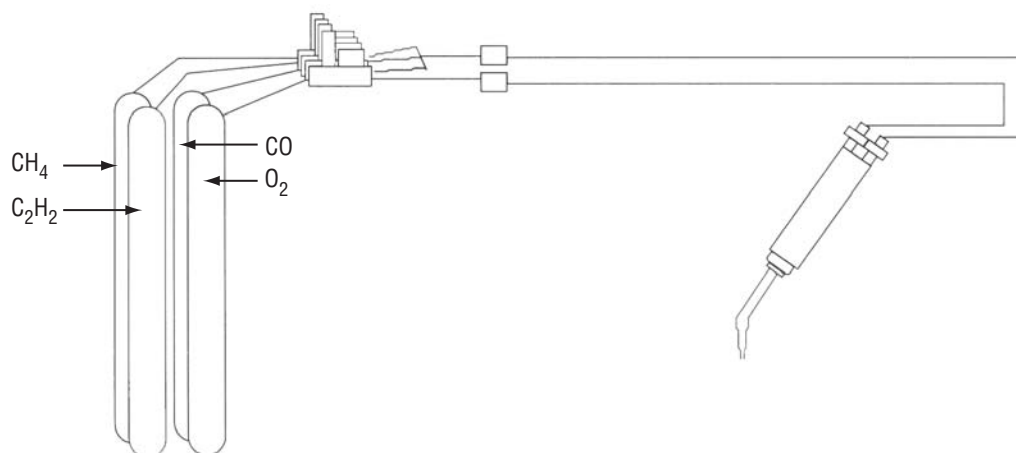


Figure 5.  $O_2$ - $C_2H_2$  torch diamond deposition gas flow path setup.

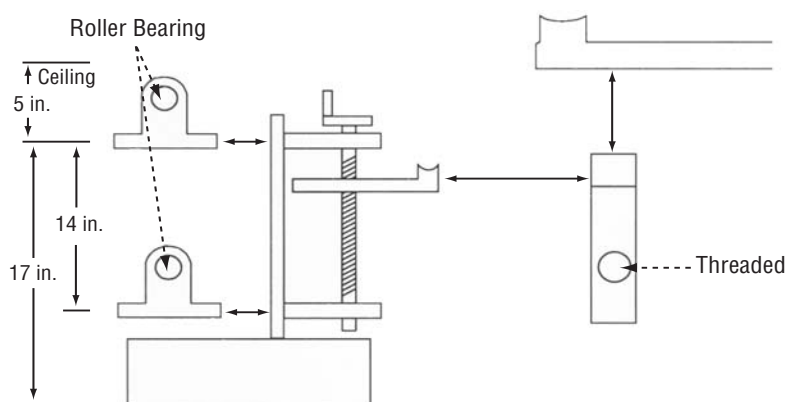


Figure 6. Torch positioning and mounting apparatus.

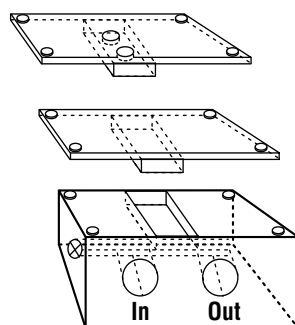


Figure 7. Substrate cooling block showing interchangeable mounting plates.

Several different holders were used. Two are shown in the conceptual drawing; the top one that houses Mo screws and the lower one that is, itself, a Cu substrate. The temperature and emissivity of the substrate were monitored using an optical pyrometer. The optical pyrometer was a pyrolaser from the Pyrometer Instrument Company. The use of a pyrolaser warrants some brief discussion. The pyrolaser is a narrow bandwidth optical pyrometer coupled with an active laser reflectometer. A low-powered pulsed GaAs laser is fired at the target surface. The reflectance is measured and the emissivity of the surface is calculated. Through the same optical path, infrared (IR) radiation on the 865-nm bandwidth is used for determination of the temperature based on the emissivity reading. For diamond film growth, it would be impossible to use an optical pyrometer without this emissivity measurement feature since the surface starts out as one material and then progresses toward a C form or a mixture of C forms with different emissivities. Both emissivity and temperature data were taken continuously during all experimental runs due to the use of the pyrolaser.

Motion control of the sample in the  $x$ - $y$  plane was controlled using a special designed motion controller developed by Delta Systems for a previous KC-135 flight experiment. This system was geared for an extremely slow translation rate, diamond-deposition work, which was fortuitously in the range required by the torch.

The computer used to control the system was a Macintosh IIX series running at 25 MHz. The system used three input/output (I/O) data acquisition and control boards. A Lab-NB board by National Instruments received gas flow levels and controlled the remote activation switch on the PIM controller. National Instruments' AO-6 board set the levels for the mass flow controllers. Both the optical pyrometer and the motion controller were controlled by serial port Super ComCard boards by Taniwa Systems. It was possible to use the modem and printer ports provided on the Macintosh system; however, it was suspected that this might have resulted in an anomalous system interrupt priority.

### **2.2.2 Software**

The diamond torch system is started from an auto initiation program called the auto system setup program. This setup program configures the system hardware connections, provides a convenient system shutdown option, and places the torch control system in a ready idle mode. The auto system setup program, using a global case structure for each setup option, calls the motion controller setup, the pyrometer auto setup, the flow control setup remote control, and the torch control system programs.

The motion controller setup program sends an initiation pulse followed by a discreet jog signal and a duration/length of command so that the motion controller executes a series of discrete jogs of set size for a given time increment until instructed to cease. The motion controller starts its motion at this time.

The flow control setup remote control program configures the I/O ports for remote control of the Porter Instrument flow controllers. A cumulative I/O error is provided to indicate that ports were acceptably conditioned.

The pyrometer auto setup program accesses the pyrometer string transfer program and sends a series of pyrometer-specific commands for the setup of continuous operation in an emissivity adjusted temperature mode. These commands are sent by indexing a case statement with the index of a "for" loop. The commands may be altered for other pyrolaser operating modes.

When the torch control program is initiated, it is placed in an idle ready mode. An all-inclusive “for” loop is provided to handle file storage issues. A run file name is given for the overall test. A front panel control, requesting the number of runs, indicates the number of data files that will be created for a given test. Each data file will use the run file name with an asterisk followed by the specific run number. The duration of each run is chosen on the “desired run time” control on the front panel. An example would be if a 2-hr test were to be run, having two data files, one for each hour, with a test file name of TEST, two files, TEST\*1 and TEST\*2, would be created, each having a desired run time of 60 min. The primary reason for having more than one file for a given test is to provide manageable file sizes. Inside an overall “do while” loop, which is the principal control loop for a given file, three separate software constructs have been developed to interact with the deposition process: A statistics loop, an analysis loop, and a control loop.

The statistics loop compiles relevant statistics during the run and provides them real time on the computer screen. Statistics may be compiled for any control or measured variable. Additionally, statistics may be generated on calculated values such as  $C_2H_2/O_2$  ratios. The statistic loop is given a number of data points (sample size) on which to run the statistics from a screen control on the front panel display. Batch values are compiled from sequential data point collections of this size. The statistic loop calls the basic statistics subprogram from which all statistics are generated. As each data point is collected, it is stored in the buffer of a “for” loop. The index of the “for” loop is previously defined as the batch size. When the appropriate batch size has been reached, the “for” loop terminates and passes the collected array of data points into library routines for standard deviation, mean, variance, and root mean square (rms). A case structure is used to select the specific variable for which values are displayed. The last statistical batch may include a number of zero data points to accommodate the batch size requirements.

The control loop and the analysis loop provide the structure for straightforward and convenient modeling and simulation trials. The system control loop provides a software mounting rack onto which various control programs and simulation models may be attached.

The heart of the analysis section is a “for” loop nested inside a case structure. The specific analysis option desired is selected from a ring control on the front panel. Each analysis option has a specific case in the case structure. The specific analysis used may be chosen from the screen during the deposition run. The number of data points used for analysis is set in the analysis size control on the front panel. Data are collected for analysis as they are recorded. The data are stored in the buffer of the “for” loop until the number of iterations of the “for” loop reaches the defined analysis size. Each analysis case simply chooses which of the available readings it requires from the data structure, then passes an array of those values on to either a direct  $x$  versus  $y$  graph or an analysis filter or transform. The final  $x$  versus  $y$  graphs are sent to a multigraph module on the front panel.

Four nested, concurrent case structures are used in the body of the system control loop: A read status, an analysis status, a storage section, and a change status case structure. The read status section reads and synchronizes all of the incoming data from the process equipment. The incoming data are then sent around the loop and received by the analysis status section. The analysis status case statement allows the process control conditions to be chosen at any time from the front panel. Then, using the currently chosen control-system program, the analysis structure decides on what the deposition conditions should be, based on the current readings. The change status segment then suitably adjusts the deposition parameters as directed. The storage structure takes each one-dimensional array of data points for each of the measured



variables and places it into a spreadsheet to create the final data file and a global variable for use by other programs and concurrent structures.

In the TRUE condition, the read status case structure calls on the flow control program and the read pyrometer program. Each program is polled for the current status of its output variables and instrument readings.

The read continuous pyrometer program accesses the pyrometer string transfer program to verify the port from which to read data. The serial port is then polled for the number of bytes. When the number of bytes reaches 44, the string is read and the values of emissivity and emissivity-corrected temperature are stripped from the string. The data are sampled as often or as seldom as updates of temperature and emissivity are required. The program, however, will wait until a full set of data is available at the serial buffer before data will be provided to the program. The longest time interval in the pyrometer operation loop is the sampling time of the pyrometer. This is also the longest data collection interval in the current data acquisition and control system.

The flow controller program is a case statement that draws on three subprograms: Volts in, volts out, and constituent's calculations. The two cases represent a situation where the flow needs to be changed and a situation where the current readings are desired.

For the TRUE case where the flow needs to be changed, the required settings are sent through a curve-fitting (linear) equation relating sLpm flow to voltage. These calibration curves are derived from the calibration curve from each flow controller. The corresponding voltage is provided as an input to the "volts in" subprogram. The "volts in" subprogram takes the voltages supplied, scales them, and writes out to the appropriate analog port.

For the FALSE case of the flow controller main case statement, the "volts out" subprogram reads and scales the analog output values from the appropriate ports and sends these data to a curve-fitting (linear) equation relating Lpm flow to voltage. These calibration curves are derived from the calibration curve from each flow controller and are identical to the equations used for the input calculations. These values are then sent to the constituents' calculations subprogram that calculates the percentage of H<sub>2</sub>, C, and O<sub>2</sub>. The current readings of each flow gas, along with selected calculated parameters, are sent as outputs from the flow controller program shown in figure 8.

$\begin{aligned}\text{Total oxygen} &= (2 \times O_2) + CO \\ \text{Total carbon} &= (2 \times C_2H_2) + CO + CH_4 \\ \text{Total hydrogen} &= (2 \times C_2H_2) + (4 \times CH_4) \\ \text{Hydrogen-carbon line percent H} &= \text{total H}_2 / (\text{total C} + \text{total H}_2) \\ \text{Carbon-oxygen line percent C} &= \text{total C} / (\text{total O}_2 + \text{total C}) \\ \text{Oxygen-hydrogen line percent O} &= \text{total O}_2 / (\text{total O}_2 + \text{total H}_2)\end{aligned}$
---

Figure 8. Constituent calculation subprogram equations.

Data points are collected into a local variable data type called "bundle" and sent into a loop variable. During the FALSE condition of the read status case statement (never used because the variable is hard-wired true), a zero value is sent to all array values.

The control system selection case structure receives the bundled data provided. Each case is prewired to receive all available system data. When a new analysis routine or scheme is desired, a subprogram is built to define the method of analysis, and this subprogram is then wired into a new case of the existing case statement. This involves only wiring in the required data from the bundled data packed to a newly written analysis routine. Several control systems have been written and are currently used. They include the screen flow comparison, the bounded CO line, the logarithmic switch, the sine wave switch, and the temperature-only control.

The screen flow comparison simply compares screen flow settings and current readings. A variation of  $\pm 0.03$  is considered to not require correction. The bounded CO line subprogram compares the percent C with a specified value. If there is a variation from this number by  $\pm 0.02$ , the  $O_2$  level is adjusted to bring the value back within specification. The sine wave switch requires that an amplitude, period, and phase angle be preset for each flow gas on the front panel of the subprogram prior to the start of a test. A base level or zero point for the sine wave is then set for each process gas, and the flow rate will then be sinusoidally varied according to the period, phase angle, and amplitude requested. The logarithmic switch varies the flow of each process gas logarithmically if a period for decay and a restart time, over which to calculate the logarithmic curve, are given. The temperature-only control stops the deposition if the temperature or emissivity rises above a preset value.

The change-status case structure receives modified gas settings from the control system case selected and an indication of whether the flow needs to be adjusted. The change-status case structure provides a safety switch that receives all of the data. It first checks to see if a blowout condition has been set and, if so, extinguishes the flame by blowing it out with an excess of  $O_2$  and then sets all of the gas levels to zero. If a blowout condition has not been met, the flows are passed on to the flow control program and the flows are adjusted using the “volts in” subprogram discussed previously.

One of the system’s main advantages comes from the versatility provided by the analysis loop and the analysis section of the control loop. A system model or feedback procedure can be created and placed into a case in the analysis loop case structure with only a very small programming effort. The newly created system model may then run concurrent with the deposition. When data received from the monitoring section do not agree with model predictions or lie outside the error limits of the feedback loop, the system will alter the deposition conditions to bring the deposition into agreement or note the disagreement for future analysis.

## **2.3 Torch Operation**

Gas regulators are opened and pressures used at the inlet of the flow controllers are set during a typical operation. A sample is loaded onto the cooling block, the water flow is started, and the diamond torch software is run through the setup procedures. Next, the optics of the pyrolaser is focused on the sample deposition region and the pyrolaser data are checked on screen. The deposition parameters or the software control method is set as previously mentioned, and the torch is then lit away from the sample. In bringing the torch over the sample, the sample is covered with a shield, typically of stainless steel or Al. Once the torch is in position, the shield is quickly removed and the sample is exposed to the flame. The normal torch tip for all experiments is a size 1 torch tip, which corresponds to a 0.040-in. hole. Torch tip design will be covered more fully in the description of the experiment dealing with torch tip modification.



## 2.4 Sample Preparation

The samples were rough polished with alumina ( $\text{Al}_2\text{O}_3$ ) grit to a rough mirror-like finish. They were then washed with acetone, followed by a thorough deionized water rinse. The operation and the sample preparation is common to all of the torch deposition experiments, with the exception of the silicon carbide (SiC) substrates, which were used in an as-supplied condition.

## 2.5 GAMoly Experiment

The acronym GAMoly stands for gas additions on molybdenum substrates. This designed experiment started in a region of diamond growth as defined by the three-component diagram compiled by Bachmann.<sup>9</sup> The total amounts of C,  $\text{H}_2$ , and  $\text{O}_2$  were kept so that the deposition remained within this region, while varying amounts of CO and  $\text{CH}_4$  were added to the process gases of  $\text{C}_2\text{H}_2$  and  $\text{O}_2$ . The experiment was run to maintain a constant flow rate and constant gas ratio. Temperatures during deposition were maintained at 800–850 °C for the first hour. Thereafter, the temperature was allowed to run with only periodic corrections where applicable. For substrates, one end of a threaded Mo rod was polished to provide a deposition surface. The rod was then threaded into a receptacle in a cooling block mounting plate as shown previously. The temperature of the substrate may be altered by turning the screw and thus increasing or decreasing the distance between the hot substrate surface and the interface with the cooling block mounting plate. The temperature is controllable to within 10 °C when this substrate is used.

Looking first at the process gases chosen for addition, CO was selected because it is suspected to be an atomic precursor to diamond embryo. Because CO is possibly the most stable species in the flame-feather environment, it was suspected that it might have a strong effect on embryos but should not affect a surface nucleation process as strongly. Methane was chosen because of the high amount of  $\text{H}_2$  it adds to a mixture and because of the postulations by Frenklach and Spear<sup>158</sup> that the  $\text{CH}_3$  radical might be the precursor to diamond embryo.

A design experiment shown in table 2 was put together using only the addition of CO and  $\text{CH}_4$  as factors. The experiment was run to account for quadratic effects on the primary factors and interactions. It also allowed for interaction between factors. This experimental design was chosen based on preliminary trials with addition of the gases that showed a marked change in flame structure. This change in flame structure was an excellent indication of a change in the gas-phase environment since it was felt that if nucleation were initiating in the gas phase, then the addition of CO and  $\text{CH}_4$  would have some effect. The limits chosen for the addition of gas were based on the blowout limits of the flame using flow parameters that were known to produce reasonable diamond films. For practicality, these limits were then reduced slightly to facilitate the reasonable maintenance of a flame.

Three  $\approx$ 60-min periods were used for each sample run. They were approximate because the Macintosh internal clock that was accessed for timekeeping the Macintosh IIX is constantly a fraction of a percent off. These runs were later glued together for data analysis. During each run, the temperature and the surface were constantly monitored automatically, as discussed above, and also manually. For several of the runs, a large C buildup would occur very quickly (1 or 2 min) and would form a large spike that would grow up into the flame. These large spikes would quench the flame when they reached a sufficient height. When these blowouts occurred, the flame was immediately relit and the C spike was broken off and removed to allow the experiment to run its course. At the completion of the experiment, the flame was immediately

removed from the substrate and extinguished at a distance away from the substrate. Every attempt was made to leave the surface inviolate following the deposition; and in most cases, optical photographs were taken soon after deposition.

Table 2. Designed experiment for GAMoly trials.

Run No.	CO Addition (sLpm)	CH <sub>4</sub> (sLpm)	Optical Microscopy (Qualitative Rating)	Raman Linewidth (cm <sup>-1</sup> )	AFM Hardness (100) (kg/mm <sup>2</sup> )	AFM Young's Modulus (100) (GPa)	AFM RMS (100) (RMS Å)	AFM Ra (100) (Å)	AFM Hardness (111) (kg/mm <sup>2</sup> )	AFM Young's Modulus (111) (GPa)	AFM RMS (111) (RMS Å)	AFM Ra (111) (Å)	Raman to Back-ground Intensity (Delta Counts)
1	—	0.1	—	—	—	—	—	—	—	—	—	—	—
2	—	0.2	—	—	—	—	—	—	—	—	—	—	—
3	—	—	—	—	—	—	—	—	—	—	—	—	—
4	—	0.2	—	—	—	—	—	—	—	—	—	—	—
5	—	0.1	—	—	—	—	—	—	—	—	—	—	—
6	—	—	—	—	—	—	—	—	—	—	—	—	—
7	—	—	—	—	—	—	—	—	—	—	—	—	—
8	—	0.1	—	—	—	—	—	—	—	—	—	—	—
9	—	0.2	—	—	—	—	—	—	—	—	—	—	—

## 2.6 Gas Flow and Substrate Experiment

The gas flow and substrate experiment was undertaken to look at the effects of changing the gas flow rate and the substrate. The deposition gases used for this experiment were C<sub>2</sub>H<sub>2</sub>, O<sub>2</sub>, and CO, with substrates of Cu, SiC, or Mo. Since the flow rate and the molar gas ratio are linked, a program had to be written that would find flow rates with identical proportions of C, H<sub>2</sub>, and O<sub>2</sub> (i.e., it had to remain consistently on the same point of phase space in the diagram developed by Bachmann<sup>9</sup>). This program and its results are shown in the appendix on developed computer software.

A designed experiment, shown in table 3, was put together using only the change in substrate type and the flow rate as factors. The experiment was run to account for quadratic effects on the primary factors and interactions. It also allowed for interaction between factors. This experimental design was chosen based on tests we performed experimenting with different substrates and on literature work suggesting an effect due to flow rate. Preliminary work with alternate materials had shown a strong change in surface structure based on the substrate used for deposition. For the Mo substrates, the polished screw tops were used just as in the GAMoly experiment. For Cu substrates, polished mounting plates were used without modification. For the SiC substrates, Union Carbide 1/8-in.-thick substrates were used. The SiC was attached to a thin Cu mounting plate using C adhesive residue produced during torch deposition of other samples.

Each experiment run consisted of one 90-min segment. The shorter run time was used to accentuate the effect of flow rate. The temperature was held constant for each of the runs. At the completion of the experiment, the flame was immediately removed from the substrate and extinguished at a distance away from the substrate. Every attempt was made to leave the surface inviolate following the depositions, and in most cases, optical photographs were taken soon after deposition.

Table 3. Designed experiment for flow trials.

Run No.	Substrate Type (Cu/Mo/SiC)	Flow Rate (sLpm)	Raman Linewidth (cm <sup>-1</sup> )	Optical Microscopy (Qualitative Rating)	Raman D/G Intensity (Delta Counts)	Raman Linewidth Adj. (cm <sup>-1</sup> )	Hexagonal Diamond Peak (Qualitative Measurement)	Raman D/A Intensity (Delta Counts)
1	0	3	—	—	—	—	—	—
2	0	6	—	—	—	—	—	—
3	0	8	—	—	—	—	—	—
4	1	3	—	—	—	—	—	—
5	1	6	—	—	—	—	—	—
6	1	8	—	—	—	—	—	—
7	2	3	—	—	—	—	—	—
8	2	6	—	—	—	—	—	—
9	2	8	—	—	—	—	—	—

## 2.7 Torch Tip Modification Experiments

For these experiments, the gas phase nucleation environment was affected by modifying the shape of the torch tip nozzle. Several very useful discussions were held with Fred Stepner and Jerry Mitchell of the Uniweld Torch Company on the practical structure and properties of torch flames and how tip modifications affect properties of the flames. For the first experiment, a two-factor design was conducted as shown in table 4; however, no quadratics or interactions were considered this time. The two factors were substrate type and the use of a normal or modified torch tip. Each experimental run consisted of one 60-min run on SiC substrates. The torch tips used in this experiment were type 1 torch tips made by Uniweld. The size of a type 1 torch tip exit-plane surface is defined by a No. 60 drill hole (0.040 in.) drawn down from a No. 53 drill hole (0.060 in.). The drill hole is drawn down such that the length of the No. 60 drill hole section is at least five times the inner bore of the hole. Modification to a No. 1 torch tip for this experiment was performed at Charles Jewelers in Huntsville, AL. The torch tip was initially a welding tip from Uniweld, type 13, size 1. A “cone bur” was used to bore out the exit region of the torch tip. The cone bur had dimensions of 1.25 mm high and 1.35 mm in diameter. The imprint left by the bur was 1.27 mm in diameter at the exit plane of the torch tip. This was measured using a high magnification micrometer at the jeweler’s facility.

Table 4. Gas tip modification designed experiment.

Run No.	Gas Modification (CO-CH <sub>4</sub> )	Tip Type (N-M)	Raman Linewidth (cm <sup>-1</sup> )	Optical Microscopy (Qualitative Rating)	Raman D/G Intensity (Delta Counts)	Raman D/A Intensity (Delta Counts)	Hexagonal Diamond Peak (Qualitative Measurement)	Raman Linewidth Adj. (cm <sup>-1</sup> )
1	0	0	—	—	—	—	—	—
2	1	0	—	—	—	—	—	—
3	0	1	—	—	—	—	—	—
4	1	1	—	—	—	—	—	—

The second experiment was conducted using the modification of the tip and substrate type as the two factors. This is shown in table 5. At the completion of the experiment, the flame was immediately removed from the substrate and extinguished at a distance away from the substrate. Every attempt was made to leave the surface inviolate following the deposition and, in most cases, optical photographs were taken soon after deposition.

Table 5. Designed substrate tip experiment.

Run No.	Tip Type (N-M)	Substrate Type (Cu/SiC)	Raman Linewidth (cm <sup>-1</sup> )	Optical Microscopy (Qualitative Rating)	Raman D/G Intensity (Delta Counts)	Raman D/A Intensity (Delta Counts)	Hexagonal Diamond Peak (Qualitative Measurement)	Raman Linewidth Adj. (cm <sup>-1</sup> )
1	0	0	—	—	—	—	—	—
2	1	0	—	—	—	—	—	—
3	0	1	—	—	—	—	—	—

## 2.8 High-Velocity Oxygen Fuel Gun Experiments

A great number of applications for which diamond provides excellent coating properties require a low coating cost, a reasonable coating deposition time, and the ability to coat large complex structures. The purpose of this work was to examine the feasibility of the HVOF diamond jet gun as a diamond-coating application procedure. HVOF<sup>159</sup> is typically used in the thermal spray industry involving the continuous internal combustion of O<sub>2</sub> and a fuel gas within an air-cooled chamber. After combustion, a powder (typically ceramic or metal) is fed axially into the flame-front gas stream. The flame is characterized<sup>159</sup> by a high-velocity plume capable of accelerating the powder to supersonic speeds. Flame velocities exiting the nozzle can be in the range of 4,000 to 4,500 ft/sec. This compares to a conventional combustion flame velocity of 300 to 500 ft/sec.<sup>160</sup> Temperature is a critical consideration in the ability to deposit diamond coatings. Unlike many of the combustion production methods, the heat flux onto a sample used for HVOF deposition is extraordinarily high. Our goal in this series of experiments was to show that the combustion environment of the HVOF allows the deposition of C, preferably in the form of diamond, as a coating onto a Mo substrate using HVOF. The advantage of the HVOF method is that the high heat loads were caused by very high mass-transport rates. The high mass-transport rates and the yield efficiency of the combustion methods in combination provide a reasonable coating deposition time for large-scale complex structures in an ambient environment.

### 2.8.1 Background

High-quality diamond films have been produced at high deposition rates at atmospheric pressure using a variety of combustion methods. First among these are the O<sub>2</sub>-C<sub>2</sub>H<sub>2</sub> torch and the plasma jet.<sup>89</sup> A comprehensive collection of deposition chemistries was put together by Bachmann<sup>9</sup> on the backdrop of a C, H<sub>2</sub>, and O<sub>2</sub> molecular percentage diagram. The Bachmann<sup>9</sup> diagram indicated that although the absence of appropriate thermal or surface structure conditions could certainly inhibit nucleation/growth, successful nucleation and growth of diamond had only occurred in a section of diagram space bounding the CO line.

The HVOF diamond jet gun was selected because of the high flame turbulence and the ability to tailor combustion precursors to mimic the successful results in  $O_2$ - $C_2H_2$  flames. Turbulent flames have been noted for an ability to provide higher quality diamond films with correspondingly lower growth rates in comparison to their laminar counterparts.<sup>81,82</sup> Mixing of the turbulent flame species can be one to two orders of magnitude larger than that in laminar flames due to the presence of eddies. Simulations of the primary flame environment were attempted using the two-dimensional kinetics (TDK) combustion computer code.

Previous work, modeling the combustion process for HVOF,<sup>161</sup> used the CONCOM computer code to calculate the exit conditions in a convergent nozzle combustion gun using propene ( $C_3H_6$ ) as a fuel. Their code input involved combustion product flow rates, specific heat of the mixture, combustion temperature, stagnation pressure, and nozzle geometry. They assumed that the combustion and mixing took place in the converging nozzle, the combustion temperature occurred at the exit plane of the nozzle, the Mach number was 1.0, and the combustion products acted as a perfect gas. A two-dimensional axisymmetric model called TORCH was used to solve mass, energy, and conservation equations.<sup>61</sup> Particles were predicted to lie within 2 mm of the plume centerline for their experimental conditions. Matsui<sup>74</sup> has also done an excellent simulation on diamond  $O_2$ - $C_2H_2$  torch deposition using the equilibrium concentrations and the thermochemical data in the Joint Army-Navy-Air Force tables. Matsui<sup>74</sup> notes that the main gaseous species are CO and  $H_2$ , an encouraging relation to our own simulation results.

### 2.8.2 Experimental

Molybdenum sheet squares (74.8 mm) of 0.232-mm nominal thickness were used as substrates. A windowpane cooling block was fabricated to provide a heat sink for the Mo substrates. The cooling block was produced from a solid block of Cu. A cavity  $\approx 15$  mm deep and 75.5 mm square was milled in the block for the substrates to lie in. Substrates were placed with their edges under the window frame and a face oriented toward the flame. The window frame was secured by four screws positioned on the corners of the frame. Water flow of  $\approx 50$  gal/min was provided through the cooling block during each of the test runs. The entire cooling block was held in a clamp stand so that the substrate face was perpendicular to the floor. The diamond jet gun was held in place using a Miller Thermal model 6000 positioning robot. Conventional process gases were brought from pigtailed bottles through Metco flow controllers into the diamond jet gun. Three experiments, one gas flow and two liquid toluene ( $C_7H_8$ ), were performed in an effort to deposit C onto a water-cooled Mo sheet. A coincident TDK computer simulation was run in parallel with the most successful experiments.

### 2.8.3 High-Velocity Oxygen Fuel—Carbon Monoxide Gas Flow Trials

The gas flow experiment was conducted with process gases of air,  $O_2$ , CO, and propylene. Carbon monoxide feed gas was brought in from a gas bottle through a regulator and a safety check valve to the power feed connection of the diamond jet gun. The regulator and the safety check valve were purposely oversized to allow for the highest flow rate and the greatest pressure against the combustion back pressure (into the powder flow tube). The feed tube for CO was shortened to provide better flow, reduced back pressure, and better upstream gas mixing prior to combustion. Trial runs were conducted to determine blowout limits of the flame with increasing additions of CO. Because of the difficulty inserting enough CO into the flame, the experiments were run with as high a gas throughput as possible. This was achieved by running without a regulator on the bottle of CO and by oversizing all check valves. The measurement of

CO addition was taken as regulator bottle pressure since each bottle was used “wide open.” When 50 passes across the substrate surface were successfully made, the test was considered complete.

Ratio calculations were performed to determine the amount of CO required to bring the carbon-hydrogen-oxygen (CHO) bond ratio into the diamond growth region as defined by the CHO diagrams produced by Bachmann et al.<sup>9</sup> The flame was initiated as fuel-rich as possible without blowing out. The calculation results are shown in figure 9 using constant amounts of O<sub>2</sub> and fuel.

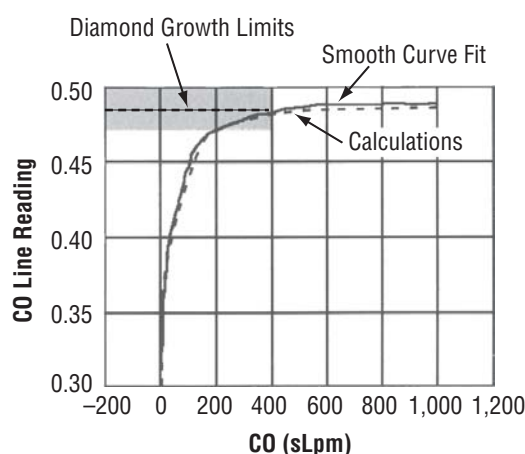


Figure 9. Carbon monoxide addition versus CO line position as relevant to Bachmann diagrams.

Clearly, relying on bottled gas, we were unable to achieve appropriate gas flow rates of CO assuming the flame would be stable in that region. A six-run designed experiment was conducted to examine the effect of CO addition and distance to the substrate. Distance to the substrate incorporates several factors, among them are surface temperature (since cooling is constant rate) and position in flame of the substrate (species concentration is relative to the position in the flame).

#### 2.8.4 High-Velocity Oxygen Fuel—Toluene Fluid Flow Experiments

For the liquid flow experiments, C<sub>7</sub>H<sub>8</sub> was pumped using an FMI lab pump, model QV metering pump, with an FMI stroke-rate controller, model v100. The liquid was put through a standard powder feed tube to deposit the liquid into the combustion region. In both the liquid and the gas experiments, deposition occurred during successive scans of the diamond jet gun across the exposed substrate surface. Ratio calculations were performed to bring the CHO ratio into the diamond growth region as defined by Bachmann.<sup>9</sup> Temperature measurement was attempted with a Pyrolaser optical pyrometer; however, the pass rate of the robot across the substrate required that the pyrometer be synchronized with the robot movement to get accurate measurements of the surface as the flame front passed across the substrate. This was not feasible with our equipment, so a rough temperature of 900 °C was assumed based on the readings we were able to obtain. By setting the O<sub>2</sub> constant at 27.187 sLpm and the propylene constant at 7.27 sLpm, we developed a chart showing the effect of C<sub>7</sub>H<sub>8</sub> addition on species relative to the CO line on the Bachmann diagram (fig. 10). The initial results of flame compositions within the diamond region suggested that our surface temperature was above that recommended for growth of diamond on Mo and above the 900 °C we had



assumed. We therefore designed the two experiments shown in table 6 with the aim of C deposition based on the perceived safety limits of the diamond jet gun and the assumption that we were above the temperature region in which diamond growth was feasible.

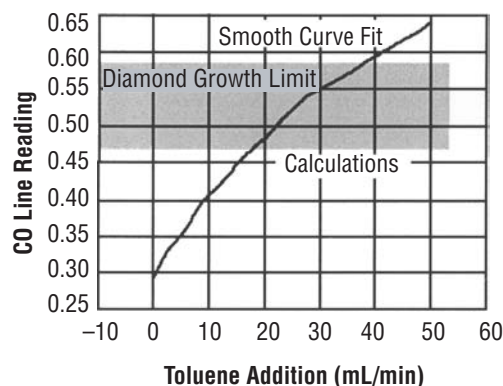


Figure 10. Toluene addition relative to CO line position on a Bachmann diagram.

Table 6. Designed experiments for  $C_7H_8$  addition.

Run No.	Distance (in.)	Amount of $C_7H_8$ (mL/min)	Amount of C (cps)	Run No.	Distance (in.)	Amount of $C_7H_8$ (mL/min)	Amount of C (cps)
1	8	35	—	1	8	70	—
2	14	35	—	2	20	70	—
3	8	105	—	3	8	105	—
4	14	105	—	4	20	105	—

## 2.9 Two-Dimensional Kinetics Simulations

Simulations were run for both the  $O_2-C_2H_2$  torch and the HVOF flame. The simulations utilized the TDK nozzle-performance evaluation software.<sup>162</sup> This software was developed for analysis of nozzle combustion flow fields. The TDK program is commonly used in the analysis of exhaust plume gas-phase constituents for rocket nozzles. The TDK program is well adapted for nonequilibrium chemical processes. The characteristic equations governing the fluid dynamic variables are integrated using a modified Euler-explicit integration method, with the chemical relaxation equations integrated by a first-order implicit integration method to ensure numerical stability in near equilibrium flows.<sup>162</sup> A full discourse on the procedure and numerical methods used can be found in reference 162.

A trial simulation experiment was run in parallel with the GAMoly experiment, and a simulation was performed in parallel with the HVOF  $C_7H_8$  addition experiment. The simulation results provide calculated flame temperatures and equilibrium concentrations of radicals present in the flame as a function of combustion gases. The variation in combustion gases during the experiment in progress provides us with possible differences in the species available for embryonic nucleation and macroscopic film growth affecting the final film structure and composition. The parallel nature of the simulation and the experiments allows us to correlate the results of the simulation with experimental analysis on the obtained sample depositions.

### 3. ANALYSIS METHODS

There have been three principal analysis methods used for this work—optical microscopy, Raman spectroscopy, and atomic force microscopy (AFM). A few scanning electron micrographs were taken for samples resulting from the HVOF diamond jet work; however, in general, the charging on diamond was sufficiently high to have created difficulties in the use of electron microscopy. In this section, a state-of-the-art review of each technique is presented as well as the specific procedures used in this research. A standard approach for optical microscopy and Raman spectroscopy was used. A novel approach was developed for determination of hardness and Young's modulus numbers for the AFM portion of the work.

#### 3.1 Optical Microscopy: A Study of Morphology

Diamond coordinates each C atom to four other C atoms using  $\sigma$  bonds arising from  $sp^3$  hybrid atomic orbitals. Two methods of stacking of layers are possible—cubic (fig. 11) and hexagonal (fig. 12). If the bonds between layers are staggered, the structure is the more common cubic diamond. If the bonds are eclipsed, the hexagonal form of diamond called lonsdaleite develops.<sup>163</sup> The eclipsed bonds in lonsdaleite produce a greater repulsive interaction between nearest neighbors.<sup>163</sup>

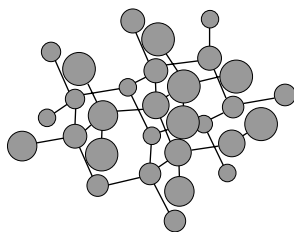


Figure 11. Cubic diamond showing staggering of interlayer bonds.

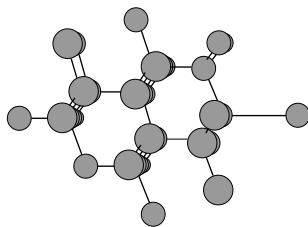


Figure 12. Hexagonal diamond showing eclipsed bonds.

Diamond films typically fall into one of two growth regimes: One dominated by aggregation of clusters, ballistic particles, and fractal geometry and the other controlled by the energetics of crystal faceting.



Looking first at the region dominated by ballistic particle interaction, thin film morphology is generally classified into structure zone models.<sup>164</sup> These structures have been shown to have a strong similarity over six orders of magnitude in film thickness and three orders of magnitude in magnification for a given thickness.<sup>164</sup> The common link for anisotropic amorphous and microcrystalline thin film morphology is the preparation of films in conditions of low mobility ( $T/T_m < 0.5$ ). Approaches to classification of this morphology have included atomic shadowing, selective diffusion and nucleation, coalescence-induced void formation, stability of surface irregularities, energy minimization of topology, and cone growth.

Two types of nucleation and growth are considered in the case of cone growth—singly nucleated and regeneratively or continuously nucleated.<sup>164,165</sup> For pyrolytic graphite, the aspect ratio of the cones of the singly nucleated films is much higher and all of the cones appear to nucleate on the surface. For the continuously nucleated case, new nucleation centers are constantly formed throughout the thickness of the films. Cone growth is a fractal construction (bounded) in that it can be carried on as long as desired and the geometrical shape would remain constant through the corresponding orders of magnitude of magnification, which would return to the initial cone size.<sup>165</sup> Cone growth appears to be relevant for films with strong amorphous content or diamond films that are predominantly microcrystalline. Although diamond films are typically grown under conditions such as  $T/T_m = 0.3$ – $0.4$ , most diamond films may be classified as large grained.<sup>166</sup> Indeed, most of the results shown in the literature indicate that the growth is obviously controlled by the energetics of crystal faceting.

Much of the literature on diamond morphology deals with the formation of the  $\{100\}$  and  $\{111\}$  planes as these are the two most commonly grown surface planes in diamond deposition. An early but comprehensive paper by Kobashi et al.<sup>167</sup> clarified the different regions of morphology based on  $\text{CH}_4$  content in CVD-based films. Films are shown to clearly indicate columnar growth. Whether this is cone or columnar growth is questionable. At low  $\text{CH}_4$  concentrations of  $< 0.4$  percent, the film surfaces are predominantly  $\{111\}$ . Above 0.4 percent, the morphology changes rather completely to  $\{100\}$  planes appearing on the surface. Methane microcrystalline features predominate above  $\approx 1.2$  percent. They note that in competition between  $\{100\}$  faces, some of the  $\{100\}$  faces appear to overlap as a consequence of interference during growth.<sup>167</sup> They reference Messier<sup>166</sup> to note that the grain that is most perpendicular to the substrate plane takes over. If this is the case, then the planes would become more perpendicular to the substrate as the deposition proceeds. Setaka<sup>21</sup> also observes this phenomena. The important results are the use of traditional or low-mobility cone growth to describe the microcrystalline growth and the relevance of crystal energetics in describing faceted growth.

In looking at diamond synthesis at 0.3-percent  $\text{CH}_4$ , Setaka<sup>21</sup> notes that initial particles have a cuboctahedral shape and that no nucleation starts between particles. Subsequently, the well-defined faces enlarge and step structures are seen on the  $\{100\}$  faces. In contrast, they note that no growth structures are seen on the  $\{111\}$  faces. When they increase the  $\text{CH}_4$  concentration, they note that when the substrate is covered, a secondary growth takes place between the particles. Resulting from a 1.2-percent concentration of  $\text{CH}_4$ , the substrate starts out with a coverage of small  $\{100\}$  grains, a secondary growth then covers, and the existing faces enlarge as the result of a 1.2-percent concentration of  $\text{CH}_4$ .<sup>21</sup> The large faces eventually dominate the growth region. Once the surface is composed of well-defined  $\{100\}$  faces, a tertiary growth of small crystallites begins again. This process appears to repeat cyclically for them.<sup>21,168</sup> They note that the  $\{100\}$  faces result from anisotropic growth of the film and contradict the periodic bond chain (PBC) theory used for high-pressure diamond growth.

Williams and Glass corroborated the effects of  $\text{CH}_4$  on the surface morphology of diamond.<sup>169</sup> For lower concentrations, the  $\{100\}$  appears to be the fastest growing plane with some  $\{111\}$  planes present, and for higher concentrations, the  $\{111\}$  planes grow faster and a few  $\{100\}$  planes are present. They also note surface steps on both sets of facets and suggest a two-dimensional growth process. Secondary nucleation was noted to have an orientational relationship for  $\{111\}$  faces; however, on the  $\{100\}$  grains, nucleation was predominantly between grains and was randomly oriented.<sup>170</sup>

Je and Lee<sup>170</sup> presented work on the  $\text{CH}_4$  dependence, substrate pretreatment dependence, and a temperature dependence of the surface morphology change between  $\{100\}$  and  $\{111\}$  planes. Their results agree with the results from reference 169 and others for the increase in  $\text{CH}_4$  concentration. They, however, propose that the change in morphology can be well explained by the initial surface growth of the particles.<sup>170</sup> With a high substrate temperature, a low deposition rate, and a low concentration of chemical species, they note that absorbed particles have enough time to diffuse on the surface to energetically favorable positions (i.e., the  $\{111\}$  plane). Where the conditions were opposite of the above, the amount of time would favor a less dense plane (i.e., the  $\{100\}$  plane). They attribute the change of the surface plane from  $\{111\}$  to  $\{100\}$  to an increase in the concentration of chemical species. The increase in concentration also relates to the apparent effect of substrate temperature. An increase in substrate temperature increases the amount of decomposed  $\text{CH}_4$  and increases the surface mobility.

Derjaguin et al., from Kobashi,<sup>167</sup> determined growth rates in the  $\langle 111 \rangle$  and  $\langle 100 \rangle$  directions. Upon increasing the substrate temperature, the crystal habits changed from regular octahedral to cubic. This would explain conflicting results. It also helps to explain the effect of substrate pretreatment that they observed.<sup>170</sup> They suggest that the material used for pretreatment and the pretreatment method affects the crystallinity and the nucleation density. They witnessed  $\{111\}$  surfaces for ultrasonically treated (with diamond in water) substrates and  $\{100\}$  surfaces for abraded diamond surfaces. With respect for deposition time and sample thickness, they noted that in their depositions there was a facetless phase on the contact boundary between the growing particles. The “nondiamond percentage” is greater when there are more crystal boundaries and more of this facetless phase.

Wild et al.<sup>171</sup> have provided an alternate explanation for the competition between  $\{100\}$  and  $\{111\}$  facets, which describes well their work on smooth  $\{100\}$  faceted diamond films and also appears to fit well with the predominance of current experimental results. They apply the model of evolutionary growth described by Van Der Drift based on a lack of secondary nucleation and a crystalline morphology independent of the crystallite orientation as in the example of high surface diffusion. They clearly explain the main determinant of film texture as the direction of fastest growth. During the growth process, more and more grains are buried by neighboring grains. The degree of texturing increases with increasing thickness such that the crystals with the direction of fastest growth perpendicular to the sample substrate will survive.<sup>171</sup> As the growth rate of the  $\{100\}$  faces increases with relevance to the  $\{111\}$  face, the growth habit progresses from left to right, as shown in figure 13. Most telling is the arrow pointing along the direction of fastest growth for each crystal.

Putting this model to work in simulation, they noted that the film surface is completely covered by  $\{100\}$  facets. This is an interesting contrast to crystal growth where the fastest growing surface typically grows to extinction and the slower growth surfaces remain. In their work, they describe a two-step CVD process that starts with preferred texturing and then progresses to a high growth rate to seal the surface with

the  $\{100\}$  facets. The process of Wild et al.,<sup>171</sup> however, does not account for twinning as in hot filament films, which exhibit a  $\langle 110 \rangle$  texture and a  $\{111\}$  surface regardless of growth conditions.

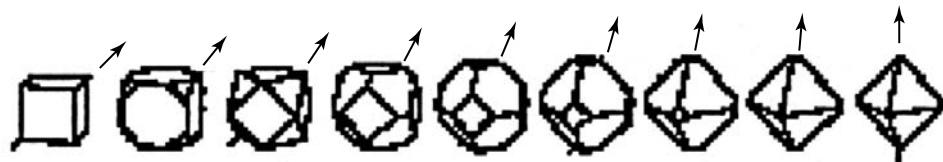


Figure 13. Competition between  $\{100\}$  and  $\{111\}$  facets, growth habit progressing left to right.

Sun et al.,<sup>172</sup> using HREE LS data, present a corresponding argument for the surface species of  $\text{CH}_4$  and  $\text{C}_2\text{H}_2$ , dominating the development of morphology. Their results correlate well with observed temperature dependencies and with  $\text{CH}_4$  concentration results. They suggest that, based on homoepitaxial measurements,  $\{111\}$  growth is controlled by  $\text{C}_2\text{H}_2$  so as the surface concentration increases, so does the  $\{111\}$  character of the deposit.<sup>172</sup>

A similar cutoff point for microcrystalline versus faceted growth involving deposition pressure was noted in an early paper by Kikuchi et al.<sup>173</sup> and later by Kweon and Lee.<sup>174</sup> The two reports produced opposing results. Kikuchi et al. indicated that lower pressures produced microcrystalline growth where faceted growth occurred for higher chamber pressures. Kweon and Lee, however, found that the conditions with lower pressure produced smooth cuboctohedral shapes whereas the higher pressure deposition produced smooth  $\{100\}$  faces and rough  $\{111\}$  faces. Because of the small particles on the  $\{111\}$  faces, they note that the  $\{111\}$  faces disappear and only  $\{100\}$  faces are observed. In referring to previous work by Zhu,<sup>175</sup> they note that graphite preferentially deposits on the  $\{111\}$  planes, thus suppressing the  $\{111\}$  growth. A similar result is attributable to  $\text{O}_2$  concentration in both hot filament<sup>176</sup> and ECR systems.<sup>52,53</sup>

Hirabayashi<sup>176</sup> considers that two-dimensional crystal growth is controlled by the waiting time for the nucleation and the time for lateral growth across the surface. Microstructures on the  $\{111\}$  faces of hot filament CVD change when  $\text{O}_2$  is added to the source gas. A change in surface morphology occurs between 0.7 and 0.8 oxygen-to-carbon (O/C) ratios when looking across an O/C of 0.5–0.8. The change goes from a growth mode, where the nucleation wait time is much less than the coverage wait time, to the converse, then from a multinucleation mode to a single nucleation growth model.<sup>176</sup> They suggest that without the addition of  $\text{O}_2$ , even for low growth rates and low  $\text{CH}_4$  concentrations, secondary nucleation will occur on the surfaces. With the addition of  $\text{O}_2$ , the graphite, which is typically formed on the  $\{111\}$  faces and inhibits diamond growth, is removed at high O/C ratios, where the OH radicals remove the diamond, leaving clean  $\{111\}$  surfaces for growth of diamond from  $\text{C}_x\text{H}_y$  radicals.<sup>10</sup>

Using growth rate readings and a local feed of both  $\text{CH}_4$  and  $\text{C}_2\text{H}_2$ , Sun et al.<sup>172</sup> arrived at different growth species for the  $\{100\}$  and  $\{111\}$  faces in hot filament CVD. Their results indicate that both  $\text{C}_2\text{H}_2$  and  $\text{CH}_4$  contribute to growth of the diamond  $\{111\}$  face. In conjunction with Frenklach's mechanism,<sup>177</sup> they suggest that  $\{111\}$  facets consist of  $\{111\}$  faces and  $\{110\}$  growth steps. They suggest that in a two-stage formation mechanism, a kernel is first nucleated by  $\text{H}_2$  abstraction and either  $\text{CH}_4$  or  $\text{C}_2\text{H}_2$  addition. In the propagation stage, the  $\{111\}$  face is grown only using  $\text{C}_2\text{H}_2$ . Unlike Frenklach's mechanism, they note that the ledges form at about the same rate as they grow, such that the rate-limiting step is the surface

concentration of  $C_2H_2$  to propagate the growth planes.<sup>172</sup> For the  $\{100\}$  faces, only  $CH_3$  is utilized as a growth species. They reconciled the  $1\times 1$  reconstruction as a low-temperature reconstruction and the  $1\times 2$  reconstruction as a higher temperature effect likely to occur during diamond deposition.<sup>172</sup>

In ECR depositions, the addition of small amounts of  $O_2$  changes the morphology from predominantly  $\{111\}$  to a mixture of  $\{111\}$  and  $\{100\}$ .<sup>52</sup> For O/C ratios up to 0.5, the cauliflower morphology dominates when the O/C climbs into the regions between 0.7 and 1, and strong  $\{111\}$  facets dominate. Large crystallites form with near perfect  $\{111\}$  facets and elongated  $\{110\}$  surfaces above an O/C of 1.5 but below 2.<sup>53</sup> Miyata et al. present very similar work considering the morphology change using the addition of diborane ( $B_2H_6$ ).<sup>178</sup> Using growth conditions that typically produced  $\{111\}$  surfaces, increasing  $B_2H_6$  addition was shown to suppress diamond nucleation or to significantly slow the growth, eventually providing a graphite surface layer. For conditions in which undoped would produce  $\{100\}$  surfaces, increasing  $B_2H_6$  rapidly changed the morphology to a  $\{111\}$  surface and then again brought on graphite growth.<sup>178</sup>

Some of the first papers on diamond identified  $\{110\}$  faceting of diamond.<sup>178–181</sup> In 1983 the landmark paper by Matsumoto and Matsui<sup>179</sup> showed electron micrographs and x-ray diffraction (XRD) patterns of single crystalline particles with the  $\langle 110 \rangle$  orientation. The nearly perfect five-fold symmetry shown by their particles led them to postulate a twinning mechanism for  $\{110\}$  facet formation.<sup>182</sup> Narayan et al.<sup>154</sup> propose a model for nucleation and formation of five-fold diamond microcrystallites. They also agree that twinning in the  $\{111\}$  planes produces the observed  $\{110\}$  oriented microcrystals. They suggest that the crystals nucleate at a surface step on the  $\{001\}$  plane of the substrate and as soon as one crystal nucleates, the others are formed by twinning.<sup>154</sup>

Based on the model of evolutionary selection, Wild et al.<sup>180</sup> showed that the  $\langle 110 \rangle$  direction was the direction of fastest growth when the appropriate twinning mechanisms are active.<sup>180</sup> They complement this study with films of  $\{100\}$  texturing which will be addressed later. Kobashi et al.<sup>181</sup> looked at  $\langle 110 \rangle$  oriented diamond films grown as bilayer films from Si. They identified regions of morphological growth of  $\{110\}$  planes based on the concentration of  $CH_4$  in the first and second portion of the bilayer films. The morphological dependence they found was quite different from their work on  $\{111\}$  and  $\{100\}$  faceting dependence on  $CH_4$  concentration. In their bilayer films, the characteristic pyramidal features appeared below a concentration of 0.8 percent only in the second layer of the films.<sup>181</sup> These films, however, did show a crossover to  $\{100\}$  faceting at higher concentrations and eventually to microcrystals at high  $CH_4$  concentrations.

### 3.2 Chemical Vapor Deposition Homoepitaxial Morphological Background

Many of the morphological studies have been done on homoepitaxial growth of diamond. Neglecting for the moment the results from work performed using the torch method, the growth and morphology of  $\{100\}$ ,  $\{110\}$ , and  $\{111\}$  surfaces have been studied. The PBC theory has been used successfully to describe the morphology of natural diamonds. Within the PBC theory, an uninterrupted chain of C–C bonds is called a PBC, and the faces of diamond crystals are classified based on the number of PBC's contained in a surface layer. The  $\{111\}$  face contains more than two PBC's in a layer and is predicted to undergo a layer growth at low C saturations. The  $\{110\}$  face has only one PBC and the  $\{100\}$  faces have no PBC; therefore, they are predicted to have the highest growth rate since no nucleation is needed for growth.<sup>167</sup>

The relevance of the PBC theory for low-pressure deposited diamond is still contested. DeNatale et al.<sup>183</sup> noted a low level of observable defects on their {100} face. Their {111} face exhibited well-defined triangular defects on an otherwise exceedingly smooth surface, and they saw a high degree of surface texture on their {110} face when using a growth temperature of 650 °C in MPCVD. The {110} face also demonstrated a growth rate roughly twice that of the other orientations.<sup>183</sup> Using the PBC theory, they suggest that the high growth rate is due to the presence of a PBC on the surface (providing sites for lateral growth) and a PBC normal to the surface (providing strong bonding for the attachment of the next plane of atoms). The {100} face is not expected to occur in a perfect diamond structure. Based entirely on PBC analysis, they attribute the strong presence of this face to surface reconstruction in the growth environment.<sup>183</sup> This is partially corroborated by AFM atomic level results from Sutcu et al.<sup>184</sup>

Boron-doped homoepitaxial crystals grown on {100} faces of type IIa natural diamond have grown edges aligned with the <110> direction and the corners point in the <100> direction.<sup>185</sup> They refer to the structures as pyramids with a “step-like” structure that, in a later paper,<sup>186</sup> correlate with reconstruction of the {100} plane. This corresponds with Sutcu et al.<sup>184</sup> who observed pyramidal and sharp triangular features on their {100} substrates. They identify the pyramids as {111} faces and the sharp triangular features as penetration twins with a rough {111} face and smooth {100} sides. Everson et al.,<sup>187</sup> by identifying pairs of these triangular features, uniquely determine the slope of the large {111} plane of the triangular feature and confirm the penetration twin structure.<sup>26</sup>

Like DeNatale et al.,<sup>183</sup> Sutcu et al.<sup>184</sup> reconcile the PBC theory with their results by using the proposition of Giling and Van Enckevort that the dimer bonds supplied by the surface reconstruction provide the missing PBC bonds to provide the smooth growth surfaces. They also note that the PBC theory assumes that the unsatisfied valence on the surface atoms remains a dangling bond, where, in CVD diamond conditions, these bonds are most likely saturated with H<sub>2</sub>, thereby forming the monohydride.

Sutcu et al.,<sup>184</sup> on their {110} sample, noted a distinct absence of faceted growth. The deposit consisted of hills with slopes as large as 46°. The importance noted on the absence of faceting is that the {100} and the {111} planes should be exposed locally on the surface with angles of 45° {100} plane and 35.3° {111} plane. As these planes are exposed to the growth environment, their absence suggests that growth of the {110} plane is at least partially stable. Correspondingly, Zheng, from DeNatale et al.,<sup>183</sup> reports a lower oxidation rate for {110} than {111} or {100} faces, suggesting that atoms on the {110} face have a higher bonding energy. The {111} homoepitaxial film of Sutcu et al.<sup>184</sup> underwent a significant amount of cracking.

DeNatale et al.<sup>183</sup> suggest an effect of incorporated graphite to spur growth rates larger than those that would be derived from layer-by-layer growth rates. Hu et al.<sup>188</sup> use reflection electron microscopy to show cleaving grooves along the <110> direction when using a {111} 2b substrate. These cleaving grooves are well explained by rapid lateral growth (as predicted by PBC) and fractures on epitaxial {111} surfaces as observed above. Variations in growth conditions are capable of producing smooth films on {110} and {111} diamond surfaces.<sup>189</sup> The CH<sub>4</sub> conditions for growth of smooth {100} surfaces appear to be higher than those required for {111} surfaces.<sup>189</sup>

Looking at work on the surface structuring of diamond faces during growth, the structure is not yet completely clear. On a {111} surface, Sun et al.<sup>190</sup> first noted that H<sub>2</sub> abstracts adsorbed H<sub>2</sub> on the {111}



surface and then replaced atoms adsorbed on the  $\{110\}$  steps. Busmann et al.<sup>191</sup> propose an intriguing surface structure for the  $\{111\}$  surface of growing films again, allowing addition of a  $C_2H_2$  molecule where the stabilizing  $H_2$  has been abstracted. They propose a  $(\sqrt{3} \times \sqrt{3}) R30$  reconstruction that takes place on a portion of the  $\{111\}$  surface. They note that a fully hydrogenated surface should be stable against reconstruction for a one-dimensional surface. However for a three-dimensional surface, complete hydrogenation will provide a high surface energy due to the steric repulsion. For the three-dimensional surfaces, on a portion of the surface it will be favorable to reconstruct into two conceivable trimer structures<sup>191</sup> based on hydrogenation of the surface. This, they note, will require, unlike the mechanism of Frenklach,<sup>177</sup> a mechanism with two separate processes for reaction and growth.<sup>191</sup> Lee and Apai,<sup>192</sup> however, note that the  $\{111\}$  surface of diamond undergoes a  $(2 \times 1)$  reconstruction where three rotated domains of  $(2 \times 1)$  symmetry provide an observed  $(2 \times 2)$  pattern. For the  $\{100\}$  faces, a  $(2 \times 1)$  reconstruction seems almost agreed upon during growth.

Sun et al.<sup>190</sup> from RHEED data convincingly suggest that following the mechanism of Frenklach and Spear,<sup>177</sup> on a  $\{100\}$  surface H corrodes the C atoms on the surface first and then saturates the dangling bonds of the next layer. Oxygen, however, at a lower temperature abstracts adsorbed  $H_2$ , allowing addition of a  $C_2H_2$  molecule. Sutcu et al.<sup>184</sup> reconcile the PBC theory with their results by using the proposition of Giling and Van Enckevort that the dimer bonds supplied by the surface reconstruction provide the missing PBC bonds to provide the smooth growth surfaces. Sun et al.<sup>190</sup> propose the  $(1 \times 1)$  reconstruction as a low-temperature reconstruction and the  $(2 \times 1)$  reconstruction as a higher temperature effect likely to occur during diamond deposition.<sup>190</sup> Lee and Apai<sup>192</sup> note, however, that an observed  $(2 \times 2)$  is the superposition of two rotated  $(2 \times 1)$  domains of symmetry that can be reversibly converted to  $(1 \times 1)$  symmetry by H dosing.

### 3.3 Natural Diamond and Other Diamond Morphological Notes

Natural diamonds, as studied by Tolansky,<sup>193</sup> display cube faces with a surface roughness caused by square pyramidal pitting called tetragons. Synthetic diamonds can display faces of both cubic and octahedral forms, depending on the crystallization temperature. A new phase of C has been proposed (H-6, H-8) based on results from the Fe-Ni-C system at HPHT that relates to structures in the electrically conducting surface of CVD diamond.<sup>182</sup> Ideal diamond has a cube length of  $a = 3.567$ , almost 10 percent larger than graphite, but the density of diamond ( $1.77 \times 10^3 \text{ g cm}^{-3}$ ) is 56 percent higher than graphite due to the anisotropy of graphite.<sup>194</sup> Microcrystals of natural diamond show structural differences from macrocrystals of natural diamond. Microcrystals show a similarity with the properties of HPHT synthetic diamond. HPHT synthetic diamond frequently exhibits  $\{110\}$ ,  $\{311\}$ , and  $\{221\}$  distinct plane faces. Microcrystals of diamond have shown a hexoctahedron shape.<sup>195</sup> Because of the similarity in structure, it has been proposed that the formation process used in HPHT diamond is identical to that of microcrystals but not of macrocrystals.<sup>195</sup>

### 3.4 Prior Morphology Studies Using the Oxygen-Acetylene Torch

One of the first studies in the U.S. was conducted by Snail et al.<sup>82</sup> using an oxygen-acetylene ( $O_2$ - $C_2H_2$ ) torch. Note that the annular ring mentioned by other researchers appears absent in their results on abraded Mo surfaces. With run times of 90 min, they obtained cuboctahedrons with well formed  $\{100\}$  facets. By switching their substrates from moly to MoC, they noted similar growth with no apparent change in nucleation density. Using a substrate of DLC deposited prior to diamond deposition, they developed

relatively fine-grained contiguous films.<sup>82</sup> They suggest that the enhancement of diamond nucleation by DLC layers is due to a regasification of C from the DLC providing more C in the near surface gas phase, a solid-state renucleation from DLC to diamond, an increase in the density of surface defect sites for nucleation, or the functioning of the DLC layer as a source of H during deposition.<sup>82</sup> Importantly, in the absence of high nucleation density, the morphology appears to be related to surface energies, growth anisotropies, and the chemistry of the gas in the diamond synthesis ambient.

When substrate temperatures are higher, the cube morphology tends to dominate while octahedral faces tend to form at lower temperatures.<sup>2</sup> There is a large portion of {110} orientation in this region, indicating decomposition from {100} crystals to {111} oriented crystals.<sup>84</sup> This is complemented by studies where the radial temperature distribution is correlated with the dominant growth habit.<sup>85</sup> The growth toward the center of the flame appears dominated by {111} facets. Traveling radially outward, {100} planes start to appear with {111} planes growing or twinning from the {100} planes.

A noteworthy presentation of morphological instability in the low-pressure synthesis of diamond films presents data based on the classification of diamond growth being a combination of diffusion-limited and ballistic aggregation, with the process becoming increasingly ballistic as the growth rate increases.<sup>87</sup> They note that vapor growth is essentially an unstable process where vapor etching is essentially a stable process. By varying only the growth times, they observe an onset of morphological instabilities relating to nutrient starvation and competitive shadowing.<sup>87</sup> Another early look at torch-grown morphologies by Ravi et al.<sup>196</sup> investigates morphology changes, which they identify as an indicator of changes in nucleation.

For the torch process, the effect of precursor composition on diamond synthesis has been studied, using the ratio of feed gases. Typically, this is reported in terms of  $R$ . Surprisingly, this report appears to be the first work that incorporates CO as a feed gas. Hanssen et al.,<sup>68</sup> during some of the earlier torch work in the U.S., found ball-like growth below  $R=0.9$ , well faceted crystals between  $1.2 > R > 0.9$ , and no growth where  $R$  was put above 1.2. Hanssen's XRD patterns showed peaks for {111}, {220}, and {311} orientations.

Carrington et al.,<sup>71</sup> in a related paper, used  $R$  to denote an oxygen-to-ethylene ratio. In this case, a ratio of 1:3 was required for growth, ratios of less than this produced no crystal growth, and even at a ratio of 1:3 crystal growth occurred only on the outer edge of the deposits.<sup>71</sup> These gas ratios have been easily plotted onto the diamond phase chart of Bachmann et al.<sup>9</sup> where they compare favorably with the conditions used in this work. Growth of transparent diamonds and diamond films has been produced on nondiamond substrates by a couple of labs<sup>80,88</sup> where results from Snail et al.<sup>80</sup> provide cohesive, free-standing films of sufficient quality through which newsprint can be read.<sup>80,88</sup> Hirose et al.,<sup>88</sup> in looking at the changes in morphology for transparent diamond, noted that transparent diamonds were obtained with ratios between 0.85–0.9. The temperature requirements of torch-produced diamond films are similarly vague. Hanssen et al.<sup>68</sup> first remarked that the temperature range in which crystal growth occurs increases as  $R$  is increased from 0.9–1.2. They note a temperature range of 650–1,050 °C. Carrington et al.,<sup>71</sup> a year later from the same laboratory, expanded the range from 650–1,150 °C. Hanssen et al.<sup>68</sup> note that the inner cone flame temperature varies from 2,960 °C at  $R = 0.8$  to 3,162 °C at  $R = 1.5$ .

Hirose et al.<sup>88</sup> more recently reported diamond growth in the temperature range of 370–1,200 °C and produced transparent diamond samples in the region between 500 and 750 °C. However, these results were contested by Snail et al.<sup>82</sup> Ravi<sup>87</sup> has provided some results on the orientation effects in torch-

produced diamond. They contend that the surface temperature controls the faceting of the diamond film surface. At high temperatures,  $>1,000\text{ }^{\circ}\text{C}$ , a  $\{100\}$  orientation is assumed, whereas for lower temperatures,  $\{111\}$  facets are formed.<sup>87</sup> They explain their results by considering that oxidizing species in the flame selectively etch ledges. Because ledge creation is easiest on the  $\{100\}$  faces, these faces propagate smoothly and eventually dominate the structure at temperatures where the oxidizing radicals are more prevalent. Additionally, the taller crystals are at a higher temperature, again encouraging the continued growth of  $\{100\}$  faces.

Schermer et al.<sup>197</sup> have used  $\text{C}_2\text{H}_2$  supersaturation to define their gas composition instead of a direct ratio as described previously. The  $\text{C}_2\text{H}_2$  flow is the  $\text{C}_2\text{H}_2$  flow minus the  $\text{C}_2\text{H}_2$  flow of a neutral flame divided by the  $\text{C}_2\text{H}_2$  flow of a neutral flame. This ratio provides a more appropriate measure of the  $\text{C}_2\text{H}_2$  used in the feather region than does the parameter  $R$ , predominantly because the  $R$  of a neutral flame is known to depend on the total flow, the diameter of the orifice, and the geometry of the torch burner.<sup>197</sup> They point out that this results in an undefined zero point for results reported using the direct gas ratio,  $R$ . Below a supersaturation of 8 percent, the growth rate is approximately linear with respect to the supersaturation percentage. At 8 percent, the central region of growth breaks into a central film of crystallites that are still octahedrally shaped. At 10-percent supersaturation, the crystals grown produce a cubic signature.<sup>198</sup> Furthermore, at low  $\text{O}_2$  flows, their morphology changed from octahedral  $\{111\}$  to cuboctahedral  $\{111\}$  and  $\{100\}$  as noted previously.

The radial dependence of morphology also traces a dependence to variation in the active flame species, with position.<sup>86</sup> As  $R$  decreases in a flame, the C supersaturation should increase while the fraction of H may decrease. The  $\text{H}_2$  termination of the growth surface will be reduced at higher temperatures as thermal desorption of  $\text{H}_2$  takes place; therefore, the interaction between increasing supersaturation of C and the increased  $\text{H}_2$  content in the higher temperature regions of the flame can help account for the growth-oriented morphology variances. Ravi<sup>87</sup> divides the typical flame-formed deposition region into three areas. Schermer et al.<sup>197</sup> define an inner region with high temperatures ( $>1,000\text{ }^{\circ}\text{C}$ ) which promotes  $\{100\}$  morphologies; next an annular ring with high temperatures but higher concentrations of oxidizing species due to ambient air diffusion where again the  $\{100\}$  plane dominates but shows higher lateral growth, and finally an outer region with predominantly  $\{111\}$  faces.

Frey et al.,<sup>198</sup> in looking at the radial variation of morphology, produce  $\{100\}$  facets in the center region of the flame. They also note a pair of twin boundary-separated  $\{100\}$  planes at intermediate radial distances.<sup>198</sup> It should be noted that Frey et al.<sup>198</sup> appear to report and discuss these particles first in the literature; however, Schermer, on page 1,154 of reference 197, has previously grown this structure. The outermost region of Frey's deposit is a contiguous film of the twinned  $\{100\}$  planes.

### 3.4.1 Temperature Effects

In the absence of high nucleation density, the morphology appears to be related to surface energies, growth anisotropies, and the chemistry of the gas in the diamond synthesis ambient. When substrate temperatures are higher, the cube morphology tends to dominate while octahedral faces tend to form at lower temperatures.<sup>199</sup> Zhu et al.<sup>200</sup> note a large portion of  $\{110\}$  oriented crystal faces indicating decomposition from  $\{100\}$  crystals to  $\{111\}$  oriented crystals as the temperature decreases. They also provide excellent scanning electron micrographs of two-dimensional spiral steps on  $\{111\}$ ,  $\{110\}$ , and  $\{100\}$  planes.



They note that the appearance of spiral layers on  $\{110\}$  diamond supports the BCF growth mechanism (growth by screw dislocation spiral growth), and is in contradiction to the PBC theory mentioned earlier. These results are complemented by studies of Okada et al.<sup>201</sup> where the radial temperature distribution is correlated with the dominant growth habit. The growth toward the center of their flame appears dominated by  $\{111\}$ . Going radially outward,  $\{100\}$  planes start to appear with  $\{111\}$  planes growing or twinning from the  $\{100\}$  planes toward the outside where the  $\{111\}$  planes dominate.

### 3.4.2 Surface Reconstruction

Okada et al.<sup>202</sup> examined the step reconstruction on both  $\{111\}$  and the  $\{100\}$  faces of  $O_2$ - $C_2H_2$  torch-produced diamond. Comfortingly, the  $\{100\}$  ( $2 \times 1$ ) reconstruction noted in CVD diamond is borne up by the etch pits aligned along the  $\langle 110 \rangle$  direction as noted on their  $\{100\}$  sample surfaces. For  $\{111\}$  surfaces, they provide excellent illustration of steps that are perpendicular to the base of the triangle  $\{111\}$  planes oriented in the  $\langle 112 \rangle$  direction.<sup>49</sup> This is indicative of the slowest lateral growth rate on the crystal. Without reconstruction, according to the PBC theory noted above, the  $\langle 112 \rangle$  direction has fewer dangling bonds and a slower and more stable growth rate (and should, therefore, be present). If the surface reconstructs such that an additional surface bond is created between atoms in the  $\langle 112 \rangle$  direction, this then would stabilize these steps and provide the slower lateral growth rate.<sup>202</sup> These steps and stabilization have been noted as well by Janssen et al.<sup>203</sup>

### 3.4.3 Homoepitaxy and Single-Crystal Experiments

Because of its high growth rate, the  $O_2$ - $C_2H_2$  torch method of diamond production is especially attractive for single-crystal growth. Single-crystal growth has been performed on  $\{110\}$ ,<sup>204</sup>  $\{111\}$ ,<sup>82,205</sup>  $\{100\}$ ,<sup>205</sup> and  $\{113\}$ <sup>203</sup> facets of natural diamond crystals. Janssen et al.<sup>204</sup> first used polished  $\{110\}$  plates of type Ia and type IIa natural diamond. Their FTIR results suggest a broad band due to O-H stretching that has not been reported for other methods of diamond growth. They also note that  $H_2$  was present in their single-grain sample. As there were no grain boundaries for the  $H_2$  to segregate to, it seems that  $H_2$  impurities may be distributed throughout the lattice.<sup>204</sup> Both Snail et al.<sup>82</sup> and Hirabayashi et al.<sup>205</sup> have produced homoepitaxial diamond on  $\{111\}$  surfaces. Snail et al.<sup>82</sup> used a cylindrical  $\langle 110 \rangle$  oriented seed crystal and a turbulent flame to grow homoepitaxial diamond on  $\{111\}$  and  $\{100\}$  surfaces. Hirabayashi et al.<sup>205</sup> note the appearance of triangular microstructures on the surfaces of single, as-grown, crystal  $\{111\}$  faces. This they relate to multinucleational growth. Similarly, they attribute the smooth faces of the  $\{100\}$  faces on the same crystal to single-nucleational growth.<sup>205</sup> In a less than clear treatment, Hirabayashi attributes the morphology difference from  $\{111\}$  to  $\{100\}$  faces to the absorbance of C and graphitic species on the surface.

Janssen et al. provide the first study of  $\{113\}$  diamond facets.<sup>203</sup> Some of their results, regarding the stability of these faces, were confirmed by Snail et al.<sup>82</sup> From work referenced to Gardner on Si, Janssen et al.<sup>203</sup> argue that dimer formation in the  $[011]$  zone can occur predicting both  $\{100\}$  and  $\{113\}$  faces. They note that a further reduction in the surface tension can be brought about by adsorption of gas species onto dangling bonds of the surface. The absolute change in surface tension is determined by the surface coverage and the density of surface sites. This means that different orientations can have a different behavior on the surface tension based on the surface coverage. They predicted that above a certain coverage the  $\{113\}$  faces would become rough. Since the surface coverage increases upon lowering the

temperature, they further predicted that the {113} faces would not grow planar below a given temperature.<sup>20</sup> This has been partially confirmed by Snail et al.<sup>82</sup> Their results arise from homoepitaxial studies performed on a cylinder cut from <110> oriented natural diamond and growth temperatures >1,225 °C.

### 3.5 Morphology Method of Study (Optical Microscopy)

For all of the morphological work performed, a Nikon UFX IIA camera was used with 35-mm color film and automatic determination of exposure times. The film was typically 400 or 100 ASA and filters were occasionally used to highlight contrast. All film was developed commercially. Some morphological study was performed using scans from the atomic force microscope. That methodology will be covered in a following section.

### 3.6 Raman Spectroscopy Background

The Raman effect was first theoretically predicted by Smekal<sup>206</sup> and later experimentally demonstrated by C.V. Raman. Two of the energy contributions to a molecule are its molecular vibrations and its rotation. Radiation and molecules share the properties of energy and frequency. By observing the change in energy when a molecule and photon of radiation interact, information can be obtained about the vibrational and rotational frequencies of the molecule. When radiation interacts with a molecule, the collision can occur as either an elastic or as an inelastic collision. If the radiation occurs as an elastic collision, the system neither gains nor loses energy and the rotational and vibrational energy of the molecule is unchanged. This elastic interaction is Rayleigh scattering and by far the strongest component of scattered incident radiation.<sup>206</sup> When a photon of the incident radiation interacts with a molecule at a ground state  $E_1$ , the molecule absorbs the energy. The molecule is raised to a higher energy level, which is not a stable energy level. The molecule then immediately loses the energy and returns to the ground state, emitting a photon at the same wavelength as was absorbed. This scattering or emitted photon is Rayleigh scattering.

If, however, instead of falling to the ground state level, the excited molecule falls to a higher or lower energy level, the emitted photon is not of the same energy as the incident or exciting photon. Only a small proportion of excited molecules fall into a state other than their ground state, and these photons of different energy are termed Raman photons. From a wave perspective, when radiation of a specific frequency is incident onto the energy spectrum of a molecule, the ability of the molecular vibration to interact with that vibration is determined by the phase and the frequency of the incident radiation. The incident radiation must correspond to a natural frequency of some form of energy storage for the molecular vibration. This can be either an electron frequency, a frequency of nuclear vibration, a frequency usable for translational energy, or a frequency acceptable to vibrational or rotational energy. Some form of energy storage must have an available energy state (as determined by frequency) to accept, even temporarily, the energy in the incident photon. Of the incident photons, only those that are in phase with the vibration at the occurrence of interaction will actually be absorbed; the others will simply be turned away. Of the ones absorbed, these are then able to emit a Raman photon upon deexcitation.

Raman spectroscopy, therefore, looks at the scattered radiation that undergoes a change in frequency due to an energy transfer with the scattering medium (center/molecule).<sup>206</sup> First-order scattering involves single photons near the center of the Brillouin zone.<sup>207</sup> When energy is added to the incident radiation, the scattering is termed Stokes Raman scattering. When energy is taken from the incident radiation, the result is anti-Stokes Raman scattering.

Raman scattering may be divided into first- and second-order Raman scattering. Second-order scattering involves scattering from a pair of photons having equal but opposite unrestricted wave vectors.<sup>208</sup> Rayleigh scattering can occur when radiation does not undergo a change in wave number and scatters from scattering centers smaller than the wavelength of the incident radiation, such as molecules. In practice, this includes Brillouin scattering (a Doppler effect from change of frequency) and Mie scattering (scattering from larger scattering centers).<sup>207</sup> One of the primary advantages of using Raman spectroscopy in the investigation of diamond and diamond-like films is the ability of Raman spectroscopy to differentiate between C in its various forms. Raman spectra are available in the literature for a-C ( $C_{60}$  and  $C_{70}$ ), graphite, microcrystalline graphite, lonsdaleite, and diamond. Many of the diamond films produced in thin-film form are composites of these varied C species.

### 3.6.1 Cubic Diamond

The first-order Raman spectrum of diamond consists of a single line at  $1,332.5\text{ cm}^{-1}$  when measured at room temperature.<sup>208</sup> This corresponds to a zone center Raman active mode vibration as shown in figure 14.<sup>209</sup> The active Raman line at  $1,332\text{ cm}^{-1}$  can be clearly seen in a type IIa diamond sample used for calibration. For the Raman system used here, a representative spectrum is shown in figure 15. The first-order Raman line of diamond shows almost no change in position or width from 14.9 K to room temperature.<sup>210</sup> The first-order spectrum shows a definite broadening and shifting<sup>211</sup> of the Stokes and anti-Stokes spectrum lines at temperatures  $>1,000\text{ K}$ . Unfortunately, this study stopped short of the graphitization region at 2,100 K. The diamond Raman mode is also sensitive to C isotopes present. This effect is caused by the change in lattice constant between isotopes of C present; the lattice change reflects a bond length and thus a frequency change.<sup>212</sup> The second-order spectrum of diamond has been extensively studied and reference is made to Solin and Ramdas.<sup>210</sup>

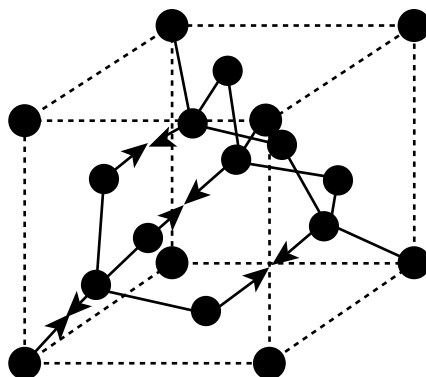


Figure 14. Primary active Raman mode of cubic diamond.

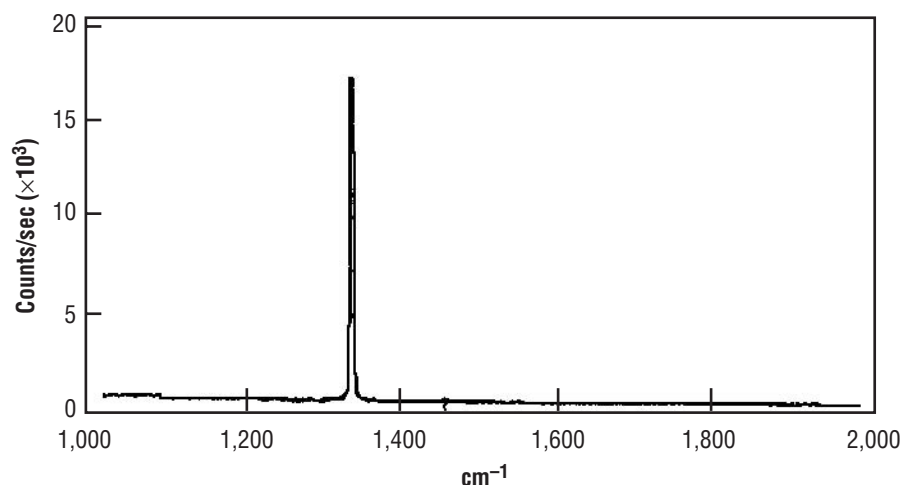


Figure 15. Primary diamond Raman signal at 1,332  $\text{cm}^{-1}$ .

### 3.6.2 Lonsdaleite—Hexagonal Diamond

The General Electric company first synthesized a hexagonal polymorph of diamond in 1967.<sup>213</sup> The Raman mode vibrations have been attempted on a commercial lonsdaleite diamond produced by a shock loading process.<sup>214</sup> Their spectrum consisted of a broadened line at 1,315- $\text{cm}^{-1}$  wave numbers and a hint of a band at 275- $\text{cm}^{-1}$  wave numbers. This does not agree well with the theoretical calculations of Mehl and Pickett<sup>209</sup> that arrive at three Raman active modes at 1,269  $\text{cm}^{-1}$ , 1,215  $\text{cm}^{-1}$ , and 430  $\text{cm}^{-1}$ . A satellite band at 1,319  $\text{cm}^{-1}$  occasionally appears on cut diamond surfaces, suggesting that the shear forces may have produced local regions of hexagonal structure. The very low intensity of the experimental observations on hexagonal diamond may account for its absence in the analysis of multicarbon surfaces.<sup>215</sup> These Raman modes have seldom been mentioned as relevant for thin-film diamond. Their absence offers an intriguing clue as to the mechanism of diamond nucleation and growth as the cubic sequence seems so dominant.

### 3.6.3 Graphite

The literature on the Raman spectrum of graphite seems to divide itself into data on highly-oriented pyrolytic graphite (HOPG)/single-crystal samples or data on microcrystalline graphite. Two Raman modes are predicted to be active in graphite.<sup>215</sup> The first is a stretching of the individual graphite sheets and the second is a shear mode between the top and bottom sheets in the hexagonal unit cell. Single-crystal graphite shows a sharp, intense, first-order band at 1,580  $\text{cm}^{-1}$  (G-band) and a low-intensity, interplanar, first-order shear band at 42  $\text{cm}^{-1}$ .<sup>206</sup> The low-intensity shear band is difficult to find and reflects the low level of interaction between the hexagonal sheets.<sup>216</sup> Nemanich and Solin<sup>216</sup> have suggested that the graphite peak at 1,581  $\text{cm}^{-1}$  is actually a doublet, with a sharp higher frequency component at 1,620  $\text{cm}^{-1}$  (fig. 16).

The Raman spectrum of microcrystalline graphite shows lines that are not present in large or single crystals.<sup>215,216</sup> A peak specific to microcrystalline graphite is found at wave number 1,355  $\text{cm}^{-1}$  (D-band). The intensity of the peak was found by Tuinstra and Koenig<sup>217</sup> to vary inversely with crystal planar domain

size. This peak has been suggested to be due to first-order scattering from a zone boundary activated by the small crystallite sample size. This effect would result from the breakdown of the  $K=0$  selection rule, allowing an  $M$ -point phonon to contribute to the Raman scattering.<sup>215</sup> In figure 17,<sup>217</sup> the first Brillouin zone of the two-dimensional lattice is shown for reciprocal space. Each of the points inside the boundary and on its periphery represent possible phonons. Due to the irregular shape of the boundaries, we can reject standing waves resulting from reflection from the boundaries. The  $K=0$  center point and the boundary points remain. The zone center Raman frequency is the difference between the ground energy state and the first excited state:  $\nu=(E_1-E_0)/h$ . The center point has the full symmetry of the lattice and produces the 1,581  $\text{cm}^{-1}$  line. The other point with high enough symmetry to give an A1G mode is the  $M$  point. In a crystal of infinite size, this mode is inactive because the polarization cancels over the infinite crystal.<sup>218</sup> As the crystal size decreases, the appearance of the 1,355- $\text{cm}^{-1}$  feature can be seen in figure 18. The graph shown from Nemaich and Solin<sup>216</sup> demonstrates the effect of crystal size.

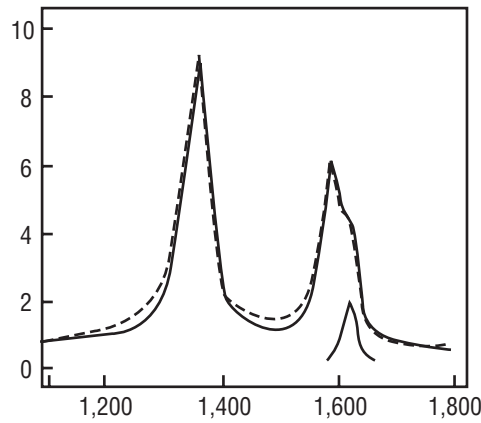


Figure 16. First-order Raman spectrum of graphite.<sup>216</sup>

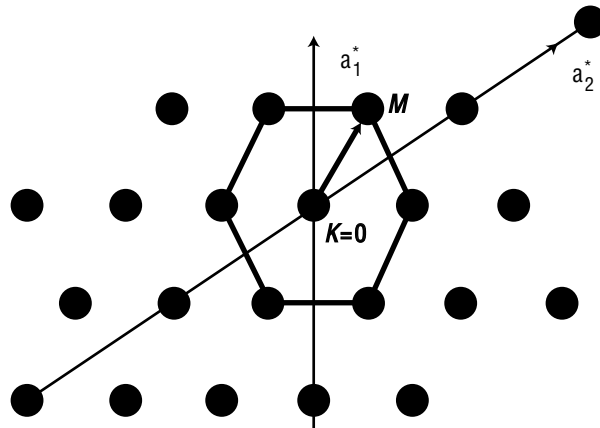


Figure 17. First Brillouin zone of a two-dimensional lattice.<sup>217</sup>

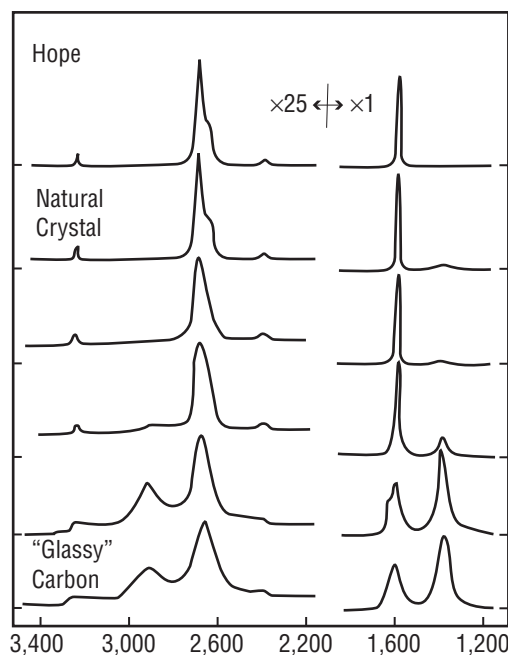


Figure 18. The  $1,355\text{ cm}^{-1}$  peak appearance with graphite crystal size.<sup>216</sup>

### 3.6.4 Buckminsterfullerene

Room-temperature Raman spectra of  $\text{C}_{60}$  and  $\text{C}_{70}$  solid films show characteristic vibrational spectra differing strongly from those of other C forms.<sup>219</sup> The  $\text{C}_{60}$  high-symmetry molecule has 10 active Raman modes predicted, and the  $\text{C}_{70}$  molecule has 21 reported features. The reported spectrum of  $\text{C}_{60}$  is shown in figure 19. It has been suggested that, given enough C atoms, the spectra of large fullerenes should approach those of microcrystalline graphite.

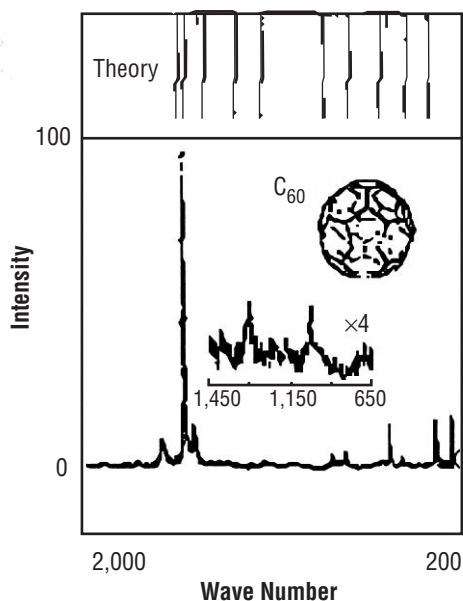


Figure 19. Raman spectra of  $\text{C}_{60}$ .<sup>219</sup>

### 3.6.5 Amorphous Carbon

Amorphous carbon or glassy C has two strong diagnostic features at 1,357 and 1,580  $\text{cm}^{-1}$ . The highly disordered C's such as charcoal and coke have broad bands, whereas the lines are more narrow in glassy C and microcrystalline graphite.<sup>215</sup> Linewidths are typically smaller in glassy C's, as opposed to very disordered C's, due possibly to a more homogeneous distribution of defect types in the glassy C.<sup>220</sup> The 1,350- $\text{cm}^{-1}$  peak is very broad and can be decomposed into two bands attributable to specific types of defects.<sup>221</sup> A diagram may be found in reference 215 that shows four types of a-C and their associated Raman spectrum. A comprehensive relation of Raman spectrum to structure was performed by Lespade et al.<sup>222</sup> and is shown in table 7.

Table 7. Carbon Raman peaks.

Wave Number ( $\text{cm}^{-1}$ )	Linewidth	Characteristics
1,332	Narrow	Truth test for cubic diamond
1,315	Broad	Experimental results for hexagonal diamond
275	Small	Lonsdaleite
1,269	?	Theoretical results for hexagonal diamond
1,215	?	?
430	?	Lonsdaleite
1,580	Narrow	Characteristic of graphite doublet
1,620	Shadowed	Other one-half of doublet
42	Elusive	Graphite shear mode
1,355	Broad	Microcrystalline graphite D-band
1,350	Broad	a-C
1,580	Broad	a-C
1,140	Broad	Unknown
+21 peaks for $\text{C}_{60}$ and $\text{C}_{70}$		

### 3.6.6 Diamond Film

The characterization of deposits as diamond-like or diamond film have become commonplace with the advent of technologies able to produce diamond outside the region of thermodynamic stability. Diamond and its Raman spectrum have been noted previously. The form of C classified as diamond results in a Raman peak at 1,332  $\text{cm}^{-1}$ . Films classified as diamond either possess a Raman peak at 1,332  $\text{cm}^{-1}$  or they are mislabeled. The confusion in the literature arises from the existence of C composite films.<sup>223,224</sup> Films of C material that contain, as a component, diamond showing a distinct 1,332- $\text{cm}^{-1}$  peak, also often display many attributes and peaks from other C forms. Alternately, films not showing a distinct 1,332- $\text{cm}^{-1}$  peak often will display characteristic properties such as hardness and transparency that are between diamond and graphite. The first occurrence is referred to as a diamond film even though the film may contain substantial amounts of foreign C. The second type of film is referred to as diamond-like.

Diamond-like C shows a characteristic intense broadband, usually with a pronounced shoulder<sup>225</sup> lying between the wave numbers of the diamond and graphite bands.<sup>225</sup> Diamond-like C films show a distinctly different Raman spectrum than that of other C materials. This has led to their occasional characterization as an independent and distinct form of C.<sup>215,224</sup> An unexplained feature of diamond-like films



shows up as a structure around  $1,140\text{ cm}^{-1}$ . This feature has been proposed as unique to diamond-like films and is attributed to disordered  $\text{sp}^3$  bonding, the presence of amorphous diamond, or a polytype of the wurtzite structure.<sup>223</sup> This peak has been noted as appearing in conjunction with the  $1,332\text{ cm}^{-1}$  Raman diamond line.<sup>226</sup>

One debated feature reported in films of diamond-like C is a feature at  $1,500\text{ cm}^{-1}$ . This broad peak has been correlated with the formation of C-rich amorphous- $\text{Si}_x\text{-C}_x\text{H}$  alloys.<sup>224,226</sup> In all noted cases, Si substrates were used; in one case,<sup>20</sup> secondary ion mass spectroscopy (SIMS) was used to verify the presence of Si in the films.

The  $1,332\text{-cm}^{-1}$  line in diamond is the highest energy vibration mode of the structure<sup>223</sup> in graphite; however, the highest energy feature is due to vibrations at  $1,620\text{ cm}^{-1}$ . Therefore, modes with energies higher than  $1,332\text{ cm}^{-1}$  cannot be attributed to diamond structures with long-range order.  $\text{Sp}^3$  bonding yields Raman peaks at  $1,332\text{ cm}^{-1}$  or lower, and  $\text{sp}^2$  bonding yields strong scattering with peaks<sup>224</sup> between  $1,355$  and  $1,600\text{ cm}^{-1}$ .

An interesting correlation of the photoluminescence intensity with characteristics of the Raman spectrum has given some unique insight into the structure and bonding of diamond films.<sup>227</sup> Four features were noted as changing in an interrelated manner:

1. The linewidth of the diamond Raman peak
2. The breadth of the tail of the Raman line
3. The intensity of the  $\text{sp}^3$  C line
4. The intensity of the photoluminescence background.

The interrelation between these features is suggested as being indicative of a spectrum of film defect density, with gem-quality diamond on one side and highly defective diamond films on the other. They suggest that, because of the correlation of linewidth and photoluminescence background intensity (relative to the diamond line intensity) and the correlation of linewidth and crystalline domain size, many or most of the  $\text{sp}^3$  bonded structures were dispersed within diamond crystallites rather than in a spatially separated phase. None of their samples showed a large increase in linewidth without a corresponding increase in  $\text{sp}^3$ -bonded C. They also show a strong correlation between the intensity of the photoluminescence background intensity relative to diamond and the nondiamond Raman signal.

### 3.7 Prior Raman Spectroscopy on Diamond Films

Raman has emerged as the primary technique for evaluation of diamond films. Although diamond presents both first- and second-order spectra, the predominance of the published work looks at the first-order spectra. For brevity, only the first-order spectra is considered in the following review. Raman has proved to be a much more sensitive characterization technique than electron or XRD.<sup>11,21</sup> Raman is much more sensitive to the presence or inclusion of graphitic or a-C, and the results of Raman are, in general, more clear in their interpretation for C species.<sup>21</sup>



Etz et al.<sup>228</sup> present early interpretive results based on line shape, linewidth, and frequency position of the Raman peaks. For CVD diamond, they note that it becomes useful to examine the peak-to-background ratio at the Raman frequency of the diamond line ( $1,332\text{ cm}^{-1}$ ) as a measure of defects in the diamond phase. The shape of the line is related to the distribution of distortions in the lattice. Specifically, they attribute the full width at half maximum (FWHM) as a measure of this distribution.<sup>228</sup> Some of their samples are superimposed on a rising background showing a broad band centered on  $1,510\text{ cm}^{-1}$ . They attribute this peak to diamond-like C sp<sup>2</sup> bonding, and thus infer its presence mixed with the sp<sup>3</sup> bonding primarily present. Their spectra included a strong luminescent background, which they begin to characterize as related to impurities incorporated into the diamond matrix.

Another early paper by Buckley et al.<sup>229</sup> interprets Raman spectra as demonstrating a multiphase nature for all of their diamond films. They notice in their work that there is a strong dependence of Raman linewidth on total gas pressure in filament-assisted CVD. The decrease in linewidth with pressure reduction is attributed to an increase in lattice defects in both diamond and graphite components of the film. In addition, in their results they notice that the line position is independent of gas pressure. In interpreting the multiphase nature of their deposits to evaluate the graphite phase, they detect its presence by peak intensity at the  $1,579\text{-cm}^{-1}$  line, and because of a well-developed feature at  $1,360\text{ cm}^{-1}$ , they infer that the crystal size for the graphite component is small. This approach is supported by Yanez-Limon<sup>230</sup> who note that in the spectrum of small graphite crystals, an additional disorder line appears at  $1,350\text{ cm}^{-1}$  as the crystal size decreases. Amorphous carbon is footprinted by a broad peak at  $1,550\text{ cm}^{-1}$ .

Buckley et al.<sup>229</sup> also refer to prior work relating to a Raman peak at  $1,140\text{ cm}^{-1}$ . They note only that the strength is unrelated to the strength of the graphite line. Bonnot,<sup>231</sup> in looking at the FWHM on a number of individual diamond crystals, shows the range of breadth of 8 to  $<21\text{ cm}^{-1}$ . This is well above the resolution of their Raman apparatus. As the diamond linewidth increases, they note the appearance of the two bands at  $1,350$  and  $1,540\text{ cm}^{-1}$ . Overall, they reference the Raman spectrum of diamond as dependent on temperature, pressure, and C isotope concentration. With temperature, the Raman shift decreases and the width of the line increases; with pressure, the Raman shift increases and the linewidth increases; and with an increase in C-13 concentration, there is a monotonic decrease of the Raman shift and linewidth. References from Bonnot<sup>231</sup> note that hexagonal diamond may show positions from  $1,315$  to  $1,350\text{ cm}^{-1}$ .

Bonnot<sup>231</sup> and Stuart et al.<sup>232</sup> present a very detailed examination of changes in Raman spectra directed on different crystal faces and of varying degrees of faceting. A brief summary of their results is presented in the following paragraphs. It should be moderated by an understanding that they have studied only one set of process conditions, and their results are probably more specific to the conditions used to produce their films than the overall structure or composition of low-pressure diamond. This said, their work presents useful insights into the interpretation of diamond spectra.

Stuart et al.<sup>232</sup> show photographs of both  $\{100\}$  and  $\{111\}$  crystals with an incident, microfocused laser spot. Looking first at crystals showing a  $\{100\}$  facet, Stuart notes that the diamond line is observed to split into two peaks— $1,334$  and  $1,340\text{ cm}^{-1}$ . This, they note, is consistent with an internal stress of  $\approx 50$  kbar. Bonnot<sup>231</sup> observes that crystals of this type are systematically broader (at least  $8.5\text{ cm}^{-1}$ ) than natural diamond and shifted toward lower wave numbers. In crystals showing a  $\{111\}$  facet parallel to the surface, Stuart et al. note a definite peak at  $1,326\text{ cm}^{-1}$ . They perform a number of experiments to determine the basis of the  $1,326\text{-cm}^{-1}$  peak in their samples; and to summarize the majority of their work, they

attribute the existence of this peak to stacking faults in the  $\{111\}$  structure. These stacking faults will have the same structure as hexagonal diamond. Very few stacking faults are needed to cause a breakdown in symmetry without having enough hexagonal material to appear as a signal between 1,326 and 1,350  $\text{cm}^{-1}$ . Bonnot<sup>231</sup> again only notes that broadening occurs relative to natural diamond samples.

In situ Raman work in a microwave plasma reactor is presented by Fayette et al.<sup>233</sup> Their first signal was noted at 1 hr of deposition; however, when the half width at half maximum (HWHM) values are plotted, there was no change noticed, indicating that the structural quality of the diamond was constant. A consistent shift of the peak was noted over time, which was interpreted as an increasing compressive stress in the film. The amorphous phase of diamond was not noted until 3 hr of deposition had gone by. Since the appearance of the amorphous phase occurred near the coalescence of isolated crystals, this peak was interpreted as being caused by grain boundary material.

Nemanich,<sup>234</sup> using an analysis method developed for Si from one of his references, equates Raman linewidths of 4–12  $\text{cm}^{-1}$  with domain sizes from 200–50 Å. He then equates the domain size measured from the Raman spectra with the spacing of stacking faults and twin planes within the structure to account for the apparent contradiction with optical crystal sizes well above 1 mm. Nemanich also notes a difference in linewidth and peak shift with the alternate substrate materials. This is attributable to varying internal stresses caused by mismatch with the substrate.

Only Harshavardhan et al.<sup>226</sup> have spent detailed effort discussing the Raman interpretation of the spectra, specifically focusing on prior torch interpretation; although, most diamond produced using an  $\text{O}_2\text{-C}_2\text{H}_2$  torch has used Raman characterization (presence or absence of the 1,332- $\text{cm}^{-1}$  line) for their films. Although Harshavardhan et al.<sup>226</sup> note the presence of a broad 1,350- $\text{cm}^{-1}$  peak indicating micro-crystalline graphite, they also observe no discernible 1,580- $\text{cm}^{-1}$  peak required for predominant graphite growth. This is especially relevant as the Raman cross section for sp<sup>2</sup>-bonded C is  $\approx 50$  times higher than sp<sup>3</sup>-bonded C. This makes Raman spectra especially sensitive to the presence of sp<sup>2</sup>-bonded C. A broad band at 1,180  $\text{cm}^{-1}$  (possibly corresponding to the CVD 1,140- $\text{cm}^{-1}$  peak) is attributed to a diamond-like precursor phase. Looking at the deposit radially, they notice a reduction in diamond line intensity as a scan is taken radially outward.

### 3.8 Raman Spectroscopy Method

Looking at the determination of the relative amounts of sp<sup>3</sup>- to sp<sup>2</sup>-bonded C, Nemanich<sup>234</sup> notes that since the relative Raman cross sections have been determined for diamond and graphite, a determination of relative amounts is theoretically possible. The quantitative analysis is complicated by the variance in the optical properties of graphite and diamond. Because graphite is highly optically absorbing, it may not be measured as efficiently as transparent diamond regions. The analysis is typically dependent on the domain size of the absorbing regions, which is complicated by the defect structure of the crystal. Further, Nemanich notes that the intensity dependence versus linewidth must be determined prior to an accurate quantitative analysis.<sup>234</sup>

Sample data were obtained at the microanalysis laboratories of the National Institute of Standards and Testing (NIST) in Gaithersburg, MD. With the assistance of Edgar Etz<sup>228, 235</sup> from NIST, survey spectra were conducted on two separate spectroscopy machines.

Spectra were obtained using a multichannel detection Raman microprobe using the 514.5-nm excitation line of an Ar laser. The spectra were taken over the Raman range of 300 to  $\approx 1,800\text{ cm}^{-1}$ . These instrument settings provide a spectral resolution of approximately  $5\text{--}6\text{ cm}^{-1}$ . The lateral spatial resolution of the probing focused laser spot was  $\approx 3\text{ }\mu\text{m}$  using a  $\times 32$  focusing objective.

We then examined the spectra of a few reference diamond samples in three categories:

1. A NIST reference gem diamond (type IIa) showing a narrow diamond peak at  $1,334.2\text{ cm}^{-1}$  (peak in channel No. 391). The half width of that line was  $\approx 3.5\text{ cm}^{-1}$  (inclusive of instrument effects).
2. A Norton Company high optical-quality CVD diamond wafer slice. This also showed a peak at  $1,334.2\text{ cm}^{-1}$  but a bit broader at  $\approx 6.5\text{ cm}^{-1}$  at FWHM. This sample showed differing levels of luminescence on the top and bottom surfaces.
3. Spectra of several NIST samples of CVD-produced diamond films on Si and SiC substrates were recorded. On these samples, we noted a variety of luminescence emissions from bright yellow to an orange-red. Microfocus spectra were then taken on the GAMoly samples; because as diamond samples reach even higher purity and structural perfection, visible excited Raman may not be sensitive enough to detect nondiamond C.

All diamond of high quality may be considered to have substantially the same clean Raman spectrum when excited in the visible region. Fourier Transform Raman (FTRaman) spectroscopy, using excitation in the near infrared (IR) at  $1.064\text{ }\mu\text{m}$ , provides improved Raman detection for diamond characterization by providing enhanced scattering of all nondiamond C.<sup>235</sup>

Raman spectra were also taken on a commercial Bruker (opus) RFS 100 FTRaman spectrometer. This spectrometer was used for all of the flow rate and tip modification samples. Several of the GAMoly samples were analyzed on this machine as well for comparative purposes.

### 3.9 Atomic Force Microscopy Background

The scanning tunneling microscope is only the fourth invention to receive a Nobel prize in physics since the award was first given in 1901.<sup>236</sup> The scanning tunneling microscope, invented by Binnig and Rohr, achieves a precision capable of imaging individual atoms by using the sensitivity of tunneling current to interatomic distance. When an interatomic distance is spanned by a tunneling current, the magnitude of the interatomic distance varies logarithmically with the magnitude of the current. For example, a change in distance of  $1\text{ }\text{\AA}$  changes the tunneling current by a factor of 10.

In 1985, the atomic force microscope (AFM) was introduced by Binnig, Quate, and Gerber.<sup>237</sup> The development of the atomic force microscope enabled images of strongly nonconductive samples for which the measurement of tunneling current was impractical. The original atomic force microscope design placed a diamond tip of approximately one atom width in contact with the surface. The repulsive force generated between the tip and surface is held constant as the tip is dragged across the sample surface. Deflections of the cantilever on which the tip is mounted provide a quantitative map of the surface

topography. Newer instruments use the reflection of a laser beam off the cantilever surface to provide measurement of the deflection between the tip and surface.

Current AFM include contact and noncontact modes in ambient and ultrahigh vacuum (UHV) environments. Additional development of scanning probe microscopies<sup>238</sup> has included noncontact mode AFM, friction force microscopy, magnetic force microscopy, electrostatic force microscopy, attractive mode force microscopy, scanning thermal microscopy, optical absorption microscopy, scanning ion-conductance microscopy, scanning near field optical microscopy, and scanning acoustic microscopy.

### 3.10 Previous Results of Atomic Force Microscopy Work on Diamond

Due to its use as a tip material and its extreme hardness, diamond is an excellent material for AFM study. The high hardness makes deformations due to tip sample interactions less severe. Results to date in the literature are on either natural diamond or CVD-produced films.

Topographic results, not from AFM, include results by Van Enkevort et al.<sup>239</sup> where the growth mechanisms of hot filament and torch-produced diamond were examined based on surface topography measurements made by Normarski differential interference-contrast microscopy (NICM) and phase shifting interferometry (PSI). On natural type IIa diamond substrates, they observed only two orientations with flat faces as described by the PBC. They also note that regardless of substrate temperature, all of their  $\{111\}$  macrosteps show a sharp discontinuity in the slope of the steps. They relate this as an indication of transport-limited growth. For flame-grown  $\{111\}$  surfaces, they note that after prolonged growth, the  $\{111\}$  faces become multiply twinned. The steps cannot pass the twin boundaries. This constrains the growth to small islands. For  $\{100\}$  facets, they note square elevations parallel to the PBC directions, again indicating that the steps are nucleated at foreign particles or lattice defects.

Early in the paper, they assume that since no foreign particles are present at growth centers, steps are generated by lattice defects rather than contact nucleation. This assumption is valid except for the possibility of diamond or other foreign particles nucleated in the gas phase that initiate the presence of growth steps. This possibility is covered in their conclusions. Bogli et al.<sup>240</sup> present work on laser irradiated samples of CVD-grown diamond films where the graphitic layer and the surface stable conductive layer could be measured with an atomic force microscope, owing to the concomitant smoothing process during etching.

Turner et al.<sup>241</sup> provided some of the first published scanning probe examination of the nucleation behavior of diamond films using the scanning tunneling microscope. Their work provided images and I–V curves of formative diamond nuclei on Si. They do note a change in surface roughness between samples, but they do not provide a quantitative measure.<sup>24</sup> Sutcu et al.<sup>242,243</sup> provided some of the first atomic force microscope high-magnification work on homoepitaxial-grown CVD diamond by using substrates of  $\{100\}$ ,  $\{110\}$ , and  $\{111\}$  diamond surfaces. Sutcu et al. used a pyramidal silicon nitride ( $\text{Si}_3\text{N}_4$ ) tip and acquired images within a few weeks of growing most samples. Sutcu provides atomic scale images that support the  $(2 \times 1)$  reconstruction of the diamond surface at an antiphase domain interface. Everson et al.<sup>244</sup> were able to provide positive identification of the ubiquitous triangular defect on the  $\{100\}$  faces of vapor-grown diamond by using AFM.

Using quantitative AFM, they provide proof of the appropriate angles identifying the common defect as the penetration twin we refer to elsewhere in this work. George et al.<sup>245</sup> provide an investigation of nucleation and growth processes of diamond films by AFM that focuses on atomic force microscope studies of the substrate face and the backside of free-standing films. They did not have acceptable success with high aspect ratio Si tips so they opted to use Si<sub>3</sub>N<sub>4</sub> tips instead. They provide excellent images of early stage growth of diamond on an initially Si substrate.

Turner et al.<sup>241</sup> note a change in surface roughness between samples when looking specifically at the use of AFM in surface roughness measurements; but unfortunately, they do not provide a quantitative measure. Sutcu et al.,<sup>242,243</sup> however, provide a few quantitative surface roughness measurements on their samples of {100} orientation growth. They report roughness variations <5 nm in amplitude. When measuring their as-polished diamond {111} substrates, they measured scratches 5 to 10 nm in height and a total height variation <100 nm. Finally, on their {110} sample, they reported a 2 peak-to-peak roughness. However, on this sample, despite the smoothness, they were not able to achieve atomic imaging. Gruen et al.<sup>246</sup> present the first atomic force microscope images where quantitative surface roughness is characterized by the rms roughness values.

Yanez-Limon et al.<sup>247</sup> characterize C film microstructure by AFM using a Park Scientific SFM BD2. They look at the surface roughness of both hydrogenated and nonhydrogenated C films and may be the first to relate surface roughness with nucleation centers. They suggest that an increase in the power density of a glow discharge will provide samples with smoother surfaces because the arriving species will be smaller and produce a more uniform a-C film.

### 3.11 Atomic Force Microscopy Method

Each diamond film was scanned for the presence of crystal faces that were oriented perpendicular to a surface normal of the original substrate. The crystal faces were required to be within  $\approx 15^\circ$  of the original substrate plane. Larger angles than this exceeded the limits of correction on the cantilever positioning mechanism and the scan typically would fail to image over a large portion of the area. Occasionally, a sample would have only high angle planes in evidence and, in these cases, we elected to work only within the region of the scan that provided a quality image. Additionally, the crystal face of interest had to be the highest point in the local area. When crystal faces were bounded by taller crystals, the cantilever would catch or become blocked by the taller nearby crystals and imaging was impossible or inaccurate. Once a suitable crystal face was located on a surface, images were obtained from each sample followed by force versus distance measurements. Typically, 5–10 force versus distance measurements were taken on each scan. The measurements were taken in the four corners and the center of the scan. Additionally, noted contrast regions (hills, valleys, ridges, unknown areas, etc.) had measurements taken on them as well.

All of the topographic microscopy was performed on a Park Scientific autoprobe LS. Sample images were taken in air using the repulsive (contact) mode. The instrument was calibrated just prior to taking sample images, in most cases, calibrating with the scan speeds and distances used in the subsequent scans. All images were taken using 512 data points per scan line in the fast scan direction in order to achieve the maximum lateral resolution. The tip used was a Si ultra/microlever, produced by Park Scientific Instruments, having a conical tip profile. The humidity in the laboratory for the samples varied over a reasonable range, as the results from sample to sample were conducted over a number of months. The humidity was not considered a strong contribution for samples where atomic resolution was not used. This



was primarily based on the results of Thundat et al.<sup>248</sup> who note that the sharpness of the image is the main characteristic affected by humidity outside of the preferred range.

Considering the force versus distance curves, the ultralever Si tips that were used in my experiments were high aspect ratio conical tips with an average tip radius of curvature of 100 Å. The Si tips used in the Park Scientific LS had a conical tip, as opposed to a more conventional pyramidal tip. The conical tip provided a sharper tip that was able to image sharper surface features than a traditional Si<sub>3</sub>N<sub>4</sub> pyramidal tip. This also improved calculation of the average and rms roughness. Each force versus distance measurement was an average of eight individual force versus distance scans. Data files were imported into Matlab and transformed into ASCII files for use in Kaliedigraph. Measurements of specific data points were then extracted from the graphs produced, and the standard curve-fitting routines provided in Kaliedigraph were used to provide the line equations and slopes.

### 3.11.1 Introduction

Diamond, because of its high bandgap and associated affinity for charging, presents one of the more challenging materials to image directly. The sample surfaces used are torch-produced diamond crystal faces in their as-grown condition. In other cases, a diamond surface has required polishing or smoothing to provide a surface suitable for scanning probe microscopy imaging.<sup>249,250</sup> Torch-produced diamond films are notorious for their extremely rough surface morphology.<sup>251,252</sup> The high growth rate, typical of torch-grown films, produces spectacular proliferations of crystal spires and connected fields of cauliflower or random crystallites. Amorphous carbon films,<sup>247,253</sup> hot filament,<sup>242</sup> and CVD<sup>240,241,243–246</sup> films have been successfully imaged with AFM as discussed previously. However, torch-produced diamond films heretofore have not been imaged with scanning force microscopy in their as-grown condition. As yet, the atomic scale force-versus-distance measurements capability with an atomic force microscope has not been applied to diamond samples.

### 3.11.2 Surface Roughness Measurements

Statistics for the surfaces profiled provided median height, mean height, peak-to-valley distance average, rms roughness, arithmetic (Ra) mean roughness, and bearing ratio. However, the measurement of surface finish requires the use of parameters that are meaningful to the experiment in progress. For example, my samples have little to no use for bearing ratio calculations. (Ironically, bearing ratio curves have been used on AFM investigations of diamond films. However, these AFM results were taken on diamond films that had been subjected to pin-on-disk tribological testing, and as such the bearing ratio is an appropriate measure.<sup>254</sup>) The most traditional parameters for surface finish measurement are the Ra mean and the rms of profile height about the geometric centerline of the profile. Most discussion and specifications for surface finish refer to these parameters. Other parameters could prove of more utility to look at nucleation of diamond-faceted material versus other C forms without distinct faceting.

The skew and kurtosis of the amplitude curve both provide a measure of the overall flatness or spikiness of the profile. For example, a profile with many large spikes and a flat base may have the same Ra and rms values as a profile with many deep crevices and a flat upper surface. The slope of the profile peaks relative to the center line may provide information about the condition of initial or present nuclei. The average frequency-weighted wavelength of the profile also provides a measure of surface smoothness and

the relative sharpness of the profile peaks.<sup>251,252</sup> The skew of the profile is the third moment of the amplitude distribution curve. The skew may be positive or negative, where a positive skew indicates a concentration of material near the bottom or surface of the profile, providing a more faceted-like surface.

Kurtosis is the fourth moment of the amplitude distribution curve. It provides a measure of the sharpness of the amplitude distribution curve. A high value of kurtosis, typically  $>3$ , indicates a sharp amplitude distribution curve that relates to large sharp peaks and valleys on the original surface. A low value of kurtosis, typically  $<3$ , shows a smoother amplitude distribution curve and more numerous and more round profile peaks.

Fortunately, the data presented here are on specific crystal facets. With the statistics currently available, rms roughness would probably give the best indication of profile sharpness. Since the rms value first squares the height and takes the mean of the squared values, thereafter taking the root of the values, a sharper sample would arrive at a higher rms value due to the increased importance of the highest peaks. Indeed, this very property of the rms value has caused it to be preferred for surface finish specifications as it provides additional confidence on overall smoothness.

### 3.11.3 Indentation Measurements

Burnham and Colton<sup>255,256</sup> were pioneers in the use of nanoindentation techniques to derive hardness and elastic modulus. As the instrumentation capability of indentation techniques has improved, the ability to derive more information on local materials' properties has begun to improve dramatically. The use of nanoindentation is beginning to show the promise of material measurements impossible to obtain in any other fashion. In a natural progression of the nanoindentation work, we use an atomic force microscope for indentation studies of elastic modulus and hardness. In the work presented, a commercially available Park Scientific Instrument autoprobe LS instrument is used for microindentation and imaging.

**3.11.3.1 Hardness Measurements.** Several considerations arising from the inherent anisotropy of diamond are important in the measurement of diamond hardness. Experimentally, the orientation between the sample surface and the indenter can cause variation by a factor of as much as 1.5. The hardness of diamond has been shown to vary considerably between diamond types (table 8). Because of the anisotropy, the hardness value is also critically dependent on the plane and direction of the hardness measurements (table 9 from reference 257). In what appears to be some of the pioneering work, Burnham and Colton<sup>255</sup> estimate a tip radius for their nanoindenter and, using their measured load and displacement, calculate a hardness value. They use the maximum load divided by the projected area of contact after the sample has recovered elastically.<sup>258</sup>

Table 8. Variation of diamond hardness with type, direction, and plane.<sup>257</sup>

Author	Date	Young's E N/m <sup>2</sup>	Poisson's
B&B	1946	$4.552 \times 10^{11}$	0.291
P&W	1953	$6.385 \times 10^{11}$	0.231
M&B	1957	$8.728 \times 10^{11}$	0.104
M	1965	$6.787 \times 10^{11}$	0.204
M&A	1972	$8.772 \times 10^{11}$	0.103
G&R	1975	$8.729 \times 10^{11}$	0.104

Table 9. Published literature on Young's modulus of diamond.

Plane	Direction	Type I	Type II	Australian
(001)	[110]	8,300	9,100	0.291
(001)	[100]	9,800	10,300	0.231
(110)	[110]	8,800	9,400	0.104
(110)	[110]	10,800	11,500	0.204
(111)	[110]	5,600	7,600	0.103
(111)	[112]	6,300	11,000	0.104

Looking at hardness, calculations are started with the definition of hardness as equivalent to the average pressure under the indenter, calculated as the applied load divided by the projected area of contact between the indenter and the sample (eq. (61)):

$$\text{Hardness} = \frac{\text{Applied Load}}{\text{Projected Area of Contact}} \quad (61)$$

With knowledge of the shape of the indenter, the plastic depth can be used to calculate the projected area of contact. The depth measured during indentation includes both elastic and plastic displacements. To obtain an accurate measurement of hardness, the elastic displacements must be subtracted from the measured values.<sup>258</sup> The initial slope of the unloading curve provides an intercept that may be read as the plastic depth of penetration to be used in calculating the projected area of contact.

For AFM conducted outside of a hard vacuum, the unloading curves are burdened with a contribution from the effects of surface adhesion and capillary forces.<sup>259–266</sup> Upon unloading, there are unknown contributions to the attractive forces due to chemical attractions between tip and surface or surface bound contaminants. For high hardness materials, it is unclear that plastic deformation is a requirement of the atomic force indentation process. For these reasons, the approach of Doerner and Nix,<sup>258</sup> wherein the data along the loading curve may be used to generate hardness as a function of depth, seems an appropriate starting point. In this approach, it is necessary to estimate the elastic displacements as a function of depth. The elastic displacements may then be subtracted from the total displacement to obtain plastic displacement if it exists. They calculate elastic displacement using the elastic compliance, where the elastic compliance relates to the compliance at maximum depth, by eq. (62):

$$\frac{dh}{dP} = \left[ \left( \frac{dh}{dP} \right)_{\max} - (b) \right] \times \frac{h_{\text{eff}\max}}{h_{\text{eff}}} + b \quad (62)$$

where  $b$  is the  $y$  intercept from a plot of the compliance versus  $1/\text{depth}$  plot. This equation can require an iterative solution using a shape calibration procedure noted in reference 258. The projected area of contact must be corrected by using the true plastic depth and an appropriate correction for the true shape of the indenter, as noted above.



The distance measurements on the Park Scientific Instrument register zero distance at the initial point of the force versus distance scan. Appropriately, this joint is far enough above the sample surface so as to provide no tip-to-sample influence. In order to calculate the depth of penetration, we reference the point at which the applied load returns to zero following the Van Der Waals attractive dip on the loading portion of the trace. This point is noted on the raw distance measurement, and the data are shifted such that my distance measurements read that point as zero distance or surface/cantilever equilibrium. Similarly, the zero point for the load was corrected to the initial portion of the trace where the distance versus load was located and showed no change in load with a continuous change in distance. In many instances, at the high load portion of the curve, the detectors would overload and the load reading would remain constant at a particular value. No data were used from these regions. In my work, the loading curves are composed, in general, of one or two linear segments.

Starting with Sneddon's solution<sup>267,268</sup> for a flat-ended cylindrical punch of radius  $a$ , in my case  $100 \text{ \AA}$ , we calculate  $2Ea/(1-\nu^2)$  from the least-squares line of the first half of the loading curve where we have the highest expectations of linear elastic behavior. When my curves were plotted by taking the segments into first and second halves, the bulk (98 percent) of the data exhibited the expected behavior of a lower slope at the start of the curve than at the bottom. Using this derived value of  $2Ea/(1-\nu^2)$ , we extrapolate the linear fit of the lower half of the curve and plug into the original linear elastic equation of

$$p = \frac{2 \times E \times a \times h}{(1 - \nu^2)} \quad (63)$$

to get

$$h = \frac{(1 - \nu^2) \times p}{2 \times E \times a} \quad , \quad (64)$$

using the measured value of  $p$  from the top of the top half of the measured curve and the derived value of  $(1-\nu^2)/2Ea$  from the least-squares fit of the lower portion of the measured curve. This gives us a measure of the elastic value of  $h$ . This value is then compared against the probable standard error for the lower curve and, provided the deviation is larger than the standard error, subtracted from the measured value of  $h$ . This provides the plastic depth to be used in hardness calculations.

This method has the advantage of not requiring an exact location of the surface. Once we have the plastic depth, we calculate hardness based upon a spherical indenter,<sup>269</sup> using the displayed series of equations. Conventional hardness measurements are traditionally obtained with a hold time at maximum load during which creep processes are active. A sample calculation is shown with typical values in figure 20.

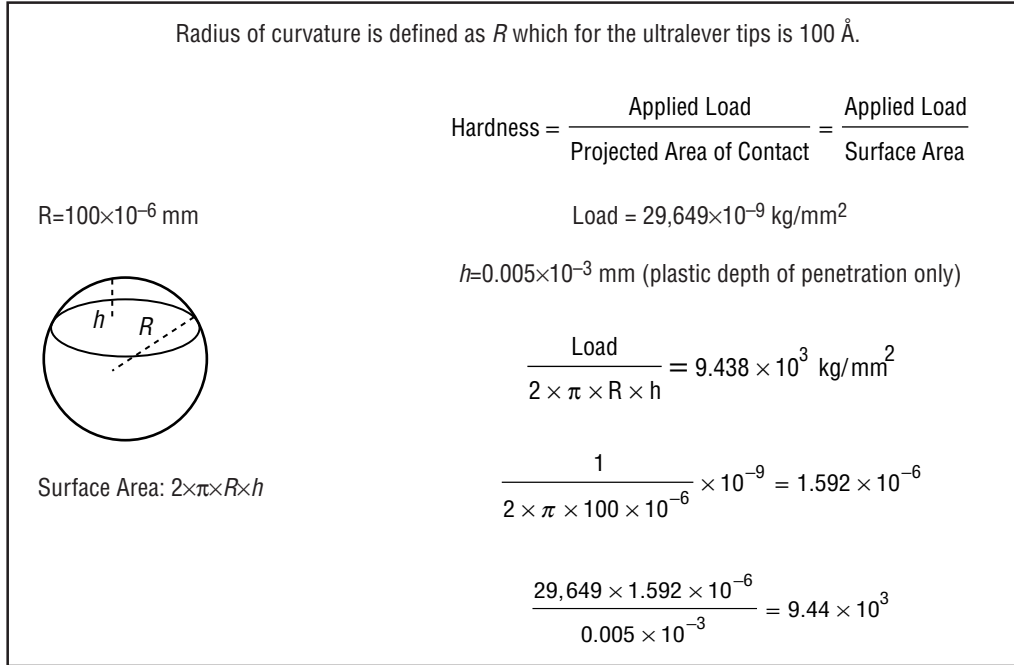


Figure 20. Demonstration of hardness calculation.

Hardness may show a dependence on depth of penetration due to indenter shape, if not corrected for ideal versus actual indenter shape. The effect is most pronounced at small depths where the actual indenter shape is considerably more blunt than the ideal pyramid.<sup>258</sup> There is a strong strain rate dependence as the size of the indentation decreases. This effect can be severe when the load-versus-depth curves are used to calculate the hardness, as opposed to indentations that allow for stress relaxation under the indenter by incorporating a hold time at the position of maximum load. This may be easily seen in a definition of strain rate as:

$$\text{Strain Rate} = \text{Constant} \times \left( \frac{1}{\text{Measured Depth}} \times \frac{d\text{Measured Depth}}{dT\text{ime}} \right) . \quad (65)$$

For my measurements, the change in measured depth versus time can be calculated from the measurement frequency and the percentage of full-scale measurement time taken during the time from zero load increasing to zero load decreasing. While it is possible to calculate the strain rate for a given measurement, the effect of strain rate on hardness measurements, made using the atomic force microscope, cannot be accurately addressed until measurements can be made that allow a hold time during the indentation to allow for stress relaxation.

**3.11.3.2 Young's Modulus Measurements.** In references 255 and 258, Sneddon's<sup>267</sup> treatment of the Boussinesq problem is referenced using his solution for a flat-ended cylindrical punch. Doener and Nix<sup>258</sup> rely on work by Loubet et al.<sup>270,271</sup> where an approximation of the flat-ended cylindrical punch solution is used to relate the slope of the initial portion of the unloading curve. This is in effect how we obtained my hardness values as described previously. Figure 21 shows a sample calculation from my data.

$$R=100 \times 10^{-10} \quad \text{Slope} = \sqrt{\frac{2}{\pi}} \times R \times E_{\text{meas}}$$

Using the equation and solving for reciprocal  $E$  with the slope from the loading curve gives

$$\text{Slope}=23,556 \quad E_{\text{meas}} = \frac{\text{Slope}}{\sqrt{\frac{2}{\pi}} \times R}$$

Then taking the published values for the Poisson's ratio and Young's modulus of the Si indenter and solving for  $E_{\text{meas}}$ ,

$$\nu=0.240, \nu_{\text{Si}}=0.223, \text{ and } E_{\text{Si}}=1.629 \times 10^{11}$$

$$E_{\text{samp}} = \frac{1 - \nu^2}{\left( \frac{1 - \nu_{\text{Si}}^2}{E_{\text{Si}}} - \frac{1}{E_{\text{meas}}} \right)}$$

$$E_{\text{samp}} = 1.715 \times 10^{11}$$

Figure 21. Sample of Young's modulus calculation.

According to Doerner and Nix,<sup>258</sup> it is not necessary to know the value of Poisson's ratio with great precision to obtain a good  $E$  value. My values of  $E$  varied over a range of  $\pm 0.1 \times 10^{11}$  when we varied the Poisson's ratio between 0.2 and 0.3 (a typical range for most materials). This was done as the published values assumed a certain quality of diamond that was unquestionably not appropriate for some of my samples. We would have preferred to use Sneddon's solution for a spherical tip; however, it required that the penetration of the sphere would never pass beyond the midpoint during the measurement. This arose from the assumption that the sphere would fit the elastic half space on a given radius. On typical atomic force microscope tips, penetration is significantly larger than the tip radius, thus making the assumption of a flat-ended cylindrical punch more appropriate.

### 3.11.4 Force Versus Distance Curves

Much has been said of the adhesive capillary force produced by surface films on surfaces under measurement.<sup>259–266</sup> My measurements were made over several weeks and the conditions of humidity and temperature were not controlled. The hydrostatic surface forces were not only a result of the ambient conditions but also were affected by the makeup of the contamination layer (surface), which was expected to vary considerably due to the experimental variations in levels of the precursor gases.

Two representative curves from two different samples are shown from my data in figures 22 and 23. Images and surface analysis results were taken for each measurement and will be discussed later. The

sample GAM6s5p2 shows a typical one-segment curve where the loading curve shows only one segment, up until the load reversal. This curve is broken into a top half and a bottom half as shown in the small graphs. An important aspect to this was that in all of my curves, the slope of the top half was higher than the slope of the lower portion. The appropriate linear fit to the top and bottom curves are shown above their respective graphs. The sample GAM5s5p5 shows a typical two-component curve with saturation of the detector at the high end of the load. Many of my curves showed this type of behavior, and in all cases we used only the first portion of the loading curve. Typically the cutoff point has its coordinates printed.

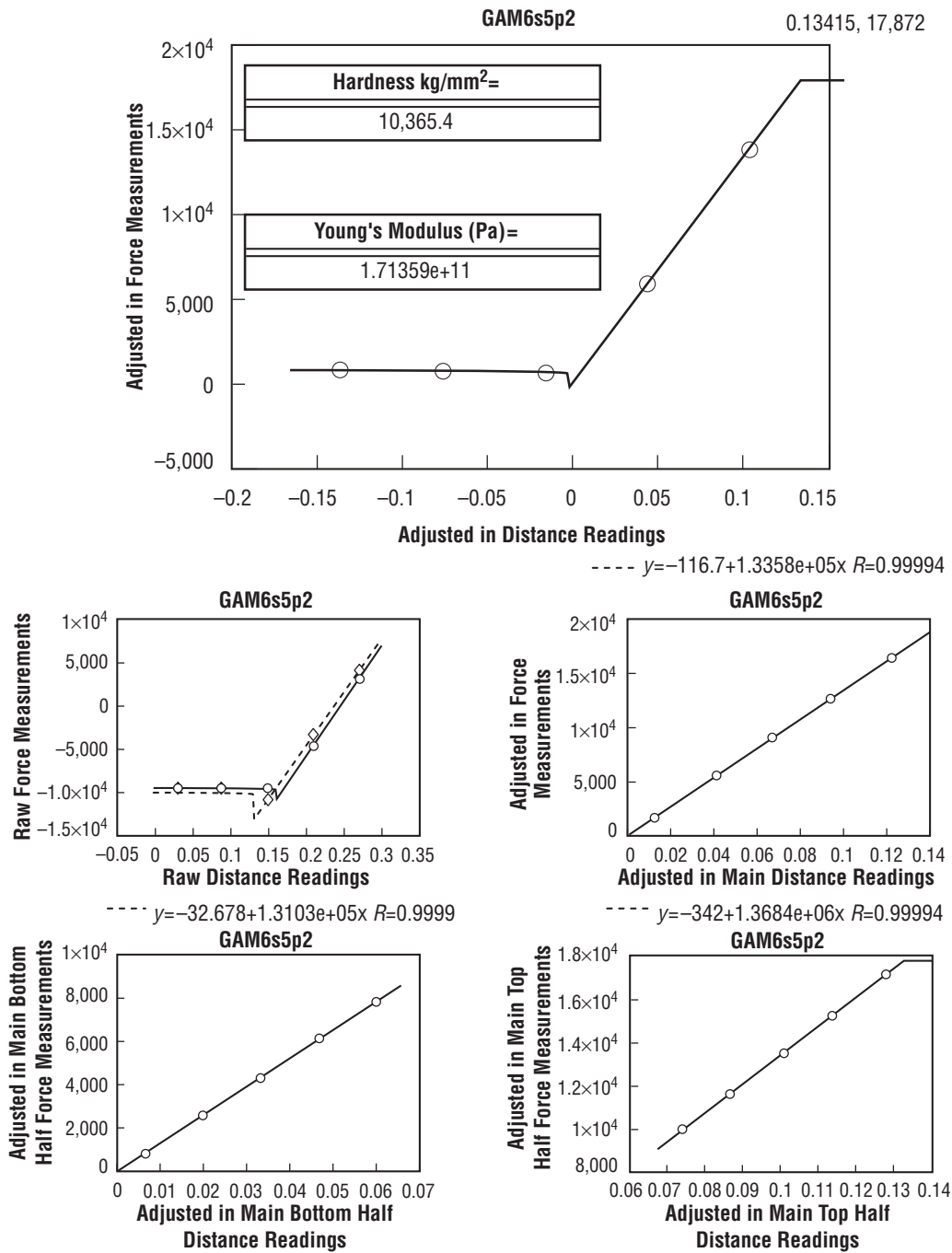


Figure 22. Typical one-segment curve.

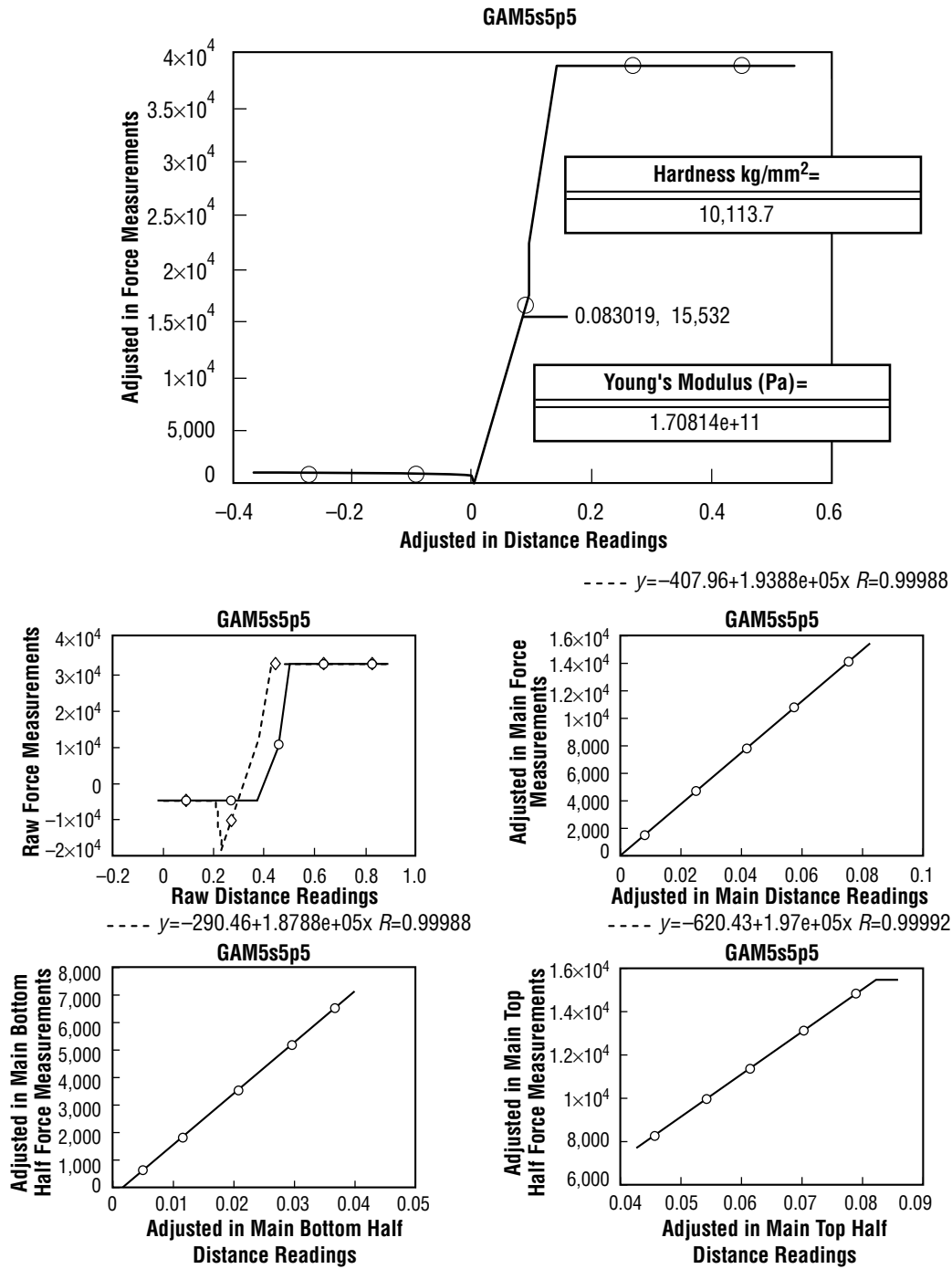


Figure 23. Typical two-segment curve.

### 3.11.5 Overall Statistics on Hardness and Modulus Calculations

My hardness data agree very well with the published data. Looking at both plots of the compiled data in figure 24, the range of my data is fairly widespread; however, the bulk of my data and the calculated average are well within the appropriate range for diamond. My data also show a somewhat higher hardness for the 100 family as contrasted with the 111 family, which also agrees with the published literature. A size

effect has been noted that accounts well for the data points that appear to have too high a hardness. As my samples often may have contained C impurities, the data that appear low in hardness may well be due to local hardness variations away from pure diamond.

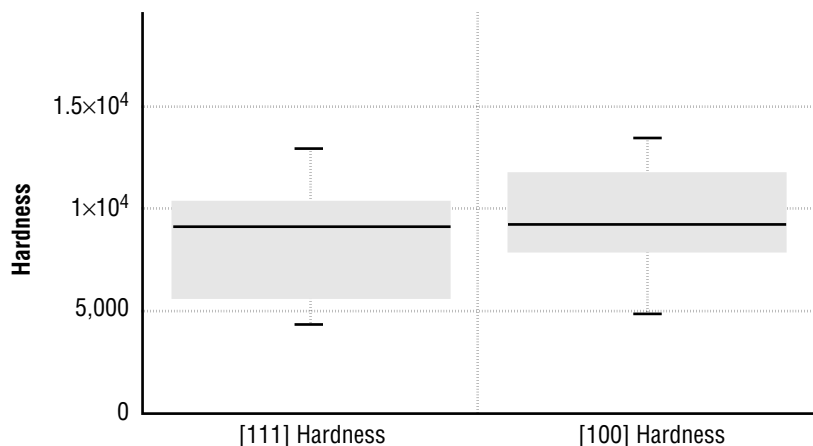


Figure 24. Box plots of hardness.

Using the method of Doerner and Nix/Loubet for calculation of elastic modulus, my values predictably fall about a comparable distance away from the published values of Young's modulus (i.e., about a factor of 4). The spread of the data is reasonably small. The discrepancy between my data and published results is either due to the assumptions required for calculations or the impurity of my diamond.

It should be noted on the raw curves that the slope of the unloading curve is lower than that of the loading curve. For very small plastic deformations, we expected to see very little change in the behavior from loading to unloading curves. In all of my cases, the sample appeared to experience a higher repulsive force on the way out as opposed to during the initial indentation. A number of possibilities could be responsible for this behavior. The behavior might be explained by considering high entrapped stresses within the torch-produced diamond samples. These stresses could be released during the indentation process and thus provide a greater force on the indenter during the unloading curve. The most plausible and best documented explanation, however, would be a simple effect of adhesive force from a surface contamination layer where the difference in slope is a result of the sliding fluid friction between the tip and the contamination layer.

### 3.11.6 Viscoelastic Modulus

Groundbreaking work<sup>255</sup> on mechanical property measurements using force microscopy has used a strictly elastic response analysis on the obtained force versus distance curves. The nature of the majority of force microscopy measurements takes place over a timescale in which it is appropriate to consider the viscoelastic response of both the material and the probe tip. Sneddon's work, on which my procedure is based, has been followed by Graham<sup>272,273</sup> and Ting<sup>274</sup> who have extended the work into the realm of viscoelasticity. A numerical solution is well presented by Calvit.<sup>275</sup> The linear equation of the force versus distance line, including the measurement frequency of the microscope, should provide the time-dependent

distance equation necessary to extend the work into the realm of viscoelasticity. While that work is not presented here, it appears a plausible extension of the current work.

### **3.11.7 Conclusions on the Atomic Force Microscopy Methodology**

A novel extension of the method for nanoindentation measurements on AFM samples was successful in its evaluation of torch-produced diamond films. The procedure used for calculations of hardness provided a wide but appropriate range of values for a large number of samples. My premise, that deviation from linearity on individual linear segments of the curve is due to plastic deformation and can be taken as the plastic contribution to the depth, was well supported. Wherein, on effectively all of my curves, the slope of the top half was larger than the slope of the lower portion. This provided a curve shape similar to traditional load displacement curves. As noted, the method provided shows promise for expansion into the viscoelastic range.

### **3.12 Designed Experiments**

All of the experiments presented in this work are designed experiments. Most of the designs are orthogonal since they allow separation of the process variables to determine individual effects on response variables, independent of the other process variables. Several texts are available on designed experiments and the interested reader is referred to references 276 and 277. The BBN/Catalyst software was used in preparing the graphs produced in this work.

## 4. EXPERIMENTAL RESULTS

### 4.1 GAMoly Experimental Results

#### 4.1.1 Run-Specific Results

Analytical results from the various experimental conditions will be covered case by case. For the GAMoly experiments, visible Raman spectra were taken for all samples; however, during the latter portion of the experiment, FTRaman spectroscopy became available. Unfortunately, the GAMoly experiment was unable to take full advantage of this capability; but, a few comparative spectra were taken. The other torch experiments described hereinafter exclusively used FTRaman because of its higher sensitivity to nondiamond C. Fortunately, the results using visible Raman spectra provide a sufficiently clear picture. Although the TDK simulation might be considered a separate experiment, because the experimental conditions for the simulation mirror those of the GAMoly experiment, simulation results will be covered within the framework of these experimental results.

The GAMoly No. 1 samples provide the condition where no CO is used and the setting for CH<sub>4</sub> is at its intermediate level. The results detail two separate morphology regions—a main growth mound and a radial boundary region. Both regions are composed of diamond crystallites. The main growth mound shows a very high growth rate, probably the best for all samples. The clean surfaces on the top of the mound are rough and have angles near perpendicular in many cases (fig. 25). Five-sided growth structures are noted, that do not resemble anything in the literature; rather, they are more akin to five cubes from a central core. Growth steps are notably present on most of the exposed crystal faces (fig. 26) especially in the central mound. The main growth mound slopes down toward the plateau of the sample surface and the radial boundary region. The radial boundary region shows strong {111} diamond faceting. A sharp boundary is shown between the mound and the boundary region (fig. 27). On the inner side of the boundary, on the foothills of the growth mound, the crystals retain their rough but faceted morphologies. On the outer side of the boundary the crystals show clear <111> faces.

The following different characteristics are noteworthy:

1. Some very clean faces are evident without discernible growth ledges and other facets can be found showing growth that appears to be highest at the crystal edges but deficient toward the crystal center.
2. A few separate nests of <111> faceted crystals were found (fig. 28). A reason for the high local growth at these nest sites is not known; however, a surface C particle/source is suggested.
3. In the boundary region, a strong change in morphology is also noted with a change in height within the film. The outer areas are predominantly <111> faceting and, at the periphery, these crystals may be isolated.





Figure 25. GAMoly No. 1 five-sided growth structures,  $\times 40$ .

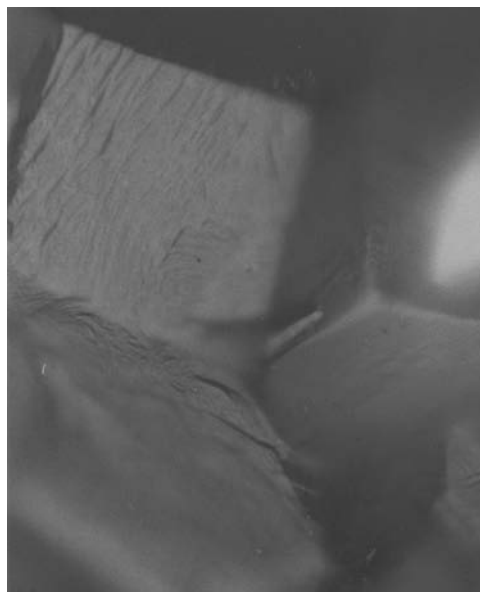


Figure 26. GAMoly No. 1 growth steps,  $\times 100$ .

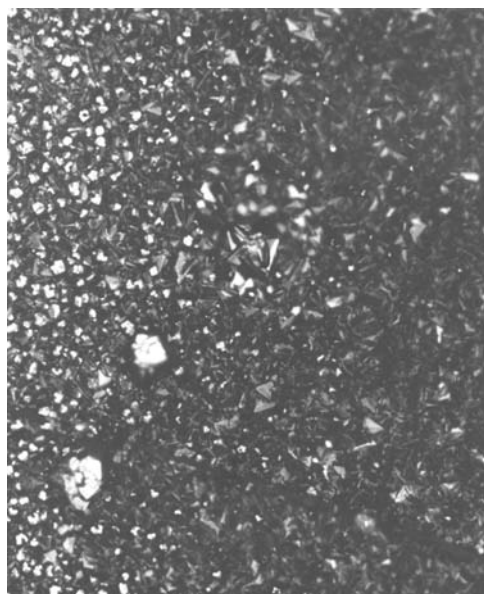


Figure 27. GAMoly No. 1 boundary and mound-region boundary,  $\times 20$ .

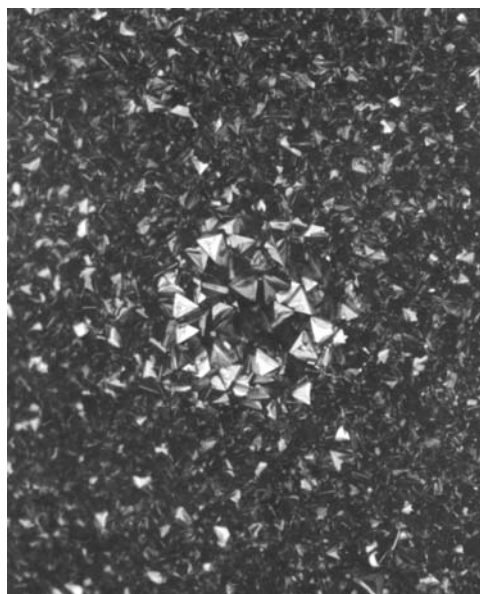


Figure 28. GAMoly No. 1 nest of  $\langle 111 \rangle$  facets,  $\times 20$ .

4. Below this at a reasonably discreet lower level/focus, a series of square terminated pillars are clearly seen, very reminiscent of the primary growth mound structures (fig. 29).

Visible Raman results on GAMoly No. 1 show a strong diamond peak at  $1,337\text{ cm}^{-1}$ . In the visible results, a small shoulder is seen at  $1,351\text{ cm}^{-1}$ , indicating the presence of some microcrystalline graphite (fig. 30).



Figure 29. GAMoly No. 2 lower-level focus showing a series of square-terminated pillars,  $\times 40$ .

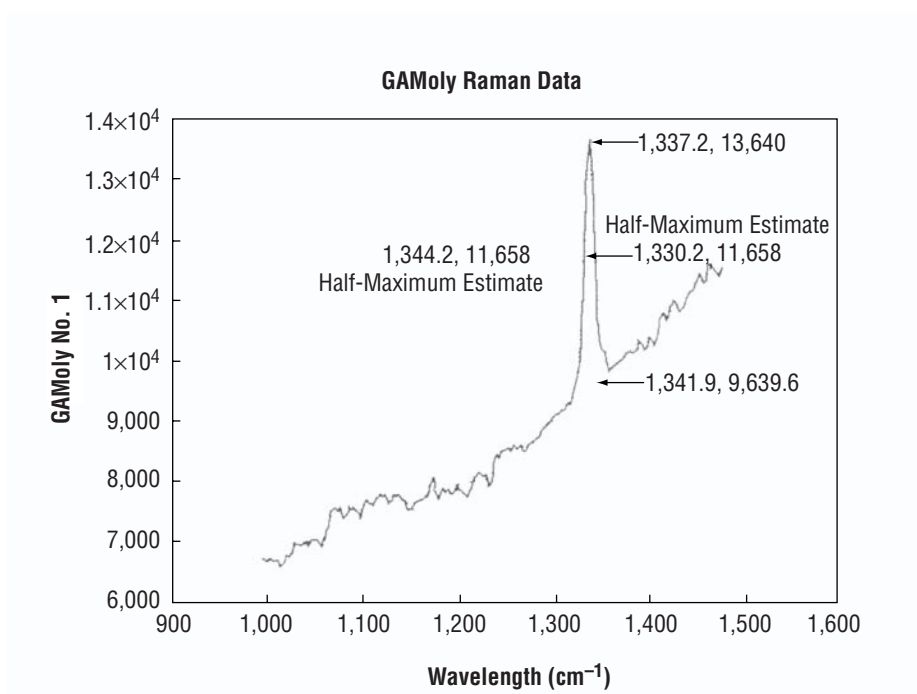


Figure 30. Visible Raman results on GAMoly No. 1.

On a few of the GAMoly samples, FTRaman spectra were taken to look at the increased sensitivity of the FTRaman in contrast to the visible Raman spectra (fig. 31). FTRaman results on GAMoly No. 1 presented a much broader peak combining the 1,350- and 1,332-cm<sup>-1</sup> peaks. Additionally, a shoulder on the combined peak was discernible at 1,193 cm<sup>-1</sup> where a-C might be expected.

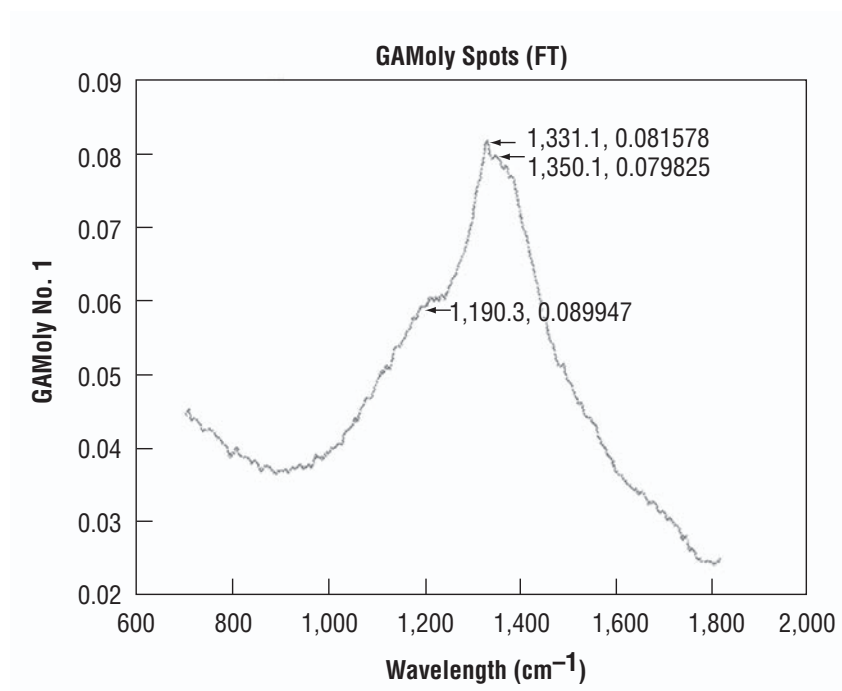


Figure 31. FTRaman results on GAMoly No. 1.

AFM results on GAMoly No. 1 were only provided on {111} or unconstrained facets. The scans were of good quality and generally were taken on crystal facets of approximately 1–4 mm (figs. 32–34). The force versus distance curves that were taken were also of good quality.

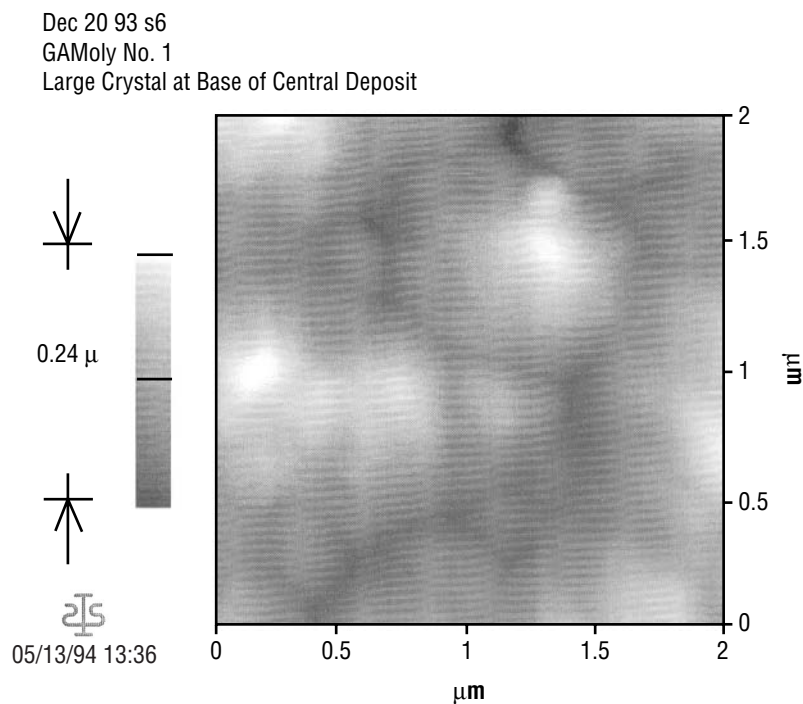


Figure 32. AFM two-dimensional scan for GAMoly No. 1.

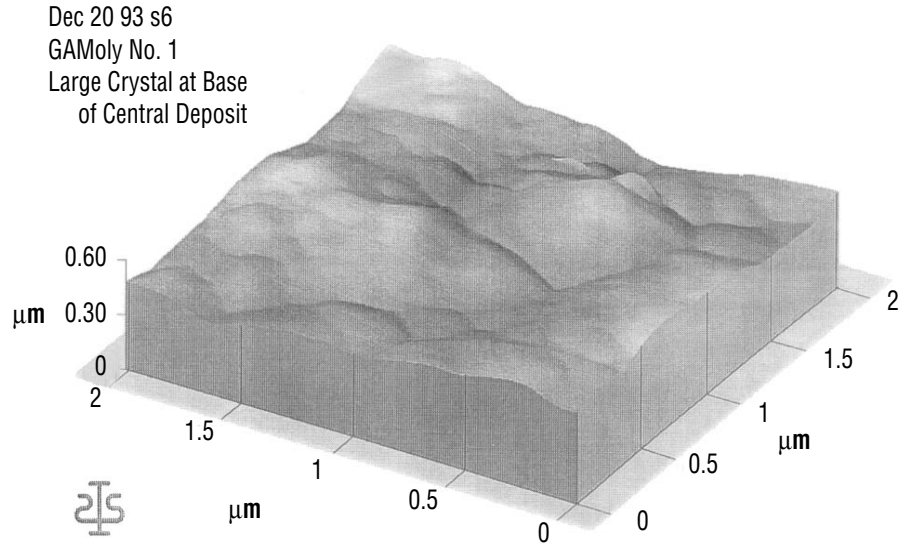


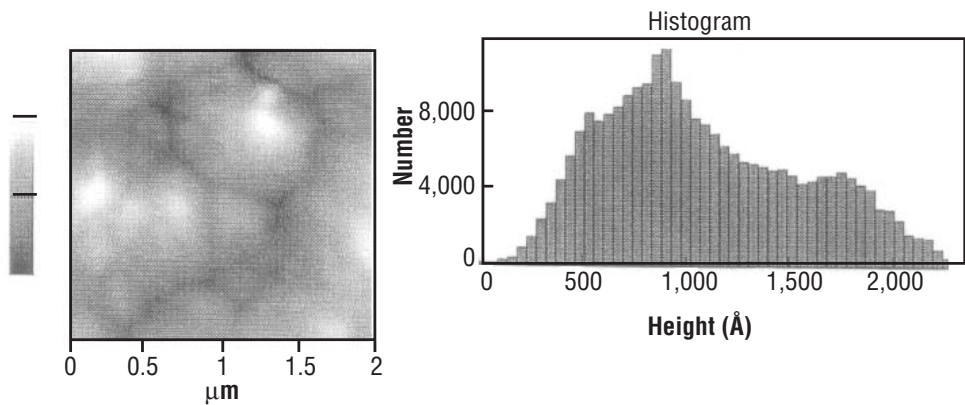
Figure 33. AFM three-dimensional scan for GAMoly No. 1.

#### Region Analysis

Dec 20 93 s6  
GAMoly No. 1  
Large Crystal at Base  
of Central Deposit



5/13/94 13:38



#### Area Statistics:

Median Height: 1,046 Å  
Mean Height: 1,086 Å  
Peak to Valley: 2,324 Å  
Surface Area: 4.38  $\mu^2$   
Projected Area: 3.97  $\mu^2$   
Volume: 0.43  $\mu^3$   
Rms Rough: 485 Å  
Ave Rough: 404 Å  
Bearing Ratio @ 75%: 813 Å

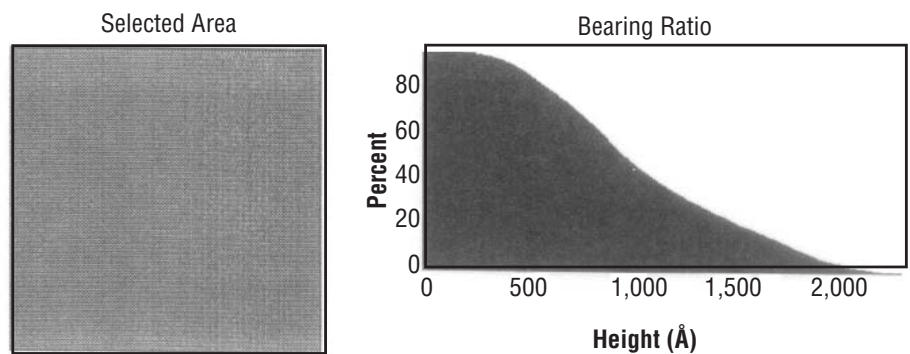


Figure 34. AFM scan analysis for GAMoly No. 1.

The curves generally showed a two-stage indentation trace (fig. 35). The first stage was used for measurement of the hardness and the Young's modulus. The curves were relatively clean during the indent trace, indicating light contamination and a single-phase material.

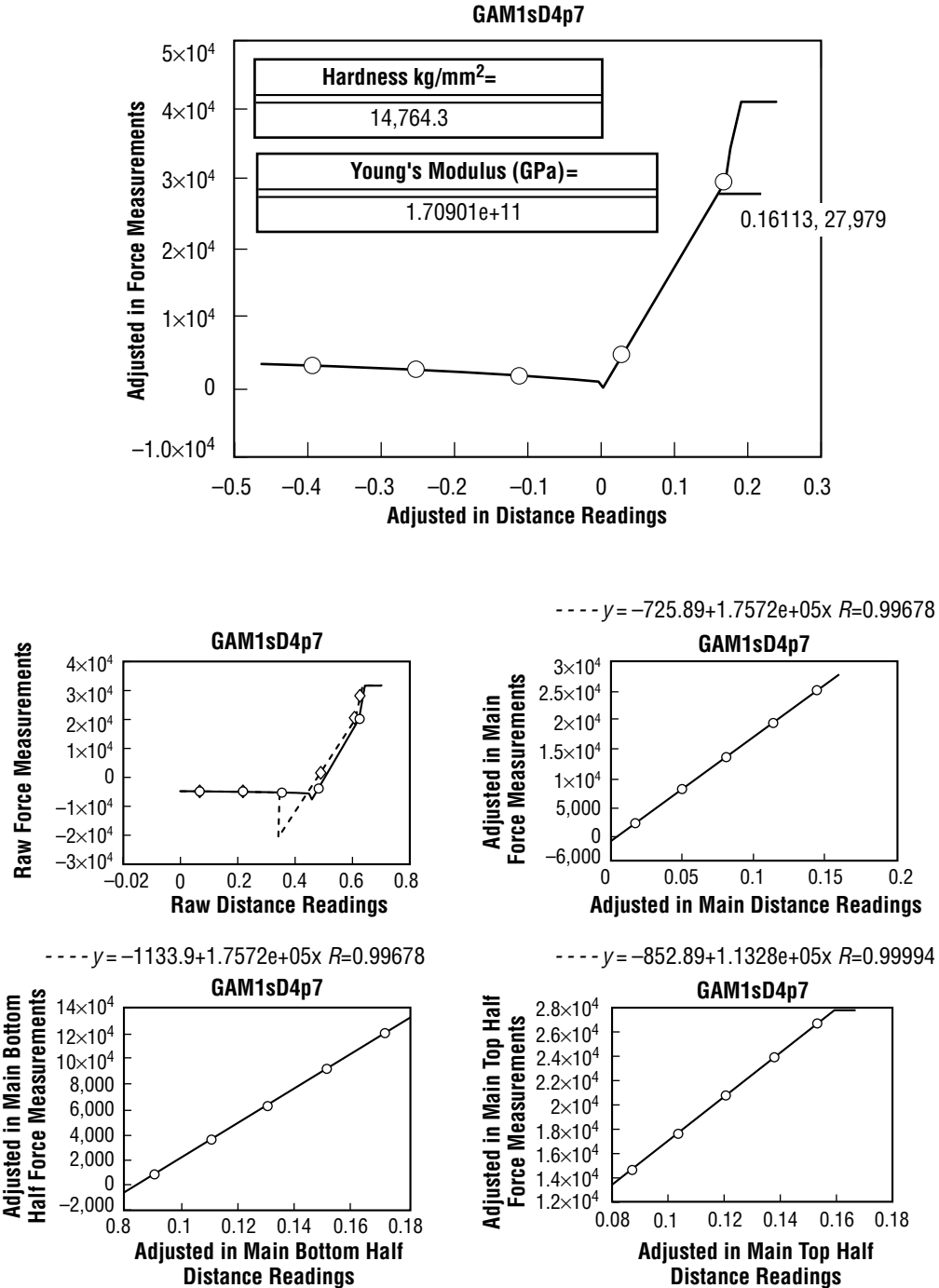


Figure 35. Force versus distance trace breakdown for GAMoly No. 1.

GAMoly No. 2 provides the midrange setting for addition of CO and the highest setting for addition of CH<sub>4</sub>. The dominant morphology in GAMoly No. 2 is the appearance of a large number of basically identical pillars forming a forest (fig. 36). There is a drastic change in morphology with height above the surface. A strong increase in faceting occurs moving away from the substrate. Faceting tends to be predominantly <111> (fig. 37) until the pillar summit, at which point the termination facets are predominantly <100> (fig. 38). The terminating square facets tend to be clean, and the supporting <111> facets are very



rough. Twinning pyramids are found on many of the supporting  $\langle 111 \rangle$  structures. Very strong faceting (predominantly  $\langle 111 \rangle$ ) is also observed on the edge of the sample. The faceting and high growth is limited to a very narrow radius on the sample edge, but the crystal size is as large as any of the inner sample crystal facets (fig. 39).

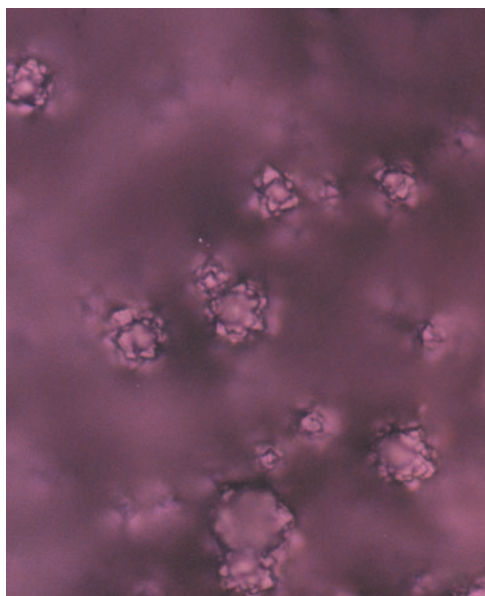


Figure 36. GAMoly No. 2 identical pillars forming a forest,  $\times 100$ .

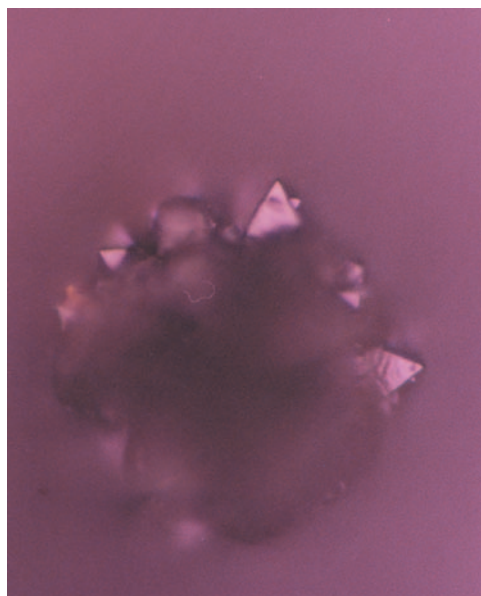


Figure 37. GAMoly No. 2  $\langle 111 \rangle$  faceting at midlevel heights,  $\times 100$ .

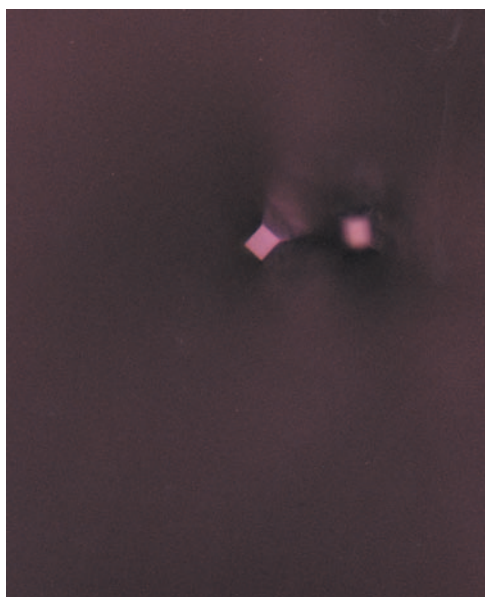


Figure 38. GAMoly No. 2  $\langle 100 \rangle$  summit faceting,  $\times 100$ .

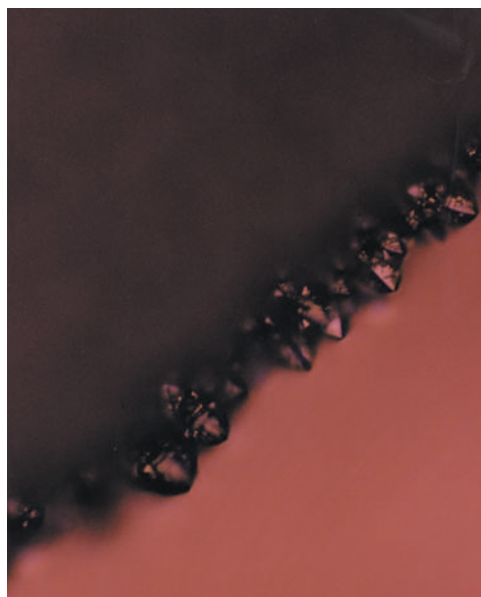


Figure 39. GAMoly No. 2 edge faceting,  $\times 40$ .

The Raman results for GAMoly No. 2 using visible light show a small but well-defined peak at  $1,338\text{ cm}^{-1}$  (fig. 40). In the FTRaman results, a rounded peak is noted at  $1,325\text{ cm}^{-1}$ , which is supported by a companion pair of shoulders at  $1,388$  and  $1,193\text{ cm}^{-1}$ . The stronger return for nondiamond C is very apparent when the two spectra are compared (fig. 41).

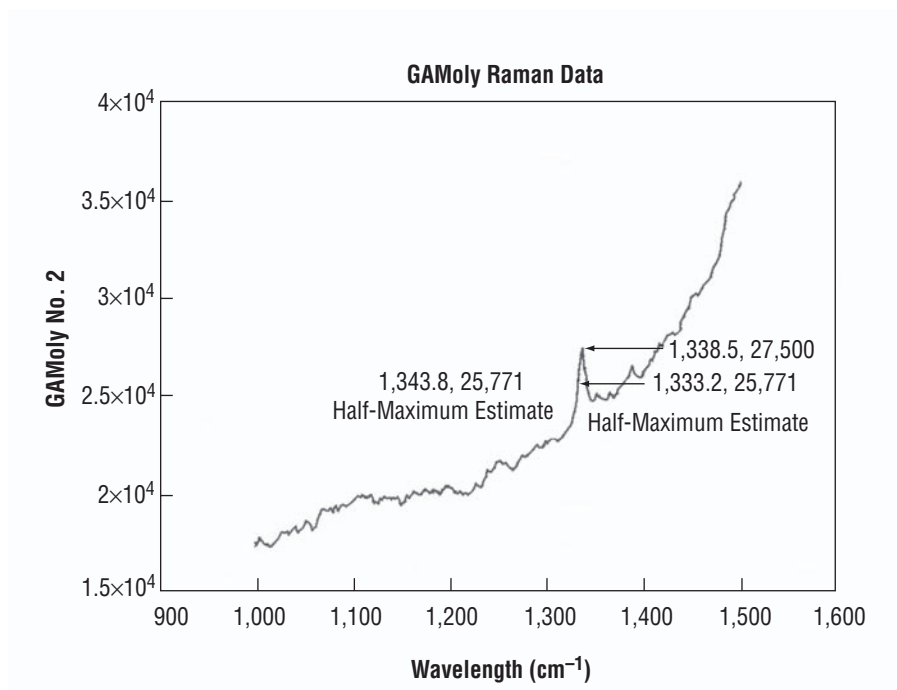


Figure 40. Visible Raman results for GAMoly No. 2.

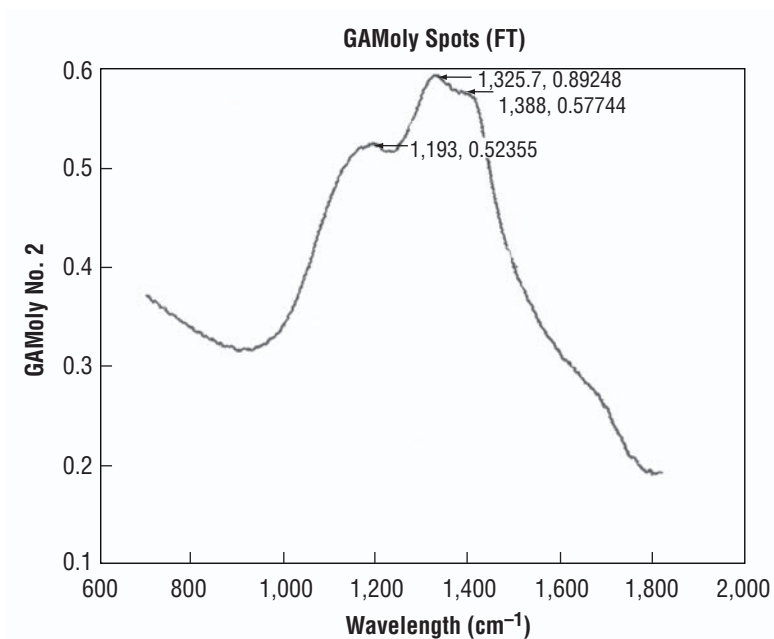


Figure 41. FTRaman results for GAMoly No. 2.

AFM results on GAMoly No. 2 were achieved for both {100} and {111} facets. The scan areas were typically 2,000–4,000 square Å (figs. 42–44). Optically, the upper surface facets appeared smooth and defect free. Generally, the AFM scans supported this with scattered, poorly defined hillocks and the lowest surface finish numbers of any sample set. The force versus distance traces show some two-stage traces but predominantly one-stage traces were recorded (fig. 45). Strong contamination layers were noted for these samples.

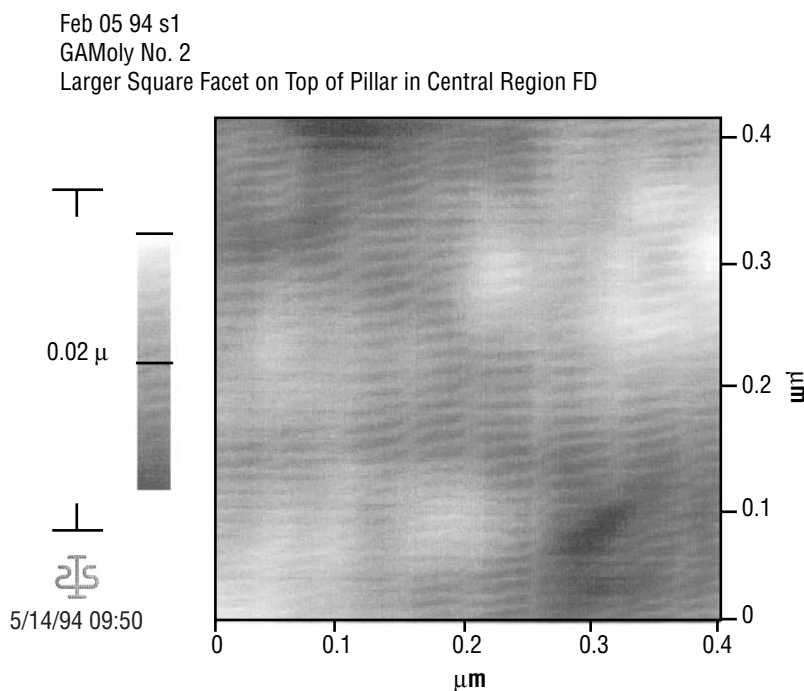


Figure 42. AFM two-dimensional scan for GAMoly No. 2.

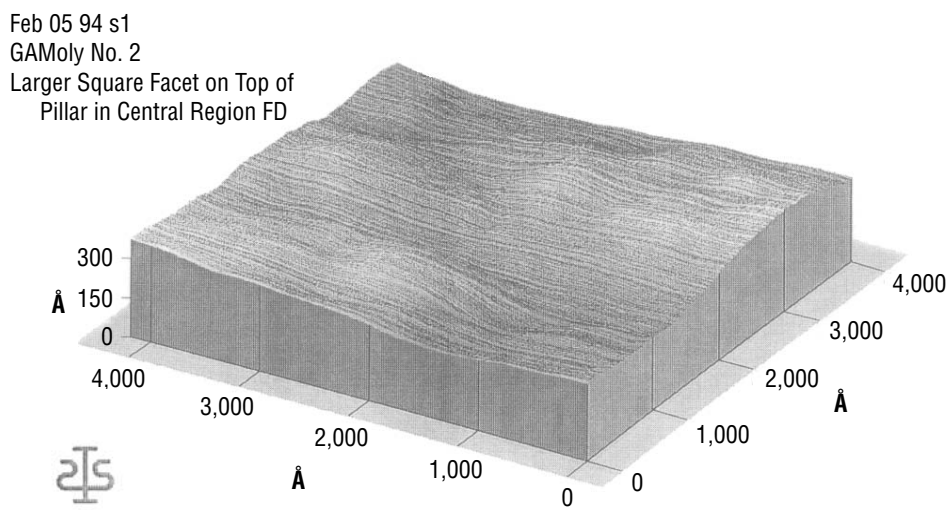


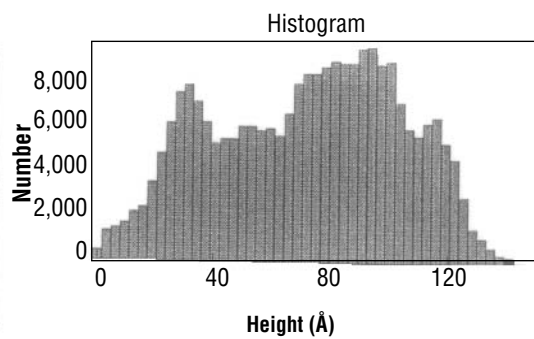
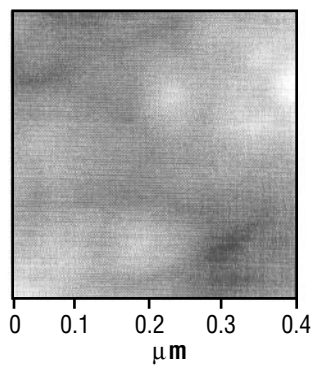
Figure 43. AFM three-dimensional scan for GAMoly No. 2.



Feb 05 94 s1  
 GAMoly No. 2  
 Larger Square Facet on Top  
 of Pillar in Central  
 Region FD



5/14/94 9:56



#### Area Statistics:

Median Height: 85 Å  
 Mean Height: 77 Å  
 Peak to Valley: 154 Å  
 Surface Area: 0.17  $\mu^2$   
 Projected Area: 0.17  $\mu^2$   
 Volume: 1.3e+09 Å<sup>3</sup>  
 Rms Rough: 34 Å  
 Ave Rough: 28 Å  
 Bearing Ratio @ 75%: 54 Å  
 Bearing Ratio @ 50%: 85 Å

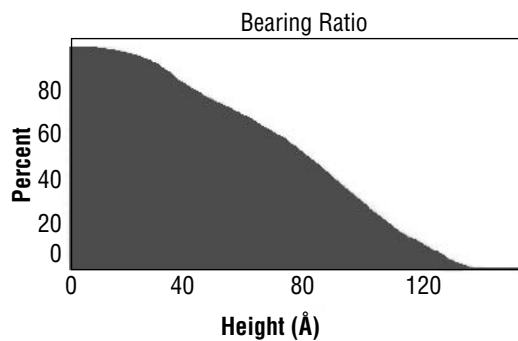
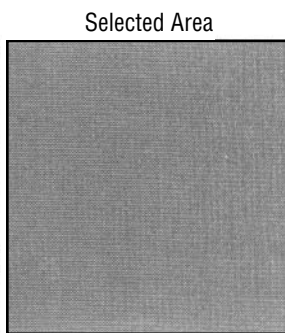


Figure 44. AFM scan analysis for GAMoly No. 2.

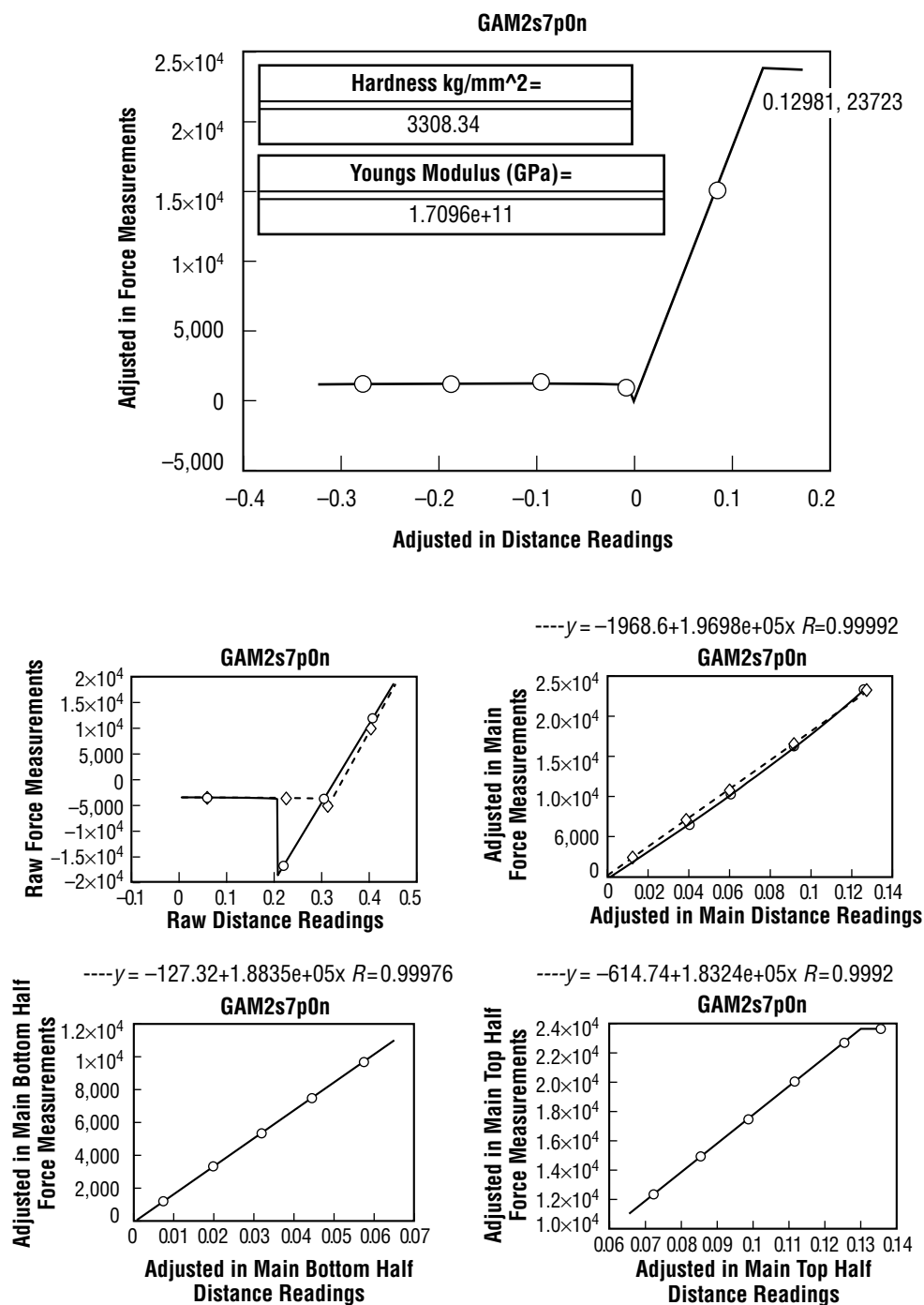


Figure 45. AFM force-versus-distance breakdown for GAMoly No. 2.

GAMoly No. 3 was the sample run where no addition of gases were used. This corresponds most closely with the results in the literature for deposition conditions and morphological results. The surface shows predominantly a mixture of small  $\langle 111 \rangle$  and  $\langle 100 \rangle$  facets (figs. 46 and 47). The crystal facets are well defined and tend to slightly resemble pillar-type growth structures. Most facets show a few defined growth steps. Outside of the central region, the faceting leans toward  $\langle 111 \rangle$  facets; however, in all parts of the film, both  $\langle 111 \rangle$  and  $\langle 100 \rangle$  facets may be found.

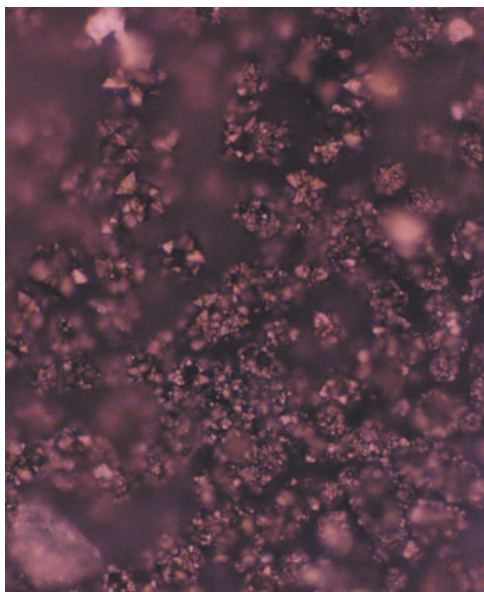


Figure 46. GAMoly No. 3 surface  
 $\langle 111 \rangle$  facets,  $\times 40$ .

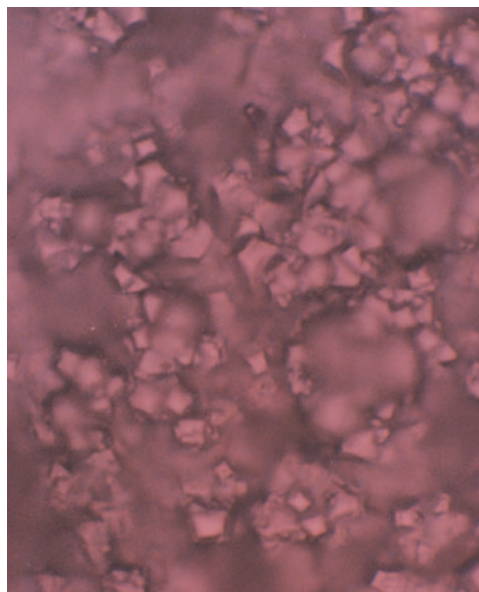


Figure 47. GAMoly No. 3 surface  
 $\langle 100 \rangle$  facets,  $\times 150$ .

Raman results on these samples showed a very strong, very narrow diamond peak at  $1,338.5 \text{ cm}^{-1}$ . The peak to background height was the highest on these samples (fig. 48).

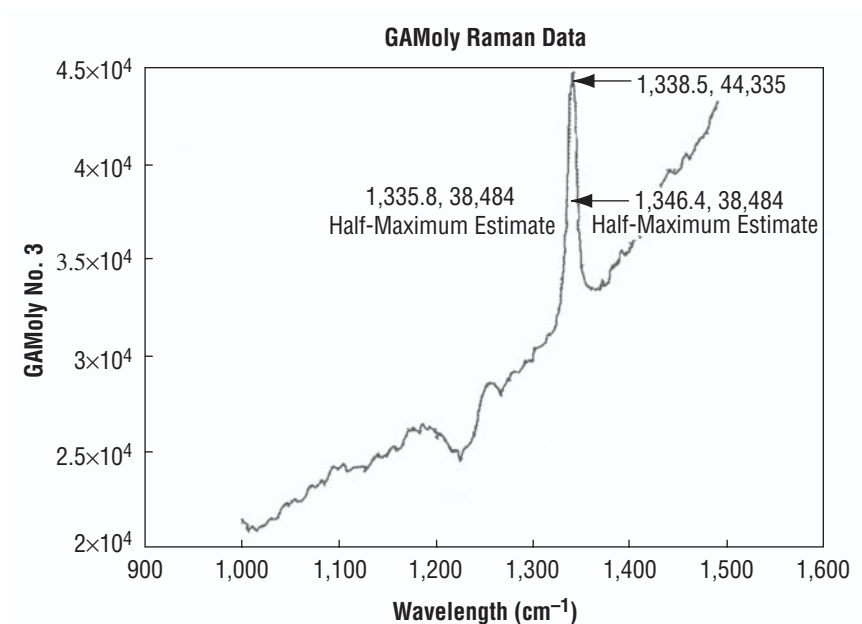


Figure 48. Raman results for GAMoly No. 3.

AFM scans of these samples were excellent. A good view of growth steps (figs. 49–51) can be seen on a {111} surface, which was scanned at a strong angle to the surface parallel. Force versus distance curves could not be obtained on these samples so the contribution has been excluded in the designed experiment calculations of hardness and Young's modulus.

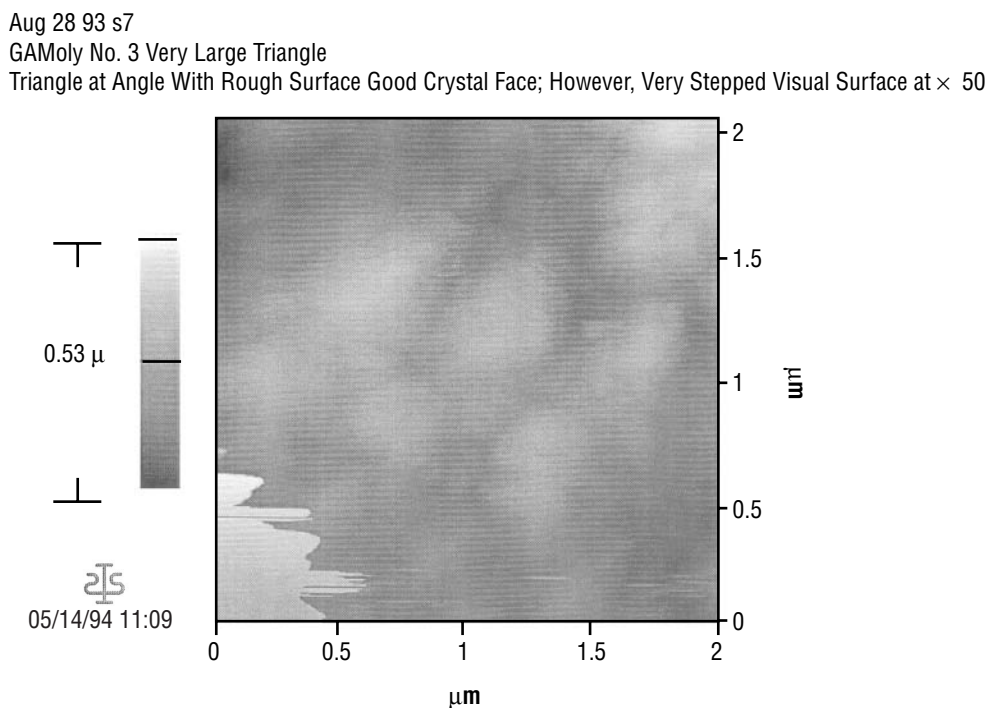


Figure 49. AFM two-dimensional scan for GAMoly No. 3.

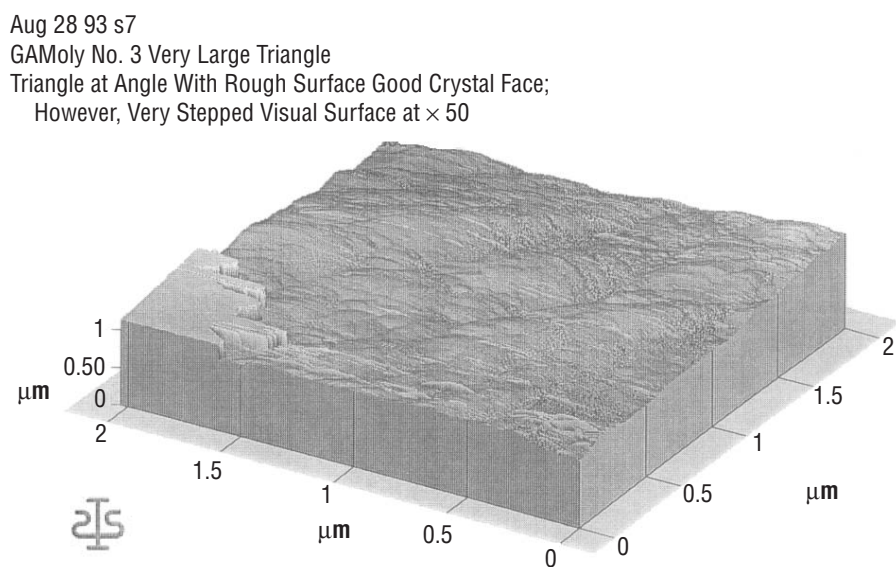
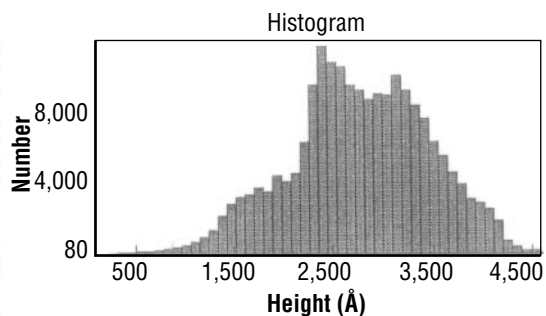
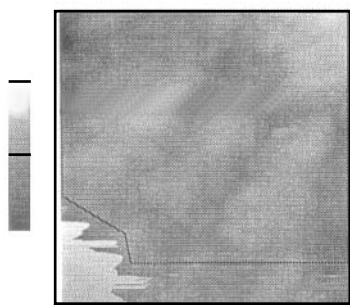


Figure 50. AFM three-dimensional scan for GAMoly No. 3.

Aug 28 93 s7  
 GAMoly No. 3 Very Large Triangle  
 Triangle at Angle With Rough  
 Surface Good Crystal Face;  
 However, Very Stepped  
 Visual Surface of  $\times 50$ .



05/14/94 11:11



#### Area Statistics:

Median Height:	2,815 Å
Mean Height:	2,757 Å
Peak to Valley:	4,632 Å
Surface Area:	43,737,000.00 $\mu^2$
Projected Area:	3.23 $\mu^2$
Volume:	0.89 $\mu^3$
Rms Rough:	722 Å
Ave Rough:	579 Å
Bearing Ratio @ 75%:	2,316 Å
Bearing Ratio @ 50%:	2,779 Å

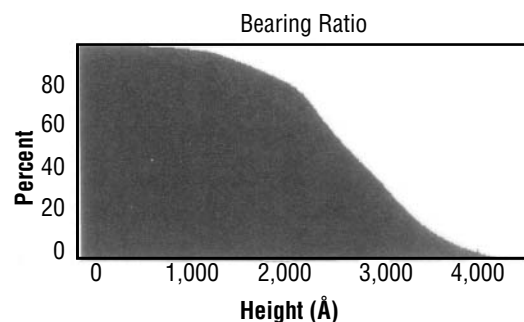
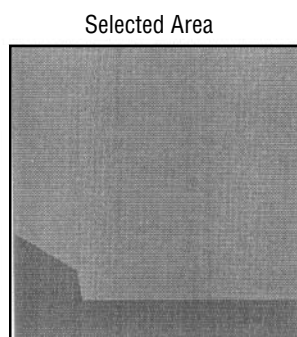


Figure 51. AFM scan analysis for GAMoly No. 3.

The GAMoly No. 4 samples provided the highest addition of CO and the highest addition of  $\text{CH}_4$ . These samples were very difficult to produce as the flame was unstable and frequently blew out, ruining some samples. The reasons behind the blowout behavior of the flame will be discussed in the following section. For the successful samples, the entire surface is apparently covered by a-C and a cauliflower morphology of nonfaceted C (fig. 52). One small triangular structure was noted (fig. 53). The triangle was very small and it was the only structure found with any arguable faceting. Toward the edge of the sample, the surface became sharper in its surface roughness appearance with the presence of whiskers or sharper bends in the cauliflower. Overall, there is no optical evidence of crystals of any type; however, pillaring is noted as the depth of focus changes on the sample.

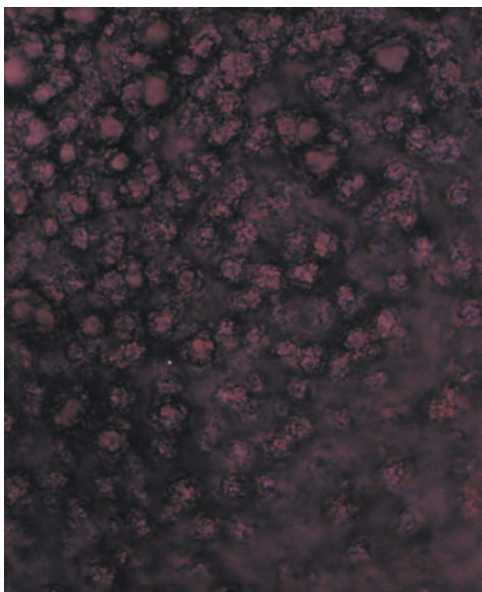


Figure 52. GAMoly No. 4 a-C and cauliflower morphology,  $\times 100$ .

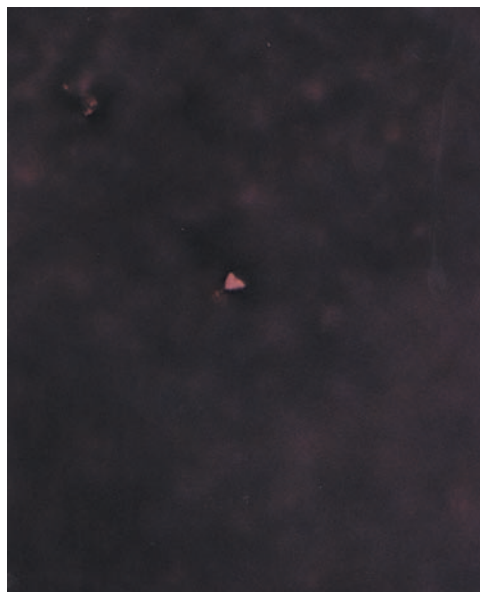


Figure 53. GAMoly No. 4 small triangular structure,  $\times 100$ .

The Raman results for this sample were a surprise considering the optical appearance of the sample. In fact, visible Raman data did show a defined peak at  $1,338\text{ cm}^{-1}$  with a stronger  $1,357\text{-cm}^{-1}$  peak (fig. 54). FTRaman spectra were taken on this sample as well. They also confirmed the presence of a diamond peak with micrographitic and a-C peaks at lower levels (fig. 55).

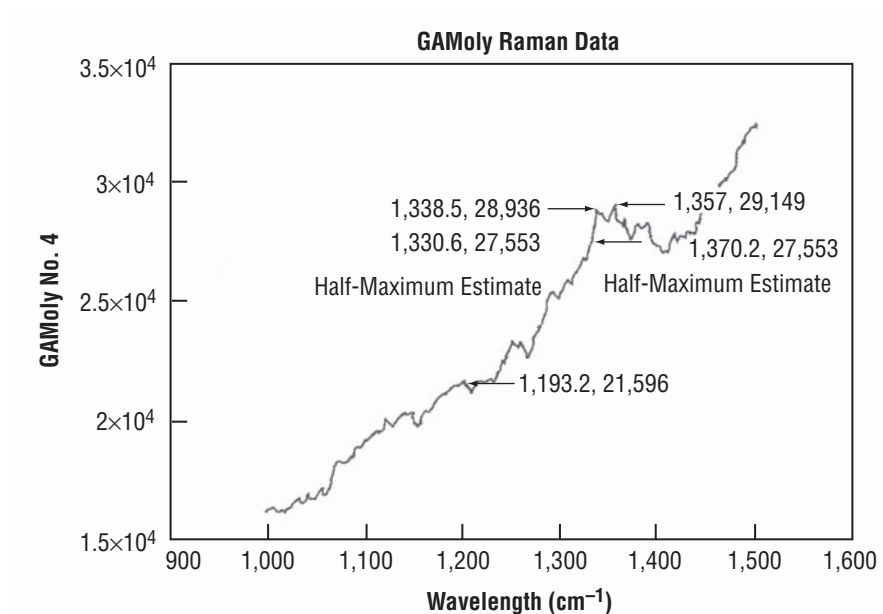


Figure 54. Visible Raman spectra of GAMoly No. 4.



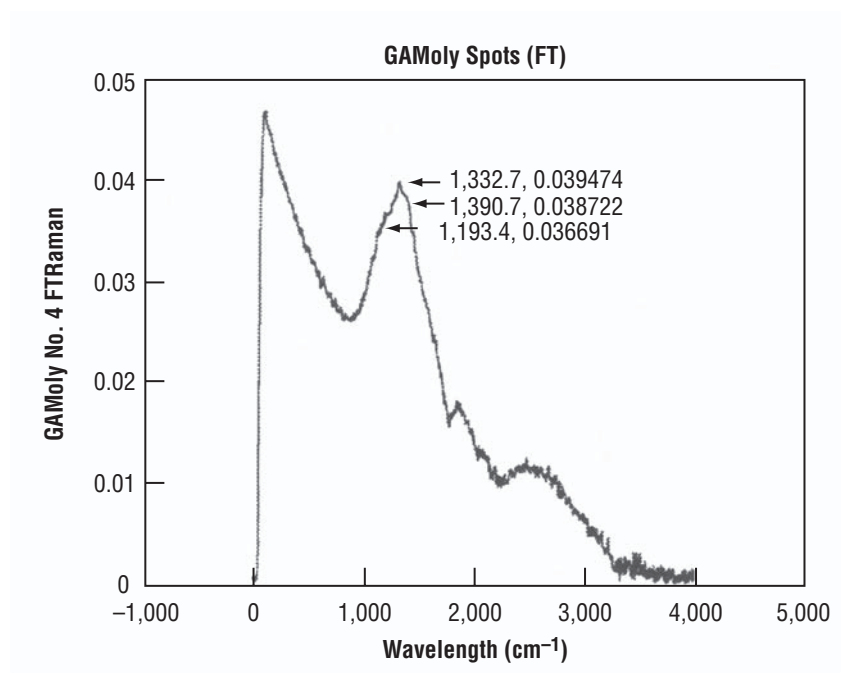


Figure 55. FT-Raman spectra of GAMoly No. 4.

AFM data were not used for this sample because no faceted surfaces could be found on which to take data. Scans of the surface were taken; however, they were not used in calculations.

The GAMoly No. 5 result arose from the highest additive level of CO and the midrange additive level of CH<sub>4</sub>. The surface was well covered with pillars that, on their top surface, show small <111> and <100> facets (fig. 56). In general, the surface looks much like that of GAMoly No. 3 with fewer pillars (fig. 57) so that the pillars appear more isolated and less like a continuous surface. The triangular facets are mostly covered with growth, cauliflower roughnesses, or secondary growths (fig. 58). This usually appears to be a layer or partial layer of noncrystalline material. A number of <111> facets, whose pillar is terminated by a <100> face, appear less contaminated or to have less secondary growth on their exposed surface.



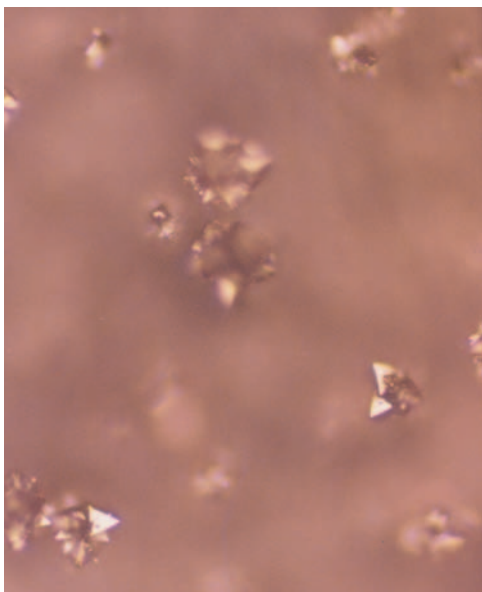


Figure 56. GAMoly No. 5 pillars with  $\{111\}$  and  $\{100\}$  facets,  $\times 40$ .

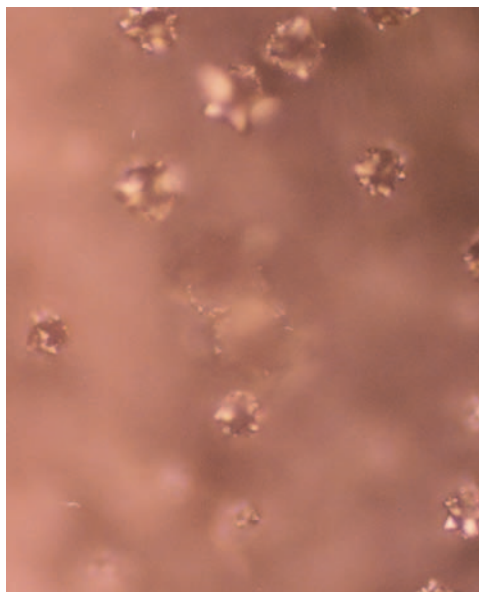


Figure 57. GAMoly No. 5 isolated pillars,  $\times 40$ .

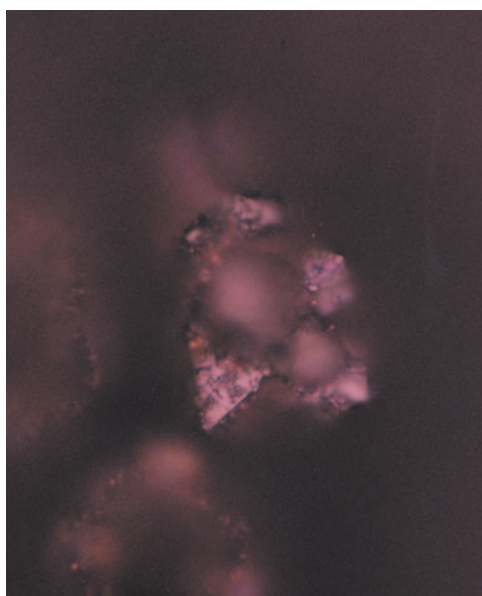


Figure 58. GAMoly No. 5 covered  $\{111\}$  surfaces,  $\times 100$ .

The visible Raman data from this sample set surprisingly showed only the smallest of diamond peaks (fig. 59). Only the presence of clear faceting encourages the identification of the  $1,338.5\text{-cm}^{-1}$  peak from the background.

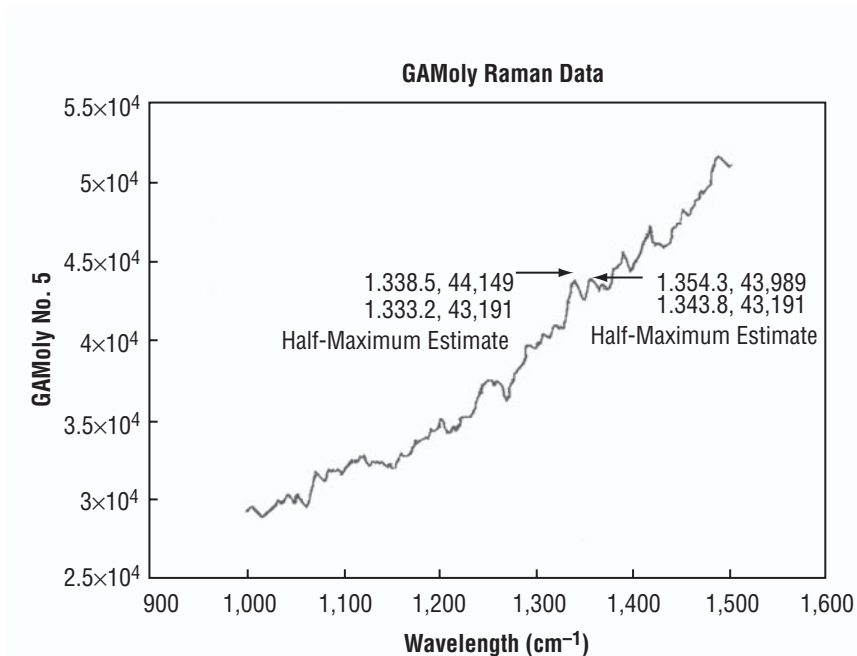


Figure 59. Visible Raman data for GAMoly No. 5.

AFM data on these samples provided data only on  $\{111\}$  surfaces. Scans were difficult to acquire, and most scans had some region that had to be removed from the calculation of surface roughnesses. Scans typically were taken over areas of  $1 \text{ mm}^2$  or less. The  $\{111\}$  facets were clean but showed a rough surface typical of this deposit (figs. 60–62). Force versus distance scans were all two-stage traces where the first trace was used for calculation. Some of the indentation traces were often slightly jagged or rough, characteristic of other than a single-phase material. The first stage was, in general, shorter than the second trace (fig. 63) unlike the previous two-stage traces.

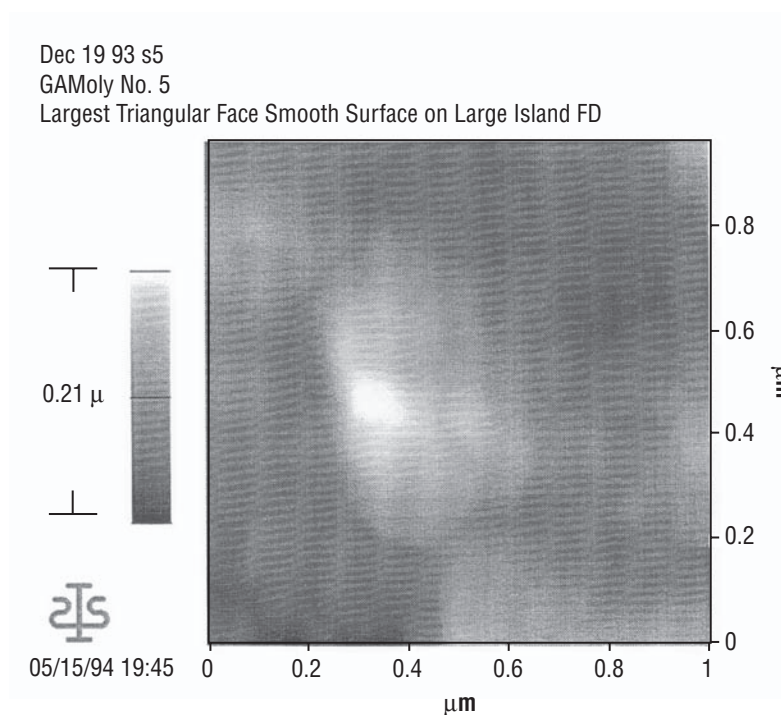


Figure 60. AFM two-dimensional scan for GAMoly No. 5.

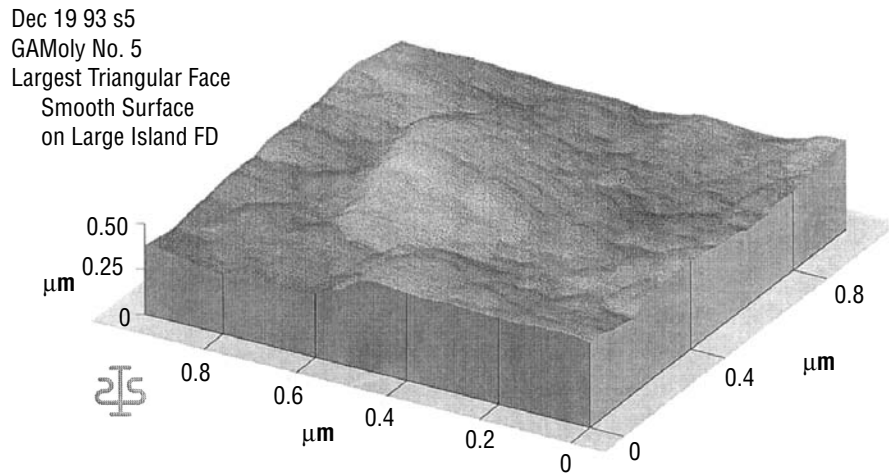


Figure 61. AFM three-dimensional scan for GAMoly No. 5.

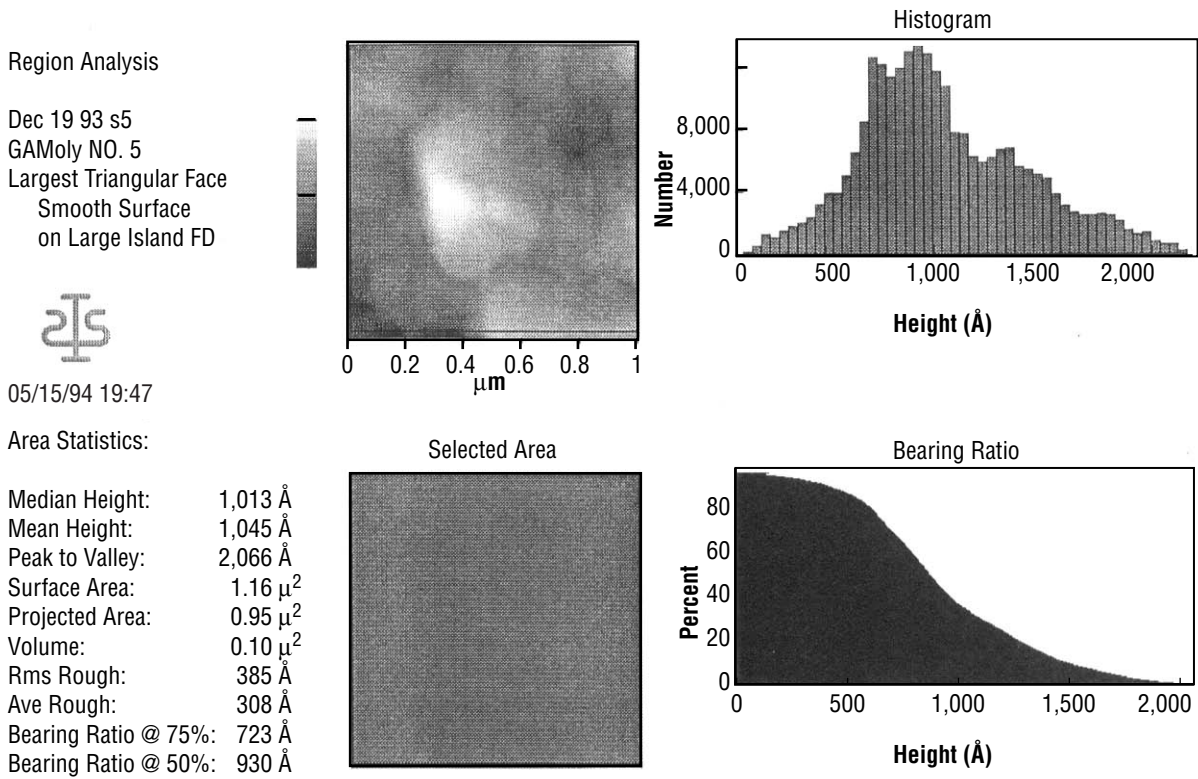


Figure 62. AFM scan analysis for GAMoly No. 5.

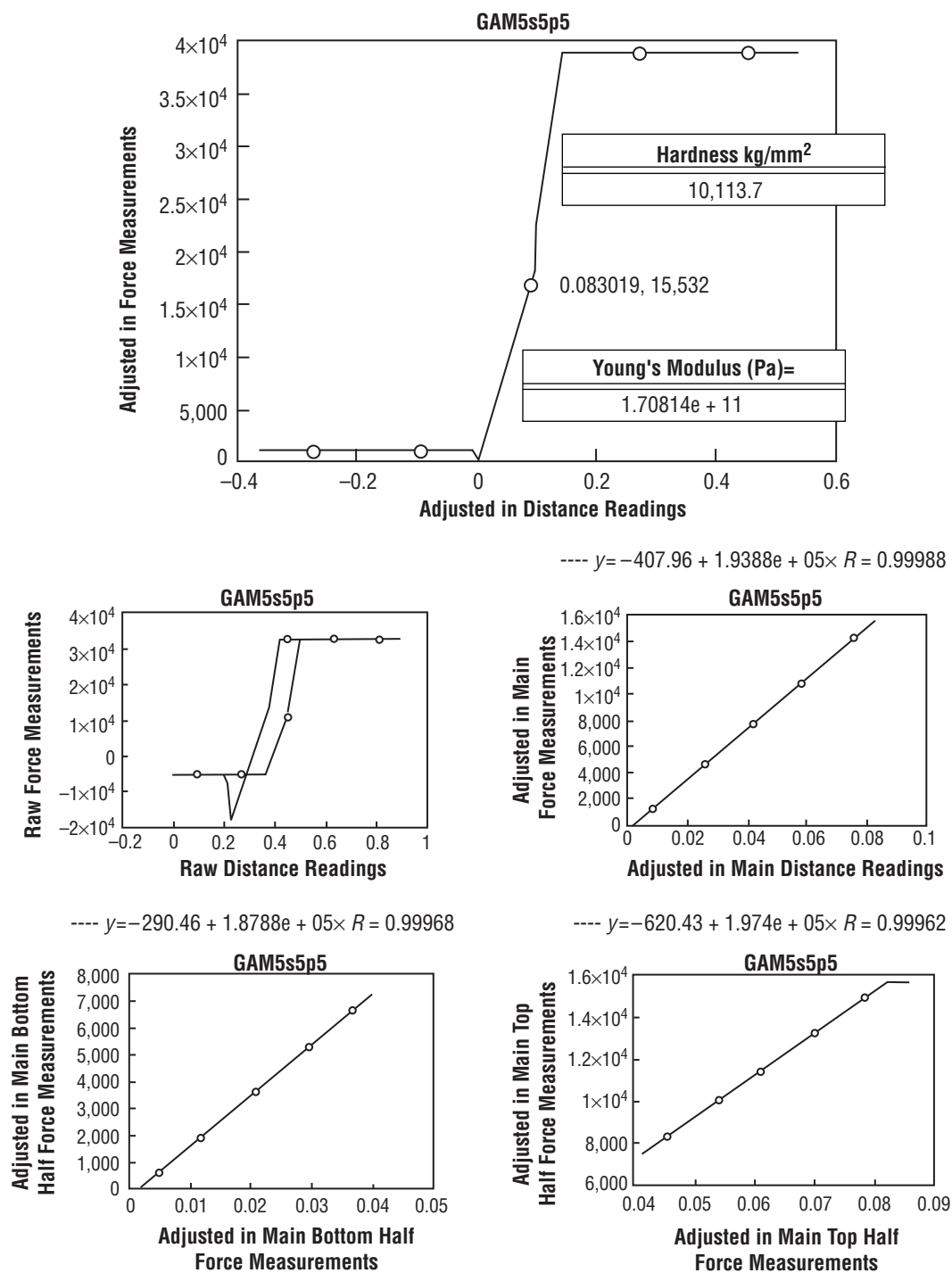


Figure 63. AFM force-versus-distance breakdown for GAMoly No. 5.

GAMoly No. 6 samples were deposited with the highest addition of CO and no CH<sub>4</sub> at all. In general, the samples separated from the Mo substrate leaving a freestanding film and a portion remaining adhered to the substrate. This behavior is typical for thicker diamond films on Mo. The portion remaining

on the substrate shows predominantly  $\langle 100 \rangle$  facets with secondary growth or intermittent nondiamond coverage (fig. 64). The freestanding film portion of GAMoly No. 6 also shows all exposed faces with what appears to be three-dimensional secondary growths. These growths are nonfaceted (figs. 65 and 66). Most crystalline faces show some layered growth, and a significant number of growths are sharp facets without a defined geometry, much like those found in GAMoly No. 1 but at a reduced level of growth. Photos were taken of the backside of the freestanding films. In no case did they show any faceting; however, the film backside was for the most part continuous (fig. 67). The film backside also showed no obvious relationship to surface preparation of the samples. Significantly, unlike several of the other samples, there is not a substantial change in morphology noted with depth where pillars can be found.

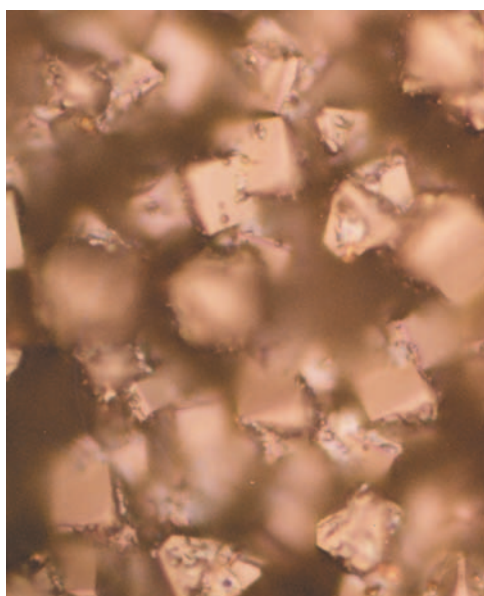


Figure 64. GAMoly No. 6  $\{100\}$  facets with secondary growth,  $\times 100$ .

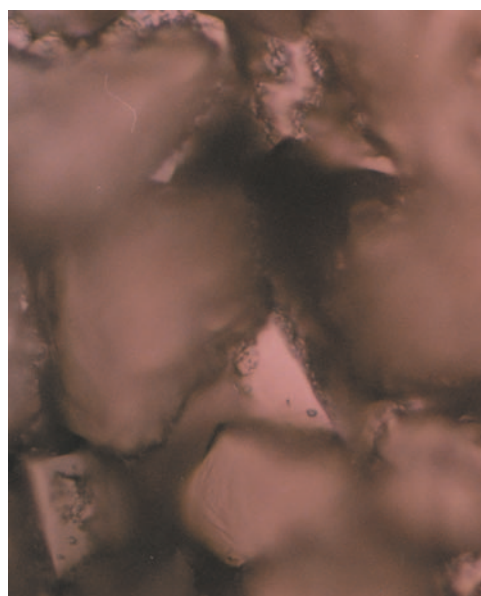


Figure 65. GAMoly No. 6 secondary growth on midlevel facets,  $\times 100$ .



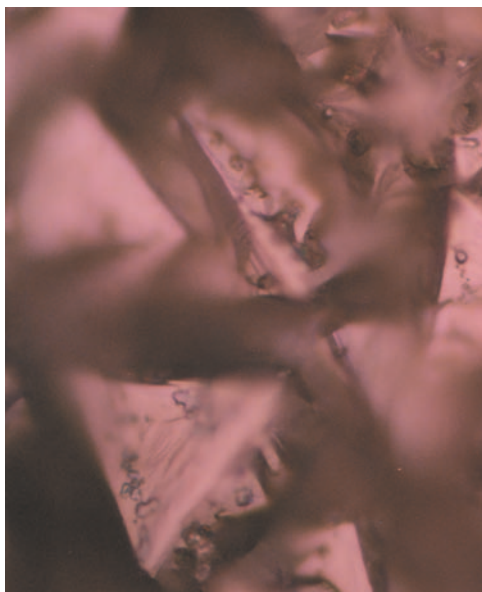


Figure 66. GAMoly No. 6 surface facets with growths,  $\times 100$ .

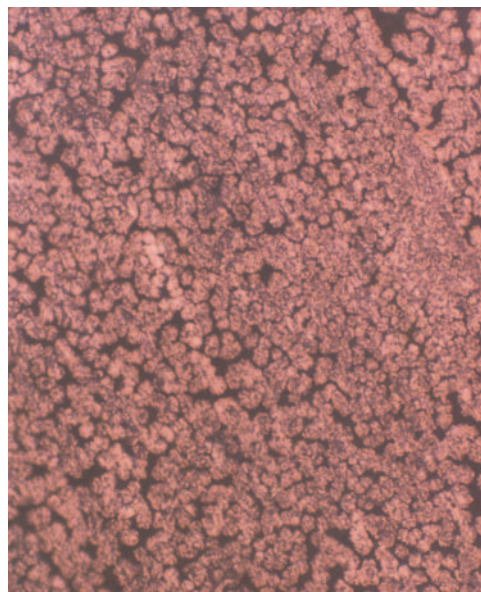


Figure 67. GAMoly No. 6 sample backside,  $\times 20$ .

The visible Raman data on GAMoly No. 6 show a strong diamond peak at  $1,341\text{ cm}^{-1}$  with no graphitic or a-C shoulder. The linewidth, FWHM, of the diamond signal for this sample is very narrow (fig. 68).

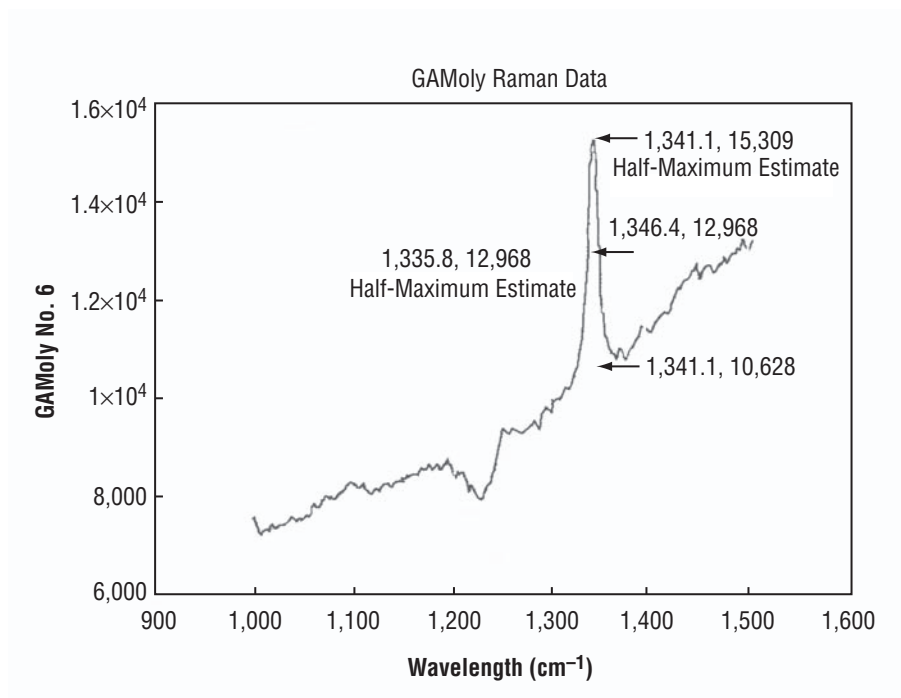


Figure 68. Visible Raman results on GAMoly No. 6.

AFM scans and force-versus-distance traces were taken on both  $\{111\}$  and  $\{100\}$  facets. Typical of this deposit, garbage or nonfaceted material covered many of the exposed crystal faces (figs. 69–71). Scans were generally taken over 2–3  $\text{mm}^2$  areas; however, most scans, such as the previous example, had regions that were removed prior to calculation because of the difficulty getting complete data. All of the force-versus-distance traces were single-stage traces; however, many of them were rough (fig. 72), indicative of the surface material noted in the scans.

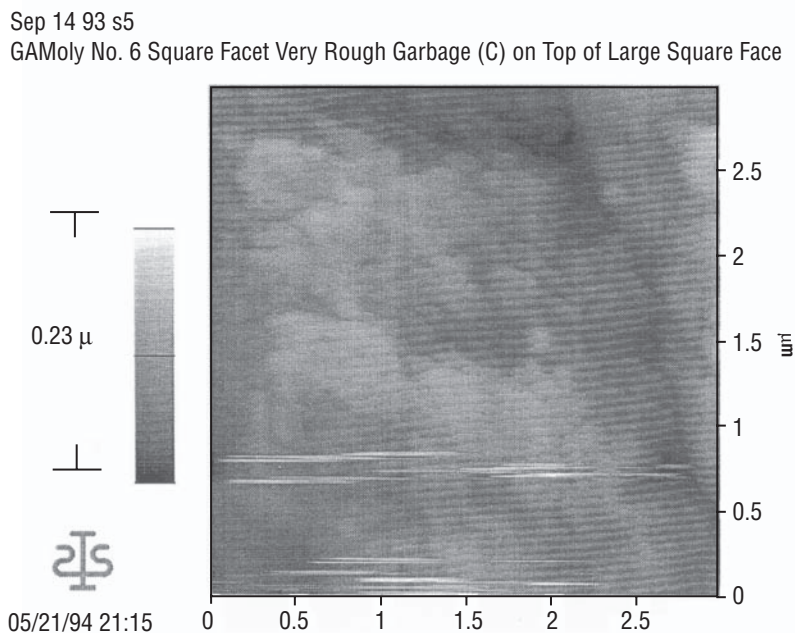


Figure 69. AFM two-dimensional scan for GAMoly No. 6.

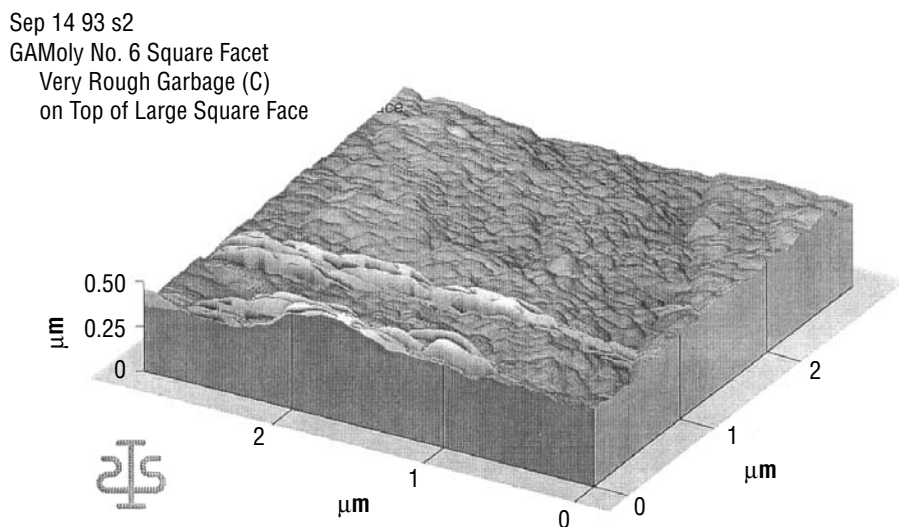


Figure 70. AFM three-dimensional scan for GAMoly No. 6.



# Region Analysis

Sep 14 93 s2  
 GAMoly No. 6 Square Facet  
 Very Rough Garbage (C)  
 on Top of Large Square Face



05/21/94 21:19

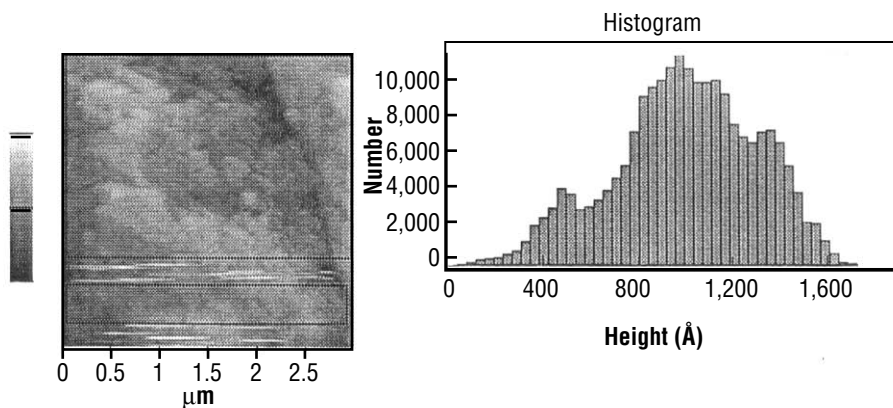


Figure 71. AFM scan analysis for GAMoly No. 6.

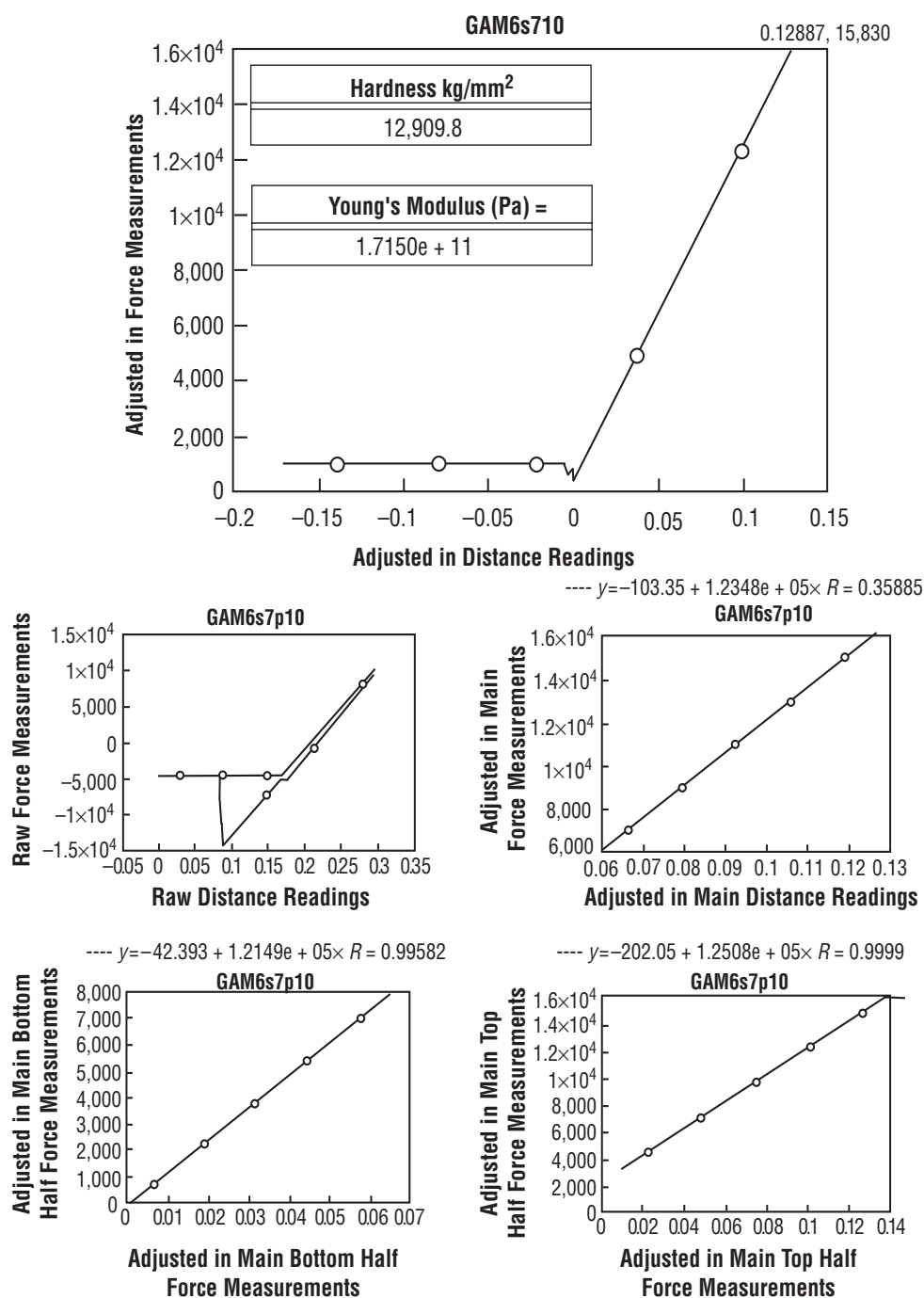


Figure 72. AFM force-versus-distance breakdown for GAMoly No. 6.

GAMoly No. 7 was produced with a medium level of CO addition and no  $\text{CH}_4$ . Just as with the previous sample, this one also produced a freestanding film and a portion of adhered material. Unlike several of the other samples, there is not a substantial change in morphology noted with depth and there are no discernible pillars on either the freestanding film or the portion of the deposit remaining on the substrate. The outer radius of deposit shows a well-developed blanket of crystals of mostly  $\langle 100 \rangle$  facets (fig. 73). These facets are clean with no visible growth steps but occasional three-dimensional secondary growths or contaminants. The extreme outer radius of the deposit that remains attached to the moly substrate shows three-dimensional crystallites (predominantly  $\{111\}$  facets), with no underlying blanket of

material. These crystals appear scattered onto the surface. The freestanding film shows both  $\{111\}$  and  $\{100\}$  facets, with the  $\{100\}$  facets being, in general, clean and well formed (fig. 74). The  $\{111\}$  facets are predominantly truncated and they show evidence of layer growth. The  $\{111\}$  facets may be typically covered with growth steps or heavily twinned (fig. 75). Looking at the bottom of the sample, whiskers are clearly present on the freestanding film (fig. 76). The backside surface is, in general, not crystalline nor are facets present (fig. 77).

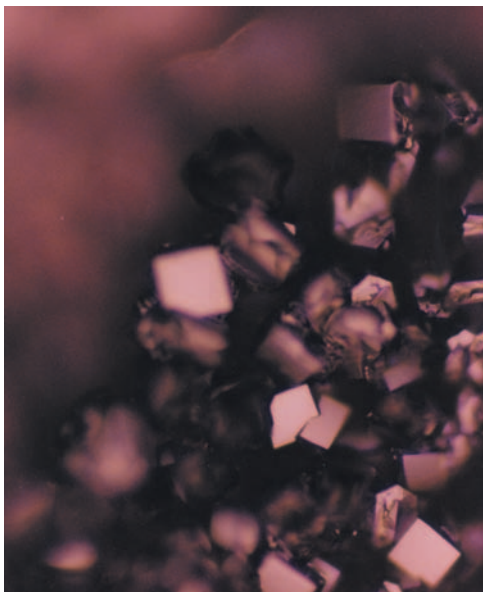


Figure 73. GAMoly No. 7 blanket of crystals of mostly  $\{100\}$  facets,  $\times 40$ .

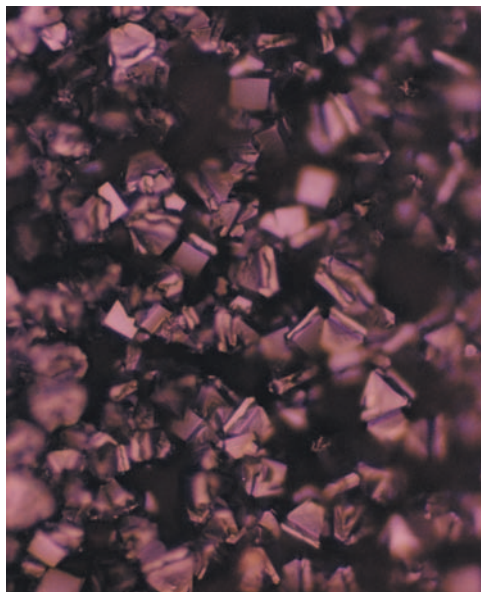


Figure 74. GAMoly No. 7 clean faceting,  $\times 40$ .



Figure 75. GAMoly No. 7 growth steps or heavily twinned facets,  $\times 100$ .

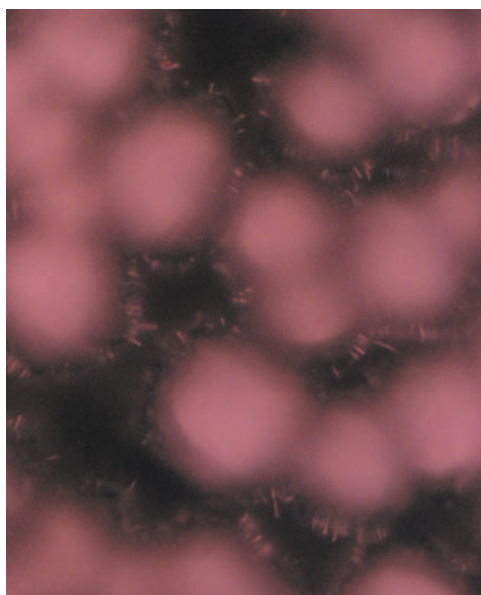


Figure 76. GAMoly No. 7 whiskers on bottom of sample,  $\times 100$ .

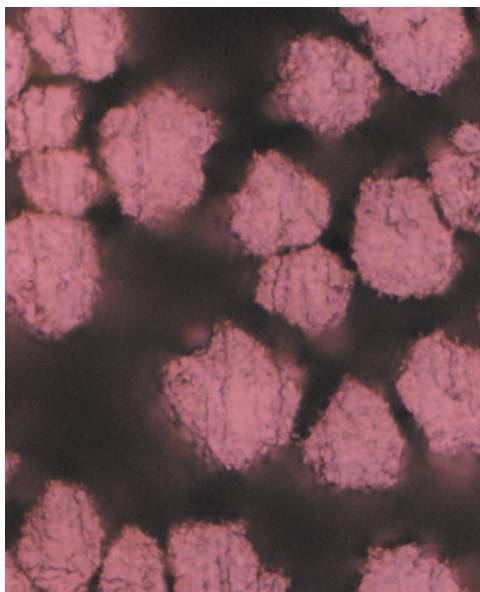


Figure 77. GAMoly No. 7 bottom of sample,  $\times 100$ .

The visible Raman data for GAMoly No. 7 show one of the stronger diamond peaks at  $1,338\text{ cm}^{-1}$ , where the linewidth is small and there is no indication of graphitic or amorphous peaks (fig. 78).

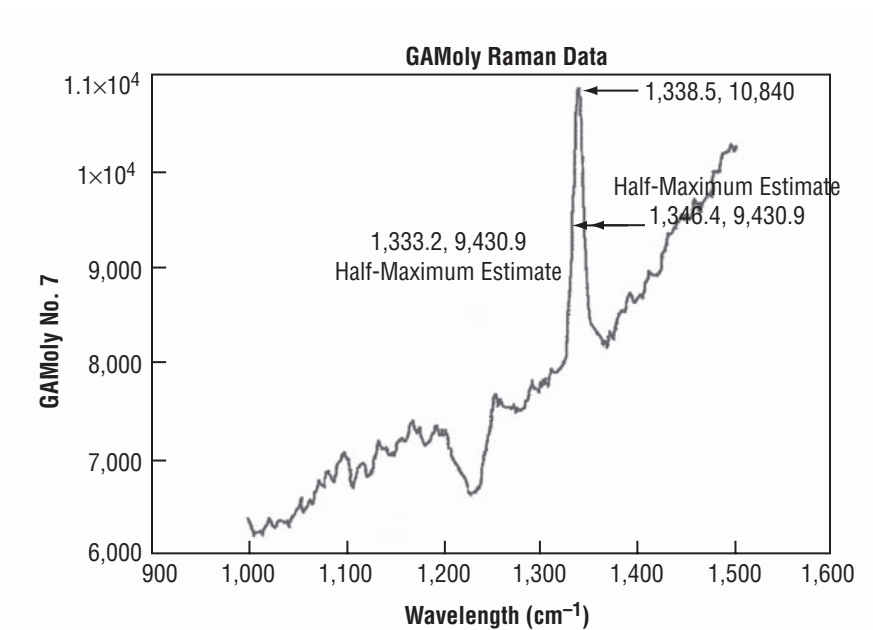


Figure 78. Visible Raman for GAMoly No. 7.

The AFM scans taken on GAMoly No. 7 were of excellent veracity. Scans were taken on both  $\{100\}$  and  $\{111\}$  facets with equal success. The  $\{100\}$  facets tended to show less surface roughness (figs. 79–81) than the  $\{111\}$  facets (figs. 82–84). Angstrom level scans were attempted in air on these

surfaces with questionable success (figs. 85–87). The bright lines are separated by  $\approx 5 \text{ \AA}$ , the lattice spacing on the  $\{100\}$  surface of diamond is  $\approx 5.04 \text{ \AA}$ , assuming a  $(2 \times 1)$  surface reconstruction.<sup>278</sup> However, these scans should exhibit a separation along the rows of  $\approx 2.52 \text{ \AA}$  between surface atoms, which is not noted. Nevertheless, potentially these are the first atomic level images of torch-produced diamond. The force versus distance traces were all single-stage traces that were smooth and continuous (fig. 88).

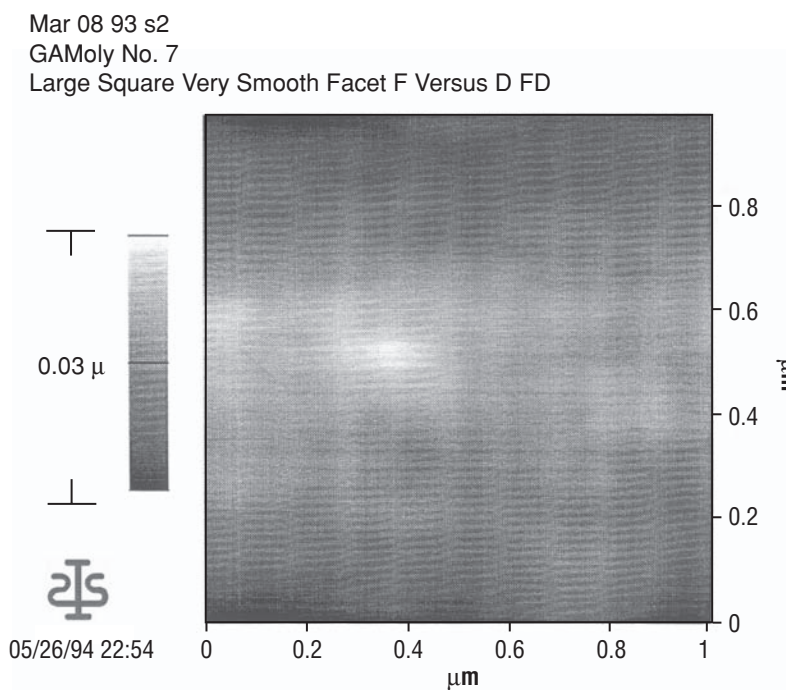


Figure 79. AFM two-dimensional scan for GAMoly No. 7.

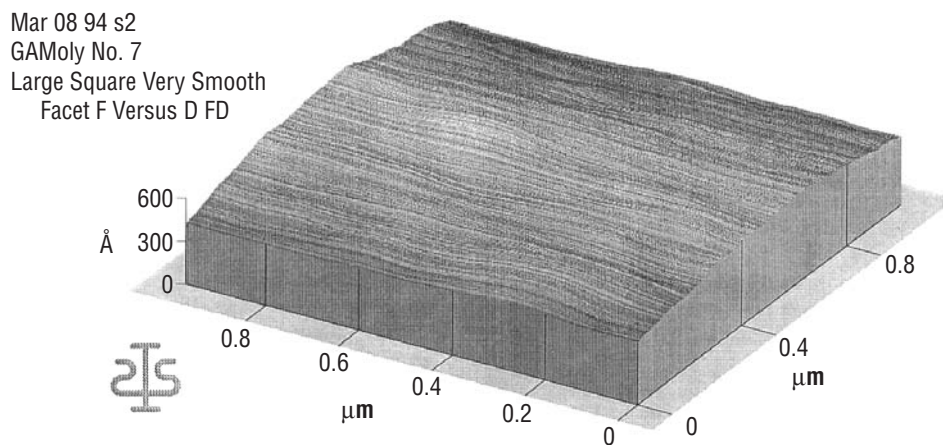


Figure 80. AFM three-dimensional scan for GAMoly No. 7.

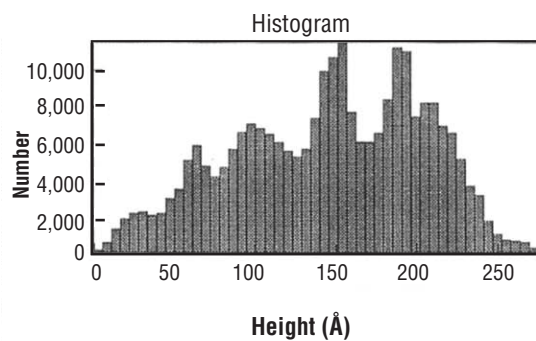
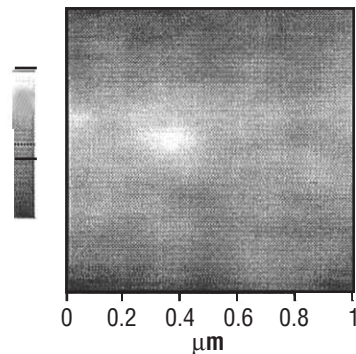


# Region Analysis

Mar 08 94 s2  
GAMoly No. 7  
Largest Square  
Very Smooth Facet F  
Versus D



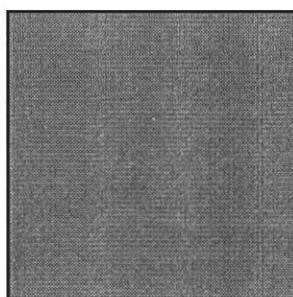
05/26/94 22:56



## Area Statistics:

Median Height: 154 Å  
Mean Height: 147 Å  
Peak to Valley: 279 Å  
Surface Area:  $0.96 \mu^2$   
Projected Area:  $0.95 \mu^2$   
Volume:  $0.01 \mu^2$   
Rms Rough: 59 Å  
Ave Rough: 49 Å  
Bearing Ratio @ 75%: 111 Å  
Bearing Ratio @ 50%: 153 Å

## Selected Area



## Bearing Ratio

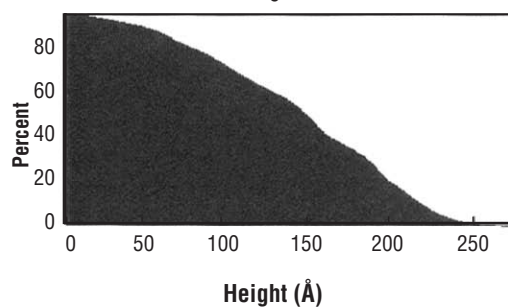


Figure 81. AFM scan analysis for GAMoly No. 7.

Mar 12 93 s26  
GAMoly No. 7  
Triangular Facet No. 16 Rough

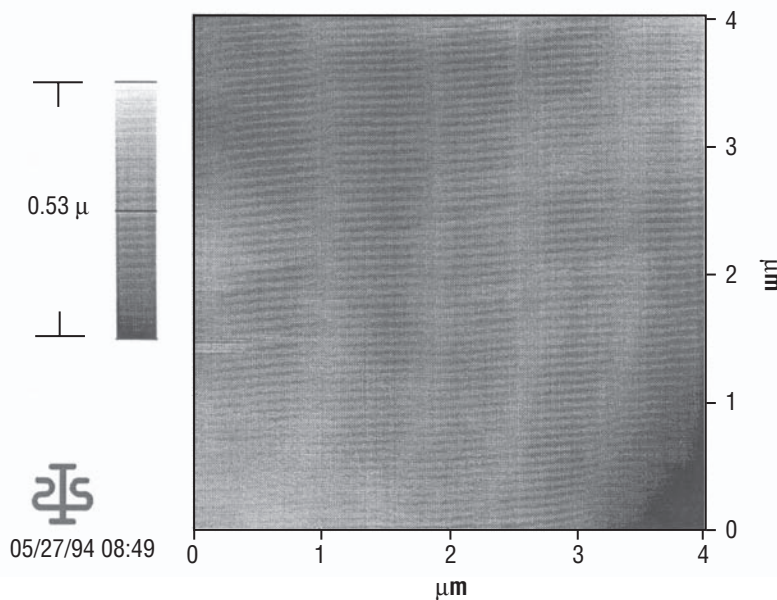


Figure 82. AFM two-dimensional scan for GAMoly No. 7.

March 12 93 s26  
 GAMoly No. 7  
 Triangular Facet  
 No. 16 Rough

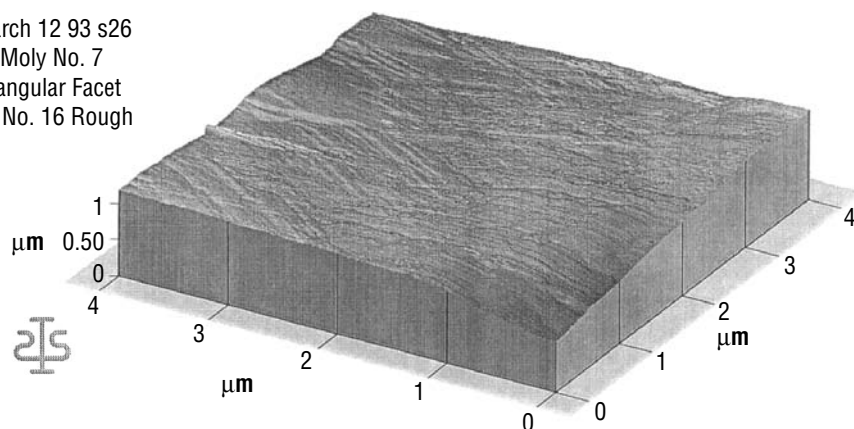


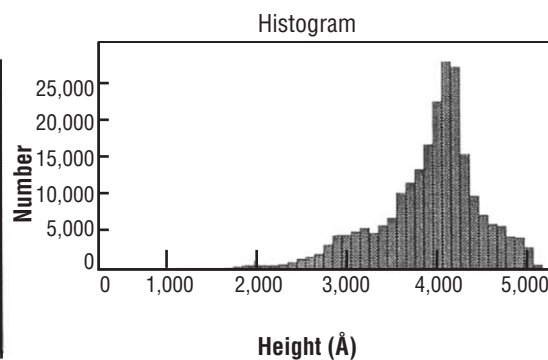
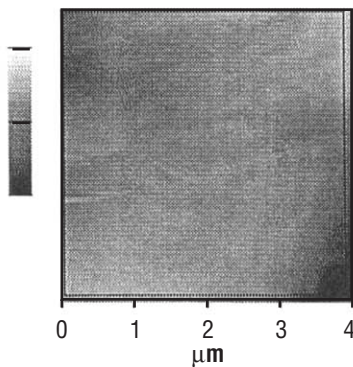
Figure 83. AFM three-dimensional scan for GAMoly No. 7.

#### Region Analysis

Mar 12 93 s26  
 GaMoly No. 7  
 Triangular Facet  
 No. 16 Rough



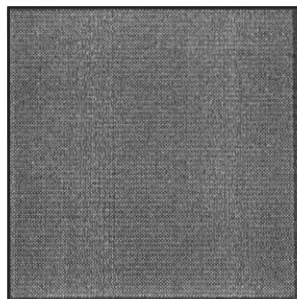
05/27/94 08:51



#### Area Statistics:

Median Height: 4,260 Å  
 Mean Height: 3,891 Å  
 Peak to Valley: 5,009 Å  
 Surface Area: 17.10 μ<sup>2</sup>  
 Projected Area: 15.19 μ<sup>2</sup>  
 Volume: 5.91 μ<sup>2</sup>  
 Rms Rough: 644 Å  
 Ave Rough: 473 Å  
 Bearing Ratio @ 75%: 3,507 Å  
 Bearing Ratio @ 50%: 4,008 Å

#### Selected Area



#### Bearing Ratio

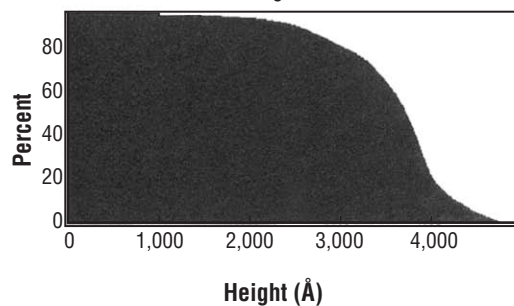


Figure 84. AFM scan analysis for GAMoly No. 7.



Mar 11 93 s24  
 GAMoly No. 7  
 Square Crystal No. 3 Smooth

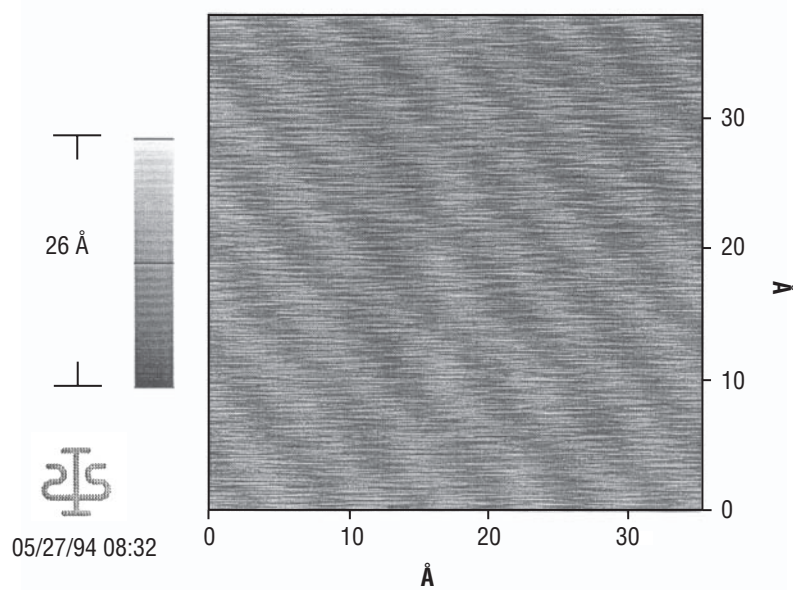


Figure 85. AFM two-dimensioinal scan for GAMoly No. 7.

Mar 11 93 s26  
 GAMoly No. 7  
 Square Crystal  
 No. 3 Smooth

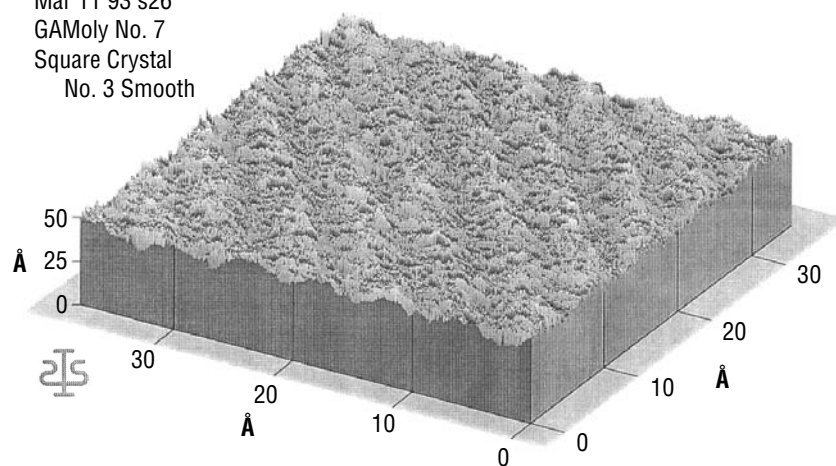


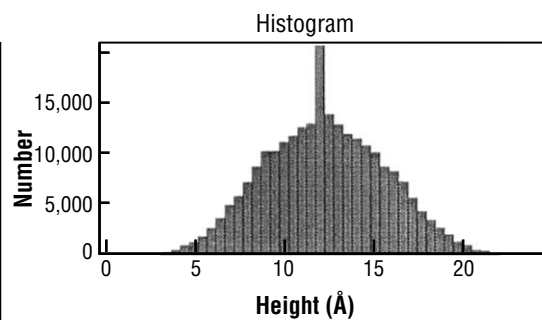
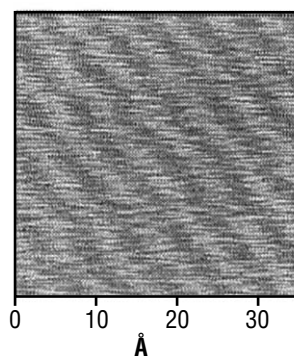
Figure 86. AFM three-dimensioinal scan for GAMoly No. 7.

### Region Analysis

Mar 11 93 s24  
GaMoly No. 7  
Square Crystal No. 3 Smooth



05/27/94 08:34



### Area Statistics:

Median Height: 12 Å  
Mean Height: 13 Å  
Peak to Valley: 25 Å  
Surface Area: 686,271 Å<sup>2</sup>  
Projected Area: 1,276 Å<sup>2</sup>  
Volume: 1.6e+04 Å<sup>3</sup>  
Rms Rough: 3.4 Å  
Ave Rough: 2.7 Å  
Bearing Ratio @ 75%: 11 Å  
Bearing Ratio @ 50%: 12 Å

### Selected Area

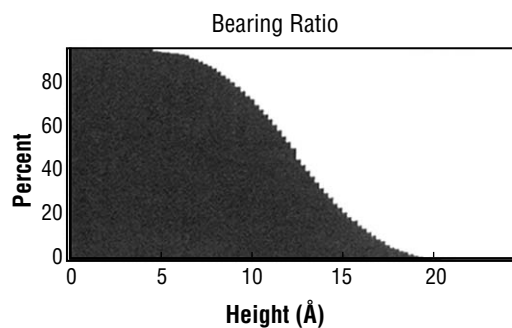
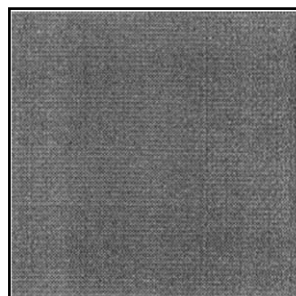


Figure 87. AFM scan analysis for GAMoly No. 7.

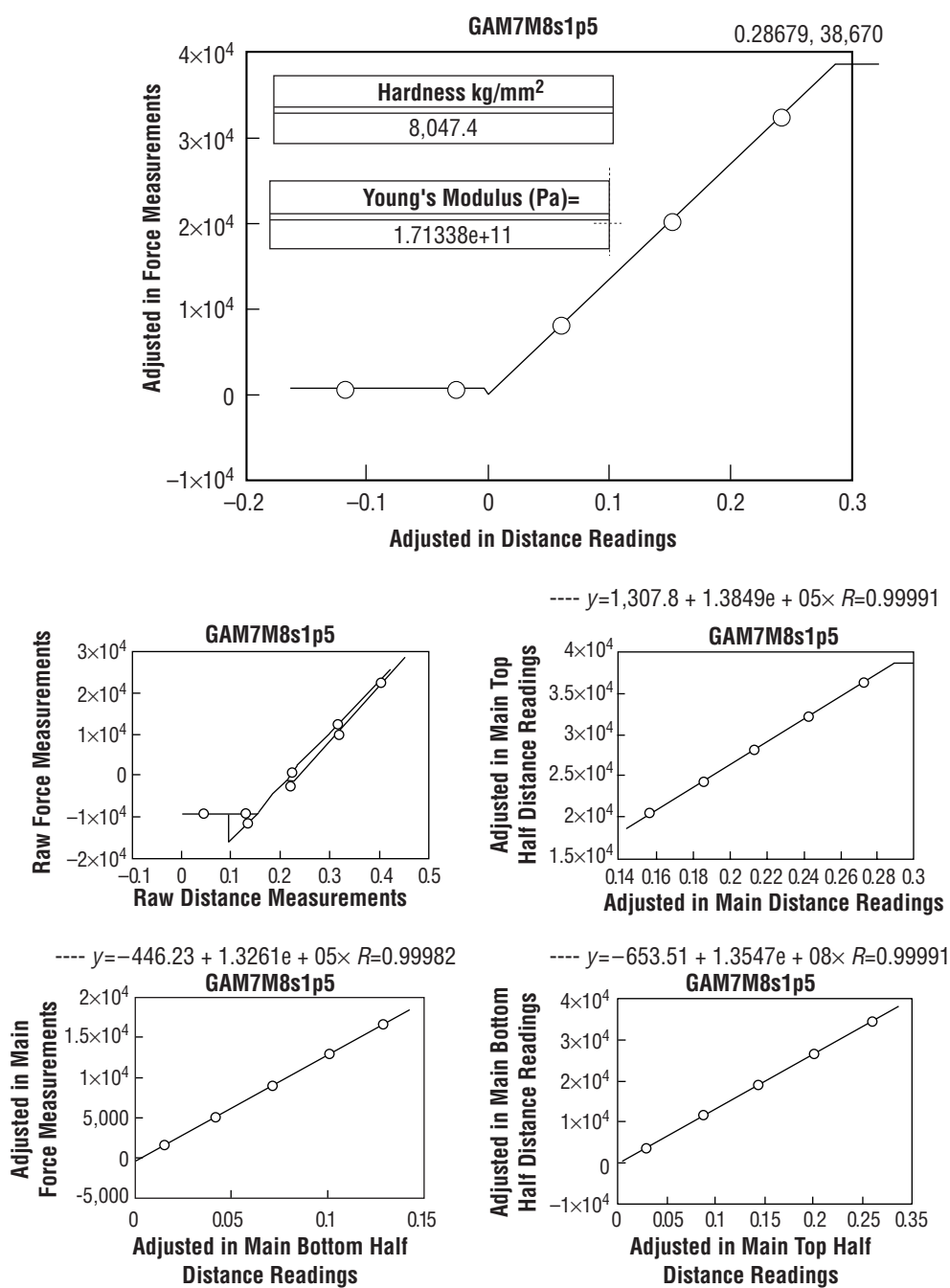


Figure 88. AFM force-versus-distance breakdown for GAMoly No. 7.

GAMoly No. 8 was produced with a medium level of CO addition and a medium level of CH<sub>4</sub> addition. These samples showed no discernible crystallinity. There are definite pillar structures with an underlying blanket (fig. 89). However, the pillars all terminate in rounded cauliflower-like structures. A scratch mark across the sample had preferential growth; however, again no discernible crystallinity could be found (fig. 90).

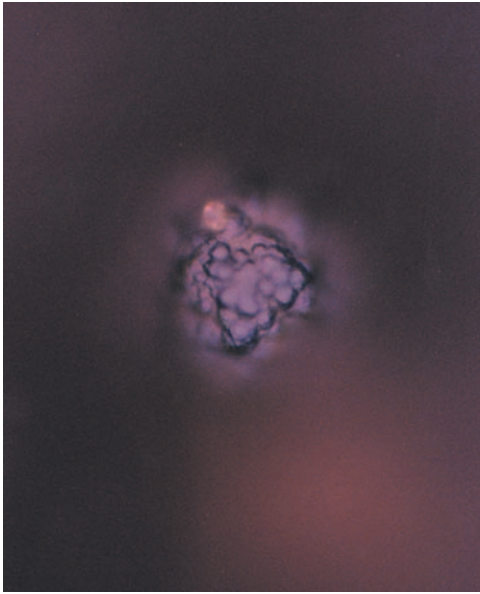


Figure 89. Lack of faceting in GAMoly No. 8,  $\times 100$ .

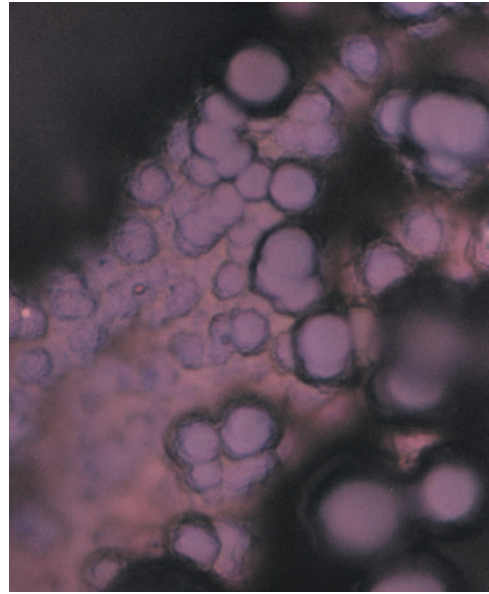


Figure 90. GAMoly No. 8 lack of facets on scratch,  $\times 100$ .

Visible Raman data for GAMoly No. 8 showed a strong  $1,180\text{ cm}^{-1}$  peak and a strong peak at  $1,359\text{ cm}^{-1}$  but no indications were present for a diamond peak (fig. 91). AFM data were collected and used in calculations. These readings were taken on the substrate surface and used for both types of crystal facets.

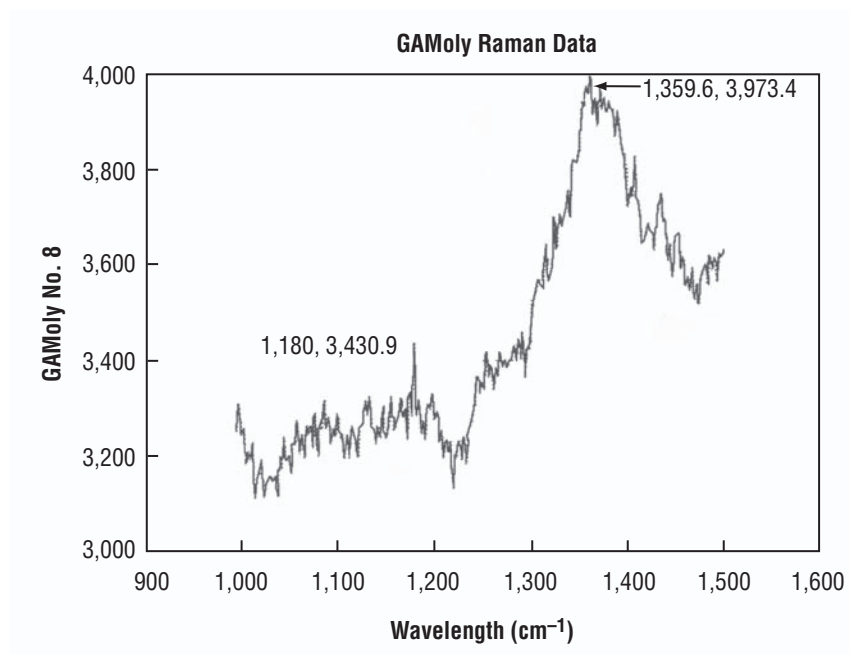


Figure 91. Visible Raman data for GAMoly No. 8.

The GAMoly No. 9 samples were produced without the addition of CO but with the largest addition of  $\text{CH}_4$ . The samples typically had a radial distribution of morphology. The inner sample section was composed almost exclusively of facets that were clean  $\langle 100 \rangle$  pillars (fig. 92). The surfaces are typically complete and smooth, with one or no secondary growth sites observable (fig. 93). The deposit does show a change in morphology with depth; however, instead of a supporting base with clear  $\langle 111 \rangle$  facets, the support is  $\langle 100 \rangle$  facets or poorly formed crystallites (fig. 94). The lowest focus on the central pillars does not show a comprehensive underlying blanket of material, rather the pillars join with each other or no support is evident. Moving out radially on the sample, the free crystal surfaces show more growth surfaces and much more secondary growth. Eventually, at the periphery, the film breaks up and the crystalline pillars are isolated (fig. 95). The isolated pillars are typically covered with contaminants or secondary growth. The faceting is predominantly  $\langle 100 \rangle$  facets with a few  $\langle 111 \rangle$  facets visible but also heavily covered with contaminant or secondary growth (fig. 96).

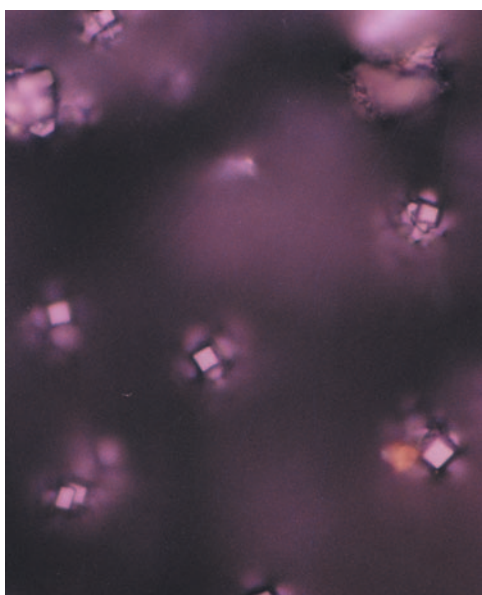


Figure 92. GAMoly No. 9 clean  $\{100\}$  pillars,  $\times 100$ .

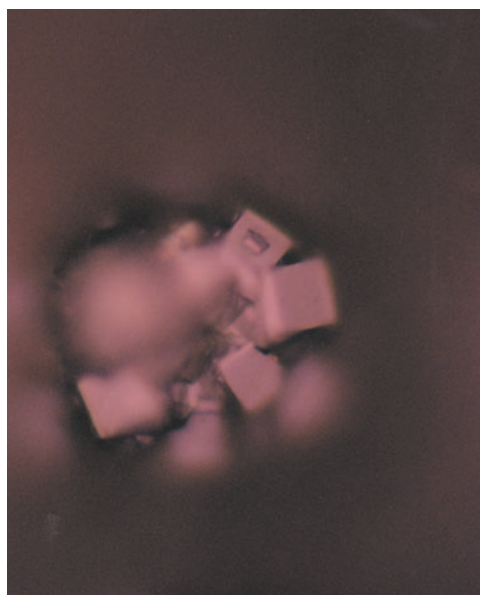


Figure 93. GAMoly No. 9 smooth facets with one or no secondary growth sites,  $\times 100$ .



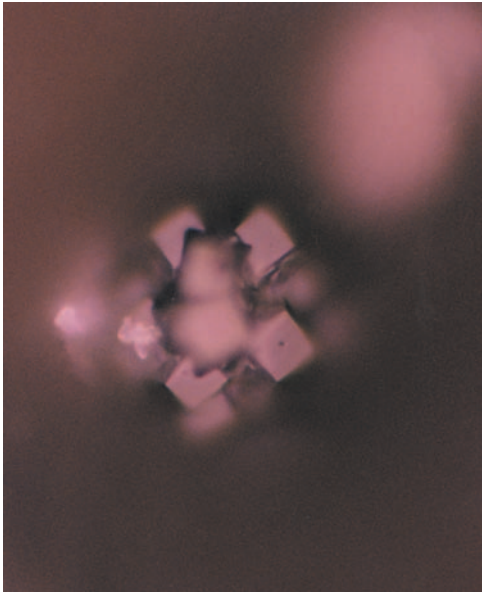


Figure 94. GAMoly No. 9 base of pillar,  $\times 100$ .

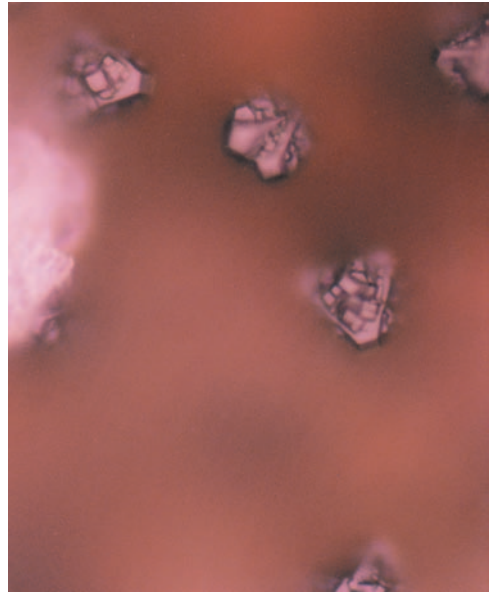


Figure 95. GAMoly No. 9 isolated pillars,  $\times 100$ .

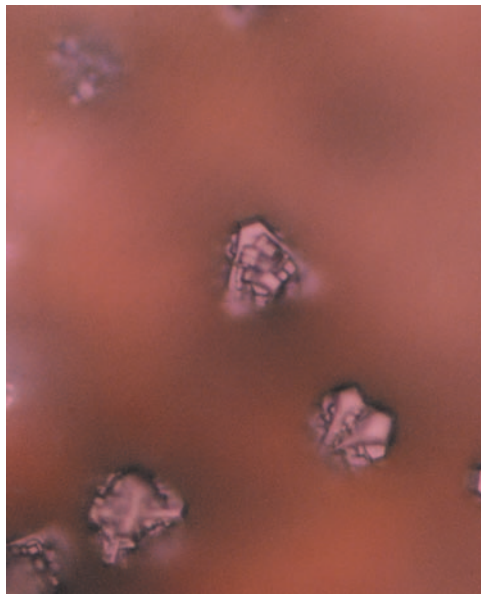


Figure 96. GAMoly No. 9 heavy secondary growth,  $\times 100$ .

One of the samples had heavy foreign material interspersed with the isolated crystals on the sample edge. Interestingly, this appeared to have no effect on the creation of crystals. A few of the crystals showed somewhat cleaner facets than those radially inward (fig. 97). At an intermediate distance radially, just where the pillars become isolated, there were a number of triangle structures covered with small, square or cubical formations. The cubes or squares were generally uniform in size and generally rose perpendicular to the triangular substructure (figs. 98 and 99). Occasionally the cubes would grow together; however,

more often they formed very dense clusters of crystallites. The visible Raman data showed a very strong diamond peak at  $1,341\text{ cm}^{-1}$ , with a noticeable graphitic contribution at  $1,351\text{ cm}^{-1}$ . The peak width for the diamond was narrow except for the broad micrographitic shoulder (fig. 100).

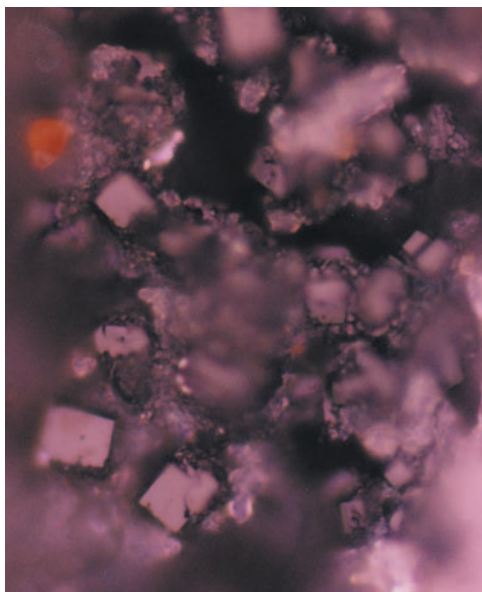


Figure 97. GAMoly No. 9 foreign material interspersed with crystallites,  $\times 100$ .

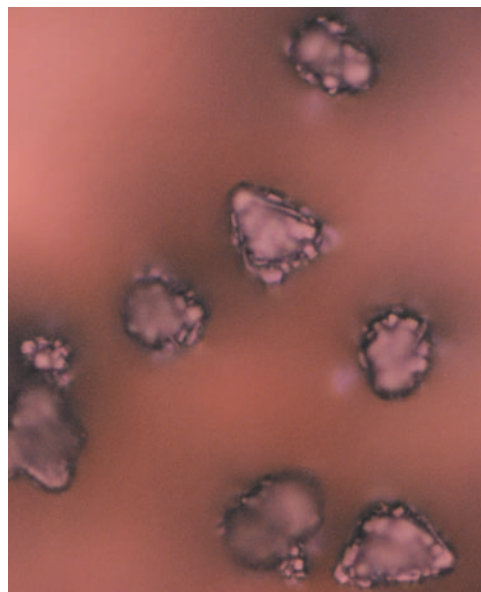


Figure 98. GAMoly No. 9 coverage by small square facets,  $\times 100$ .

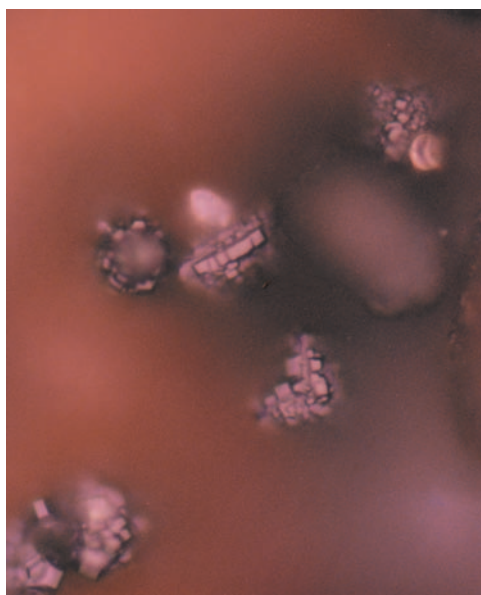


Figure 99. GAMoly No. 9 coverage by small square facets,  $\times 100$ .



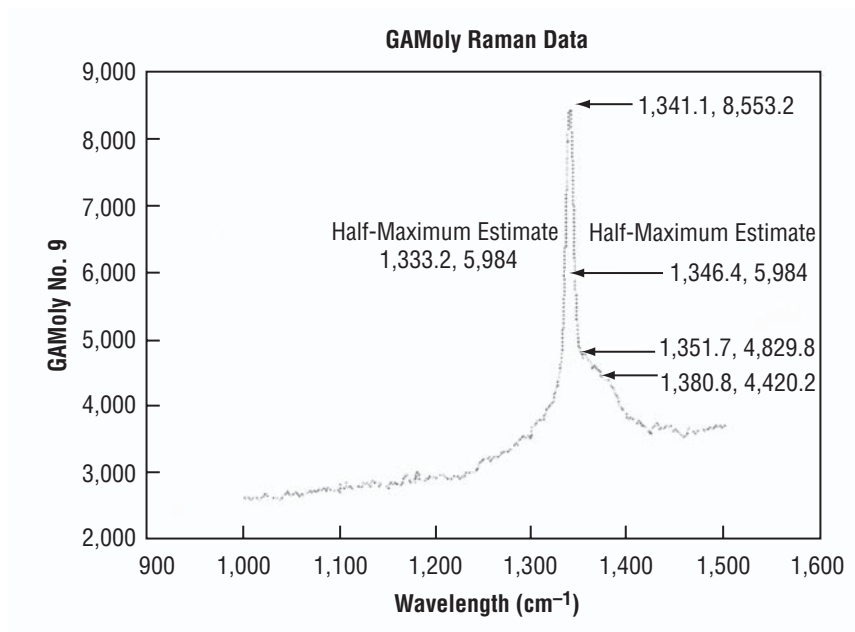


Figure 100. Visible Raman data for GAMoly No. 9.

Many AFM scans were taken on the GAMoly No. 9 samples with excellent results. Nucleation sites are arguable for several of the scans based on the scan data and the surface roughness measurements. Figures 101 through 103 show several of these possible sites with different regions selected for surface roughness measurements. Atomic level scans were attempted on these samples but without success. The force versus distance curves were only successful on {100} facets for GAMoly No. 9. Consequently, this sample was removed from calculation for {111} faceted readings. The traces were all single-stage traces showing very smooth indentation paths (fig. 104).

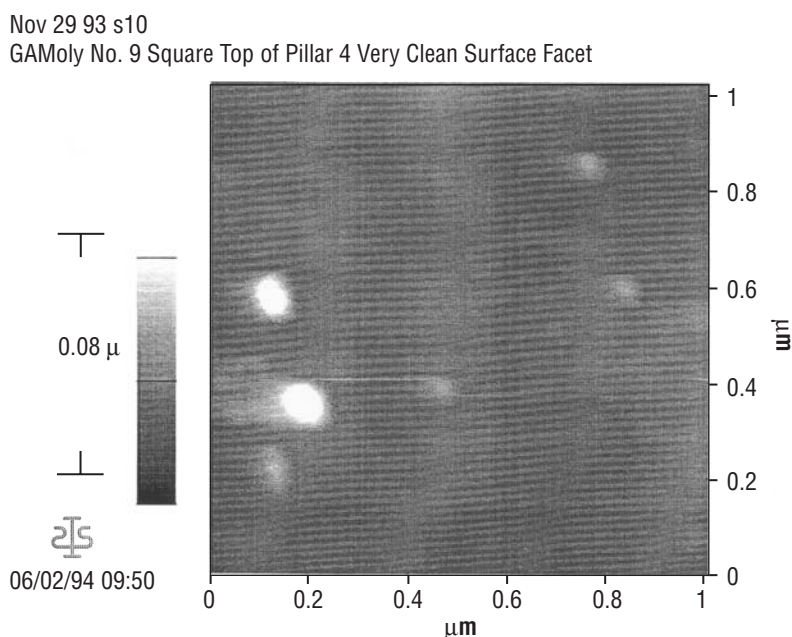


Figure 101. AFM two-dimensional scan for GAMoly No. 9.

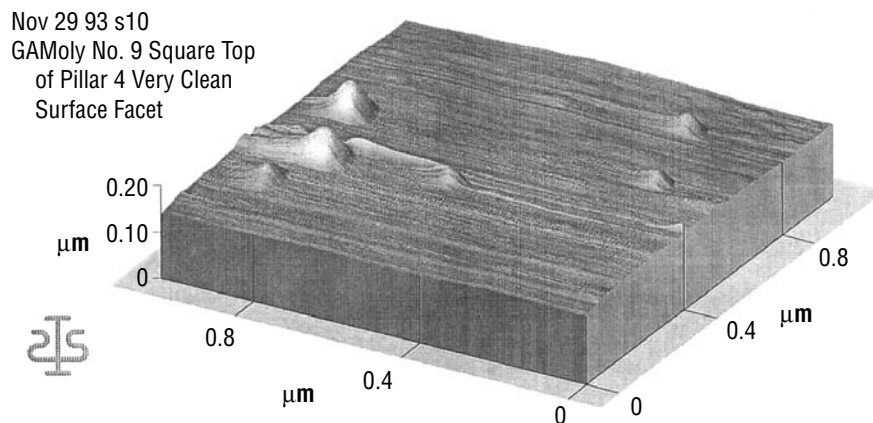
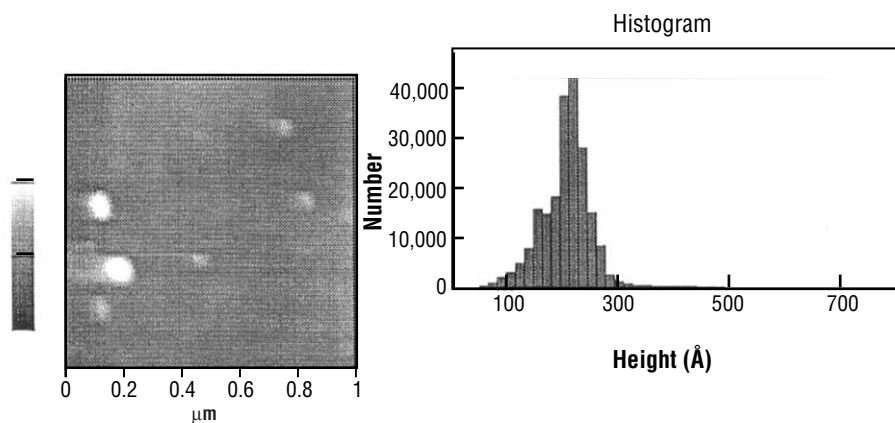


Figure 102. AFM three-dimensional scan for GAMoly No. 9.

#### Region Analysis

Nov 29 93 s10  
GaMoly No. 9 Square Top  
of Pillar 4 Very Clean  
Surface Facet

06/02/94 09:51



#### Area Statistics:

Median Height:	250 Å
Mean Height:	223 Å
Peak to Valley:	803 Å
Surface Area:	1.07 $\mu^2$
Projected Area:	1.02 $\mu^2$
Volume:	0.02 $\mu^2$
Rms Rough:	71 Å
Ave Rough:	41 Å
Bearing Ratio @ 75%:	201 Å
Bearing Ratio @ 50%:	241 Å

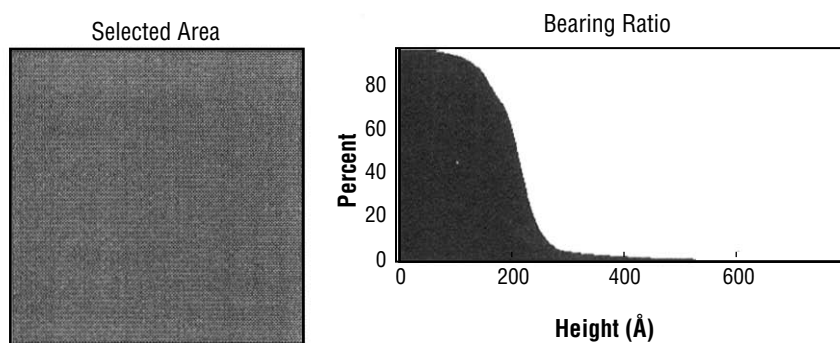


Figure 103. AFM scan analysis for GAMoly No. 9.

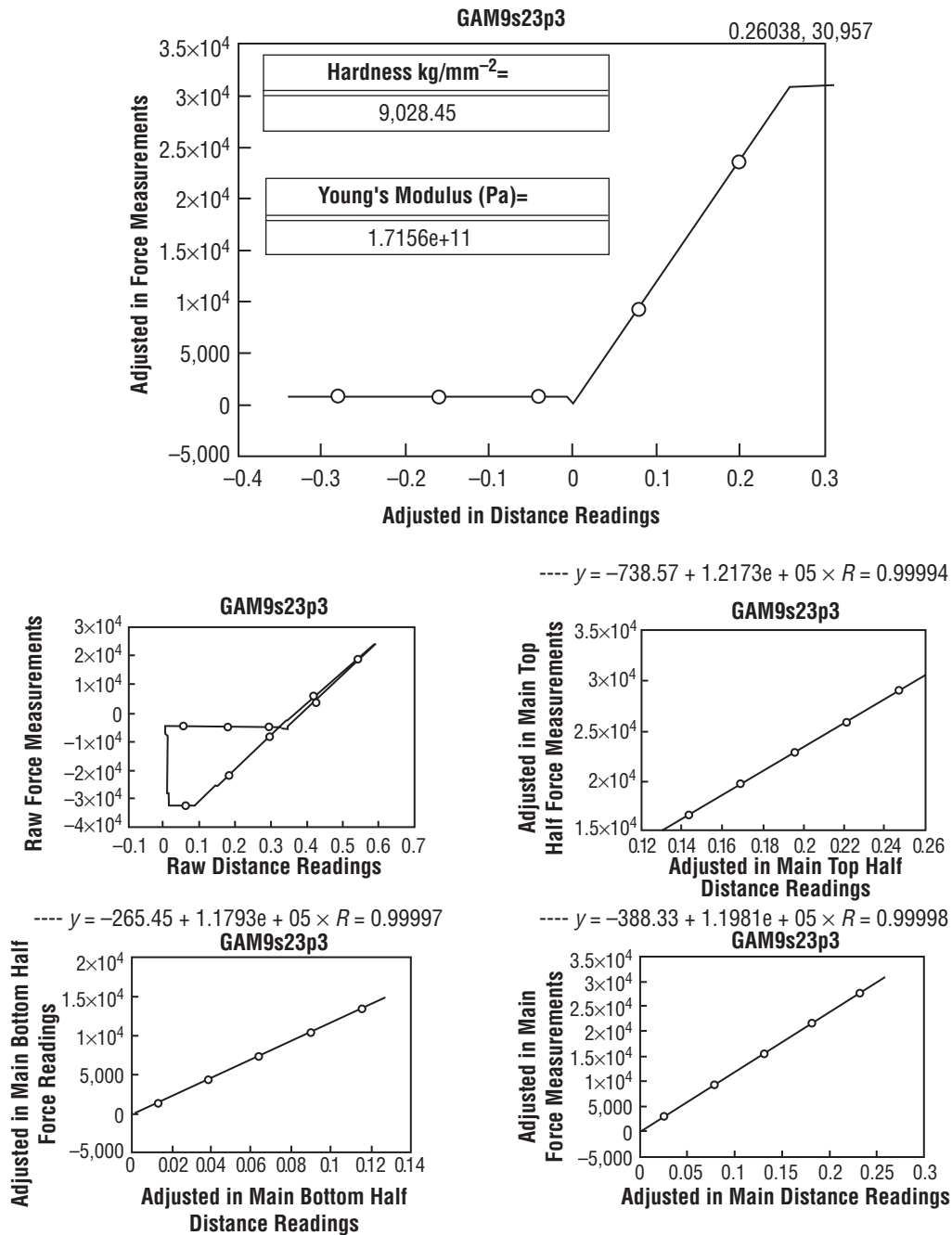


Figure 104. AFM force-versus-distance breakdown for GAMoly No. 9.

#### 4.1.2 Pillar Morphology Depth Profile Comparisons

A significant number of the samples produced pillar-like growths on some portion of the sample. Here, a quick review is presented of depth profiles taken along each of the samples. Figures from this review are presented in the appendix.

GAMoly No. 1 shows an extremely dense film. At the top focus level, a predominance of  $\langle 111 \rangle$  facets is shown of relatively consistent size. Focusing deeper into the film, the pillars terminate in typically

square facets. The film base of joined crystallites typical of diamond films is fairly clear. GAMoly No. 2, at the top focus level, shows widely separated pillars terminated by clean square facets. Traveling toward the surface, the pillars show predominantly  $\langle 111 \rangle$  faceting along their exposed surfaces. Directly above the surface, the density of the pillars predictably increases. The visible surface of the deposit shows a continuous film but not any discernible faceting.

In GAMoly No. 3, the upper focus shows a very dense (most dense of any pillaring sample) clustering of pillars, with  $\langle 111 \rangle$  faceting as the focus progresses toward the surface. The morphology does not really seem to change; however, there is not the thickening of the pillars nor does there seem to be more connection between the pillars deeper within the films. At the base, there is a continuous film of microcrystalline or noncrystalline material thinly covering the surface or scattered on the surface.

GAMoly No. 4 showed small, very densely spaced pillars of nonfaceted cauliflower-like material. The morphology does not change appreciably with depth of focus. This material is described as microcrystalline material at best.

GAMoly No. 5 displays pillars that are not terminated in  $\langle 100 \rangle$  facets. The GAMoly No. 5 pillars continuously show well-developed  $\langle 111 \rangle$  facets all along the length of the pillar and on the upper surface. At the base of the pillars where they join to the continuous film, the material appears to be much the same as the base material in GAMoly No. 4; i.e., noncrystalline cauliflower-like material.

GAMoly Nos. 6 and 7 did not produce pillar growths. GAMoly No. 8 produced pillars of nonfaceted material that were more separated than those in GAMoly No. 4. The pillars had a somewhat rougher appearance with slightly more variation in distance between the base material and the top surfaces.

The upper surfaces of pillars on GAMoly No. 9 are clean, large  $\langle 100 \rangle$  facets. Progressing toward the surface, the pillars are unique in that they continue to show well-developed, distinct  $\langle 100 \rangle$  faceting along their sides. Directly above the surface, the pillars appear much less faceted and more cauliflower-like in appearance. The bottom, or connection with the continuous film or substrate, appears identical with that of GAMoly No. 3. For example, there is a continuous film of microcrystalline or noncrystalline material thinly covering the surface or interspersed with the molysubstrate material to produce the surface.

#### **4.1.3 Designed Experiment Results**

For the gas additions on the Mo experiment, a three-level, two-factor, full-factorial design was used. This provided the quadratic incorporation for each gas added and provided for an interaction term between the additions. Because of the lack of AFM data from run Nos. 3 and 4, all of the terms from those runs were removed from the experiment analysis except for the qualitative results and the Raman results. While interpreting the Raman spectra, the Raman linewidth was measured at an estimate of half-maximum peak height. The linewidth was measured on the measured peak only, and the relative Raman peak height to background was measured using an estimate of background position under the Raman peak.

The quality of the deposit, as viewed in optical microscopy, was measured on a qualitative scale. Generally, higher rankings were given to deposits with more macroscopic faceting and higher film density. Using these criteria, the qualitative assessment decreased with the addition of CO and increased very

slightly with the addition of  $\text{CH}_4$ . The most significant fact from this assessment is the second curve, which shows the effect of the interaction of CO and  $\text{CH}_4$ . With the addition of both gases, the qualitative assessment decreases sharply as the amount of total gas added increases. Figure 105 shows the graphic results from the designed experiment with optical quality as a response variable.

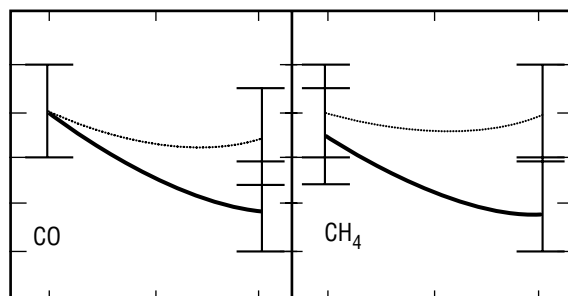


Figure 105. Response of qualitative optical rating.

Two responses were considered related to the Raman measurements; these were the linewidth and the height of the diamond peak as related to the background signal. For the linewidth, shown in figure 106, the addition of CO was shown to broaden the linewidth as the amount increased, and the  $\text{CH}_4$  addition was shown to have a small advantageous quadratic effect. As the  $\text{CH}_4$  went through its midlevel position, the linewidth decreased. At the higher setting, however, the addition of  $\text{CH}_4$  was found unfortunate.

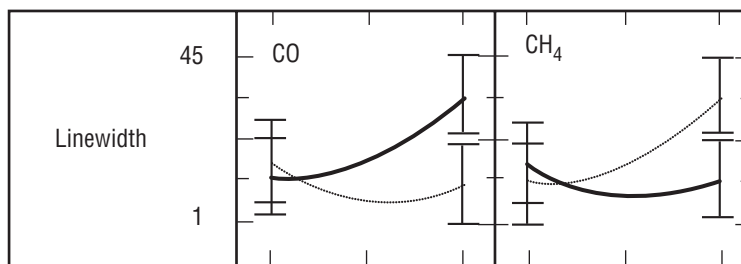


Figure 106. Response of Raman linewidth for GAMoly.

For the relative height of the diamond peak to the background signal, a strong quadratic effect was noted for the addition of CO and the addition of  $\text{CH}_4$ . Additionally, a strong interaction was noted between the addition of the two gases. Digressing slightly to a discussion of the results, the strong interaction may be seen as follows:

1. Carbon monoxide addition is beneficial only if there is an appropriate amount of excess  $\text{H}_2$  available.
2. Methane addition is desirable only up to the point at which all of the gas phase C surfaces are stabilized, but not past that point at which etching of surface species becomes more prevalent.

The designed experiment curves are shown in figure 107.

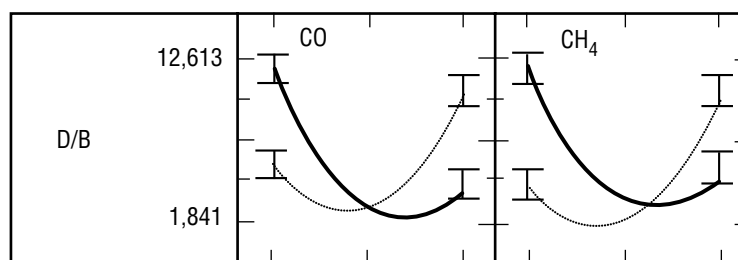


Figure 107. Response of relative peak height between diamond and the background.

There are eight response variables concerned with the atomic force measurements of the free upper crystal surfaces. These responses are divided into those on {111} faces and those on {100} faces. Certain failings are inherent in this experiment, namely that the designed experiment statistics require the use of data from either GAMoly Nos. 4 or 8 to be included in the calculations for the interaction terms to be relevant. Accordingly, I have used the atomic force results from GAMoly No. 8 and used these as data from both {100} and {111} facets. This is clearly in error as there were no facets found on this sample. Because the surface roughness became worse with the addition of both gases, as in both sample Nos. 4 and 8, the midlevel results from No. 8 provide conceptually accurate results. Also, for the use of these numbers in Young's modulus and hardness calculations, although not strictly on crystal faces, the hardness and modulus are certainly a result of the structure measured. Again, the results are felt to be conceptually accurate.

The first set of responses below refers to the surface finish. Ra and rms values were taken. The behavior of the response did not differ between {100} and {111} crystal surfaces or between the rms and Ra values so they will be grouped together. In figure 108 the surface finish may be seen to show a critical point at which the surface finish reaches a point where there is a balance between the addition of CO and CH<sub>4</sub>. The surface finish is apparently very sensitive to the addition of alternate process gases, with the effect of CO strongly mediated by CH<sub>4</sub>. The interpretation of this will be covered in the following section.

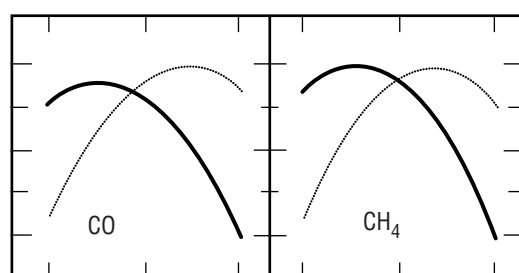


Figure 108. Surface finish response.

The remaining measurements are related to the measurements of hardness and Young's modulus. The variance of Young's modulus was unacceptably high for the results presented here to carry much veracity. They are presented below for completeness; however, they will not be covered in the discussion section because of the questionable nature of the method of measurement. The Young's modulus measurements show a stronger effect for CH<sub>4</sub> addition than for CO. On {100} crystals, shown in figure 109, CH<sub>4</sub> is shown as bringing about a higher modulus material when the CO is minimized. The results on {111} crystals are similar and not presented.

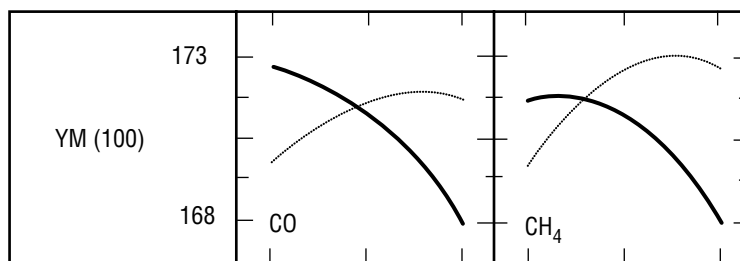


Figure 109. Young's modulus results.

The following results present the effects of the process gases on the hardness measurements. These results were significantly different for  $\{100\}$  and  $\{111\}$  facets. For  $\{100\}$  facets, shown in figure 110, the process gases have a strong interaction and a strong quadratic component. The behavior for each process gas is substantially the same and the important factor appears to be the interaction between the gases for the determination of  $\{100\}$  hardness. As the hardness will later be related to specific crystal facets and thus to the growth and nucleation environment, these results are significant.

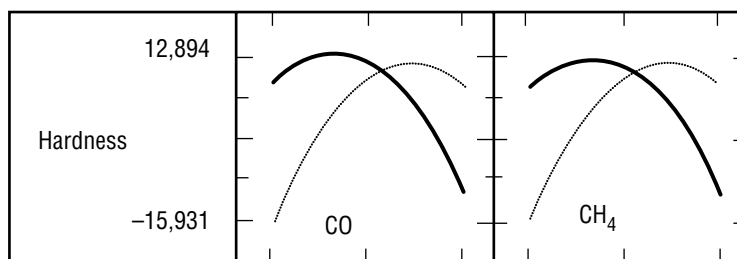


Figure 110. Graph of  $\langle 100 \rangle$  hardness results.

The effect on hardness for  $\{111\}$  crystal facets is shown to be more strongly dependent on the presence of  $\text{CH}_4$  than on the presence of  $\text{CO}$  (fig. 111).  $\text{CH}_4$  additions increase the hardness with a slight quadratic effect such that the beneficial effect tapers at the higher  $\text{CH}_4$  addition levels.  $\text{CO}$  is shown in all cases to either counterbalance the effect of  $\text{CH}_4$  or to significantly decrease the hardness on its own.

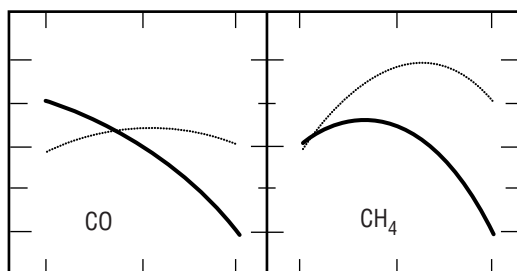


Figure 111. Graph of  $\langle 111 \rangle$  hardness results.

#### 4.1.4 Two-Dimensional Kinetics Simulation Results

Results of the two-dimensional (chemical) kinetics simulations using the conditions of the GAMoly experiment are presented below. The first response variable that relates to the addition of  $\text{CO}$  and  $\text{CH}_4$  is the combustion temperature (fig. 112). No interaction is noted between the gases; however, both  $\text{CO}$  and  $\text{CH}_4$ , as would be expected, lower the combustion temperature and thus the temperatures seen in the flame



plasma.  $\text{CH}_4$  is shown to have a stronger effect, which accounts well for the blowout of the flame (thermal quenching) as too much  $\text{CH}_4$  and CO were added (GAMoly No. 4).

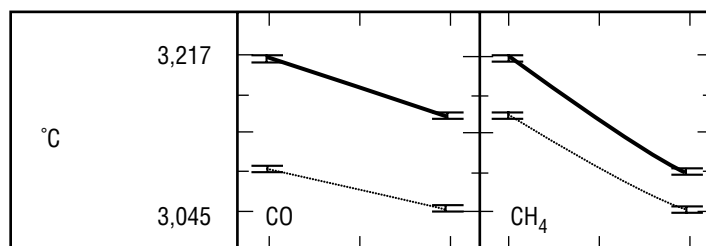


Figure 112. Combustion temperature response of GAMoly simulation.

Enthalpy of the flame also showed no interaction between the process gases; however, CO was shown to significantly decrease the enthalpy of the mixture as its additive level increased (fig. 113).

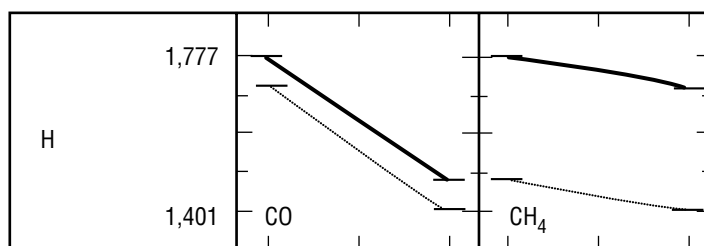


Figure 113. Enthalpy response of GAMoly simulation.

Entropy of the mixture showed no interaction of the gases. CO decreased the overall entropy and  $\text{CH}_4$  increased the entropy as the level increased (fig. 114).

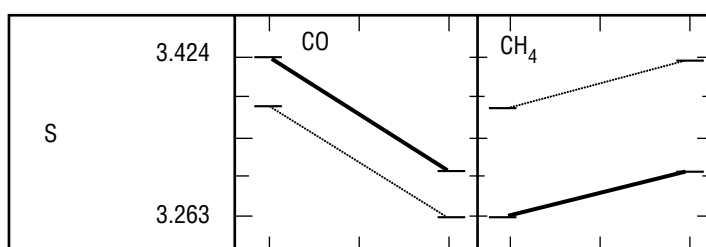


Figure 114. Entropy response of GAMoly simulation.

The fraction of species was derived at the exit plane. This was the best guess as to a position corresponding to the downstream edge of the torch flame feather but not very far into the diffusion region. Gases not listed as response variables did not appear in any significant quantities in the combustion stream. CO has been noted as the most stable gas at the operating temperatures of the  $\text{O}_2\text{-C}_2\text{H}_2$  torch. Predictably, as the level of CO addition was increased, the fraction present in the plasma rose accordingly (fig. 115). This premise was the initial driving force behind the GAMoly experiment. As  $\text{CH}_4$  was added, the fraction of CO decreased accordingly.

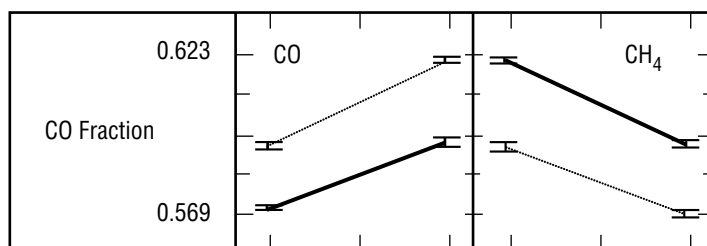


Figure 115. Carbon monoxide fraction from GAMoly simulation.

Looking at the fraction of carbons found, C and C<sub>2</sub> behave in substantially the same manner (only C is shown (fig. 116)), with CO and CH<sub>4</sub> scavenging C and C<sub>2</sub> from the gas. This would be expected to form C<sub>2</sub>H<sub>2</sub> and CO<sub>2</sub> byproducts and is reflected in the C<sub>2</sub>H<sub>2</sub> graph shown later.

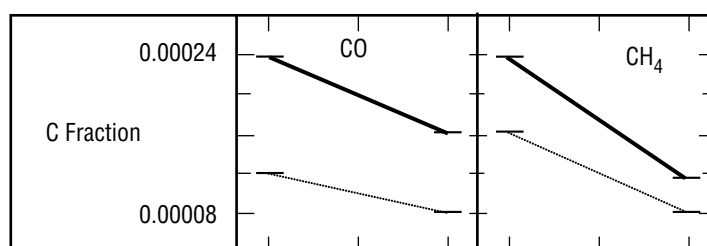


Figure 116. Carbon fraction from GAMoly simulation.

For C<sub>3</sub> the principal difference in behavior from C and C<sub>2</sub> is that the CH<sub>4</sub> does not affect the C<sub>3</sub> as strongly so that there is a quadratic effect such that only at the higher levels of CH<sub>4</sub> addition does the C<sub>3</sub> fraction begin to decrease (fig. 117). The CO is as effective in decreasing the production of C<sub>3</sub> as that of C and C<sub>2</sub>.

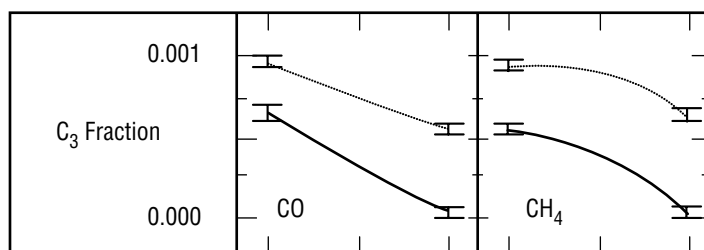


Figure 117. Triatomic carbon fraction from GAMoly simulation.

Several hydrocarbons are present (CH, C<sub>2</sub>H<sub>2</sub>, and singly terminated diatomic carbon (C<sub>2</sub>H)). The fraction of CH is decreased linearly by the addition of either CO or CH<sub>4</sub> as shown in figure 118.

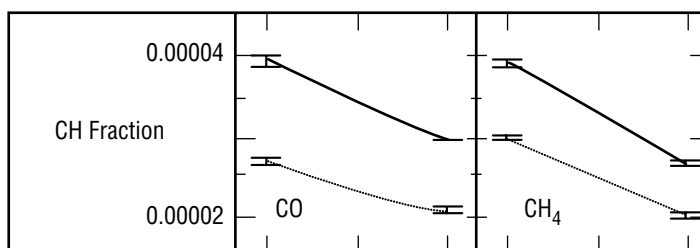


Figure 118. Hydroxide fraction from GAMoly simulation.

For  $C_2H$ ,  $CH_4$  is shown to increase the fraction present in the gas.  $CO$ , however, strongly inhibits the presence of  $C_2H$  in the gas (fig. 119).

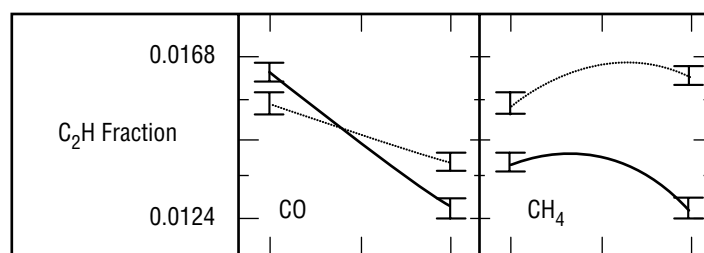


Figure 119. Singly terminated, diatomic carbon fraction from GAMoly simulation.

Acetylene is the principal C source of the process gases. However, the raw  $C_2H_2$  concentration was not adjusted so that any change is due to disassociation resulting from  $CO$  and  $CH_4$  addition. Methane is shown to greatly increase the levels of  $C_2H_2$  present. Carbon monoxide decreases the fraction of  $C_2H_2$  present, as shown in figure 120. There is a small interaction effect such that, if  $CO$  is present with  $CH_4$ , there is a negative synergistic effect, so that the  $C_2H_2$  level is initially slightly higher when the  $CO$  is present. As  $CH_4$  is added, the  $C_2H_2$  will not reach as high a level as it would if only the  $CH_4$  were added. Conversely, with no  $CH_4$  present,  $CO$  addition slightly increases the amount of  $C_2H_2$  but the overall amount is low. When  $CH_4$  is added, the overall level of  $C_2H_2$  is higher but the  $CO$  tends to reduce the fraction present. This interaction can be seen most clearly as the  $CH_4$ -addition response crosses itself. The level of initial concentration is higher for the  $CO$ -added curve, but as the level of  $CH_4$  addition increases, the curves cross and the curve representing no  $CO$  addition provides the highest final level of  $C_2H_2$ .

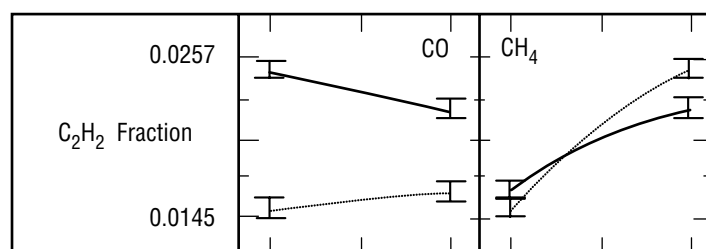


Figure 120. Acetylene fraction from GAMoly simulation.

The final two responses are related to the amounts of H and molecular H that are present for surface stabilization. In figure 121, both  $CO$  and  $CH_4$  are seen to scavenge H quite readily.

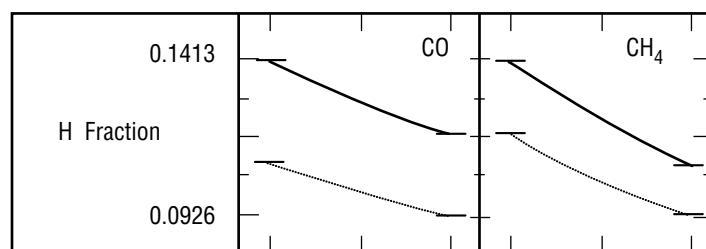


Figure 121. Atomic hydrogen fraction from GAMoly simulation.

For diatomic hydrogen, CO is shown to have little effect, while CH<sub>4</sub> greatly increases the fraction of molecular hydrogen present (fig. 122).

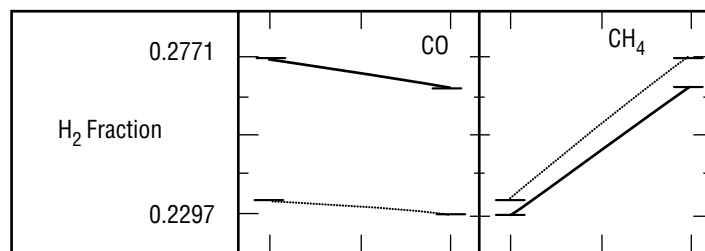


Figure 122. Hydrogen fraction from GAMoly simulation.

## 4.2 Flow Rate and Substrate Experimental Results

### 4.2.1 Run Specific Results

Again, the individual results from each process condition will be covered in sequence. Following the case-by-case results, the results from depth profile comparisons will be presented. Finally, results from the analysis of the designed experiment will be presented.

Flow No. 1 run represents the lowest flow rate condition on a Cu surface. This would be a low-flow, low-carbide capability run. Flow No. 1 micrographs do not show any clear-cut crystalline deposits (fig. 123). Two larger, typical faceted growths are shown—one is octagonal (fig. 124) and the other rectangular (fig. 125). Both of these growths are covered with smaller deposits and neither has any depth component. No optical indication of diamond is present in any of the photos from this condition.

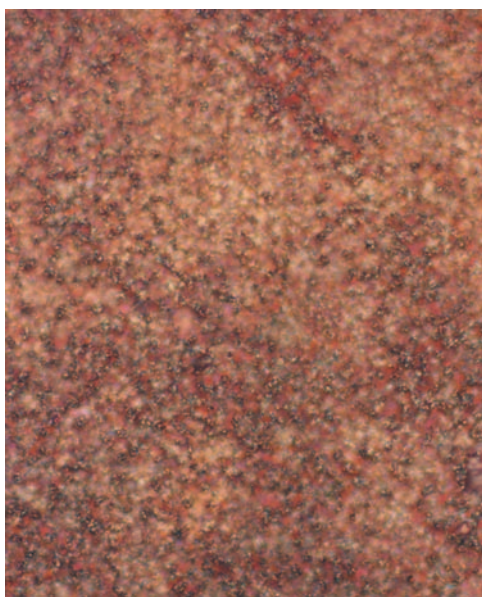


Figure 123. Flow No. 1 general deposit,  $\times 40$ .

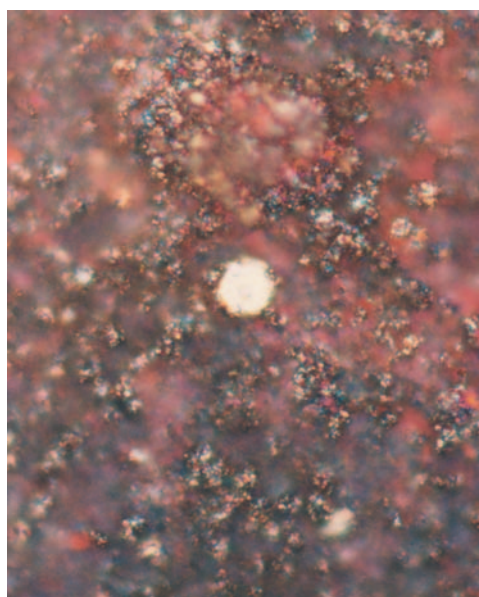


Figure 124. Flow No. 1 octagonal faceted growth,  $\times 40$ .



Figure 125. Flow No. 1 rectangular faceted growth,  $\times 40$ .

Raman data show a clear diamond peak at  $1,332\text{ cm}^{-1}$ . An indication of graphite is observed from a peak of equal count intensity at  $1,367\text{ cm}^{-1}$ . An occluded a-C Raman peak is suspected at  $1,180\text{ cm}^{-1}$  from a shoulder on the main peak (fig. 126). The Raman data were taken from individual surface growths such as those seen in figure 125.

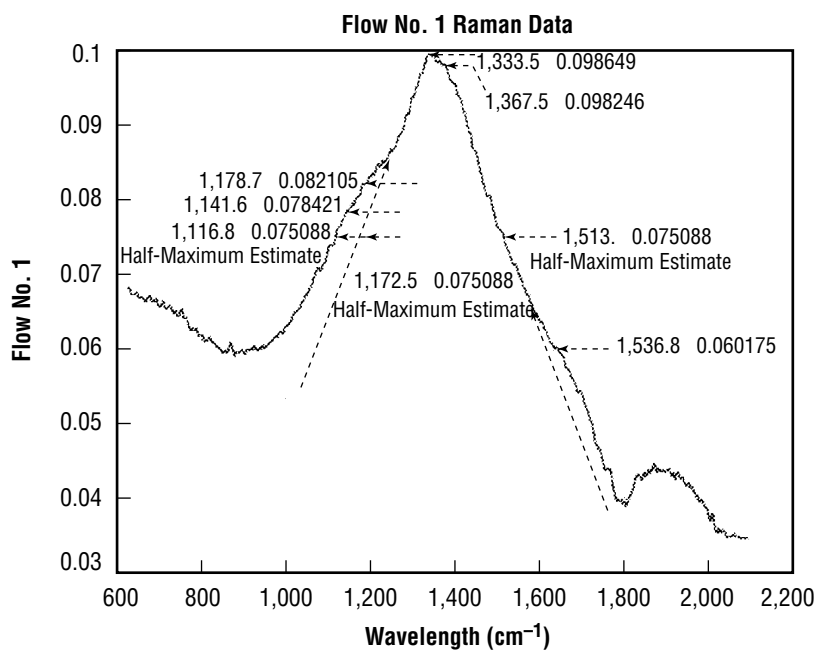


Figure 126. FTRaman data for flow No. 1.

Flow No. 2 run is a midlevel flow rate on a Cu surface. Deposits of what appear to be C material are scattered on the surface (fig. 127). Clusters show some faceting on the upper surfaces. The upper surface faceting shown is typical of diamond {100} and {111} surfaces; however, never more than one, or at most two, facets appear to be present in a particular cluster or pillar. Depth profile and magnification photographs of a larger macroscopic cluster show some poorly faceted surfaces (fig. 128); however, no clear optical indication of diamond is present in the larger clusters. The background underneath the clusters shows no faceting or indications of crystalline material (fig. 129).

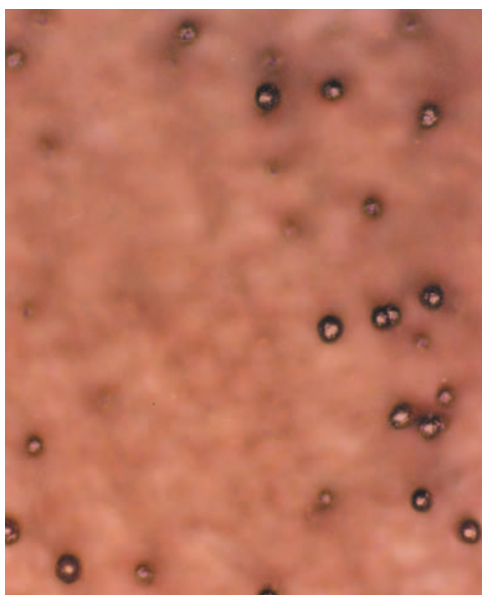


Figure 127. Flow No. 2 carbon-like surface material,  $\times 40$ .

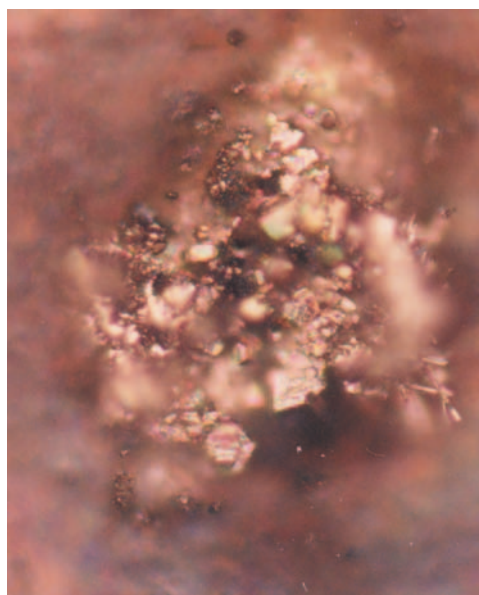


Figure 128. Flow No. 2 poorly faceted material,  $\times 100$ .



Figure 129. Flow No. 2 background, underneath pillar,  $\times 100$ .



Raman data for the flow No. 2 samples show definite diamond presence in the small isolated clusters that are widely scattered as shown in figure 128. There are clear indications for both an a-C peak and a microcrystalline graphite peak (fig. 130). No diamond is noted in spectra from the larger clusters.

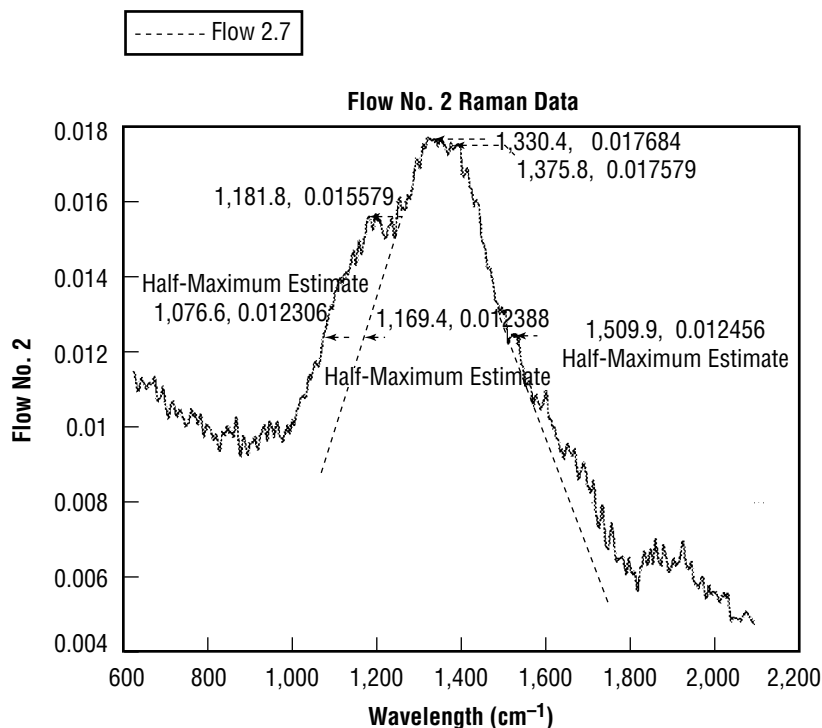


Figure 130. FTRaman data for flow No. 2.

Flow No. 3 run again used Cu substrates; however, the flow conditions were substantially higher than in the previous runs. This would be a high-flow, low-carbide capacity run. As in flow Nos. 1 and 2, small, isolated deposits are seen with facets only present on the upper surfaces (fig. 131). Larger deposits appear to be primarily nondiamond materials without discernible facets (fig. 132). The background is again completely lacking in either faceted material or crystalline indications (fig. 133).

Raman data on flow No. 3 samples show the characteristic double peak of graphite for the background of the substrate (fig. 134). One of the sharper diamond peaks is well noted for the small faceted cluster deposits that are scattered over the substrate. In this case, the diamond peak is very well defined and reasonably sharp but without as strong a graphite presence as the other SiC substrates. A clear-cut peak is noted at 1,200 cm<sup>-1</sup> and was substituted in the calculations for the expected 1,180-cm<sup>-1</sup> peak.





Figure 131. Small, isolated deposits on flow No. 3 with primarily top surface faceting,  $\times 40$ .

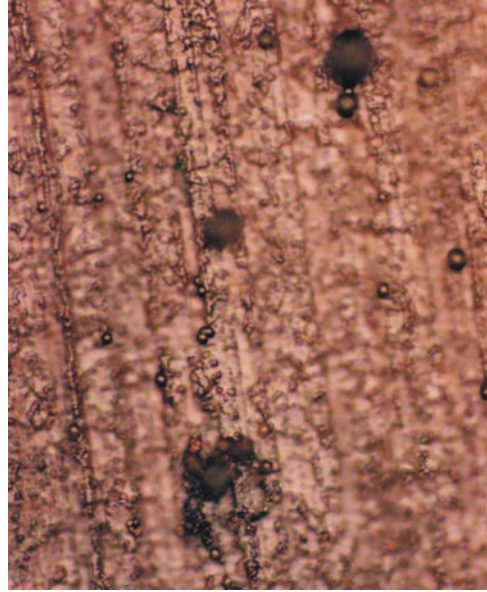


Figure 132. Larger deposits on flow No. 3 showing no faceting,  $\times 40$ .

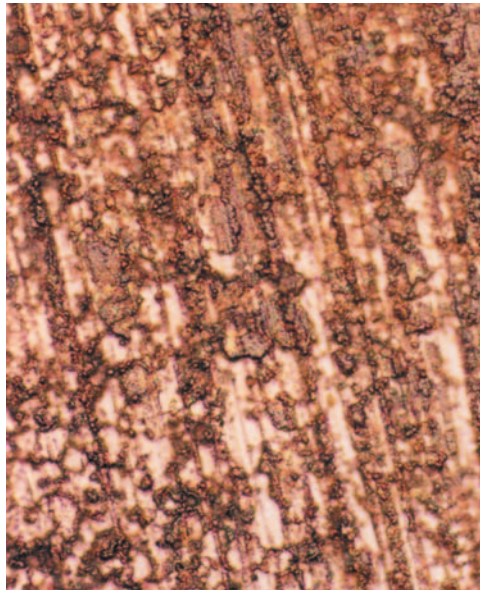


Figure 133. Background of flow No. 3 showing no faceted material,  $\times 40$ .

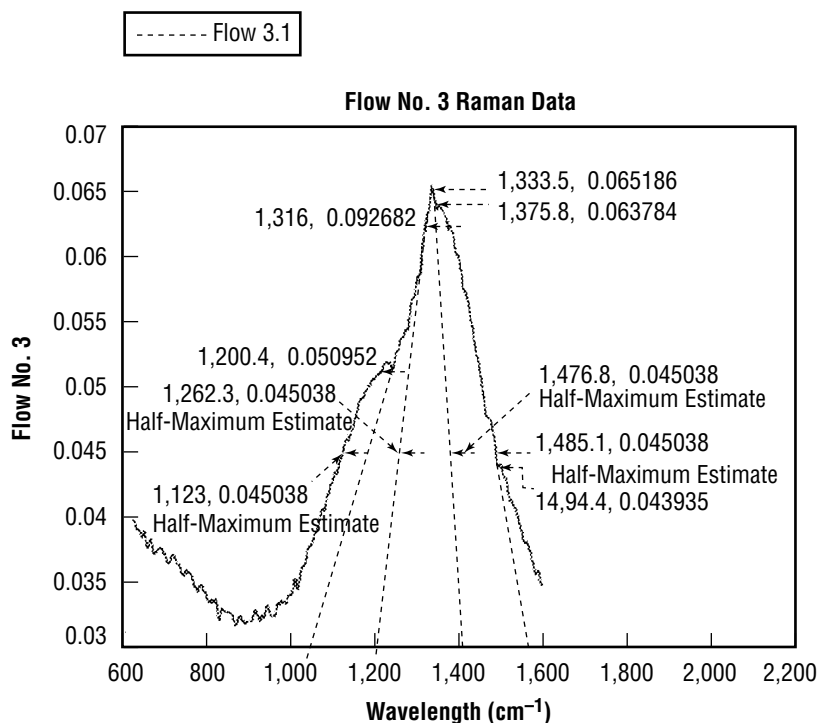


Figure 134. FTRaman results on flow No. 3.

Flow No. 4 sample was representative of a low-flow condition on a Mo substrate. Virtually no deposit was found for these samples. Optically small islands of discoloration were noted on the surface (fig. 135) and one larger collected region of what optically appeared to be unfaceted material was present. As a result of the lack of deposit, no Raman data were able to be collected from this sample.

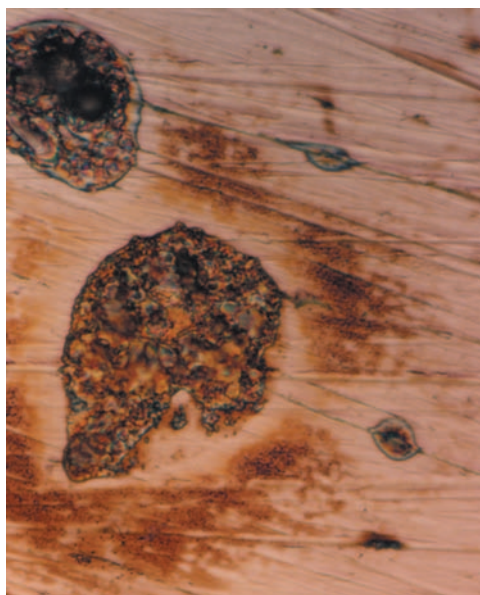


Figure 135. Discolorations noted on flow No. 4,  $\times 100$ .

Flow No. 5 is the midflow condition on Mo substrates. This run has a large number of virtually continuous isolated pillars of heavily faceted crystalline material. This may be seen in figures 136 and 137. The facets are alternately [100] and [111] facets, with a number of pillars having a hexagonal aspect directly pointing upward, such as in figure 138. Pitting and alternate growths can be seen on all upper surfaces as in figure 139. The [111] facets are, in general, heavily twinned with growth ripples on the exposed faces.

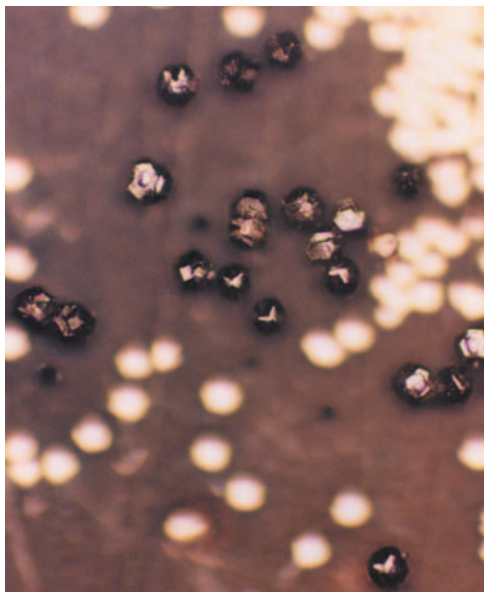


Figure 136. Isolated pillars of heavily faceted crystalline material flow No. 5,  $\times 20$ .

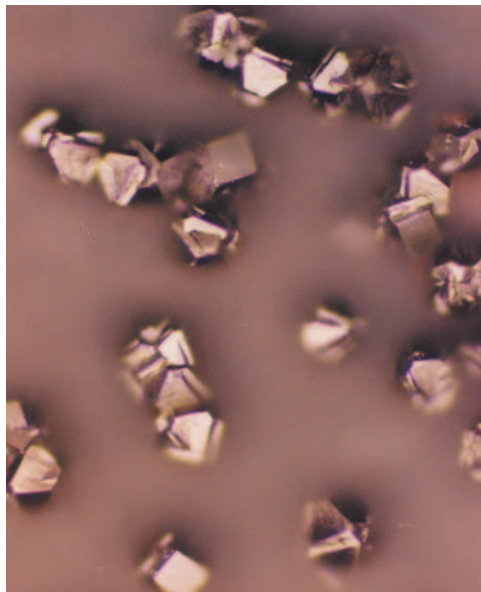


Figure 137. Isolated pillars of heavily faceted crystalline material flow No. 5,  $\times 40$ .

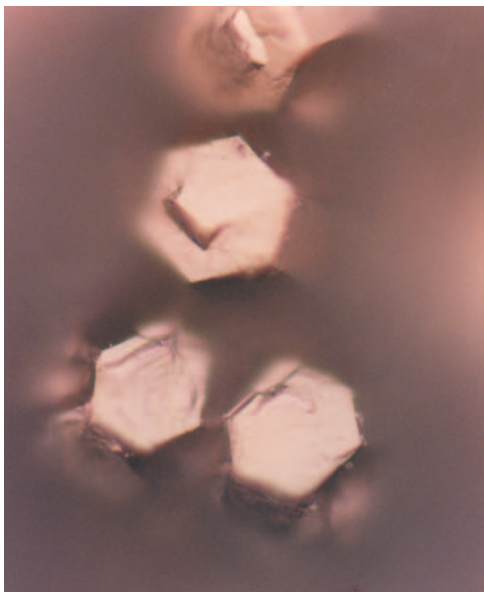


Figure 138. Flow No. 5 facets showing hexagonal aspects,  $\times 100$ .



Figure 139. Pitting on upper surface of flow No. 5 facets,  $\times 100$ .

Raman data from the flow No. 5 run show a very strong diamond signal with a spread shoulder at  $1,180\text{ cm}^{-1}$ . The combined diamond microcrystalline graphite peak is broad without a sharp clear-cut dropoff (fig. 140).

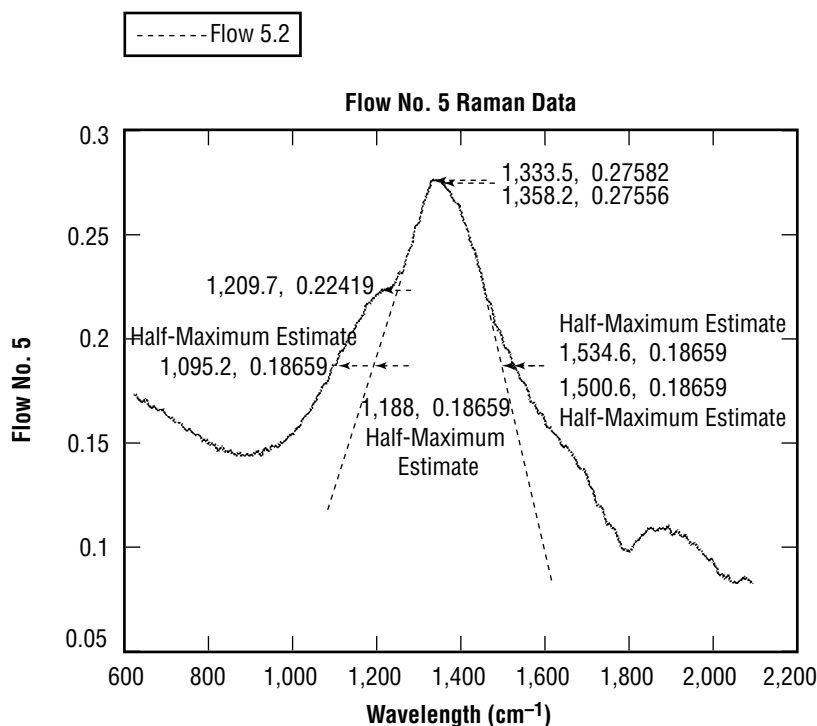


Figure 140. FTRaman data for flow No. 5.

Flow No. 6 run is the high flow condition on the midlevel, carbide-potential substrate of Mo. This run presents a very surprising morphology. Again, isolated pillars of obvious diamond facets are noted (fig. 141). The pillars have, however, a fairly regular shape with a [100] face parallel with the surface and eight [111] pyramids below and surrounding the [100] facet (fig. 142). The [111] facets are branching off in a direction such that the [100] direction of the associated crystal is perpendicular to the facet parallel with the surface. These flower structures are surprisingly regular in shape, separation, and size. The [100] top facets are very clean. The {111} facets, however, are very cluttered with secondary and nonfaceted deposits (fig. 143).



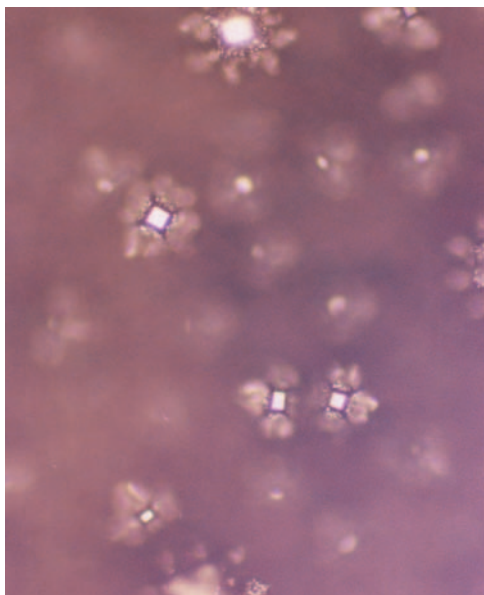


Figure 141. Flow No. 6 isolated pillars of faceted material,  $\times 20$ .

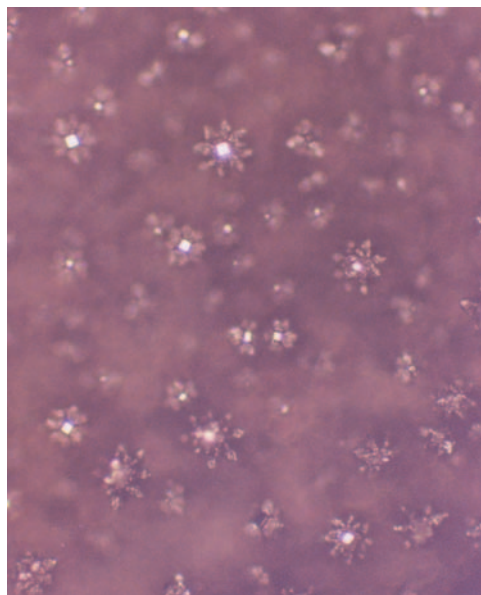


Figure 142. Regular flower structure of  $\langle 111 \rangle$  and  $\langle 100 \rangle$  facets,  $\times 10$ .

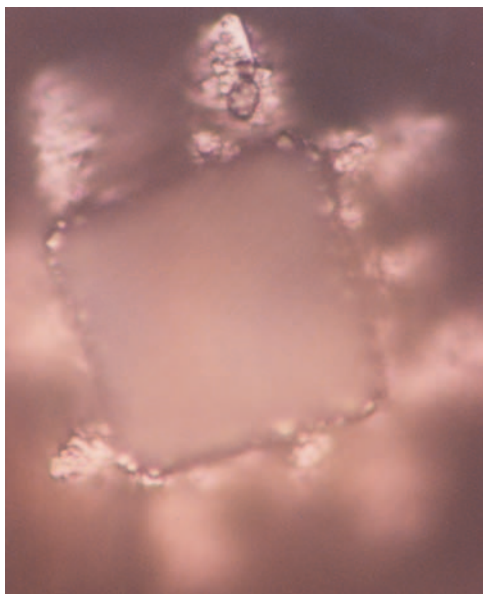


Figure 143. Picture of  $\langle 111 \rangle$  facets with secondary growths,  $\times 100$ .

Raman data from the flow No. 6 results show a low graphite peak in relation to a strong diamond line. A weak broad shoulder may be seen in figure 144 at the a-C peak of  $1,180\text{ cm}^{-1}$ .

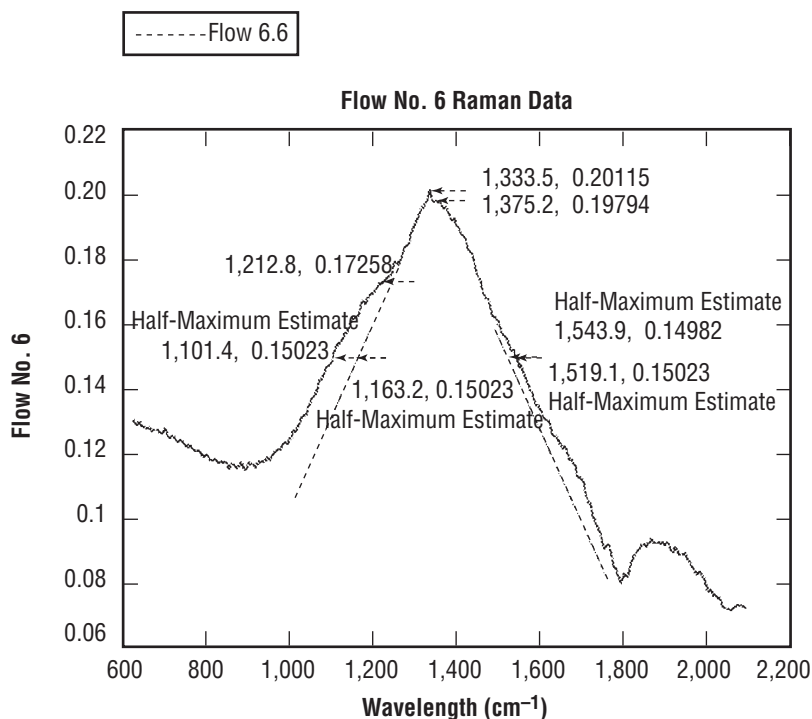


Figure 144. FTRaman data for flow No. 6.

Flow No. 7 results represent the low flow region and the highest carbide potential substrates SiC. These samples had three distinct deposition regions—two that debonded from the substrate surface and one that remained adhered. The adhered region was typically centrally located. This region typically showed no faceting at any magnification (fig. 145). The two debonded regions showed dense coverage by almost exclusively very small {111} facets (figs. 146 and 147). A series of photos ranging in magnification from  $\times 40$  to  $\times 150$  (figs. 148–150) details well the small size but uniform coverage of the crystals. The size here is relevant only in that no other samples from any of the other experiments showed crystals of this size that also were densely packed. A depth profile of clusters on one of the raised surfaces shows only a consistency of structure such that the base morphology is a densely packed compact of [111] faceted crystals and disordered material and the pillars seem to be rounded globules composed of a densely packed compact of [111] crystals (figs. 151–153).

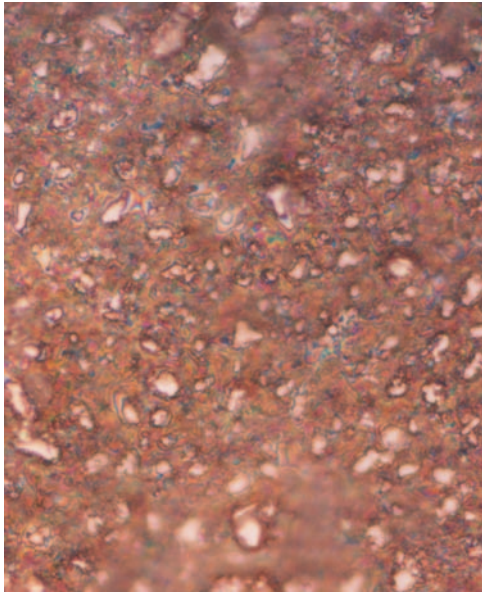


Figure 145. Flow No. 7 adhered region showing no faceting,  $\times 100$ .

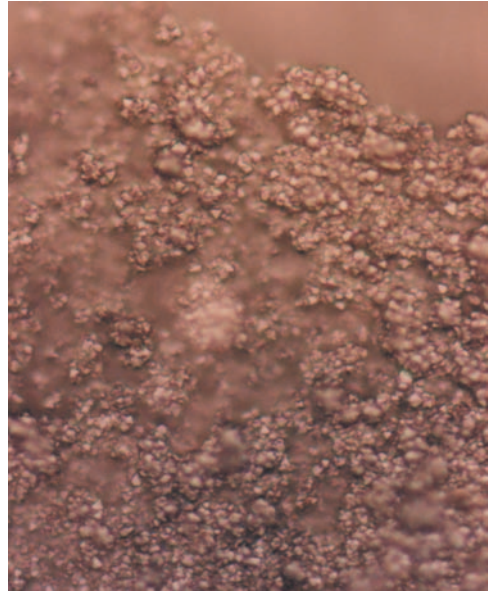


Figure 146. Flow No. 7 debond region showing strong small  $\{111\}$  faceting,  $\times 100$ .

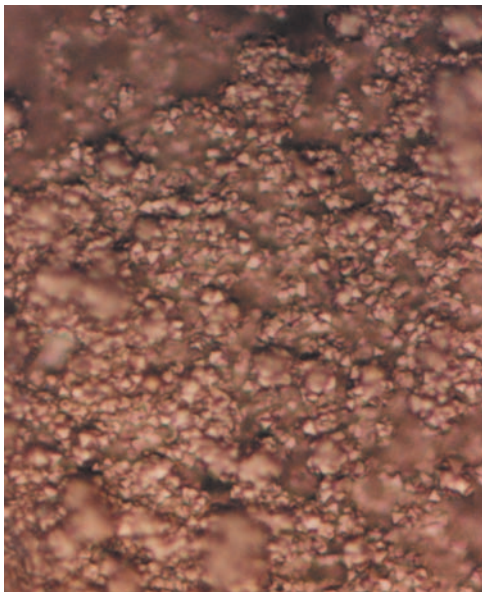


Figure 147. Flow No. 7 debond region showing strong small  $\{111\}$  faceting,  $\times 100$ .



Figure 148. Small  $\langle 111 \rangle$  crystals showing uniform coverage of GAMoly No. 7,  $\times 40$ .



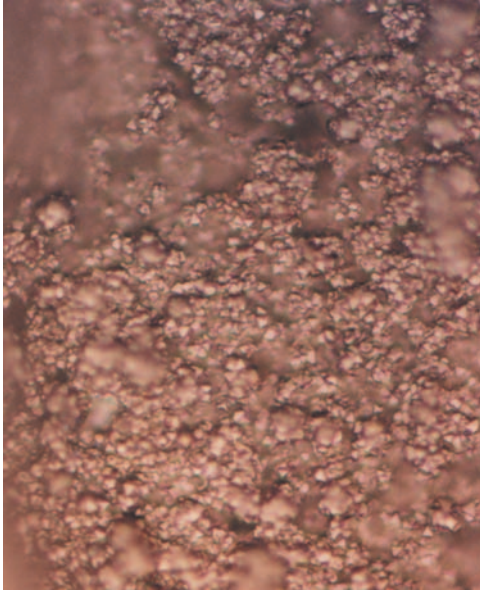


Figure 149. Small  $\langle 111 \rangle$  crystals showing uniform coverage of GAMoly No. 7,  $\times 100$ .

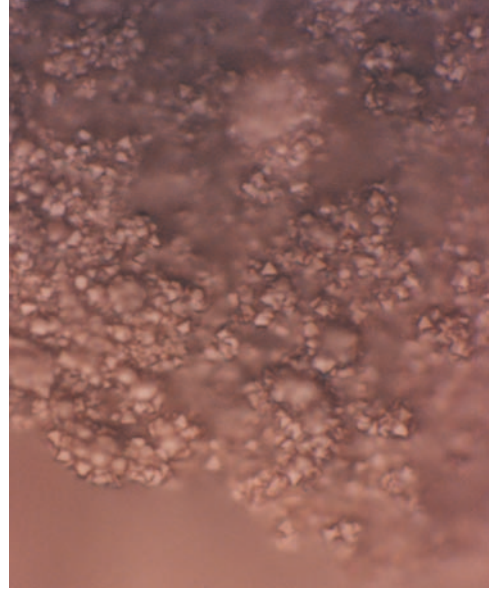


Figure 150. Small  $\langle 111 \rangle$  crystals showing uniform coverage of GAMoly No. 7,  $\times 150$ .

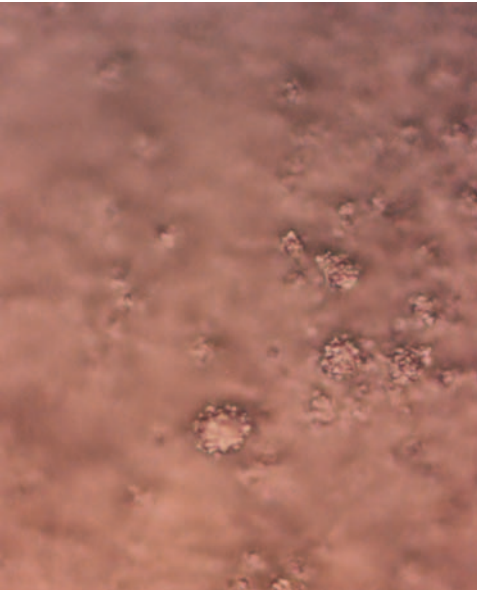


Figure 151. Flow No. 7  $\langle 111 \rangle$  compact of facets,  $\times 100$ .

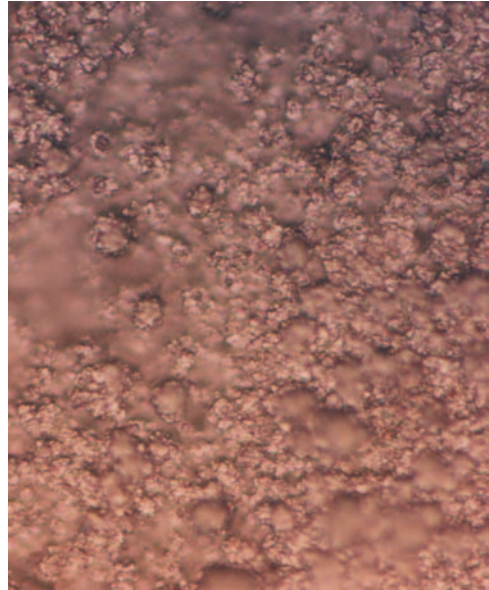


Figure 152. Flow No. 7  $\langle 111 \rangle$  facets on raised portion,  $\times 100$ .

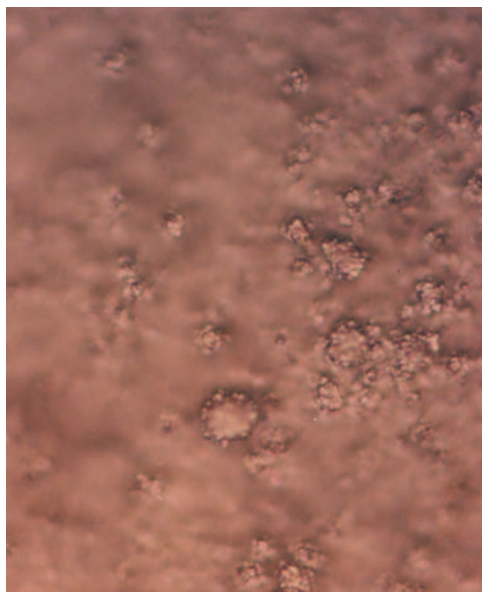


Figure 153. Flow No. 7  $\langle 111 \rangle$  facets in dense compact film,  $\times 100$ .

Raman data from the flow No. 7 results were very rough between the diamond and microcrystalline graphite peaks (fig. 154). The two peaks were clustered together on the top of a broad peak with few shoulders or clearly defined peaks. Reasonable strength is seen at the  $1,308\text{-cm}^{-1}$  line; however, it is moderately suspect due to the overall peakiness of the spectra.

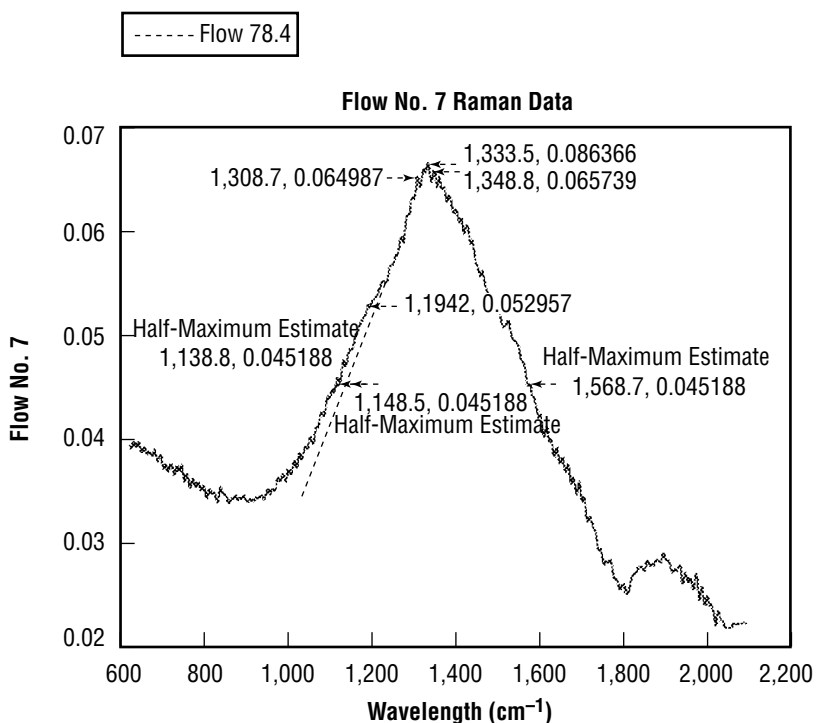


Figure 154. Raman results on flow No. 7.

Flow No. 8 samples are the midflow results on SiC substrates. A series of depth profiles on the flow No. 8 results show that the deposit is entirely composed of pillars that show no tendency to widen or join (figs. 155–157). At the top of a typical pillar is a large  $\{111\}$  facet or very small  $\{100\}$  facet. In the topmost focus, the crystal faces appear relatively free of debris. At a midlevel focus, the samples larger  $\{111\}$  facets are heavily covered by debris or nonfaceted residue. The substrate base is clearly seen through the pillars at the lowest focus and the substrate base shows no faceted material at all (figs. 158 and 159).



Figure 155. Flow No. 8 pillars depth profile top,  $\times 40$ .

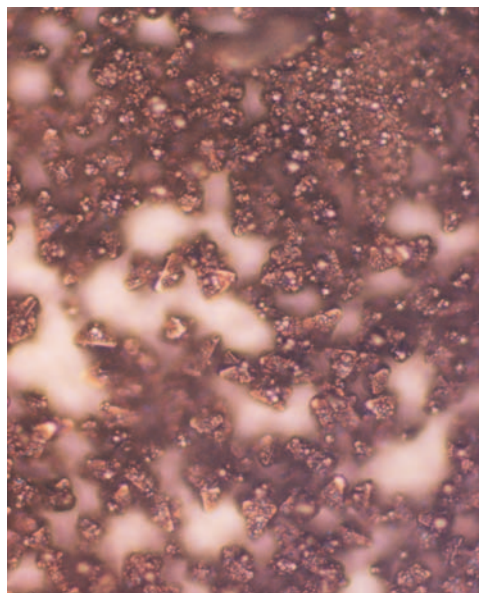


Figure 156. Flow No. 8 pillars depth profile middle,  $\times 40$ .

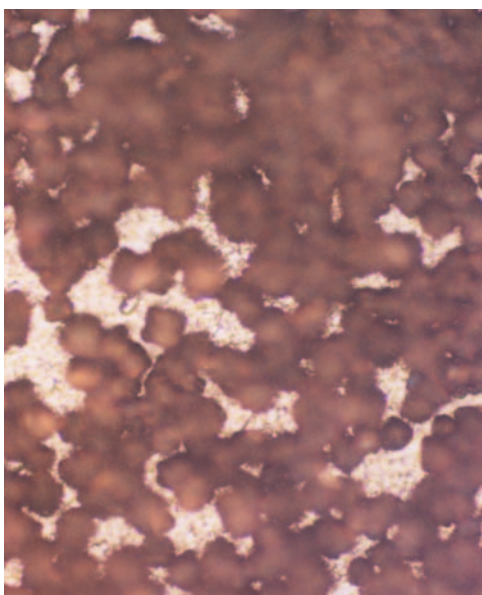


Figure 157. Flow No. 8 pillars depth profile base,  $\times 40$ .

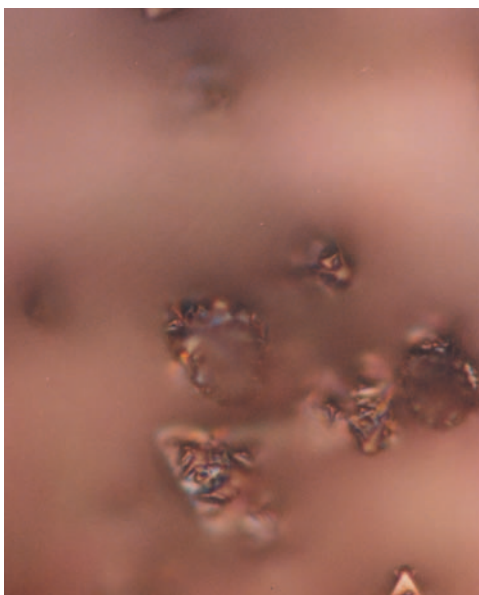


Figure 158. Flow No. 8 outlier pillars top focus,  $\times 100$ .

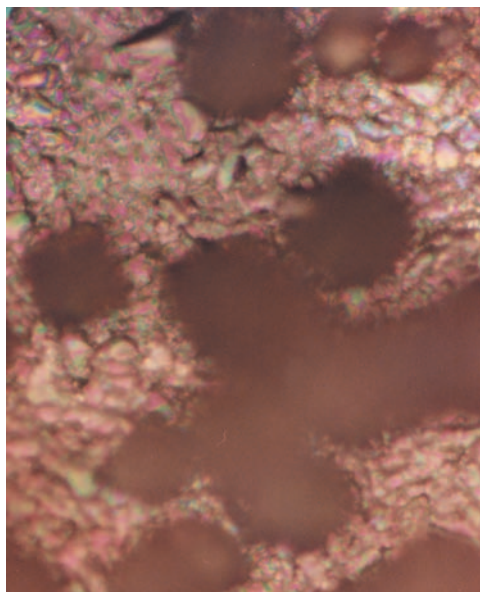


Figure 159. Flow No. 8 outlier pillars base,  $\times 100$ .

Raman data for these samples showed a strong shoulder for the a-C peak and a weak microcrystalline graphite peak. The strength of the amorphous shoulder made it easy to estimate the diamond peak without occlusions (fig. 160).

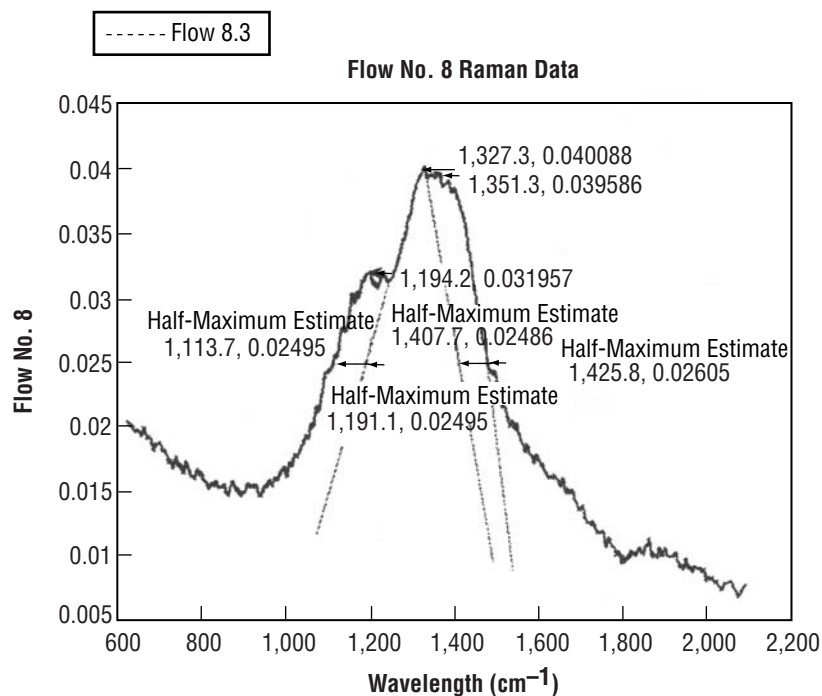


Figure 160. Raman data for flow No. 8.

Crystals were noted at the center and on the edges of flow No. 9 samples. These samples were the highest flow rate runs with the highest carbide potential. Center crystals were exclusively  $\{100\}$  faceted



crystals that grew from a few isolated clusters (fig. 161). These clusters were surrounded by pillars of material that were nonfaceted at the magnifications used (figs. 162 and 163). Crystals at the edge of the deposit arose from discrete pillaring. The pillars showed an increasing tendency to broaden toward the center of the deposits (figs. 164–166). In general, this was inversely related to cleanliness of the facets. In addition, traveling away from the center of the deposit there appeared to be an increase in twinning. Many structures were observed that consisted of  $\{111\}$  twins or growths on a table-like surface of a  $\{100\}$  face (fig. 167).

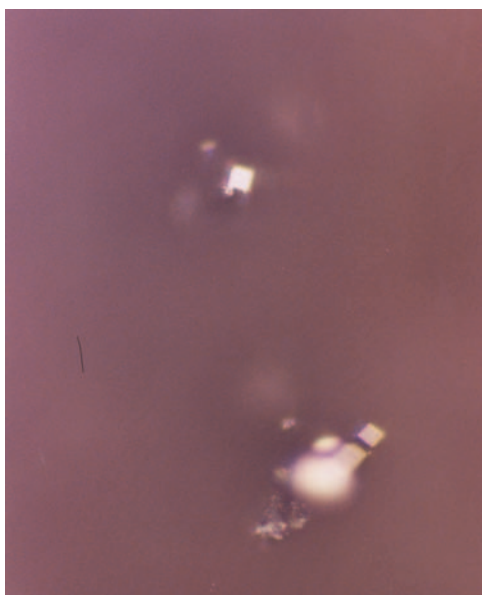


Figure 161. Flow No. 9 samples center crystals top,  $\times 40$ .

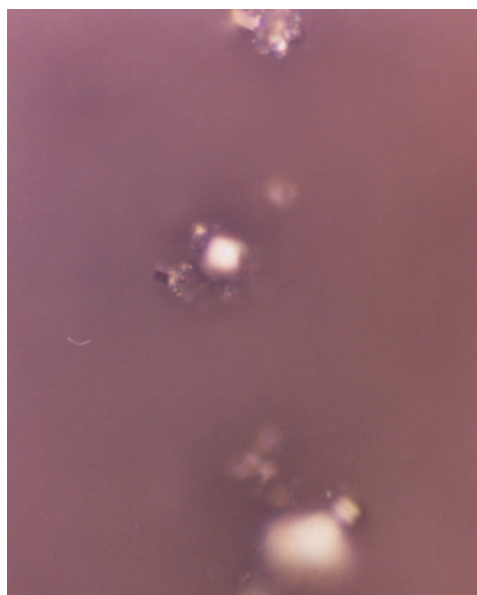


Figure 162. Flow No. 9 samples center crystals midlevel,  $\times 40$ .

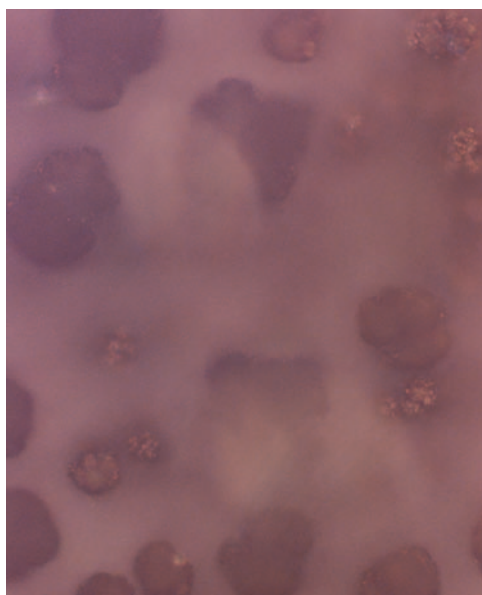


Figure 163. Flow No. 9 samples center crystals base,  $\times 40$ .

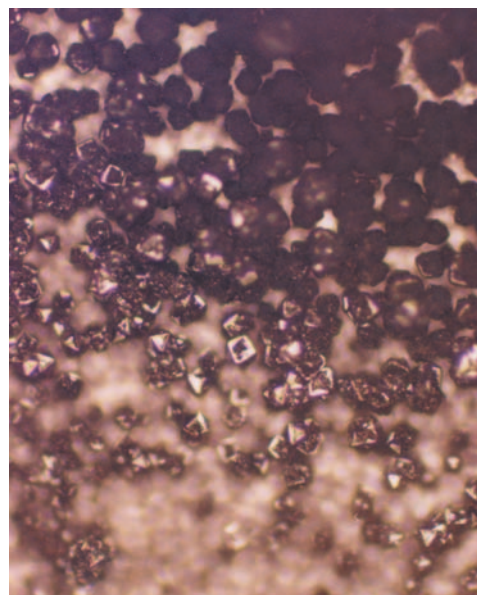


Figure 164. Flow No. 9 edge pillars showing tendency to broaden,  $\times 20$ .

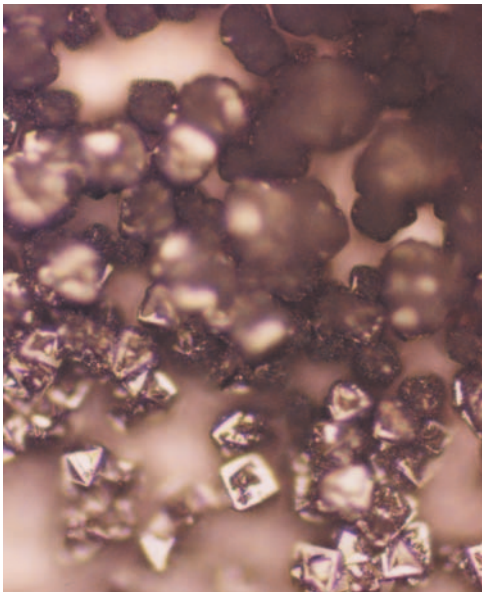


Figure 165. Flow No. 9 edge pillars showing tendency to broaden midlevel,  $\times 40$ .

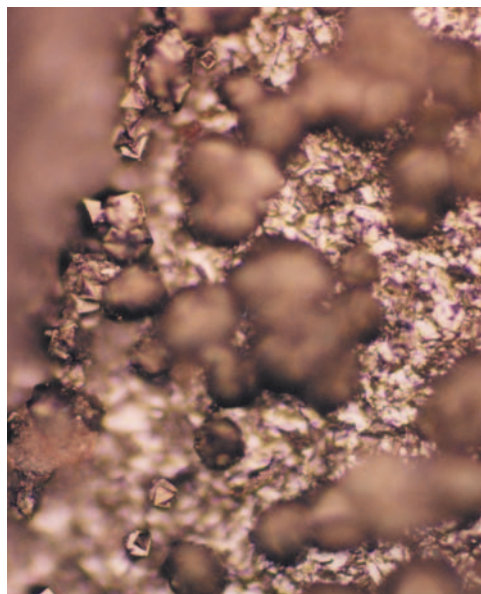


Figure 166. Flow No. 9 edge pillars showing tendency to broaden base,  $\times 40$ .

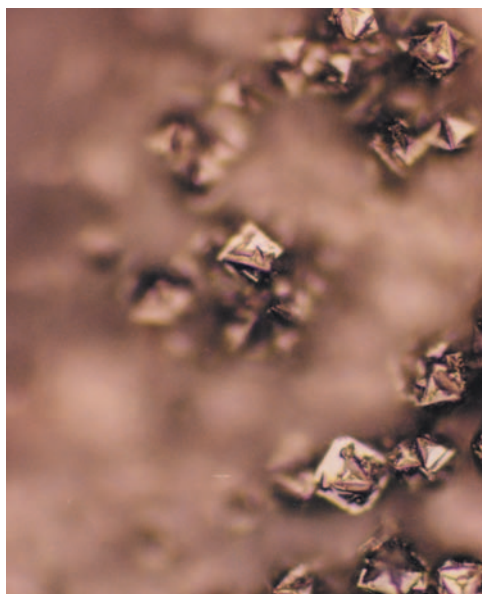


Figure 167. Twin-like structures on tabletop  $\langle 100 \rangle$  facets,  $\times 40$ .

Raman results on these samples showed some of the strongest and narrowest diamond peaks at  $1,330\text{ cm}^{-1}$ . The microcrystalline graphite and the a-C peaks are both shallow but clear in contrast to the diamond peak (fig. 168). A clear hexagonal diamond peak is also found at  $1,308\text{ cm}^{-1}$ . This hexagonal peak is the best indication of hexagonal diamond or heavily faulted material on any of the flow samples.



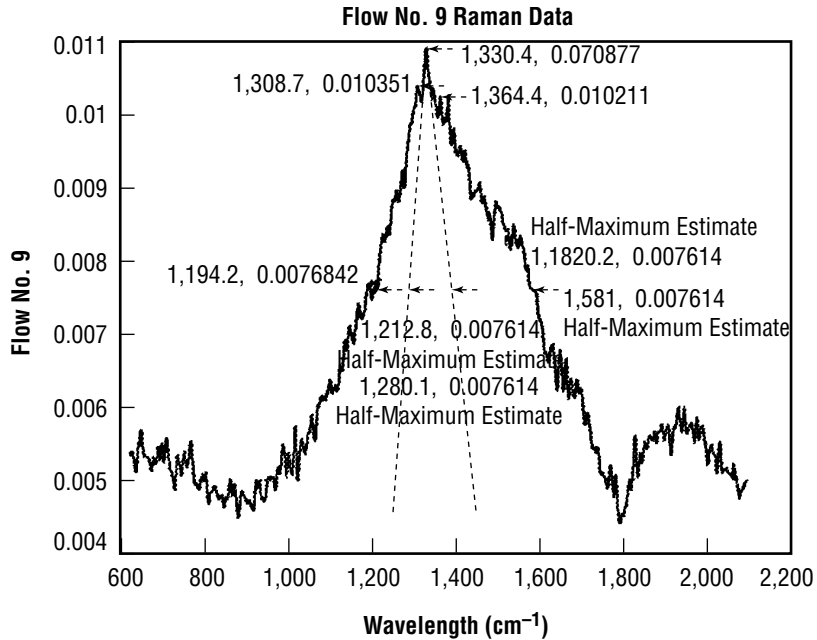


Figure 168. FTRaman results on flow No. 9.

Several Raman spectra of interest showed weaker signal-to-noise ratio but produced conclusive data nonetheless. Spectra from flow samples Nos. 3 and 6 provided very strong diamond line readings with almost no graphite present (figs. 169 and 170). Weak signal data from flow No. 9 samples provided more conventional spectra (fig. 171), while flow No. 7 weak signal spectra provided strong evidence for hexagonal or heavily faulted diamond (fig. 172).

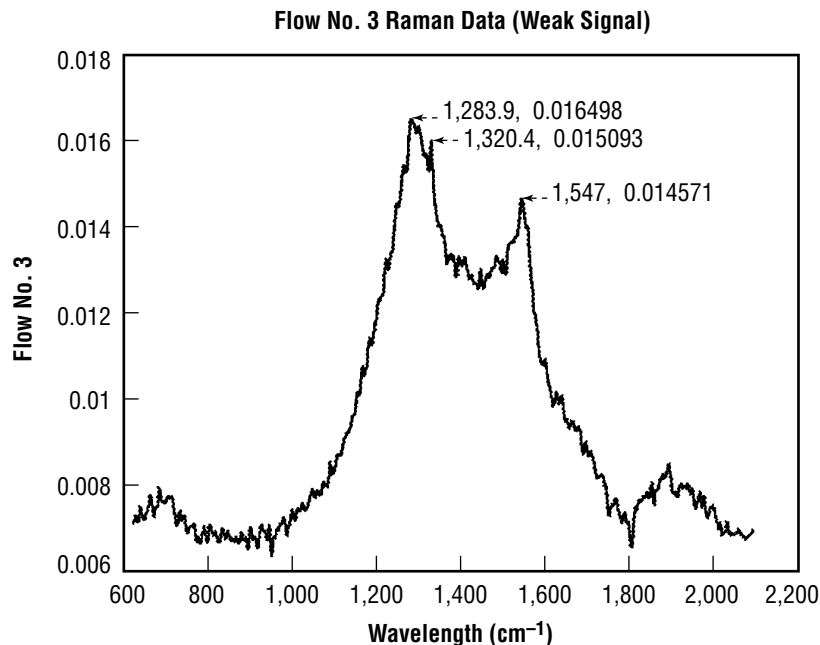


Figure 169. Weak signal FTRaman data flow No. 3.

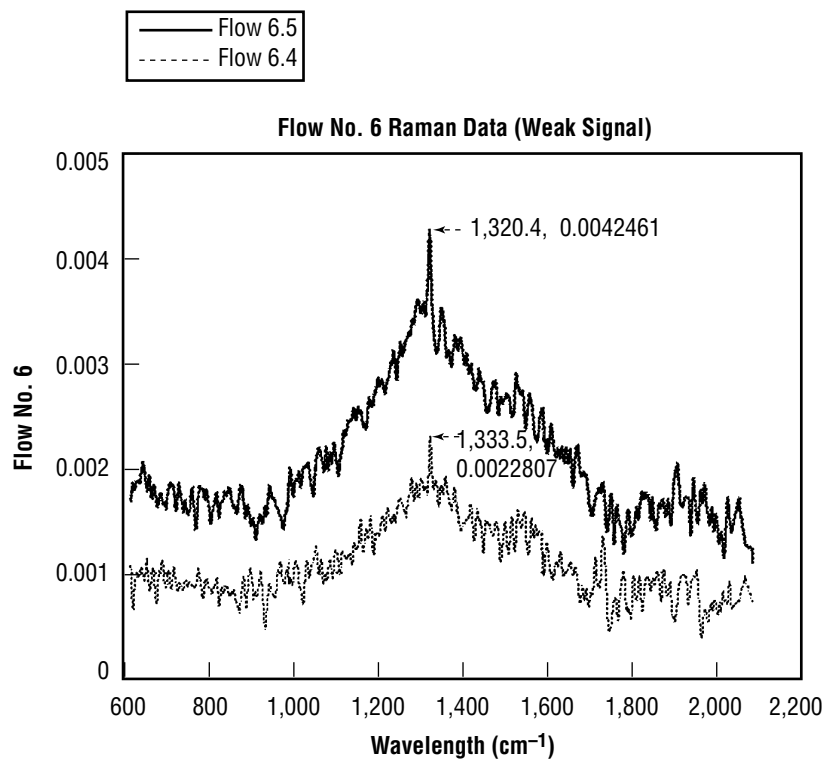


Figure 170. Weak signal FTRaman data flow No. 6.

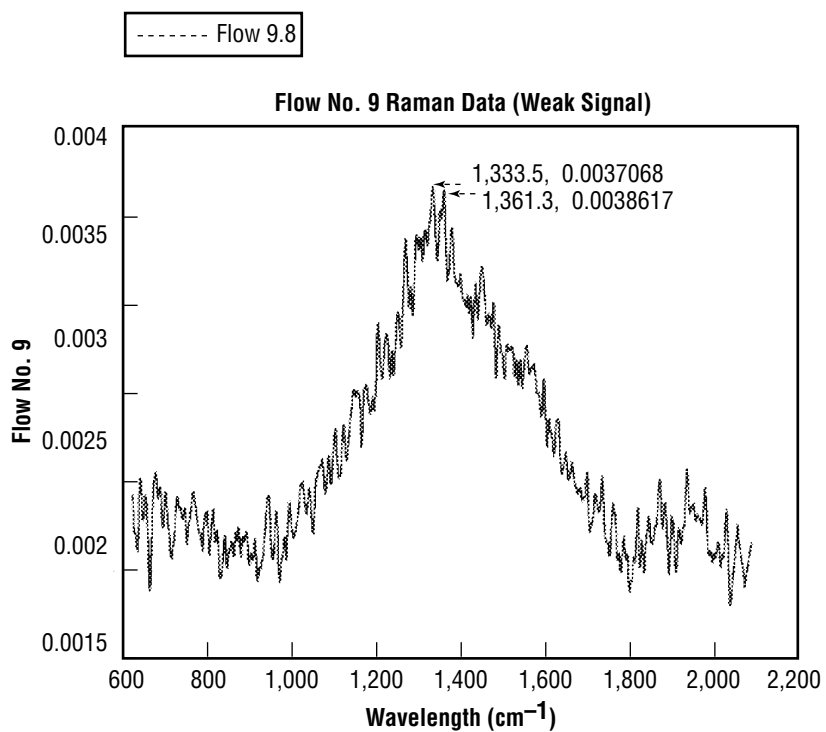


Figure 171. Weak signal FTRaman data flow No. 9.

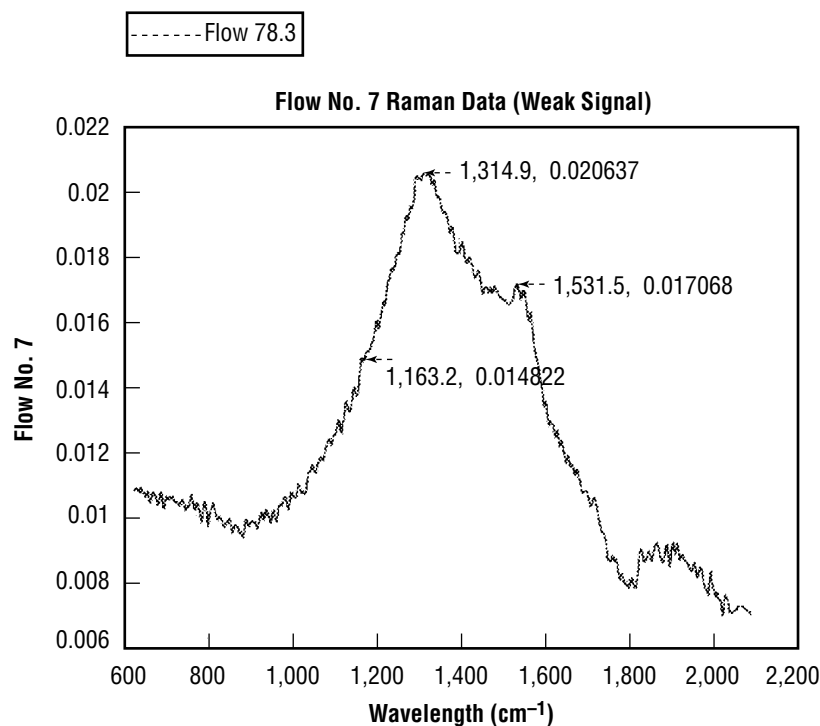


Figure 172. Weak signal FTRaman data flow No. 7.

#### 4.2.2 Designed Experiment Results

For the flow rate and substrate experiment, a three-level, two-factor, full-factorial design was used. This gave quadratic term incorporation for use in the effect of flow rate on the measured parameters and provided for an interaction term between the substrate material effect and the effect of flow rate. Because of the lack of data from run No. 4, all of the terms from that run were removed from the experiment analysis except for the qualitative results on the optical microscopy and the hexagonal diamond peak.

While interpreting the Raman spectra, the Raman linewidth was measured at an estimate of half-maximum peak height. The linewidth was measured on the measured peak only. Typically, this included occluded graphite or an occluded a-C peak or both. The adjusted Raman linewidth was a measure of the linewidth between estimated projections of the diamond peak where an attempt was made to isolate the diamond peak. For the diamond-to-graphite and the diamond-to-a-C ratios, peaks near the 1,360-cm<sup>-1</sup> peak were used as the microcrystalline graphite peak. Peaks near the 1,180-cm<sup>-1</sup> a-C peak were used as the a-C peak. Typically, these peaks were present.

In a few instances, there may be some doubt as to the presence of a discernible peak. In these cases, the presence of an expanding shoulder was considered sufficient grounds to use the intensity measured at the expected position of the peak. Any peak between 1,310 and 1,326 cm<sup>-1</sup> was considered indication of hexagonal diamond. As mentioned in the previous section on morphology and the section on Raman spectroscopy, an indication of hexagonal diamond may indicate either hexagonal diamond or the presence of a high number of stacking faults in a diamond where the Raman spectra were taken on a {111} surface perpendicular to the Raman microfocus laser.

Two of the responses were measured on a relative scale. The first was the quality of the deposit as viewed in optical microscopy. Generally, higher rankings were given to deposits with more macroscopic faceting and higher film density. Using these criteria, the substrate and the flow rate were found to have a small effect on optical film quality. Figure 173 shows the graphic results from the designed experiment with optical quality as a response variable. As the carbide-forming capability of the substrate increases from left to right, so does the corresponding optical quality. Higher flow rate is also found to be beneficial to subjective film quality.

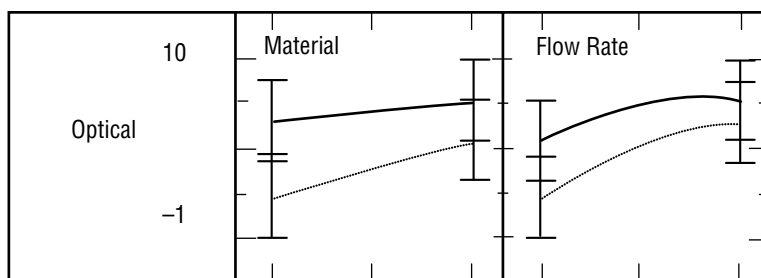


Figure 173. Qualitative optical results from flow and substrate experiment.

The second subjective ranking was the determination of hexagonal diamond peaks. Any peak between 1,310 and 1,326  $\text{cm}^{-1}$  was considered an indication of hexagonal diamond; however, a distinct peak was required in this area and no shoulder region or occlusions were thought to be acceptable. The strength of the peak was rated subjectively from 0–10 and the results are shown in figure 174. The results in this case are confusing; however, the graphs are more easily understood when the raw data are considered. A low-grade response for hexagonal diamond was found on sample No. 3, which was the high-flow, low-carbide run. A high-grade response was found on flow No. 9 samples, which was a high-flow, high-carbide capacity run. Graphic results then show an improvement with the carbide capacity of the surface and a drastic quadratic improvement with the flow rate.

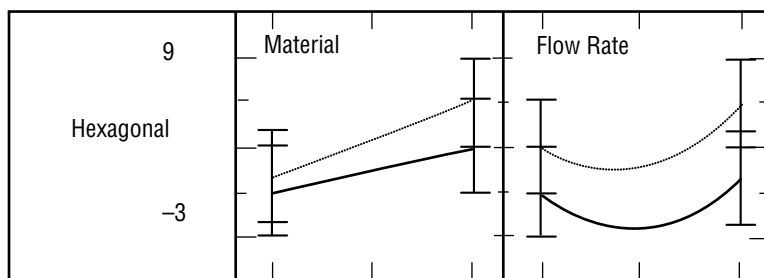


Figure 174. Qualitative hexagonal diamond results from flow and substrate experiment.

The response of Raman linewidth to variations in flow rate and substrate material is shown in figure 175. Both factors show some effect on the Raman linewidth. The substrate has either a positive or a negative effect on linewidth. In either case, the effect is tied to the flow rate. The flow rate seems to present a critical value situation. Below a certain flow rate, the quality, as defined by linewidth, drops off linearly with the flow rate. Above the critical flow rate, the quality no longer follows flow rate but instead is affected more by substrate type.

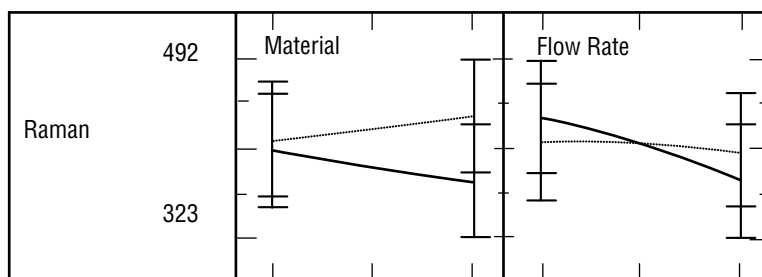


Figure 175. Raman diamond linewidth results from flow on substrate experiment.

The response of Raman linewidth was also considered when an adjusted measurement was made. For these measurements, an attempt was made at the half maximum value to estimate the linewidth of the diamond peak without incorporating occluded peaks. These estimations are very rudimentary and, as might be expected, they show similar results as presented above; however, the effects are not as strongly represented in the estimations. In figure 176, the quadratic effect is somewhat more pronounced with respect to flow rate in the adjusted measurements. The quadratic effect predicts a stronger effect of increased flow and less of a critical point. This would indicate that the effect of flow becomes more pronounced after the critical point, but increasing flow rate increases quality on either portion.

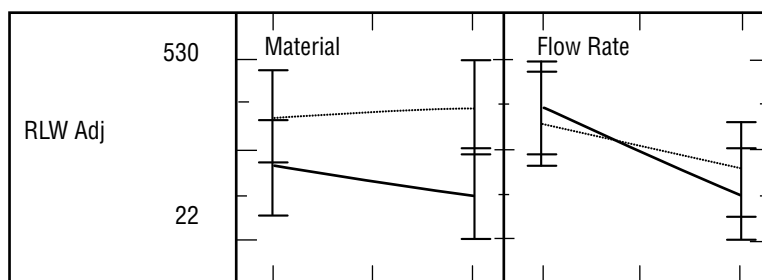


Figure 176. Raman diamond linewidth results from flow and substrate experiment.

Two measures of relative peak height measurement were used—a ratio with the microcrystalline graphite peak and a ratio with the a-C peak. The peak-height ratio is a good quantitative measure of quality because it does not depend on the laser power applied for a given sample nor does it require interpretation of the Raman counts received as this quantity is ratioed out. Graphic results from peak ratios correlate very well with results from the linewidth measurements. In figure 177 for the diamond to microcrystalline graphite peak, the substrate type may be seen to have an effect that is amplified by the flow rate. A strong effect is noticeable for the flow rate. For the linewidth measurements, not much of the effect was found to be quadratic; however, the relative strength of the peaks appears more strongly affected by changes in flow rate.

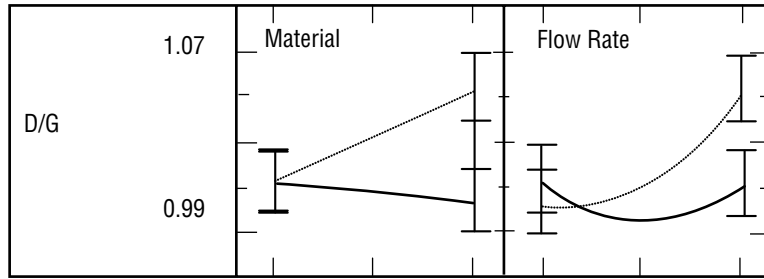


Figure 177. Raman diamond linewidth versus graphite linewidth results from flow and substrate experiment.

For the ratio of diamond to a-C peak, similar effects are noted, but the strength of the responses is less, as seen in figure 178.

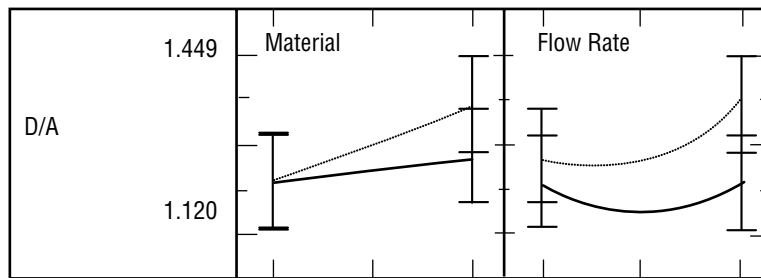


Figure 178. Raman diamond linewidth versus a-C linewidth results from flow and substrate experiment.



### 4.3 Tip Modification Experiment Results

#### 4.3.1 Run Specific Results

Tip No. 1 results were based on a SiC substrate using an unmodified No. 1 torch tip with the addition of small amounts of  $\text{CH}_4$ . The island morphology of these samples is clearly seen in the survey photo in figure 179. Agglomeration of the islands is seen in the primary growth regions. Typically, the pillars terminate with either clean  $\{100\}$  facets (fig. 180) or dirty  $\{111\}$  facets (fig. 181). A depth profile of a larger pillar (figs. 182–185) shows  $\{100\}$  termination at the top and protruding  $\{111\}$  facets along the sides with poorly faceted material at the base.

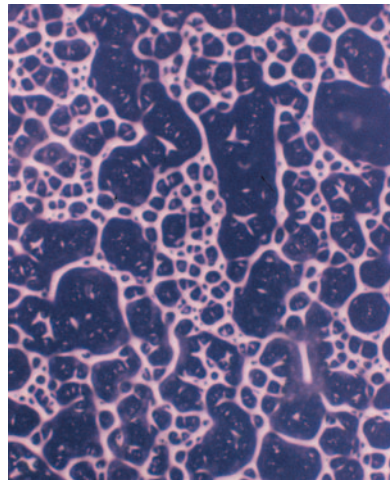


Figure 179. Gas tip No. 1 island morphology in tip No. 1 samples,  $\times 5$ .

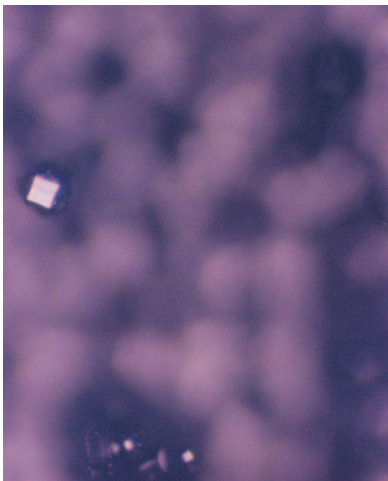


Figure 180. Gas tip No. 1 clean  $\langle 100 \rangle$  terminated facets,  $\times 10$ .

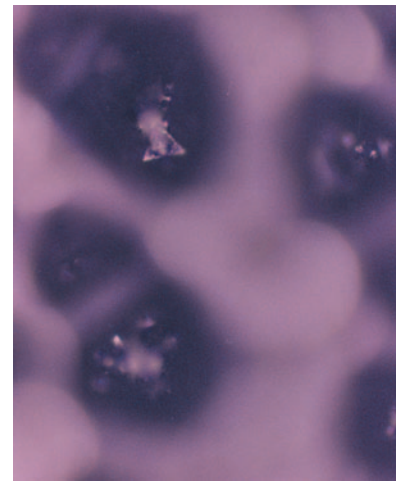


Figure 181. Gas tip No. 1  $\{111\}$  terminated facets with growth structures,  $\times 40$ .

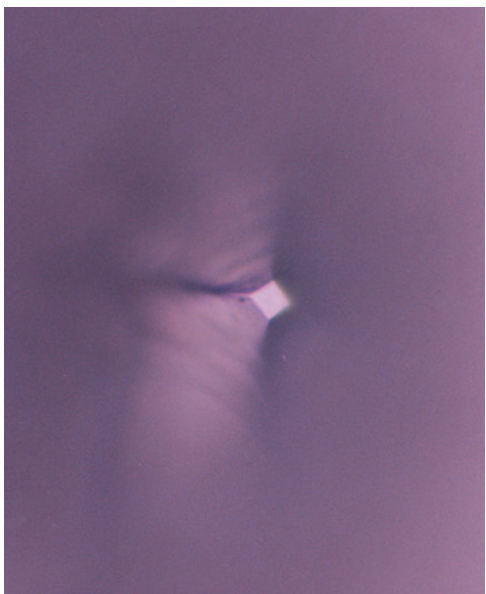


Figure 182. Gas tip No. 1 depth profile {100} top surface,  $\times 100$ .

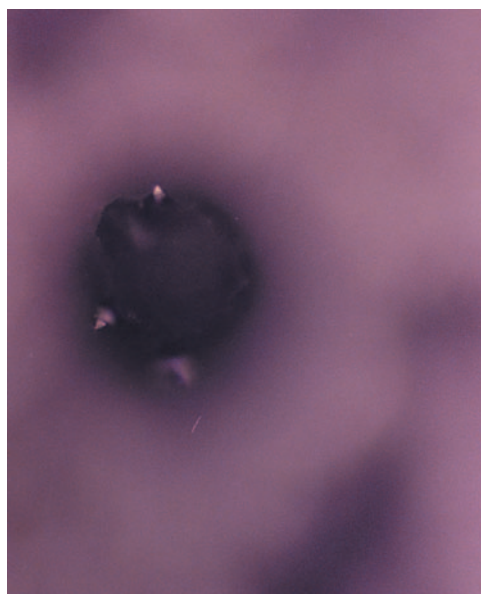


Figure 183. Depth profile for gas tip No. 1 samples, {111} midlevel facets,  $\times 40$ .

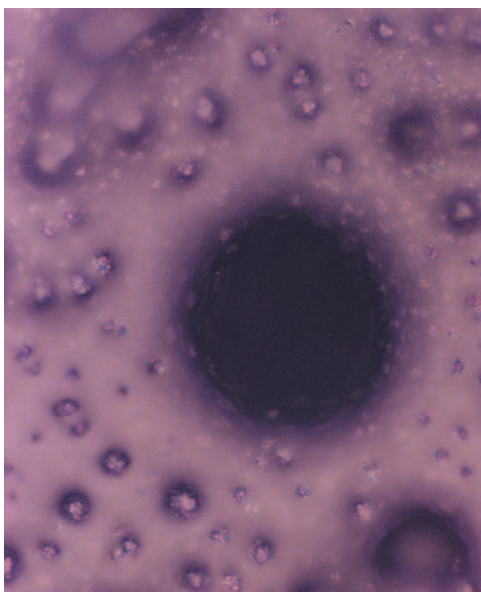


Figure 184. Depth profile for gas tip No. 1 samples, {111} midlevel facets,  $\times 40$ .

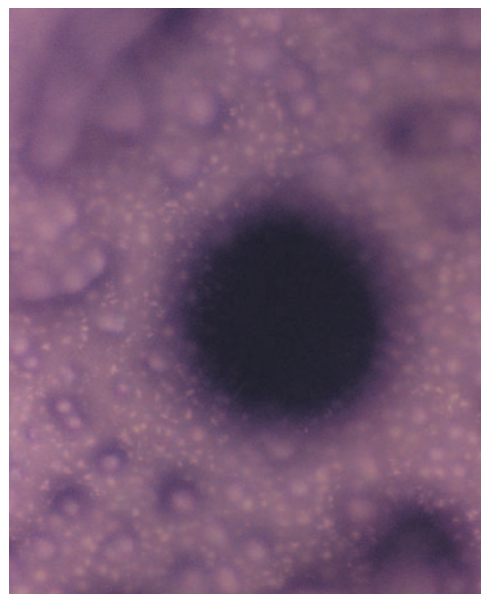


Figure 185. Depth profile for gas tip No. 1 samples, unfaceted base material,  $\times 40$ .

Raman data for tip No. 1 samples show a very strong amorphous shoulder at  $1,180\text{ cm}^{-1}$  and a weak microcrystalline graphite peak (fig. 186). The combined diamond/microcrystalline graphite peak is, however, very broad.

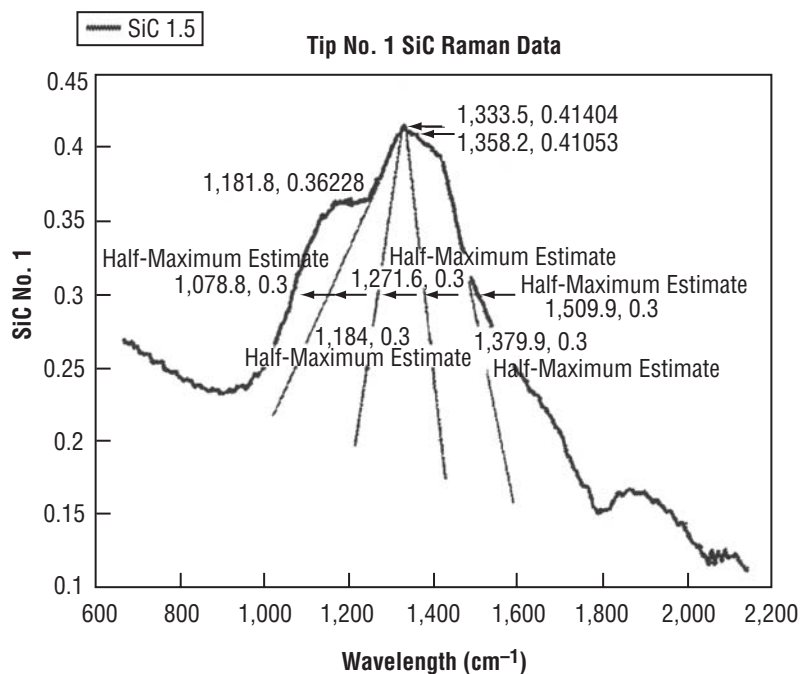


Figure 186. FTRaman data for tip No. 1 samples.

Tip No. 2 samples were produced using an unmodified No. 1 torch tip on SiC substrates with small additions of CO. No faceting was noted on tip No. 2 deposits (fig. 187). Deposits were predominantly granular. Two structures were noted (figs. 188 and 189) that may be related to the growth of noncomposite material. These were, by far, the exception and not the rule.

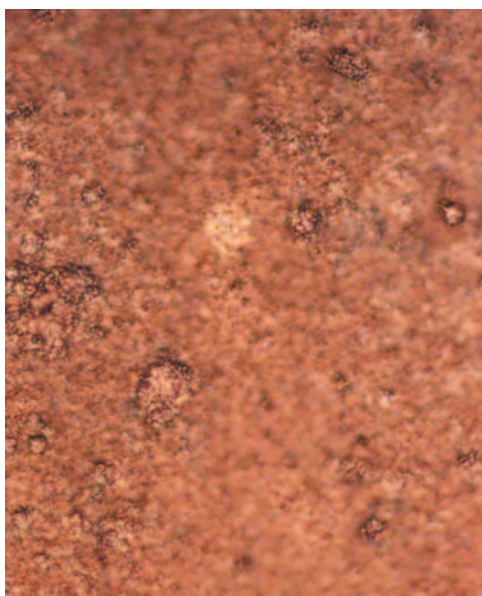


Figure 187. Gas tip No. 2 samples showing a lack of faceting,  $\times 40$ .



Figure 188. Gas tip No. 2 unusual structures,  $\times 100$ .

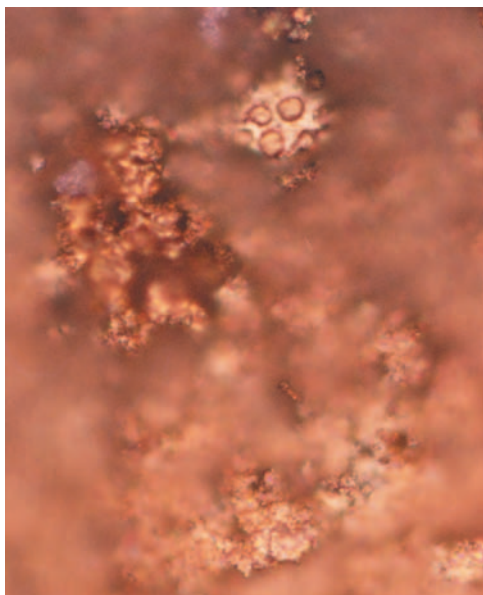


Figure 189. Gas tip No. 2 unusual structures,  $\times 100$ .

Raman data on tip No. 2 showed no evidence of diamond. A significantly minor peak was noted at  $1,494\text{ cm}^{-1}$ , which may be attributable to the  $1,500\text{-cm}^{-1}$  line of graphite. It is, however, barely above the noise level (fig. 190).

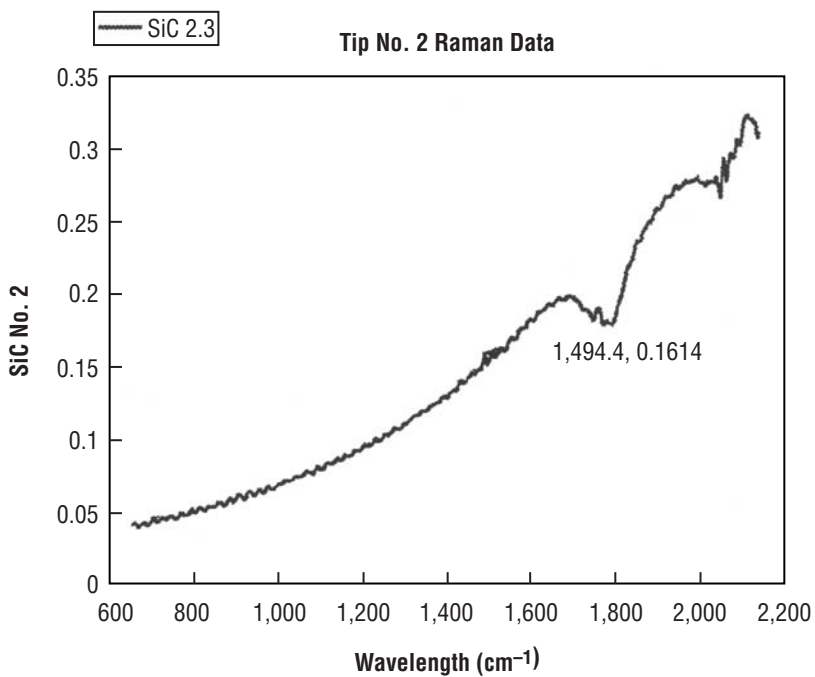


Figure 190. FTRaman data for tip sample No. 2.

Tip No. 3 samples resulted from a modified torch tip, described previously, and the addition of small amounts of  $\text{CH}_4$  onto a SiC substrate. The results were divided into the center region where large



isolated pillars of  $\{111\}$  faceting were observed. In the center, a depth profile typically shows a column with little or no broadening toward the bottom. The pillar is typically composed of many medium-sized pyramidal facets (figs. 191–193). The outer edges showed a somewhat denser cluster of smaller crystallites that form more of a contiguous film and fewer pillar structures. These facets, however, are typically covered and/or surrounded by nonfaceted material (figs. 194–196).

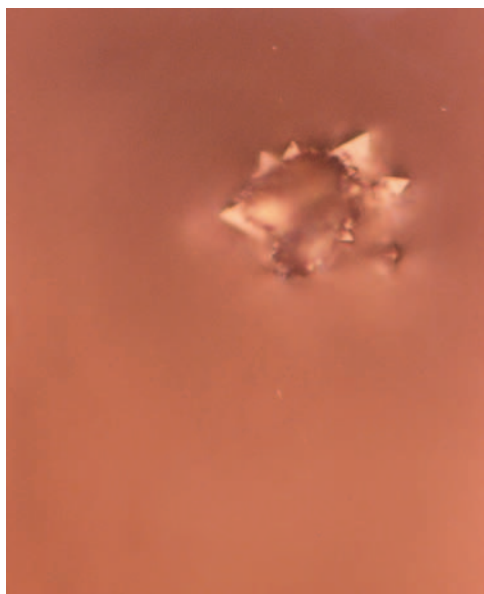


Figure 191. Faceted pillars for gas tip No. 3,  $\times 100$ .

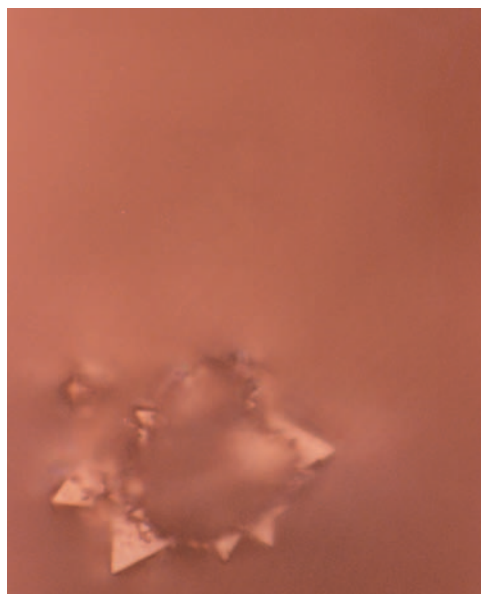


Figure 192. Faceted pillars for gas tip No. 3,  $\times 150$ .

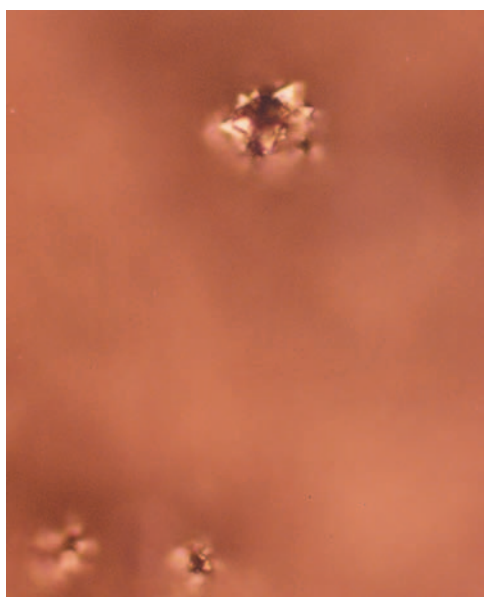


Figure 193. Faceted pillars for gas tip No. 3,  $\times 40$ .

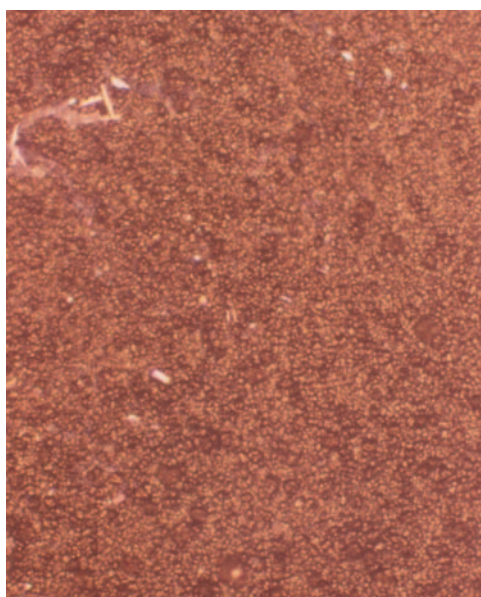


Figure 194. Pillars and nonfaceted material for gas tip No. 3,  $\times 10$ .

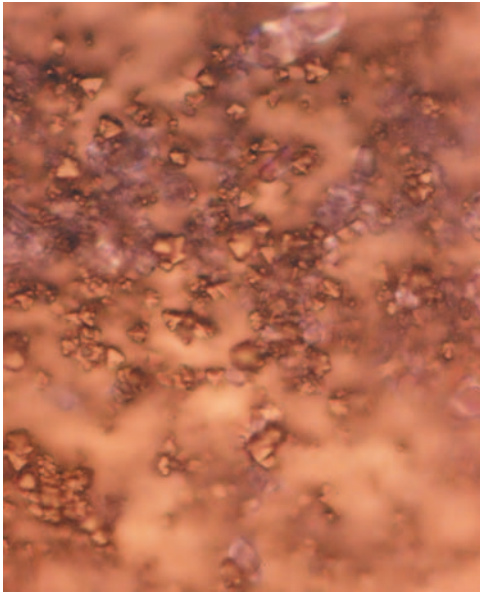


Figure 195. Pillars and nonfaceted material for gas tip No. 3,  $\times 100$ .

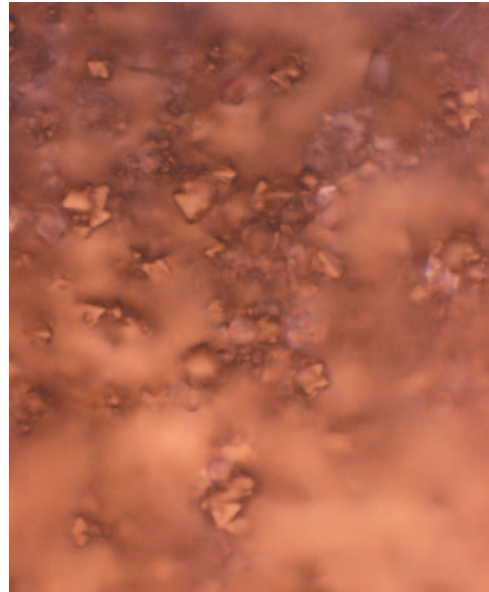


Figure 196. Pillars and nonfaceted material for gas tip No. 3,  $\times 150$ .

Raman data for tip No. 3 samples show a very rounded and smooth combination of microcrystalline graphite and the diamond peak. A strong shoulder is again seen near the  $1,180\text{-cm}^{-1}$  a-C peak (fig. 197).

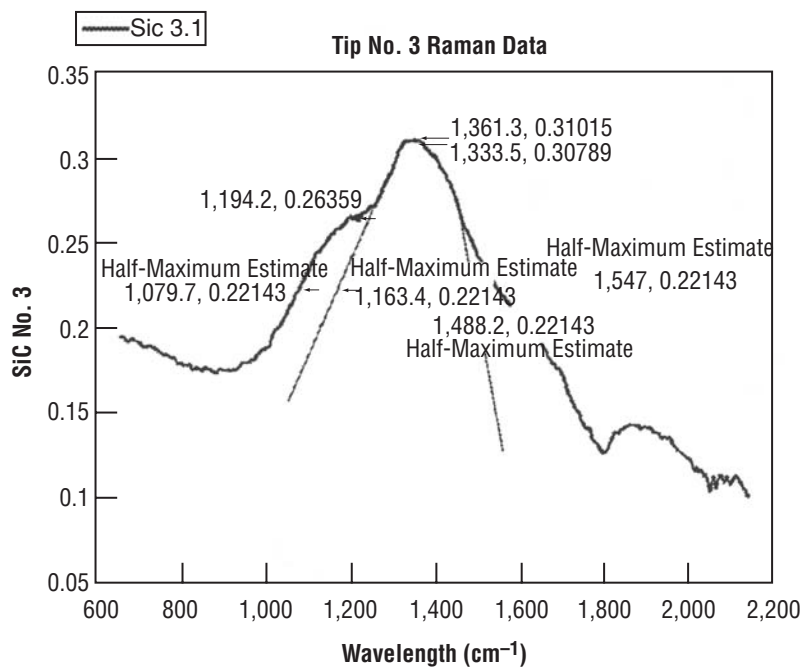


Figure 197. Raman data for tip No. 3 samples.



Tip No. 4 sample had a number of curious anomalies, but results of the Raman spectroscopy indicate that no diamond was produced. Both hexagonal structures (fig. 198) and transparent anomalies (figs. 199 and 200) were present. No Raman signal was present for either of them. A large cluster with well-defined, triangular-faceted material also failed to produce a Raman signal (fig. 201) for diamond or any form of C. The results were very disappointing; however, they were repeated and the equipment veracity checked against known samples. The results have been put aside for later study.



Figure 198. Hexagonal structures on tip No. 4 samples,  $\times 100$ .

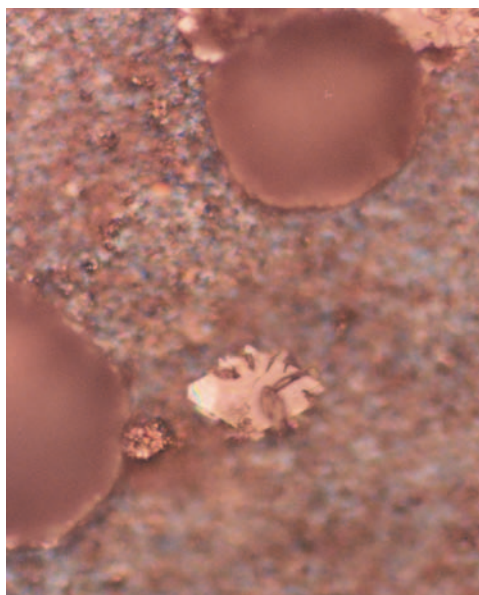


Figure 199. Transparent structures on tip No. 4 samples,  $\times 40$ .

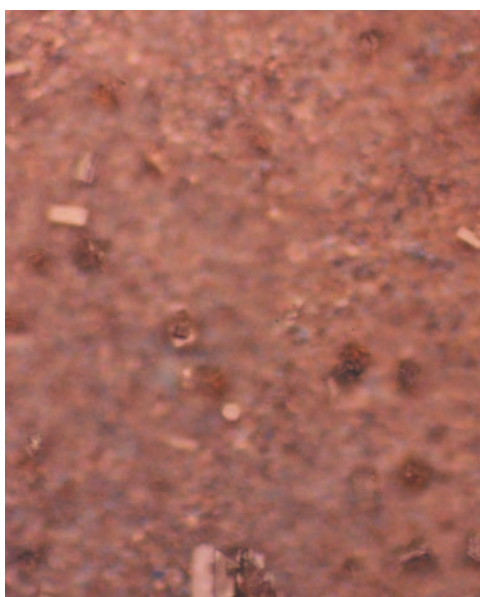


Figure 200. Transparent structures on tip No. 4 samples,  $\times 40$ .

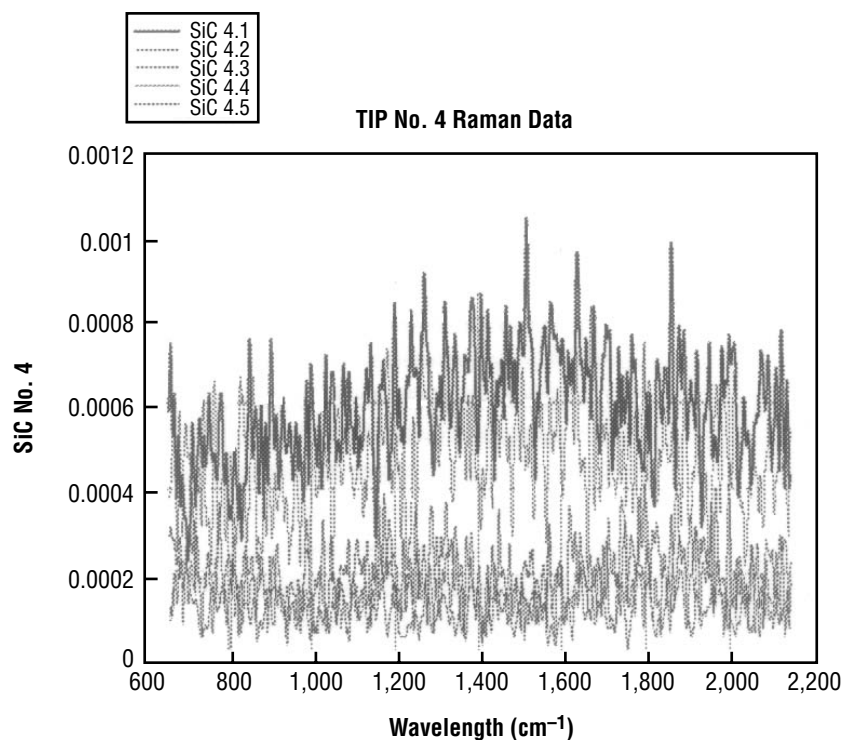


Figure 201. Raman data for tip No. 4 samples.

### 4.3.2 Designed Experiment Results

For the gas type and tip modification experiment, a two-factor, full-factorial design was used. The results using the addition of CO were disappointing and provided no crystals for measurement and comparison. The effect of the tip modification did spur the following experiment on tip modification and substrate type. The only results worthy of note from this designed experiment was the effect of the tip modification on Raman linewidth. The Raman linewidth is shown drastically increasing for the change in gas type. This is due to the use of an arbitrarily high value to indicate the lack of a diamond line in the Raman spectra. More importantly, the diamond linewidth was shown (fig. 202) to broaden slightly due to the modification of the torch tip.

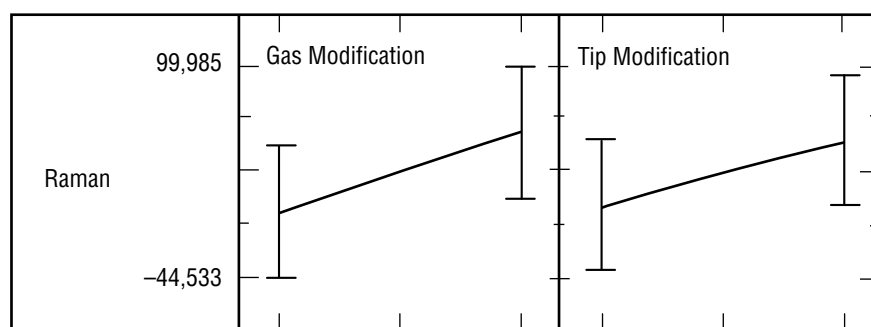


Figure 202. Raman linewidth for gas tip experiment.

## 4.4 Substrate Tip Experiment Results

### 4.4.1 Run Specific Results

Pictures from the subtip No. 1 sample contrast strongly with the Raman results. The subtip No. 1 sample was run onto a Cu substrate using an unmodified torch tip. Raman results show a diamond peak only barely above the noise level of the instrument (fig. 203), without a background noise reduction correction (i.e., these are raw spectra). Because of the much higher sensitivity to sp<sup>2</sup>-bonded material on the FT instrument on which the Raman were taken, one would expect, perhaps, to see only a very small diamond crystal or a transparent diamond with no surrounding sp<sup>2</sup> material. Instead, the optical micrographs show a proliferation of nonfaceted material, with only one series of photographs showing a possible faceted pillar (figs. 204–207).

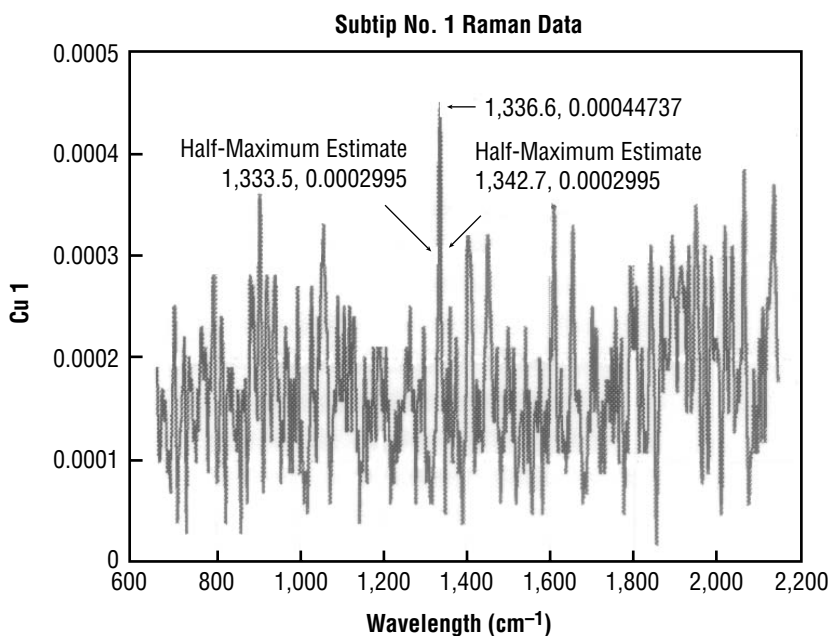


Figure 203. Substrate tip No. 1 Raman results.

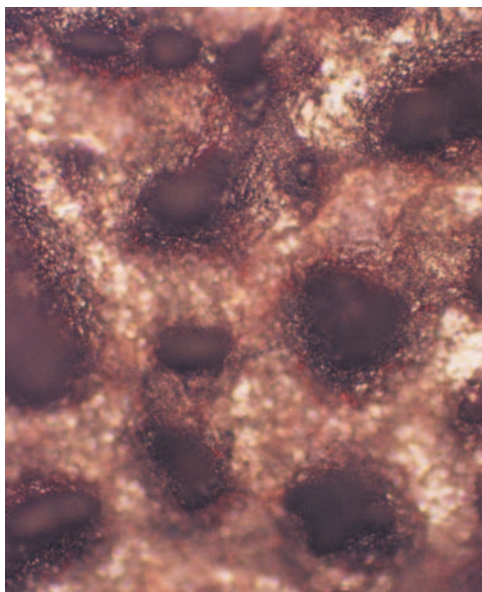


Figure 204. Substrate tip No. 1 nonfaceted material,  $\times 10$ .

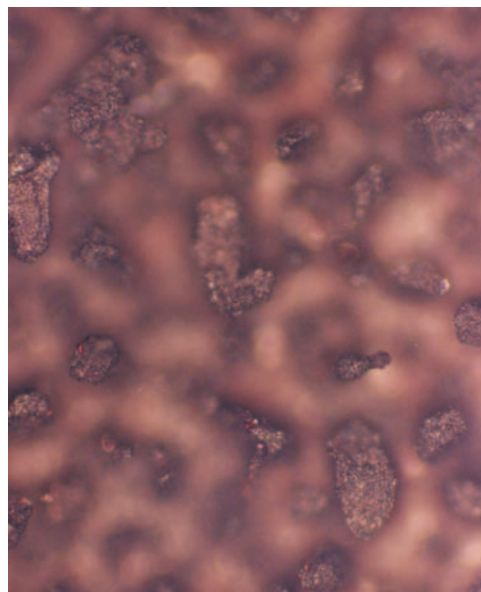


Figure 205. Substrate tip No. 1 nonfaceted material,  $\times 10$ .

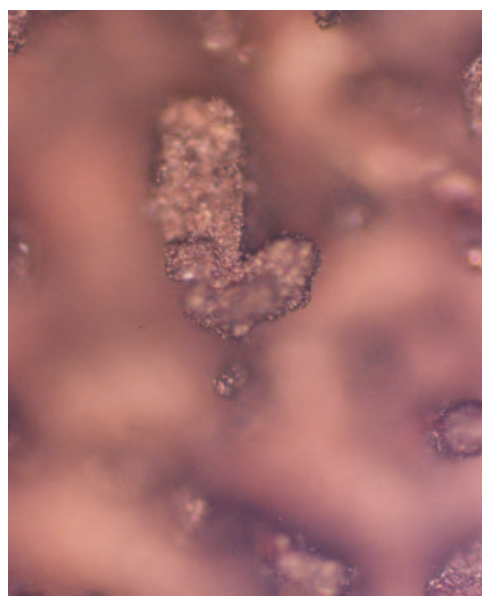


Figure 206. Substrate tip No. 1 nonfaceted material,  $\times 20$ .

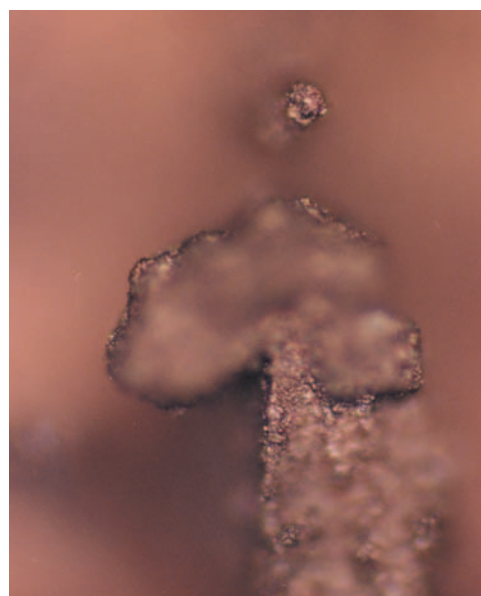


Figure 207. Substrate tip No. 1 nonfaceted material,  $\times 40$ .

Subtip No. 2 provided almost no crystalline facets (fig. 208). One depth profile shows what may be transparent diamond (figs. 209 and 210) (this photographs poorly) covered by nonfaceted material on most surfaces. Most of the deposit appears to be small contiguous clusters of ball-like growth or large very nonfaceted structures (fig. 211). Subtip No. 2 samples were run using a modified torch tip onto a Cu substrate.



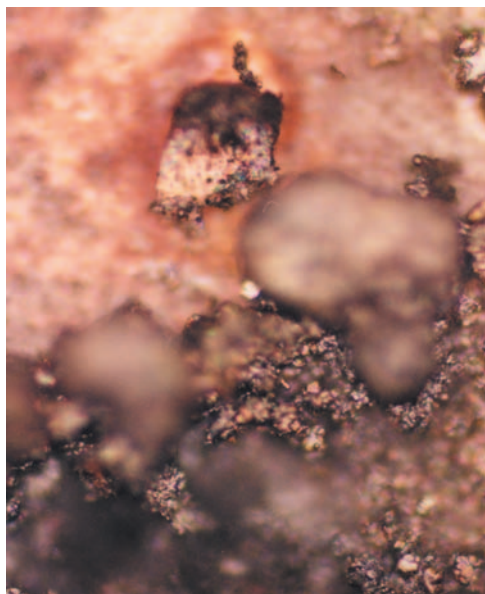


Figure 208. Substrate tip No. 2 nonfaceted material,  $\times 40$ .

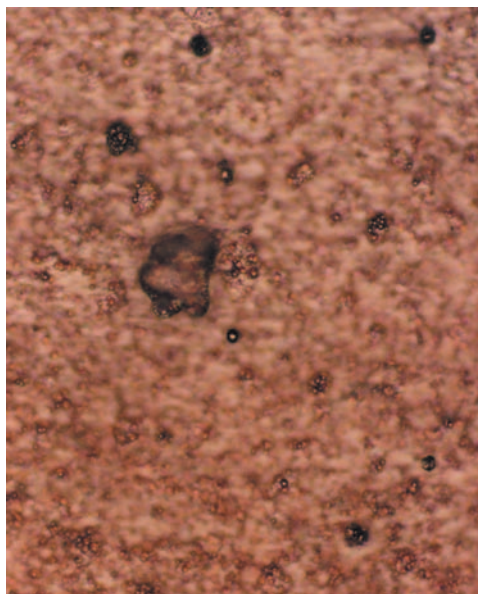


Figure 209. Substrate tip No. 2 transparent structure,  $\times 40$ .

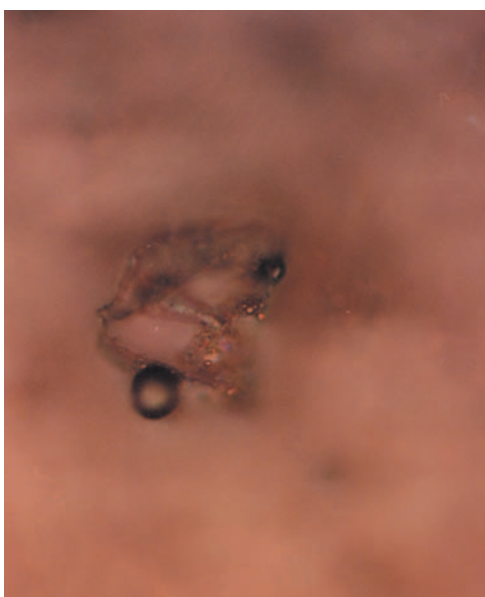


Figure 210. Substrate tip No. 2 transparent structure,  $\times 100$ .

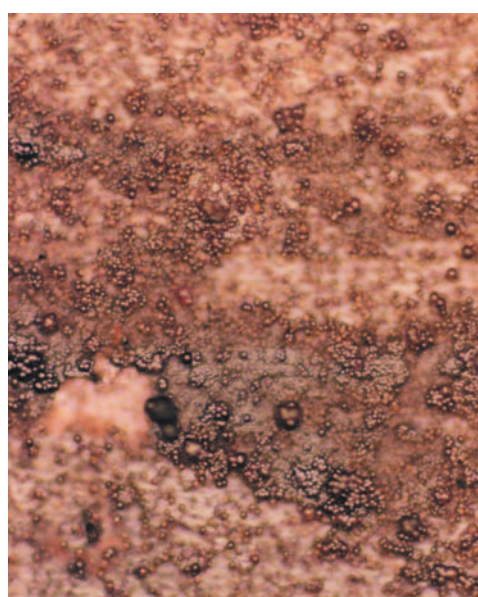


Figure 211. Substrate tip sample No. 2 ball-like growths,  $\times 40$ .

Raman results from these samples show a strong diamond peak with a weak microcrystalline diamond peak and a peak at  $1,150\text{ cm}^{-1}$  corresponding to a-C (fig. 212). There is also a small rounded peak at  $1,321\text{ cm}^{-1}$  that may be a result of hexagonal diamond or a significant number of stacking faults.

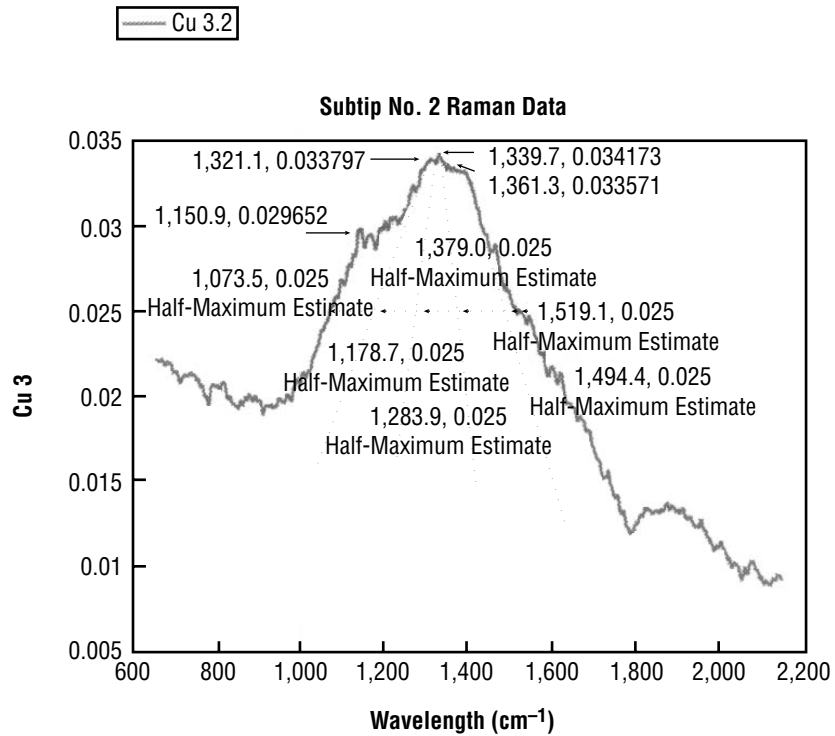


Figure 212. FTRaman results for subtip No. 2.

Subtip No. 3 results were based on a SiC substrate using an unmodified No. 1 torch tip. These samples show an island morphology, which is clearly seen in figure 213. The pillars are terminated with clean {100} facets (fig. 214).

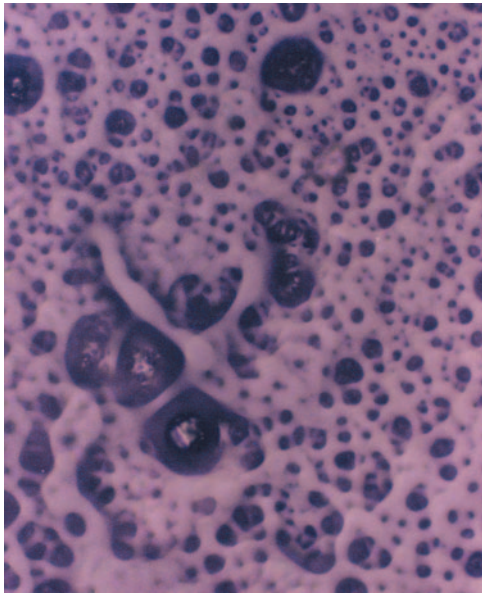


Figure 213. Substrate tip No. 3 island-like morphology,  $\times 40$ .

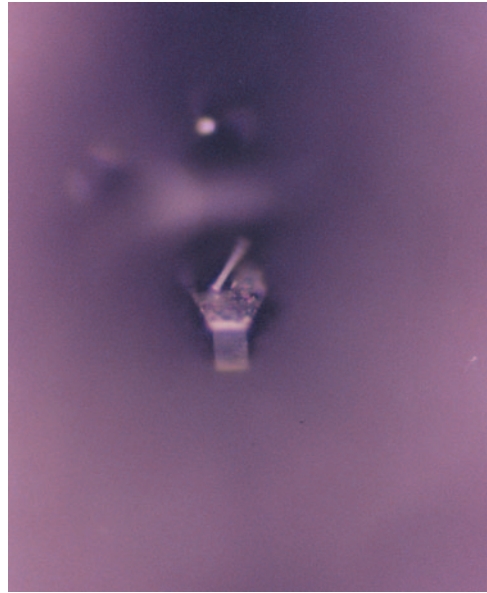


Figure 214. Substrate tip No. 3  $\langle 100 \rangle$  terminated facets,  $\times 20$ .



Raman data for subtip No. 3 samples show a very strong amorphous shoulder at  $1,180\text{ cm}^{-1}$  and a weak microcrystalline graphite peak (fig. 215).

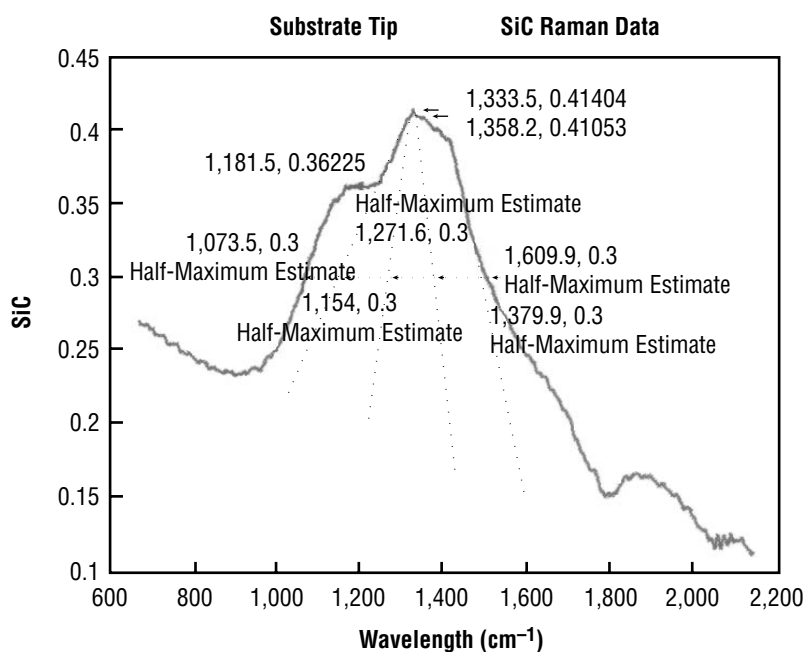


Figure 215. FT-Raman results for substrate tip No. 3.

Subtip No. 4 samples resulted from a modified torch tip, onto a SiC substrate. The results showed isolated pillars of  $\{111\}$  faceting (fig. 216). In the center, a depth profile (figs. 217 and 218) shows a column with no broadening toward the bottom. The pillar is composed of medium-sized pyramidal facets. The facets are typically covered by nonfaceted material.



Figure 216. Isolated pillars of  $\{111\}$  faceting on substrate tip No. 4,  $\times 40$ .

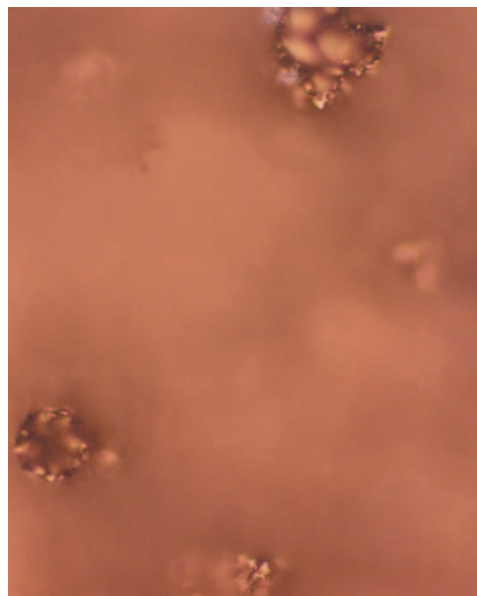


Figure 217. Substrate tip No. 4 depth profile No. 1,  $\times 40$ .

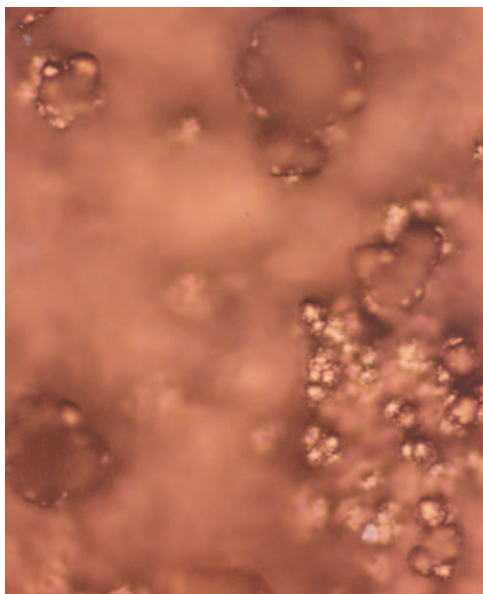


Figure 218. Substrate tip No. 4 depth profile No. 2,  $\times 40$ .

Raman data for subtip No. 4 samples show a very rounded and smooth combination of microcrystalline graphite and the diamond peak. A strong shoulder is seen near the  $1,180\text{-cm}^{-1}$  a-C peak (fig. 219).

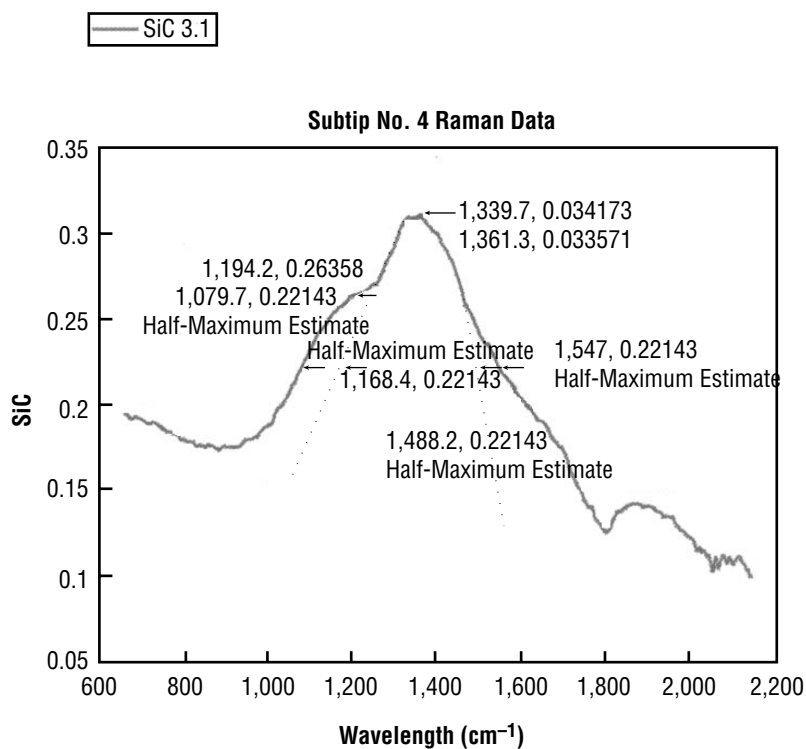


Figure 219. FTRaman results for substrate tip No. 4.

#### 4.4.2 Designed Experiment Results

For the substrate and tip modification experiment, a two-factor, full-factorial design was used. While interpreting the Raman spectra, the Raman linewidth was measured at an estimate of half-maximum peak height. The linewidth was measured on the measured peak only. Typically, this included either an occluded graphite or an occluded a-C peak or both. The adjusted Raman linewidth was a measure of the linewidth between estimated projections of the diamond peak where an attempt was made to isolate the diamond peak. For ratios of diamond to graphite and diamond to a-C, peaks near the  $1,360\text{-cm}^{-1}$  peak were used as the microcrystalline graphite peak, and peaks near the  $1,180\text{-cm}^{-1}$  a-C peak were used as the a-C peak. In most cases, the presence of an expanding shoulder was considered sufficient grounds to use the intensity measured at the expected position of the peak.

For the quality of the deposit as viewed in optical microscopy, higher rankings were given to deposits with more macroscopic faceting and higher film density. Shown in figure 220 are the graphic results from the designed experiment with optical quality as a response variable. As the carbide-forming capability of the substrate increases from left to right, so does the corresponding optical quality. The modified tip is also found to be beneficial to subjective film quality.

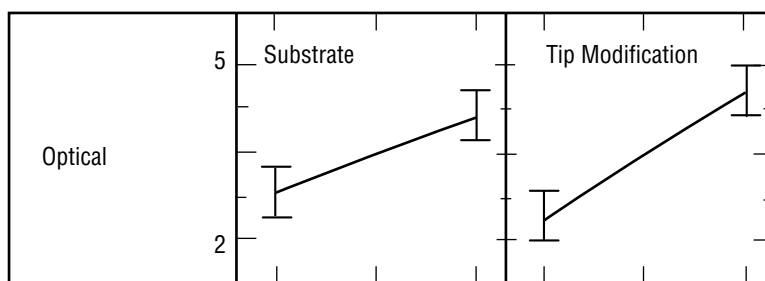


Figure 220. Tip suboptical response.

Determination of hexagonal diamond peaks is of questionable relevance in this study as no peaks were distinctly identified. The response of Raman linewidth to variations in substrate material and the modified tip are shown in figure 221. Both factors show some effect on the Raman linewidth. As the carbide capacity of the substrate increases, the width of the diamond line seems to increase as well. The width of the diamond line also increases when the change is made to the modified torch tip.

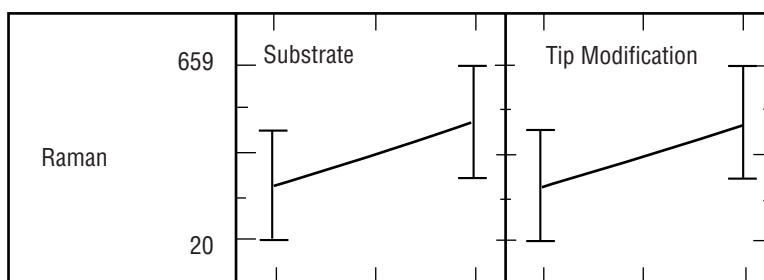


Figure 221. Tip sub-Raman linewidth response.

The response of Raman linewidth was also considered when an adjusted measurement was made. For these measurements, an attempt was made at the half maximum value to estimate the linewidth of the diamond peak without incorporating occluded peaks. These estimations are very rudimentary; however, they track the results as presented previously (fig. 221).

The two measures of relative peak height were the ratio with the microcrystalline graphite peak and the ratio with the a-C peak. The ratio of peak height is a good quantitative measure of quality because it does not depend on the laser power applied for a given sample nor does it require interpretation of the Raman counts received, as this quantity is ratioed out. The graphic results from the peak ratios correspond with the results from the linewidth measurements. In figure 222, on the diamond-to-microcrystalline graphite peak, the ratio of diamond-to-graphite is seen to decrease with an increase in carbide capacity of the substrate and with modification of the tip.

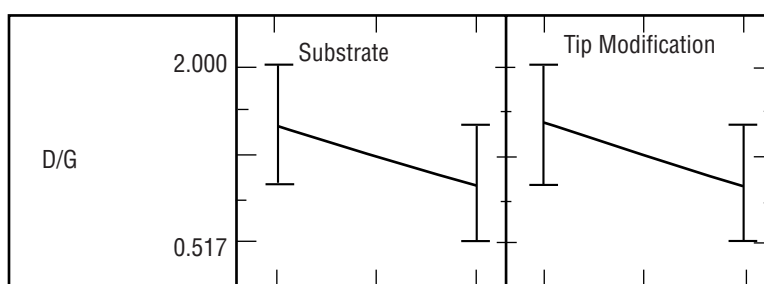


Figure 222. Tip sub-Raman linewidth comparison between diamond and graphite.

For the ratio of diamond-to-a-C peak, similar effects to the response of the diamond-to-graphite peak are seen in figure 223.

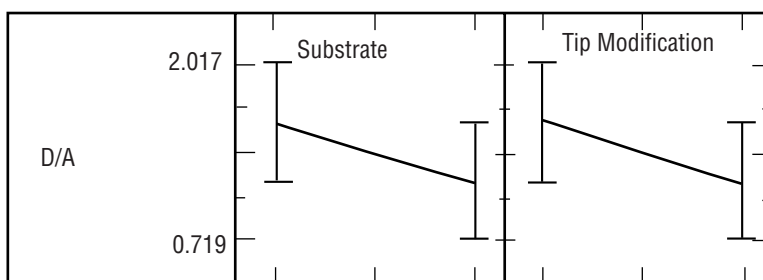


Figure 223. Tip sub-Raman linewidth comparison between diamond and a-C.

#### 4.5 High-Velocity, Oxygen Fuel Gun—Discussion of Results

The HVOF diamond jet gun was selected because of the high flame turbulence and the ability to tailor the combustion precursors to mimic the successful results in  $O_2-C_2H_2$  flames. Turbulent flames have been noted for an ability to provide higher quality diamond films with correspondingly lower growth rates in comparison to their laminar counterparts.<sup>81,82</sup>

### 4.5.1 Carbon Monoxide Gas Addition Results

Clearly in the gas phase experiments, even if the temperatures could be maintained at an appropriate level for stable diamond growth, the flow rates of CO required are economically prohibitive. The use of the HVOF deposition system with strictly gas-phase initial constituents will probably require the use of  $C_2H_2$  as the fuel gas. Currently, federal regulation does not provide for convenient examination of this processing route.

### 4.5.2 Addition of Liquid Toluene Results

The addition of  $C_7H_8$  to the flame was attempted in order to achieve the appropriate CHO flame species ratio for embryonic nucleation and eventual film growth within the flame. The two experiments, described in a previous section, provided optical and scanning electron microscope (SEM) micrographs of the resulting films. The micrographs did not reveal any diamond or diamond-like material. Raman spectra were obtained from all of the samples and the results are tabulated in the following paragraphs.

Our spectra investigated primarily the region between 500 and 2,000  $cm^{-1}$  wave numbers. Several of the known Mo-C-O vibrations are below this in the 400–500  $cm^{-1}$  wave number region. Considering oxide formation, several references appear to be of value. Reference 279 displays vibrational modes at 318, 841, and 894  $cm^{-1}$  for  $(MoO_4)_2$ , but the best display for interpretation of our spectra appears to be in reference 280, which provides a picture of active Raman at  $\approx 904\text{--}907\text{ }cm^{-1}$  {v1} for this compound. Additionally, solid-state  $MoO_2$  ( $S_2CNMe_2$ )<sub>2</sub> has IR peaks at 908 and 873  $cm^{-1}$ .

Looking at carbonate complexes, a variation of molybdenum carbonate  $Mo(CO)$  indicates that our consistent peak at 726–743  $cm^{-1}$  may be related to Trans  $[Mo(CO)_4(P(OMe)_3)_2]$ , which is listed as having a Raman peak at 740  $cm^{-1}$ .<sup>279</sup>  $Mo(CO)_{6-n}L_n$  ( $n=1,2$ ) displays bands near 650  $cm^{-1}$ ,<sup>279</sup> a variation of which may be related to the 663–664 peak shown in the nongraphite samples.

For pure C deposition, only sample Nos. 2 and 3 displayed unambiguous peaks. Specifically, graphite displays a well-known pair of peaks at 1,341 and 1,601  $cm^{-1}$ . Using the higher  $C_7H_8$  flow experiment as the only one from which interpretation is relevant, the distance to the substrate appears to have a stronger effect than the effect of additional  $C_7H_8$ . This is shown in the factor-response graphs from the designed experiment (fig. 224). The importance of tip substrate distance correlates well with traditional  $O_2$ - $C_2H_2$  torch work where the interaction between the flame feather and the substrate is critical.

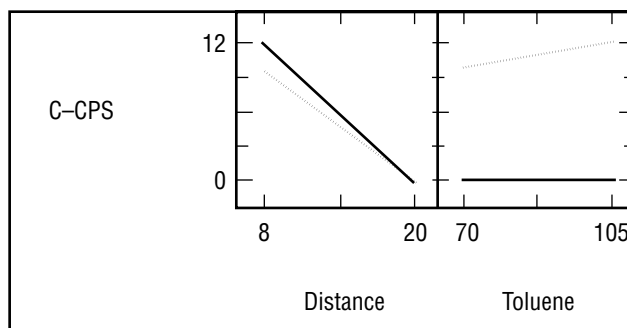


Figure 224. Designed experiment for addition of toluene.

### 4.5.3 Two-Dimensional Kinetics Simulation Results

The TDK results presented are necessarily independent of tip-to-substrate distance (table 10). The results are useful since they provide a good general picture of the combustion environment. Our results are indicative of species present at the exit plane of a nozzle following combustion in the combustion chamber using the constituents present in our prior flame experiments. The most notable result of the simulation is the correlation between the addition of  $C_7H_8$  and the flame temperature. As the  $C_7H_8$  level is increased, the flame temperature increases and the moles of  $H_2$  increase. These effects would be thought to counterbalance each other with respect to diamond growth. Additionally, as the  $C_7H_8$  is increased, the CO percentage appears to pass through a maximum, while the production of graphite disappears completely. Also, there is no discernible  $C_2$  or CH as discussed by Matsui et al.<sup>74</sup> who correlate this with the growth rate in the feather or growth region of  $O_2$ - $C_2H_2$  torch flames.

Table 10. TDK results for  $C_7H_8$  addition.

$C_7H_8$ Level (mL/min)	Temperature (°R)	Moles of C(Gr)	Moles of $C_2H_2$	Moles of $CH_4$	Moles of CO	Moles of H
35	2,757	0.28636	6.0000e-6	0.000512	0.30965	1.4000e-5
70	4,290	—	—	—	0.58838	0.0089920
105	5,570	—	—	—	0.47474	0.078714



## 5. DISCUSSION

In starting a discussion of this work, a preface is required of previous studies that have examined the nucleation of diamond. Following this review, the mechanism for nucleation of  $O_2-C_2H_2$  torch diamond, the principal result of this work, will be presented. Each experiment will then be reviewed in comparison to the literature, and the relevance of the experiment to the nucleation mechanisms will be discussed. Finally, brief examples addressing the proposed mechanism will be drawn from the literature.

### 5.1 Previous Work on the Low-Pressure Nucleation of Diamond

#### 5.1.1 Diamond Nucleation on Surfaces

By far, most of the nucleation studies on diamond films have either presented evidence for nucleation on the surface or performed their nucleation studies starting from that premise. Although any nucleation mechanism for diamond ideally would encompass all of the deposition techniques, it is not yet clear as to whether this is appropriate or not.

In review and analysis of my experimental data, I have found that much of the work on microwave-plasma deposition and the high-rate diamond deposition methods of dc plasma-jet and combustion synthesis appear to behave in a substantially similar manner. The hot filament method of production, because of the thermal equilibrium production of activated gas species and the frequent use of a heated substrate, may well nucleate diamond via a different mechanism. In fact, I have found much of the conflicting data in the literature arise between hot filament and other systems. I will separate the discussion of prior work into a section for hot filament work and a general section. Although my work is strictly relevant for  $O_2-C_2H_2$  torch production, the most comprehensive nucleation work was performed on the hot filament method of diamond nucleation and growth, and a review is appropriate.

#### 5.1.2 Hot Filament Surface Nucleation Work

Hyer et al.<sup>281</sup> present one of several studies that find that crystallites in hot filament systems are deposited predominantly along the scratch marks. Their results find that nucleation is almost instantaneous and new nuclei cease appearing after 30 to 60 min. They remark that it is interesting to note that the nucleation process terminates with a significant area of the substrate still unnucleated. This result is explained well by using a starvation mechanism that depletes the surface of species used to form nuclei in the process of growth.

Kim et al.<sup>282</sup> present an effect of reaction pressure on the nucleation behavior that they are able to adapt to produce diamond films on Si substrates without the use of scratches. They find that at low pressures, higher nucleation densities are observed. They relate their results convincingly to a higher nucleation of SiC sites at lower pressures.

Jackman et al.<sup>28</sup> present a different picture of diamond nucleation based on H-driven addition of hydrogenated forms. Using a hot filament system, they investigate the interaction of activated CH<sub>4</sub>/H<sub>2</sub> mixtures with a Si {100} surface. They provide experimental evidence which they interpret as showing that the surface is initially host to both C<sub>2</sub>H<sub>2</sub> and ethylene (C<sub>2</sub>H<sub>4</sub>) species, with H<sub>2</sub> abstraction converting the C<sub>2</sub>H<sub>4</sub> to C<sub>2</sub>H<sub>2</sub> thereafter. This suggests that H<sub>2</sub> only arises from the decomposition of C<sub>2</sub>H<sub>2</sub> and other organic fragments on the surface and not from reaction with the hot filament.<sup>28</sup>

Singh<sup>35,36</sup> is the primary developer of a theory of hot filament diamond nucleation that is based on the renucleation of C directly into diamond. Singh and Vellaikal<sup>35</sup> grew diamond directly on Cu TEM grids. High-resolution TEM images revealed an amorphous layer supporting the diamond crystals. Based on these results, they suggest that the bombardment of H<sub>2</sub> converts sp<sup>2</sup> bonding to sp<sup>3</sup> bonding; and following this, a rearrangement will occur to lower the H<sub>2</sub>-stabilized surface energy. This results in the formation of the diamond crystal structure.

Excellent models of nucleation have been presented by several laboratories in Italy, notably the Universita di Roma and the Istituto di Metodologie Avanzate Inorganiche. Tomellini et al.<sup>283</sup> present a model for describing nucleation of diamond in CVD processes. They assume nucleation at a surface defect based on thermodynamic or structural arguments. In their treatment, no assumptions are made on the structure or composition of the germs or the nuclei. The difference between nuclei and germs is the ability of a germ to desorb while a nucleus must grow. They produce a system of three differential equations that give an account of the nucleation centers, germs, and nuclei for the evolution in time. The model requires formation of germs as intermediates. This seems appropriate to account for generation of germs in the gas phase. Germs grow to the nuclei phase on the surface in accordance with a probability determined by the growth conditions. In a related paper on nucleation, Polini<sup>284</sup> notes that the occurrence of edges is a necessary but inadequate condition for nucleation. He interprets his results to indicate that particular atomic arrangements are required for the diamond nucleus formation.

A series of papers by Molinari et al.<sup>285,286</sup> follows the results of Tomellini's work with experimental determination and kinetic analysis of the surface density of active nucleation sites, germs, and nuclei. They then provide a molecular model based on their kinetic analysis. One important requirement of Tomellini's work is the predicted presence of a flex point in the shape of surface density of nuclei  $N(t)$ .

Molinari et al. use a distribution function of the particle size, which in turn requires a function describing the growth of a single nucleus to calculate the nucleation rate in the limit of low surface coverage. Analysis of data, in conjunction with the formation of germs from active sites and the growth of nuclei from germs, is well handled by their interpretation modified to incorporate the creation of centers. These centers are created when two germs link through propagation of acetelynic growth. Although the model is well thought out, this paper makes a number of suggestions as to methods of improving the accuracy of the calculations. Relevant at this point might be the suggestion of a different reactivity of the C species desorbed. Instead, a suggestion might be to use a more reactive site activator such as C<sub>2</sub>H. They also mention that they must assume a 1:1 ratio of nuclei to observed nuclei in the SEM photographs for their calculations to be valid.

Further analysis of the dependence of the long-term observed nucleation density<sup>286</sup> requires the use of a cutoff criteria where only nucleation centers with heats of desorption larger than that applied by the

surface temperature and gas composition conditions will be created. They also mention indications in their data of a surface phase forming that cannot be accounted for within their current model. An intermediate phase is formed as a two-dimensional phase rather than as a fully stable SiC. They discuss at length the effects of their use of diamond polishing pretreatment of their samples.<sup>285</sup> They note that if seeding by a polishing mechanism is important, the final number of nucleation sites observed should not vary with temperature or pressure; however, these sites actually do vary with temperature and pressure. Furthermore, they do not notice a bimodal distribution of sizes corresponding to some seeds and some conventional nucleation. Their position would be significantly strengthened by experimental data that did not start from seeded samples.

The study by Tomellini and the papers by Molinari are complemented by a model developed by Ascarelli and Fontana.<sup>287</sup> They note that the nucleation kinetics observed depict the nucleation rate as reaching a maximum and then tapering to zero for longer deposition times. A total number of activated nucleation surface sites and a temperature-dependent incubation time, related to the time to form critical diamond nuclei, are required to support this observation. They present a model and a discussion of transient nucleation time. Most relevant is that their incubation time is temperature dependent and largely a function of the misfit strain energy between the substrate surface and the diamond nuclei.

### 5.1.3 Torch and General Nucleation Studies

An early look at the nucleation of low-pressure diamond is presented by Spitsyn<sup>135</sup> where he considers nucleation of metastable phases from the vapor. Diamond is metastable at any temperature when the pressures are  $<13,800 \text{ kg cm}^{-2}$ . The free energy difference between diamond and graphite varies between 0.564 kcal/mole at 0 K to 2.5 kcal/mole at 2,000 K. Spitsyn notes that single C atoms do not represent suitable building blocks for diamond because the C atom, in its ground state, is divalent. He also notes that molecules of C containing compounds with more than four to five C atoms are unsuitable for defect-free growth of diamond.

Kikuchi et al.<sup>174</sup> separate growth conditions into conditions where nucleation is preferred to growth and conditions where growth is preferred to nucleation. In cases where nucleation is preferred, they note that they believe the larger nondiamond C peak that is observed in the Raman spectra is predominantly material between grains and not part of the nuclei that have grown.

Turner et al.<sup>241</sup> investigate microwave plasma films using Raman spectroscopy and scanning tunneling microscopy. They provide a picture of nucleation that occurs along the scratches in their substrate. They note a roughening of the surface between their 60-min and 30-min depositions; however, within these timeframes, complete films of diamond were not produced. Ohl et al.,<sup>288</sup> in a well-controlled examination of the effect of  $\text{H}_2$  on nucleation, note that while crystal size may be linked to H concentration, measured nucleation density was independent of  $\text{H}_2$  concentration. They interpret this by complete control of nucleation by pretreatment-induced nucleation sites. Rankin et al.<sup>289</sup> note that better diamond grows on the oxide surfaces in conjunction with higher gas flow rates. They interpret this as an indication of the surface altering the plasma near the growth surface primarily by  $\text{H}_2$  recombination.

#### 5.1.4 Surface-Stable Nuclei Using Substrate Pretreatment

A significant amount of study relevant to nucleation has focused on the ability to direct and control nucleation by substrate pretreatment. Substrate pretreatment can be considered either the activation of surface sites for surface nucleation or the activation of the surface to promote surface attachment and survival of diamond nuclei germs formed in the gas phase.

Much controversy continues on the actual effect on nucleation of diamond prescratching of surfaces. A provocative experiment was performed<sup>7</sup> where a wafer was polished along a strip in an east/west direction with diamond powder. Following that polish, it was repolished along a perpendicular strip in a north/south direction with cubic boron nitride (BN). The nucleation density was found to strongly follow the diamond polishing and not the BN. Although it might seem that this experiment provided strong evidence of diamond nucleation sites, there are still significant questions, some of which are discussed in the following paragraphs.

Ma et al.,<sup>290</sup> relatively early, demonstrated excellent control of stable diamond nuclei using a combination of pretreatment strategies. They placed silicon dioxide ( $\text{SiO}_2$ ) dots on a Si substrate and then diamond polished the entire surface. This treatment was not enough to achieve selective growth; however, following the polish, the surface was subsequently irradiated with an oblique Ar beam, producing an edge effect and excellent nuclei stabilization. In interpreting the success of the Ar beam in selectively placing nuclei, they attribute the lack of nucleation on the Si or silica surface as the result of amorphitization of the surface.

In a related study, they found that the first stable nuclei are observed on the edge of the silica dot away from the Ar radiation. Their interpretation is contrasted by the high-resolution electron microscopy (HREM) data of Jiang et al.<sup>291</sup> where they present convincing HREM images of diamond that have formed predominantly on an amorphous layer between Si and the diamond overgrowth. Jiang also paradoxically shows diamond growing on Si nonamorphous surfaces and they present reasonable evidence of diamond formation based on SiC crystallites formed in the amorphous intermediate layer. Maeda et al.<sup>292</sup> have provided work on the role of abrasion provided by an extensive array of nonoxide ceramic particles. They found that specifically MoB, lanthanum boron-6 ( $\text{LaB}_6$ ), and tantalum diboride ( $\text{TaB}_2$ ) provided the largest nuclei stabilization within the decreasing order of diamond population, borides > carbides > nitrides > silicides.

Itoh et al.<sup>293</sup> compared the traditional technique of diamond polishing with the additional treatment of microflawing the substrate in an ultrasonic bath using diamond of various particle sizes suspended in ethanol. In a study on cemented carbide substrates, they found that the density of stable nuclei increased with the decreasing grain size of microflawing of the diamond powder. The grain size of their samples decreased with microflawing time. Je and Lee<sup>169</sup> compared vibration in SiC medium with diamond polishing and ultrasonic agitation in a diamond/acetone suspension. They also found more stable nuclei present using ultrasonic agitation.

Bauer et al.<sup>294</sup> consider the nucleation behavior of untreated substrates contrasted with substrates that were diamond-polished, SiC-scratched,  $\text{Al}_2\text{O}_3$ -scratched, graphite-wiped, and spin-coated with PMMA. Only diamond polishing was shown to have a substantial effect on the stable nuclei density. They infer a

short burst of nucleation followed by growth without any nucleation. The most striking results from their study are their lack of a nucleation incubation time and the consistency of diamond nucleation. Even on the diamond-polished samples, which show increased nuclei stability, their nucleation rarely corresponded with the scratches from the diamond polishing on the surface. They also note that no Ostwald ripening occurred between small crystals and growing larger crystals. Boundaries between growing crystallites show no indication of motion or grain size changes as the films develop. Their nucleation calculations are based on Volmer's model of homogeneous nucleation. For their data, they assume heterogeneous nucleation on the Si and no deviations in the surface on which nuclei are measured. They note that the growth of their diamond crystallites extrapolates to zero size at zero time, providing no incubation time within the experimental error for nucleation.

Substrate biasing has been shown to have a beneficial effect on the density of plasma-grown films. Stoner et al.<sup>295</sup> used this effect in an in situ study of diamond growth. They note here the deposition of a surface C layer resulting from the pretreatment. Yugo et al.<sup>296</sup> present a nucleation mechanism based on their data of negative biasing of substrates in a microwave plasma. They maintain that the negative bias collects C ions on the surface and into a subsurface layer more rapidly than if a negative bias is not present. The model also considers that the sp<sup>3</sup> bond form will be more stable under the surface bombardment of energetic ions, leading to a greater number of sp<sup>3</sup>-bonded C-cluster diamond precursors on the surface. Jiang et al.<sup>297</sup> performed a study on the crystals formed using substrate bias by employing the atomic force microscope and the SEM.

A study by George et al.<sup>245</sup> also used AFM to directly study nucleation; however, they predominantly presented geometric data that they noted with a strong influence by tip convolution effects. Work by Jiang et al.<sup>297</sup> was also plagued by tip convolution; however, they used the AFM data only for nuclei height determinations and then used the data from the SEM to follow the kinetics proposed by Tomellini et al. They found that with a careful determination of coefficients they reproduced the flex point experimentally and computationally, indicating that the active site-germs-nuclei sequence may be applicable for the bias-enhanced nucleation conditions. The primary focus of their work was an examination of nearest neighbor distance and improvements on surface diffusion, which they measured from an enlargement of nearest neighbor distance. They recognized the possible influence of a high C supersaturation at the surface because of the bias conditions.<sup>297</sup>

No studies have been performed to separate the effect of substrate bias with the effect of the initial C layer put down in these pretreatments. However, a number of studies have shown the beneficial effects on nucleation density of initial use of a high supersaturation level, or an initial above-average amount of hydrocarbon. For example, Mitsuda et al.<sup>298</sup> find that a 5-min supersaturation, followed by a change in parameters to those encouraging traditional growth, provides an increase in the number of stable nuclei. They mention that as of their paper, the nucleation site had not yet been identified, but the a-C deposited in their early supersaturation step might play the role of a nucleation site when a sufficient size had been reached. Menningen et al.<sup>299</sup> consider substantially the same pretreatment method using either CH<sub>4</sub> or C<sub>2</sub>H<sub>2</sub> as the pretreatment high-supersaturation gas; however, they conduct their work in a hot-filament system. They note no beneficial effect of a higher initial supersaturation for either CH<sub>4</sub> or C<sub>2</sub>H<sub>2</sub>. Principally, they relate the effects of a higher supersaturation in a hot-filament system to poisoning of the W filament surface by C saturation.

Supersaturation has also been used in  $O_2$ - $C_2H_2$  torch systems by Von Windheim et al.<sup>300</sup> who performed nucleation studies using the pretreatment method of an initially high hydrocarbon-torch pretreatment as described by Tseng et al.<sup>94</sup> or Ravi et al.<sup>83</sup> In their nucleation experiments, they first ultrasonically cleaned the substrates with diamond suspension and used a number of pretreatment strategies. They show improved diamond film coverage for the pretreated samples with complete disk-like coverage deposition areas as opposed to annular ring deposition areas for the control samples. They interpret their work primarily based on previous studies where silica was used to mask certain areas from diamond growth. An oxide forms during their nucleation experiments, and the precursor for diamond nucleation competes with  $O_2$  on the Si surface in the early stages of deposition.

### 5.1.5 Flame Chemistry and Relevant Torch Work

Little work has been done for the addition of gases into a diamond-producing  $O_2$ - $C_2H_2$  torch and the effect on flame chemistry (and none on the effect of nucleation environment). Several books and journals are devoted to the study of flames; however, incorporated here are references appropriate to my work. Oakes et al.<sup>89</sup> at the NRL studied the effects of  $H_2$  additions to an  $O_2$ - $C_2H_2$  flame, and Matsui et al.<sup>74,301</sup> have investigated the structure of flames for diamond deposition and compared diamond growth in  $C_3H_8$  flames to that present in  $C_2H_2$  flames.

Oakes et al.<sup>89</sup> added  $H_2$  to the flame and substituted  $H_2$  for  $C_2H_2$  in their flames. They interpreted their results based upon the intensity difference between the diamond peak and the a-C peak. High-quality diamond was noted upon the addition of  $H_2$  and attributed to a higher etching rate of nondiamond C. They also note that the increase in  $H_2$  may perturb the gaseous composition of the flame feather, adding heat capacity to the flame or consuming  $H_2$  by  $O_2$ , thus reducing the flame temperature.<sup>89</sup> In the  $H_2$  substitution experiments, they produced only nondiamond C and they attribute this to an unacceptable ratio of C to  $H_2$  and  $O_2$  in a previously reported no-growth region. My calculations of their ratios put them into a no-growth region of the Bachmann diagram as well.

Matsui et al.<sup>74,301</sup> provide a structural look at flames used for diamond deposition. Using laser fluorescence and mass spectrometry, they provide experimental determinations of radical species present in the flame. They provide their results based on  $R$ . Experimentally, they grew their diamond at an  $R$  value between 1 and 1.2. The etching reaction was so fast in the intermediate and outer zones that the diamond crystals of some micrometers disappeared within a few minutes. They focus their attention on  $C_2$  and  $C_3$  concentrations in the flame and flame feather, and with the fluorescence, they provide axial concentration profiles for  $C_2$ .<sup>74</sup> These results are qualitatively supported by data from their SIT camera experiments.<sup>301</sup> They conclude that the  $C_2H_2$  flame for diamond growth consists of a C radical-rich feather and an  $O_2$  radical-rich intermediate zone. Their mass spectrometric measurements support the qualitative measurements, but quantitative analysis was not carried out for the species of most relevance to this work; i.e., the higher hydrocarbons. They specifically note, however, that higher hydrocarbons are detected in the feather but disappear in the intermediate zone.<sup>74</sup> They also note that for other fuels where the flame temperature is not so high, the C radicals are replaced by C particles.

Miller et al.<sup>302</sup> note, in a treatise on combustion modeling, the higher heat of formation required for  $C_2H$  in fuel-rich, high-temperature  $C_2H_2$  flames. In the simulation results presented in this work, the enthalpy of the gas mixture and the  $C_2H$  track each other quite well.



### 5.1.6 Gas-Phase Nucleation Work

It is difficult to pinpoint the first mention of gas-phase nucleation of diamond; however, the notion has been recorded several times in the early 1980's through the present literature. Gas-phase nucleation has been observed in conventional materials such as Si in conventional reactor systems.<sup>303</sup> Much of the serious investigation of gas-phase nucleation of diamond was spurred by related work on diamonds in the interstellar medium, most recently the work by Allamandola et al.<sup>304</sup>

Matsumoto and Matsui,<sup>178</sup> in looking at the development of twins composed of 2, 5, and 20 single crystal units, have suggested adamantane as an unstable cage-type precursor for diamond embryo nucleation, taking advantage of H<sub>2</sub> stabilization. The embryos already have structures that lead to the formation of the twins during growth. They suggest that diamond nucleates in the gas phase or the nuclei are probably hydrocarbons that have weak interactions with the Si surface before degradation of the CH.<sup>178</sup>

Mitura<sup>305</sup> presents another very early look at the possibility of diamond nucleation not only on the surface but also in the gas phase. He grows films on a Si surface using an rf electrode. As the pressure increases in his deposition system, noncohesive diamond spherical agglomerates are noted on the surface. These spherical agglomerates, he proposes, are nucleated in the gas phase and remain in the plasma until the effects of gravity bring them onto the substrate.<sup>305</sup> Using the rationale proposed by Feedosev, they consider that a diamond phase of several nanometers in size may be due to the Laplace pressure inside such a small structure. This pressure can attain the level of several gigapascals. Angus and Hayman<sup>306</sup> mention similar work on the occurrence of gas-phase nucleation.

Some of the strongest supporting work for diamond nucleation in the gas phase is a result of evidence from Nuth.<sup>307</sup> He proposes a stability reversal between diamond and graphite relative to particle size, where at very small particle sizes, diamond becomes the stable phase of C and is correspondingly preferred over graphite. This argument is predicated on differences between the molar volume for diamond and the molar volume for graphite. Because of the larger number of less dense graphite particles occupied in one mole of C when compared to the smaller number of diamond particles for the same mole of C, the surface diamond will be the stable form of C. This can most easily be seen in the following calculation from Nuth, in which he assumes equilibrium at some size between diamond and graphite, and proceeds to find the required surface energy for which the assumption is valid:

$$(\text{area} \times \text{surface energy})_{\text{diamond}} + G_{\text{diamond}} = (\text{area} \times \text{surface energy})_{\text{graphite}} \quad (66)$$

The determination of stability, directly based on the surface free energy, is difficult to test because the values for the surface free energy of diamond and graphite are at this time unreliable. The calculation of Nuth is based on a similarity of surface free energy of diamond and graphite based on the assumption of a  $\pi$ -bonded C layer surface for diamond. The above calculation allows for the preferred stability of diamond even if the surface free energy of diamond is slightly higher than that of graphite.<sup>307</sup>

In a related paper, Nuth<sup>308</sup> again holds diamond to be more stable at small particle sizes <50. Given that the surface free energy values numerically contain a large uncertainty, he performs a calculation wherein he shows that because of the larger number of less dense graphite particles needed to contain one mole of C, the surface free energy of diamond does not actually need to be smaller than that of graphite for diamond

to be more stable. He notes that it can be larger because of the difference in density and the quantity of surface per molecule.

In an approach with similar results, Badzig et al.<sup>309</sup> provide a theoretical H-to-C (H/C) ratio for the stability crossover between diamond and graphite. Their results are based on calculated heats of formation of various C cluster sizes where specific energies were assigned to the C-H and C-C<sub>tetrahedral</sub> bonds used in creation of the clusters. Predictably, they arrived at two bands of values, tetrahedral molecules and hexagonal molecules. Small tetrahedral molecules were shown to be more stable than small hexagonal molecules until a specific crossover value of H/C (surface terminating H<sub>2</sub> atoms/tetrahedral or hexagonal C atoms). When the H/C is plotted against the binding energy, the sp<sup>3</sup> (tetrahedral) molecules have a negative slope and the sp<sup>2</sup> (hexagonal) molecules have a slope near zero. They performed particle size calculations based on their calculated critical H/C. The calculations gave a critical particle size of  $\approx 3$  nm where the tetrahedral and hexagonal structures are of equal heats of formation (i.e., where diamond and graphite particles of equal size are equally stable). This work assumes additional relevance in light of soot-particle production in flames, on which the literature is voluminous.

Frenklach et al.<sup>310</sup> present evidence for homogeneous nucleation of diamond powder in the gas phase in a microwave plasma reactor. In their experiments, diamond was nucleated in the plasma and collected downstream on filter paper. The diamonds were nucleated in dichloroethylene or dichloromethane O<sub>2</sub> flames, typically a blue conical flame. They noted the formation of cubic diamond, lonsdalite, and 6H-hexagonal diamond.

Buerki and Leutwyler<sup>311</sup> also demonstrate gas-phase nucleation of diamond using laser-driven gas-phase reactions. They produced diamond using a primary C source of C<sub>2</sub>H<sub>4</sub>, both with and without the addition of gas-phase H<sub>2</sub>. They did not attempt to concentrate the diamond and no oxidation steps to remove nondiamond C were performed. They determined that the formation of the diamond phase is critically dependent on the residence time in the reaction flame.<sup>311</sup> However, they could not completely separate time effects due to a temperature dependence from the residence.

In a later paper by Howard et al.,<sup>312</sup> the same group as in Frenklach's paper<sup>310</sup> presents work on synthesis of diamond powder in O<sub>2</sub>-C<sub>2</sub>H<sub>2</sub> microwave plasma. They obtained diamond over a limited range of composition and pressure. As suggested in work by Cappelli and Paul,<sup>76</sup> they found that diamond phases were formed over narrower ranges in premixed flames than in diffusion flames. Their ratios for diamond formation of O<sub>2</sub> to C<sub>2</sub>H<sub>2</sub> were similar to that of Hanssen et al.,<sup>68</sup> i.e.,  $0.83 \geq C/O \geq 1$ , and of the diamonds produced in this study. However, they also noted diamond formation in diffusion flames with ratios as low as  $C/O \geq 0.22$ . As in previous work, their diamonds were a mixture of cubic and hexagonal polytypes. Their Raman signatures are very similar to several produced in this work, with special reference to the shape of the 1,332-cm<sup>-1</sup> diamond peak. They confirm that particle size is primarily determined by the reaction time.

## 5.2 Outline of the Proposed Mechanism for Nucleation of Diamond

With consideration of the previous work in mind, data presented by the series of several experiments discussed below has suggested a mechanism for the nucleation of diamond. The nucleation mechanism I propose builds on the work of previous researchers, specifically those suggesting gas-phase nucleation, but presents an approach to nucleation in a detail and direction not fully presented before.

Diamond produced using an  $O_2$ - $C_2H_2$  torch on the surface of any number of substrates is the result of germ or embryo formation in the gas phase. Germs and nuclei are, by definition, pseudo stable. The formation of germs is not complex. Traditional, although not equilibrium, thermodynamics and kinetics are appropriate for the description of formation. Transition of germs or embryos into stable surface nuclei is affected by a variety of concurrent phenomena. However, the crucial contribution of this work is identification of the gas phase as the controlling environment for the initial formation steps leading to nucleation.

Identification of the structures formed in the gas phase as germs is perhaps slightly misleading. A traditional explanation of germ formation to nuclei formation to growth of nuclei assumes a spatial location with a consistent environment. The  $O_2$ - $C_2H_2$  torch system presents a path through a series of environments through which hydrocarbon-precursor species pass.

A very traditional nucleation and growth scenario would describe the behavior in the nucleation region under nucleation conditions in the gas phase. However, motion of the species from this environment into spatial regions (gas and surface) with alternate conditions rapidly places previously formed nuclei into a position where continued growth or survival may be unlikely. Because of the transient nature of diamond nuclei stability, I have elected to use the nomenclature of germs to describe the initial precursors to stable diamond nuclei. This is considered because, although under formation conditions the diamond formed may be stable nuclei, they must also pass through additional gas-phase conditions and additional surface stability conditions before they are capable of growth. Only nuclei that may no longer regress (or progress) into alternate forms may be awarded the status of nuclei. A brief stepwise progression of the mechanism path is presented as follows:

1. Gas-phase nucleation/stabilization of the diamond phase
2. Possible regression of nuclei to germ stage due to—
  - a. Downstream gas environment
  - b. Surface stability environment
3. Accommodation with surface resulting in—
  - a. Stable diamond nuclei
    1. Rearrange epitaxially with surface
    2. Create new nucleation sites
  - b. Unstable diamond germs that—
    1. Grow to diamond
    2. Do not form diamond.

Although it was not a focus of this work to identify the species responsible for nucleation or growth, simulation results suggest that  $C_2H$  may be the species initially responsible for nucleation. Relevance of this mechanism to other types of diamond synthesis will also be discussed; but of necessity, there is no experimental substantiation within the scope of this work.

### 5.3 Discussion of Experimental Conditions Similar to GAMoly

A reasonable number of studies have been performed using the addition of various process gases into diamond deposition systems (ref. 18). There are even more studies concerned with optimizing the existing process gases but they are not particularly relevant in discussing this work. Certainly, other than the addition of alternate species for the modification of chemical constituents, no studies have used the addition of process gases to significantly modify the gas-phase environment.

#### 5.3.1 Carbon Monoxide as a Process Gas

Carbon monoxide has only been reported as a process gas for microwave-plasma deposition systems. In microwave systems, CO has been used successfully as the source gas for C in the production of diamond.<sup>21,26,313–316</sup> In microwave systems with H<sub>2</sub>, CO has been noted to provide twice the growth rate as the traditional CH<sub>4</sub> and H<sub>2</sub> system<sup>316</sup> and, in very early work, improved deposition rates for diamond were related to the formation of CO and CO<sub>2</sub>.<sup>21</sup>

Muranaka et al.<sup>313</sup> investigated the CO/He/H<sub>2</sub> system by adding various amounts of H<sub>2</sub>. Their optical emission results indicated that H in the ground state suppresses the formation of C and C<sub>2</sub> in the gas, yielding higher concentrations of CH<sub>x</sub>. Most importantly, they suggest that pathways for diamond growth occur both in the gas phase and through surface reactions. In both cases, they approach this result from the elimination of C and C<sub>2</sub>. The same authors, in a following related paper,<sup>314</sup> investigate the effect of O<sub>2</sub> additions on the CO/H<sub>2</sub> system. They relate the Raman linewidth, a measure of diamond quality, to the inclusion of polyacetylene inclusion in the grown films. In their work, surface temperatures between 403 and 1,023 K were used with a noticeable change in quality at 406 K. The addition of O<sub>2</sub> was found to suppress polyacetylene formation and the counted nucleation densities were observed to increase dramatically with a worsening of film quality at 406 K.

Cerio et al.<sup>315</sup> investigated the CO/H<sub>2</sub> system to determine the efficiency of CO as a C source. Their substrate preparations included diamond seeding so that their study focuses on growth of diamond. They support results of prior studies; however, they conclude that hydrocarbons formed in the CO/H<sub>2</sub> plasma are responsible for diamond growth. Indeed, adding O<sub>2</sub> enhances formation of these hydrocarbons.

Johnson and Weimer present the most relevant work for this publication and the most conclusive paper on the role of CO.<sup>316</sup> They compare gaseous microwave plasma mixtures of C–13 CH<sub>4</sub> and C–13 CO with C–13 present in diamond films. Using 0.68-percent C–13 CH<sub>4</sub>, 59 percent of the diamond was judged to have arisen from the C–13 CH<sub>4</sub> and 41 percent from the 99+ percent CO. An important issue brought up in their work is that CO/H<sub>2</sub> is only an effective diamond-precursor system in plasma systems but not in hot filament systems. By looking at calculated equilibrium concentrations, they conclude that the chemistry in a microwave system does not tend toward thermal equilibrium because of the high-energy electrons present in the plasma. A hot filament system is, however, a thermally driven system that approaches thermal equilibrium. At thermal equilibrium, CO is preferred over hydrocarbons by four orders of magnitude. Therefore, in a hot filament system, a significant number of hydrocarbons cannot be formed for diamond production from the CO.

### 5.3.2 Methane Additions to Process Gases

Methane has often been used as the primary process gas in diamond deposition. The studies that use both  $\text{CH}_4$  and  $\text{C}_2\text{H}_2$  typically contrast the two for efficiency of diamond growth. Yarbrough et al.<sup>317</sup> found a dramatic change in film quality and growth rate associated with the addition of  $\text{CH}_4$  versus  $\text{C}_2\text{H}_2$  directly above the surface, but downstream of hot filaments in a hot filament system. Acetylene feed was found to have little or no effect, but  $\text{CH}_4$  was observed to enhance the growth rate and the uniformity of diamond growth. Earlier work by Johnson et al.<sup>318</sup> is similar to their work on  $\text{CH}_4$  labeling with C-13 for CO studies. Comparing C-13 labeled  $\text{CH}_4$  and  $\text{C}_2\text{H}_2$ , they found a primary role for  $\text{CH}_4$  and a secondary role for  $\text{C}_2\text{H}_2$  in the production of their films. They interpret their results as supporting the methylene radical formation of diamond.

Methane injection has been performed in  $\text{H}_2\text{O}_2$  flames by Glumac et al.<sup>90</sup> supplying  $\text{CH}_4$  and  $\text{C}_2\text{H}_2$  locally to the surface in the presence of an  $\text{H}_2\text{O}_2$  flame. Diamond is grown successfully; however, their results are not applicable to nucleation studies due to pretreatment of substrates by both diamond polishing and  $\text{O}_2$ - $\text{C}_2\text{H}_2$  torch pretreatment. They find the growth of diamond occurs through the methylene radical mechanism.

### 5.3.3 Elastic Constants

Elastic constants of a variety of natural diamonds have been well documented by a number of authors (ref. 194). Chandra and Clyne<sup>319</sup> have looked at the in-plane modulus of deposited thin diamond films. They used an ultrasonic technique to measure the composite resonant frequency of the substrate and diamond film composite. Although they obtained relatively appropriate values for diamond hardness, they were unable to obtain relative information about the deposition from the technique. A calculation of the appropriate elastic constants for hexagonal diamond has been made by Phelps,<sup>320</sup> but the veracity of these measurements will be left for others.

### 5.3.4 Surface Finish

Other studies such as Ong and Chang,<sup>321</sup> Wu et al.,<sup>322</sup> and Sutcu et al.<sup>184</sup> have reported rms roughness data from AFM; but in general, these have been large area scans on complete films rather than scans of individual crystal facets. Only Sutcu et al. is appropriate to discuss in conjunction with our results as they have made mention of scans on local (crystal faces) areas. They mention local smoothness of {100} areas on the 1- to 100-nm scale. Assuming (because it is not mentioned) that this is an  $R_a$  measurement, these results are smoother than mine, which would be expected from the comparison of CVD films and  $\text{O}_2$ - $\text{C}_2\text{H}_2$  flame films. The difference averages one order of magnitude for the films and can be most easily attributed to the alternate growth rates of the processes. The Sutcu et al.<sup>184</sup> study displays {111} AFM surfaces in the form of penetration twins and mentions the much higher surface roughness of the {111} faces; however, no quantitative data for comparison were presented. Sutcu also presents an attempt at atomic-level imaging that has scant indications of five separations at a juncture on a  $(2 \times 1)$  film. These images are not similar to mine. My images are, as Sutcu's, less than compelling.

## 5.4 Discussion of Relevant Simulation Prior Work

Because of the ease with which simulations may be run, the literature of relevant experiments is voluminous. Simulation review is presented as general and torch specific. An enormous amount of prior work is not mentioned here because I felt it was only of peripheral relevance to the current torch-produced diamond nucleation study. The general simulations mentioned are in all probability not the only ones relative to my results. They are only the most relevant to the work reviewed.

### 5.4.1 General Simulations

Frenklach and Wang<sup>323</sup> have presented an extremely comprehensive simulation of a one-dimensional, hot-filament reactor. They use a chemical-reaction mechanism developed for flame-like environments. They calculate the reactive-gas compositions with burner code from Frenklach and Wang.<sup>323</sup> They assume surface nucleation and no interaction on the gas-phase species by their surface reactions. Much of their work is specific to the hot filament system. However, two points are of relevance to this work:

1. They propose the dominant deposition of diamond by a  $\text{H}_2$ -abstraction,  $\text{C}_2\text{H}_2$ -addition reaction mechanism. They note that the last reaction step of the addition of a  $\text{C}_2\text{H}_2$  molecule to a diamond surface radical proceeds essentially irreversibly. Their reactions show a large number of surface reactions with gas phase  $\text{C}_2\text{H}$  and they also mention experimental observation of catalytic conversion of  $\text{C}_2\text{H}$  on diamond surfaces to  $\text{CH}_3$ . It is not an enormous leap to envision the catalytic process connected with a growth process using  $\text{C}_2\text{H}$  as the precursor.
2. The other important result from their work is that they note a critical dependence on gas history both in the prefilament and postfilament zones. This would lend support to a gas-phase nucleation mechanism.

Harris et al.<sup>34</sup> also provide a simulation of hot-filament diamond growth using a one-dimensional reactor flow code. They successfully predict growth rates of filament, plasma torch, and  $\text{O}_2$ - $\text{C}_2\text{H}_2$  torch systems. They base their success on the assumption that the chemistry of diamond surfaces is fundamentally similar to the chemistry of gas-phase alkanes. The advantage to this is that the gas-phase chemistry is controlled by local properties of the molecule. For example, enthalpy and entropy of the hydrocarbon bonds are typical of the gas. Belton and Harris<sup>324</sup> also propose a mechanism for the addition of  $\text{C}_2\text{H}_2$  to a (110) diamond surface based on gas-phase hydrocarbon chemistry; however, they use a  $\text{CH}_3$  radical as the growth species.

Rau and Picht<sup>325</sup> present a simulation that my work may support. Using a combination of simulation and experiment, they compare deposition profiles of diamond films against assumptions of C-containing active (for growth) species. The best fit to their data arises from the use of  $\text{C}_2\text{H}$  as the growth species. In their simulation, they let each hydrocarbon in the gas phase be assumed to incorporate into the growing crystal with a deposition coefficient of 0.1 from their microwave plasma experimental work. Other species such as  $\text{CH}_3$  and  $\text{C}_2\text{H}_2$  do not agree with either the observed layer thickness or the temperature and pressure dependencies. Unlike other microwave work, for the conditions used in their experiments, the gas phase approaches equilibrium. They attribute this to the higher pressure at which they operate.



In defense of  $C_2H$  as a growth species, they note that  $C_2H$  is the most strongly bound species on a diamond surface.  $C_2H$  is stronger than  $H$ ,  $CH_3$ , or  $C_2H_2$ . Methane should displace  $H_2$  from the surface and, once bonded, remain. This mechanism is akin to the previously proposed acetylinic mechanism with the  $C_2H$  molecule not being created by the formation of diatomic  $H$  and the  $C_2H$  growth species radical, but rather directly approaching from the gas phase. Although not a focus of the current report, my work lends strong support to the use of  $C_2H$  as the primary growth species. Hyman et al.<sup>326</sup> also identify  $C_2H$  as the second most prominent  $C_2$  species in microwave plasma reactors in their simulation work.

#### 5.4.2 Torch Specific Simulations

Perhaps the first simulation work on the  $O_2$ - $C_2H_2$  torch came from the labs of Y. Hirose where simulation results from Matsui et al.<sup>74</sup> provided a study of the radical behavior in the flame. They organize their results around the  $R$ . Using the stoichiometric reaction equation ( $R = 1$ ),



The concentrations of radical species are, therefore, quite different for  $R < 1$  and  $R > 1$ . They note that for  $R < 0.95$ , the  $O_2$ -containing radicals are so prevalent that some  $CO$  is formed into  $CO_2$ . However, when  $R > 1.04$ , their simulation then places  $C_2H_2$  and  $C_2H$  as the two dominant species. Their results also show that the  $C$ -containing radicals rapidly decrease below 3,000 K and then are replaced by solid  $C$ 's.<sup>74</sup> I attribute the pillaring shown in the GAMoly samples, to this trend—with the addition of  $CH_4$ . They discount the growth via  $C_2H$  or  $C_2H_2$  by a disagreement of  $R$ -dependence, and the indications that growth is limited by mass transport and surface reactions must be rate determining if they are the precursors. This is a consistent chain of reasoning only if the nucleation is assumed to occur on the surface. When nucleation is presented in the gas phase, the nucleation is then mass-transport limited, using  $C_2H$  as building embryos, and the growth would appear to be based on sites upon which the nucleation is grown.

Cappelli and Paul<sup>76</sup> employ CHEMKIN®, a standard flame-kinetics package, to compute the major flame species and compare these with their laser emission results. They note that  $H$  should be the primary radical in the postprimary flame front, and that  $C_2H$  should reach a maximum stable point at this location by a balance of  $C_2H_2$  oxidation and ethynyl oxidation. They emphasize that the region of the substrate in contact with this portion of the gas stream contains nondiamond  $C$  only. Kim and Cappelli<sup>327</sup> followed with a study where only  $H$ , diatomic  $H$ , and  $CH_3$  are assumed to react with a growing diamond surface. Using traditional flame-reaction mechanisms that include large amounts of  $Ar$ , but accounting for cyclical aromatics, they also support a balance for  $CH_3$  radicals between oxidation and cyclization.

More recently, Matsui et al.<sup>328</sup> have expanded on their previous simulation work. Recognizing that the low-temperature boundary layer adjacent to the surface is impractical to experimentally approach, they again compare simulation with growth rate and include a discussion of surface reaction. They compare  $CH_3$  with  $CH_2$ ,  $C_2H_2$ , and  $C_3H_2$  as diamond precursors. A strong correlation with temperature dependence of the growth rate is founded for  $CH_3$ .

Finally, a molecular simulation has been performed by Xing and Scott wherein they use a kinetic Monte Carlo method, employing a potential function by Brenner, that was designed for condensed phase

hydrocarbon modeling. Most relevant to this work is their finding that by using  $C_2H_2$ , a crystalline film clearly grows more rapidly when surface desorption of C surface species occurs.

### 5.5 Relevance of GAMoly and Simulation to Proposed Mechanism

The GAMoly experiment looks at changing the gas precursor species while retaining the atomic proportions required for diamond growth. The changes in the gas-phase environment strongly affect the conditions present during gas-phase nucleation, but affect less the surface mobility and surface conditions that drive surface nucleation. The GAMoly experiment is analyzed in conjunction with results from the parallel TDK simulation.

In many cases, the GAMoly films were found to show various densities of pillaring. A natural result of fewer initial diamond nucleation sites at the onset of film growth would be to apply the proposed mechanism when graphite, a-C, and diamond are all simultaneously depositing from the gas-phase pillaring. For each of the samples, the substrate material and the surface temperature were constant. If the amount of etchant changes in the gas phase, it will slow film growth or create lower grade films; however, pillaring is not caused by etching. Restated, when a diamond nucleus (germ) approaches the surface with sufficient energy, if it lands on a graphite or C surface, it may reorient in favor of the existing structure. The same is true when it lands near a diamond nucleation site. Thus, the surface sites that are diamond may remain so. Typically, pillaring is avoided when nucleation of other C forms is avoided in the gas phase. Diamond is, of course, etched more slowly than other forms of C, and this makes diamond more stable in the environment of the surface gas-phase species. However, pillaring is controlled by the number of nuclei of each C form impacting the surface.

The addition of  $CH_4$  into the precursor gases was found to be responsible for pillaring of the films. In each of the runs where  $CH_4$  was not added, pillaring was not observed. In all of the runs where  $CH_4$  was added, pillaring was found. The surface mobilities of the substrates are unchanged in that the surface temperatures remain within identical bounds to those of the other samples. The clear case of  $CH_4$ -dependent pillaring is best explained by drawing from the results of the parallel simulation. The calculated flame temperature for each experimental trial without  $CH_4$  was higher than the calculated flame temperature for any of the trials with  $CH_4$  added.

Looking at the results from the designed experiment, no interaction is noted between the gases; however, both CO and  $CH_4$ , as would be expected, lower the combustion temperature and thus the temperatures seen in the flame plasma. Methane is shown to have a much stronger effect. This again points back at gas-phase nucleation, considering the well-known suppression of soot formation in higher temperature flames. As soot (graphite and a-C) is suppressed from nucleation in the flame, the fraction of diamond nuclei present correspondingly rises and the surface is more completely covered with diamond nucleation sites. When other nuclei are present in the gas phase (notably soot), they cover a significant percentage of the substrate surface, inhibiting the growth and stability of diamond nuclei. Stabilizing  $H_2$  is abstracted by surface C and diamond merges with a graphitic or amorphous surface.

Looking at the other effects of  $CH_4$ , for the linewidth, the  $CH_4$  addition was shown to have a small advantageous quadratic effect. As the  $CH_4$  went through its midlevel position, the linewidth decreased. At the higher setting, the addition of  $CH_4$  was unfortunate. Methane is shown to provide more diatomic H,

which provides more species available for surface etching. This explains why the diamond line initially decreases as small amounts of  $\text{CH}_4$  are added. They etch more nondiamond species from the diamond that is growing. At higher levels of  $\text{CH}_4$  addition, the effect of increasing the C nuclei content overcomes the effect of increased etching. This is also seen in the hardness data. The effect on hardness for  $\{111\}$  crystal facets is shown to be more strongly dependent on the presence of  $\text{CH}_4$  than on the presence of CO. Methane additions increase the hardness with a slight quadratic effect, such that the beneficial effect tapers off at the higher  $\text{CH}_4$  addition levels.

Considering now the support for  $\text{C}_2\text{H}$  as a growth species for  $\text{C}_2\text{H}_2$ ,  $\text{CH}_4$  is shown to slightly increase the fraction present in the gas. Methane is shown to greatly increase the levels of  $\text{C}_2\text{H}_2$  present. Assuming that the beneficial effects of  $\text{CH}_4$  are not due to etching, and when comparing the two slightly beneficial results noted for the early stages of the quadratic behavior shown for  $\text{CH}_4$  addition, the results correspond much more closely to the increase in  $\text{C}_2\text{H}$  than the drastic increase noted in  $\text{C}_2\text{H}_2$ .

Methane also increases the entropy of the system. This correlates well with the decrease in temperature. Less heat is transferred into the system for the oxidation of  $\text{CH}_4$  than for the oxidation of  $\text{C}_2\text{H}_2$ . When  $\text{CH}_4$  adds unreacted  $\text{H}_2$ , this adds heat capacity to the gas and thus reduces the flame temperature. The temperature must become low enough for the change in entropy to remain positive in order for the entropy to increase for the process as the change in heat becomes less positive.

Carbon monoxide is the most stable constituent in the flame at the operating temperatures. It does not appear to be a primary precursor to diamond nucleation or diamond growth. The addition of CO in the GAMoly experiment is expected to suppress nucleation, if nucleation is occurring in the gas phase. The observed effect of CO addition on nucleation was to suppress nucleation as well as growth of diamond. Several effects of CO show reduced diamond content in the films and in the crystals, although the total fraction of C,  $\text{H}_2$ , and  $\text{O}_2$  was still comfortably within the appropriate regions for diamond growth. It was difficult to definitively separate the effects of CO on nucleation from the effects on growth; however, the AFM surface roughness data provide a reasonable look at the suppression of nucleation by CO. The surface finish data were taken on crystal surfaces that were open to the nucleation environment and generally parallel to the substrate surface. These surfaces were measured as an independent measure of the instantaneous nucleation environment.

Atomic-force, surface-finish data analysis is complicated by the need to locate facets of each type,  $\{100\}$  and  $\{111\}$ , on each sample. Because of the different growth rates of the different crystal faces and thus the assumed difference in the number of growing layers, comparisons are made only between different runs but on the same crystal facets. Ra and rms values were taken. The behavior of the response did not differ strongly between  $\{100\}$  and  $\{111\}$  crystal surfaces or between the Ra and rms values. The principal result of the surface roughness study details the difference in crystal growth and not in nucleation. Surface roughness values of the  $\{111\}$  facets are, in general, higher values than those for the  $\{100\}$  facets and can easily be seen in the box plot shown in figure 225. This has been suggested and qualitatively documented in other work as due to greater ease in ledge formation on  $\{111\}$  faces. My data show clearly that CO softens  $\{111\}$  faces, whereas  $\text{CH}_4$  does not. It is possible to explain this within the proposed framework as slowing the deposition of germs onto a growth/nucleation surface. This would smooth the surface by providing fewer new layer nucleation sites for growth.

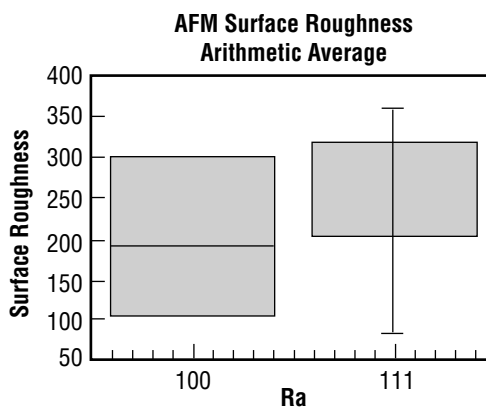


Figure 225. Surface roughness by facet.

Simulation results parallel to the GAMoly experiment show that the effect of CO addition is strongest on entropy of gas, enthalpy of gas, and a strong decrease of  $C_2H$  fraction. This is perhaps the primary support of  $C_2H$  as the diamond precursor. As well as decreasing the  $C_2H$  fraction, CO also decreases the fraction of  $C_2H_2$  present. The rise in diamond linewidth closely parallels the reduction in  $C_2H$  as a function of CO addition. The enthalpy and the entropy of the flame did not show interaction between the process gases.

Hardness is also related to specific crystal facets and thus traceable to the growth and nucleation environment. Hardness results support the above interpretation although the results were significantly different for  $\{100\}$  and  $\{111\}$  facets. For  $\{100\}$  facets, the process gases have a strong interaction and a strong quadratic component. The important factor appears to be the addition of CO for the determination of  $\{100\}$  hardness. Because the  $\{100\}$  face is a slower growing face, the effect of lower nucleation densities does not seem to strongly affect the hardness a crystal demonstrates. The addition of CO is again notable in that, in conjunction with reduced nucleation, the effect on growth (presumably  $C_2H$  growth species) strongly affects the composition and the hardness of the grown crystal.

The effect on hardness for  $\{111\}$  crystal facets is shown to be more strongly dependent on the presence of  $CH_4$  than on the presence of CO. Methane additions increase the hardness with a slight quadratic effect such that the beneficial effect tapers at the higher  $CH_4$  addition levels. In the proposed mechanism, a slight reduction in nucleation would result in slower growth of the  $\{111\}$  facet, resulting in less possible sites for incorporation of nondiamond material. However, the beneficial effect is lost, as demonstrated by the data, as the  $CH_4$  level increases and the number of nondiamond nuclei increases.

## 5.6 Discussion of Experimental Conditions Similar to the Flow and Substrate Experiment

### 5.6.1 Gas Flow Prior Work

Work has been performed in hot filament,<sup>329</sup> microwave plasma,<sup>330</sup> and the  $O_2-C_2H_2$  torch<sup>75,76,81,92,226</sup> on the effects of flow rate. As flow rate is primarily a process parameter, of necessity, its effect must be interpreted within the process used. For example, in the hot filament study performed by Kweon et al.,<sup>329</sup> the nature and amount of various species is noted to be dependent on the hot filament temperature, system pressure, composition of the incoming gas, and the flow rate of the incoming gas. In

this case, gas flux influences nothing more than the mass flux which in turn controls the mass transport. As flow rate increases, a decrease in ratios of the intensities of the diamond line to a nondiamond line at  $1,550\text{ cm}^{-1}$  is noted. At low temperatures, the growth rate of diamond does not change with gas flow rate; however, at high temperatures, the growth rate follows the flow rate of the gas. Kweon et al.'s results imply that in the lower temperature region, surface reaction kinetics is limiting the deposition, and in the higher temperature region, the growth rate is mass transport controlled.<sup>329</sup>

Celii et al.,<sup>330</sup> in an MPCVD system, used flow rate to control chamber residence times. In a microwave system, the flow rate is decoupled from other processing parameters, making their study reasonably specific to flow rate in an MPCVD system. They calculated that the effect of substrate heating, due to the change in gas flow rate, was only  $5\text{ }^{\circ}\text{C}$ . Their results pointed to dominant faceting at intermediate flow rates of 100 and 200 sccm with rough intergranular material present for flow rates at 25 and 50 sccm. Their study also used various substrates, in their case microcrystalline diamond and Si. On the microcrystalline diamond, {100} faces were seen only at 100 sccm, while at other flows, the films had a random distribution of facets. They do not mention orientation, if any, of their microcrystalline diamond substrate. Given that their results on Si seem inconclusive with regard to flow rate, I believe that the substrate texture may have been significant. In their results, they noted an insensitivity of deposition rate on flow rate. This was found to be principally due to the gas flow pattern in their reactor.

Most work concerning flow rate has been conducted using the  $\text{O}_2\text{-C}_2\text{H}_2$  torch process. The predominance of flame processes in flow rate investigation is easily seen due to gas flow parameters in the sensitivity of the process. Flame configuration,<sup>75</sup> convective heat flux,<sup>76</sup> stagnation point,<sup>92</sup> flame composition,<sup>226</sup> and flame temperature<sup>22</sup> are all related to the gas flow with flame-formed diamond.

Cappelli and Paul<sup>76</sup> note that all else being equal, the surface kinetics are controlled by the surface temperature. He estimates that to a first-order approximation, the convective heat flux is the product of the heat of combustion, the volumetric flow rate of  $\text{C}_2\text{H}_2$ , and the surface area of substrate in contact with the flame. Cappelli, however, looks only at the effect of flow rate on substrate temperature and the requirements to maintain sufficient thermal sinks in order to avoid the high-temperature production of graphite. In related work on flat flame burners, Murayama et al.<sup>92</sup> look at the importance of gas flow in determining the change in stagnation point with gas flow. In a related paper by Kim and Cappelli,<sup>327</sup> they note that increasing the flow velocity should result in significant increases in growth rate. They note that  $\text{CH}_3$  surface flux should be significantly increased by increases in the volumetric flow rate. No mention is made if the increase directly tracks the increase in  $\text{CH}_3$  species due to the sensitivity of the process.

Harshavardhan et al.<sup>226</sup> undoubtedly produce the most complete experimental results with respect to gas flow. They varied their total gas flow from 1.25 to 3 sLpm; however, they make only a token attempt to keep the gas composition constant with changes in flow rate. Their Raman results indicate an optimum flow rate of 2 sLpm. At low flow rates, they show primarily graphitic results; and at flow rates  $>2$  sLpm, they note that they have created a strong intermixing peak with the substrate on Si (in their case, SiC has been assumed). The high flow rate samples also show a weaker diamond peak with respect to the background spectra. They note that as their deposition proceeds, they observe a  $100\text{--}150\text{ }^{\circ}\text{C}$  temperature variation due to the thermal conductivity of the deposit. The issue of thermal conductivity of the sample brings up the relation of substrate material to diamond nucleation and deposition.



The effect of gas flow on the laminar or turbulent nature of the flame appears to be one of the more crucial parameters for diamond growth. Snail et al.<sup>82</sup> have produced some of the highest transparency torch-produced film using turbulent flames. Alers et al.<sup>81</sup> have performed an excellent study decoupling the effect of flow rate from tip geometry that will be covered in the discussion of our tip geometry modifications.

### 5.6.2 Prior Work on Substrate Effect

Sutcu et al.<sup>184</sup> suggest that differences may result from perturbation of gas-phase chemistry due to the surface recombination rate of  $H_2$  on each particular surface. Surface recombination is due to abstraction of surface  $H_2$  by  $H_2$  in the gas phase. This is different on different substrates and will affect diamond nucleation in the affected region. This region may of course relate to surface or gas phase nucleation.

**5.6.2.1 Diamond as a Substrate.** As a substrate, diamond offers the easiest material to nucleate and grow on. Diamond, however, has the advantage of allowing studies of the structure and texturing of deposited films. Diamond substrates have elucidated many of the effects of substrates on diamond film production.

Some of the first work on growing diamond films was implemented on diamond substrate because of the lattice match. Derjaguin et al.,<sup>331</sup> using a microwave plasma, have looked closely at defect structures that were caused by stresses on various natural crystal faces. Although their epitaxy was perfect, periods of the natural and deposited lattices were different. Stresses resulting from the mismatch of lattice cells were found sufficient to cause significant twinning. Sutcu et al., in comparing morphological similarities using an AFM, remark also that the structure of individual faces of CVD-grown diamond will not, in general, be comparable to the local structure of a homeoepitaxial film of the same orientation.<sup>184</sup>

Miyata et al.<sup>178</sup> have used CVD diamond as a substrate for their B-grown samples. In their experiments, there was no noticeable effect due to the use of a CVD layer as a substrate for B-doped CVD. In addition, looking at B doping, Everson and Tamor<sup>185</sup> show growth on a type II natural diamond substrate. Their results were very similar to others where gross defects were found in linear arrays. These were found to have a step-like structure under scanning tunneling microscopy and this step-like structure was interpreted as lateral epitaxy.

**5.6.2.2 Silicon as a Substrate.** Because of its high band gap and high thermal conductivity, diamond, as an electronics substrate, is substantially superior to the current substrate of choice, Si. However, because of the ease of preparing single-crystal Si substrates, much work is being put into epitaxial growth of diamond onto Si wafers. Narayan et al.<sup>332</sup> have shown in an early paper that  $\langle 011 \rangle$  textured diamond films could be grown on  $\{100\}$  Si substrates by matching a  $\{111\}$  or a (200) plane of the diamond with the  $\{022\}$  plane of Si. They suggested magnesium oxide (MgO) as a preferred material, again with a better match of lattice parameter. Ikoma and Yamanaka<sup>333</sup> pretreat a  $\{111\}$  Si substrate, forming various amounts of SiC to form as nucleation sites. In fact, they found that SiC is not thought to be a nucleating agent for diamond but rather diffused Si atoms are more likely to be the nucleation site. Recently, Jiang et al.,<sup>297</sup> using HREM, show compelling results for diamond nucleation on a stressed Si surface or preferentially on an amorphous layer of Si.



**5.6.2.3 Platinum as a Substrate.** Platinum (Pt) is an interesting substrate because it is considered an excellent catalyst for reactions involving hydrocarbons. Harris et al.<sup>334</sup> noted that Pt does not have a significant effect on the gas phase chemistry at the substrate surface. They suspect that a surface hydrocarbon layer is converted to or replaced by diamond. They also bring up the possibility of diamond nucleation on graphite islands that were incompletely etched away. Belton and Schmieg<sup>335</sup> observe that on Pt, the addition of O<sub>2</sub> causes the suppression of diamond nuclei by preferentially removing graphitic C precursors used as nucleation sites.

**5.6.2.4 Titanium Nitride as a Substrate.** Titanium nitride (TiN) has been studied as a substrate for diamond. It has been studied because of the possibility of using it as a barrier layer applied to tool steel onto which diamond might be adherently bonded. Weiser et al.<sup>336</sup> first showed that TiN was a sufficient barrier to C diffusion to allow the deposition of diamond onto TiN onto an Fe base. In a related paper,<sup>337</sup> they note that an a-C layer forms on the TiN and it is onto this a-C layer to which diamond bonds.

**5.6.2.5 Stainless Steel as a Substrate.** Using a thin layer of Mo as a pretreatment, Heidarpour and Namba<sup>338</sup> were able to produce a strongly adherent diamond phase C film onto stainless steel. In their work on TiN coating layers, Weiser et al.<sup>337</sup> found that a graphitic layer was deposited onto Fe prior to the growth of diamond.

**5.6.2.6 Silicon Dioxide as a Substrate.** Fused quartz has been very successfully used as a substrate material. Praver et al.<sup>339</sup> have produced films of  $<3\text{ cm}^{-1}$  Raman linewidth using a parallel flow configuration in a microwave plasma system. Sun et al.<sup>340</sup> very successfully used an overlayer of zinc oxide-aluminum compound (ZnO:Al) on silica to produce diamond films. Under the same conditions, the films on the coated surface were larger with smaller crystallites than on the uncoated silica surface. This they interpret as a greater nucleation density on the ZnO:Al coating.

**5.6.2.7 Tungsten Carbide as a Substrate.** Flame work on tungsten carbide (WC) was performed early by Matsui et al.;<sup>74</sup> however, the investigation of the substrate effects were minimal. Work on WC with cobalt (Co) used heavily pretreated substrates.<sup>341</sup> The pretreatment was an ultrasonic bath containing a diamond suspension. They suggest, based on their work, that the nucleation on their substrates is primarily due to contamination by diamond particles on the surface. They also confirm the deleterious effect of Co on diamond growth reported in a prior paper.

**5.6.2.8 Aluminum as a Substrate.** Aluminum is difficult to deposit onto because of the low temperatures that must be used during deposition so as not to harm the substrate. Eddy et al.<sup>50</sup> have successfully deposited diamond onto Al using an ECR system. I have also been able to deposit diamond onto Al 2219 and 6061 substrates using the oxygen-acetylene torch; however, the results on Al are not presented as part of this work. Results by Eddy et al.<sup>50</sup> indicate only successful deposition of crystallites on pretreated substrates. It is noted here again that in my work on Al, pretreatment was not found necessary.

**5.6.2.9 Single-Crystal Beryllium Oxide as a Substrate.** Argoitia et al.<sup>342</sup> provide very interesting results about the diamond nucleation process using beryllium oxide (BeO) as a substrate material. Different planes of the BeO surface should favor the epitaxial growth of alternately hexagonal or cubic diamond. They were careful with their substrates and only SiC was used in pretreatment abrasion. Much like the results found in this work on the tip modification experiments to be discussed later in this section,

they were able to grow diamond particles that, in microscopy, were hexagonal in form. Their samples of this type produced very clearcut cubic diamond Raman spectra.<sup>342</sup> They noted the presence of beryllium carbide (BeC). This helps exemplify my use in the substrate experiment of the carbide potential of a substrate. Substrates with higher potential or lower energetic cost to form carbides are considered more likely precursor substrates for diamond. Argoitia et al.<sup>342</sup> notice in their work that where hexagonal diamond should have been favored, none was observed. They explain this with use of a rapidly developed stacking fault that would grow a thin layer of hexagonal diamond but quickly attain the more stable cubic form after the early stages of diamond growth.

**5.6.2.10 Titanium as a Substrate.** Interestingly, titanium (Ti) has been used as a substrate material, looking at carbide formation during diamond growth. Carbide formation has been suspected as a necessary or advantageous precursor phase in a number of systems such as Si, Mo, W, Ti, and Ta. Park and Lee<sup>343</sup> use Ti, simultaneously growing titanium carbide (TiC), to nucleate diamond and investigate the importance of a carbide layer and the importance of the surface concentration of C as determined by the available thickness of the carbide layer. In their experiments, diamond and TiC grew simultaneously. They surmise that the nucleation of diamond does not require either the carbide layer or any specific surface concentration of C.

**5.6.2.11 Nickel as a Substrate.** Nickel is a typical catalyst in HPHT diamond growth and, because of the close lattice parameter, is an obvious choice for a substrate material. In CVD systems, however, Ni typically has grown diamond using a graphite overlayer. This is due to a high solubility of C in Ni and a strong catalytic effect of Ni for hydrocarbon dissociation. Yang et al.,<sup>344</sup> in working with Ni substrate, grow oriented diamond using seeding during a substrate pretreatment step. They attribute the orientation to a realignment of the seed with the grain of the substrate. They also inhibit the growth of a graphitic overlayer by melting the surface Ni during deposition. They note that, according to Badzian, the formation of nickel hydride (NiH) may be responsible for the lack of the graphitic growth.

**5.6.2.12 Copper as a Substrate.** In comparative work with Si substrates and colloidal graphite suspensions, Feng et al.<sup>345</sup> look at the growth of diamond on Cu substrates. Because of the formation of diamond on Cu, they surmise that a carbide layer is not a requirement for diamond growth; however, they also note that the particle size on Cu is smaller than that on Si and the growth rate on Cu is less than that of Si.

**5.6.2.13 Molybdenum as a Substrate.** A large number of torch experiments have been carried out using Mo as the substrate material; however, little work has been done considering the relative effects of Mo as a substrate material. Meilunas et al.<sup>346</sup> indicate that early in their plasma production of diamond, MoC is formed as an intermediate layer and diamond is formed after surface saturation of the carbide.

**5.6.2.14 Silicon Carbide as a Substrate.** Silicon carbide has been suggested as an interface material for growth of diamond on Si, and it has been extensively used as a substrate material (primarily the alpha phase). Of several papers that cover SiC as an interface layer on Si substrates, work by Belton et al.<sup>347</sup> is significant in their use of in situ x-ray photoelectron spectroscopy (XPS) to obtain a time-dependent surface species characterization. They definitively observe the formation of an intermediate SiC layer before the deposition of diamond. They estimate the depth of the SiC layer at 90 Å. Silicon carbide, in the phase, has been used as a substrate for textured growth by Stoner and Glass<sup>348</sup> where a biasing

pretreatment was used to grow a 50-percent textured film on SiC. In their work, they suggest that the primary advantage of the pretreatment for SiC is the removal of surface oxides. Grannen and Chang<sup>349</sup> also provide work using fluorine (F) chemistry for nucleation and growth of diamond on reaction-bonded SiC samples. They provide excellent growth without the use of any pretreatment on their SiC and on WC samples. They also stabilize diamond nuclei on SiC powder. Their SEM photographs support a gas-phase nucleation mechanism; however, no mention of this is made, nor would the F-based microwave method have any necessary applicability.

**5.6.2.15 Properties of Carbon Coatings on Substrates.** In looking at C substrates other than diamond, the use of a hydrocarbon immersion prior to deposition is a very effective pretreatment for diamond growth. Using several hydrocarbon coatings, even ballpoint pen ink,<sup>350</sup> produces effective nucleation enhancement. Ignoring only other C phases as independent substrate materials, thin films of colloidal graphite, when applied to {100} Si substrates, were found by Feng et al.<sup>345</sup> to have a critical thickness for the enhancement of diamond nucleation. In their work, thick films of graphite, deposited from a colloidal isopropyl alcohol suspension, inhibited nucleation, whereas films at 0.2 mm had the most positive impact on nucleation. Looking at the results of a critical C layer thickness, they note that the results are related to the composition of the gas phase. They suggest that a relatively high C concentration in the gas phase is not conducive to diamond growth. Indeed, if the diamond is nucleating in the gas phase, requiring H for surface stabilization, excess C will then not allow a sufficient percentage of surface to be stabilized.

In a related paper,<sup>351</sup> thin, hard C films were produced on Si substrates and subsequently diamond was grown. Three stages of diamond growth were noted as follows:

1. Gradual growth of spherical nanoparticles with primarily a graphitic Raman peak
2. Roughening and enlargement of the existing particles with the emergence of diamond as the primary Raman peak
3. Coalescence and increases in crystallinity were noted.

Turbostratic C films deposited onto Cu substrates increase the nucleation of diamond when heated in an H-rich environment.<sup>352</sup> This illustrates the possibility of surface nucleation because the rates of nucleation are much faster than typical with the growth conditions used for hot filament growth onto other substrates.

Dubray et al.<sup>353</sup> used an amorphous hydrogenated-C coating on graphite, Si, and SiAlON substrates to show that the presence of surface sites of disordered C are required for increasing the nucleation density of diamond films. Johansson et al.<sup>354</sup> vapor deposited graphite as a coating onto Monel and Ni substrates and used them for diamond deposition in a hot filament reactor. Their work, with varying thicknesses of starting graphite films and various deposition times, provides the interesting result that the nucleation of diamond does not depend on these parameters. They note that regardless of the initial thickness on their substrates or the deposition time, a {100} film was noted onto which the diamond nucleated. They present a mechanism for the surface nucleation of diamond based on fractured graphite ring starting points.

The presence of these graphite ring starting points is enhanced for rougher surface finish surfaces and grain boundaries. This, correlates well with the previously mentioned work of Dubray.

### 5.6.3 Substrate Comparison Work

More closely related to the current work are those studies where a comparison of the behavior was noted across a range of substrates. Everson and Tamor<sup>185</sup> used Cu, Si, Mo, and SiO<sub>2</sub> and found similar growth rates when they used ultrasonic cleaning in a diamond-loaded hydrocarbon bath as a pretreatment. Youchison et al.<sup>51</sup> examined simultaneous deposition with a diamond-polished Cu substrate, a diamond-polished Al substrate, a diamond-polished Si {100} substrate, and an ultrasonically diamond-polished Si {100} substrate. Only the Cu substrate did not produce continuous films. They assumed that it was prohibited by excessive a-C growth.

Kobayashi et al.<sup>355</sup> looked at Si substrates and Si substrates coated with Fe to investigate the importance of a SiC layer and carbonization of the substrate surface. Their procedure was to form a carbide layer by heating in CH<sub>4</sub>, then removing the graphite overlayer by heating in H<sub>2</sub> gas. This produced a SiC surface and a C-rich Fe surface above the Si base. They suggest that on Si, polishing cleaves the natural oxide, and diamond nucleation sites are fabricated by C diffusion into the Si substrate. When they only perform the H<sub>2</sub> treatment, the diamond nucleation decreases slightly. However, when only the carburization treatment was used, the diamond nucleation decreased drastically. This was probably due to the nature of their growth conditions and the ratio of surface C to stabilizing H<sub>2</sub> required for diamond formation.

An early study was performed on a number of metal (Ni, Co, W, Cu, and Mo) and ceramic (SiO<sub>2</sub>, Al<sub>2</sub>O<sub>3</sub>, ZrO<sub>2</sub>, AlN, SiC) substrates by Saito et al.<sup>356</sup> for the CO-H system. This study covers each of the substrates used in the flow rate and substrate experiment. They conclude that the nucleation density is an order of magnitude higher for the carbide-forming (and carbide-formed) substrates; i.e., Mo, W, and SiC.

Chen and Narayan<sup>357</sup> recently published an excellent investigation on substrate effect on diamond film formation. They use the transition metals of Cu, Ni, and Fe with their corresponding alloys of Si and Al to vary the activity of three-dimensional electrons on the substrate surface. They did not use any diamond scratching or abrading for any of their substrates when preparing their samples for hot filament deposition. This practice is not followed in many of the literature references; however, it does lend much more credibility to their investigation of surface effects.

Looking at the ability of a hot surface to catalyze and stabilize the production of graphite, they relate the catalyzing effect to the level to which the outer three-dimensional electron shell is filled in the substrate material. They note that the amount of graphite deposition decreases along the path of Fe ≥ Ni ≥ Cu as the electron shell is gradually filled. This relates to a greater percentage of diamond growth along this same path in their experiment. The inability to form stable carbides maintains the open electron shells of the Fe and Ni substrates so that graphite is continuously formed (stabilized) on the surface. When stable carbides may be formed, they surmise that graphite is no longer catalyzed and diamond may be formed. They postulate that the bonding of the diamond with the substrate should be via  $\sigma$  bonds and that the sp<sup>3</sup> configuration should remain unchanged.

#### 5.6.4 Torch-Specific Substrate Comparisons

The torch process is very amenable to production of diamond on a wide variety of substrates; however, detailed results are difficult to find on the effect of various substrates on the nucleation process. In one of the first U.S. papers, Hanssen et al.<sup>68</sup> mention success on Si {100}, Si {111}, BN, Mo {100}, Nb {100} tantalum (Ta) foil, TiC, and Cu. They actually report no results other than successful deposition of diamond. Hirose et al.<sup>88</sup> report torch diamond work on TiN, Mo, Al<sub>2</sub>O<sub>3</sub>, and Si; however, with regard to substrate work, they only report that successful transparent diamond was grown on TiN and Mo samples.

#### 5.6.5 Hexagonal Diamond From Chemical Vapor Deposition Sources

Silva et al.<sup>358</sup> used a plasma-enhanced CVD process to observe hexagonal diamond microcrystals by means of Raman spectroscopy and XRD. In their work, however, they consider the 1,170-cm<sup>-1</sup> peak as a hexagonal diamond peak. Strong exception is taken to the use of 1,170 cm<sup>-1</sup> as a hexagonal peak. Silva et al. also note but do not explain the previous work on HPHT shock-produced hexagonal diamond, which did not show a peak at 1,170 cm<sup>-1</sup>. I will continue to refer to the Raman mode vibrations produced from commercial lonsdaleite diamond produced by a shock loading process<sup>214</sup> at the General Electric Corporation. Their spectrum consisted of a broadened line at 1,315-cm<sup>-1</sup> wave numbers and a hint of a band at 275-cm<sup>-1</sup> wave numbers.

### 5.7 Relevance of Flow Rate and Substrate to Proposed Mechanism

The FLOW experiment changes conditions on the surface of the sample by increasing the gas flow rate while remaining on a consistent point of the CHO diagram and by changing the carbide potential of the substrate.

Increasing the flow rate increases the number of germs present on the surface. This in turn decreases the distance a surface species needs to travel to form or add to a growing nucleus. If diamond forms on a substrate, this should have a large effect on the amount and consistency of the film.

The change in the carbide potential of the substrate is done by varying the substrate material. Substrate type affects the electronic structure available for surface nucleation and the mobility of surface species. The substrate type was varied over a range of carbide potentials. This is a rough description of the solubility of C in the substrate, and ease and type of carbide bond formed with the substrate. The changes in the substrate material drastically affect the surface mobility and surface stability of the surface species or surface germs. Surface stability is primarily a result of the bonding mechanism between the surface and either a surface stable molecule or a germ/nucleus.

From the perspective of the proposed mechanism, the ability of the surface to retain appropriate nucleation sites for diamond as opposed to graphite and a-C varies with carbide potential. When a-C and graphitic nuclei arrive at the surface along with diamond, they may present a surface appropriate for diamond nucleation or one appropriate for continued graphitic nucleation. The gas-phase nucleation conditions in this experiment are affected only slightly and primarily by the increase in gas flow rate. The flow rate affects the number of arriving growth species available for growth or nucleation for surface nucleation.



Following the proposed mechanism, we should expect the strongest substrate effect to be found in the comparisons between C-phase peak intensities. If the surface stabilizes one form of C better than another substrate, then since the gas conditions do not change, the forms of C should be found in varying amounts on the different substrates. This is best seen in the relative Raman-peak heights. In fact, the strongest effect seen in the relative peak heights is for the change in substrate material. The cooperative effect noticed in the peak ratio and the linewidth results is explained well with the proposed mechanism. Without the effect of high flow (low flow) condition, the ratio of the peaks gets worse as the carbide potential increases. This is because the surface better stabilizes more forms of C nuclei. However, when the flow rate increases, growth conditions favor those substrates that best stabilize diamond relative to other forms of C, and the higher carbide potential substrates provide stronger diamond-to-other-C-peak ratios.

Because of the high solubility of C in Cu, reviewers have noted that the surface cannot passivate and C is expected to continuously diffuse into the substrate. Looking at the proposed mechanism, the reason diamond is seen at the high flow rates on Cu is because diamond absorbs less readily into the substrate than does C or graphite so that diamond germs that land on the substrate are left behind more readily than germs from other forms of C. Carbon of all forms is able to reorient and desorb into the substrate in the low flow condition. Molybdenum forms a stable carbide and by the proposed mechanism at deposition temperatures, the surface will passivate. It will passivate most readily with C and graphite nuclei or radical desorbed species. Diamond nuclei will stabilize most readily on the surface when sufficient C flow is present to passivate the surface. SiC does not require passivation, being already in the carbide form. All forms of C are expected to be relatively stable on SiC so that all forms of C should deposit. According to the proposed mechanism, only the quality of the diamond should improve with flow rate as the samples are in a diamond growth environment. On a stable surface such as passivated moly or SiC, the increase in flow rate should improve the quality and amount of the diamond grown.

Although the occurrences of hexagonal diamond are not strongly noted in the Raman spectra, it should be noted that the Raman response of lonsdaleite is much less than that of cubic diamond.<sup>312</sup> In my work, any peak between 1,310 and 1,326  $\text{cm}^{-1}$  was considered an indication of hexagonal diamond; however, a distinct peak was required in this area and no shoulder region or occlusions were thought to be acceptable. A strong indication of gas-phase nucleation is found with the drastic quadratic improvement with flow rate of hexagonal diamond. The indications of hexagonal diamond are important in that the prior work with gas-phase nucleation in plasmas typically demonstrates a significant amount of hexagonal diamond.

## **5.8 Work Related to Torch Tip Modification**

An obvious experimental approach in investigating gas-phase nucleation is the modification of the time-gas-plasma environment. For the  $\text{O}_2\text{-C}_2\text{H}_2$  torch, the time of residence for an assumed nucleus in the nonequilibrium formation environment of the flame feather and the mixing of embryonic precursors are two parameters, both tied to the pressure drop across the nozzle. The pressure drop and the gas velocity are both easily modified by geometric changes to the tip/nozzle exit. Work with variations of the nozzle to date is comprised of studies of turbulence or laminar versus turbulent behavior. Frey et al.<sup>198</sup> provide an excellent picture of the flow field involved in torch deposition; however, they do not investigate modifications to the flow field in any detail.



In work unrelated to diamond deposition, Kappes et al.<sup>359</sup> used conical nozzles in supersonic molecular beams to maximize the generation of large clusters. They considered the expansion of a metal vapor previously heated, but the conical nozzle provided better mixing and a slightly higher gas phase residence time.

For turbulent flames, Sivanathan and Faeth<sup>360</sup> noted that the soot spoke found in laminar flames is comparable in terms of maximum soot-volume fractions. In addition, maximum soot-volume fractions and temperature ranges within laminar and turbulent soot spikes were essentially the same for  $C_2H_2$  and  $C_2H_4$  flames. For the current work, the relevance of this is the similar number of nucleated soot particles in the gas-phase environment of laminar and turbulent flames.

Alers et al.<sup>81</sup> provided a sound investigation of the properties of commercial torch tips by comparing laminar and turbulent flames. They noted that although the Reynolds number is sufficiently high for the onset of turbulence on commercial burners, to transition a flow between laminar and turbulent requires a sufficiently long opening section.<sup>81</sup> Furthermore, they note that it is impossible to stabilize both a laminar and a turbulent flame on the same commercial burner using the same total gas flow. In their work, they note the modification of a commercial burner by adding a turbulence-creating step. They do not provide details of this modification. For their flames, they note that the growth rate of the turbulent flames was approximately twice that of the laminar flames at the same flow rate. They performed two experiments—one in which the gas ratio was altered and one in which the total gas flow rate was altered. They did not notice a strong change with gas flow rate; however, they did notice a proportionally larger effect on growth rate as the  $R$  decreased from 1.1 to 1.07 in the turbulent flames. They draw the conclusion from their work that the deposition process is mass transport limited.

Snail et al.<sup>82</sup> present work on the deposition of transparent diamond in turbulent flames on a commercial torch. They verify the presence of turbulence by flame characteristics and Reynolds number. In contrast to the work of Alers,<sup>81</sup> Snail et al. notice no growth rate difference between the laminar and turbulent flames. They suggest that the higher quality observed is due to an increase in the etchant species at the substrate surface. I believe this would correspond to an increase in the mixing between the intermediate region and the feather region of the flames.

## 5.9 Relevance of Torch Tip Modifications to Proposed Mechanism

The two tip modification experiments look at the behavior of gas-phase nucleation by modifying the shape and behavior of the flame plasma in which diamond nucleation is suspected to occur. The experiments also perform a verification function in that they each duplicate, on a reduced scale, one of the previous experiments. In each case, the tip experiment is expected to show an effect due to the tip modification and an effect that correlates to the results from previous work. The first tip experiment changes the tip and gas constituents, whereas the second tip experiment changes the tip and surface conditions.

In the first experiment that used either CO or  $CH_4$  with either a modified or a traditional tip, the addition of CO provided no crystals for measurement and comparison. The effect of the tip modification, did spur the following experiment on tip modification and substrate type. CO completely inhibited diamond formation on SiC. The tip modification increased the Raman linewidth. This directly correlates to the

previous GAMoly results, but the slower velocity of the flame amplifies the effect. The tip effects are seen most clearly in the tip/substrate experiment, because in the tip gas experiment, both the gas addition and the modification to the tip negatively affect the gas nucleation environment so that data from grown diamond is weak, negative, or nonexistent.

In the tip substrate experiment, because the flow rate effect is not present when the substrate carbide potential increases, the number of stable C nuclei increases, the Raman linewidth increases, and the peak differential shifts in favor of other C forms. An interesting effect is the possibility of hexagonal diamond that would follow the noted pattern of diamond being stabilized on the higher carbide surfaces. Both variations in substrate material and the modified tip show some effect on the Raman linewidth. As the carbide capacity of the substrate increases, the width of the diamond line seems to increase as well. The width of the diamond line also increases when the change is made to the modified torch tip. The results from the increase in substrate carbide capacity support the previous results obtained in the flow experiment.

Looking at the effects of the tip modification, the flow is separated into at least three separate regions of flow transport as follows:

1. The first is a region corresponding to the stoichiometric combustion of torch gases.
2. The second is an intermediate region, the flame feather, that is composed of excess reaction products engaged in combustion.
3. The third is a diffusion flame region in which combustion occurs using  $O_2$  that diffuses into the flame region from the surrounding atmosphere.

The previously described modification to the torch tip produces a slower flame and a reduction in the transient pressure spike due to expansion at the nozzle exit. Slower gas flow from the flame provides better mixing of the initial and intermediate zones because the combustion speed has not changed. Better mixing near the flame feather introduces OH and O etchants from the intermediate region which destroy diamond and graphite nuclei. The better mixing of regions will occur because the species present in the combustion reaction remain in the combustion zone for a longer period. This provides more etching species in the primary feather. Looking at the proposed mechanism, more etching species in the flame feather will decrease the probability of nucleation in this region and fewer diamond nuclei will result. This will result in a lower grade diamond film due to carbide formation on the surface from the hydrocarbon species that are able to nucleate on the surface.

The difficulty provided by the better mixing on nucleation of diamond in the gas phase also may be seen in the diamond to microcrystalline graphite peak and the diamond to a-C peak. In both cases, the ratio of diamond to C is seen to decrease with an increase in the substrate carbide capacity and with the modification of the tip. The carbide capacity decrease is expected as above, based on the previous experiment, and the tip modification again is shown to decrease gas-phase nucleation.

### 5.10 Diamond Jet High-Velocity Oxygen Fuel Experiment

Diamond nucleation and growth is impractical at this point using  $C_3H_6$  as the fuel-gas phase precursor. The appropriate C-to-etchant ratio does not appear to be economical or practical. Looking at the results from  $C_7H_8$  addition to the HVOF flame, the progression of our samples on a Bachmann diagram is shown in figure 226. Both of the samples displaying graphite samples were grown in the nondiamond growth region. Several factors may explain the lack of diamond on our substrates. The first supposition is temperature. We have no accurate measurement of surface temperature during the deposition. In our initial assumptions, we considered that the surface temperature at some point would, on a heating or a cooling curve, be appropriate for diamond stability.

Upon examining the experimental results, it is quite possible that stable diamond embryos are subject to sufficient etchant or carburization forces over the range of unfavorable temperatures, as to prevent microscopic observation of any diamond. The strong effect of low surface temperature may indicate that phase quenching plays a more important role than surface diffusion in the generation of diamond. This hints at gas-phase formation of the diamond embryo. A second possibility may well be the flame turbulence. Diamond growth has not been reported in gas streams with the high flow rates that were prevalent in our experiments. As a final note, the presence of nondiamond C is encouraging in its adherence to the Bachmann diagram. It would appear that both the temperature concerns and the turbulence concerns might be overcome experimentally.

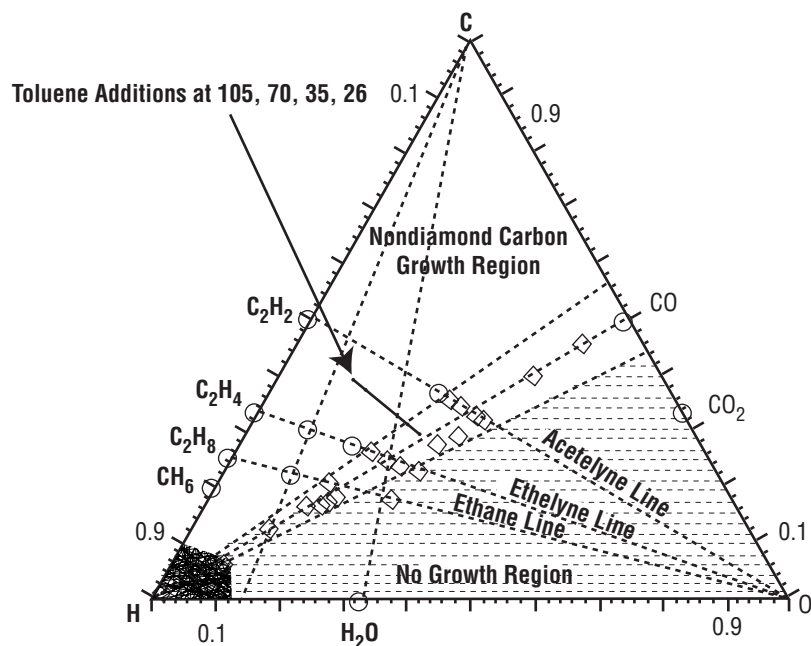


Figure 226. Plot of  $C_7H_8$  experiment on Bachmann diagram.

## 5.11 Relevance of Proposed Mechanism to Prior Literature

It is necessary that any mechanism proposed should be supported by the current experimental work as well as the bulk of the previous experiments in the literature. The following discussion attempts to address most of the concerns and highlights strong experimental support from other works, although it is by no means comprehensive. Looking first, systematically, at the proposed mechanism of diamond nucleation in an  $O_2$ - $C_2H_2$  torch, relevant literature is noted in conjunction with the portion of the proposed mechanism to which it is relevant.

### 5.11.1 Gas-Phase Nucleation/Stabilization of the Diamond Phase

In the  $O_2$ - $C_2H_2$  torch, embryonic nucleation of the diamond occurs in the gas phase. Carbon nucleates in flame and picks up growth species that stabilize the diamond form in the secondary flame front. The diamond form is stabilized at high temperatures by the acquisition of growth species. Diamond surfaces are normally terminated by  $H_2$ ; however, at 1,000 °C they lose this layer and can begin to reconstruct.<sup>6</sup> At very small sizes, because of an energetic advantage due to surface energy, diamond is the more stable form of C. This means that diamond is the preferred form for C at the sizes appropriate for germination.

In 1967, Homann<sup>72</sup> presented a strong treatise on the formation of C in premixed flames. In this work, he treats the behavior of the unmistakable formation of C (soot) in  $C_2H_2$  flames. As a very simple starting point, the nucleation of diamond in the gas phase can be taken from the obvious nucleation of soot and the energetic preference of diamond for small-sized particles developed by Nuth.<sup>307</sup> Homann states that carbon formation in flames start when the first yellow or orange luminosity is observed by eye. He also suggests that C formation is inhibited by OH concentrations. Relative to my tip experiments, he notes that 10 times more soot was produced in flat laminar flames than in turbulent flames. For my experiment, this corresponds to the low output of diamond in the turbulent slow flames present in the torch modification experiments. Homann also notes that in all measurements, the first phase of particle growth to the {100} orientation is extremely rapid.

Matsui et al.<sup>74</sup> showed that the bright, nonluminous feather formed in  $O_2$ - $C_2H_2$  flames exactly corresponds to the range of diamond formation. The formation of a bright, nonluminous feather in the work of Matsui, with creative interpretation, supports the nucleation of diamond germs in the gas. Just as C particles produce a luminous cone, diamond, due to its more difficult oxidation, might well produce the bright, nonluminous feather noted. Matsui et al.<sup>74</sup> also note that the growth rate is determined by mass transport and so sticking probability will be important. Interpreting this with the proposed mechanism, the sticking probability is actually the stabilization probability of germs on the substrate surface, and the mass transport that determines the growth rate is the germ mass transport.

Tseng et al.<sup>361</sup> demonstrated that when using alternating periods of growth and etching in a laminar flame, better phase purity is obtained with higher cycling frequencies. This strongly supports the proposed mechanism through the following interpretation. As all forms of C nucleate and deposit in the gas and stabilize on a diamond surface, brief etching periods will preferentially remove the nondiamond forms. The higher cycling frequency can be seen as producing the highest continual flux of diamond germs toward the surface while never allowing nondiamond nuclei to have any opportunity to stabilize or become trapped on the surface. The higher temperature flames have been found to suppress the formation of soot.

Although not noted, this is because the additional energy in the system is readily disrupting the sp<sup>1</sup> and sp<sup>2</sup> bonds typically found in soot. The sp<sup>3</sup> bonds required for diamond formation are more likely to survive as the flame temperature rises.

Lee et al.<sup>362</sup> produced conditions where CH<sub>3</sub> radicals were separated from H and the gas-phase environment was unreactive until they came within a few mean free paths of the surface by using a supersonic free jet of CH<sub>3</sub> radicals. They were able to grow diamond quite well on seeded substrates, but no diamond nucleation was observed. Their experiments provide strong support in that their lack of nucleation is predicted by the current mechanism. This lack of nucleation could be predicted due to the inhibition of gas-phase reactions. Machlin<sup>363</sup> suggests that the role of H may be to promote the sp<sup>3</sup> bond configuration on C clusters and to maintain this configuration on surface clusters.

Vitkavage et al.<sup>364</sup> produce films where they mention that the residence time of their CH<sub>4</sub> is too low to allow any gas-phase polymerization to occur. Their results seem to support gas-phase nucleation in that the published Raman spectroscopy data, from the sample for which they claim diamond, show no diamond peak. Rather, their data show a microcrystalline graphite peak for the conditions produced for their films. The current mechanism would indeed predict the Raman results presented for the conditions where insufficient residence time for gas-phase nucleation was permitted. Badziag<sup>309</sup> presents an analysis based on the experimental work of Deryagin and Feedosev.<sup>5</sup> Relevant to the current work, he mentions that homogeneous nucleation is possible in a supersaturation layer that is adjacent to the growing crystal surface.

### 5.11.2 Etching and Destabilization of Created Nuclei

As the formed diamond embryo passes into lower temperature regions of the flame, the surface reconstruction is stabilized by H<sub>2</sub>. Growth of these embryos to a diamond nucleus requires sufficient H and a sufficient surface roughness. As C atoms agglomerate, sufficient H must be available to saturate a critical percentage of the embryo surface in order for continued stable growth to occur. In the O<sub>2</sub>-C<sub>2</sub>H<sub>2</sub> torch, the embryo will survive only in specific flame regions. Outside of the survival regions, the etching conditions or the addition of too much C will destroy the stability of the diamond form. Most likely, this occurs by either the removal of H<sub>2</sub> by excess O<sub>2</sub> or by too much C being present to allow stabilization by the available H<sub>2</sub>. Matsui et al.<sup>74</sup> specifically note that higher hydrocarbons are detected in the feather but disappear in the intermediate zone.

Using an alternate approach to emission intensity measurement, Cappelli and Paul<sup>76</sup> localized the C<sub>2</sub> and CH radicals at the feather boundary while OH radicals are found primarily in the intermediate zone. The passage into the intermediate zone by the diamond nuclei is where the proposed mechanism redefines the diamond nuclei created previously as germs. These nuclei are capable of completely regressing into constituents.

Homann,<sup>72</sup> in his work on C formation in flames, notes that particles <100 nm have almost disappeared at a height of 50 nm above the flame. This corresponds to work by Snail and Craige<sup>80</sup> where they have determined that diamond is present only when the flame feather is near or over the surface. These papers demonstrate that a diamond nuclei formed outside of this region becomes a germ when entering because of the destructive effect of the flame radicals at this position.

An investigation by Frey et al.,<sup>198</sup> using an upward directed  $O_2$ - $C_2H_2$  torch, showed a strong variation of morphology with radial position on the substrate. They relate this to the gas-phase composition. Within the proposed mechanism, the nucleation density of germs or the amount of etching due to  $O_2$  species from the ambient will vary with radial position. Thus, the growth rate (germ incorporation) in the regions will vary, providing different morphologies. In their work, they anticipate the effects of buoyancy, due to the propagation of their system against gravity.<sup>198</sup> Clearly, if buoyancy effects are present, they would be most pronounced on a gas-phase nucleation system.

Belton et al.,<sup>347</sup> in a plasma system, noted that diamond nucleation and growth were able to be controlled by  $O_2$  content. With decreasing  $O_2$  content, diamond did not nucleate or grow, grew only, or nucleated and grew. The proposed mechanism relates this to the aggressiveness of the etchant prior to surface accommodation of diamond nuclei. For low  $O_2$  content, we could expect nucleation and growth. With higher  $O_2$  content and greater gas-phase etching, we could expect small germs suitable for growth but too small to remain stable on the substrate. Finally, for high  $O_2$  content, germ formation is completely suppressed, resulting in no nucleation or growth.

Wang et al.,<sup>93</sup> in their work with large area deposition using an  $O_2$ - $C_2H_2$  flame, provided Ar shielding for the primary flame and the flame feather. The Ar shielding was provided to eliminate  $O_2$  attack of the diffusion flame surrounding the  $C_2H_2$  feather. By interpreting this in terms of the proposed mechanism, many of the OH and O species present that attack the diamond nuclei as they pass from the nucleation region of the feather toward the substrate are basically removed. This should increase the number of diamond nuclei present. If the flame temperature is kept high to prevent the formation of C or soot nuclei, the additional nuclei will provide a larger area for diamond growth. Wang et al.<sup>93</sup> note that the deposition area increases by a factor of 2.

### 5.11.3 Surface Stabilization of Nuclei

Once a diamond germ has passed through the etching region of the flame, it makes contact with the surface where it may be accommodated. Germs, at this point, may experience growth on the surface to become nuclei or they may fail to maintain the diamond configuration. A surface can provide an energetic advantage to nucleation for a given volume of a condensed phase by reducing the area multiplier for a given interface free energy contribution. In the literature where zero nucleation rates are observed, usually in the later stages of growth, these interpretations are due to germ or embryo capture by diamond surfaces on which nucleation is not detected, treated as a twin formation (most likely), or the germ is incorporated into the crystal and does not become a nucleus.

In the paper where Rau and Picht<sup>325</sup> present  $C_2H$  as a growth species, they use Mo substrates in a microwave plasma reactor with cones in the substrates produced by placing indents in the substrate backside. The tips of these cones show noticeably higher nucleation and growth rates. In support of the proposed mechanism, they note that the substrate temperature is nearly the same at the center of a cone as around it. The cone tip sees a larger spherical angle of the gas phase. If the current mechanism holds for plasma systems, the nuclei would (as other plasma species) approach the surface through diffusion such that a greater number of nuclei would indeed deposit on the cone structures.



Spitsyn et al.,<sup>365</sup> in their review covering diamond and diamond-like film, note that a substantial factor in the formation of diamond-like films is the quenching by the substrate of the metastable C forms. The quenching of C forms is an analogous way of looking at the stability of germs or nuclei on the surface. The proposed mechanism, in a parallel fashion, stresses the importance of substrate temperature. Spitsyn also considers, in the deposition of diamond without concurrent formation of other forms of C, that the controlling variable is the time of formation of either graphite or diamond nuclei. He proposes that the lack of a requirement to reorient will favor the production of diamond. This approach is well supported by the current proposed mechanism in that, with germ formation in the gas phase, both the sticking probability and the surface stability will favor the formation of diamond and again favor the production of diamond from a time-of-formation approach.

Summing over individual bond energies, Machlin<sup>363</sup> calculated the free energy of substrate graphite and substrate diamond systems. He found that for a diamond substrate, any graphite-bonded cluster of two atoms or more will gain in stability by transforming to the diamond structure. His results demonstrated that the deposit surface-interface energy controls the stability in the early stages of growth. If the embryo, upon contact with the substrate, gains enough energy to reorient, then the surface onto which the diamond embryos are sent will significantly impact the morphology and the existence of the C/diamond film that results.

Muranaka et al.,<sup>366</sup> in considering CO-based plasma systems, noted a sharp increase in the nucleation density and a worsening of the film quality as the substrate temperature fell below 406 K. They also noted that the ratio of peak intensities for diamond to a-C significantly increased over the same range. They attribute this to polyacetylene formation at low substrate temperatures. As the surface temperature falls, the ability to stabilize any form of C improves and the competition for surface stabilization begins to favor nondiamond C species.

A number of researchers have presented mechanisms for controlling the initial stable nucleation sites of diamond typically on Si substrates in CVD systems. Diamond does not stick to Si well because of the higher surface energy of diamond ( $6 \text{ J cm}^{-2}$ ) compared to Si ( $1.5 \text{ J cm}^{-2}$ ).<sup>297</sup> DeNatale et al.<sup>367,368</sup> used a proprietary photoresist that inhibited stabilized nucleation sites. Nuclei were observed first on the edges between the photoresist and the uncovered Si and then on the uncovered Si. Narayan and Chen<sup>369</sup> used a laser patterning method where regions of a diamond-prescratched substrate were protected from laser annealing. Diamond nuclei were found to be stable only in the protected regions.

In none of the above studies was diamond nucleation found to occur without diamond pretreatment of the substrate before patterning. Ramesham and Ellis,<sup>370</sup> however, provide pyramids with exposed Si apexes. The pyramids are surrounded by  $\text{SiO}_2$  and nuclei are noted only on the bare Si. They also show results for diamond-pretreated and nondiamond-pretreated samples. Most relevant to this work is the demonstration of selective area deposition using  $\text{SiO}_2$  masking in an  $\text{O}_2\text{-C}_2\text{H}_2$  torch system.<sup>371</sup> They use a pretreatment to inhibit a  $\text{SiO}_2$  layer from forming, thus improving their nucleation density. Their work strongly demonstrates the absence of stable nuclei where  $\text{SiO}_2$  has grown. The proposed mechanism shows us that diamond nuclei should be easier to stabilize on a Si surface with C rather than on an oxidized Si surface.

#### 5.11.4 Further General Mechanism Discussion

The current mechanism explains some of the difficulty that has been found in producing single-crystal epitaxial films. In the high rate processes, there are a large number of nucleation centers constantly under construction in the gas phase when the chemistry is such that sufficient  $H_2$  is available to stabilize the gas-phase surfaces. Zhimeng et al.<sup>372</sup> added  $H_2$  to an  $O_2$ - $C_2H_2$  flame to modify the concentration of C atoms in the flame. They were primarily concerned with improvements in diamond quality provided by the additional surface etching of the  $H_2$ ; however, they mention that the addition will also stabilize the diamond phase. The large number of nucleation centers precludes single-crystal growth. In the case where the conditions are changed so that gas-phase nucleation of all C forms is possible, excess C is formed and deposited. If there is enough  $H_2$  so that diamond is going to form or grow in this environment, diamond embryos will form on the edges of surface structures. Again, the situation of many such surface sites, being available through the nature of the deposition, provides multiple nucleation sites, precluding single-crystal growth.

Using a rationale proposed by Feedosev, consider that a diamond phase of several nanometers in size may be due to the Laplace pressure inside a small structure. This pressure can attain the level of several gigapascals. In the torch system, the highest temperature is attained near the location of the largest pressure drop. The diamond melting temperature decreases with a drop in pressure.<sup>373</sup> As C passes through this region, the formation of melted diamond becomes favored as the next step in an Ostwald progression. Then this progresses, based on the small particle size, into diamond nuclei.

Nuth<sup>307</sup> proposes a stability reversal between diamond and graphite relative to particle size, where at very small particle sizes, diamond becomes the stable phase of C and is correspondingly preferred over graphite. Because of the larger number of less dense graphite particles occupied in one mole of C when compared to the smaller number of diamond particles for the same mole of C, the diamond surface will be the stable form of C. Nuth<sup>308</sup> shows that, because of the larger number of less dense graphite particles needed to contain one mole of C, the surface free energy of diamond does not actually need to be smaller than that of graphite for diamond to be more stable. He notes that it can be, in fact, larger because of the difference in density and the quantity of surfaces per molecule.

#### 5.11.5 Support of Singly Terminated Diatomic Carbon as the Primary Precursor to Diamond

The simulation results suggest that  $C_2H$  may be the species initially responsible for nucleation. Singly terminated  $C_2$  bonds the strongest with a diamond surface. This means the  $H_2$  abstraction, proposed by Frencklach et al., used in the first stage of  $C_2H_2$  bonding, is not necessary. Singly terminated  $C_2$  may directly displace a surface  $H_2$  and, once replaced, it has the highest probability of remaining. In a recent study of C-H bond disassociation energies, Curtiss and People<sup>374</sup> have calculated that the  $C_2H$  neutral molecule has the minimum C-C bond distance (1.180) for any of the  $C_2H_2$ -based neutrals or ions.

Rau and Picht<sup>325</sup> present a simulation that my work may support. Using a combination of simulation and experiment, they compare deposition profiles of diamond films against assumptions of C-containing active (for growth) species. The best fit to their data arises from the use of  $C_2H$  as the growth species. In their simulation, they let each hydrocarbon in the gas phase be assumed to incorporate into the growing

crystal. They use a deposition coefficient of 0.1 from their microwave plasma experimental work. Other species such as  $\text{CH}_3$  and  $\text{C}_2\text{H}_2$  do not agree with either the observed layer thickness or the temperature and pressure dependencies. Unlike other microwave work, for the conditions used in their experiments, the gas phase approaches equilibrium. They attribute this to the higher pressure at which they operate. In defense of  $\text{C}_2\text{H}$  as a growth species, they note that  $\text{C}_2\text{H}$  is the most strongly bound species on a diamond surface. Singly terminated  $\text{C}_2$  is stronger than H,  $\text{CH}_3$ , or  $\text{C}_2\text{H}_2$ .  $\text{C}_2\text{H}$  should displace  $\text{H}_2$  from the surface and, once bonded, remain.

## 6. CONCLUSIONS

In summary, this work presents a mechanism for the nucleation of diamond in the combustion flame environment. A series of six experiments and two associated simulations provide results from which the mechanism was derived. A substantial portion of the prior literature was reviewed, and data and conclusions from previous experimenters were found to support the proposed mechanism. The nucleation mechanism builds on the work of previous researchers but presents an approach to nucleation in a detail and direction not fully presented heretofore.

Diamond produced using an  $O_2$ - $C_2H_2$  torch on the surface of any number of substrates is the result of germ or embryo formation in the gas phase. Germs and nuclei are, by definition, pseudostable. The significant contribution of this work is the identification of the gas phase as the controlling environment for the initial formation steps leading to nucleation. Identification of the species formed in the gas phase as germs is perhaps slightly misleading. The traditional explanation of germ formation to nuclei formation to growth of nuclei assumes a spatial location with a consistent environment. The  $O_2$ - $C_2H_2$  torch system presents a path through a series of environments, through which hydrocarbon-precursor species pass. The motion of the species from stable regions into etching flame regions rapidly places previously formed nuclei into a position where continued growth or survival is in question. Because of the transient nature of diamond nuclei stability, I have elected to use the nomenclature of germs to describe the initial precursors to stable diamond nuclei. In brief, this may be because, although under formation conditions, the diamonds formed may be stable nuclei. They must also pass through additional gas-phase conditions and additional surface stability conditions before they are capable of growth. Only nuclei that may no longer regress (or progress) into alternate forms may be awarded the status of nuclei. A stepwise progression of the mechanism path has been presented.

Strong support for the mechanism has been noted in prior literature. In the  $O_2$ - $C_2H_2$  torch, embryonic nucleation of the diamond occurs in the gas phase. Gas-phase nucleation has been proposed as mentioned by several authors.<sup>179,303–307</sup> Carbon nucleates in flame and picks up growth species which stabilizes the diamond form in the secondary flame front. The diamond form is stabilized at high temperatures by the acquisition of growth species. At very small sizes, because of an energetic advantage due to surface energy, diamond is the more stable form of C. This means that diamond is the preferred form for C at the sizes appropriate for germination. The nucleation of diamond in the gas phase can be taken from the obvious nucleation of soot and the energetic preference of diamond for small-sized particles developed by Nuth.

Some of the strongest supporting work for diamond nucleation in the gas phase is a result of evidence from Nuth.<sup>307</sup> He proposes a stability reversal between diamond and graphite relative to particle size. At very small particle sizes, diamond becomes the stable phase of C and is correspondingly preferred over graphite. This argument is predicated on differences between the molar volume for diamond and the molar volume for graphite. Because of the larger number of less dense graphite particles occupied in one mole of C, when compared to the smaller number of diamond particles for the same mole of C, the surface diamond will be the stable form of C. The calculation of Nuth is based on a similarity of surface free energy

of diamond and graphite based on the assumption of a  $\pi$ -bonded C layer surface for diamond. The above calculation allows for the preferred stability of diamond, even if the surface free-energy of diamond is slightly higher than that of graphite.<sup>307</sup>

In a related paper, Nuth<sup>308</sup> again holds diamond to be more stable at small particle sizes  $<50$ , but given that the surface free-energy values numerically contain a large uncertainty, he performs a calculation wherein he shows that because of the larger number of less dense graphite particles needed to contain one mole of C, the surface free-energy of diamond does not actually need to be smaller than that of graphite for diamond to be more stable. He notes that it can be larger because of the difference in density and the quantity of surfaces per molecule. Looking at the density approach by Nuth and using the rationale proposed by Feedosev, a diamond phase of several nanometers in size may be more stable due to the Laplace pressure inside such a small structure. This pressure can attain the level of several gigapascals.

In an approach with similar results, Badziag et al.<sup>309</sup> provide a theoretical H/C for the stability crossover between diamond and graphite. Their results are based on calculated heats of formation of various C cluster sizes where specific energies were assigned to the C-H and C-C<sub>tetrahedral</sub> bonds used in creation of the clusters. Predictably, they arrived with two bands of values—tetrahedral and hexagonal molecules. Small tetrahedral molecules were shown to be more stable than small hexagonal molecules until a specific crossover value of the H/C (surface terminating H<sub>2</sub> atoms/tetrahedral or hexagonal C atoms). When the H/C is plotted against the binding energy, the sp<sup>3</sup> (tetrahedral) molecules have a negative slope and the sp<sup>2</sup> (hexagonal) molecules have a slope near zero. They performed particle size calculations based on their calculated critical H/C. The calculations gave a critical particle size of  $\approx 3$  nm where the tetrahedral and hexagonal structures are of equal heats of formation (i.e., where diamond and graphite particles of equal size are equally stable).

Frencklach et al.<sup>310</sup> present evidence for homogeneous nucleation of diamond powder in the gas phase in a microwave plasma reactor. In their experiments, diamond was nucleated in the plasma and collected downstream on filter paper. The diamonds were nucleated in dichloroethylene or dichloromethane O<sub>2</sub> flames, typically a blue conical flame. They noted the formation of cubic diamond, lonsdalite, and 6H-hexagonal diamond. Howard et al.<sup>312</sup> confirm that particle size is primarily determined by the reaction time.

As the formed diamond embryo passes into lower temperature regions of the flame, the surface reconstruction is stabilized by H<sub>2</sub>. The growth of this embryo to a diamond nucleus requires sufficient H and a sufficient surface roughness. As C atoms agglomerate, sufficient H must be available to saturate a critical percentage of the embryo surface in order for continued stable growth to occur. In the O<sub>2</sub>-C<sub>2</sub>H<sub>2</sub> torch, the embryo will survive only in specific flame regions. Outside of the survival regions, the etching conditions or the addition of too much C will destroy the stability of the diamond form. Cappelli and Paul<sup>76</sup> localized the C<sub>2</sub> and CH radicals at the feather boundary with OH radicals found primarily in the intermediate zone. The point where the proposed mechanism redefines the diamond nuclei, created previously as a germ, is the passage into the intermediate zone by the diamond nuclei.

Homann,<sup>72</sup> in his work on C formation in flames, notes that particles  $<100$  Å in size have almost disappeared at a height of 50 nm above the flame. This corresponds to work by Snail et al.<sup>80</sup> where they

have determined that diamond is present only when the flame feather is near or over the surface. These papers demonstrate that a diamond nuclei formed outside of this region becomes a germ when entering because of the destructive effect of the flame radicals at this position. An investigation by Frey et al.,<sup>198</sup> using an upward-directed  $O_2$ - $C_2H_2$  torch, showed a strong variation of morphology with radial position on the substrate. They relate this to the gas-phase composition. Within the proposed mechanism, the nucleation density of germs, or the amount of etching due to  $O_2$  species from the ambient, will vary with radial position and thus the growth rate (germ incorporation) in the regions will vary, providing different morphologies. In their work, they anticipate the effects of buoyancy, due to the propagation of their system against gravity.<sup>198</sup> Clearly, buoyancy effects are most pronounced in a gas-phase nucleation system.

Once a diamond germ has passed through the etching region of the flame, it makes contact with the surface where it is accommodated. At this point, germs may experience growth on the surface to become nuclei or may fail to maintain the diamond configuration.

The current mechanism explains some of the difficulty that has been found in producing single-crystal epitaxial films. In the high rate processes, there are a large number of nucleation centers constantly under construction in the gas phase when the chemistry is such that sufficient  $H_2$  is available to stabilize the gas-phase surfaces. The large number of nucleation centers precludes single-crystal growth. In the case where the conditions are changed so that gas-phase nucleation of all C forms is possible, excess C is formed and deposited. If there is enough  $H_2$  so that diamond is going to form or grow in this environment, diamond embryos will form on the edges of surface structures. Again, the situation of many such surface sites being available through the nature of the deposition provides multiple nucleation sites, precluding single-crystal growth.

In the current series of experiments, the GAMoly experiment looked at changing the gas precursor species while retaining the atomic proportions required for diamond growth. In many cases, the films show various densities of pillaring. Considering the proposed mechanism when graphite, a-C, and diamond are all simultaneously depositing from the gas phase, pillaring is a natural result of fewer initial diamond nucleation sites at the onset of film growth. For each of the samples, the substrate material and the surface temperature were constant. If the amount of etchant changes in the gas phase, the result will be slow film growth or lower grade films; however, pillaring is not caused by etching. Restated, when a diamond nucleus (germ) approaches the surface with sufficient energy and lands on a graphite or C surface, it may reorient in favor of the existing structure. The same is true when it lands near a diamond nucleation site. Thus, the surface sites that are diamond may remain so. Typically, pillaring is avoided when other nucleation or other C forms are avoided in the gas phase. Diamond is, of course, etched more slowly than other forms of C, and this makes diamond more stable in the environment of the surface gas-phase species. However, pillaring is controlled by the number of nuclei of each C form impacting the surface.

The addition of  $CH_4$  into the precursor gases was responsible for pillaring the films. Surface mobilities of the substrates are unchanged in that surface temperatures of the substrates remain within identical bounds of the other samples. The clear case of  $CH_4$ -dependent pillaring is explained using the parallel computer simulation. The simulation shows that the effect of  $CH_4$  is to strongly lower the flame temperature. This is relevant considering the well-known suppression of soot formation in higher temperature flames. As soot (graphite and a-C) is suppressed from nucleation in the flame, the fraction of diamond



nuclei present correspondingly rises and the surface is more completely covered with diamond nucleation sites. When other nuclei are present in the gas phase, notably soot, they cover a significant percentage of the substrate surface inhibiting the growth and stability of diamond nuclei.

Carbon monoxide is the most stable constituent in the flame at the operating temperatures. It does not appear to be a primary precursor to diamond nucleation or diamond growth. The observed effect of CO addition on nucleation was to suppress nucleation and growth of diamond. Several effects of CO show reduced diamond content in the films and in the crystals, although the total fraction of C, H<sub>2</sub>, and O<sub>2</sub> was still within the appropriate regions for diamond growth. AFM surface roughness data provide a reasonable look at the suppression of nucleation by CO. The surface finish data were taken on crystal surfaces that were open to the nucleation environment and generally parallel to the substrate surface. These surfaces were measured as an independent measure of the instantaneous nucleation environment. Data show clearly that CO softens {111} faces, whereas CH<sub>4</sub> does not. It is possible to explain this within the proposed framework as slowing the deposition of germs onto a growth/nucleation surface. This would smooth the surface by providing fewer new layer nucleation sites for growth.

The simulation results, parallel to the GAMoly experiment, showed that the effect of CO addition is strongest on entropy of gas, enthalpy of gas, and a strong decrease of C<sub>2</sub>H fraction. This is perhaps the primary support of C<sub>2</sub>H as the diamond precursor. CO decreases the C<sub>2</sub>H fraction and also decreases the fraction of C<sub>2</sub>H<sub>2</sub> present. The rise in diamond linewidth closely parallels the reduction in C<sub>2</sub>H as a function of CO addition. The enthalpy and the entropy of the flame did not show interaction between the process gases.

The gas flow and substrate experiment changed the conditions on the surface of the sample by increasing the gas flow rate while remaining on a consistent point of the CHO diagram, and by changing the carbide potential of the substrate. Increasing the flow rate increases the number of germs present on the surface. This in turn decreases the distance a surface species needs to travel to form or add to a growing nucleus. The ability of the surface to retain appropriate nucleation sites for diamond was controlled with carbide potential. When a-C and graphitic nuclei arrive at the surface along with diamond, they present a surface appropriate for diamond nucleation or one appropriate for continued graphitic nucleation. The proposed mechanism suggests that the strongest substrate effect will be found in comparisons between C-phase peak intensities. The cooperative effect noticed in the peak ratio and the linewidth results are explained well with the proposed mechanism. Without the effect of high flow (low flow condition), the ratio of the peaks gets worse as the carbide potential increases, because the surface better stabilizes more forms of C nuclei. However, when the flow rate increases, the growth conditions favor those substrates that best stabilize diamond relative to other forms of C and the higher carbide potential substrates provide stronger diamond to other C peak ratios.

Because of the high solubility of C in Cu, reviewers have noted that the surface cannot passivate and C is expected to continuously diffuse into the substrate. Looking at the proposed mechanism, diamond is seen at the high flow rates on Cu because diamond absorbs less readily into the substrate than does C or graphite—so diamond germs that land on the substrate are left behind more readily than germs from other forms of C. In the low flow condition, C of all forms reorients and desorbs into the substrate. No forms a stable carbide, and by the proposed mechanism at deposition temperatures, the surface will passivate. It

passivates most readily with C and graphite nuclei or radical desorbed species. Diamond nuclei will stabilize most readily on the surface when sufficient C flow is present to passivate the surface. SiC does not require passivation, already being in the carbide form. All forms of C are stable on SiC so that all forms of C deposit. According to the proposed mechanism, quality of diamond improves with flow rate because the samples are in a diamond growth environment.

The two tip modification experiments looked at the behavior of gas phase nucleation by modifying the shape and behavior of the flame plasma in which the diamond nucleation is suspected to occur. The experiments perform a verification function by duplicating, on a reduced scale, one of the previous experiments. In each case, the tip experiment demonstrated an effect due to the tip modification and an effect that correlates to the results from previous work. The tip effects were seen most clearly in the tip/substrate experiment. In the tip gas experiment, both the gas addition and the modification to the tip negatively affect the gas nucleation environment so that data from grown diamond is weak, negative, or nonexistent.

The width of the diamond line increases when the change is made to the modified torch tip. Looking at the effects of the tip modification, the flow is separated into at least three separate regions of flow transport. The first is a region corresponding to the stoichiometric combustion of torch gases. The second is an intermediate region termed the flame feather that is composed of excess reaction products engaged in combustion. The third is a diffusion flame region in which combustion occurs using  $O_2$  that diffuses into the flame region from the surrounding atmosphere. The previously described modification to the torch tip produces a slower flame and a reduction in the transient pressure spike due to expansion at the nozzle exit. Slower gas flow from the flame provides better mixing of initial and intermediate zones because the combustion speed has not changed. Better mixing near the flame feather introduces OH and O etchants from the intermediate region which destroy diamond and graphite nuclei. The better mixing of regions will occur because the species present in the combustion reaction remain in the combustion zone for a longer period. This provides more etching species in the primary feather. Looking at the proposed mechanism, more etching species in the flame feather will decrease the probability of nucleation in this region and fewer diamond nuclei will result. This will result in a lower grade diamond film due to carbide formation on the surface from the hydrocarbon species that are able to nucleate on the surface.

The difficulty provided by the better mixing on nucleation of diamond in the gas phase also may be seen in the diamond-to-microcrystalline graphite peak and the diamond-to-a-C peak. In both cases, the ratio of diamond to C is seen to decrease with both an increase in carbide capacity of the substrate and with the modification of the tip. The carbide capacity decrease is expected as above, based on the previous experiment, and the tip modification is shown to decrease gas-phase nucleation.

Diamond nucleation and growth is impractical at this point using  $C_3H_6$  as the fuel gas-phase precursor. The appropriate C-to-etchant ratio is not economical or practical. Toluene addition to the HVOF flame produced, at best, graphite deposition. Both of the samples displaying graphite samples were grown in the nondiamond growth region. Several factors may explain the lack of diamond on our substrates. The first supposition is substrate temperature. The experimental temperatures provided so much thermal energy that all stable diamond embryos were completely desorbed. A second possibility may well be the flame turbulence. Diamond growth has not been reported in gas streams with the high flow rates that were prevalent in our experiments. The presence of nondiamond C is encouraging in its adherence to the Bachmann

diagram. It would appear that both the temperature concerns and the turbulence concerns might be overcome experimentally.

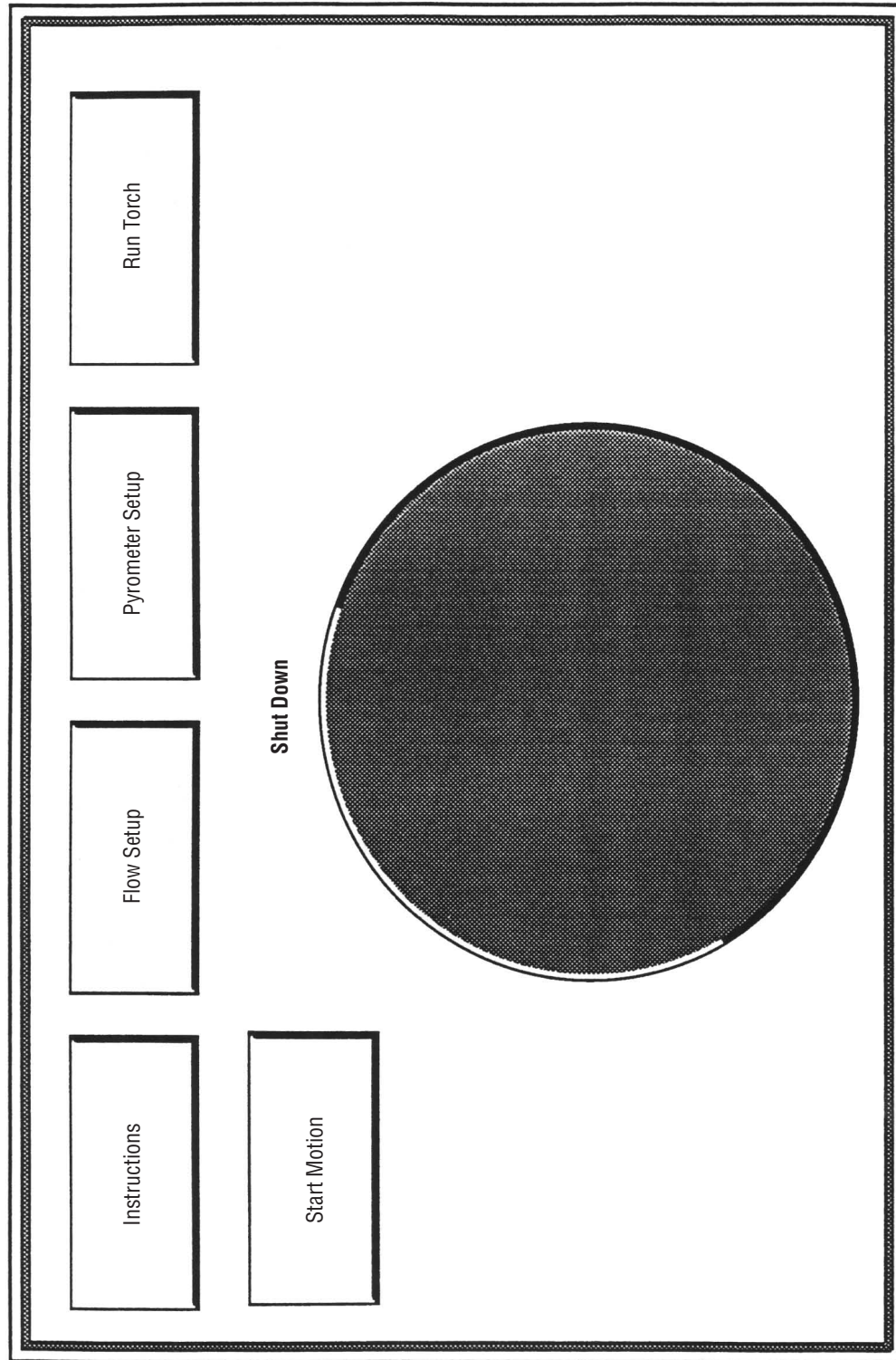
Although occurrences of hexagonal diamond are not strongly noted in the Raman spectra, it should be noted that the Raman response of lonsdalite is much less than that of cubic diamond. Indications of hexagonal diamond are important in that the prior work with gas-phase nucleation in plasmas typically demonstrates a significant amount of hexagonal diamond.

In support of  $C_2H$  as the primary precursor to diamond, simulation results suggest that  $C_2H$  may be the species initially responsible for nucleation. Singly terminated  $C_2$  bonds the strongest with a diamond surface. This means the  $H_2$  abstraction, proposed by Frencklach et al., used in the first stage of  $C_2H_2$  bonding, is not necessary. Singly terminated  $C_2$  may directly displace a surface  $H_2$  and, once replaced, it has the highest probability of remaining. In a recent study of CH bond disassociation energies, Curtiss and People<sup>374</sup> have calculated that the  $C_2H$  neutral molecule has the minimum CC bond distance (1.180 Å) for any of the  $C_2H_2$ -based neutrals or ions.

Rau and Picht<sup>325</sup> present a simulation that compares deposition profiles of diamond films against assumptions of C containing active (for growth) species. The best fit to their data arises from the use of  $C_2H$  as the growth species. In their simulation, they let each hydrocarbon in the gas phase be assumed to incorporate into the growing crystal with a deposition coefficient, from their microwave plasma experimental work, of 0.1. Other species such as  $CH_3$  and  $C_2H_2$  do not agree with either the observed layer thickness or the temperature and pressure dependencies. Unlike other microwave work, for the conditions used in their experiments, the gas phase approaches equilibrium. They attribute this to the higher pressure at which they operate. In defense of  $C_2H$  as a growth species, they note that  $C_2H$  provides stronger bonds to the diamond surface than H,  $CH_3$ , or  $C_2H_2$ . Singly terminated  $C_2$  should displace  $H_2$  from the surface and once bonded, remain.

Although it was not a focus of this work to identify the species responsible for nucleation or growth, simulation results suggest that  $C_2H$  may be the species initially responsible for nucleation. Methane is shown to slightly increase the fraction present in the gas and greatly increase the levels of  $C_2H_2$  present. Assuming that the beneficial effects of  $CH_4$  are not due to etching when comparing  $CH_4$  and  $C_2H_2$ , the slightly beneficial result noted for the early stages of the quadratic behavior shown for  $CH_4$  addition, the results correspond much more closely to the increase in  $C_2H$  than the drastic increase noted in  $C_2H_2$ .

## **APPENDIX—ALGORITHM FLOW DIAGRAMS AND BLOCK DIAGRAMS**



Block Diagram

Figure 227(a). Alto system setup.

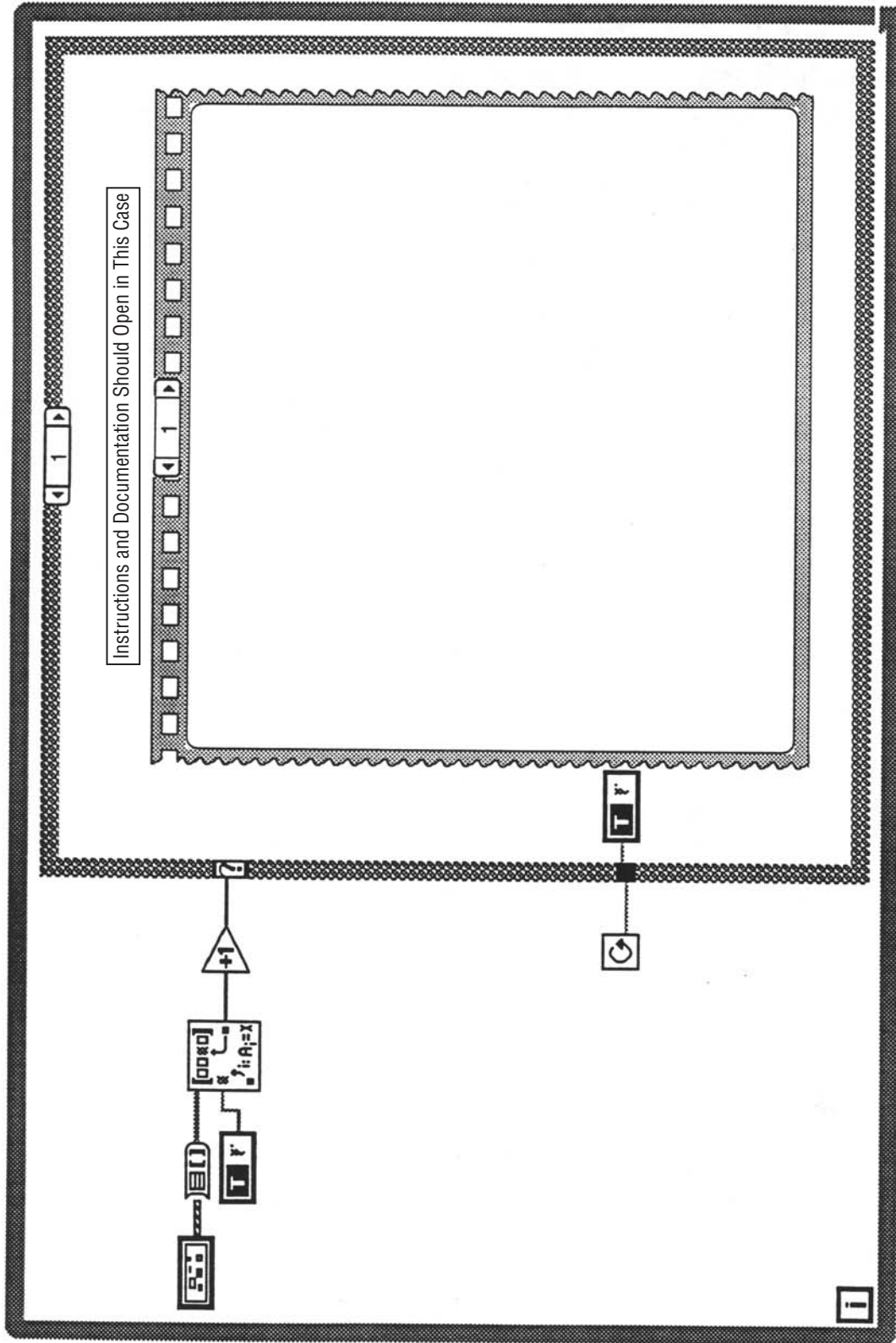


Figure 227(b). Alto system setup.



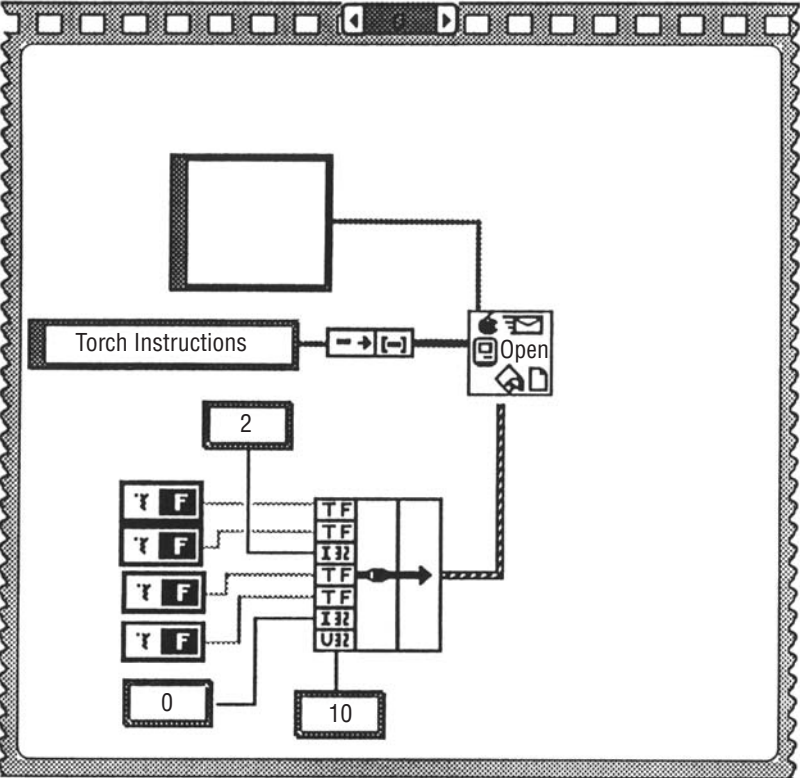


Figure 227(c). Alto system setup.

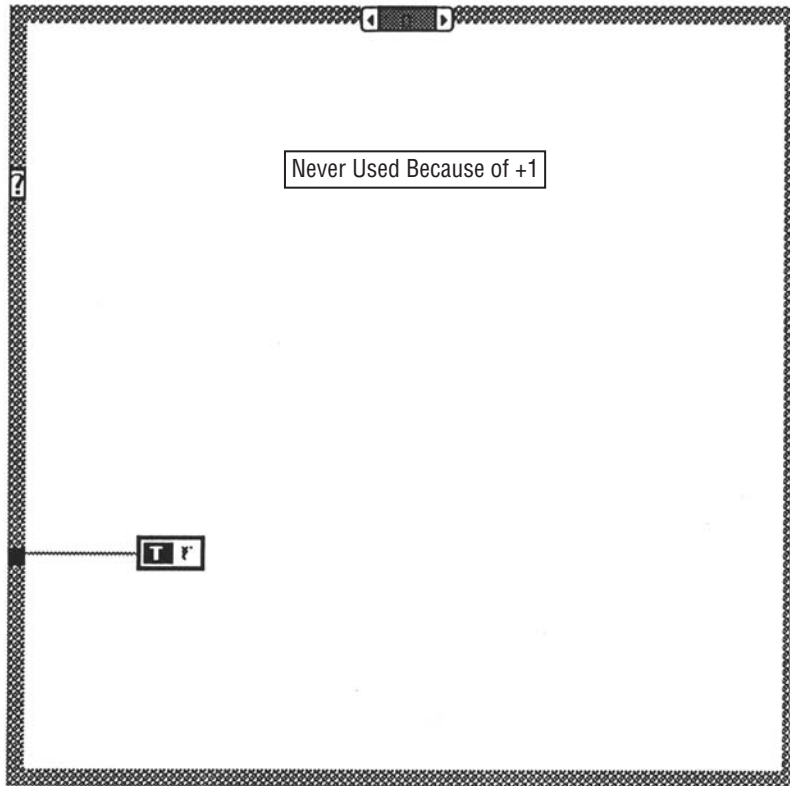


Figure 227(d). Alto system setup.

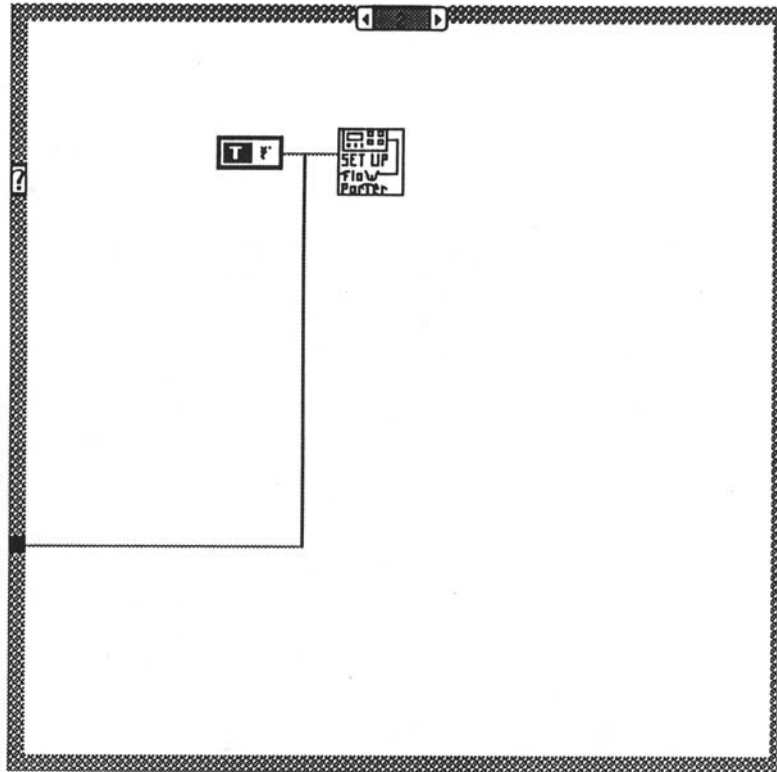


Figure 227(e). Alto system setup.

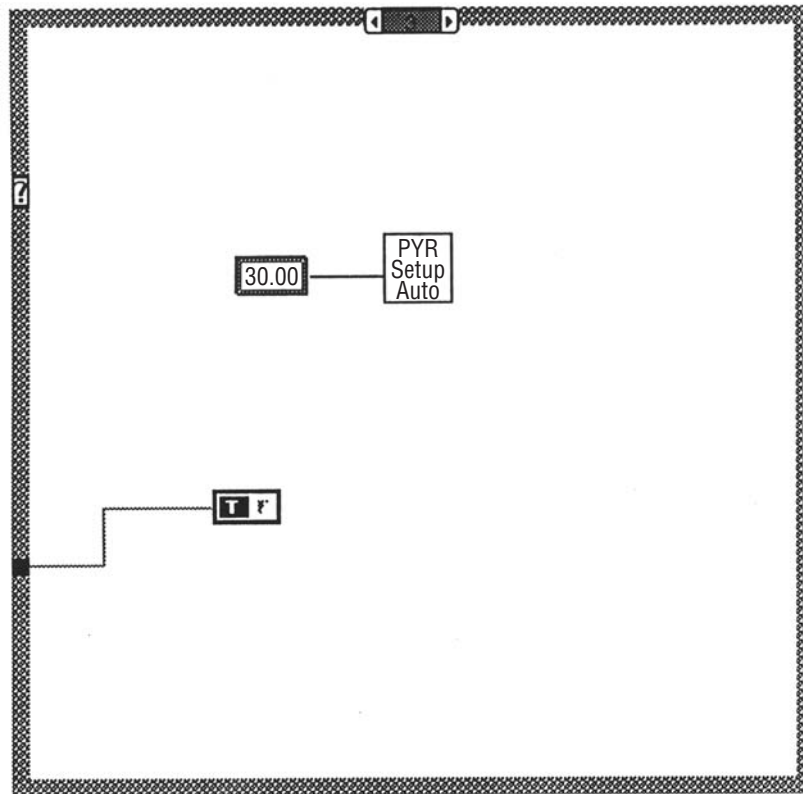


Figure 227(f). Alto system setup.

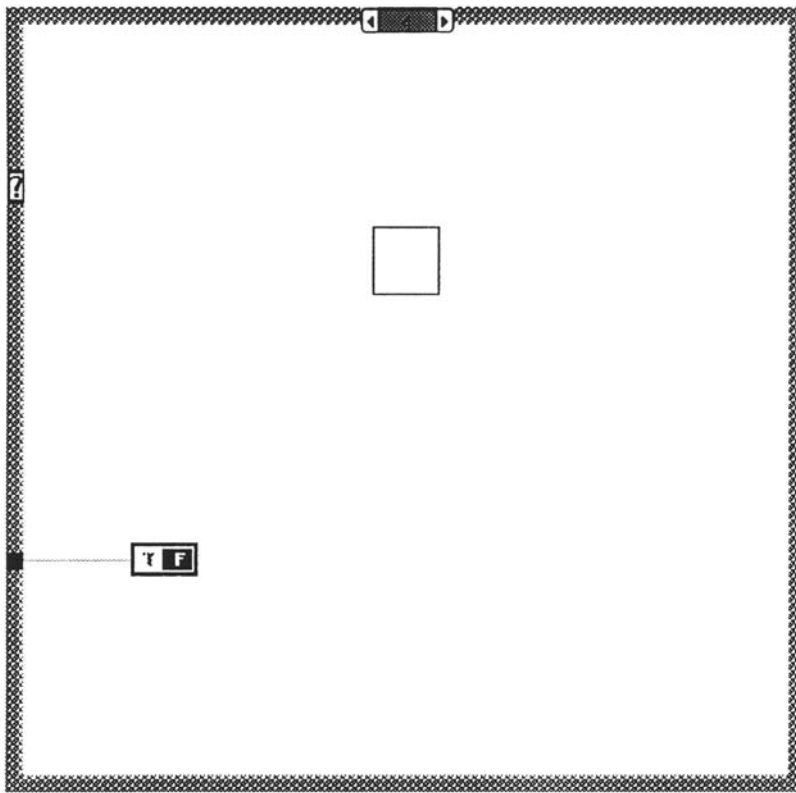


Figure 227(g). Alto system setup.

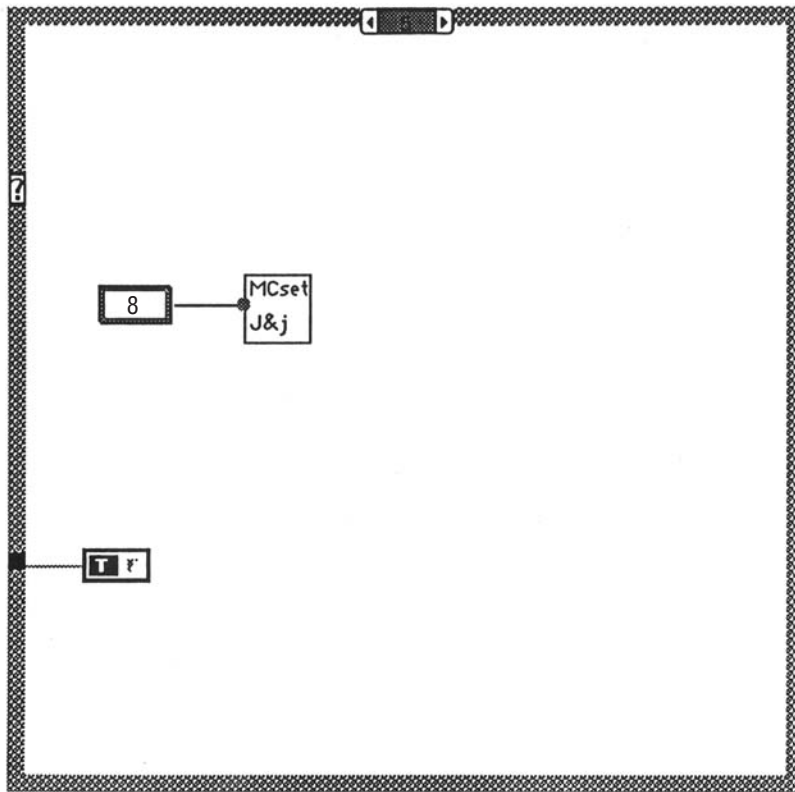


Figure 227(h). Alto system setup.



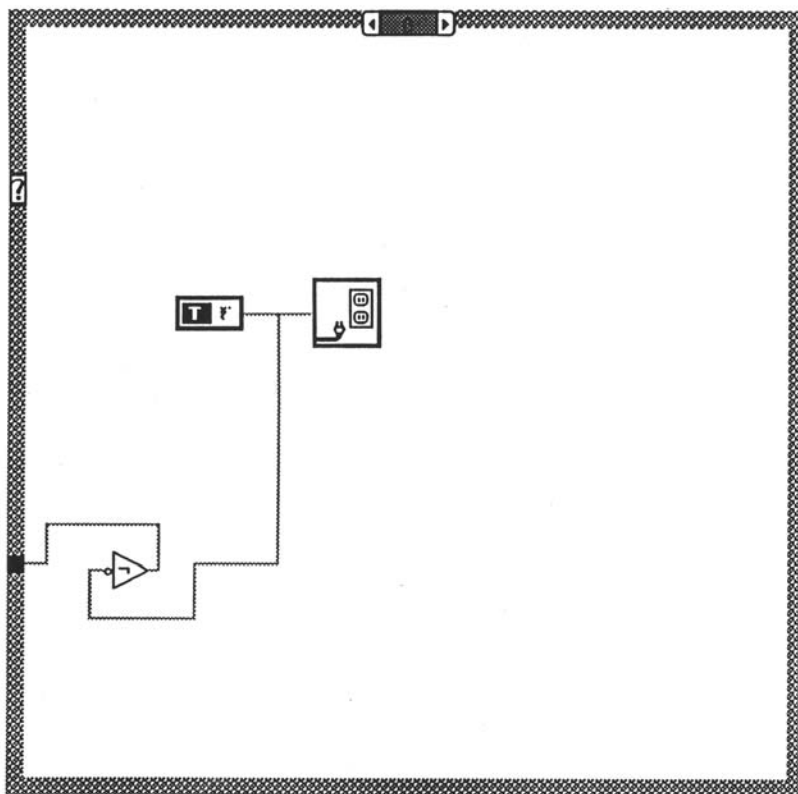
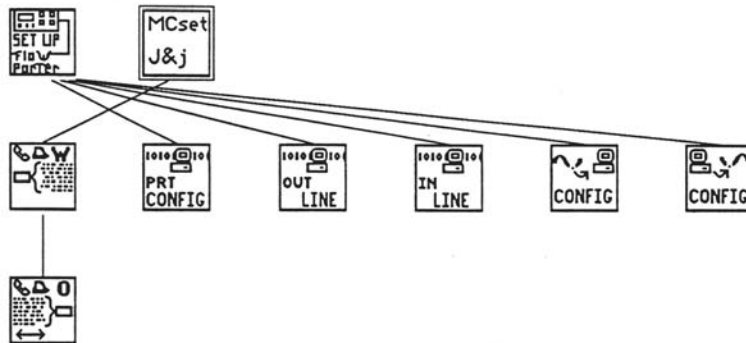
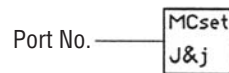


Figure 227(i). Alto system setup.

Position in Hierarchy

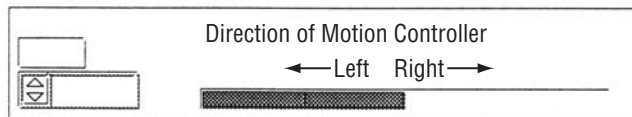


Connector Pane



Motion Controller Setup

Front Panel



Block Diagram

Figure 228(a). Motion controller setup.

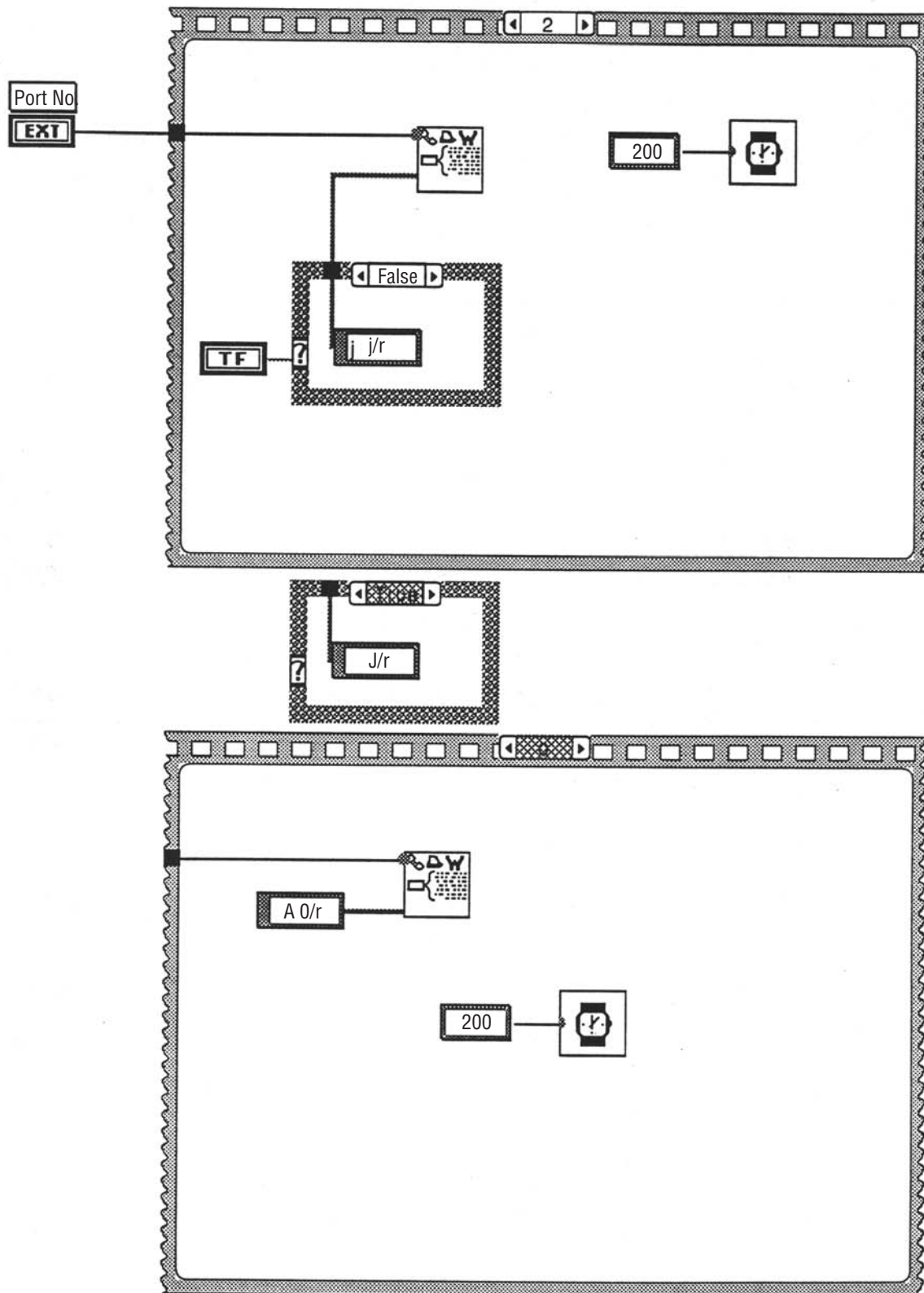


Figure 228(b). Motion controller setup.

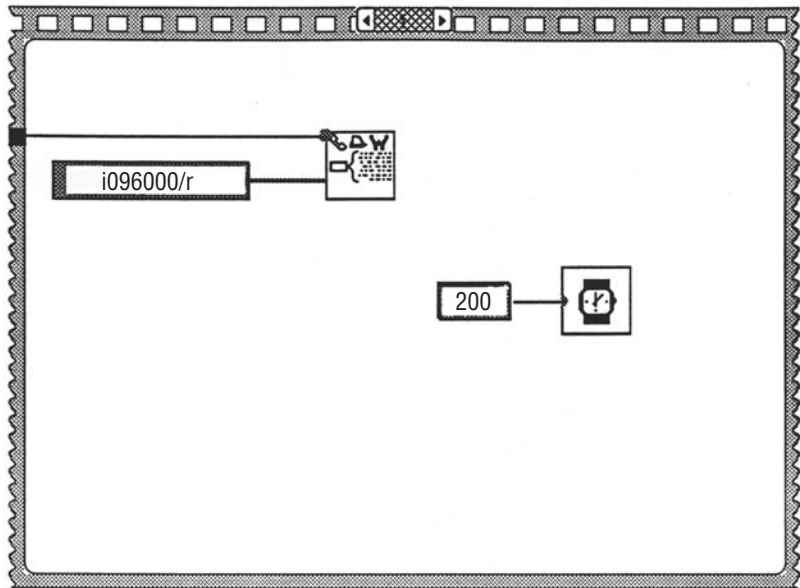
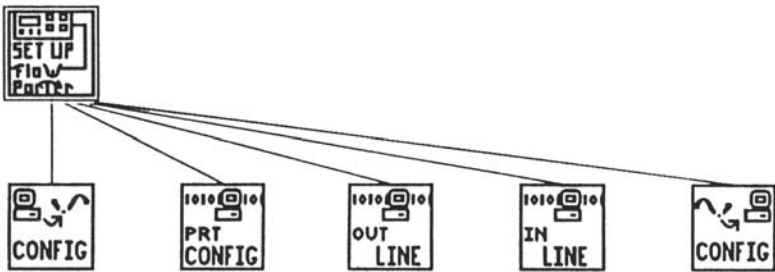


Figure 228(c). Motion controller setup.

Position in Hierarchy



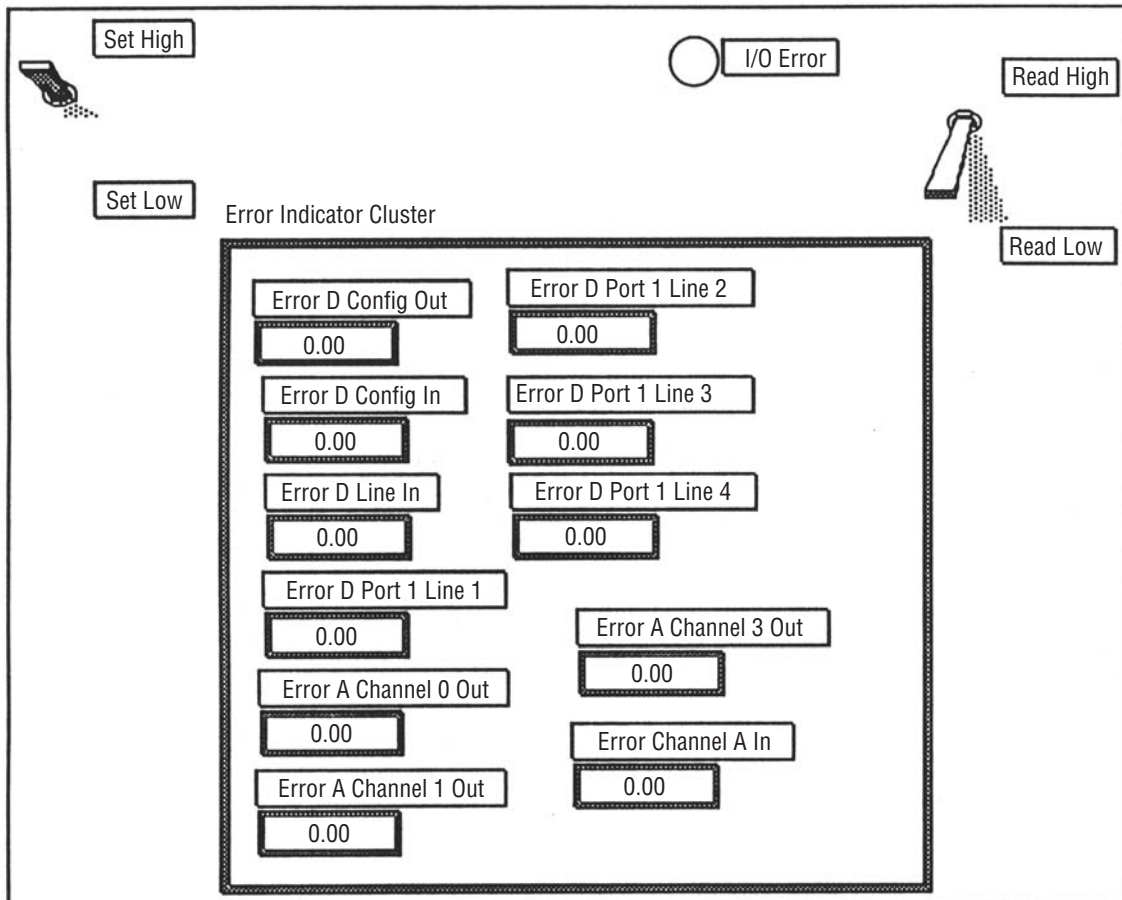
Connector Pane



Setup Remote Control for Copy

Front Panel

Figure 229(a). Setup remote control for copy.



Block Diagram

Figure 229(b). Setup remote control for copy.

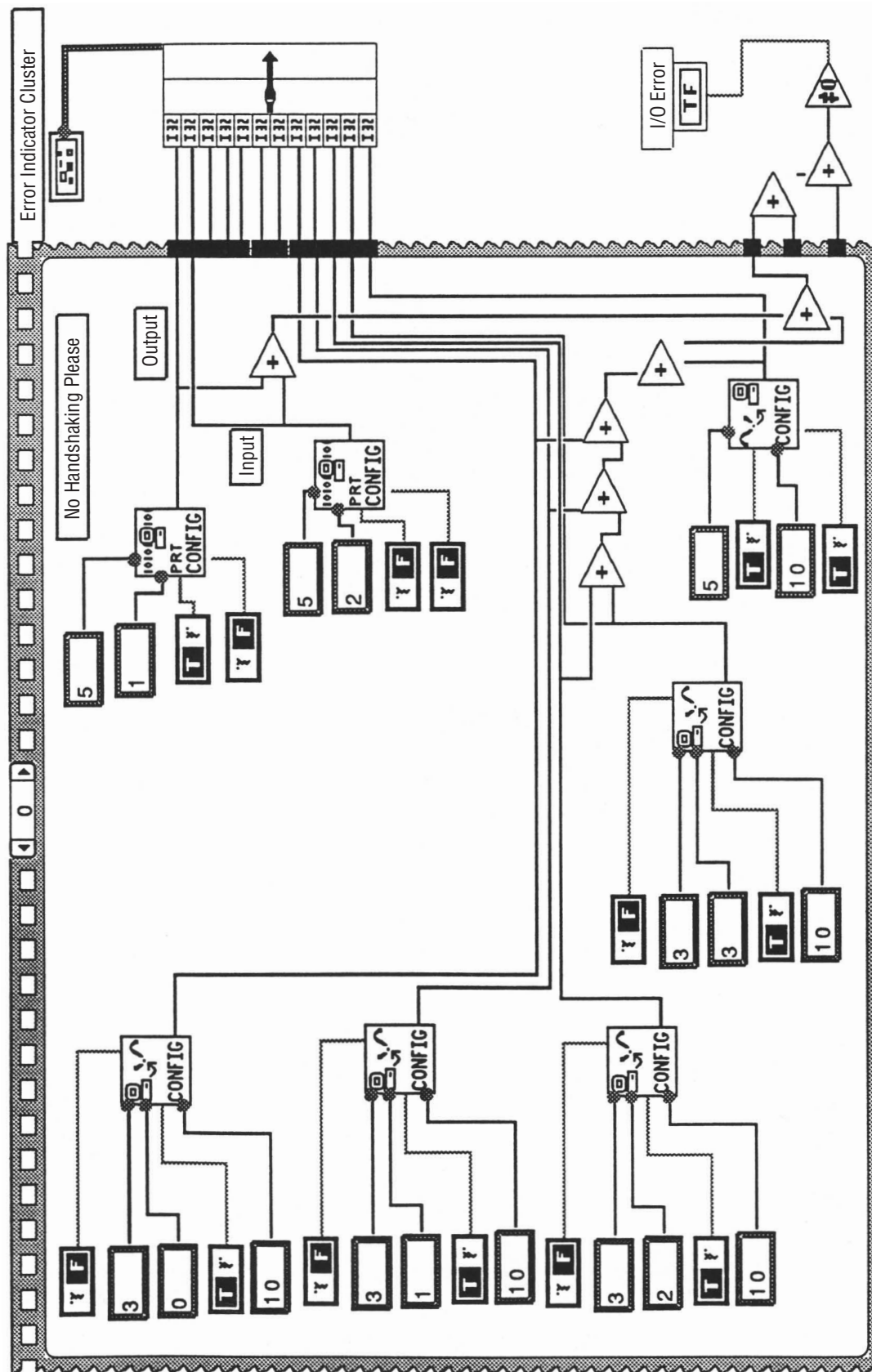


Figure 229(c). Setup remote control for copy.



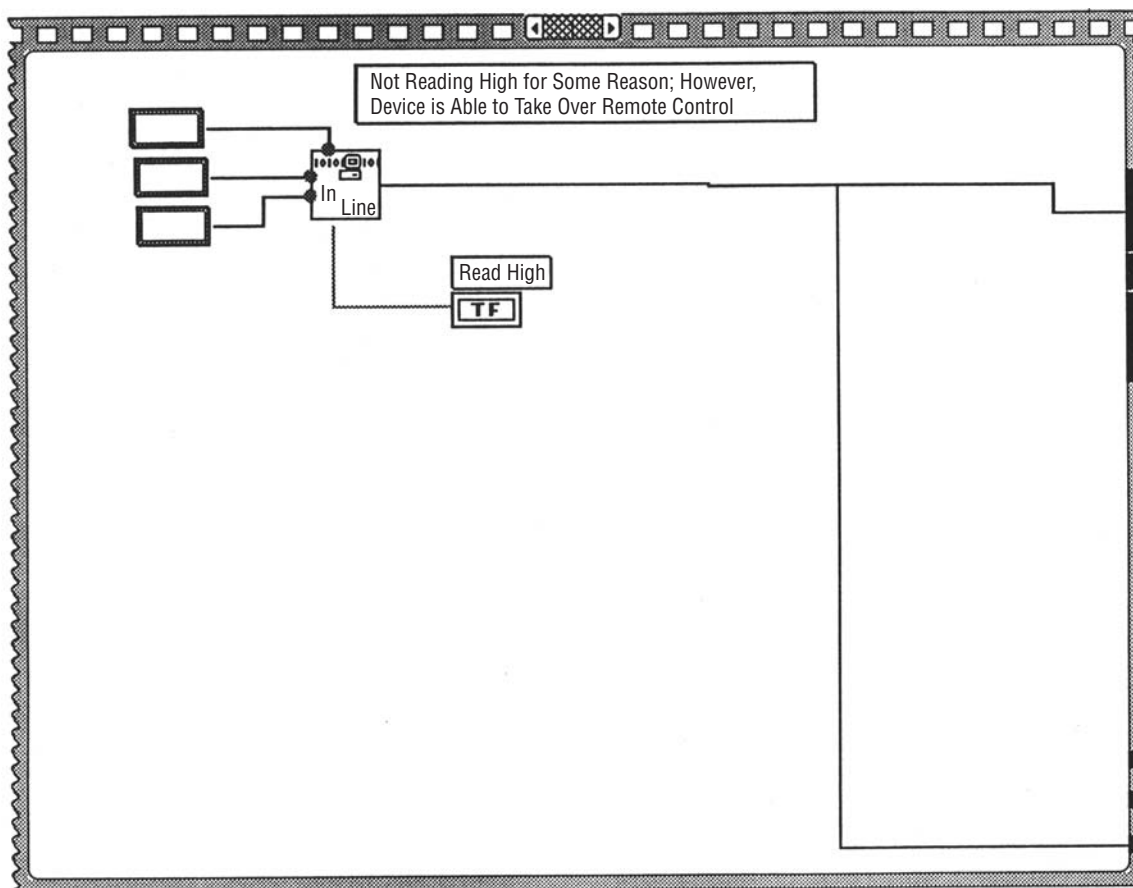


Figure 229(d). Setup remote control for copy.

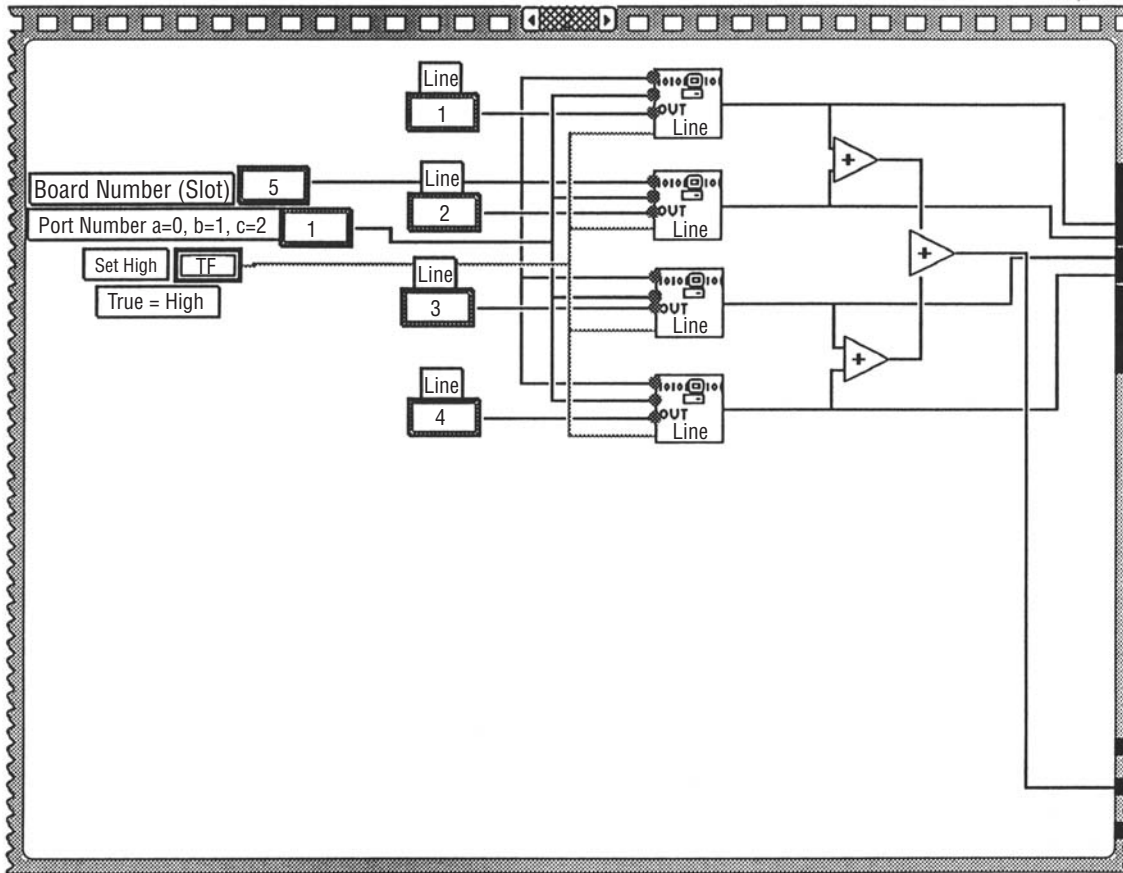
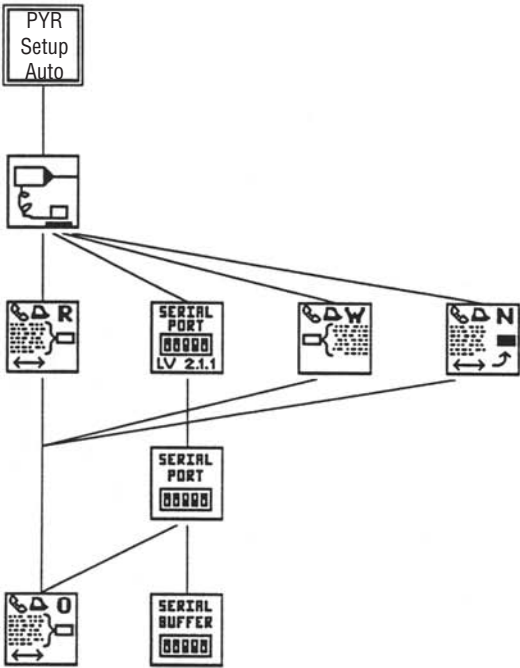


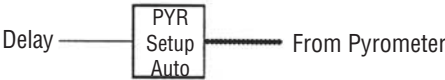
Figure 229(e). Setup remote control for copy.



Position in Hierarchy



Connector Pane



Pyrometer Auto Setup

Front Panel

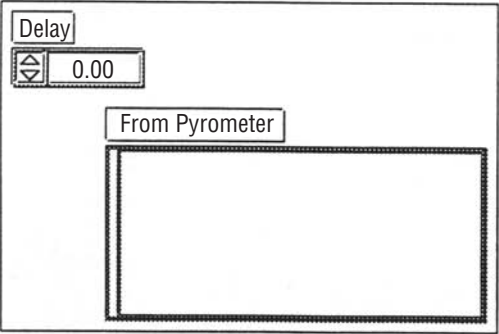


Figure 230(a). Pyrometer auto setup.

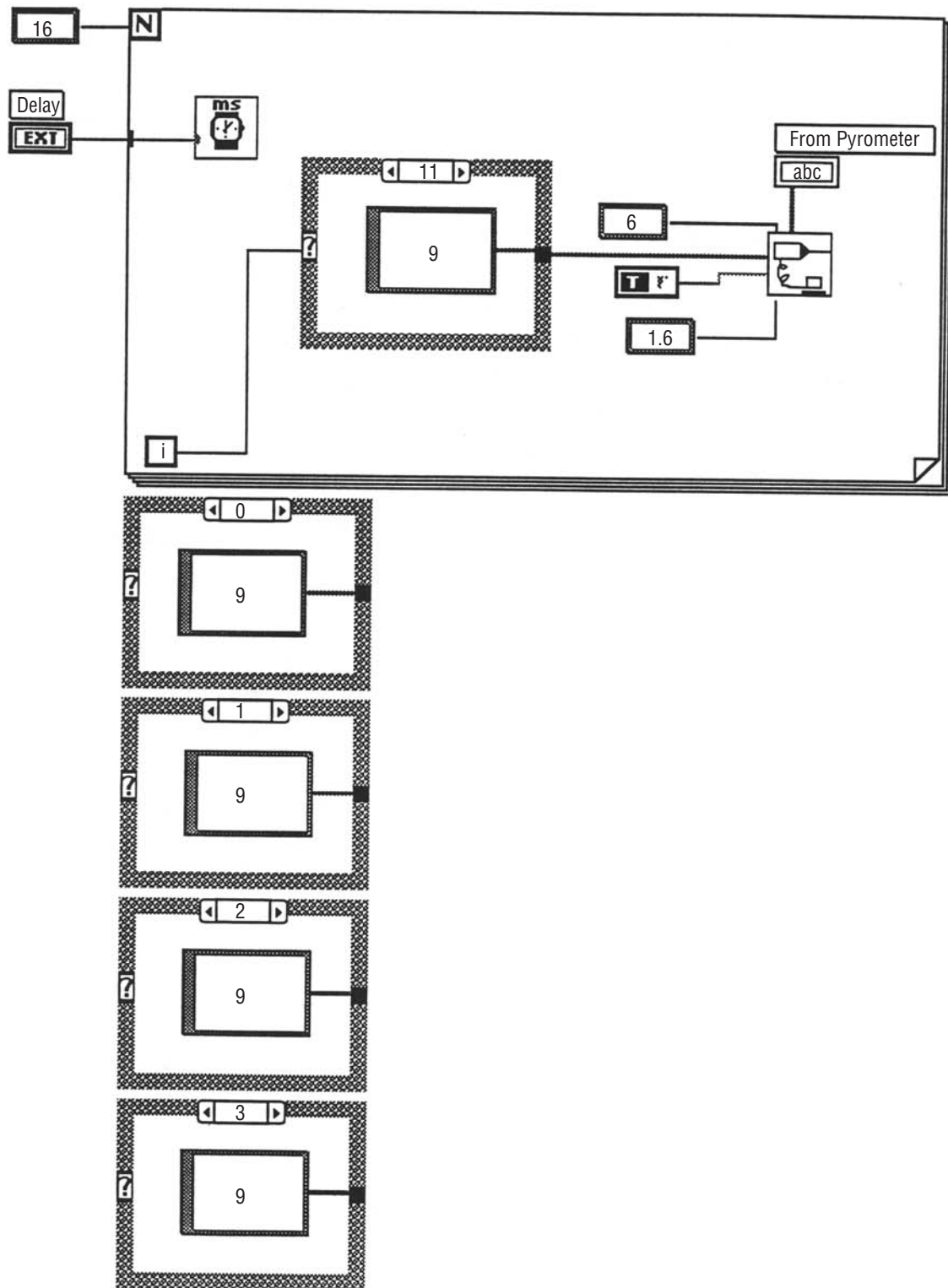


Figure 230(b). Pyrometer auto setup.

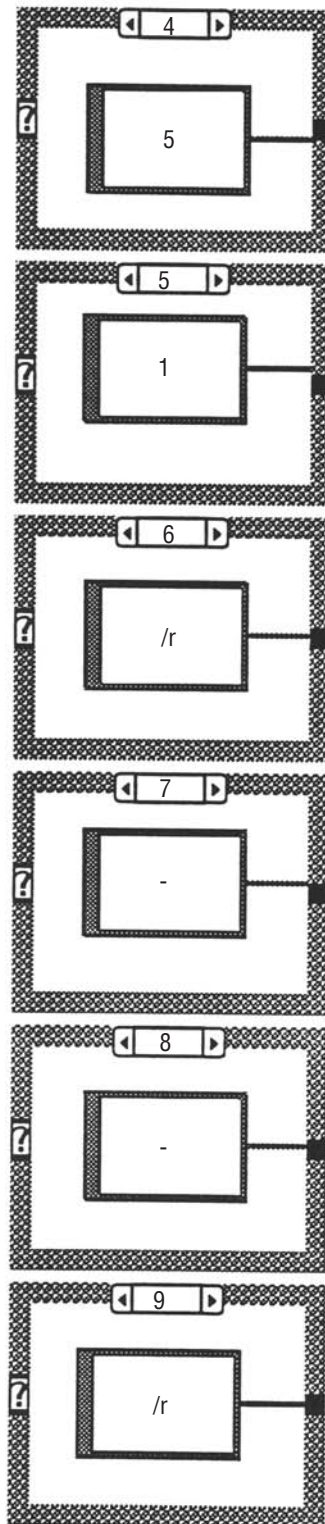


Figure 230(c). Pyrometer auto setup.

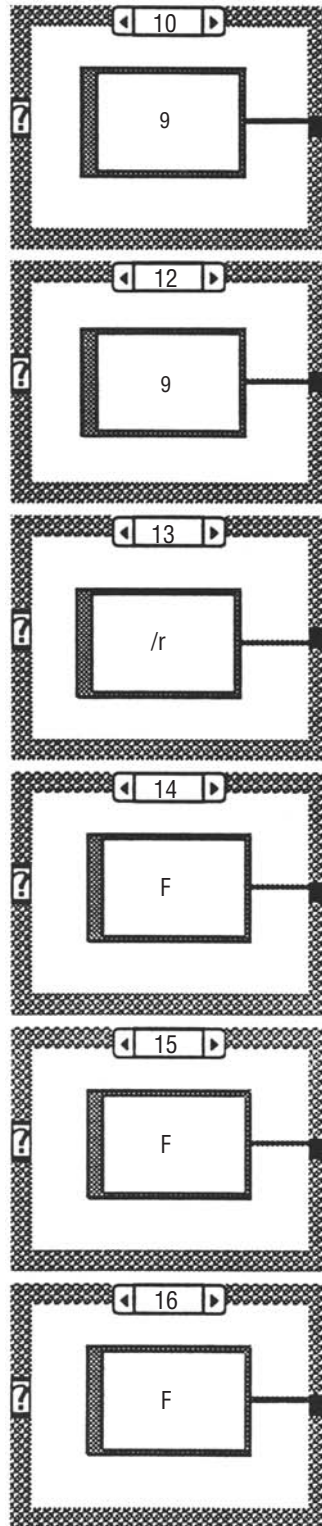
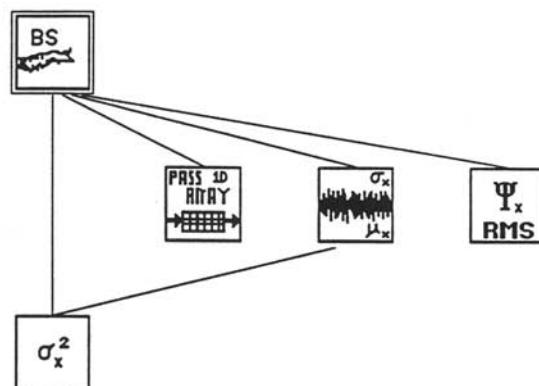


Figure 230(d). Pyrometer auto setup.

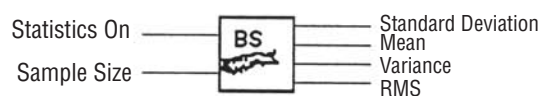




Position in Hierarchy



Connector Pane



Basic Statistics

Front Panel

Statistics On ☐

Sample Size

Standard Deviation

Mean

Variance

RMS

Block Diagram

Figure 231(a). Basic statistics.

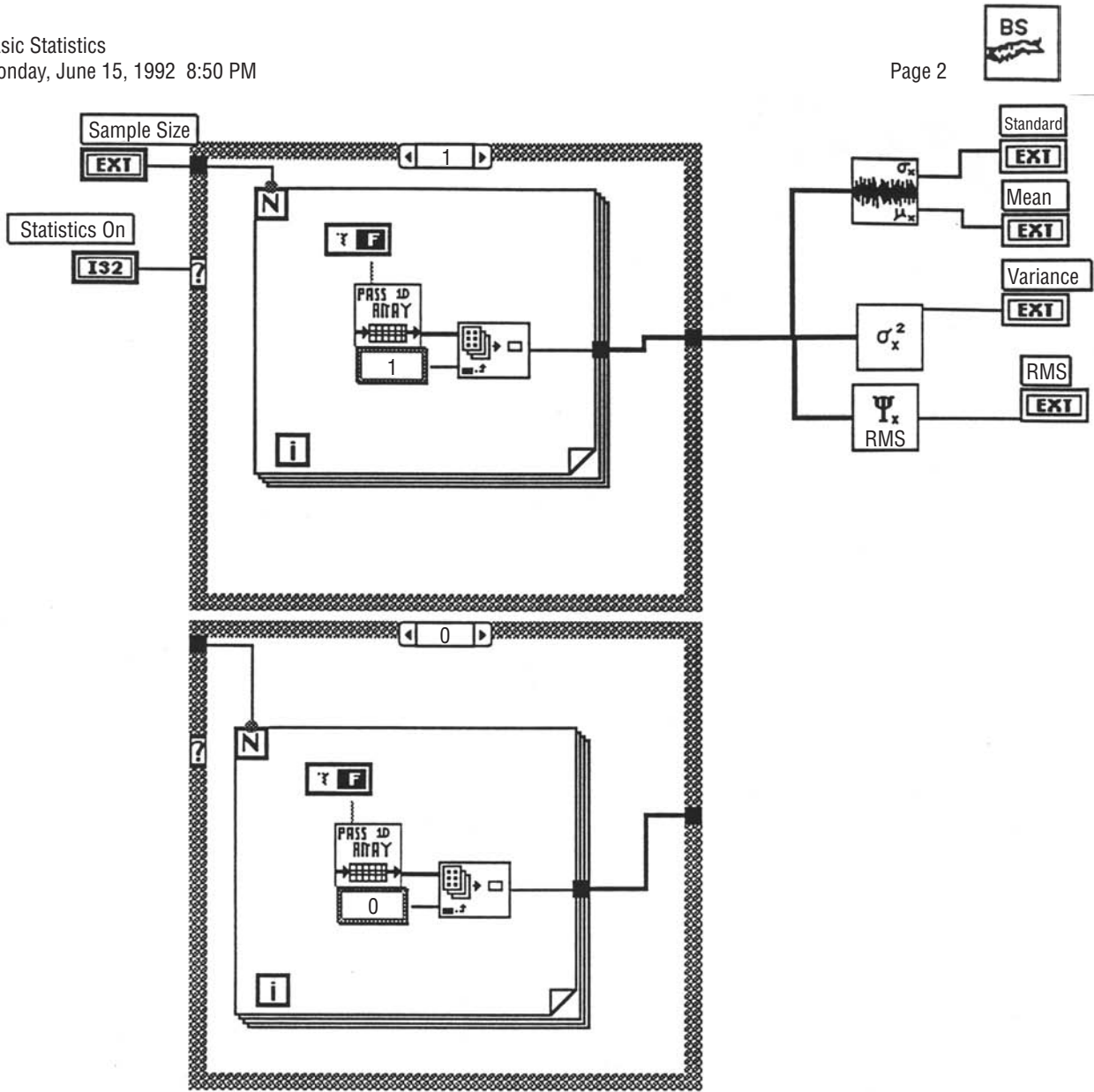


Figure 231(b). Basic statistics.

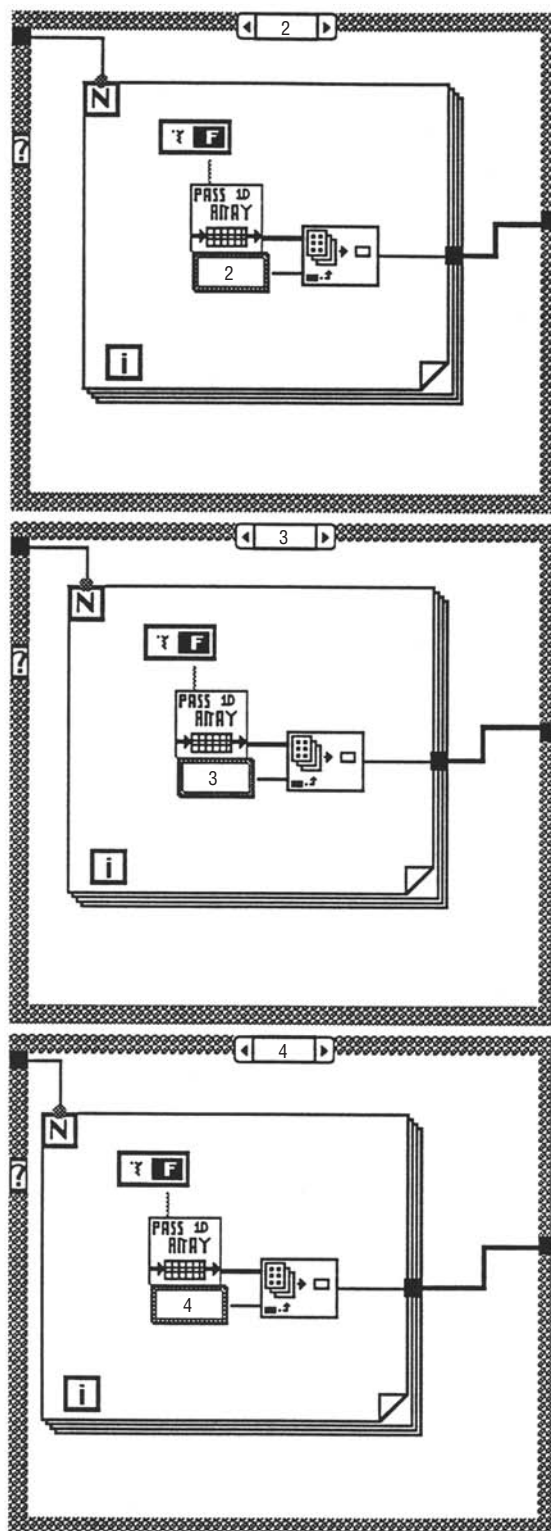


Figure 231(c). Basic statistics.

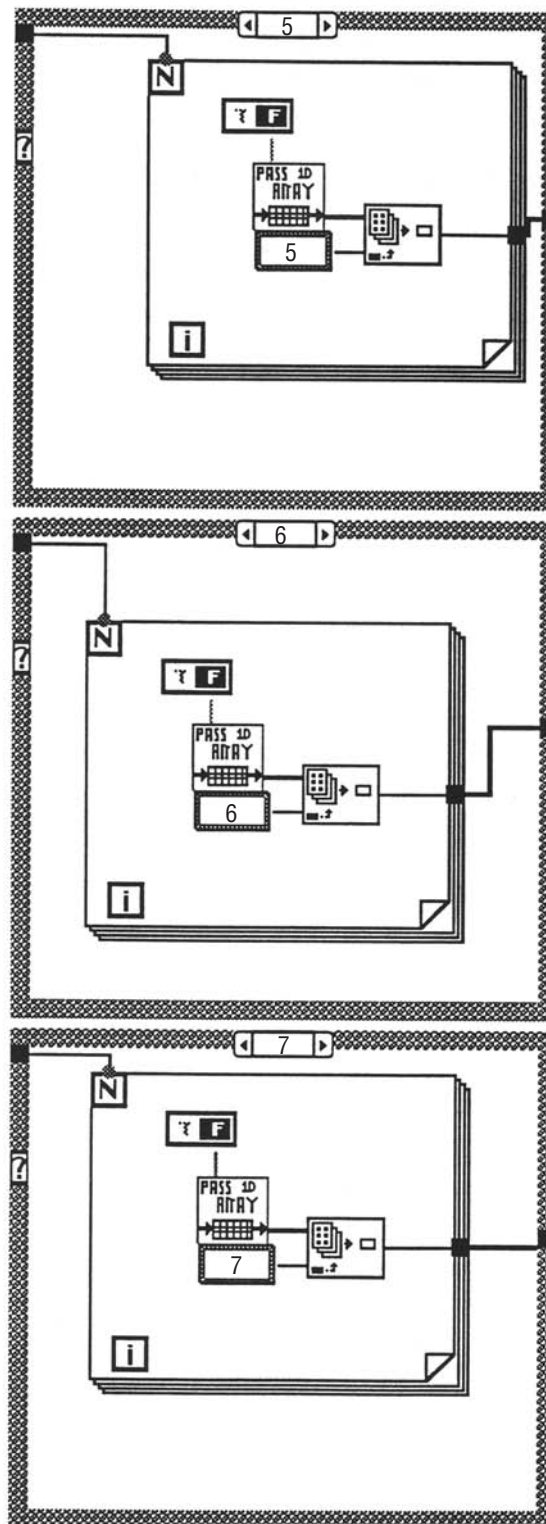


Figure 231(d). Basic statistics.

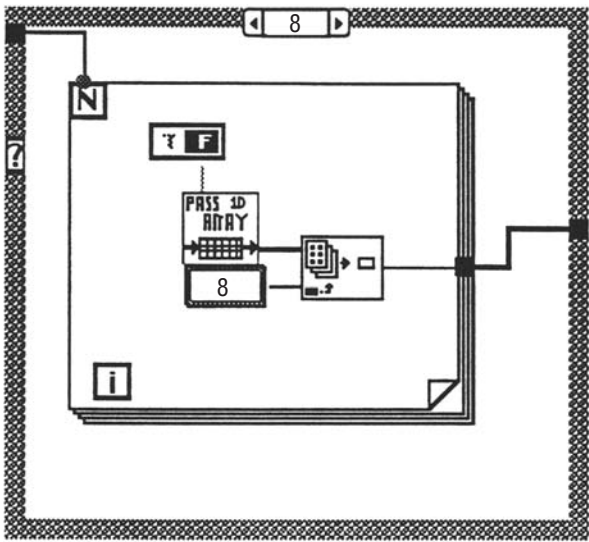
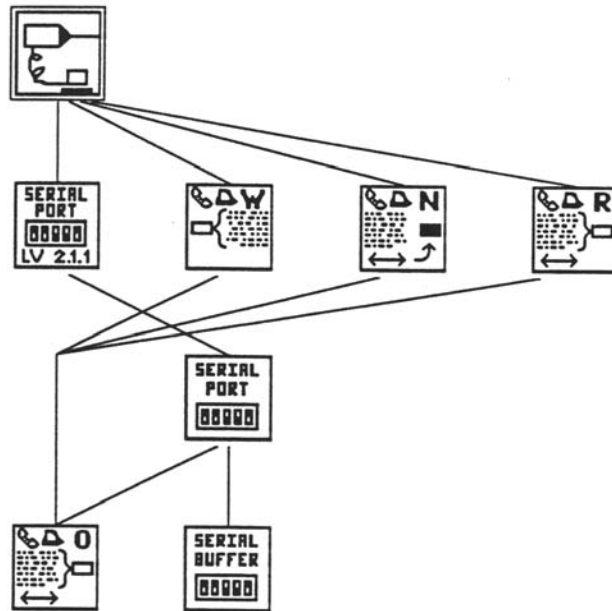
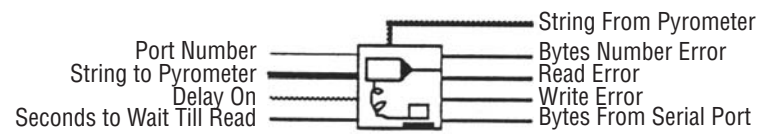


Figure 231(e). Basic statistics.

Position in Hierarchy



Connector Pane



**Pyrometer St Transfer VI**

Front Panel

Figure 232(a). Pyrometer st transfer VI.





Port Number

6

Comcard Slot 6 No. 0

String to Pyrometer

2

Delay On

1.20

Seconds to Wait Till Read

Serial Init Error

Bytes From Serial Port

45.00

Bytes Number Error

0.00

Write Error

0.00

Read Error

0.00

String From Pyrometer

Date: 91-10-06

Time: 14:01:06

(1) Set temperature mode 9 —(cr) —(cr)

(2) Set angle of incidence 5(cr)—1-3 —(cr)

(3) Set data acquisition mode 5(cr)—1—(cr)

(4) Fire (F) once in cont mode to setup

Block Diagram

Figure 232(b). Pyrometer st transfer VI.

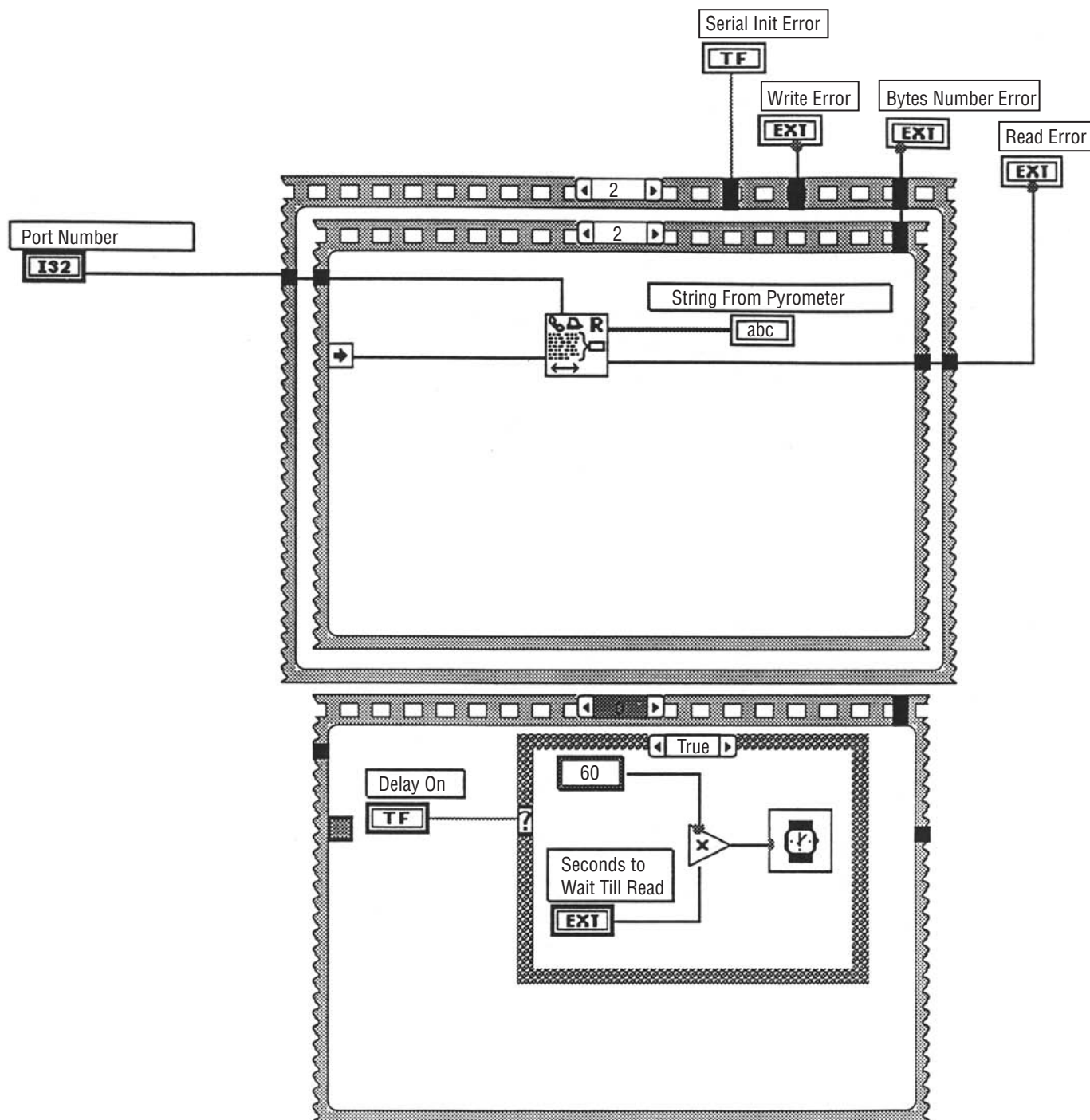


Figure 232(c). Pyrometer st transfer VI.

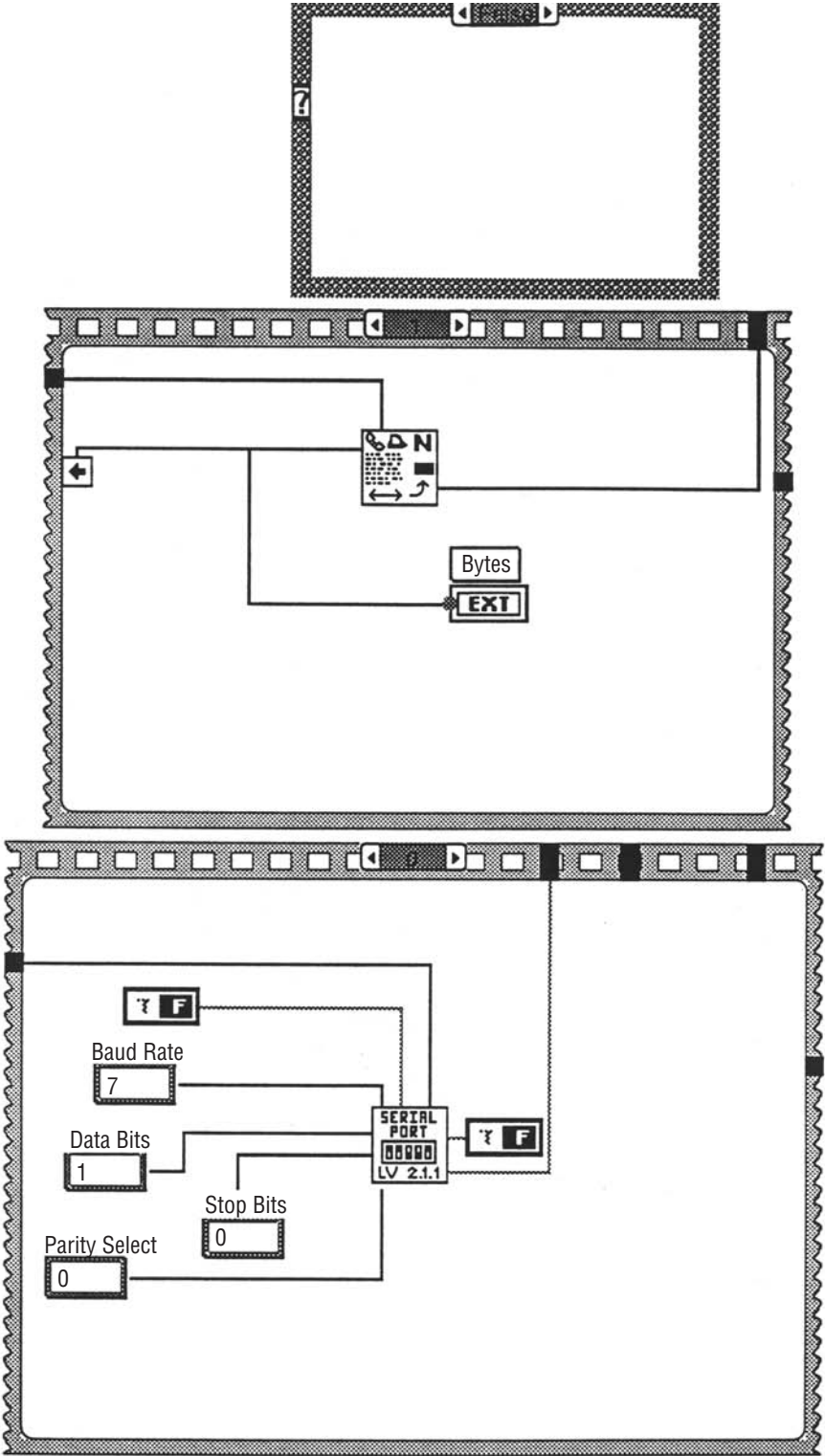


Figure 232(d). Pyrometer st transfer VI.

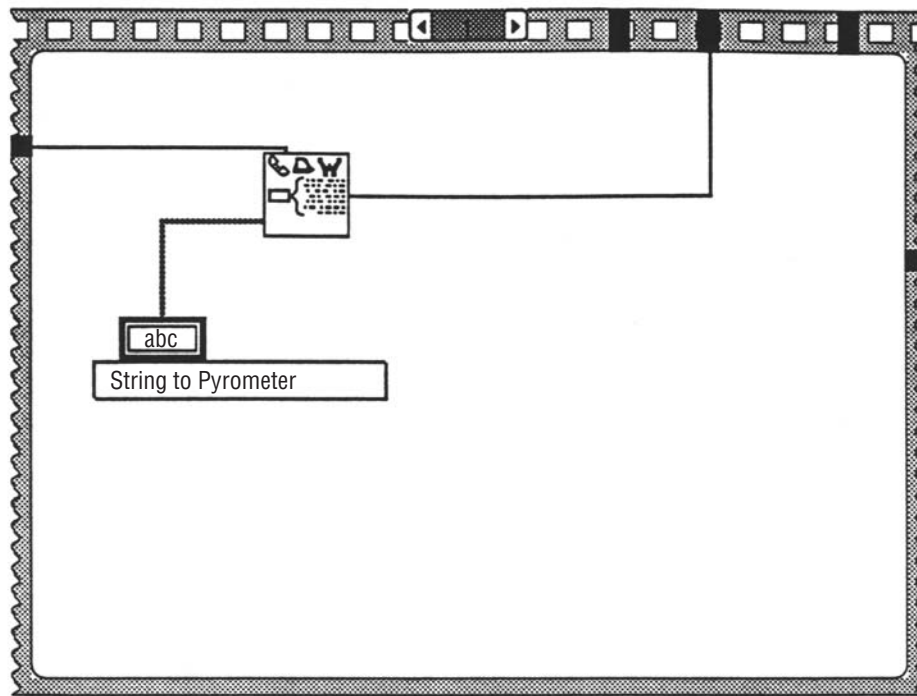
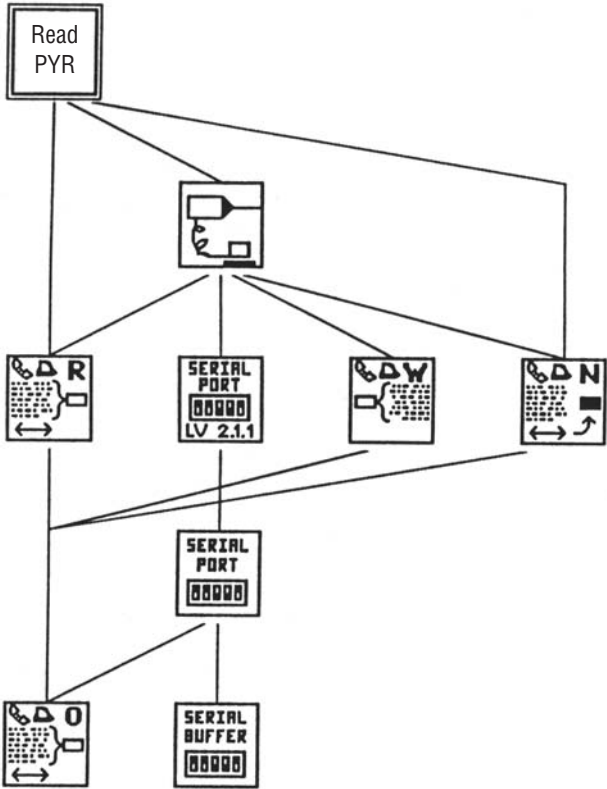


Figure 232(e). Pyrometer st transfer VI.

Position in Hierarchy



Connector Pane

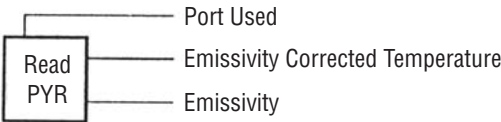


Figure 233(a). Read continuous pyrometer.

Front Panel

Port Used	0.00
Number Error	0.00
Read Error	0.00

Emissivity Corrected Temperature	950
	792
	633
	475
	317
	158
	0

Emissivity	1.00
	0.80
	0.60
	0.40
	0.20
	0.00



Block Diagram

Figure 233(b). Read continuous pyrometer.



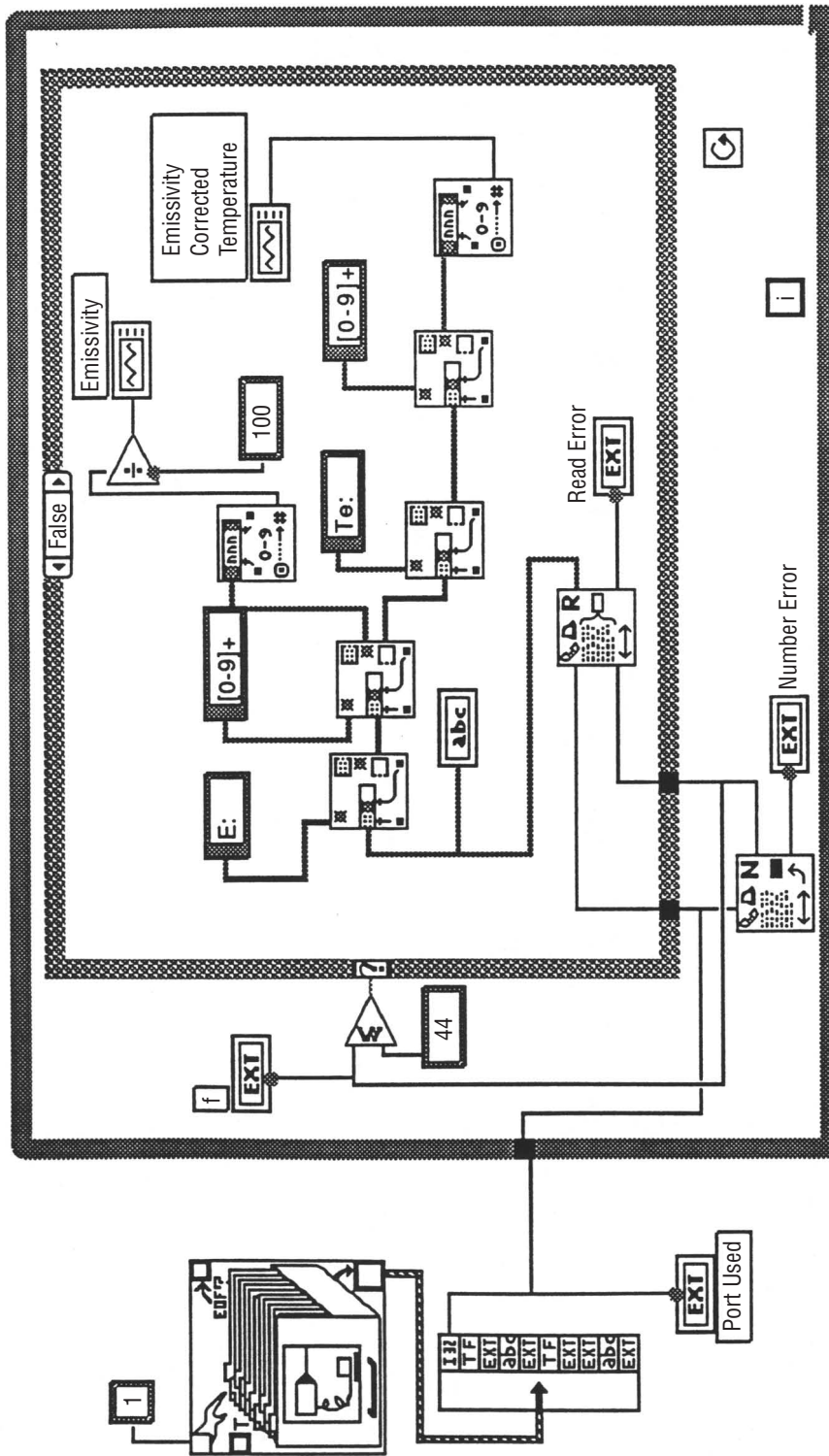


Figure 233(c). Read continuous pyrometer.

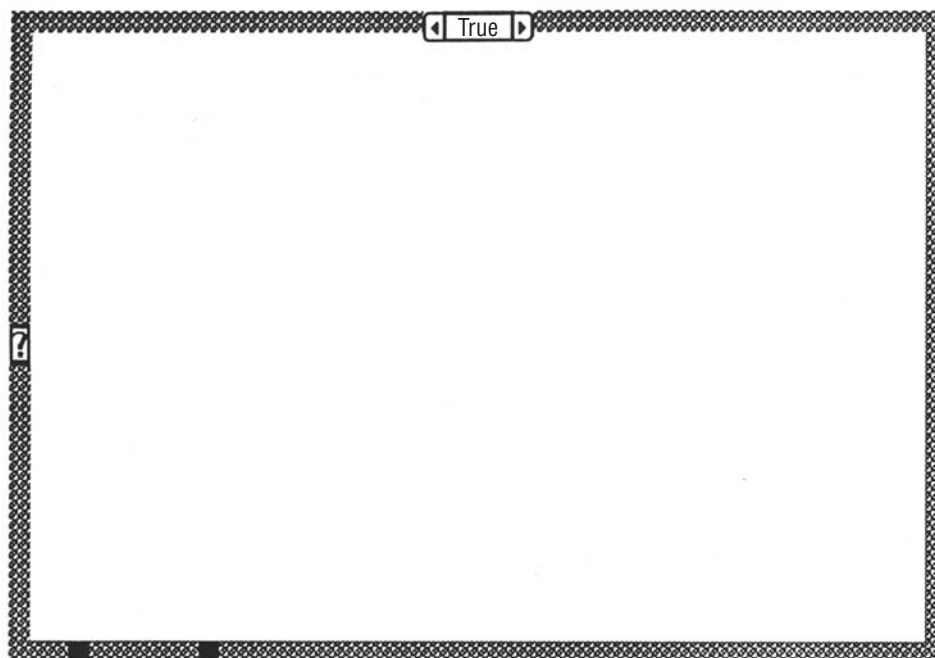


Figure 233(d). Read continuous pyrometer.



Position in Hierarchy



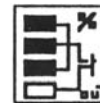
Connector Pane

Acetylene $C_2H_2$	_____		_____	Gas Ratio
Carbon Monoxide $CO$	_____		_____	C-O Line % C
Methane $CH_4$	_____		_____	H-C Line % H
Oxygen $O_2$	_____		_____	O-H Line % O

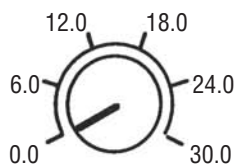
Constituent Calculations 2

Front Panel

Figure 234(a). Constituent calculations.

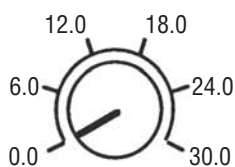


All Dials Are in Standard Liters per Minute (SLPM)



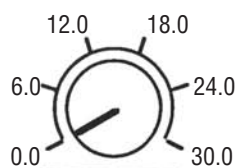
0.00

Acetylene  $C_2H_2$



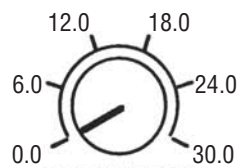
0.00

Oxygen  $O_2$



0.00

Carbon Monoxide  $CO$



0.00

Methane  $CH_4$

Gas Ratio

0.000

C-O Line % C

0.00

1.00 —  
0.86 —  
0.71 —  
0.57 —  
0.43 —  
0.29 —  
0.14 —  
0.00 —

H-C Line % H

0.00

1.00 —  
0.86 —  
0.71 —  
0.57 —  
0.43 —  
0.29 —  
0.14 —  
0.00 —

O-H Line % O

0.00

1.00 —  
0.86 —  
0.71 —  
0.57 —  
0.43 —  
0.29 —  
0.14 —  
0.00 —

Block Diagram

Figure 234(b). Constituent calculations.

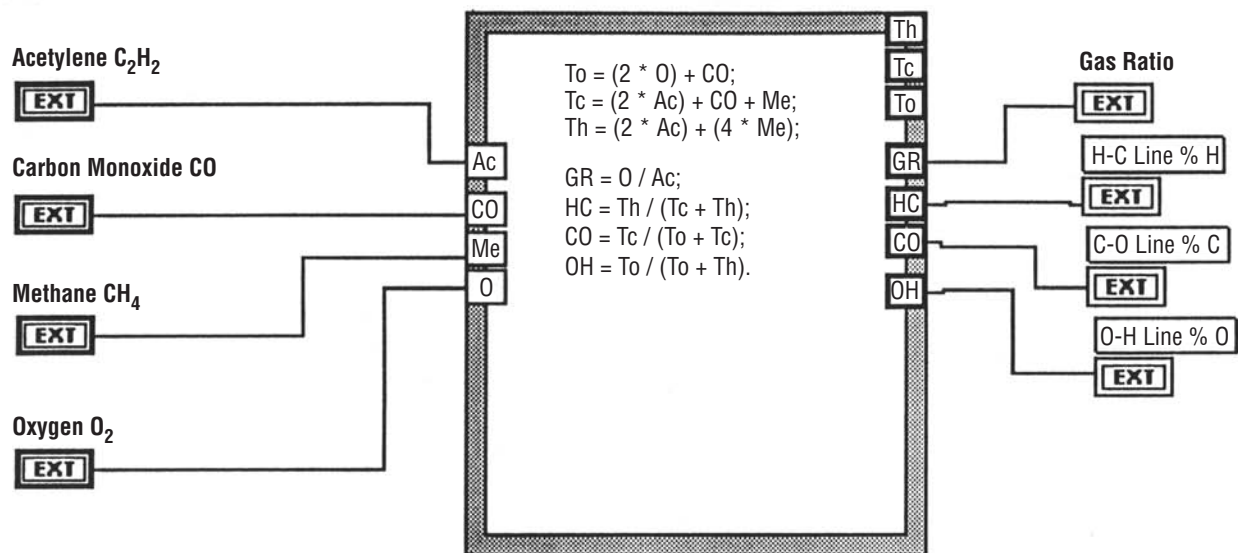
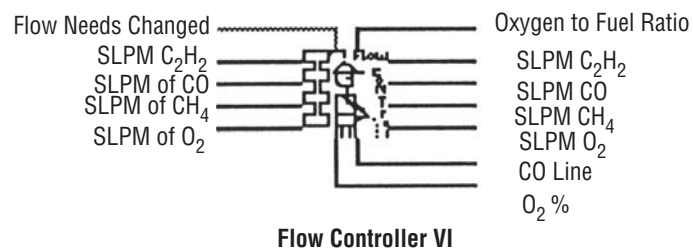


Figure 234(c). Read continuous pyrometer.

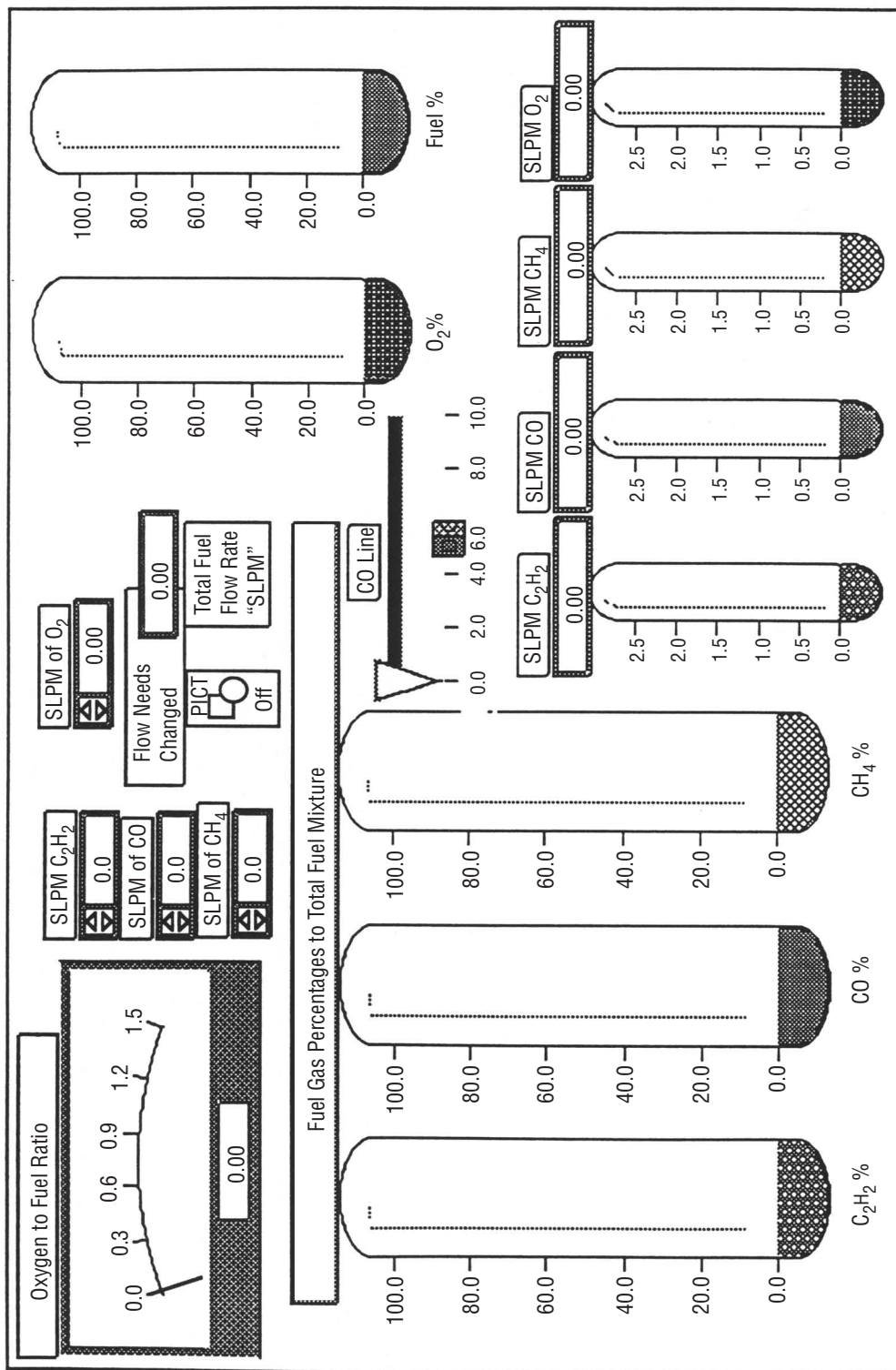


Front Panel

Figure 235(a). Flow control VI.



Flow Controller VI  
Monday, July 13, 1992 3:19 PM



Block Diagram

Figure 235(b). Flow control VI.

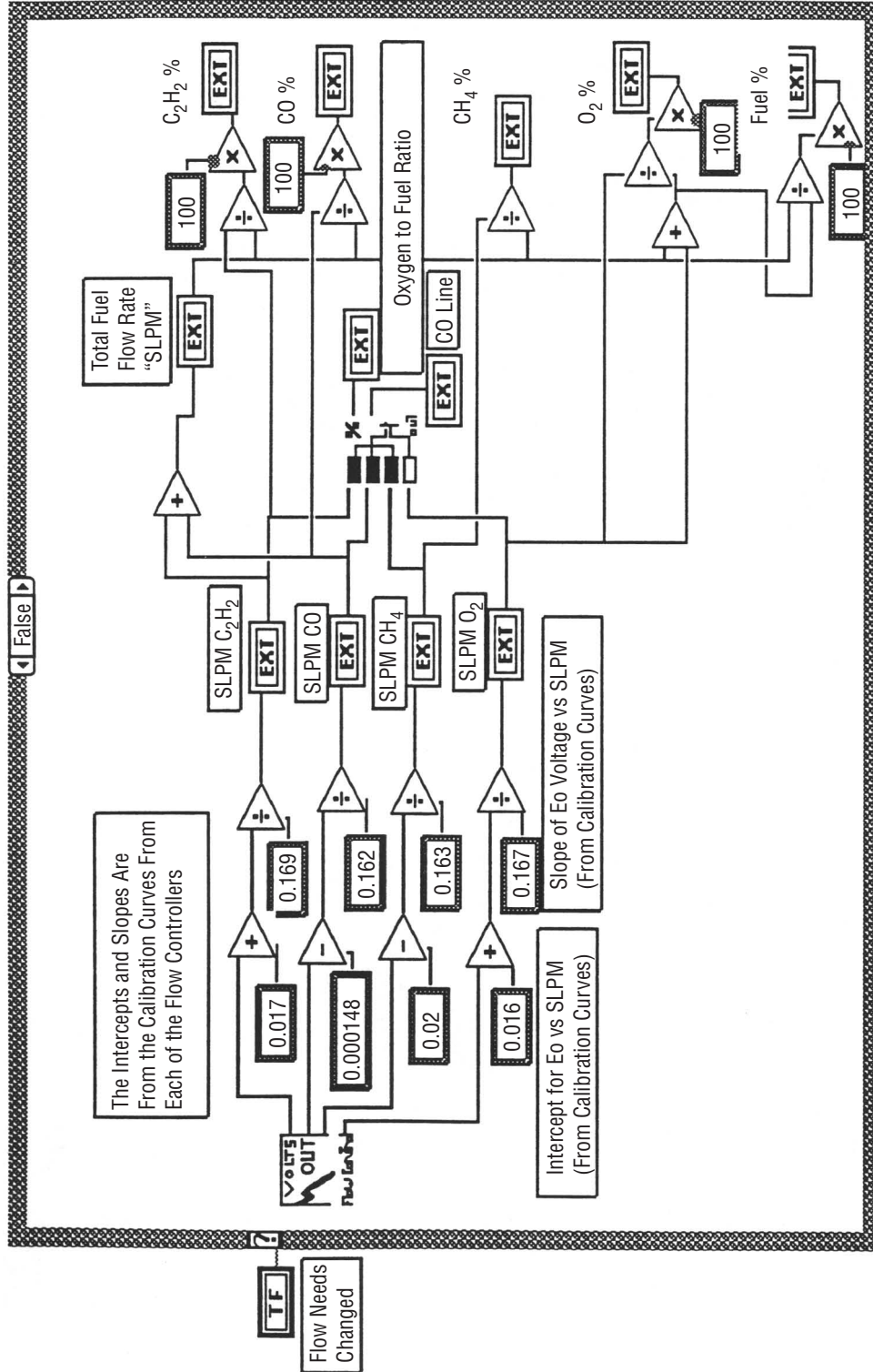


Figure 235(c). Flow control VI.



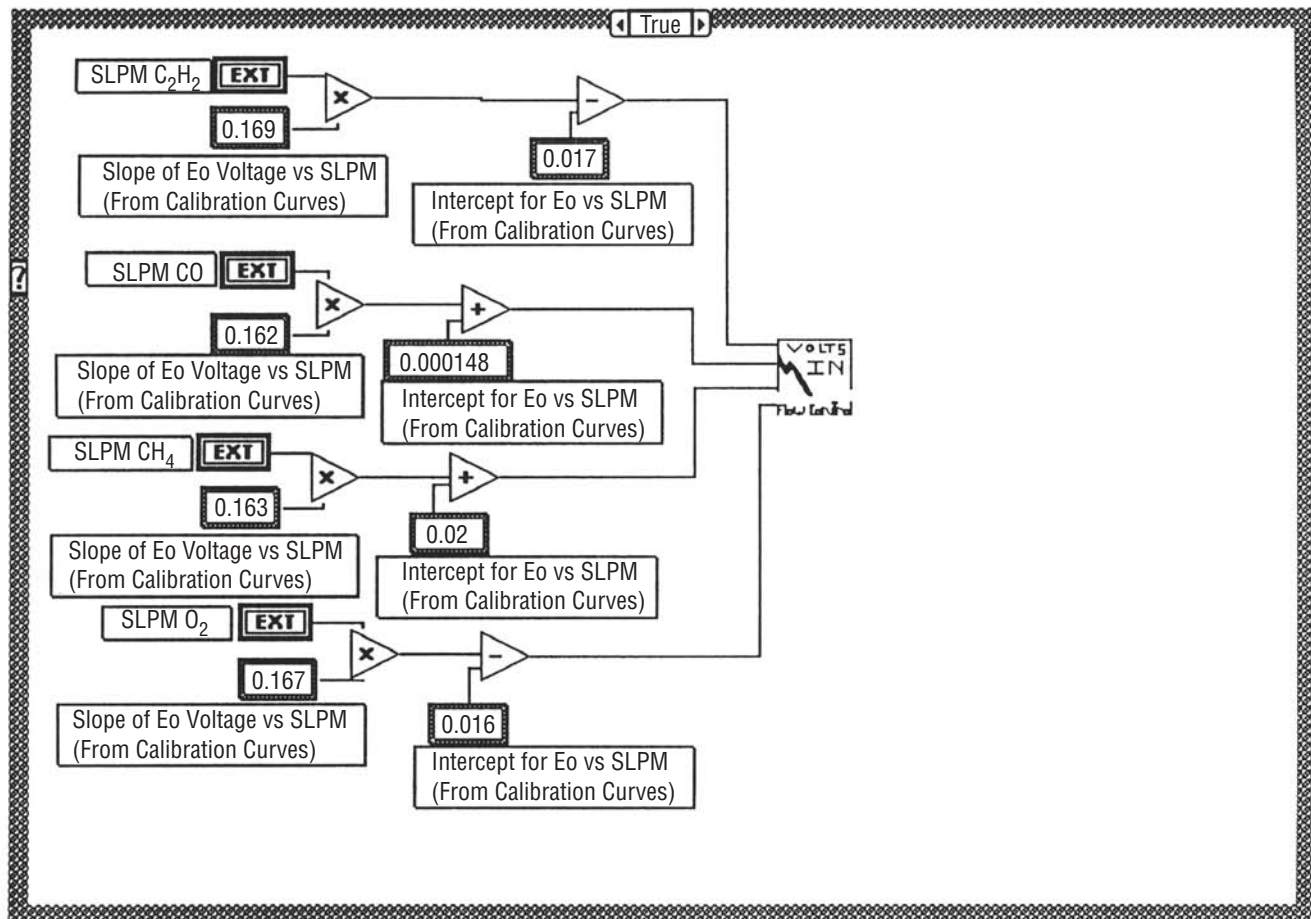
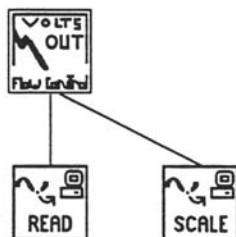


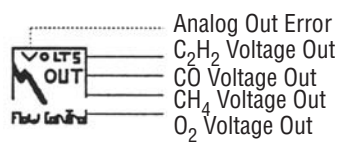
Figure 235(d). Flow control VI.



Position in Hierarchy

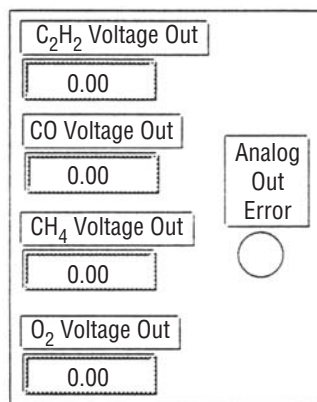


Connector Pane



### Output Voltages From Flow Controller

Front Panel



Block Diagram

Figure 236(a). Output voltages from flow control.

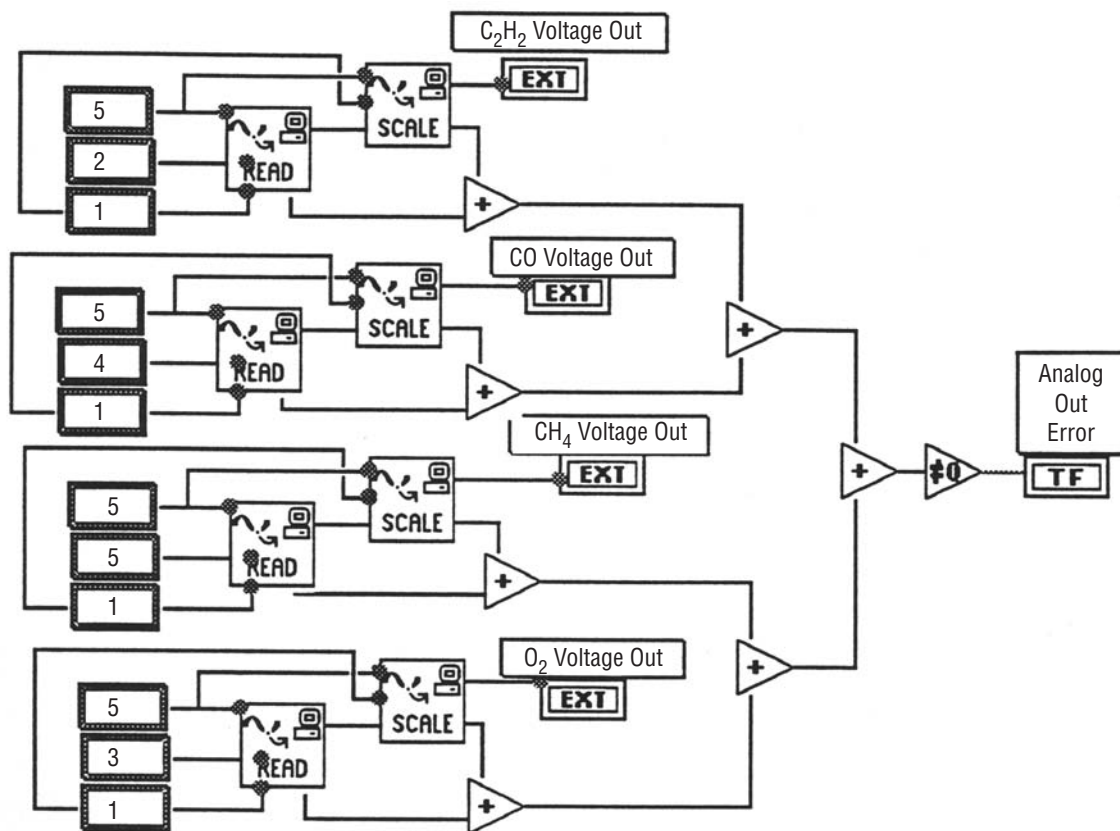
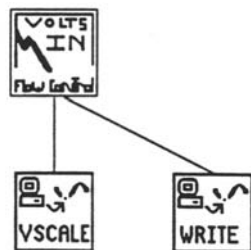


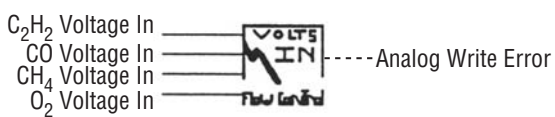
Figure 236(b). Output voltages from flow control.



Position in Hierarchy

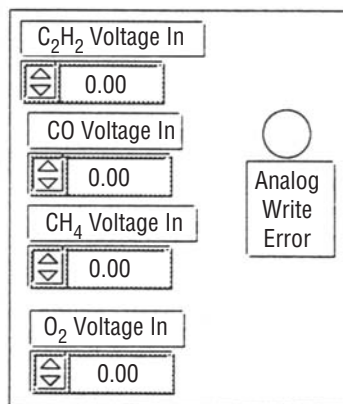


Connector Pane



Input Volages for Flow Control

Front Panel



Block Diagram

Figure 237(a). Input voltages for flow control.

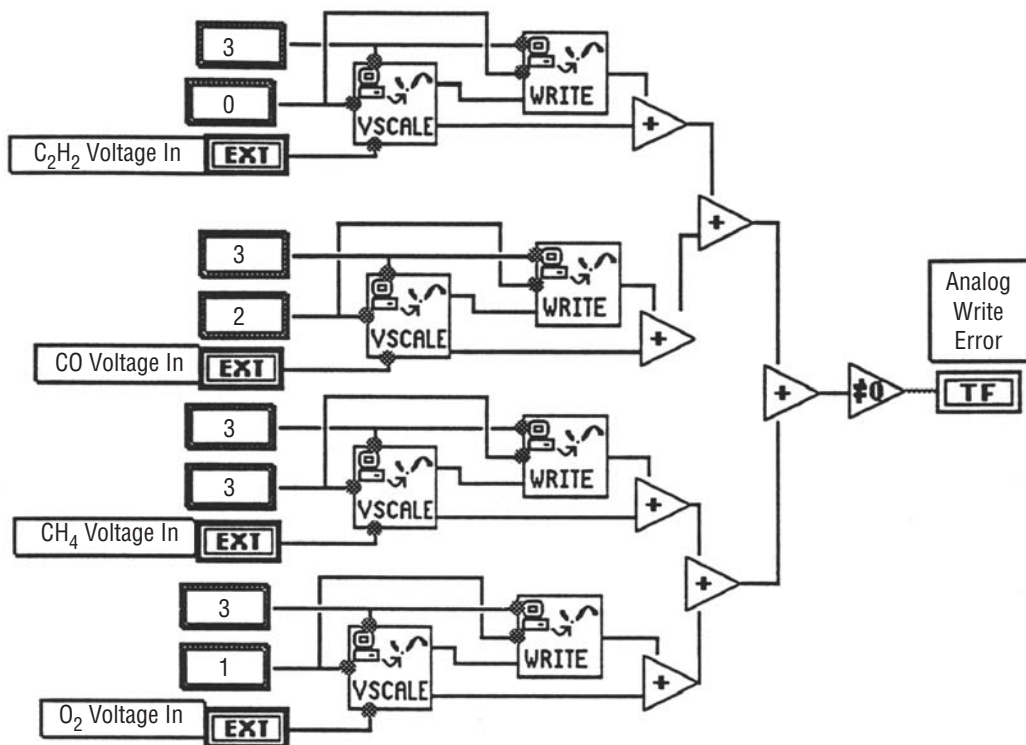


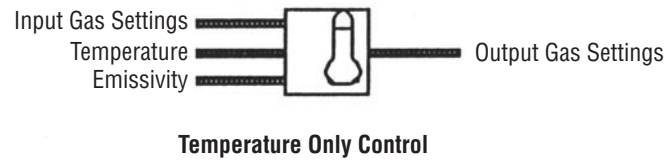
Figure 237(b). Input voltages for flow control.



Position in Hierarchy



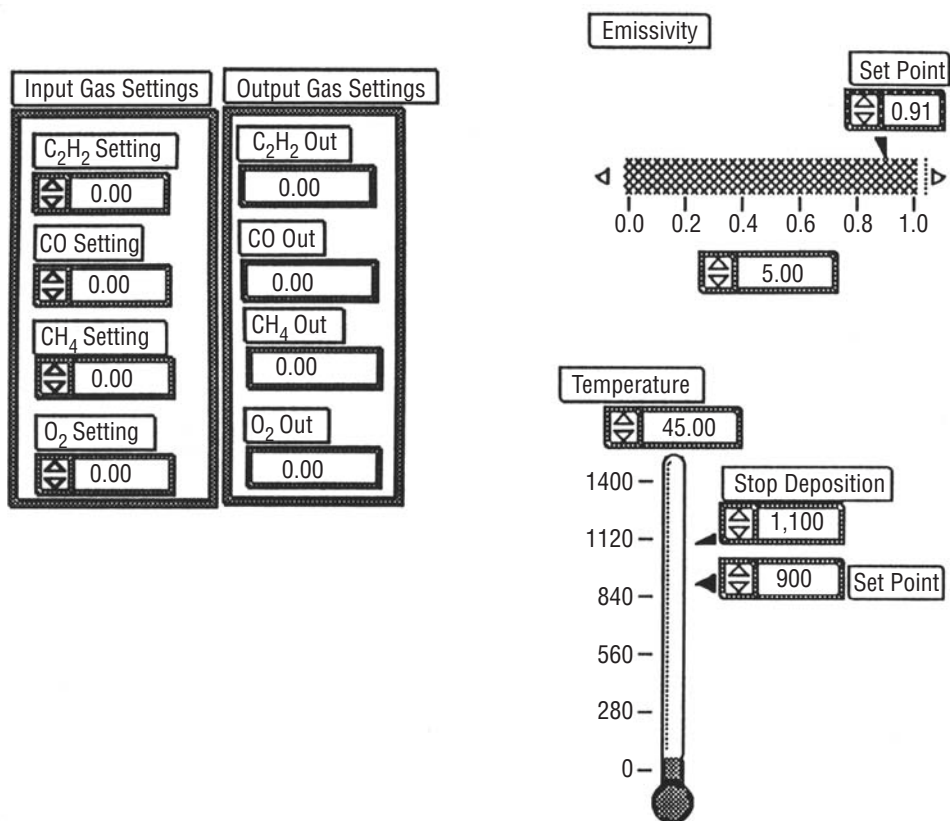
Connector Pane



Front Panel

Figure 238(a). Temperature-only control.





Block Diagram

Figure 238(b). Temperature-only control.

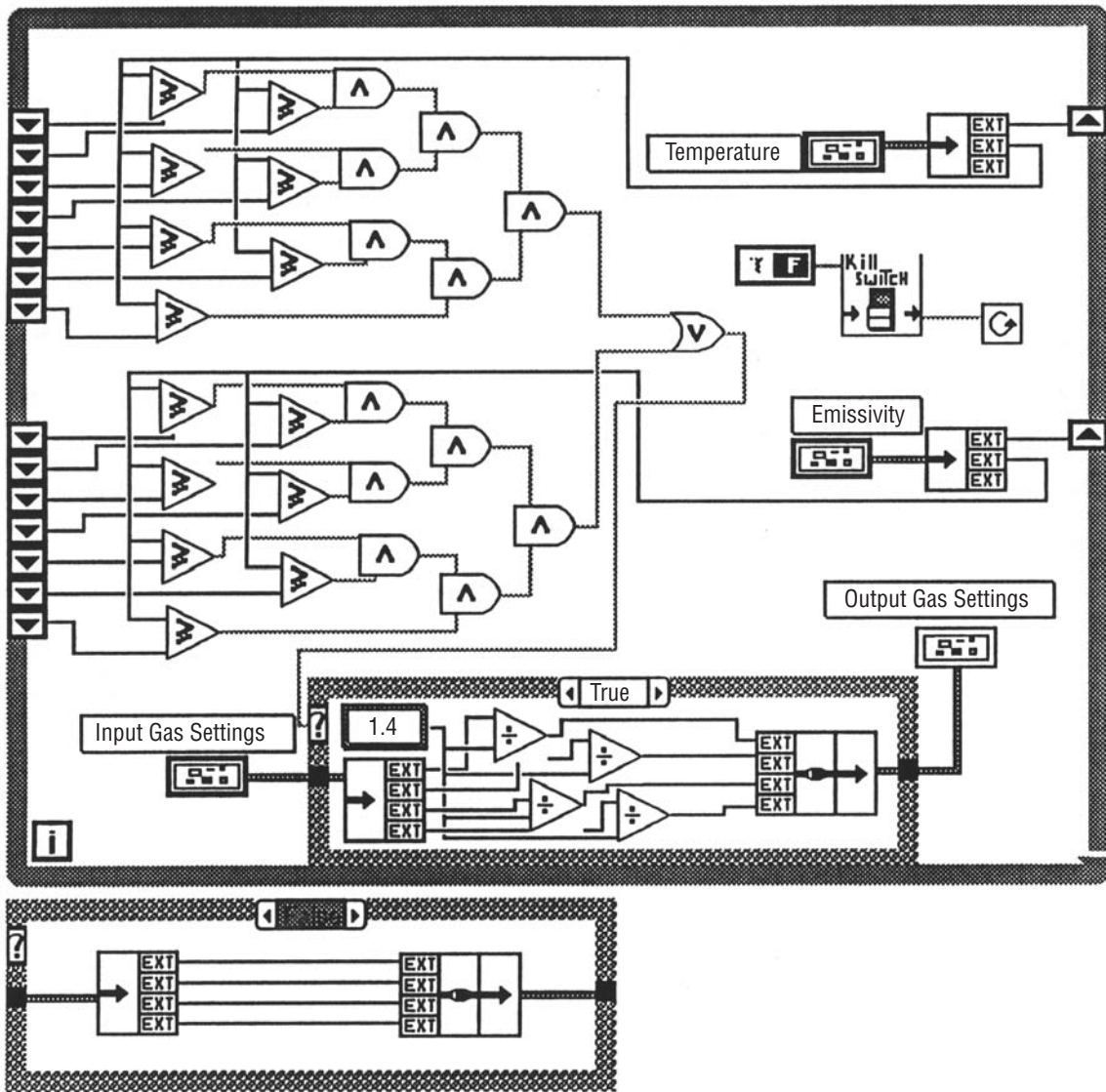


Figure 238(c). Temperature-only control.



Position in Hierarchy



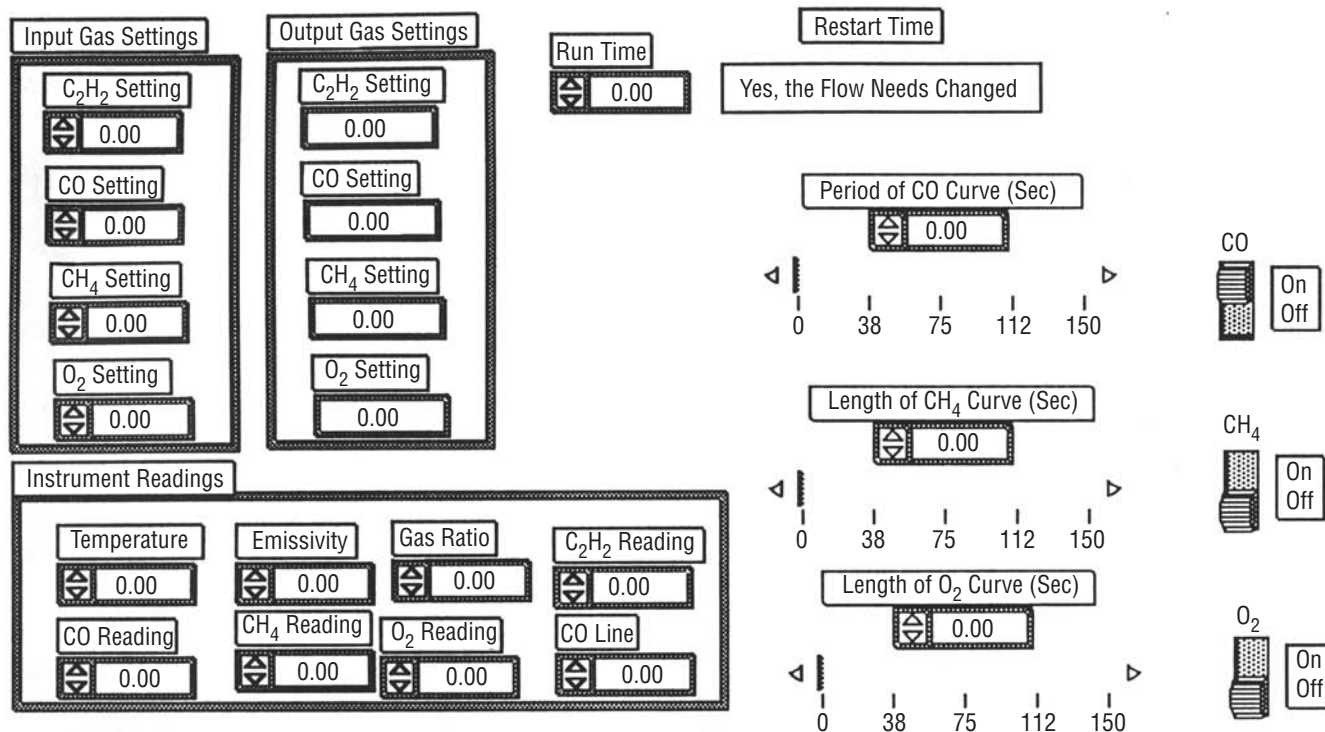
Connector Pane



Logarithmic Switch

Front Panel

Figure 239(a). Logarithmic switch.



Block Diagram

Figure 239(b). Logarithmic switch.

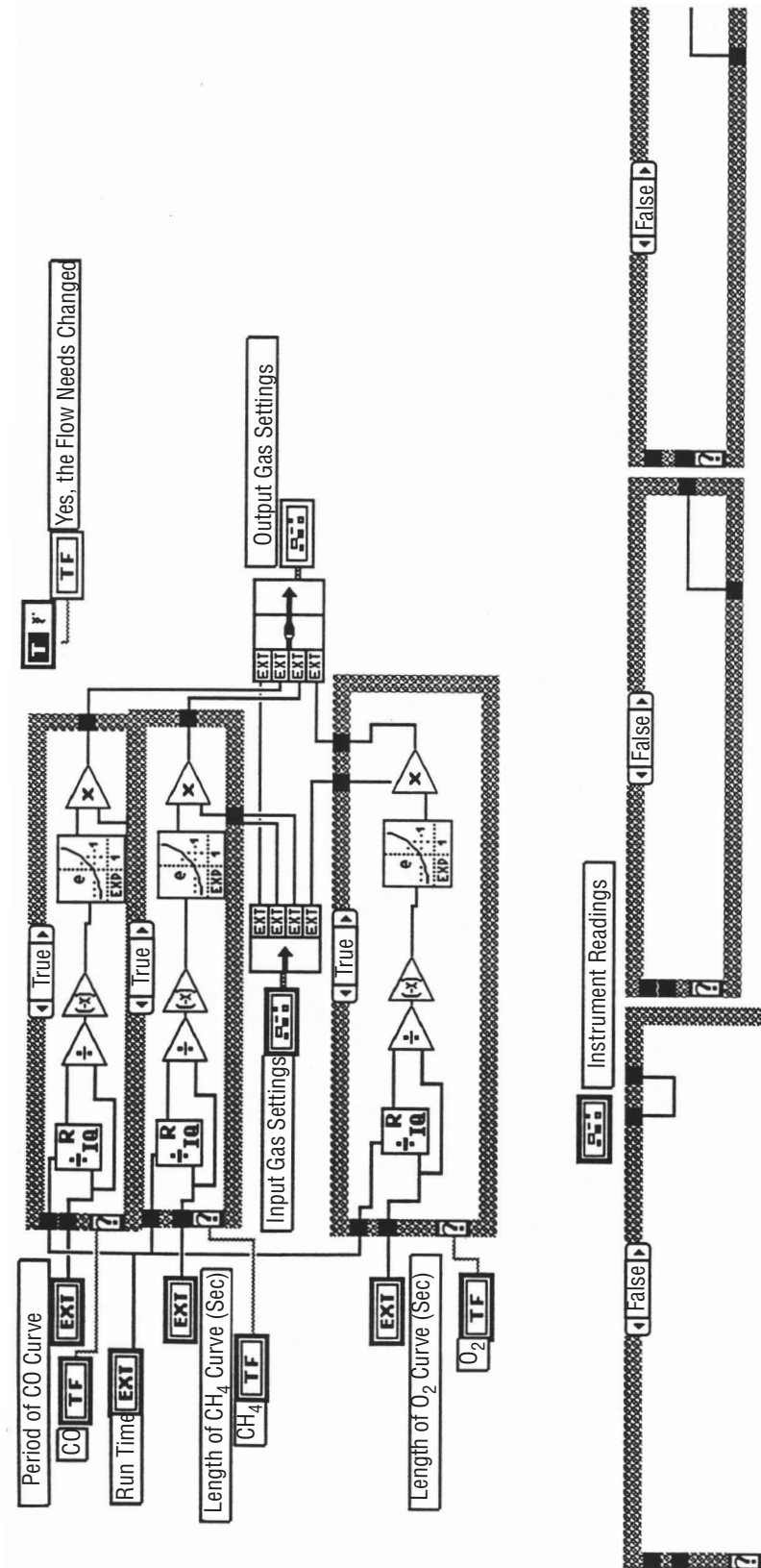


Figure 239(c). Logarithmic switch.

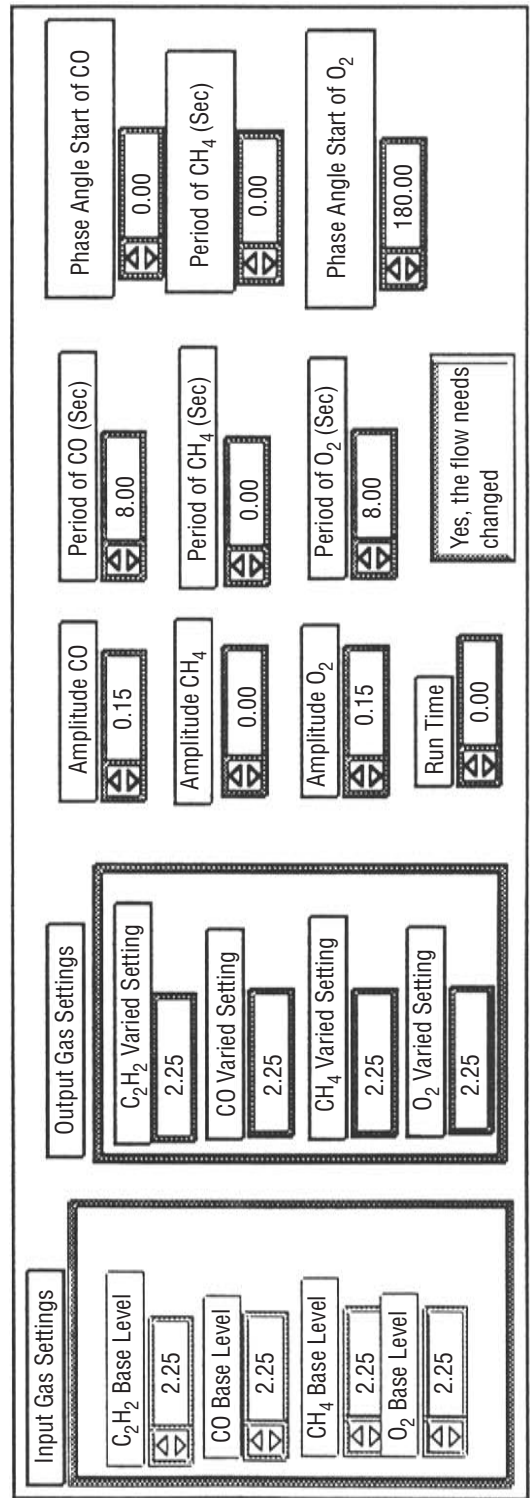


Connector Pane



Sine Wave Switch

Front Panel



Block Diagram

Figure 240(a). Sine wave switch.



Sine Wave Switch  
Thursday, July 30, 1992 12:51 PM

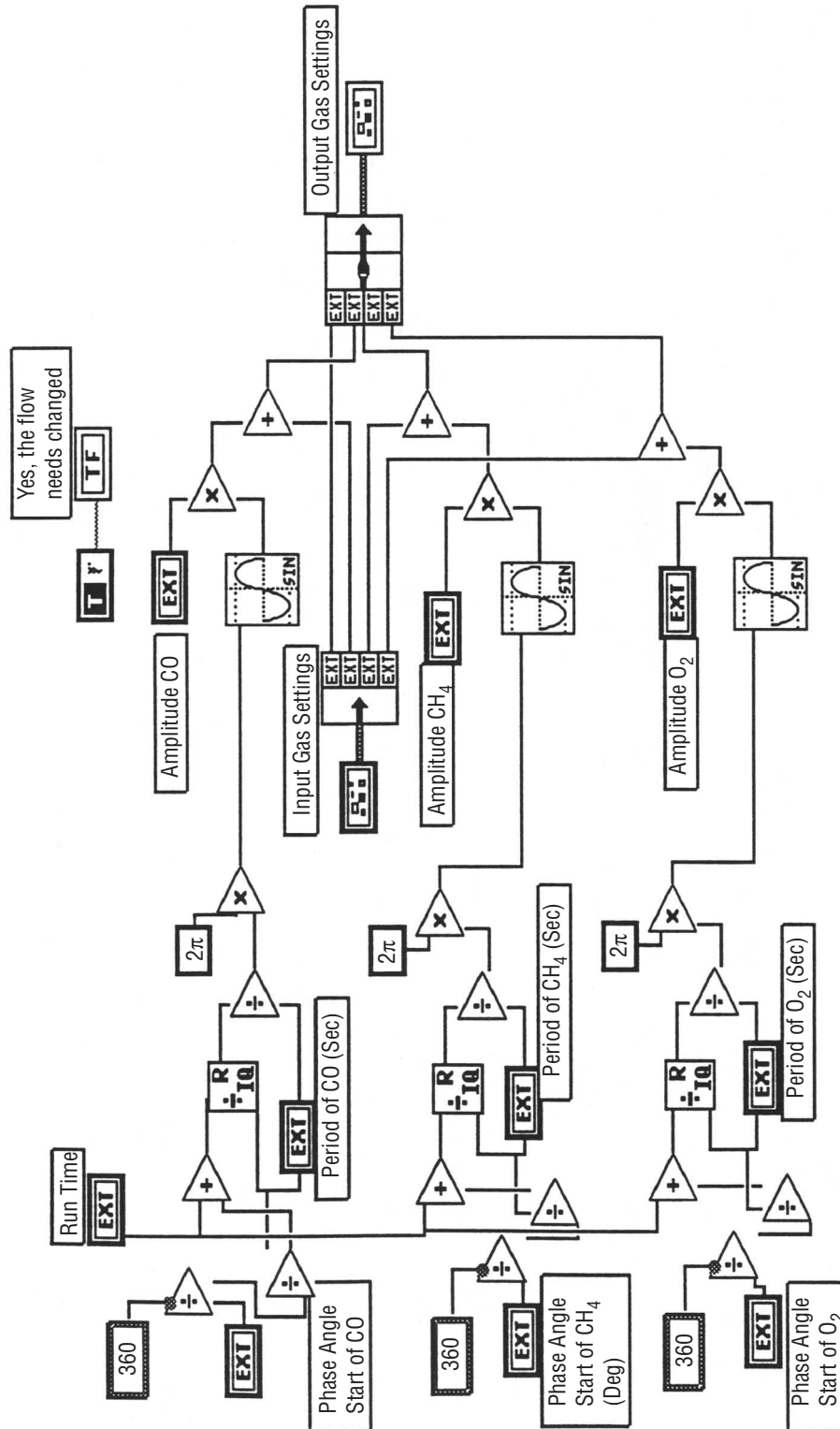
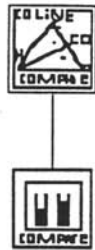


Figure 240(b). Sine wave switch.

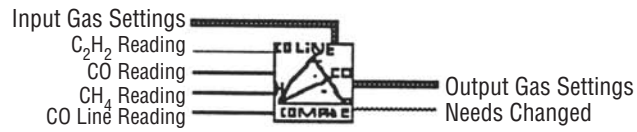




Position in Hierarchy

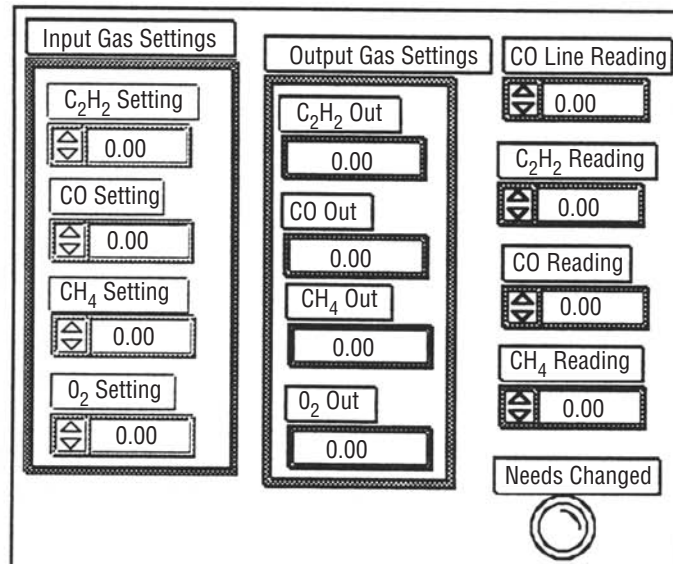


Connector Pane



Bounded CO Line

Front Panel



Block Diagram

Figure 241(a). Bounded CO line.

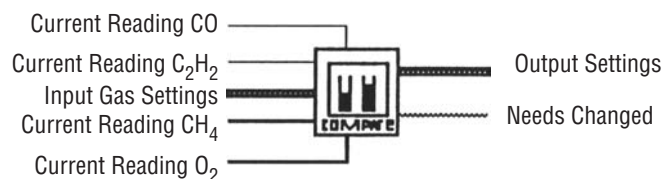




Position in Hierarchy



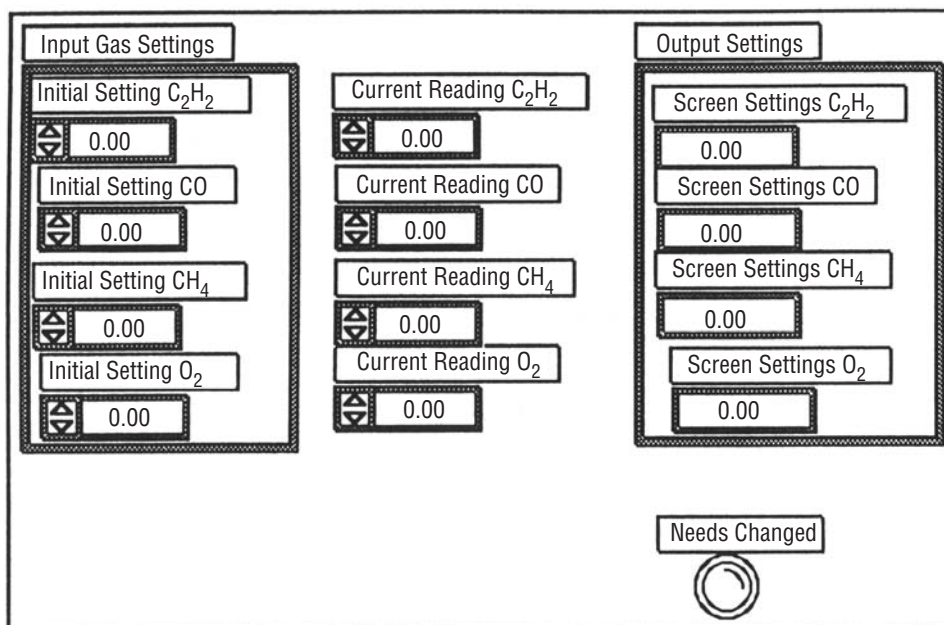
Connector Pane



Screen Flow Comparison VI

Front Panel

Figure 242(a). Screen flow comparison VI.



Block Diagram

Figure 242(b). Screen flow comparison VI.

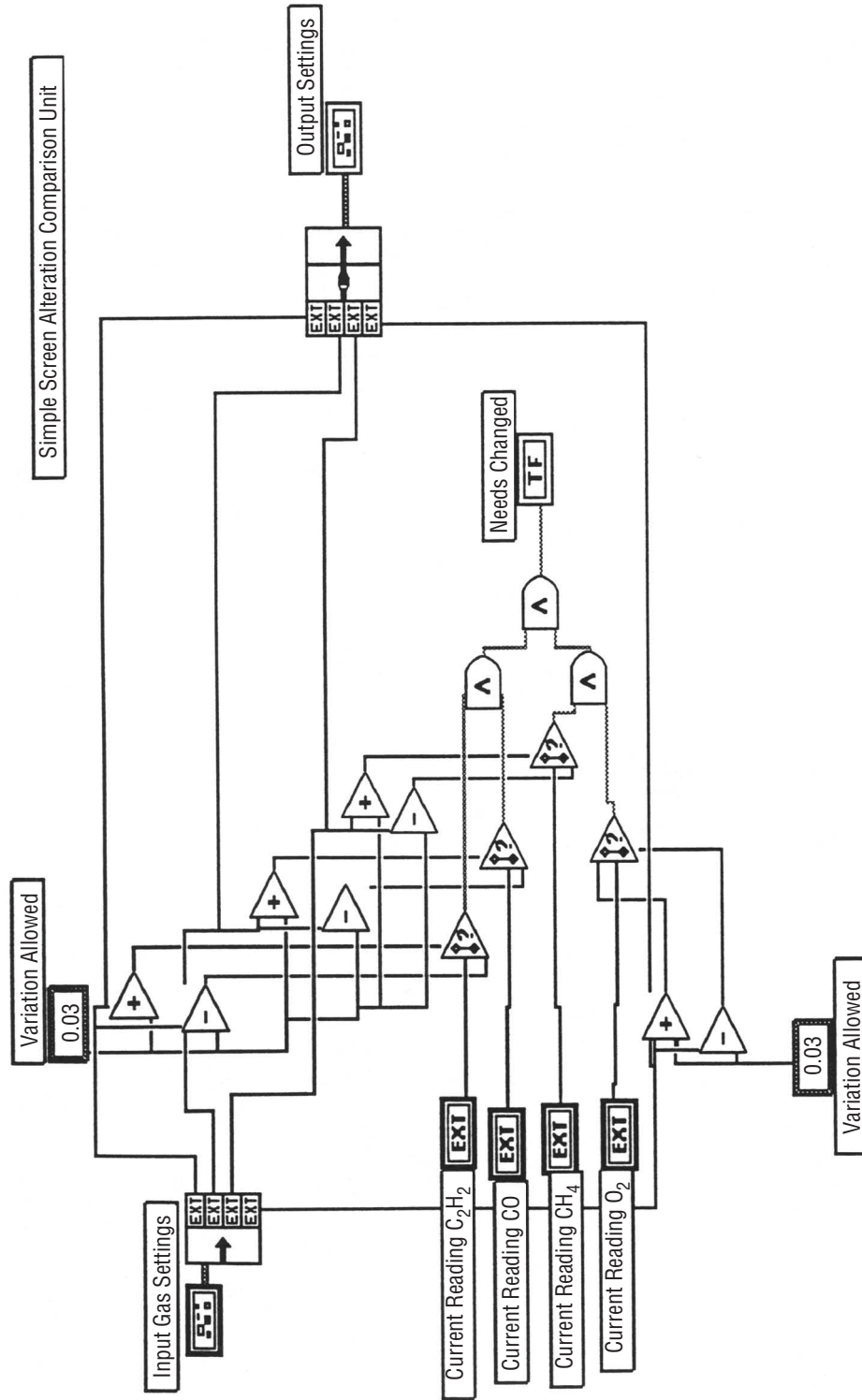


Figure 242(c). Screen flow comparison VI.



#### Position in Hierarchy



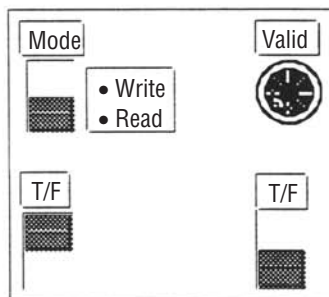
#### Connector Pane



#### Kill Switch

Set the boolean to the input value (True or False) if mode is True; otherwise, retain the last value. Return the current value of the boolean.

#### Front Panel



#### Block Diagram

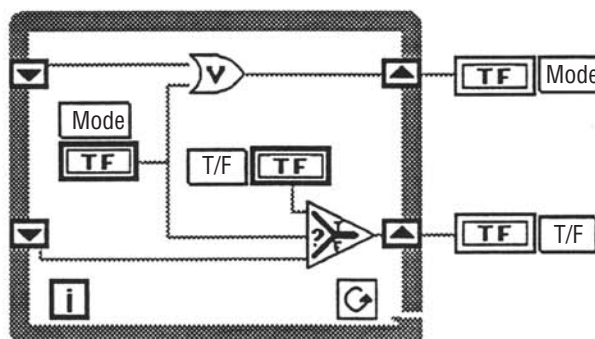


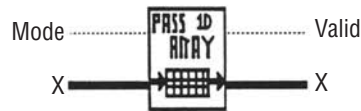
Figure 243. Kill switch.



### Position in Hierarchy



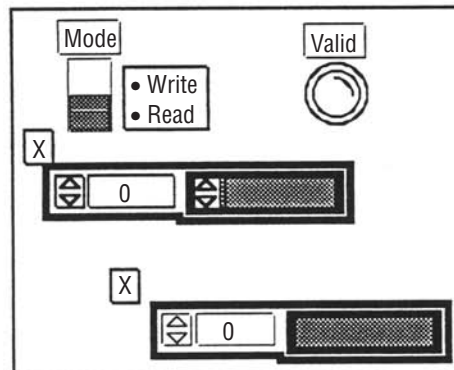
### Connector Pane



### Global Array 1D Pass

Set the variable to the input value if mode is True; otherwise, retain the last value. Return the value of the variable.

### Front Panel



### Block Diagram

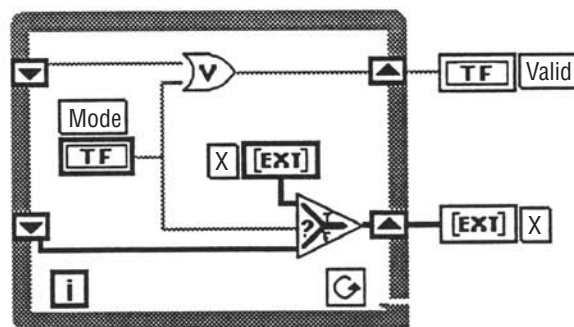


Figure 244. Global array 1D pass.

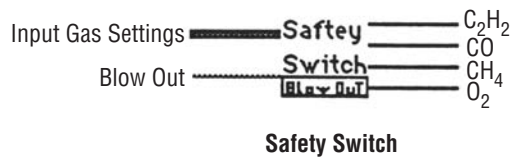




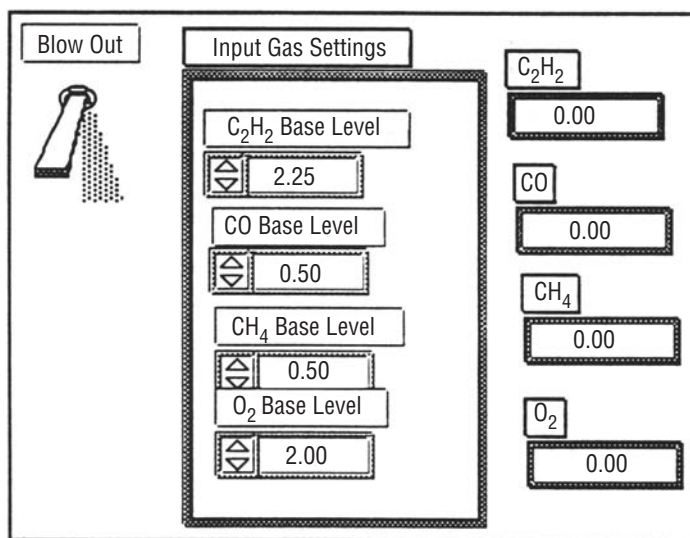
Position in Hierarchy



Connector Pane



Front Panel



Block Diagram

Figure 245(a). Safety switch.

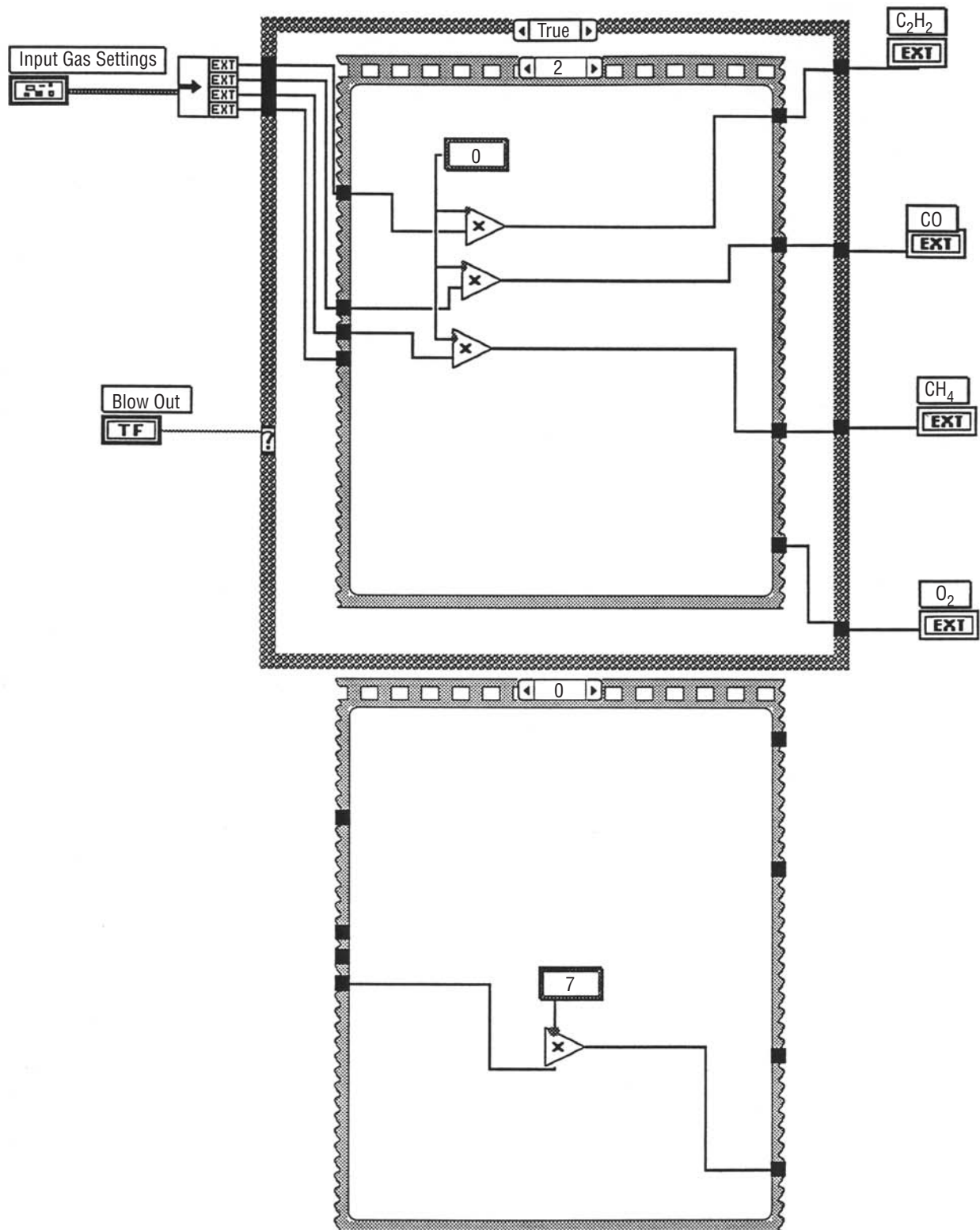


Figure 245(b). Safety switch.

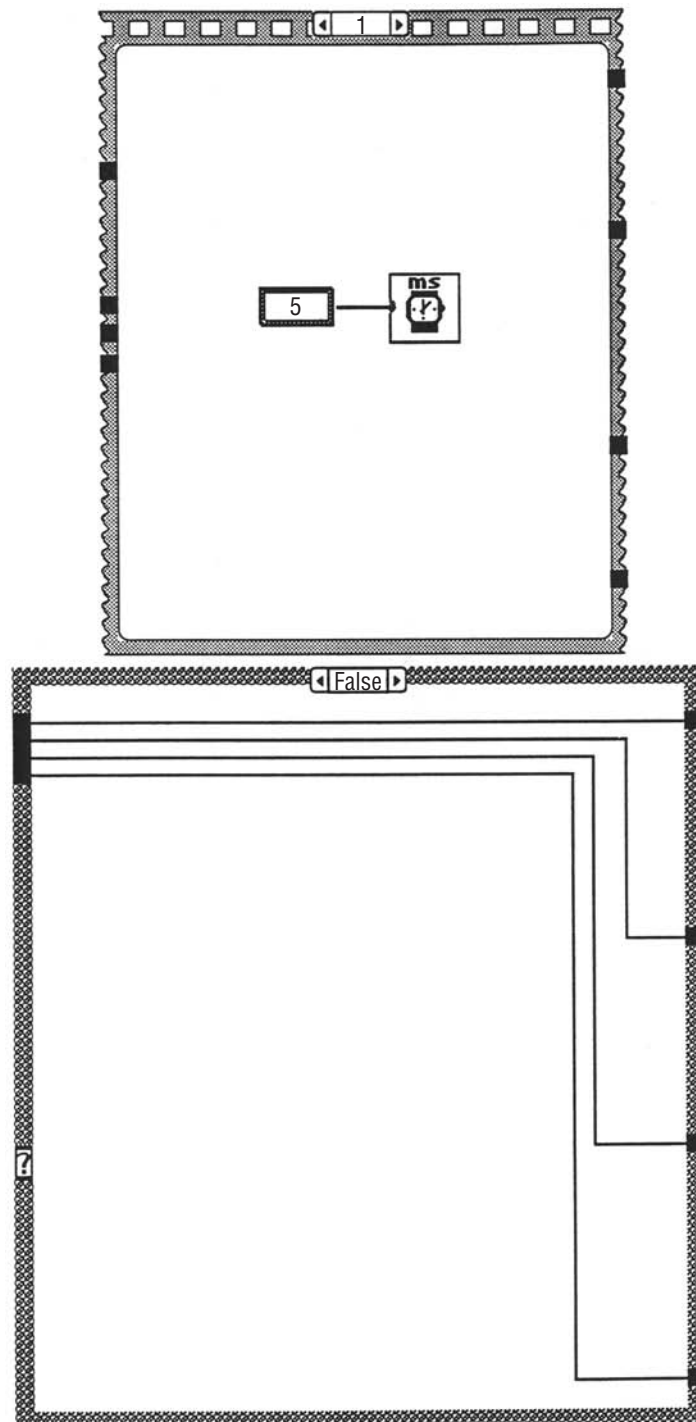


Figure 245(c). Safety switch.



---

Connector Pane

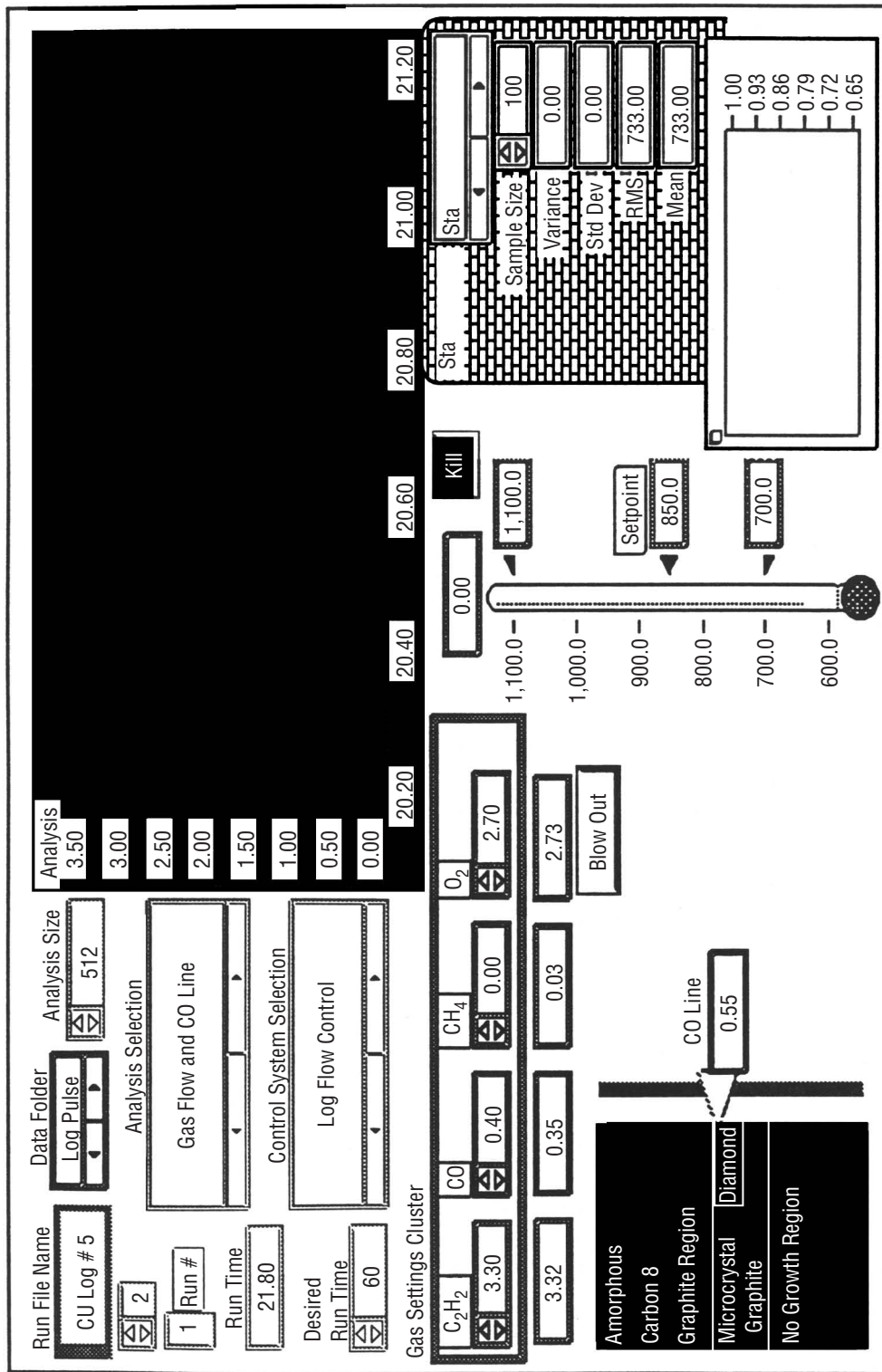


**New Torch Control System**

---

Front Panel

Figure 246(a). New torch control system.



Block Diagram

Figure 246(b). New torch control system.

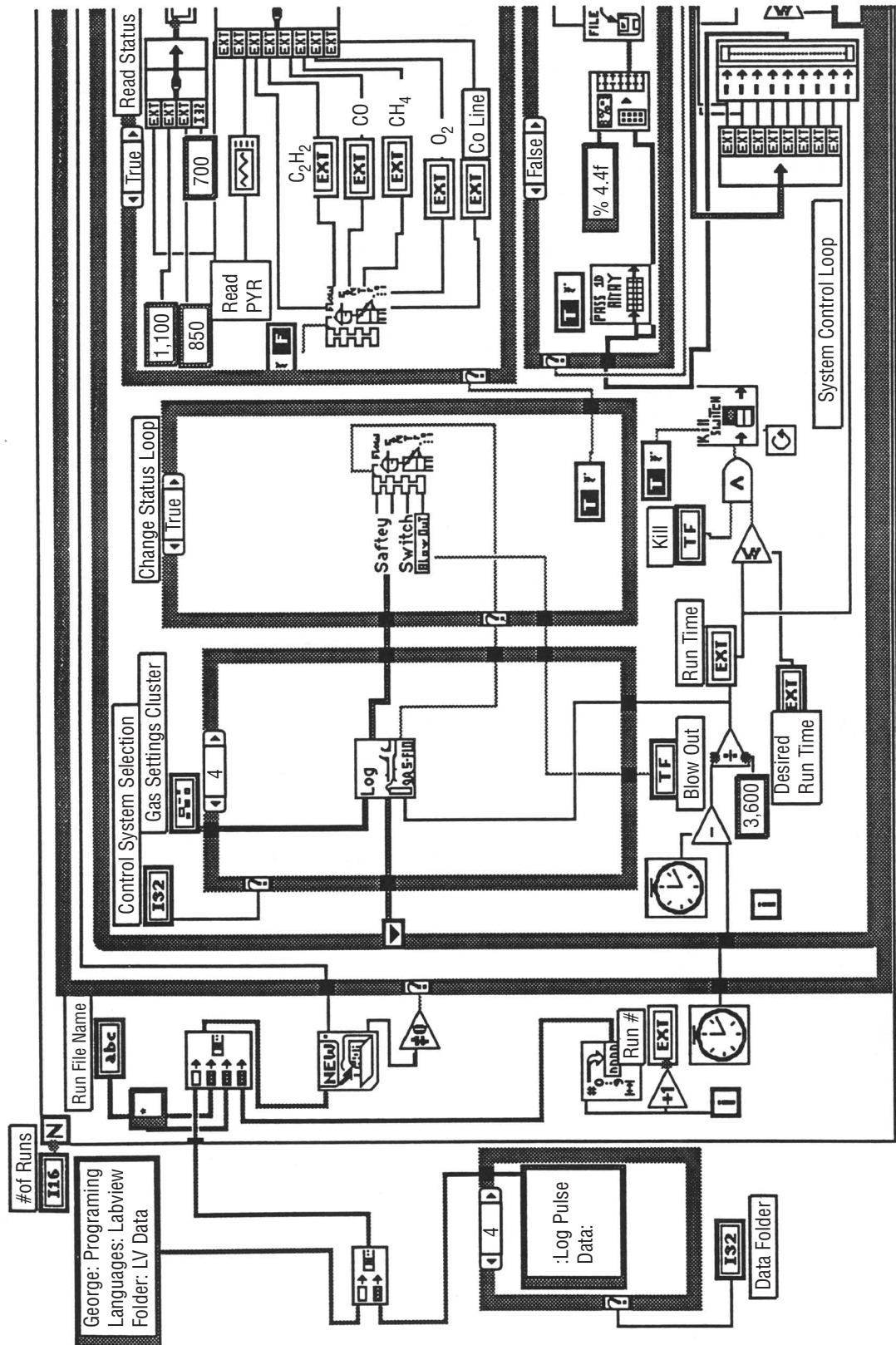


Figure 246(c). New torch control system.



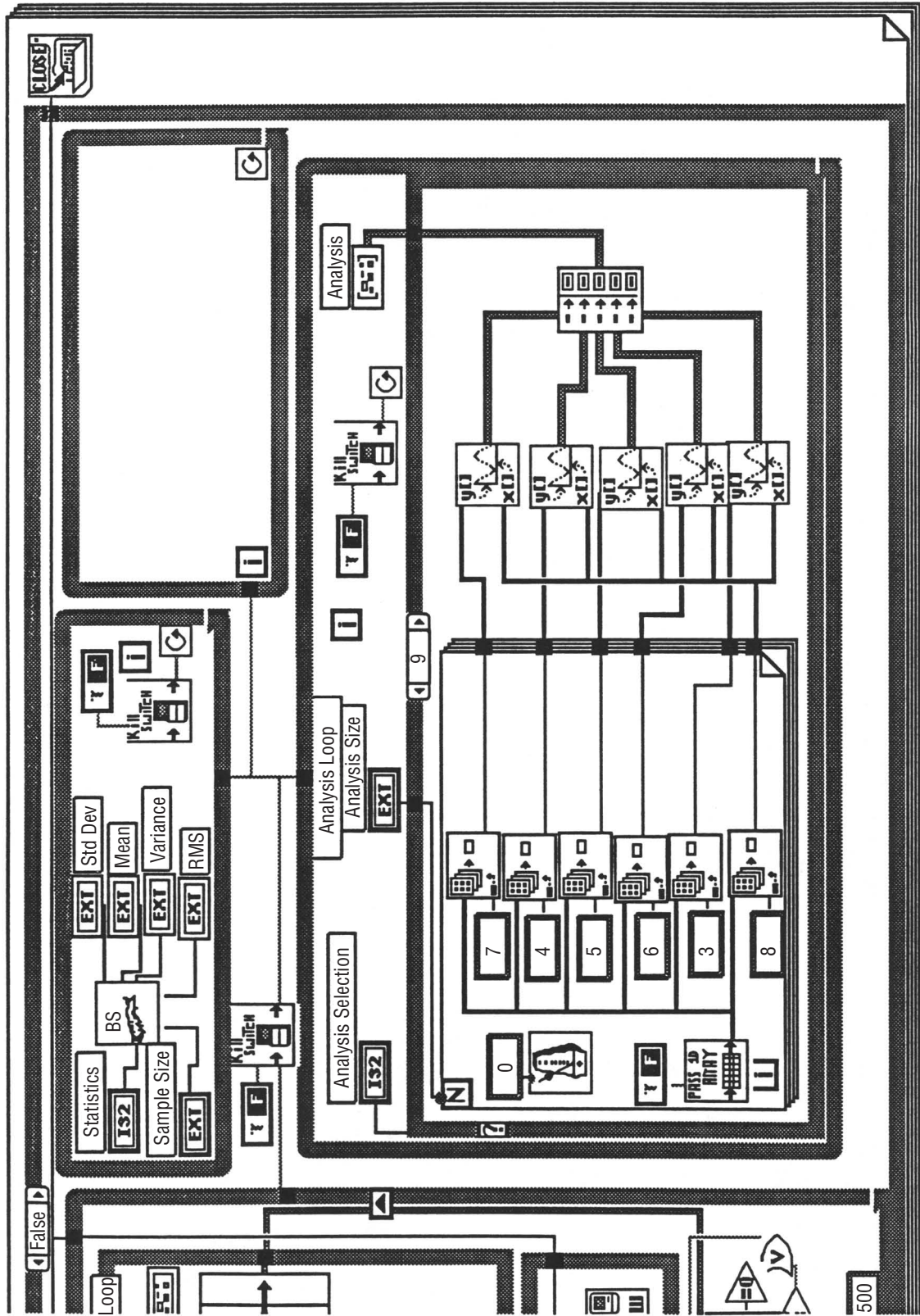


Figure 246(d). New torch control system.

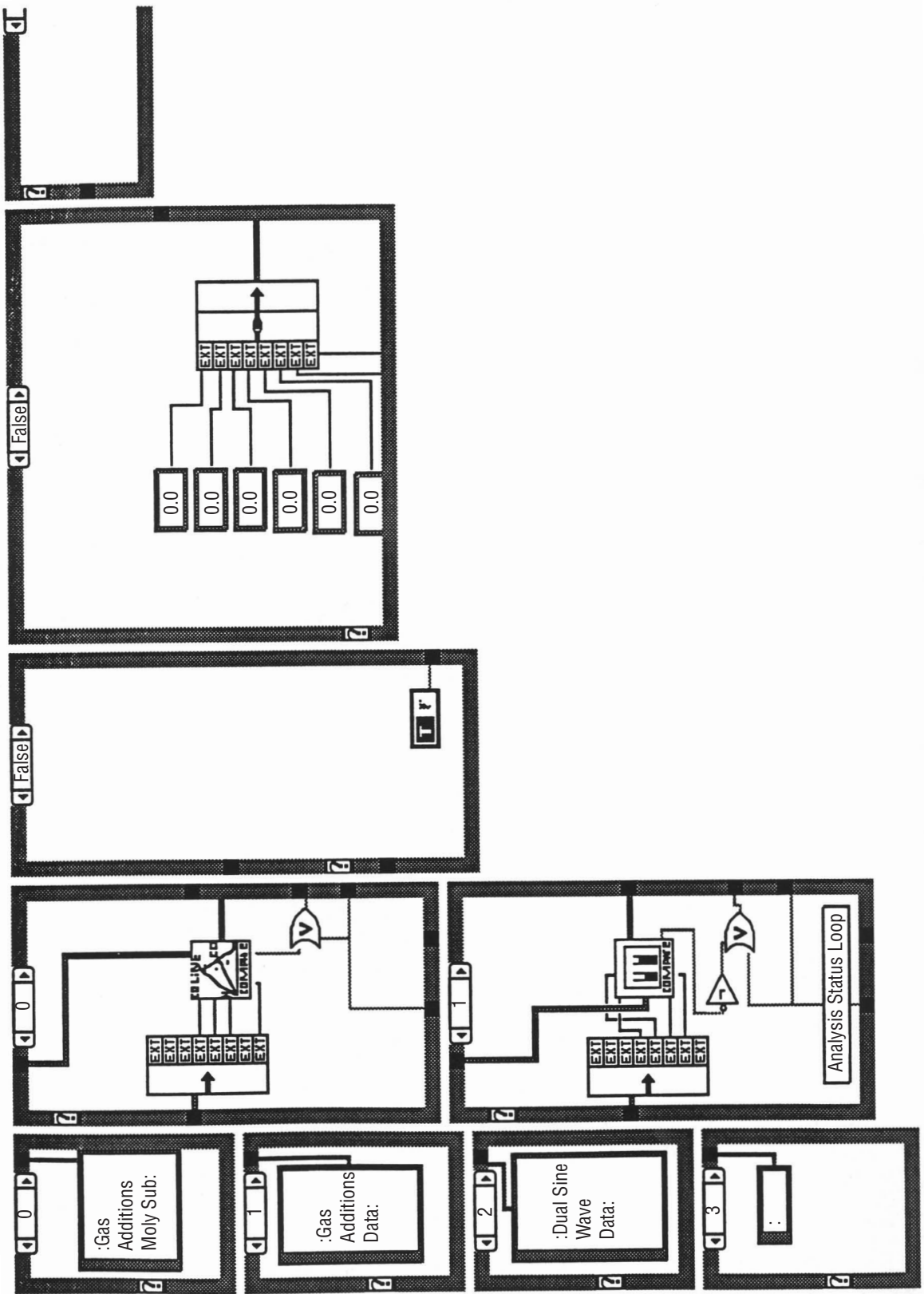


Figure 246(e). New torch control system.



True ▶

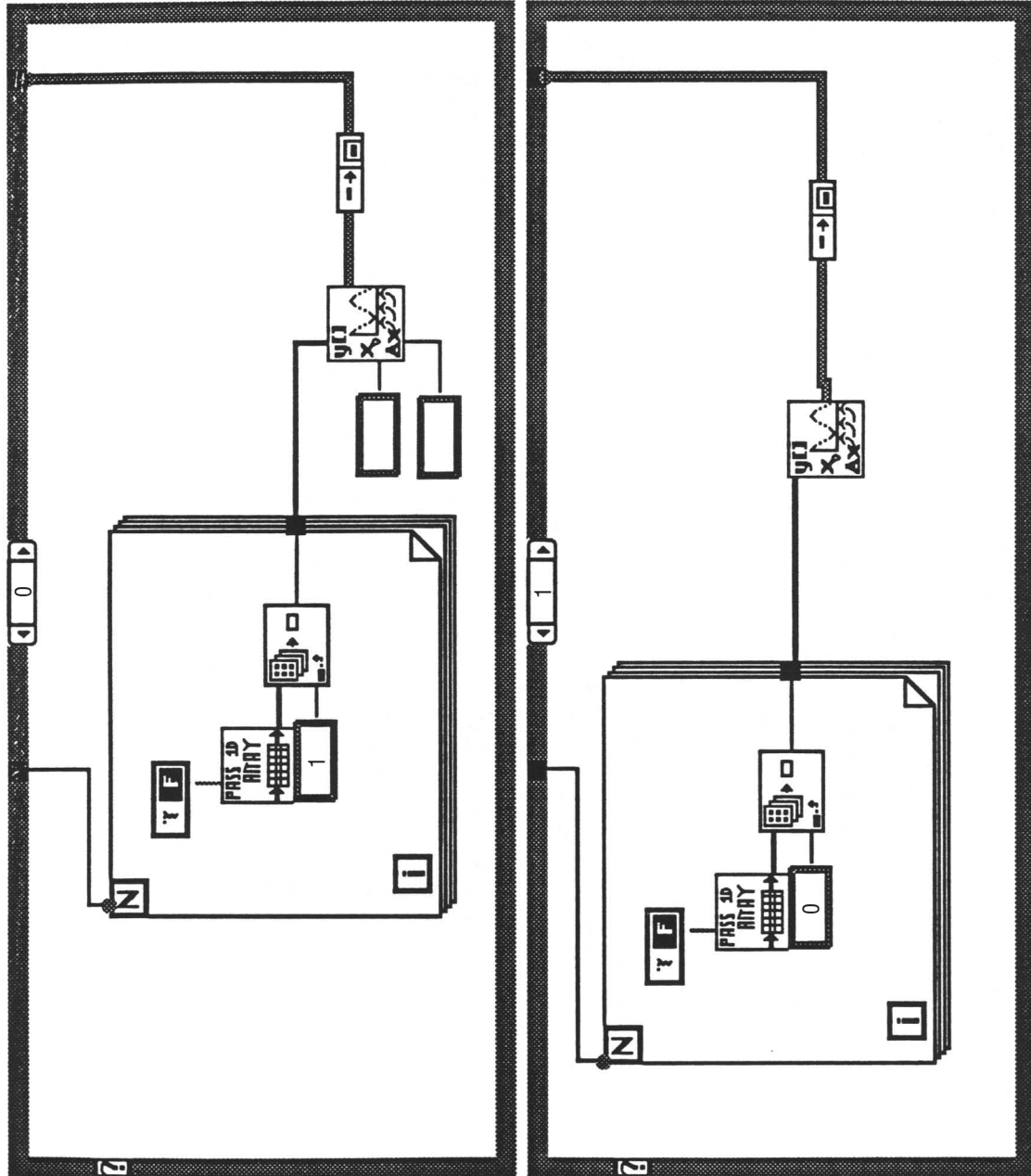


Figure 246(f). New torch control system.

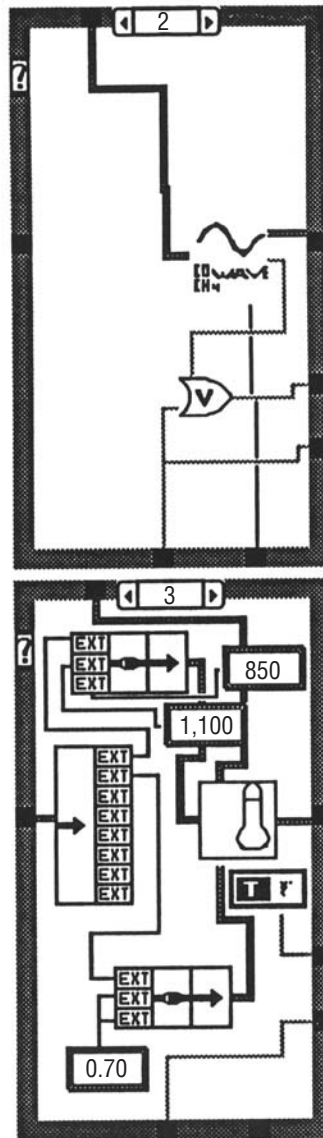


Figure 246(g). New torch control system.



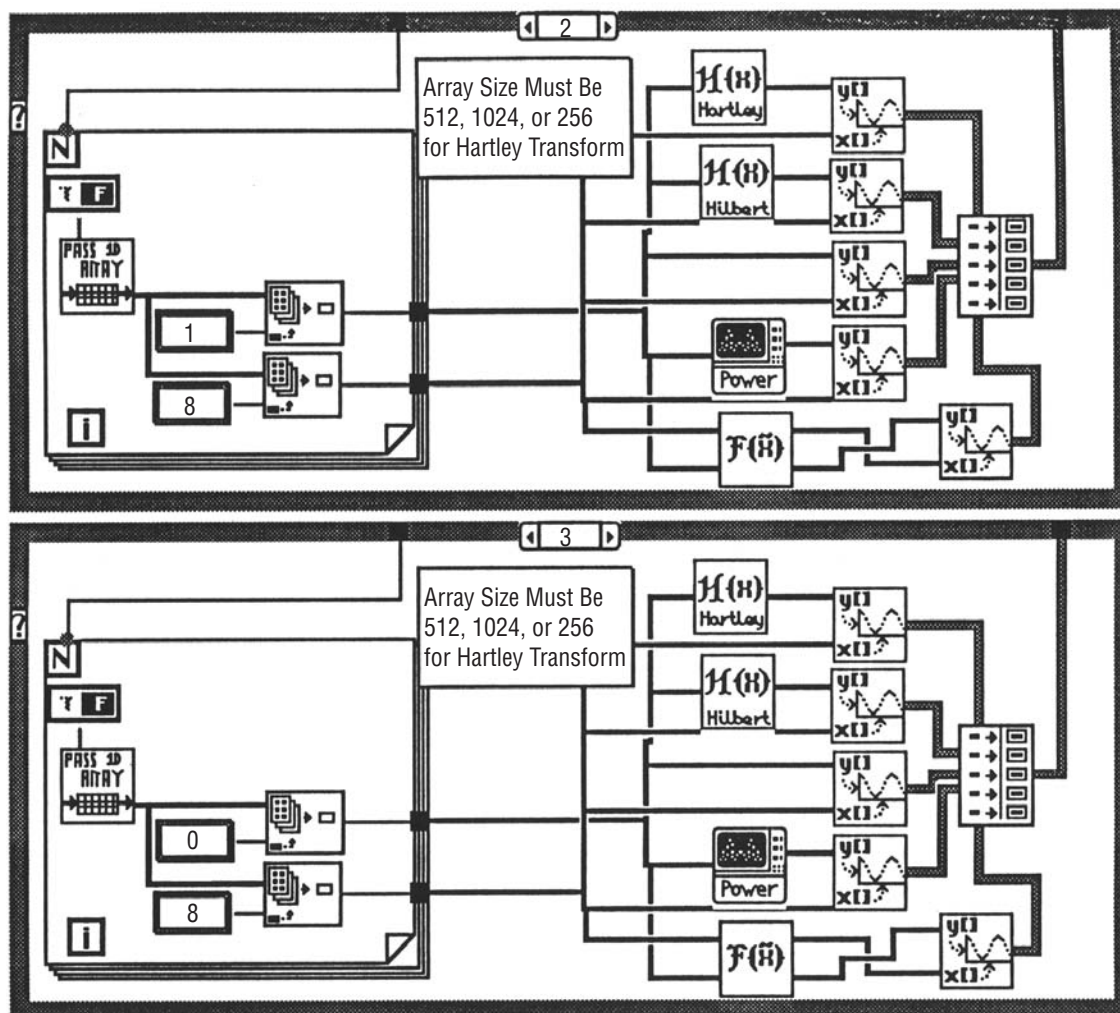


Figure 246(h). New torch control system.

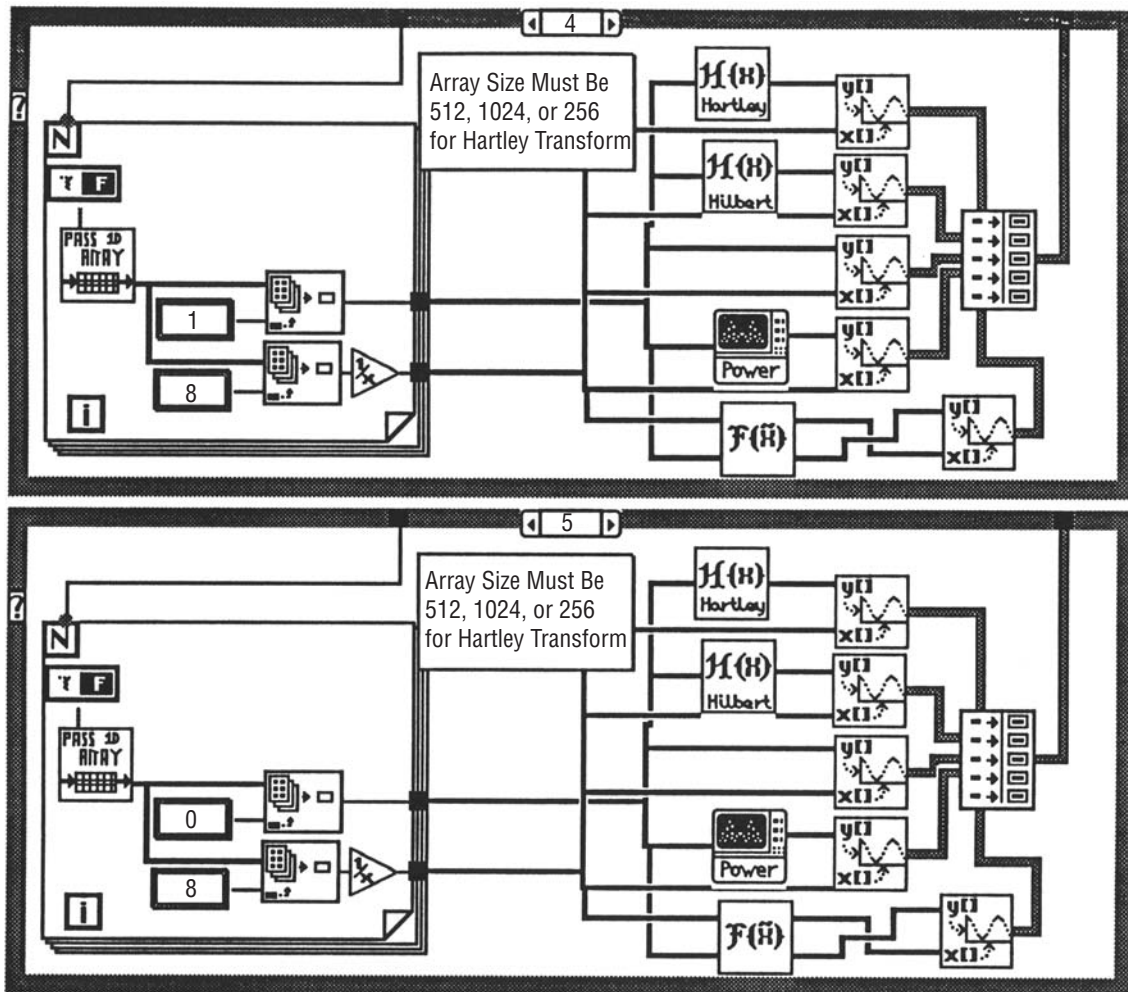
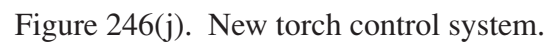


Figure 246(i). New torch control system.





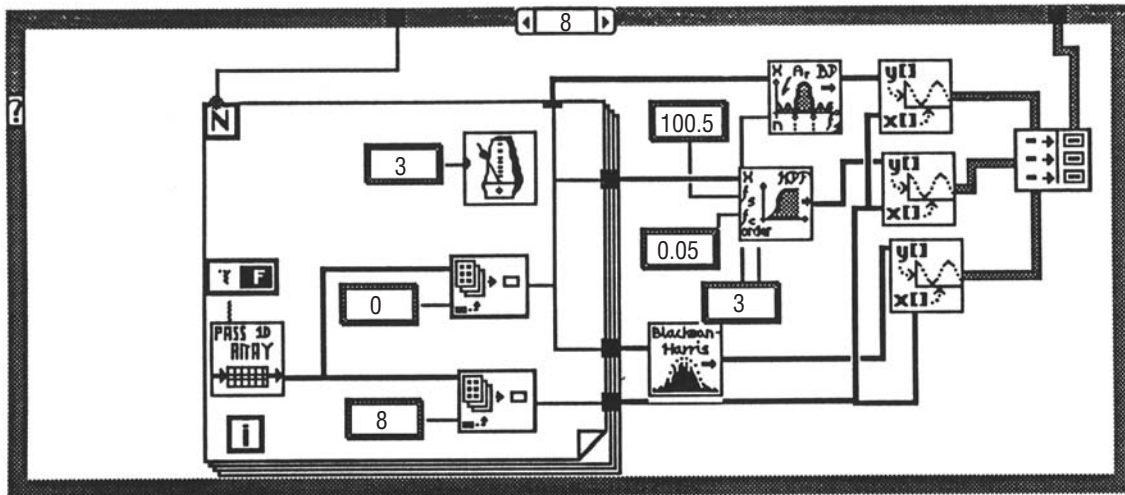


Figure 246(k). New torch control system.



Figure 246(1). New torch control system.

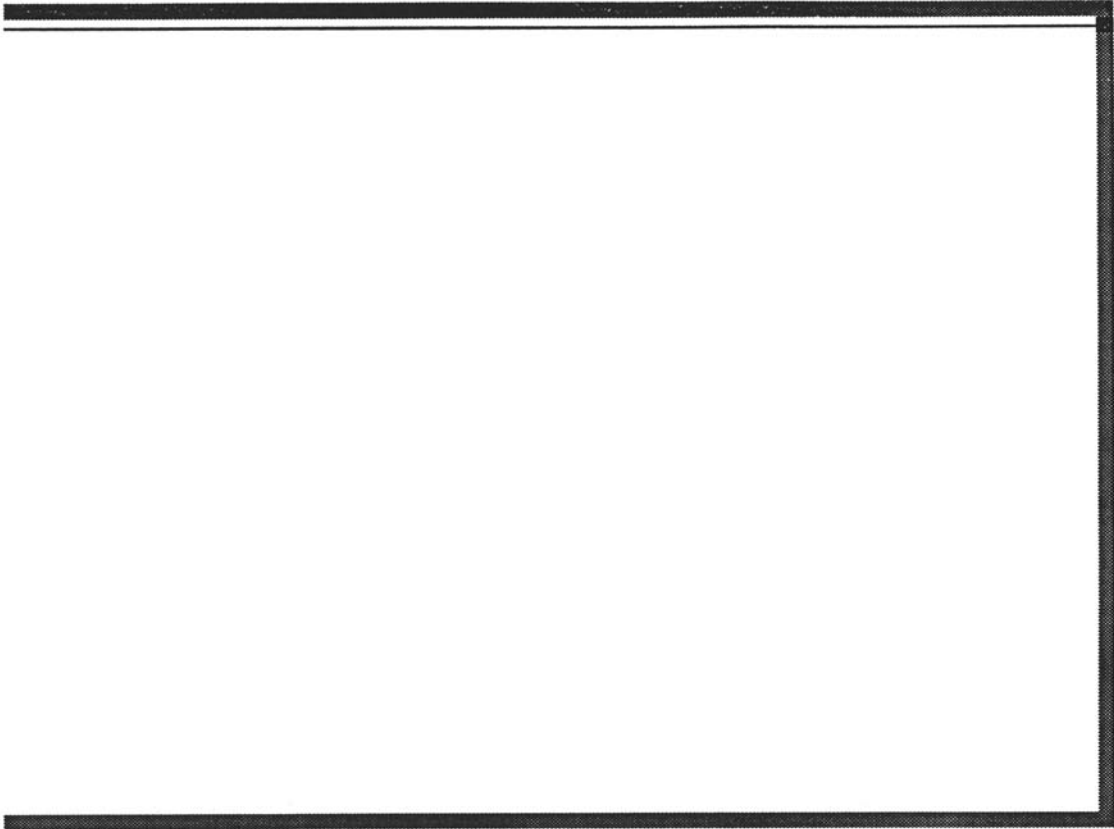
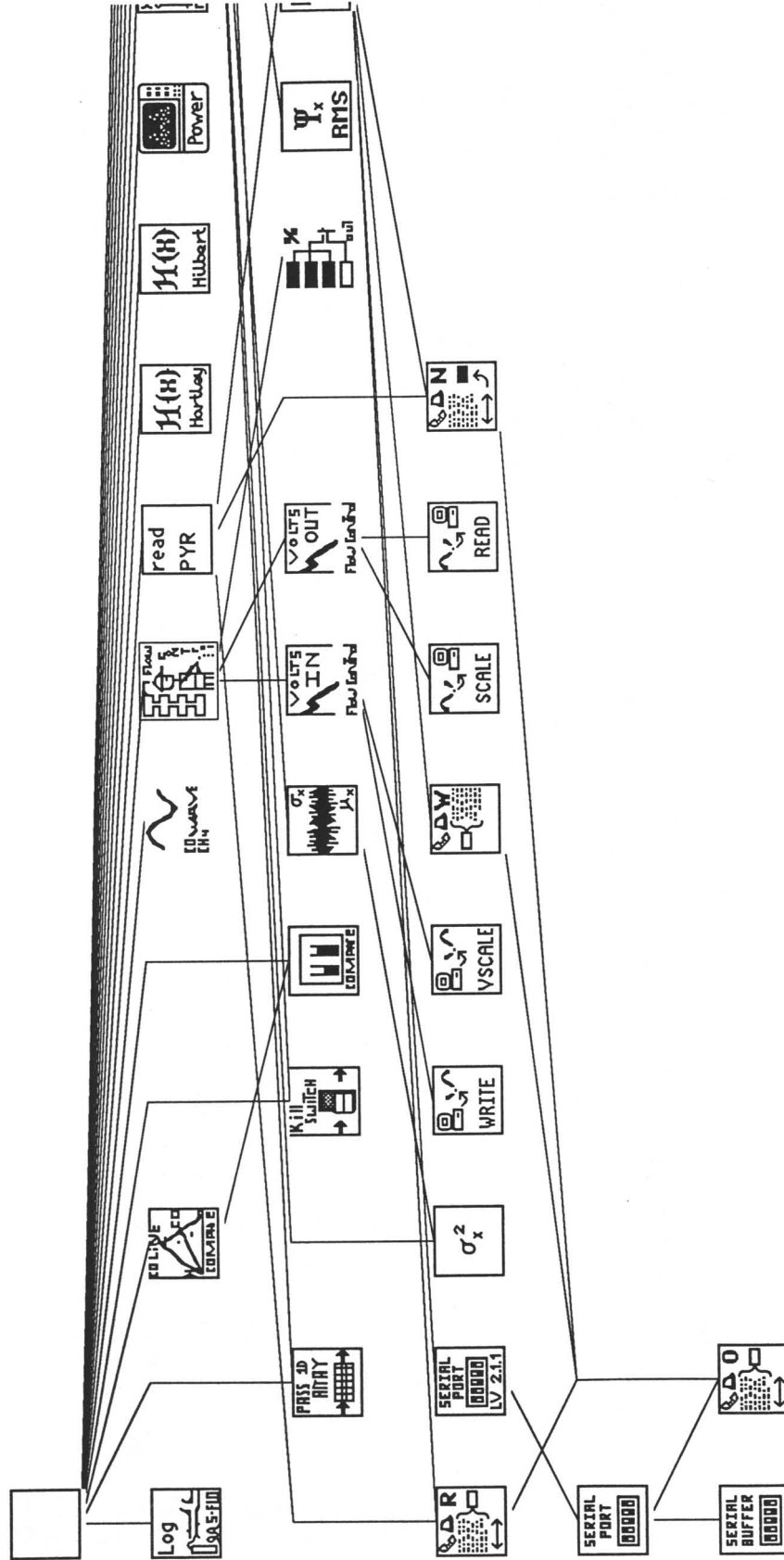


Figure 246(m). New torch control system.



Position in Hierarchy



Connector Pane

Figure 247(a). Flow controller VI.

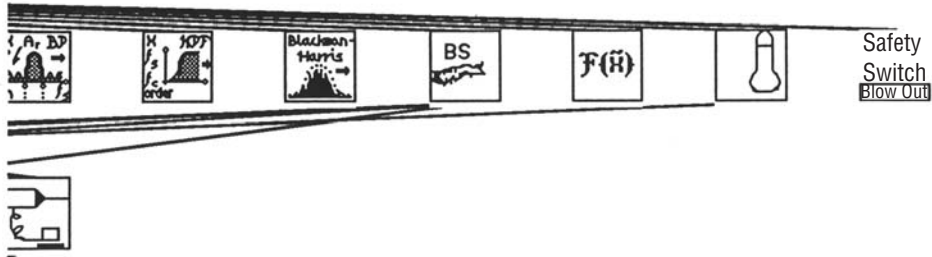


Figure 247(b). Flow controller VI.



Position in Hierarchy

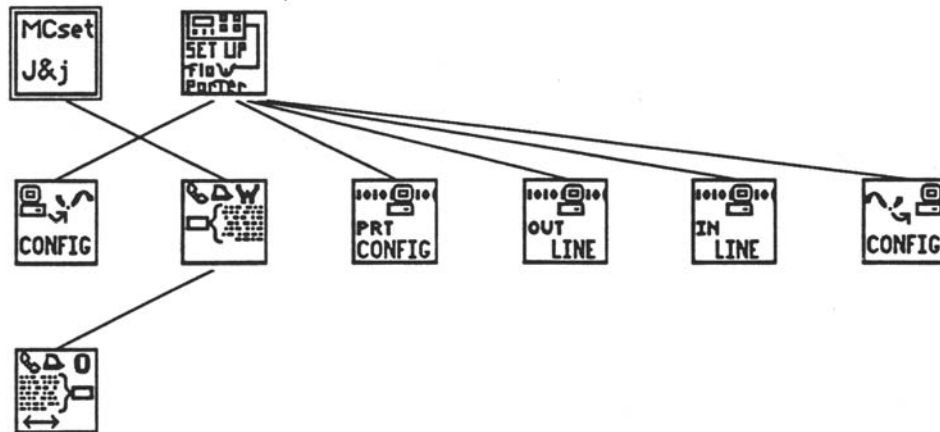


Figure 248. Motion controller setup.





Position in Hierarchy

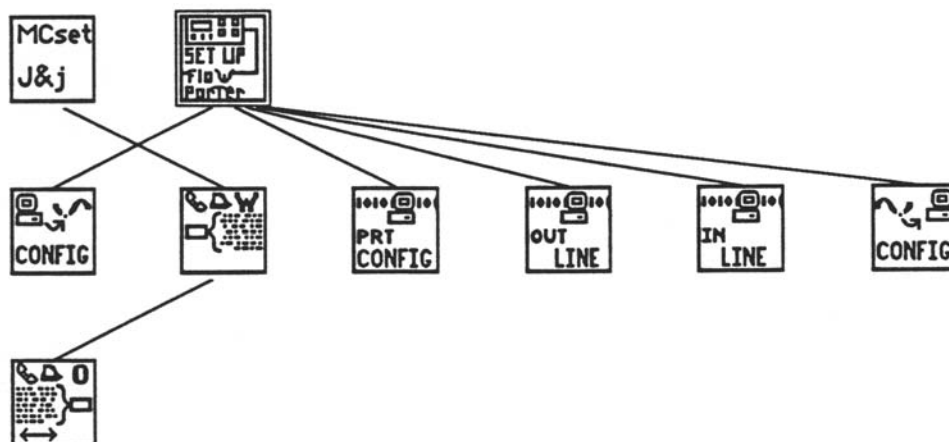
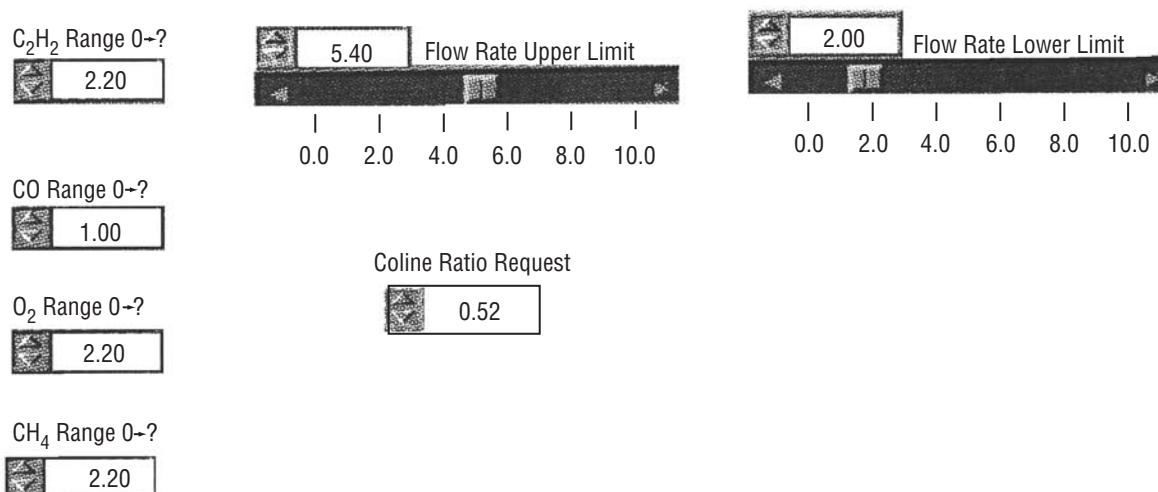


Figure 249. Setup remote control for copy.

Tuesday, December 14, 1993 12:47 AM

Front Panel



Block Diagram

Figure 250. Front panel.

## REFERENCES

1. Bundy, F.P.; et al.: *Nature*, Vol. 176(51), p. 183, 1955.
2. Komanduri, R.; Snail, K.S.; and Fehrenbacher, L.L.: *Philosophical Magazine Letters*, Vol. 62, No. 4, pp. 283–290, 1990.
3. Angus, J.C.; et al.: *Materials Research Society Bulletin*, pp. 38–47, 1989.
4. Eversole, W.G.: U.S Patent Nos. 3,030,187 and 3,030,188, 1958.
5. Deryagin, B.V.; and Feedosev, D.B.: *Scientific American*, Vol. 233, p. 102, 1975.
6. Spitsyn, B.V.; Bouilov, B.P.; and Deryagin, B.V.: *Progress in Crystal Growth Characterization*, Vol. 17, p. 79, 1988.
7. Yarbrough, W.A.: *Journal of the American Ceramic Society*, Vol. 75(12), p. 3179–2000, 1992.
8. Kosky, P.G.; and McAtee, D.S.: *Materials Letters*, Vol. 8, No. 9, pp. 369–374, 1989.
9. Bachmann, P.; Leers, D.; and Lydtin, H.: *Diamond and Related Materials*, Vol. 1, pp. 1–12, 1991.
10. Saito, Y.; Matsuda, S.; and Nogita, S.: *Journal of Material Science Letters*, pp. 565–568, 1986.
11. Spear, K.E.: *Earth and Mineral Sciences*, Vol. 56, No. 4, pp. 53–59, 1987.
12. Watanabe, I.; and Sugata, K.: *Japanese Journal of Applied Physics*, Vol. 27, No. 8, pp. 1397–1400, 1988.
13. Saito, Y.; et al.: *Journal of Materials Science*, Vol. 23, pp. 842–848, 1988.
14. Kung, P.J.; and Tzeng, Y.: *Journal of Applied Physics*, Vol. 66(10), pp. 4676–4684, 1989.
15. Gomez-Aleixandre, C.; et al.: *Journal of Applied Physics*, Vol. 74(6), pp. 3752–3757, 1993.
16. Zhang, J.; et al.: *Journal of Vacuum Science and Technology A*, Vol. 8(3), pp. 2124–2128, 1990.
17. Hirai, H.; Yazaki, Y.; and Fukunaga, O.: *Journal of Material Science Letters*, Vol. 10, pp. 330–332, 1991.
18. Mitomo, T.; et al.: *Journal of Applied Physics*, Vol. 70(8), pp. 4532–4539, 1991.

19. Joeris, P.; Benndorf, C.; and Bohr, S.: *Journal of Applied Physics*, Vol. 71(9), pp. 4638–4639, 1992.
20. Williams, B.E.; Kong, H.S.; and Glass, J.T.: *Journal of Materials Research*, Vol. 5, No. 4, pp. 801–810, 1990.
21. Setaka, N.: *Journal of Materials Research*, Vol. 4, No. 3, pp. 664–670, 1989.
22. Lee, C.H.; Fu, T.D.; and Chen, Y.F.: *Journal of Materials Sciences*, Vol. 28, pp. 170–176, 1993.
23. Wolden, C.; Mitra, S.; and Gleason, K.K.: *Journal of Applied Physics*, Vol. 72(8), pp. 3750–3758, 1992.
24. Sawabe, A.; and Inuzuka, T.: *Thin Solid Films*, Vol. 137, pp. 89–99, 1986.
25. Harris, S.J.; Weiner, A.M.; and Perry, T.A.: *Applied Physics Letters*, Vol. 53(17), pp. 155–157, 1988.
26. Corat, E.J.; and Goodwin, D.G.: *Journal of Applied Physics*, Vol. 74(3), pp. 2021–2029, 1993.
27. Celli, F.G.; and Butler, J.E.: *Journal of Applied Physics*, Vol. 71(6), pp. 2877–2883, 1992.
28. Jackman, R.B.; Chua, L.H.; and Ford, J.S.: *Surface Science*, Vol. 292, pp. 47–60, 1993.
29. Chu, C.J.; et al.: *Journal of Applied Physics*, Vol. 70(3), pp. 1695–1705, 1991.
30. McNamara, K.M.; and Gleason, K.K.: *Journal of Applied Physics*, Vol. 71(6), pp. 2884–2889, 1992.
31. Chu, C.J.; et al.: *Journal of Materials Research*, Vol. 5, No. 11, pp. 2405–2413, 1990.
32. D'Evelyn, M.P.; et al.: *Journal of Applied Physics*, Vol. 71(3), pp. 1528–1530, 1992.
33. Kondoh, E.; et al.: *Journal of Applied Physics*, Vol. 72(2), pp. 705–711, 1992.
34. Harris, S.J.; Weiner, A.M.; and Perry, T.A.: *Journal of Applied Physics*, Vol. 70(3), pp. 1385–1391, 1991.
35. Singh, J.; and Vellaikal, M.: *Journal of Applied Physics*, Vol. 73(6), pp. 2831–2834, 1993.
36. Singh, J.: *Journal of Materials Science*, Vol. 29, pp. 2761–2766, 1994.
37. Ohsawa, Y.; et al.: *Journal of Materials Science*, pp. 3748–3752, 1991.
38. Okano, K.; et al.: *Japanese Journal of Applied Physics*, Vol. 27, No. 2, pp. L173–L175, 1988.

39. Morrish, A.A.: White Paper.
40. Suzuki, K.; et al.: *Applied Physics Letter*, Vol. 50(12), pp. 728–729, 1987.
41. Kurihara, K.; et al.: *Applied Physics Letter*, Vol. 52(6), pp. 437–438, 1990.
42. Cappelli, M.A.; Owano, T.G.; and Kruger, C.H.: *Journal of Materials Research*, Vol. 5, No. 11, b pp. 2326–2333, 1990.
43. Vilotijevic, M.; Dimitrijevic, S.T.; and Randjelovic, I.: *Journal of Materials Science Letters*, pp. 1261–1263, 1993.
44. Mitsuda, Y.; Tanaka, K.; and Yoshida, T.: *Journal of Applied Physics*, Vol. 67(8), pp. 3604–3608, 1990.
45. Coltrin, M.E.; and Dandy, D.S.: *Journal of Applied Physics*, Vol. 74(9), pp. 5803–5820, 1993.
46. Takeuchi, K.; and Yoshida, T.: *Journal of Applied Physics*, Vol. 71(6), 1992.
47. Stalder, K.R.; and Sharpless, R.L.: *Journal of Applied Physics*, Vol. 68(12), pp. 6187–6190, 1990.
48. Kawarada, M.; Jurihara, K.; and Sasaki, K.: *Journal of Applied Physics*, Vol. 71(3), pp. 1442–1445, 1992.
49. Norton Diamond Film Co., 300–C West Main Street, Northboro, MA 01532–1545 (Papers such as—*N. B. Nguyen Power Conversion*, 1991, Proc—*E.F. Borchelt and G. Lu*, 6th Int SAMPE Electronics Conf—*7.8 Boudreaux/Diamond Inserts and Coated Substrates*—and others).
50. Eddy, C.R., Jr.; et al.: *Journal of Materials Research*, Vol. 7, No. 12, pp. 3255–3259, 1992.
51. Youchison, D.L.; Eddy, C.R.; and Sartwell, B.D.: *Journal of Vacuum Science and Technology A*, Vol. 11(1), pp. 103–114, 1993.
52. Youchison, D.L.; Eddy, C.R.; and Sartwell, B.D.: *Journal of Vacuum Science and Technology A*, Vol. 11(4), pp. 1875–1880, 1993.
53. Jin, S.; and Moustakas, T.D.: *Diamond and Related Materials*, Vol. 2, pp. 1355–1369, 1993.
54. Chang, J.J.; et al.: *Journal of Applied Physics*, Vol. 71(6), pp. 2918–2923, 1992.
55. Ishii, A.; et al.: *Journal of Vacuum Science and Technology A*, Vol. 12(4), pp. 1241–1243, 1994.
56. Gruen, D.M.; et al.: *Journal of Vacuum Science and Technology A*, pp. 1491–1495, 1994.
57. Harris, S.J.; and Martin, L.R.: *Journal of Materials Research*, Vol. 5, No. 11, pp. 2313–2319, 1990.

58. Martin, L.R.; and Hill, M.W.: *Journal of Material Science Letters*, Vol. 9, pp. 621–623, 1990.
59. Martin, L.R.: *Journal of Applied Physics*, Vol. 70(10), pp. 5667–5674, 1991.
60. Kitahama, K.; et al.: *Applied Physics Letters*, Vol. 49(11), pp. 634–635, 1986.
61. Celii, F.G.; Nelson, H.H.; and Pehrsson, P.E.: *Journal of Materials Research*, Vol. 5, No. 11, pp. 2337–2344, 1990.
62. O’Keefe, A.: *Deacon Research—SBIR Phase 1 Final Report Contract F49612–88–C–0099*, Sponsored by the U.S. Air Force Office of Scientific Research, Bolling Air Force Base, Washington, DC, 1989.
63. Narayan, J.; Godbole, V.P.; and White, C.W.: *Science*, Vol. 252, pp. 416–418, 1991.
64. Molian, P.A.; and Waschek, A.: *Journal of Materials Science*, Vol. 28, pp. 1733–1737, 1993.
65. Rebello, J.H.D.; and Subramanian, V.V.: *JOM*, pp. 60–63, 1994.
66. Latsch, S.; and Hiraoka, H.: *JOM*, pp. 64–65, 1994.
67. Hirose, Y.; and Terasawa, Y.: *Japan Journal of Applied Physics*, Vol. 2, p. L519, 1986.
68. Hanssen, L.M.; et al.: *Materials Letters*, Nos. 7 and 8, p. 266, 1988.
69. Hirose, Y.; and Kondo, N.: *Program and Book of Abstracts Japan Applied Physics*, p. 434, 1988.
70. Allendorf, M.D.; Bautista, J.R.; and Potkay, E.: *Journal of Applied Physics*, Vol. 66(10), pp. 5046–5051, 1989.
71. Carrington, W.A.; et al.: *Metallurgical Transactions A*, Vol. 20A, pp. 1282–1284, 1989.
72. Homann, K.H.: Vol. 11, pp. 265–287, 1967.
73. Matsui, Y.; and Nomaguchi, T.: *Nomaguchi Japanese Journal of Applied Physics*, Vol. 28, No. 9, pp. 1718–1724, 1977.
74. Matsui, Y.; et al.: *Japanese Journal of Applied Physics*, Vol. 28, No. 9, pp. 1718–1724, 1989.
75. Kosky, P.G.; and McAtee, D.S.: *Materials Letters*, Vol. 8, No. 9, pp. 369–374, 1989.
76. Cappelli, M.A.; and Paul, P.H.: *Journal of Applied Physics*, Vol. 67(5), pp. 2596–2602, 1990.
77. Hwang, J.; et al.: *Journal of Materials Research*, Vol. 5, No. 11, pp. 2334–2336, 1990.

78. Yalamanchi, R.S.; and Harshavardhan, K.S.: *Journal of Applied Physics*, Vol. 68(11), pp. 9–12, 1990.
79. Matsui, Y.; et al.: *Diamond and Related Materials*, Vol. 1, pp. 19–24, 1991.
80. Snail, K.A.; and Craige, C.J.: *Applied Physics Letters*, Vol. 58(17), pp. 1875–1877, 1991.
81. Alers, P.; Hanni, W.; and Hintermann, H.E.: *Diamond and Related Materials*, Vol. 2, pp. 393–396, 1992.
82. Snail, K.A.; et al.: *Journal of Applied Physics*, Vol. 74(12), pp. 1100–1118, 1993.
83. Ravi, K.V.; et al.: *Journal of Materials Research*, Vol. 5, No. 11, pp. 2356–2366, 1990.
84. Zhu, W.; et al.: *Diamond and Related Materials*, Vol. 2, pp. 491–495, 1993.
85. Okada, K.; et al.: *Journal of Materials Science*, pp. 3081–3085, 1991.
86. Hanssen, L.M.; et al.: *Submitted to Thin Solid Films*, pp. 798–800, 1990.
87. Ravi, K.V.: *Journal of Materials Research*, Vol. 7, No. 2, pp. 384–393, 1992.
88. Hirose, Y.; Amanuma, S.; and Komaki, K.: *Journal of Applied Physics*, Vol. 68(12), pp. 6401–6405, 1990.
89. Oakes, D.B.; et al.: *Journal of Applied Physics*, Vol. 69(4), pp. 4561–4566, 1991.
90. Glumac, N.G.; Corat, E.J.; and Goodwin, D.G.: *Diamond and Related Materials*, Vol. 2, pp. 169–173, 1993.
91. Doverspike, K.; Butler, J.E.; and Freitas, J.A.: *Diamond and Related Materials*, Vol. 2, pp. 1078–1082, 1993.
92. Murayama, M.; Kojuma, S.; and Uchida, K.: *Journal of Applied Physics*, Vol. 69(11), pp. 7924–7926, 1991.
93. Wang, D.Y.; et al.: *Diamond and Related Materials*, Vol. 2, pp. 304–310, 1993.
94. Tseng, Y.; et al.: *Applied Physics Letters*, Vol. 58(23), pp. 2645–2647, 1991.
95. Cappelli, M.A.: Private Communication, 1991.
96. Bundy, F.P.; et al.: *Nature*, Vol. 176, p. 51, 1955.
97. Pavel, E.; et al.: *Diamond and Related Materials*, Vol. 2, pp. 500–504, 1993.



98. Hong, S.; and Wakatsuki, M.: *Journal of Material Science Letters*, pp. 283–285, 1993.
99. Pavel, E.; et al.: *Journal of Materials Science*, Vol. 28, pp. 1645–1647, 1993.
100. Lee, J-K.; Park, J-K.; and Eun, K.Y.: *Journal of Crystal Growth*, Vol. 125, pp. 51–58, 1992.
101. Hirai, H.; and Kondo, K.L.: *Science*, Vol. 253, pp. 772–774, 1990.
102. Erskine, D.J.; and Nellis, W.J.: *Journal of Applied Physics*, Vol. 71(10), pp. 4882–4886, 1992.
103. DeCarli, P.S.: *Science and Technology of Industrial Diamonds*, edited by J. Buris, Proceedings of the International Industrial Diamond Conference, Oxford, pp. 49–63, 1967.
104. Regueiro, M.N.; et al.: *Physical Review B*, Vol. 46, No. 15, pp. 9903–9905, 1992.
105. Matsuoka, M.; Hoshino, K.; and Ono, K.: *Journal of Vacuum Science and Technology A*, Vol. 11(6), pp. 2994–3001, 1993.
106. Kitabatake, M.; and Wasa, K.: *Journal of Vacuum Science and Technology A*, Vol. 6(3), pp. 1793–1797, 1988.
107. Panitz, J.K.G.; et al.: *Journal of Vacuum Science and Technology A*, Vol. 12(4), pp. 1480–1486, 1994.
108. Lee, S.S.; et al.: *Science*, Vol. 263, pp. 1596–1598, 1994.
109. Ostwald, W.; and Physik, Z.: *Chemistry*, Vol. 22, p. 289, 1987.
110. Stranski, L.N.; and Totomanow, D.: *Zeitschrift Fuer Physics Chemistry*, Vol. 163A, Nos. 5 and 6, pp. 399–408, 1933.
111. Nowick, A.S.: *Comm. on Solid State Physics*, Vol. 2, p. 155, 1969.
112. Strickland-Constable, R.F.: *Kinetics and Mechanism of Crystallization*, Academic Press New York, pp. 12, 44–45, 1968.
113. Williams, F. A.: *Combustion Theory*, Benjamin/Cummings Publishing Co., 1985.
114. Toshev, S.; Milchev, A.; and Stoyanov, S.: *Journal of Crystal Growth*, Vol. 113(14), pp. 123–127, 1972.
115. Frade, J.R.: *Journal of Materials Science*, Vol. 28, pp. 6715–6718, 1993.
116. Kurz, W.; and Fisher, D.J.: *Fundamentals of Solidification*, Trans Tech Publication, Switzerland, Vol. A4, 1989.

117. Gutzow, J.; and Toshev, S.: *Kristall and Technik*, Vol. 3, pp. 485–497, 1968.
118. Gutzow, J.; and Toshev, S.: *Journal of Crystal Growth*, Vol. 7, pp. 215–220, 1970.
119. Inoue, N.; et al.: *Journal of Crystal Growth*, Vol. 84, pp. 21–35, 1987.
120. Shi, G.; Seinfeld, J.H.; and Okuyama, K.: *Physical Review A*, Vol. 41, No. 4(15), pp. 2102–2108, 1990.
121. Shi, G.; and Seinfeld, J.H.: *Journal of Materials Research*, Vol. 6, No. 10, pp. 2091–2102, 1991.
122. Turnbull, D.: *The Journal of Chemical Physics*, Vol. 18, No. 2, pp. 198–203, 1950.
123. Calvert, A.; and Uhlman, T.: *Journal of Crystal Growth*, Vol. 17, pp. 13–22, 1972.
124. Hirth, J.P.: *Journal of Crystal Growth*, Vol. 17, pp. 63–69, 1972.
125. Lewis, B.; and Halpern, V.: *Journal of Crystal Growth*, Vol. 33, pp. 39–52, 1976.
126. Trofimov, V.I.: *Journal of Crystal Growth*, Vol. 54, pp. 211–216, 1981.
127. Ookawa, A.: *Crystal Growth and Characterization*, R. Ueda, and J.B. Mullin (eds.), North Holland Publishing Co., pp. 5–19, 1975.
128. Osaka, T.; and Kasukabe, Y.: *Journal of Crystal Growth*, Vol. 73, pp. 10–20, 1985.
129. Rasmussen, D.H.; et al.: *Journal of Crystal Growth*, Vol. 64, pp. 229–238, 1983.
130. Demo, P.; and Kozisek, Z.: *Physical Review B*, Vol. 48, No. 6(1), pp. 3620–3625, 1993.
131. Jayaraman, D.; et al.: *Journal of Crystal Growth*, Vol. 79, pp. 997–1000, 1986.
132. Desre, P.J.: *Philosophical Magazine Letters*, Vol. 69, pp. 261–268, 1994.
133. Lee, C.P.; and Wang, T.G.: *Journal Applied Physics*, Vol. 71(11), pp. 5721–5723, 1992.
134. Wilcox, W.R.: *Journal of Crystal Growth*, Vol. 26, pp. 153–154, 1974.
135. Spitsyn, B.V.: *The Institute of Physical Chemistry of the USSR Academy of Sciences, Moscow Journal*, Vol. 25, pp. 23–44, 1970.
136. Martin, T.P.: *Elemental and Molecular Clusters*, G. Benedek, T.P. Martin, and G. Pacchioni (ed.), Springer Verlag Publishers, 1988.
137. Berry, R.S.: *Scientific American*, pp. 68–74, 1990.

138. Ostwald, W.: *Zeitschrift Fuer Physik. Chemie.*, Vol. 22, pp. 289–330, 1987.
139. Berry, R.S.: *The Chemical Physics of Atomic and Molecular Clusters Proceedings of the International School of Physics, <<Enrico Fermi>> G. Scoles (ed.)*, pp. 1–41, 1990.
140. Jortner, J.; Scharf, D.; and Landman, U.: *Elemental and Molecular Clusters*, G. Benedek, T.P. Martin, and G. Pacchioni (ed.), Springer Verlag Publishers, pp. 148–205, 1988.
141. Friedel, J.: *Elemental and Molecular Clusters*, G. Benedek, T.P. Martin, and G. Pacchioni (ed.), Springer Verlag Publishers, 1988.
142. Cox, D.M.; Zakin, M.R.; and Kaldor, A.: *Elemental and Molecular Clusters*, G. Benedek, T.P. Martin, and G. Pacchioni (ed.), Springer Verlag Publishers, pp. 329–349, 1988.
143. Olivei, A.: *Journal of Crystal Growth*, Vol. 22, pp. 69–79, 1974.
144. Olivei, A.: *Journal of Crystal Growth*, Vol. 26, pp. 243–254, 1974.
145. Chow, G.M.: *Materials Research Society Symposium Proceedings*, Vol. 206, pp. 315–320, 1991.
146. Klots, C.E.: *Nature*, Vol. 327, pp. 222–223, 1987.
147. Berry, R.S.: *The Chemical Physics of Atomic and Molecular Clusters Proceedings of the International School of Physics, <<Enrico Fermi>> G. Scoles (ed.)*, pp. 43–98, 1990.
148. Torchet, G.; et al.: *The Chemical Physics of Atomic and Molecular Clusters Proceedings of the International School of Physics, <<Enrico Fermi>> G. Scoles (ed.)*, pp. 513–542, 1990.
149. Shimamura, S.: *Physics and Chemistry of Small Clusters*, P. Jena, B.K. Rao, and S.N. Khanna (eds.), Scribner's, 1991.
150. Cheng, H.P.; and Landman, U.: *Science*, Vol. 260, pp. 1304–1307, 1993.
151. Zajfman, D.; et al.: *Science*, Vol. 258, pp. 1129–1131, 1992.
152. Fantucci, P.; and Koutceky, J.: *Elemental and Molecular Clusters*, G. Benedek, T.P. Martin, and G. Pacchioni (ed.), Springer Verlag Publishers, 1988.
153. Raghavachari, K.; and Binkley, J.S.: *Physics and Chemistry of Small Clusters*, P. Jena, B.K. Rao, and S.N. Khanna (eds.), Scribner's, 1991.
154. Narayan, J.; Srivatsa, A.R.; and Ravi, K.V.: *Applied Physics Letters*, Vol. 54(17), pp. 1659–1661, 1989.
155. Ott, L.S.; and Ray, A.K.: *Physics and Chemistry of Small Clusters*, P. Jena, B.K. Rao, and S.N. Khanna (eds.), Scribner's, 1991.

156. Mandich, M.L.: *The Chemical Physics of Atomic and Molecular Clusters Proceedings of the International School of Physics, <<Enrico Fermi>> G. Scoles (ed.)* pp. 635–760, 1990.
157. Jing, X.; and Chelikowsky, J.R.: *Physical Review B*, Vol. 46, No. 23, pp. 503–508, 1992.
158. Frenklach, M.; and Spear, K.E.: *Journal of Materials Research*, Vol. 3(1), pp. 133–140, 1988.
159. Kaufold, R.; et al.: *Metco Division of Perkin Elmer White Paper*.
160. Chon, T.; et al.: *Metco Division of Perkin Elmer White Paper*.
161. Varacalle, D.J.; et al.: *Proceedings of the International Thermal Spray Conference and Exposition*, Orlando, FL, 1992.
162. Nickerson, G.R.; et al.: SN91, Contract NAS8–36863, March 31, 1989, NASA–CR–183947.
163. Angus, J.C.; et al.: *Materials Research Society Bulletin*, pp. 38–47, 1989.
164. Messier, R.; and Yehoda, J.E.: *Journal of Applied Physics*, Vol. 58(10), pp. 3739–3748, 1985.
165. Messier, R.: *Journal of Vacuum Science and Technology A*, Vol. 4(3), pp. 490–495, 1986.
166. Messier, R.; et al.: *Thin Solid Films*, Vol. 153, pp. 1–9, 1987.
167. Kobashi, K.; et al.: *Physical Review B*, Vol. 38, No. 6, pp. 4067–4084, 1988.
168. Kobashi, K.; et al.: *Journal of Vacuum Science and Technology A*, Vol. 6(3), pp. 1816–1817, 1988.
169. Williams, B.E.; and Glass, J.T.: *Journal of Materials Research*, Vol. 4, No. 2, pp. 373–384, 1989.
170. Je, J.H.; and Lee, G.Y.: *Journal of Materials Science*, Vol. 27, pp. 6324–6330, 1992.
171. Wild, C.; et al.: *Diamond and Related Materials*, Vol. 2, pp. 158–168, 1993.
172. Sun, B.; Zhang, X.; and Lin, Z.: *Physical Review B*, Vol. 47, No. 15, pp. 9816–9824, 1993.
173. Kikuchi, N.; Komatsu, T.; and Yoshimura, H.: *Materials Science and Engineering*, Vol. A105–A106, pp. 525–534, 1988.
174. Kweon, D.W.; and Lee, J.Y.: *Journal of Materials Science Letters*, Vol. 11, pp. 1043–1045, 1992.
175. Zhu, W.; et al.: *Journal of Applied Physics*, Vol. 68(4), pp. 1489–1495, 1990.
176. Hirabayashi, K.: *Journal of Applied Physics*, Vol. 72(9), pp. 4083–4087, 1992.
177. Frenklach, M.; and Spear, K.E.: *Journal of Materials Research*, Vol. 3(1), pp. 133–140, 1988.
178. Miyata, K.; et al.: *Journal of Materials Research*, Vol. 8, No. 11, pp. 2845–2857, 1993.
179. Matsumoto, S.; and Matsui, Y.: *Journal of Materials Science*, Vol. 18, pp. 1785–1793, 1983.
180. Wild, C.; Herres, N.; and Koidl, P.: *Journal of Applied Physics*, Vol. 68(3), pp. 973–978, 1990.
181. Kobashi, K.; et al.: *Journal of Materials Research*, Vol. 5, No. 11, pp. 2469–2482, 1990.

182. Pavel, E.; et al.: *Diamond and Related Materials*, Vol. 2, pp. 500–504, 1993.
183. DeNatale, J.F.; Harker, A.B.; and Flintoff, J.F.: *Journal of Applied Physics*, Vol. 69(9), pp. 6456–6460, 1991.
184. Sutcu, L.F.; et al.: *Journal of Applied Physics*, Vol. 71(12), pp. 5930–5940, 1992.
185. Everson, M.P.; and Tamor, M.A.: *Journal of Materials Research*, Vol. 7, No. 6, pp. 788–791, 1992.
186. Tamor, M.A.; and Everson, M.P.: *Journal of Materials Research*, Vol. 8, pp. 1770–1772, 1993.
187. Everson, M.P.; et al.: *Journal of Applied Physics*, Vol. 75(1), pp. 169–172, 1994.
188. Hu, Z.W.; et al.: *Journal of Physics Condensed Matter*, Vol. 4, pp. 3753–3747, 1992.
189. Kondoh, E.; Tanaka, K.; and Ohta, T.: *Journal of Applied Physics*, Vol. 74(3), pp. 2030–2035, 1993.
190. Sun, B.; Zhang, X.; and Lin, Z.: *Journal of Applied Physics*, Vol. 73(9), pp. 4614–4617, 1993.
191. Busmann, H.G.; et al.: *Surface Science*, Vol. 295, pp. 340–346, 1993.
192. Lee, S.T.; and Apai, G.: *Physical Review B*, Vol. 48, No. 4, pp. 2684–2693, 1993.
193. Moore, M.: in *Properties of Diamond*, J.E. Field (ed.), Academic Press, New York, NY, 1979.
194. Implantation, Ion: in *Diamond Graphite, and Related Materials*, M.S. Dresselhaus and R. Kalish (eds.), Springer Verlag, pp. 12–13, 1992.
195. Varshavskii, A.V.; and Bulanov, G.P.: *Sov. Phys. Dokl.*, Vol. 19, No. 8, pp. 469–471, 1975.
196. Ravi, K.V.; et al.: *Journal of Materials Research*, Vol. 5, No. 11, pp. 2356–2366, 1990.
197. Schermer, J.J.; et al.: *Diamond and Related Materials*, Vol. 2, pp. 1149–1155, 1993.
198. Frey, E.A.; et al.: *Journal of Materials Research*, Vol. 9, No. 3, pp. 152–155, 1994.
199. Komanduri, R.; Snail, K.S.; and Fehrenbacher, L.L.: *Philosophical Magazine Letters*, Vol. 62, No. 4, pp. 283–290, 1990.
200. Zhu, W.; et al.: *Diamond and Related Materials*, Vol. 2, pp. 491–495, 1993.
201. Okada, K.; et al.: *Journal of Materials Science*, pp. 3081–3085, 1991.
202. Okada, K.; et al.: *Journal of Applied Physics*, Vol. 71(10), pp. 4920–4924, 1992.
203. Janssen, G.; et al.: *Journal of Crystal Growth*, Vol. 125, pp. 42–50, 1992.
204. Janssen, G.; et al.: *Journal of Crystal Growth*, Vol. 104, pp. 752–757, 1990.
205. Hirabayashi, K.; Amanuma, S.; and Hirose, Y.: *Applied Physics Letters*, Vol. 60(5), pp. 574–576, 1992.
206. Colthup, N.B.; Daly, L.H.; and Wiberley, S.E.: *Introduction to Infrared and Raman Spectroscopy*, Academic Press Inc., San Diego, CA, 1990.

207. Long, D.A.: *Raman Spectroscopy*, McGraw Hill, New York., NY, pp. 1–4, 1977.
208. Field, J.E.: *The Properties of Diamond*, Academic Press Inc., London, pp. 60–69, 1979.
209. Mehl, M.J.; and Pickett, W.E.: “Raman Scattering Luminescence and Spectroscopic Instrumentation in Technology,” *SPIE*, Vol. 1055, pp. 181–184, 1989.
210. Solin, S.A.; and Ramdas, A.K.: “Raman Spectrum of Diamond,” *Physical Review B*, Vol. 1, No. 4, pp. 1687–1698, 1970.
211. Herchen, H.; and Cappelli, M.A.: *Physical Review B*, Vol. 43, pp. 11,740–11,744, 1991.
212. Holloway, H.; et al.: *Physical Review B*, Vol. 44, pp. 7123–7126, 1991.
213. Bundy, F.P.: *J. Wash. Acad. Sci.*, Vol. 57, pp. 1–12, 1967.
214. Knight, D.S.; et al.: in *Diamond and Diamond-Like Materials Synthesis, MRS Extended Abstracts*, G.H. Johnson, A.R. Badzian, and M.W. Geis (eds.), Mat Res Soc, Pittsburgh, p. 73, 1988.
215. Knight, D.S.; and White, W.B.: *Journal of Materials Research*, Vol. 4, No. 2, pp. 385–393, 1989.
216. Nemanich, R.J.; and Solin, S.A.: *Physical Review B*, Vol. 20, No. 2, pp. 392–401, 1979.
217. Tuinstra, F.; and Koenig, J.L.: *Journal of Chemical Physics*, Vol. 53, pp. 1223–1229, 1970.
218. Tuinstra, F.; and Koenig, J.L.: *Journal of Chemical Physics*, Vol. 53, No. 3, pp. 1126–1130, 1970.
219. Meliunas, R.; et al.: *Journal of Applied Physics*, Vol. 70(9), pp. 5128–5130, 1991.
220. Vidano, R.P.; et al.: *Sol. State. Comm.*, Vol. 39, pp. 341–344, 1981.
221. Rouzaud, J.N.; Oberlin, A.; and Beny-Bassez, C.: *Raman Spectroscopy Linear and Nonlinear*, J. Lascombe, and P.V. Huong (eds.), Proceedings of the eighth international conference on Raman spectroscopy, 1982.
222. Lespade, P.; et al.: *Carbon*, Vol. 22, No. 4/5, pp. 375–385, 1984.
223. Nemanich, R.J.; et al.: *Journal of Vacuum Science and Technology A*, Vol. 6(3), pp. 1783–1787, 1988.
224. Shroder, R.E.; Nemanich, R.J.; and Glass, J.T.: *Physical Review B*, Vol. 41, No. 6, pp. 3738–3745, 1990.
225. Knight, D.S.; and White, W.B.: “Raman Scattering Luminescence and Spectroscopic Instrumentation in Technology,” *SPIE*, Vol. 1055, pp. 144–151, 1989.
226. Harshavardhan, K.S.; et al.: *Journal of Applied Physics*, Vol. 68(7), pp. 3303–3306, 1990.
227. Robins, L.H.; Farabaugh, E.N.; and Feldman, A.: *Journal of Materials Research*, Vol. 5, No. 11, pp. 2456–2468, 1990.
228. Etz, E.S.; et al.: *Proceedings of the SPIE Conference*, Vol. 969, 1988.



229. Buckley, R.G.; et al.: *Journal of Applied Physics*, Vol. 66(8), pp. 3595–3599, 1989.
230. Yanez-Limon, J.M.; et al.: *Journal of Applied Physics*, Vol. 76(6), pp. 3443–3447, 1994.
231. Bonnot, A.M.: *Physical Rev. B*, Vol. 41, No. 9, pp. 6040–6049, 1990.
232. Stuart, S.A.; Praver, S.; and Weiser, P.S.: *Diamond and Related Materials*, Vol. 2, pp. 753–757, 1990.
233. Fayette, L.; et al.: *Journal of Applied Physics*, Vol. 76(3), pp. 1604–1608, 1994.
234. Nemanich, R.J.: *Annual Review of Materials Science*, Vol. 21, pp. 535–558, 1991.
235. Etz, E.: *Published White Paper NIST*, 1991.
236. Fisher, A.: *Popular Science*, pp. 102–107, 1991.
237. Wickramasinghe, H.K.: *Scientific American*, pp. 98–105, 1989.
238. Pool, R.: *Science*, Vol. 247, pp. 634–636, 1990.
239. Van Enkevort, et al.: *Diamond and Related Materials*, Vol. 2, pp. 997–1003, 1993.
240. Bogli, U.; et al.: *Diamond and Related Materials*, Vol. 1, pp. 924–927, 1993.
241. Turner, K.F.; et al.: *Journal of Applied Physics*, Vol. 69(9), pp. 6400–6405, 1991.
242. Sutcu, L.F.; et al.: *Applied Physical Letter*, Vol. 60(14), pp. 3886–3891, 1992.
243. Sutcu, L.F.; et al.: *Journal of Applied Physics*, Vol. 71(12), pp. 5930–5940, 1992.
244. Everson, M.P.; et al.: *Journal of Applied Physics*, Vol. 75(1), pp. 169–172, 1994.
245. George, M.A.; et al.: *Journal of Applied Physics*, Vol. 76(7), pp. 4099–4106, 1994.
246. Gruen, D.M.; et al.: *Journal of the American Vacuum Society*, pp. 1491–1495, 1994.
247. Yanez-Limon,; et al.: *Journal of Applied Physics*, Vol. 76(6), pp. 3443–3447, 1994.
248. Thundat, T.; et al.: *Surface Science Letters*, Vol. 294, pp. 939–943, 1993.
249. Couto, M.S.; Van Enkevort, W.J.P.; and Seal, M.: *Philosophical Magazine B*, Vol. 69, No. 4, pp. 621–641, 1994.
250. Tsuno, R.; et al.: *Journal of Applied Physics*, Vol. 75(3), pp. 1526–1529, 1992.
251. Yarbrough, W.A.: *Journal of the American Ceramic Society*, Vol. 75(12), No. 3, pp. 179–200, 1992.
252. Ravi, K.V.: *Journal of Materials Research*, Vol. 7, No. 2, pp. 384–393, 1992.
253. Nakuamura, Y.; Watanabe, Y.; Suefuji, Y.; and Hirayama, S.: *Journal of the American Ceramic Society*, Vol. 77(5), pp. 1385–1387, 1994.

254. Languell, M.L.; et al.: *JOM*, pp. 66–70, 1994.
255. Burnham, N.A.; and Colton, R.J.: *Journal of Vacuum Science and Technology*, Vol. A7(4), pp. 2906–2913, 1989.
256. Burnham, N.A.; Colton, R.J.; and Pollock, H.M.: *Journal of Vacuum Science and Technology*, Vol. A9, pp. 2548–2556, 1991.
257. Field, J.E.: *The Properties of Diamond*, Academic Press, NY, 1979.
258. Doerner, M.F.; and Nix W.D.: *Journal of Materials Research*, Vol. 1(4), pp. 601–609, 1986.
259. Wickramasinghe, H.K.: *Scientific American*, pp. 98–105, 1989.
260. Rudd, G.I.; et al.: *Journal of the American Ceramic Society*, Vol. 76(10), pp. 2555–2560, 1993.
261. Hues, S.M.; et al.: *MRS Bulletin*, pp. 41–49, 1993.
262. Goodman, F.O.; and Garcia, N.: *Physical Review B*, Vol. 43, No. 6, pp. 4728–4731, 1991.
263. Girard, C.: *Physical Review B*, Vol. 43, No. 11, pp. 8822–8828, 1991.
264. Baselt, D.R.; and Baldeschwieler, J.D.: *Journal of Applied Physics*, Vol. 76(1), p. 6734, 1994.
265. Heinzelmann, H.; et al.: *Scanning Tunneling Microscopy and Related Methods*, R.J. Behm (ed.), Kluwer Acad Pub, Netherlands, pp. 443–467, 1990.
266. Meyer, E.; et al.: *Journal of Microscopy*, Vol. 152, Pt 1, pp. 269–280, 1988.
267. Sneddon, I.N.: *International Journal of Engineering Science*, Vol. 3, pp. 47–57, 1965.
268. Sneddon, I.N.: *Proc. Glasgow Math Assoc.*, Vol. 4, p. 108, 1960.
269. Sokolov, I.Y.: *Surface Science*, Vol. 311, pp. 287–294, 1994.
270. Loubet, J.L.; et al.: Transactions of the ASME, *Journal of Tribology*, Vol. 106, p. 4348, 1984.
271. Loubet, J.L.; Georges, J.M.; and Meille, G.: *Microindentation Techniques in Materials Science and Engineering*, P.J. Blau and B.R. Lawn (eds.), ASTM Special Publication 889, pp. 72–89, 1985.
272. Graham, G.A.C.: *International Journal of Engineering Science*, Vol. 3, pp. 27–48, 1965.
273. Graham, G.A.C.: *International Journal of Engineering Science*, Vol. 26, No. 2, pp. 167–184, 1966.
274. Ting, T.C.: Proceedings of the 11th Midwestern Mechanics Conference, *Developments in Mechanics*, Vol. 5, pp. 591–599.
275. Calvit, H.H.: *International Journal of Solids Structures*, Vol. 3, pp. 951–966, 1967.
276. Schmidt, S.R.; and Launsby, R.G.: *Understanding Industrial Designed Experiments*, Air Academy Press, 1989.
277. BBN/Catalyst Intuitive Software for Design of Experiments Handbook BBN Software Products, Cambridge, Mass, 1992.

278. Thomas, J.M.: *The Properties of Diamond*, J.E. Field (ed.), Cambridge Press, pp. 221–223, 1979.
279. Adams, D.M.: *Metal-Ligand and Related Vibrations—A Critical Survey of the Infrared and Raman Spectra of Metallic and Organometallic Compounds*, New York St Martin's Press, pp. 249–96–129, 1968.
280. Nakamoto, K.: “Infrared and Raman Spectra of Inorganic and Coordination Compounds,” Wiley & Sons Publishing Co., p. 477, 1986.
281. Hyer, R.C.; et al.: *Journal of Materials Science Letters*, Vol. 10, pp. 515–518, 1991.
282. Kim, D-G.; Lee, H-C.; and Lee, J-Y.: *Journal of Materials Science*, Vol. 28, pp. 6704–6708, 1993.
283. Tomellini, M.; Poliji, R.; and Sessa, V.: *Journal of Materials Science*, Vol. 22, pp. 504–508, 1992.
284. Polini, R.: *Journal of Applied Physics*, Vol. 72(6), pp. 2517–2519, 1992.
285. Molinari, E.; et al.: *Journal of Materials Research*, Vol. 8, No. 4, pp. 785–797, 1993.
286. Molinari, E.; Polini, R.; and Tomellini, M.: *Journal of Materials Research*, Vol. 8, No. 4, pp. 798–810, 1993.
287. Ascarelli, P.; and Fontana, S.: *Diamond and Related Materials*, Vol. 2, pp. 990–996, 1993.
288. Ohl, A.; Ropcke, J.; and Schleinitz, W.: *Diamond and Related Materials*, Vol. 2, pp. 298–303, 1993.
289. Rankin, J.; et al.: *Journal of Materials Research*, Vol. 9, No. 8, pp. 2164–2173, 1994.
290. Ma, J.S.; et al.: *Journal of Crystal Growth*, Vol. 99, pp. 1206–1210, 1990.
291. Jiang, N.; et al.: *Journal of Materials Research*, Vol. 9, No. 10, pp. 2695–2702, 1994.
292. Maeda, H.; et al.: *Journal of Crystal Growth*, Vol. 121, pp. 507–515, 1992.
293. Itoh, H.; et al.: *Journal of Materials Science*, Vol. 26, pp. 3763–3768, 1991.
294. Bauer, R.A.; Sbrokey, N.M.; and Brower, W.E.: *Journal of Materials Research*, Vol. 8, No. 11, pp. 2858–2869, 1993.
295. Stoner, B.R.; et al.: *Journal of Materials Research*, Vol. 7, No. 2, pp. 257–260, 1992.
296. Yugo, S.; Kimura, T.; and Kanai, T.: *Diamond and Related Materials*, Vol. 2, pp. 328–332, 1992.
297. Jiang, X.; Schiffmann, K.; and Klages, C.P.: *Physical Review B*, Vol. 50, No. 12, pp. 8402–8410, 1994.
298. Mitsuda, Y.; Moriyasu, T.; and Masuko, N.: *Diamond and Related Materials*, Vol. 2, pp. 333–336, 1993.
299. Menningen, K.L.; et al.: *Journal of Materials Research*, Vol. 9, No. 4, pp. 915–920, 1994.
300. Von Windheim, J.A.; et al.: *Diamond and Related Materials*, Vol. 2, pp. 438–442, 1993.
301. Matsui, Y.; et al.: *Diamond and Related Materials*, Vol. 1, pp. 19–24, 1992.

302. Miller, J.A.; Kee, R.J.; and Westbrook, C.K.: *Annual Review of Physical Chemistry*, Vol. 41, pp. 345–387, 1990.
303. Murthy, T.U.M.S.; et al.: *Journal of Crystal Growth*, Vol. 33, pp. 1–7, 1976.
304. Allamandola, L.J.; et al.: *Science*, Vol. 260, No. 2, pp. 64–65, 1993.
305. Mitura, S.: *Journal of Crystal Growth*, Vol. 80, pp. 417–424, 1987.
306. Angus, J.C.; and Hayman, C.C.: *Science*, Vol. 241, pp. 913–921, 1988.
307. Nuth, J.A., III: *Astrophysics Space Science*, Vol. 139, pp. 103–109, 1987.
308. Nuth, J.A., III: *Nature*, Vol. 329, p. 589, 1987.
309. Badziag, P.; et al.: *Nature*, Vol. 343, pp. 244–245, 1990.
310. Frenklach, M.; et al.: *Journal of Applied Physics*, Vol. 66(1), pp. 395–399, 1989.
311. Buerki, P.R.; and Leutwyler, S.: *Journal of Applied Physics*, Vol. 69(6), pp. 3739–3744, 1991.
312. Howard, W.; et al.: *Journal of Applied Physics*, Vol. 68(3), pp. 1247–1251, 1990.
313. Muranaka, Y.; et al.: *Journal of Applied Physics*, Vol. 67(10), pp. 6247–6254, 1990.
314. Muranaka, Y.; Yamashita, H.; and Miyadera, H.: *Journal of Applied Physics*, Vol. 69(12), pp. 8145–8153, 1991.
315. Cerio, F.M.; Weimer, W.A.; and Johnson, C.E.: *Journal of Materials Research*, Vol. 7, No. 5, pp. 1195–1203, 1992.
316. Johnson, C.E.; and Weimer, W.A.: *Journal of Materials Research*, Vol. 8, No. 9, p. 2245–2249, 1993.
317. Yarbrough, W.A.; Tankala,; and DebRoy, T.: *Journal of Materials Research*, Vol. 7, No. 2, pp. 379–383, 1992.
318. Johnson, C.E.; Weimer, W.A.; and Cerio, F.M.: *Journal of Materials Research*, Vol. 7, No. 6, pp. 1427–1431, 1992.
319. Chandra, L.; and Clyne, T.W.: *Journal of Materials Science Letters*, Vol. 12, pp. 191–195, 1993.
320. Phelps, A.W.: *Journal of Materials Science Letters*, Vol. 9, pp. 1096–1098, 1990.
321. Ong, T.P.; and Chang, R.P.H.: *Applied Physics Letters*, Vol. 55, p. 2063, 1989.
322. Wu, R.L.C.; et al.: *Journal of Applied Physics*, Vol. 72(1), pp. 110–116, 1992.
323. Frenklach, M.; and Wang, H.: *Physical Review B*, Vol. 43, No. 2, pp. 1520–1545, 1991.
324. Belton, N.; and Harris, S.J.: *Journal of Chemical Physics*, Vol. 96(3), pp. 2371–2377, 1992.
325. Rau, H.; and Picht, F.: *Journal of Materials Research*, Vol. 8, No. 9, pp. 2250–2264, 1993.

326. Hyman, E.; et al.: *Journal of Vacuum Science and Technology A*, Vol. 112(4), pp. 1474–1479, 1994.
327. Kim, J.S.; and Cappelli, M.A.: *Journal of Applied Physics*, Vol. 72(11), pp. 5461–5466, 1992.
328. Matsui, Y.; Yabe, H.; and Hirose, Y.: *Diamond and Related Materials*, Vol. 2, pp. 7–13, 1993.
329. Kweon, D.W.; Lee, J.Y.; and Kim, D.: *Journal of Applied Physics*, Vol. 69(12), pp. 8329–8335, 1991.
330. Celii, F.G.; White, D.; and Purdes, A.J.: *Journal of Applied Physics*, Vol. 70(10), pp. 5636–5646, 1991.
331. Derjaguijn, B.V.; et al.: *Journal of Crystal Growth*, Vol. 31, pp. 44–48, 1975.
332. Narayan, J.; et al.: *Applied Physics Letters*, Vol. 53(19), pp. 1823–1825, 1988.
333. Ikoma, K.; and Yamanaka, M.: *Journal of Applied Physics*, Vol. 74(5), pp. 3519–3522, 1993.
334. Harris, S.J.; et al.: *Journal of Applied Physics*, Vol. 66(11), pp. 5353–5359, 1989.
335. Belton, D.N.; and Schmieg, S.J.: *Journal of Applied Physics*, Vol. 69(5), pp. 3032–3036, 1991.
336. Weiser, P.S.; et al.: *Journal of Applied Physics*, Vol. 72(10), pp. 4643–4647, 1992.
337. Weiser, P.S.; et al.: *Journal of Applied Physics*, Vol. 76(4), pp. 2164–2168, 1994.
338. Heidarpour, E.; and Namba, Y.: *Journal of Materials Research*, Vol. 8, No. 11, pp. 2840–2844, 1993.
339. Prawer, S.; et al.: *Journal of Applied Physics*, Vol. 69(9), pp. 6625–6631, 1991.
340. Sun, Z.; et al.: *Journal of Applied Physics*, Vol. 76(7), pp. 4446–4447, 1994.
341. Mehlmann, A.K.; et al.: *Diamond and Related Materials*, Vol. 2, pp. 317–322, 1993.
342. Argoitia, A.; et al.: *Journal of Applied Physics*, Vol. 73(9), pp. 4305–4312, 1993.
343. Park, S-S.; and Lee, Y.: *Journal of Applied Physics*, Vol. 69(4), pp. 2618–2622, 1991.
344. Yang, P.C.; Zhu, W.; and Glass, J.T.: *Journal of Materials Research*, Vol. 8, No. 8, pp. 1773–1776, 1993.
345. Feng, Z.; et al.: *Journal of Applied Physics*, Vol. 74(4), pp. 2841–2849, 1993.
346. Meilunas, R.; et al.: *Applied Physics Letters*, Vol. 54(22), pp. 500–505, 1989.
347. Belton, D.N.; et al.: *Applied Physics Letters*, Vol. 54(5), pp. 416–417, 1989.
348. Stoner and Glass: *Applied Physics Letters*, Vol. 60(6), pp. 698–700, 1992.
349. Grannen, K.J.; and Chang, R.P.H.: *Journal of Materials Research*, Vol. 9, No. 8, pp. 2154–2163, 1994.
350. XiLing, P.: *Journal of Materials Research*, Vol. 9, No. 6, pp. 1573–1577, 1994.

351. Feng, Z.; et al.: *Journal of Materials Research*, Vol. 9, No. 8, pp. 2148–2153, 1994.
352. Oral, B.; et al.: *Diamond and Related Materials*, pp. 225–228, 1993.
353. Dubray, J.J., et al.: *Journal of Vacuum Science and Technology A*, Vol. 9(6), pp. 3012–3018, 1991.
354. Johansson, E.; Norekrans, A-S.; and Carlsson, J-O.: *Diamond and Related Materials*, pp. 383–388, 1993.
355. Kobayashi, K.; et al.: *Diamond and Related Materials*, pp. 278–284, 1993.
356. Saito, Y.; et al.: *Journal of Materials Science*, pp. 2441–2444, 1991.
357. Chen, X.; and Narayan, J.: *Journal of Applied Physics*, Vol. 74(6), pp. 4168–4173, 1993.
358. Silva, S.R.P.; et al.: *Journal of Materials Science Letters*, pp. 4962–4966, 1994.
359. Kappes, M.M.; et al.: *Chemical Physics Letters*, pp. 11–16, 1985.
360. Sivathanu, Y.R.; and Faeth, G.M.: *Combustion and Flame*, Vol. 81, pp. 150–165, 1990.
361. Tzeng, Y.; et al.: *Applied Physics Letters*, Vol. 58(23), pp. 2645–2647, 1991.
362. Lee, S.S.; et al.: *Chen Science*, Vol. 263, pp. 1596–1598, 1994.
363. Machlin, E.S.: *Journal of Materials Research*, Vol. 3(5), pp. 958–968, 1988.
364. Vitkavage, D.J.; et al.: *Journal of Vacuum Science and Technology A*, Vol. 6(3), pp. 1812–1815, 1988.
365. Spitsyn, B.V.; Bouilov, L.L.; and Derjaguin, B.V.: *Prog. Crystal Growth and Characterization*, pp. 79–170, 1988.
366. Muranaka, Y.; Yamashita, H.; and Miyadera, H.: *Journal of Vacuum Science and Technology A*, Vol. 9(1), pp. 76–84, 1991.
367. DeNatale, J.F.; Flintoff, J.F.; and Harker, A.B.: *Journal of Applied Physics*, Vol. 68(8), pp. 4014–4019, 1990.
368. DeNatale, J.F.; Flintoff, J.F.; and Harker, A.B.: *Journal of Materials Science*, pp. 553–556, 1992.
369. Narayan, J.; and Chen, X.: *Journal of Applied Physics*, Vol. 71(8), pp. 3795–3801, 1992.
370. Ramesham, R.; and Ellis, C.: *Journal of Materials Research*, Vol. 7, No. 5, pp. 1189–1194, 1992.
371. Von Windheim, J.; and Glass, J.T.: *Journal of Materials Science*, Vol. 7, No. 8, pp. 2144–2150, 1992.
372. Zhimeng, G.; Sheng, Y.; and Heyi, L.: *Journal of Material Science Letters*, pp. 244–246, 1995.
373. Galli, G.; et al.: *Science*, Vol. 250, pp. 1547–1549, 1990.
374. Curtiss, L.A.; and People, J.A.: *Journal of Chemical Physics*, Vol. 91(4), pp. 2420–2423, 1989.



REPORT DOCUMENTATION PAGE			Form Approved OMB No. 0704-0188	
Public reporting burden for this collection of information is estimated to average 1 hour per response, including the time for reviewing instructions, searching existing data sources, gathering and maintaining the data needed, and completing and reviewing the collection of information. Send comments regarding this burden estimate or any other aspect of this collection of information, including suggestions for reducing this burden, to Washington Headquarters Services, Directorate for Information Operation and Reports, 1215 Jefferson Davis Highway, Suite 1204, Arlington, VA 22202-4302, and to the Office of Management and Budget, Paperwork Reduction Project (0704-0188), Washington, DC 20503				
1. AGENCY USE ONLY (Leave Blank)		2. REPORT DATE November 2003		3. REPORT TYPE AND DATES COVERED Technical Publication
4. TITLE AND SUBTITLE Nucleation Behavior of Oxygen-Acetylene Torch-Produced Diamond Films			5. FUNDING NUMBERS	
6. AUTHORS F.E. Roberts				
7. PERFORMING ORGANIZATION NAMES(S) AND ADDRESS(ES) George C. Marshall Space Flight Center Marshall Space Flight Center, AL 35812			8. PERFORMING ORGANIZATION REPORT NUMBER  M-1094	
9. SPONSORING/MONITORING AGENCY NAME(S) AND ADDRESS(ES) National Aeronautics and Space Administration Washington, DC 20546-0001			10. SPONSORING/MONITORING AGENCY REPORT NUMBER  NASA/TP-2003-212929	
11. SUPPLEMENTARY NOTES Prepared for Materials, Processes, and Manufacturing Department, Engineering Directorate				
12a. DISTRIBUTION/AVAILABILITY STATEMENT Unclassified-Unlimited Subject Category 20 Availability: (301) 621-0390			12b. DISTRIBUTION CODE	
13. ABSTRACT (Maximum 200 words) <p>A mechanism is presented for the nucleation of diamond in the combustion flame environment. A series of six experiments and two associated simulations provide results from which the mechanism was derived. A substantial portion of the prior literature was reviewed and the data and conclusions from the previous experimenters were found to support the proposed mechanism. The nucleation mechanism builds on the work of previous researchers but presents an approach to nucleation in a detail and direction not fully presented heretofore. This work identifies the gas phase as the controlling environment for the initial formation steps leading to nucleation. The developed mechanism explains some of the difficulty which has been found in producing single crystal epitaxial films.</p> <p>An experiment which modified the initial gas phase precursor using methane and carbon monoxide is presented. Addition of methane into the precursor gases was found to be responsible for pillaring of the films. Atomic force microscopy surface roughness data provided a reasonable look at suppression of nucleation by carbon monoxide. Surface finish data was taken on crystals which were open to the nucleation environment and generally parallel to the substrate surface. These surfaces were measured as an independent measure of the instantaneous nucleation environment. A gas flow and substrate experiment changed the conditions on the surface of the sample by increasing the gas flow rate while remaining on a consistent point of the atomic constituent diagram, and by changing the carbide potential of the substrate. Two tip modification experiments looked at the behavior of gas phase nucleation by modifying the shape and behavior of the flame plasma in which the diamond nucleation is suspected to occur. Diamond nucleation and growth was additionally examined using a high-velocity oxygen fuel gun and C<sub>3</sub>H<sub>6</sub> as the fuel gas phase precursor with addition of carbon monoxide gas or addition of liquid toluene.</p>				
14. SUBJECT TERMS torch-produced diamond, diamond nucleation, diamond films			15. NUMBER OF PAGES 326	
			16. PRICE CODE	
17. SECURITY CLASSIFICATION OF REPORT Unclassified	18. SECURITY CLASSIFICATION OF THIS PAGE Unclassified	19. SECURITY CLASSIFICATION OF ABSTRACT Unclassified	20. LIMITATION OF ABSTRACT Unlimited	

National Aeronautics and  
Space Administration  
AD33

**George C. Marshall Space Flight Center**  
Marshall Space Flight Center, Alabama  
35812

---